

**Structural, Physical and Biological Studies of Gold(III)
Bis(Pyrrrolide-Imine) Schiff Base Macrocyclic and
Pseudomacrocyclic Complexes: Targeted Chemotherapeutic
Agents**

Submitted in the fulfilment of the requirements for the degree of

Doctor of Philosophy

By

Kate J. Akerman

BSc (Honours), MSc (University of KwaZulu-Natal)

November 2013



**UNIVERSITY OF
KWAZULU-NATAL**

School of Chemistry and Physics
University of KwaZulu-Natal
Pietermaritzburg

College of Agriculture, Engineering and Science

Declaration - Plagiarism

I, Kate Akerman, declare that

1. The research reported in this thesis, except where otherwise indicated, is my original research.
2. This thesis has not been submitted for any degree or examination at any other university.
3. This thesis does not contain other persons' data, pictures, graphs or other information, unless specifically acknowledged as being sourced from other persons.
4. This thesis does not contain other persons' writing, unless specifically acknowledged as being sourced from other researchers. Where other written sources have been quoted, then:
 - a. Their words have been re-written but the general information attributed to them has been referenced
 - b. Where their exact words have been used, then their writing has been placed in italics and inside quotation marks, and referenced.
5. This thesis does not contain text, graphics or tables copied and pasted from the Internet, unless specifically acknowledged, and the source being detailed in the thesis and in the References sections.

Signed.....

Kate J. Akerman

I hereby certify that this is correct.

Signed.....

Professor O. Q. Munro
(Supervisor)

School of Chemistry and Physics
University of KwaZulu-Natal
Pietermaritzburg

November 2013

Acknowledgements

I would like to acknowledge my supervisor, Prof. Orde Munro. I thank him for his advice and guidance but also for letting me follow my own ideas. I am very grateful to have had the opportunity to learn from someone who is as accomplished in his field as Prof. Munro. I appreciate the fact that he always pushed me to aim for ever higher standards.

I am very grateful to Craig Grimmer for his generosity in giving up his time and expertise. His assistance with NMR spectroscopy as well as his general support has been much appreciated.

I feel privileged to have been able to study at the Chemistry Department on the Pietermaritzburg campus of the University of KwaZulu-Natal. The environment and the people have made my time of study an enjoyable experience.

I would also like to thank the South African National Research Foundation for the funding that has allowed me to study this degree and for sponsoring me to go to the European Biological Inorganic Chemistry Conference in Spain in 2012, an experience I will not forget.

To Mintek, my grateful thanks for their sponsorship of materials and for the funding they have given me.

The collaboration with Prof. M. T. Muller's work group at the University of Central Florida has been invaluable. They have contributed many of the important results to this work. Thanks to Alex Fagenson and Vidusha Cyril for their contributions.

I appreciate all the support that my family has given me over the years. The stability, encouragement and support from my whole family has made me who I am today. I would like to thank my mother-in-law for her support and for proof-reading my thesis. I also appreciate Gran's continual interest in my work.

At certain stages during my doctorate studies I felt tired or disheartened, but my husband was constantly there to motivate and support me. I would like to thank him for all the chemistry dinner table talks, the long discussions and problem solving sessions. I appreciate his continual interest, advice and help. I cannot even begin to list everything that he has done for me but I appreciate everything and will always know how much he has done for me.

Publications

1. Kate J. Akerman and Orde Q. Munro, *Acta Cryst.* (2013). C69, m258-m262.
2. Kate J. Akerman, *Acta Cryst.* (2012). E68, o3354-o3355.
3. Desigan Reddy, Kate J. Akerman, Matthew P. Akerman and Deogratius Jaganyi, *Transition Met. Chem.*(2011), 36, 6, 593-602.
4. Matthew Akerman, Kate Akerman, Deogratius Jaganyi and Desigan Reddy, *Acta Cryst.* (2011). C67, m290-m292.
5. Matthew Akerman, Kate Akerman, Deogratius Jaganyi and Desigan Reddy, *Acta Cryst.* (2011). E67, m1075-m1076.
6. Orde Q. Munro, Matthew P. Akerman and Kate Gillham, *Acta Cryst.* (2009). C65, m343-m346.
7. Orde Q. Munro, Kate Gillham and Matthew P. Akerman, *Acta Cryst.* (2009). C65, m317-m320.

Patents

A patent was secured for the application of this class of gold(III) bis(pyrrolide-imine) Schiff base complexes as chemotherapeutic agents.

1. Orde. Q. Munro, Kate. J. Akerman and Matthew. P. Akerman, Gold Complexes, (2011), WO2011/158176 A2.

Awards

1. The initial work presented in this thesis was presented at the South African Chemical Institute Post Graduate Symposium (UKZN Westville, 2011). First place was awarded for the presentation in the oral category entitled: *Novel Macrocyclic Gold(III) Complexes: Targeted Chemotherapeutic Agents*.
2. The work presented in this thesis was presented at the COST D39 Conference (Dublin, Ireland, 2011). First place was awarded for the presentation in the poster category entitled: *Gold(III) Macrocyclic Chelates Inhibit Human Topoisomerase I and II α* .

List of Abbreviations

8-HQ	-	8-hydroxyquinoline
A	-	Absorbance/Adenine
AIDS	-	Acquired Immunodeficiency Syndrome
AIF	-	Apoptosis Inducing Factor
ATP	-	Adenosine Triphosphate
B3LYP	-	Becke three parameter Lee-Yang-Parr
Bipy	-	2,2'-bipyridine
BOC ₂ O	-	Di-tert-butylidicarbonate
bp	-	Base pair
C	-	Cytosine
c	-	Concentration
CCC	-	Closed-covalently circular
CDK	-	Cyclin-dependant kinase
CIC	-	Catalytic Inhibitor Compounds
Cisplatin	-	Diaminedichloroplatinum(II)
CNS	-	Central Nervous System
CPT	-	Camptothecin
CSD	-	Cambridge Structural Database
Ct	-	Calf thymus
Cyclam	-	1,4,8,11-tetraazacyclotetradecane
Cyclen	-	1,4,7,10-tetraazacyclotetradecane
damp	-	2-[(dimethylamino)methyl]phenyl
dbbpy	-	Dibutyl-2,2-bipyridyl
DCM	-	Dichloromethane
DFT	-	Density Functional Theory
dien	-	Diethylenetriamine
DMDT	-	Dimethyltetraathiafulvalenedithiolate
DMF	-	<i>N,N'</i> -dimethylformamide
DMSO	-	Dimethyl sulfoxide
DNA	-	Deoxyribonucleic acid
dppz	-	Dipyrido[3,2-a:2',3'-3]phenazine
dpq	-	Dipyrido[3,2-d:2'3'-f]quinoxaline
DTP	-	Developmental Therapeutic Programme
EB	-	Ethidium bromide
EDC	-	1-(3-(dimethylamino)propyl)-3-ethylcarbodiimide hydrochloride
EDTA	-	Ethylenediaminetetraacetic acid
EMSA	-	Electrophoretic Mobility Shift Assay
en	-	Ethylene diamine
EPR	-	Electron Paramagnetic Resonance
ESDT	-	Sarcosine ethyl ester dithiocarbamate
ϵ_0	-	Extinction coefficient
FID	-	Free induction decay

List of Abbreviations

FTIR	-	Fourier Transform Infrared
G	-	Guanine
G ₁	-	Gap1 phase of cell cycle
G ₂	-	Gap2 phase of cell cycle
GGA	-	gradient-corrected functional
GI ₅₀	-	Growth inhibition 50%
GSH	-	Reduced glutathione
GSSG	-	Oxidised glutathione
HCR	-	Hypoxic Cytotoxicity Ratio
HFA	-	Hollow Fibre Assay
HIV	-	Human Immunodeficiency Virus
Hpm	-	hydroxyl-methylpyridine
HOMO	-	Highest occupied molecular orbital
I	-	Intensity
IC ₅₀	-	Inoculation concentration 50%
IFP	-	interfacial poison
IR	-	Infrared
IUCR	-	International Union of Crystallographers
K _{app}	-	Apparent binding constant
K _b	-	equilibrium binding constant
KDNA	-	Kinetoplast deoxyribonucleic acid
K _{EB}	-	Ethidium bromide DNA binding constant
l	-	Path length (cm)
LANL2DZ	-	Los Alamos National Labs Double Zeta
LC ₅₀	-	Lethal concentration 50%
LMCT	-	Ligand to Metal Charge Transfer
Log P _{o/w}	-	Octanol/water partition coefficient
LUMO	-	Lowest unoccupied molecular orbital
M	-	Mitosis phase of the cell cycle
MLCT	-	Metal to Ligand Charge Transfer
MM	-	Molecular Mechanics
MS	-	Mass spectrometry
MTD	-	Maximum Tolerated Dose
n	-	non-bonding
NCI	-	National Cancer Institute
NCP	-	N-confused porphyrin
NCTPP	-	N-confused tetraryl porphyrin
NDC	-	No Drug Control
NHS	-	N-hydroxysuccinimide
NMR	-	Nuclear Magnetic Resonance
NOC	-	Nicked open-circular
NPC	-	Nasopharyngeal Carcinoma
NTC	-	No Template Control
OC	-	Open circular
PBE	-	Perdew, Burke and Ernzerhof

List of Abbreviations

PCR	-	Polymerase Chain Reaction
PDB	-	Protein Data Bank
PDT	-	Photodynamic Therapy
PES	-	Potential Energy Surface
phen	-	phenanthroline
pic	-	picolinate
pm	-	Methyl pyridine
RMS	-	Root mean square
RNA	-	Ribonucleic Acid
ROS	-	Reactive Oxygen Species
S	-	Synthesis phase of cell cycle
s	-	Binding site size
scDNA	-	Super-coiled DNA
SDS	-	Sodium dodecyl sulfate
SPR	-	Surface Plasmon Resonance
T	-	Transmittance / thymine
tacn	-	1,4,7-triazacyclononane
T _c	-	Coalescence temperature
TCA	-	Tricarboxylic acid
tdt	-	4-toluene-1,2-dithiolate
Terpy	-	2,6-bis(2-pyridyl)pyridine
THF	-	Tetrahydrofuran
T _m	-	Melting temperature
TMS	-	Tetramethylsilane
TOP1	-	Topoisomerase I
TOP2	-	Topoisomerase II
Tz	-	Time of cell inoculation with drug
UV	-	Ultra violet
VP-16	-	Etoposide

Abstract

Twelve (ten novel) bis(pyrrolide-imine) Schiff base ligands were synthesized and characterised by ^1H and ^{13}C NMR, FTIR and high resolution MS. The ligands are divided into three classes: macrocyclic, pseudomacrocyclic and open-chained. The macrocyclic ligands consist of a pair of pyrrole rings joined through a di(azomethine) linkage on one end and a quinoxaline or pyrazine tail on the other end, forming a macrocycle. The pseudomacrocyclic ligands have a pair of pyrrole rings joined at one end by a quinoxaline tail, but instead of a di(azomethine) linkage completing the macrocycle they are left open with methyl and ethyl groups joined to the imine moieties. The open-chain ligand is similar in structure to the macrocycles, but lacks the quinoxaline group. The structure of the ligands is varied through transformations of the di(azomethine) linkage as well as variations of the quinoxaline tail. Coordination of the ligands to gold(III) yielded twelve novel gold(III) Schiff base complexes. The majority of the complexes could be synthesized by direct metallation of the free ligands; however, macrocyclic ligands with substituted and extended bridging groups had to be synthesized by template reactions. Chelation of the metal ion required concomitant deprotonation of the NH groups, resulting in tetradentate, dianionic ligands. The ligands were sufficiently strong σ -donors to stabilize the gold(III) ion through chelation. The gold(III) macrocyclic complexes with a quinoxaline tail, have the following di(azomethine) linking groups: 1,3-propyl [Au(L1)](PF₆), 2,2-dimethyl-1,3-propyl [Au(L2)](PF₆), 1,4-butyl [Au(L3)](PF₆) and 2-chloro-1,3-propyl [Au(L4)](PF₆). The gold(III) macrocyclic complexes with a 1,3-propyl linkage have the following substituents on the quinoxaline tail: 6,7-dimethyl [Au(L5)](PF₆), 6-methyl [Au(L6)](PF₆) and 6-fluoro [Au(L7)](PF₆). A gold(III) macrocyclic complex with a pyrazine-3-methoxy-2-carbonitrile tail and 1,3-propyl di(azomethine) linkage, [Au(L8b)](PF₆), has been synthesized as well as two pseudomacrocyclic complexes with a quinoxaline tail. The pseudomacrocycles have methyl [Au(L9)](PF₆), ethyl [Au(L10)](PF₆) and ethanol [Au(L11)](PF₆), groups appended to the imine N atoms. The open-chain complex has no quinoxaline tail and is bridged by a 1,4-butyl di(azomethine) linkage [Au(L12)](PF₆).

The crystal structures of H₂L2, H₂L5, H₂L6, H₂L7, H₂L8a, H₂L8b, H₂L8c, H₂L9 and H₂L12 were elucidated using single crystal X-ray diffraction. The X-ray structures of the macrocyclic and pseudomacrocyclic compounds exhibit a slightly domed conformation with the pyrrole rings both canted relative to the quinoxaline or pyrazine tail. The X-ray data shows, in the form of a peak of electron density, that one pyrrole N atom and the diagonally opposite imine N atom are protonated. The configuration with the diagonally opposite N atoms protonated is favoured as the non-bonded repulsion is minimized. All the macrocyclic and pseudomacrocyclic compounds show two intramolecular hydrogen bonds. The first hydrogen bond has the pyrrole N–H acting as the hydrogen bond donor and the opposite pyrrole N atom acting as the hydrogen bond acceptor. The second hydrogen bond comprises the imine N–H acting as the hydrogen bond donor and the opposite imine N atom acting as the hydrogen bond acceptor. The gold(III) chelates: [Au(L1)](PF₆), [Au(L2)](CF₃SO₃), [Au(L3)](PF₆), [Au(L10)](AuCl₄) and [Au(L12)](PF₆) were also studied by single crystal X-ray diffraction. All showed a nominally square-planar coordination geometry at the gold(III) centre; the N–Au–N bond angles for the complexes are approaching 90° and the Au–N distances are all approximately equal, falling in the range of 1.98–2.06 Å. The average Au–N_{pyrrole} distance for the gold(III) complexes is 1.98(3) Å while the Au–N_{imine} bond distances average 2.03(6) Å. Both of the butyl-bridged complexes, [Au(L3)](PF₆) and [Au(L12)](PF₆), have larger N_{imine}–Au–N_{imine} bond angles than the propyl bridged complexes. This is expected as the longer bridge forces the imine N atoms further apart thus changing the bite angle of the ligand. The pseudomacrocyclic complex, [Au(L10)](AuCl₄), has no di(azomethine) bridging unit restricting the bite angle; it therefore exhibits the largest N_{imine}–Au–N_{imine} bond angle of all the complexes. The complexes exhibit several weak electrostatic interactions including $\pi\cdots\pi$ and Au $\cdots\pi$ interactions.

Density functional theory calculations were performed on both the metal chelates and free ligands. The level of theory used was PBE1PBE/LANL2DZ and B3LYP/6-311G(d,p), respectively. The calculations that were performed include: geometry optimizations, vibrational frequency calculations, and predictions of electronic and NMR spectral data. Geometry optimizations with several possible tautomers were calculated. The results of the calculations were particularly accurate for the ligand tautomer with the pyrrole N atom and the diagonally opposite imine N atom protonated. These calculations showed that the tautomeric form of the solid state structures was indeed the lowest energy conformation.

The gold(III) complexes were designed to act as anti-cancer agents, which exert their cytotoxicity through DNA intercalation and the inhibition of the topoisomerase enzymes. A range of experiments which show how the compounds are likely to behave under physiological conditions were performed. The DNA binding affinity of the complexes was determined by fluorescence competitive binding DNA titrations with ethidium bromide (EB). The K_{app} of the complexes range from $4.88 \times 10^5 \text{ M}^{-1}$ ($[\text{Au}(\text{L12})](\text{PF}_6)$) to $6.61 \times 10^6 \text{ M}^{-1}$ ($[\text{Au}(\text{L11})](\text{PF}_6)$). The gold(III) macrocyclic and pseudomacrocyclic complexes have a relatively high affinity for DNA. The lipophilicity of the compounds, as measured by $\log P_{o/w}$, range from -0.58(1) (for $[\text{Au}(\text{L10})](\text{PF}_6)$) to +1.468(3) (for $[\text{Au}(\text{L12})](\text{PF}_6)$). All the macrocyclic and pseudomacrocyclic chelates have a high affinity for octanol. This result is expected as the complexes consist of a large organic ligand as well as a bulky hexafluorophosphate(V) counterion which will lead to increased hydrophobicity. This large positive $\log P_{o/w}$ indicates that the complexes should move readily from the blood serum through the cell membrane. Using the binding constants, $\log P_{o/w}$ values and bridge volumes of $[\text{Au}(\text{L1})](\text{PF}_6)$, $[\text{Au}(\text{L2})](\text{PF}_6)$, $[\text{Au}(\text{L3})](\text{PF}_6)$, $[\text{Au}(\text{L4})](\text{PF}_6)$ and $[\text{Au}(\text{L5})](\text{PF}_6)$, it was determined that the binding constant increases with increasing drug hydrophobicity and decreasing bulk of the bridging unit.

Nine of the twelve gold(III) complexes synthesized were selected by the NCI for single-dose screening against their panel of sixty human cancer cell lines. These complexes are: $[\text{Au}(\text{L1})](\text{PF}_6)$, $[\text{Au}(\text{L2})](\text{PF}_6)$, $[\text{Au}(\text{L3})](\text{PF}_6)$, $[\text{Au}(\text{L4})](\text{PF}_6)$, $[\text{Au}(\text{L5})](\text{PF}_6)$, $[\text{Au}(\text{L6})](\text{PF}_6)$, $[\text{Au}(\text{L7})](\text{PF}_6)$, $[\text{Au}(\text{L10})](\text{PF}_6)$ and $[\text{Au}(\text{L11})](\text{PF}_6)$. The complex $[\text{Au}(\text{L3})](\text{PF}_6)$ is the most active macrocyclic complex. The mean GI_{50} , IC_{50} and LC_{50} values across the sixty cell line panel for this compound are: 6.4, 16.0 and $>100 \mu\text{M}$, respectively. The most active pseudomacrocyclic complex is $[\text{Au}(\text{L11})](\text{PF}_6)$ with mean GI_{50} , IC_{50} and LC_{50} values of 2.8, 5.60 and $>100 \mu\text{M}$, respectively. The complex $[\text{Au}(\text{L3})](\text{PF}_6)$ has been selected for a hollow fibre assay at the NCI. The hollow fibre assay showed that the cytotoxicity of the chelate was greatly reduced in a live animal environment.

Gel electrophoresis experiments and a novel microtiter assay proved that these gold(III) chelates have a highly specific mode of action, being catalytic inhibitors of topoisomerase I and II (TOP1 and 2). Additional gel electrophoresis experiments were used to unequivocally show that the gold(III) ion is critical to the cytotoxicity of the chelates.

New SP4 molecular mechanics (MM) force field parameters were used to determine the energetically preferred DNA binding site for $[\text{Au}(\text{L3})]^+$ using a 22-base pair duplex favoured by TOP1. It was determined that $[\text{Au}(\text{L3})]^+$ binds in the major groove at an adjacent T10-A11 base pair in dsDNA. This is also the cut-site of TOP1. When the complex is bound in this site, it prevents Arg364 of the TOP1 enzyme from recognizing the adenine base in the TA base pair by steric repulsion from the quinoxaline ring which projects into the minor groove. Binding of the complex also induces elongation at the intercalation site of the DNA. This displaces the scissile strand downstream so that Tyr723 is too far away to form a covalent P-O-C link to the enzyme. Surface plasmon resonance was used to verify these results.

List of Figures

Figure	Title	Page
1.1	General scheme of the proposed gold(III) macrocyclic and pseudomacrocyclic Schiff base complexes.	2
1.2	Diagram illustrating (a) a point mutation and (b) translocation of genetic material.	3
1.3	(a) The cell cycle where C refers to the various cellular checkpoints, G ₁ is the first gap phase, S is the synthesis phase, G ₂ is the second gap phase, M is the phase where mitosis occurs and G ₀ is the dormant phase. (b) The process of apoptosis.	5
1.4	(a) Key structural features of daunorubicin that allow for effective DNA intercalation. (b) X-ray crystal structure of daunorubicin (shown in yellow) intercalated between DNA base pairs. Water solvent molecules have been omitted for clarity.	9
1.5	X-ray structures of (a) Bleomycin A2 chelated to cobalt and intercalated between DNA base pairs. (b) Ruthenium (dppz).	10
1.6	(a) Mechanism of action of TOP1 inhibitors resulting in DNA strand breaks and cell death. (b) Structures of TOP1 inhibitors; Camptothecin and Topotecan.	12
1.7	(a) X-ray structure of DNA strand with and without TOP1 enzyme present. Note the nick that the TOP1 has created in the DNA. (b) X-ray structure of DNA strand and intercalated topotecan with and without TOP1 enzyme present. Note that the drug intercalates between bases at the nick site created by TOP1. The protein is shown as a green ribbon and the topotecan is shown with atoms at their van der Waals radii in yellow. Water solvent molecules have been omitted for clarity.	12
1.8	(a) Mechanism of action of TOP2. (b) The nicking of the DNA chain by TOP2.	13
1.9	Two-gate model for DNA transport in TOP2A.	14
1.10	(a) X-ray structure of cisplatin forming intrastrand adducts between DNA base pairs. (b) X-ray structure of cisplatin coordinated to two guanosine residues. (c) Structures of cisplatin and the second generation platinum(II) based anti-cancer drugs; carboplatin and oxaliplatin.	16
1.11	X-ray crystal structure of a dinuclear gold(II) complex; Dibromo-bis(μ ₂ -diphenyldimethylene phosphoranyl-C,C')-di-gold(II). The hydrogen atoms have been omitted for clarity.	18
1.12	(a) The hybrid orbitals ψ_1 and ψ_2 that are formed by the mixing of a dz^2 and s orbital as well as the hybrid orbitals formed from the mixing of pz and ψ_2 . ³³ (b) X-ray structure of a linear gold(I) complex; dicyano-gold(I).	19
1.13	(a) Energy level diagram for square-planar gold(III) complexes. (b) X-ray crystal structure of dicyano-(1,10-phenanthroline- <i>N,N'</i>)-gold(III), a square-planar gold(III) complex. The hydrogen atoms and counter ions were omitted for clarity.	20
1.14	X-ray structures of (a) Bromo-dicyano-(1,10-phenanthroline- <i>N,N'</i>)-gold(III) and (b) Di-iodo-bis(<i>o</i> -phenylene-bis(dimethylarsine)) gold(III). These are examples of five and six coordinate gold(III) complexes, respectively. The hydrogen atoms, counterions and solvent molecules have been omitted for clarity.	20
1.15	Oxidation of methane to methanol using a gold(I)-based catalyst.	21
1.16	(a) Mechanism of toluene oxidation-condensation to benzyl benzoate with Au-Pd catalyst (b) Absorption modes of O ₂ on gold.	22
1.17	(a) Gold(I)-catalyzed nucleophilic addition using a nitrogen nucleophile (b) Gold(I)-catalyzed nucleophilic addition using an oxygen nucleophile. (c) Gold(III)-catalyzed cyclization reaction.	22
1.18	Structure of the drugs (a) aurothiomalate and (b) urothioglucose. (c) X-ray structure of auranofin. Hydrogen atoms have been omitted for clarity.	23
1.19	(a) Gold(III) complexes with Au-N bonds tested for anti-cancer activity. (b) Gold(III) terpy derivatives.	26
1.20	Gold(III) chelates tested for anti-cancer activity in a study by Messori and co-workers.	26

List of Figures

Figure	Title	Page
1.21	(a) X-ray crystal structure of a gold(III) porphyrin, the counterion is omitted for clarity. (b) Schematic diagram of a gold(III) porphyrin with various substituents in the <i>para</i> position of the meso-phenyl rings. (c) Proposed model for the cellular mechanism of gold(III) porphyrin-induced apoptosis in NPC cells.	28
1.22	X-ray crystal structure of [Au(L1)]Cl and schematic of gold(III)bis(pyrrolide-imine) Schiff base complexes that went through 5-dose screening at the National Cancer Institute (NCI).	29
1.23	Gold(III) complexes with (a) Au-S bonds and (b) Au-C bonds that have been tested for anti-cancer activity.	29
1.24	Structures of a variety of tetrapyrrole ligands.	35
1.25	X-ray crystal structure of chlorophyll. The water solvent molecule is omitted for clarity.	35
1.26	(a) X-ray crystal structure of cyanocobalamin (vitamin B12). The hydrogen atoms and solvent molecules are omitted for clarity; (b) Diagram illustrating the saddle conformation of the corrin system and (c) stepwise reduction of the cobalt metal centre with a corresponding decrease in axial ligand coordination.	36
1.27	Various biological functions of the heme tetrapyrrole complex.	37
1.28	Protein structure of one of four subunits of hemoglobin. The water solvent molecules and protein atoms are omitted for clarity.	38
1.29	Complex structures of natural product macrocycles used in medicine; (a) Vancomycin, used as an anti-biotic (b) Epothilone B, an anti-cancer agent and (c) Amphotericin B, an anti-fungal agent. The hydrogen atoms and solvent molecules have been omitted for clarity.	39
1.30	(a) Structure of texaphyrin complexes. (b) General approach to conjugate design.	40
1.31	Proposed mechanism of action of chemotherapeutic Cu(II) macrocycles in hypoxic cells.	42
1.32	The stability constants for a variety of metal N-alkylated macrocyclic complexes.	43
1.33	Schematic of the gold(III) complexes synthesized in this study.	45
1.34	Key structural features allowing for potential DNA intercalation.	46
2.1	Structure of 1,2-bis(1 <i>H</i> -pyrrole-2-yl)ethane-1,2-dione showing the atom naming scheme.	55
2.2	Structure of 2,3-di-1 <i>H</i> -pyrrol-2-ylquinoxaline showing the atom naming scheme.	56
2.3	Structure of 6,7-dimethyl-2,3-di-1 <i>H</i> -pyrrol-2-ylquinoxaline showing the atom naming scheme.	57
2.4	Structure of 6-methyl-2,3-di-1 <i>H</i> -pyrrol-2-ylquinoxaline showing the atom naming scheme.	58
2.5	Structure of 6-fluoro-2,3-di-1 <i>H</i> -pyrrol-2-ylquinoxaline showing the atom naming scheme.	59
2.6	Structure of 5,6-di-1 <i>H</i> -pyrrol-2-ylpyrazine-2,3-dicarbonitrile showing the atom naming scheme.	60
2.7	Structure of 5,5'-quinoxaline-2,3-diylbis(1 <i>H</i> -pyrrole-2-carbaldehyde) showing the atom naming scheme.	61
2.8	Structure of 5,5'-(6,7-dimethylquinoxaline-2,3-diyl)bis(1 <i>H</i> -pyrrole-2-carbaldehyde) showing the atom naming scheme.	62
2.9	Structure of 5,5'-(6-methylquinoxaline-2,3-diyl)bis(1 <i>H</i> -pyrrole-2-carbaldehyde) showing the atom naming scheme.	63
2.10	Structure of 5,5'-(6-fluoroquinoxaline-2,3-diyl)bis(1 <i>H</i> -pyrrole-2-carbaldehyde) showing the atom naming scheme.	64
2.11	Structure of 5,6-bis(5-formyl-1 <i>H</i> -pyrrol-2-yl)pyrazine-2,3-dicarbonitrile showing the atom naming scheme.	65
2.12	Structure of 2,2,12,12- <i>t</i> -methyl-3,11-dioxo-4,10-dioxo-5,9-diazatridecan-7-ol(<i>N,N'</i> -di- <i>t</i> - <i>boc</i> -2-hydroxy-1,3-diaminopropane) showing the atom naming scheme.	66
2.13	Structure of 2-chloro-1,3-diaminopropane dihydrochloride showing the atom naming scheme.	67
2.14	Structure of 12,13-dihydro-14 <i>H</i> -6,9:17,20-diepimino[1,6]diazacyclo-heptadecino[12,13-β]quinoxalinato showing the atom numbering scheme.	68
2.15	Structure of 12,14-dihydro-13,13-dimethyl-6,9:17,20-diepimino[1,6]diazacyclo-heptadecino-[12,13-β]quinoxalinato showing the atom numbering scheme.	69

List of Figures

Figure	Title	Page
2.16	Structure of 12,13,14,15-tetrahydro-6,9:18,21-diepimino[1,6]diazacyclocta-decino[12,13-β] quinoxalinato showing the atom numbering scheme.	70
2.17	Structure of 12,13-dihydro-14 <i>H</i> -6,9:17,20-diepimino[1,6]diazacyclo-heptadecino[12,13-β]-6,7-dimethyl quinoxalinato showing the atom naming scheme.	71
2.18	Structure of 12,13-dihydro-14 <i>H</i> -6,9:17,20-diepimino[1,6]diazacyclo-heptadecino[12,13β]6-methyl quinoxalinato showing the atom naming scheme.	72
2.19	Structure of 12,13-dihydro-14 <i>H</i> -6,9:17,20-diepimino[1,6]diazacyclo-heptadecino[12,13β]6-fluoro quinoxalinato showing the atom naming scheme.	73
2.20	Structure of 12,13-dihydro-14 <i>H</i> -6,9:17,20-diepimino[1,6]diazacyclo-heptadecino-pyrazine-2,3-dicarbonitrile showing the atom naming scheme.	74
2.21	Structure of 12,13-dihydro-14 <i>H</i> -6,9:17,20-diepimino[1,6]diazacyclo-heptadecino-pyrazine-3-methoxy-2-carbonitrile showing the atom naming scheme.	75
2.22	Structure of 12,13-dihydro-14 <i>H</i> -6,9:17,20-diepimino[1,6]diazacyclo-heptadecino-methyl-3-cyanopyrazine-2-carboxidoate showing the atom naming scheme.	76
2.23	Structure of <i>N,N'</i> -{quinoxaline-2,3-diylbis[1 <i>H</i> -pyrrole-5,2-diyl(<i>E</i>)methylidene]}dimethanamine showing the atom naming scheme.	77
2.24	Structure of <i>N,N'</i> -{quinoxaline-2,3-diylbis[1 <i>H</i> -pyrrole-5,2-diyl(<i>E</i>)methylidene]}diethanamine showing the atom naming scheme.	78
2.25	Structure of {quinoxaline-2,3-diylbis[1 <i>H</i> -pyrrole-5,2-diyl(<i>E</i>)methylidenenitrilo]}diethanol showing the atom naming scheme.	79
2.26	Structure of <i>N,N'</i> -bis[(1 <i>E</i>)-1 <i>H</i> -pyrrol-2-ylmethylene]butane-1,4-diamine showing the atom naming scheme.	80
2.27	Structure of [12,13-dihydro-14 <i>H</i> -6,9:17,20-diepimino[1,6]diazacyclo-heptadecino[12,13-β] quinoxalinato] gold(III) hexafluorophosphate(V), showing the atom numbering scheme.	82
2.28	Structure of [12,14-dihydro-13,13-dimethyl-6,9:17,20-diepimino[1,6]diazacyclo-heptadecino-[12,13-β] quinoxalinato]-gold(III) hexafluorophosphate(V), showing the atom numbering scheme.	83
2.29	Structure of [12,14-dihydro-13,13-dimethyl-6,9:17,20-diepimino[1,6]diazacyclo-heptadecino-[12,13-β] quinoxalinato]gold(III) trifluoromethanesulfonate.	84
2.30	Structure of [12,13,14,15-tetrahydro-6,9:18,21-diepimino[1,6]diazacycloctadecino[12,13β] quinoxalinato] gold(III) hexafluorophosphate(V), showing the atom naming scheme.	85
2.31	Structure of [13-chloro-12,14-dihydro-6,9:17,20-diepimino-[1,6]-diazacycloheptadecino-[12,13-β]-quinoxalinato]gold(III) hexafluorophosphate(V).	86
2.32	Structure of [12,13-dihydro-14 <i>H</i> -6,9:17,20-diepimino[1,6]diazacyclo-heptadecino[12,13-β]-6,7-dimethyl quinoxalinato]-gold(III) hexafluorophosphate(V), showing the atom naming scheme.	87
2.33	Structure of [12,13-dihydro-14 <i>H</i> -6,9:17,20-diepimino[1,6]diazacyclo-heptadecino[12,13β]6-methyl quinoxalinato]gold(III) hexafluorophosphate(V), showing the atom naming scheme.	88
2.34	Structure of [12,13-dihydro-14 <i>H</i> -6,9:17,20-diepimino[1,6]diazacyclo-heptadecino[12,13β]6-fluoro quinoxalinato] gold(III) hexafluorophosphate(V), showing the atom naming scheme.	89
2.35	Structure of [12,13-dihydro-14 <i>H</i> -6,9:17,20-diepimino[1,6]diazacyclo-heptadecino-pyrazine-2,3-dicarbonitrile] gold(III)hexafluorophosphate(V).	90
2.36	Structure of [12,13-dihydro-14 <i>H</i> -6,9:17,20-diepimino[1,6]diazacyclo-heptadecino-pyrazine-3-methoxy-2-carbonitrile]gold(III) hexafluorophosphate(V), showing the atom naming scheme.	91
2.37	Structure of [<i>N,N'</i> -{quinoxaline-2,3-diylbis[pyrrole-5,2-diyl(<i>E</i>)methylidene]}dimethan-amine gold(III) hexafluorophosphate(V), showing the atom naming scheme.	92
2.38	Structure of [<i>N,N'</i> -{quinoxaline-2,3-diylbis[1 <i>H</i> -pyrrole-5,2-diyl(<i>E</i>)methylidene]}diethanamine] gold(III) hexafluorophosphate(V), showing the atom naming scheme.	93
2.39	Structure of [<i>N,N'</i> -{quinoxaline-2,3-diylbis[1 <i>H</i> -pyrrole-5,2-diyl(<i>E</i>)methylidene]}diethan-amine] gold(III) tetracholoaurate.	94

List of Figures

Figure	Title	Page
2.40	Structure of [{quinoxaline-2,3-diylbis(pyrrole-5,2-diyl(<i>E</i>)-methylylidene-nitrilo)}diethanol]gold(III) hexafluorophosphate(V), showing the atom numbering scheme.	95
2.41	Structure of <i>N,N'</i> -bis[(1 <i>E</i>)-1 <i>H</i> -pyrrol-2-ylmethylene]butane-1,4-diamine gold(III) hexafluorophosphate(V), showing the atom numbering scheme.	96
2.42	Structure of [12,13-dihydro-14 <i>H</i> -6,9:17,20-diepipimino[1,6]diazacyclo-heptadecino[12,13- β]quinoxalinato] nickel(II), showing the atom numbering scheme.	97
3.1	Solid-state reaction for the synthesis of H ₂ L11.	106
3.2	High resolution mass spectrum of [Au(L4)](PF ₆).	109
3.3	Structure of monoimidate, H ₂ L8c, formed during the reaction involving triethylamine.	111
4.1	(a) Hydrogen bonding motif consisting of a pyrrole NH and imine N. (b) Schematic diagram showing complementary hydrogen bonding in a mono(pyrrolide-imine) derivative. (c) Complementary hydrogen bonding in a bis(pyrrolide-imine) system with a flexible linker.	120
4.2	(a) X-ray structure of <i>N,N'</i> -bis[(1 <i>E</i>)-1 <i>H</i> -pyrrol-2-ylmethylene]propane-1,3-diamine. (b) Side view illustrating W-shaped conformation of the molecule. (c) Repeating unit of an infinite one-dimensional hydrogen-bonded chain.	121
4.3	(a) X-ray crystal structure of <i>N,N'</i> -bis[(1 <i>E</i>)-1 <i>H</i> -pyrrol-2-ylmethylene]benzene-1,2-diamine. (b) Hydrogen-bonded dimer structure supported by complementary hydrogen bonding between the pyrrole NH and imine N atom.	122
4.4	(a) X-ray crystal structure of (1 <i>S</i> ,2 <i>S</i>)- <i>N,N'</i> -bis[(1 <i>E</i>)-1 <i>H</i> -pyrrol-2-ylmethylene]cyclohexane-1,2-diamine monohydrate showing the water solvent molecule. (b) One dimensional polymer formed by water molecules bridging Schiff base ligands.	122
4.5	X-ray crystal structures of (a) H ₂ L1 and (b) H ₂ L3 showing intra-molecular hydrogen bonds. (b) Side view of H ₂ L1 showing the out-of-plane twisting of the pyrrole rings. (d) π - π stacking of H ₂ L3 molecules.	124
4.6	X-ray crystal structure of <i>N,N'</i> -((5,5'-(quinoxaline-2,3-diyl)bis(1 <i>H</i> -pyrrole-5,2-diyl))bis(methanylylidene))bis(4-methoxyaniline) showing hydrogen bonding to the methanol solvent molecule.	125
4.7	X-ray crystal structures of (a) (1,2-bis(pyrrol-2-ylmethyleneamino) ethane- <i>N,N',N'',N'''</i>)-iron(II) and (b) (<i>N,N'</i> -(1,2-cyclohexylene)-bis(pyrrol-2-ylmethyleneamine))-palladium(II). (c) Front view of the iron(II) and palladium(II) complexes showing the twisting of the bridge.	127
4.8	(a) X-ray structure of (<i>N,N'</i> -1,3-propylene-bis(pyrrole-2-ylmethyleneamine))-palladium(II). (b) Front view of the palladium(II) complex showing the out-of-plane nature of the central methylene carbon atom of the propyl bridge. (c) π - π stacking of the palladium(II) complex.	127
4.9	X-ray crystal structures of (a) (12,13-dihydro-6,9:17,20-diepipimino[1,6]diazacyclo-heptadecino[12,13-b]quinoxalinato)-nickel(II) and (b) (12,13,14,15-tetrahydro-6,9:18,21-diepipimino[1,6]diazacyclo octadecin [12,13-b]quinoxalinato)-nickel(II) (c) "Front view" of molecule A of the propyl-bridged macrocyclic Ni(II) chelate showing the canted quinoxaline tail and puckered propyl bridge. Molecule B shows a similar deviation from planarity. (d) "Front view" of the different molecules in the asymmetric unit of the butyl-bridged macrocyclic Ni(II) chelate. (e) M- π stacking between molecules A and B of the butyl-bridged chelate.	129
4.10	(a) X-ray crystal structure of <i>N,N'</i> -((5,5'-(quinoxaline-2,3-diyl)bis(1 <i>H</i> -pyrrole-5,2-diyl))bis(methanylylidene))bis(4-methoxyaniline)-copper(II). (b) Back view of the copper(II) complex(II) showing the domed nature of the pyrrole moieties. (c) Space-fill diagram of the copper(II) complex, illustrating why it is referred to as a pseudomacrocyclic.	130
4.11	X-ray crystal structures of (a) (5,7,12,14-tetramethyl-1,4,8,11-tetraaza-4,6,11,13-tetraene)-gold(III) bromide and (b) dichloro-(1,8-bis(hydroxyethyl)-1,3,6,8,10,13-hexa-azacyclo-tetradecane- <i>N,N',N'',N'''</i>)-gold(III) tetrachloro-gold(III). (c) "Side view" of (5,7,12,14-tetramethyl-1,4,8,11-tetraaza-4,6,11,13-tetraene)-gold(III) bromide showing the slight twist in the ethylene bridging group and overall planar nature of the ligand.	131

List of Figures

Figure	Title	Page
4.12	Thermal ellipsoid plots of (a) H ₂ L2, (b) H ₂ L5, (c) H ₂ L6 (with 50:50 site occupancy of the methyl substituent), (d) H ₂ L7 (with 80:20 site occupancy of the fluorine substituent) and H ₂ L9 showing 50% probability surfaces. Hydrogen atoms have been rendered as spheres of arbitrary radius. Hydrogen-bonding has been indicated by broken purple tubes.	134
4.13	Diagrams showing the four atom mean plane defined by the four coordinating N atoms for (a) H ₂ L2, (b) H ₂ L5 and (c) H ₂ L9 to illustrate the varying extent of doming of the molecule.	135
4.14	Tautomeric forms of (a) symmetric and (b) asymmetric macrocyclic ligands.	137
4.15	Spacefilling diagram, with atoms rendered at their van der Waals radii, of (a) a genuine macrocycle, H ₂ L2, and (b) the pseudomacrocyle H ₂ L9 showing how the coordination sphere is effectively closed by electron density from the methyl groups.	138
4.16	(a) Side view of H ₂ L2 showing the interplanar spacing between the 26-atom mean planes of two adjacent π -stacked molecules. (b) Top view of the π -stacked dimer of H ₂ L2 showing the π interactions of the quinoxaline and pyrrole rings. (c) Side view of H ₂ L5 showing the interplanar spacing between the 10-atom mean plane defined by the quinoxaline group of one molecule and the quinoxaline group of an adjacent, π -stacked molecule. (d) Top view of the π -stacked dimer of H ₂ L5 showing the π interactions between the quinoxaline rings of adjacent molecules.	140
4.17	(a) Side view of H ₂ L7 showing the interplanar spacing between the 28-atom mean plane of one molecule and the mean plane of an adjacent π -stacked molecule. (b) Top view of the π -stacked dimer of H ₂ L7 showing the π interactions of the quinoxaline and pyrrole rings. (c) Side view of H ₂ L9 showing the interplanar spacing between the 26-atom mean plane of one molecule and the mean plane of an adjacent π -stacked molecule. (d) Top view of the π -stacked dimer of H ₂ L9 showing the nature of the slipped configuration and the resulting π interactions between the pyrrole rings of adjacent molecules.	140
4.18	Thermal ellipsoid plots of (a) H ₂ L8a (b) H ₂ L8b (c) H ₂ L8c showing 50% probability surfaces, hydrogen atoms have been rendered as spheres of arbitrary radius. Intramolecular hydrogen bonding has been indicated by purple tubes.	141
4.19	Diagrams showing the four-atom mean plane defined by the four coordinating N atoms for (a) H ₂ L8a, (b) H ₂ L8b and (c) H ₂ L8c to illustrates the varying extent of doming of the molecule. (d) Least squares fit of molecules A and B of H ₂ L8a. Molecule A is shown in yellow and molecule B is shown in blue.	142
4.20	One-dimensional hydrogen-bonded chain adopted by (a) H ₂ L8a and (b) H ₂ L8b running co-linear to the a -axis. (c) Side view of H ₂ L8c showing the interplanar spacing between the 22-atom mean plane of one molecule and the mean plane of an adjacent π -stacked molecule. (b) Top view of the π -stacked dimer of H ₂ L8c showing the π interactions of the pyrazine and pyrrole rings.	144
4.21	(a) Thermal ellipsoid plot of H ₂ L12 showing 50% probability surfaces, hydrogen atoms have been rendered as spheres of arbitrary radius. (b) Infinite, one-dimensional hydrogen-bonded chain adopted by H ₂ L12. (c) Side view of two hydrogen-bonded molecules showing the relative planarity of the ten-membered hydrogen bonding ring.	145
4.22	Thermal ellipsoid plots showing a single molecule of the asymmetric unit of (a) [Au(L1)](PF ₆), (b) [Au(L2)](CF ₃ SO ₃) (c) [Au(L3)](PF ₆) (d) [Au(L10)](AuCl ₄) and (e) [Au(L12)](PF ₆) showing 50% probability surfaces; hydrogen atoms have been rendered as spheres of arbitrary radius.	147
4.23	(a) Mean plane diagram for [Au(L1)](PF ₆) showing the perpendicular displacement of each non-H atom (in units of pm) from the five-atom mean plane defined by the four coordinating nitrogen atoms and the gold(III) atom. (b) "Back view" of [Au(L1)](PF ₆) showing the deviation from the five atom mean plane. (c) Mean plane diagram for both molecules in the asymmetric unit of [Au(L2)](CF ₃ SO ₃) showing the perpendicular displacement of each non-H atom (in units of pm) from the five-atom mean plane defined by the four coordinating nitrogen atoms and the gold(III) atom. (d) "Back view" of both molecules of [Au(L2)](CF ₃ SO ₃) showing the deviations from the five atom mean plane. (e) Least squares fit of molecules A and B of [Au(L2)](CF ₃ SO ₃).	149

List of Figures

Figure	Title	Page
4.24	(a) Mean plane diagrams of all the molecules in the asymmetric unit of $[\text{Au}(\text{L3})](\text{PF}_6)$ showing the perpendicular displacement of each non-H atom (in units of pm) from the five-atom mean plane defined by the four coordinating nitrogen atoms and the gold(III) atom. (b) "Back view" of all the molecules in the asymmetric unit of $[\text{Au}(\text{L3})](\text{PF}_6)$ showing the deviations from the five-atom mean plane.	150
4.25	(a) Mean plane diagram of (a) $[\text{Au}(\text{L10})](\text{AuCl}_4)$ and (b) $[\text{Au}(\text{L12})](\text{PF}_6)$ showing the perpendicular displacement of each non-H atom (in units of pm) from the five-atom mean plane defined by the four coordinating nitrogen atoms and the gold(III) ion. (c) "Back view" of $[\text{Au}(\text{L10})](\text{AuCl}_4)$ and (d) "back view" of $[\text{Au}(\text{L12})](\text{PF}_6)$ illustrating the deviations from the five-atom mean planes.	151
4.26	(a) View of the π - π dimers formed by the cations of compound $[\text{Au}(\text{L1})](\text{PF}_6)$ in the crystalline solid state. (b) Space-filling structure diagrams (van der Waals radii) of $[\text{Au}(\text{L1})](\text{PF}_6)$ viewed perpendicular and down the axis normal to the cation's 5-atom mean plane. (b) π - π dimers formed by the cation of compound $[\text{Au}(\text{L2})](\text{CF}_3\text{SO}_3)$ in the crystalline solid state. (c) Space-filling structure diagram (van der Waals radii) of $[\text{Au}(\text{L2})](\text{CF}_3\text{SO}_3)$.	153
4.27	(a) View of the different π -stacking orientations formed by molecules A and B and molecules E and F of $[\text{Au}(\text{L3})](\text{PF}_6)$ in the crystalline solid state. Molecules C and D exhibit similar stacking to molecules E and F. (b) Space-filling structure diagrams (van der Waals radii) of molecules A and B and molecule E and F of $[\text{Au}(\text{L3})](\text{PF}_6)$ viewed perpendicular and down the axis normal to the cation's 5-atom mean plane.	154
4.28	(a) View of the different π -stacking and orientations formed by $[\text{Au}(\text{L10})](\text{AuCl}_4)$ in the crystalline solid state. (b) Space-filling structure diagrams (van der Waals radii) of $[\text{Au}(\text{L10})](\text{AuCl}_4)$ viewed perpendicular and down the axis normal to the cation's 5-atom mean plane. (c) View of the π - π dimers formed by the cation of compound $[\text{Au}(\text{L12})](\text{PF}_6)$ in the crystalline solid state. (d) Space-filling structure diagrams (van der Waals radii) of $[\text{Au}(\text{L12})](\text{PF}_6)$.	155
5.1	(a) Different modes of stretching and bending vibrational motion. (b) The approximate regions of the electromagnetic spectrum at which various bonds resonate (stretching vibrations only).	160
5.2	IR spectrum of (a) $\text{H}_2\text{L1}$ and (b) $[\text{Au}(\text{L1})](\text{PF}_6)$.	163
5.3	IR spectrum of (a) $\text{H}_2\text{L8b}$ and (b) $\text{H}_2\text{L11}$ highlighting selected resonance frequencies.	164
5.4	(a) Electronic energy levels and transitions. (b) Electronic and vibrational transitions superimposed (rotational levels have been omitted for clarity).	166
5.5	Schematic diagram of a double-beam UV/Vis spectrophotometer.	167
5.6	Electronic spectra of (a) $\text{H}_2\text{L1}$ in chloroform, (b) $[\text{Au}(\text{L1})](\text{PF}_6)$ in acetonitrile, (c) $\text{H}_2\text{L10}$ in chloroform and (d) $[\text{Au}(\text{L10})](\text{PF}_6)$ in acetonitrile.	168
5.7	^1H spectrum of (a) $\text{H}_2\text{L3}$ and (b) $[\text{Au}(\text{L3})](\text{PF}_6)$ in $\text{DMSO-}d_6$ at 303 K showing the spectral assignments.	174
5.8	Stacked ^1H NMR spectra of the imine CH for (a) $\text{H}_2\text{L3}$ in chloroform and (b) $\text{H}_2\text{L8a}$ in DMF.	176
5.9	Section of the ^1H NMR spectra of $\text{H}_2\text{L8a}$ (grey) and $\text{H}_2\text{L8b}$ (black) in $\text{DMSO-}d_6$ at 303 K.	178
5.10	Overlay of the ^1H NMR spectra of 2-chloro- and 2-hydroxy-1,3-diaminopropane dihydrochloride, shown in black and grey respectively, in D_2O at 303 K.	178
5.11	DFT optimised structures of $[\text{Au}(\text{L4})](\text{PF}_6)$ with the chlorine substituent in the (a) axial and (b) equatorial positions. The protons closest to the chlorine substituent are shown in pink and are more deshielded than the protons shown in purple. (c) ^1H NMR spectrum of $[\text{Au}(\text{L4})](\text{PF}_6)$ in $\text{DMSO-}d_6$ at 303 K showing the chemical shifts of the methylene protons on the di(azomthine) linkage adjacent to the chlorine substituent.	179
5.12	(a) UV/visible spectra of the octanol and water layers containing $[\text{Au}(\text{L1})](\text{PF}_6)$ at 298 K. Inset is the Beer-Lambert plot for $[\text{Au}(\text{L1})](\text{PF}_6)$ in acetonitrile at 300 nm. (b) Photographs of the octanol and water layers of $[\text{Au}(\text{L1})](\text{PF}_6)$ and $[\text{Au}(\text{L11})](\text{PF}_6)$.	182
5.13	X-ray Crystal structures of the (a) reduced (GSH) form and the (b) oxidized (GSSG) form of glutathione. The solvent molecules in (b) have been omitted for clarity.	186

List of Figures

Figure	Title	Page
5.14	Spectral changes in the UV/visible spectrum of 39 μM $[\text{Au}(\text{L1})](\text{PF}_6)$ in the presence of 50 μM GSH at 37 $^\circ\text{C}$ in 15% DMSO 85% 25 mM TRIS-HCl buffer (pH = 7.00). The spectrum was recorded over 24 hours at one hour intervals. The arrows indicate the spectral changes.	187
5.15	Melting point curves of DNA in the absence and presence of increasing concentrations of (a) $\text{H}_2\text{L1}$ and (b) $[\text{Au}(\text{L1})](\text{PF}_6)$.	192
5.16	(a) Displacement of ctDNA-intercalated EB by $[\text{Au}(\text{L1})](\text{PF}_6)$ ($T = 25^\circ\text{C}$, 15% DMSO-TRIS buffer, pH 7.0). Inset is a least-squares fit of the change in EB emission at 614 nm with increasing concentration of the metal chelate to determine concentration of the complex at 50% reduction in emission. (b) Stern-Volmer plot for $[\text{Au}(\text{L1})](\text{PF}_6)$.	194
5.17	(a) Absorbance plot of EB with increasing concentrations of ctDNA. The arrows indicate spectral changes. (b) Non-linear fit for the titration of EB with ctDNA at 492 nm in pH 7.0, 15% DMSO TRIS-HCl buffer at 25 $^\circ\text{C}$.	195
5.18	Graph of the ctDNA affinity constant (K_{app} , 298 K) of $[\text{Au}(\text{L1})](\text{PF}_6)$, $[\text{Au}(\text{L2})](\text{PF}_6)$, $[\text{Au}(\text{L3})](\text{PF}_6)$, $[\text{Au}(\text{L4})](\text{PF}_6)$ and $[\text{Au}(\text{L5})](\text{PF}_6)$ as a function of the steric bulk of the macrocycle's hydrocarbon bridge and the hydrophobicity of the complete Au^{3+} cation, $\log(P_{\text{o/w}})$. The 3D surface is the best-fit bivariate linear regression function to the data.	197
6.1	NH-tautomerism in porphyrins and N-confused porphyrins.	206
6.2	Least-squares fit of the non-H atoms of the DFT calculated (yellow) and the X-ray crystal structures (blue) of all the tautomers of (a) $\text{H}_2\text{L2}$, (b) $\text{H}_2\text{L7}$ and (c) $\text{H}_2\text{L9}$. The RMSD values and the relative energies of each tautomer are indicated on the diagram. The pyrrole and imine NH atoms have been included only to show the tautomeric form.	210
6.3	Change in selected N–H bond lengths with increasing optimization steps of tautomer C of $\text{H}_2\text{L2}$ with no restrictions on the bond lengths.	212
6.4	DFT-calculated structures of the tautomers of (a) $\text{H}_2\text{L1}$ and (b) $\text{H}_2\text{L11}$ at the B3LYP/6-311G(d,p) level of theory.	214
6.5	Overlay of experimental and calculated Infrared data for all tautomeric forms of $\text{H}_2\text{L1}$.	216
6.6	Overlays of the calculated electronic spectra (width at half height = 2400 cm^{-1}) of the tautomeric forms of $\text{H}_2\text{L1}$ and the experimental data. Calculated states are depicted as vertical lines with intensities given by their oscillator strengths.	220
6.7	The molecular orbitals for the tautomeric forms of $\text{H}_2\text{L1}$: (a) tautomer A (b) tautomer B (c) tautomer C and (d) tautomer D, that are responsible for the major electronic transitions.	223
6.8	Naming scheme used for the ^1H and ^{13}C NMR assignments of $\text{H}_2\text{L1}$.	227
6.9	Plot of experimental versus calculated ^1H NMR shifts for tautomer B of the imine NH protons of the macrocyclic ligands. The correlation coefficient of the linear fit as well as the equation of the line is shown in the plot.	229
6.10	Least-squares fits of the non-H atoms of the DFT-calculated structures (yellow) and the molecules in the asymmetric unit of the X-ray crystal structures (blue) for (a) $[\text{Au}(\text{L1})]^+$, (b) $[\text{Au}(\text{L10})]^+$, (c) $[\text{Au}(\text{L12})]^+$, (d) $[\text{Au}(\text{L3})]^+$, and (e) $[\text{Au}(\text{L2})]^+$. The RMSDs are indicated on the diagram.	231
6.11	Geometry optimized structures of (a) $[\text{Au}(\text{L4})]^+$, (b) $[\text{Au}(\text{L5})]^+$, (c) $[\text{Au}(\text{L6})]^+$, (d) $[\text{Au}(\text{L7})]^+$, (e) $[\text{Au}(\text{L9})]^+$, and (f) $[\text{Au}(\text{L11})]^+$ calculated at the PBEPBE/LANL2DZ level of theory.	233
6.12	Overlay of calculated and experimental frequency data for (a) $[\text{Au}(\text{L1})]^+$ and (b) $[\text{Au}(\text{L11})]^+$.	234
6.13	Plot of experimental versus calculated imine C=N stretching vibrations of the bis(pyrrolide-imine) gold(III) chelates. The correlation coefficient and the linear regression are shown on the plot.	235
6.14	Overlay of experimental and calculated UV/visible spectra (width at half height = 1000 cm^{-1}) of (a) $[\text{Au}(\text{L1})]^+$ and (b) $[\text{Au}(\text{L10})]^+$ in acetonitrile. Calculated states are depicted as vertical lines with intensities given by their oscillator strengths.	236
6.15	Selected electronic orbitals of (a) $[\text{Au}(\text{L1})]^+$ and (b) $[\text{Au}(\text{L10})]^+$.	237
6.16	Labeling scheme for $[\text{Au}(\text{L1})]^+$.	241

List of Figures

Figure	Title	Page
6.17	Plot of experimental versus calculated (a) ^1H NMR shifts and (b) ^{13}C NMR shifts of the imine protons and carbon atoms of the gold(III) chelates. The correlation coefficients are shown on the plots.	244
6.18	Non-linear least squares fits of the AMMP calculated (blue) and X-ray (orange) structures of the compounds (a) $[\text{Au}(\text{L}1)]^+$, (b) $[\text{Au}(\text{L}2)]^+$ and (c) $[\text{Au}(\text{L}3)]^+$. The RMSD errors are shown and were determined from the fit of all atoms in each structure.	247
6.19	Overlay of MM calculated (green) structure and X-ray (orange) structure of a 22 base pair DNA duplex. The H atoms and water molecules have been omitted for clarity but were included in the simulation.	247
6.20	DNA base pair specificity for $[\text{Au}(\text{L}3)]^+$.	248
6.21	(a) Plot of E_{rel} vs ΔG_{helix} for the major and minor groove intercalation adducts. (b) Stabilities of the various base pairs along the DNA helix.	249
6.22	(a) Ion-dipole and π - π stacking interactions at the T10-A11 binding site. (b) Major and minor groove-bound conformations of $[\text{Au}(\text{L}3)]^+$.	250
6.23	Model of the $[\text{Au}(\text{L}3)]^+$ DNA intercalation complex in the presence of TOP1.	250
6.24	Overlay of the pdp1a36 X-ray structure without the complex bound (pink) and the drug-bound MM structure (blue).	251
7.1	Dose-response curve of a central nervous system cancer cell line with the chemotherapeutic agent, daunorubicin.	255
7.2	Screening processes at the NCI.	255
7.3	Single-dose screening results for $[\text{Au}(\text{L}3)](\text{PF}_6)$ over the NCI's panel of sixty human cancer cell lines. The bars are coloured according to the cell line panel, from left to right: leukemia, lung, colon, central nervous system, melanoma, ovarian, renal, prostate and breast cancers.	263
7.4	Mean growth rate of the NCI's panel of sixty human cancer lines against which the gold(III) complexes were tested in the single-dose screen.	264
7.5	Dose-response curves for $[\text{Au}(\text{L}3)](\text{PF}_6)$, cisplatin and daunorubicin. The curves measure the response of the breast cancer cell line MDA-MB-468. Data were obtained from the DTP drug repository.	266
7.6	Plot of $-\log \text{GI}_{50}$ of $[\text{Au}(\text{L}3)](\text{PF}_6)$ versus the equivalent data for cisplatin.	267
7.7	Comparison of $-\log \text{GI}_{50}$ values of $[\text{Au}(\text{L}3)](\text{PF}_6)$ with commercially available chemotherapeutic agents for specific cancer cell lines. The dashed horizontal line gives the mean GI_{50} value.	268
7.8	Plot of $-\log \text{GI}_{50}$ versus single-dose growth percentage.	268
7.9	(a) Cytotoxicity Assay in HeLa cells for $[\text{Au}(\text{L}1)](\text{PF}_6)$, $[\text{Au}(\text{L}2)](\text{PF}_6)$ and $[\text{Au}(\text{L}3)](\text{PF}_6)$ tested against VP-16. (b) Dose-response function fit for the MTS assay in HeLa cells for $[\text{Au}(\text{L}1)](\text{PF}_6)$, $[\text{Au}(\text{L}2)](\text{PF}_6)$ and $[\text{Au}(\text{L}3)](\text{PF}_6)$.	270
7.10	Plot of the $-\log \text{IC}_{50}$ values for selected gold(III) complexes for four human cancer cell lines.	271
7.11	Comparison of the activity profile of commercial drugs with a known mode of action and $[\text{Au}(\text{L}3)](\text{PF}_6)$.	273
7.12	Key events in the catalytic cycle of human TOP1.	274
7.13	Electrophoretic mobility shift assay of selected compounds with supercoiled pHOT1 DNA and Nicked-open circular DNA(NOC).	275
7.14	Microtiter well-based assay for distinguishing between TOP1 IFPs and CICs.	276
7.15	TOP1 DNA relaxation assays for (a) $[\text{Au}(\text{L}1)](\text{PF}_6)$, $[\text{Ni}(\text{L}1)]$ and $\text{H}_2\text{L}1$ and (b) $[\text{Au}(\text{L}3)](\text{PF}_6)$. (c) Dose-response function fit for the TOP1 DNA relaxation assay of $[\text{Au}(\text{L}3)](\text{PF}_6)$. (d) Overlapped dose-response function fit for the TOP1 DNA relaxation assay of $[\text{Au}(\text{L}1)](\text{PF}_6)$, $[\text{Au}(\text{L}2)](\text{PF}_6)$, $[\text{Au}(\text{L}3)](\text{PF}_6)$, $[\text{Au}(\text{L}4)](\text{PF}_6)$ and $[\text{Au}(\text{L}5)](\text{PF}_6)$.	277
7.16	(a) TOP2 decatenation assays for $[\text{Au}(\text{L}1)](\text{PF}_6)$, $[\text{Au}(\text{L}2)](\text{PF}_6)$ and $[\text{Au}(\text{L}3)](\text{PF}_6)$. (b) Dose-response curves for the TOP2 decatenation of $[\text{Au}(\text{L}1)](\text{PF}_6)$, $[\text{Au}(\text{L}2)](\text{PF}_6)$ and $[\text{Au}(\text{L}3)](\text{PF}_6)$.	279

List of Figures

Figure	Title	Page
7.17	(a) Illustration of the key concepts of surface plasmon resonance. (b) On the left, graph showing DNA binding by [Au(L3)](PF ₆) and on the right DNA binding by mTOP1 in the presence (blue) and absence (red) of [Au(L3)](PF ₆) as determined by SPR. The on-chip duplex DNA sequence is illustrated above the graphs with the enzyme's TA target highlighted.	281
8.1	Schematic diagram of the gold(III) complexes synthesized in this work.	287
8.2	(a) Macrocyclic complexes with a region for hydrogen-bonding. (b) Pseudomacrocyclic complexes with increased aromaticity.	293
8.3	X-ray crystal structure of (a) α -cyclodextrin ¹³ and (b) α -cyclodextrin (<i>N,N'</i> -bis(2,6-dimethylphenyl)-4,4'-stilbenedicarboxamide)-rotaxane. ¹⁴ The hydrogen atoms and solvent molecules have been omitted for clarity.	294
8.4	An example of targeted drug delivery; (a) normal receptor function and (b) drug bound substrate. The receptor that will be targeted is biotin. (c) [Au(L11)] ⁺ tagged with biotin.	295

List of Schemes

Scheme	Title	Page
3.1	Mechanism of condensation of carbonyl compounds with primary amines.	99
3.2	Synthetic methods for the synthesis of (a) non-aqueous soluble and (b) aqueous-soluble gold(III) porphyrin complexes.	100
3.3	Template synthesis of Schiff base macrocycles in the presence of main group metal ions.	101
3.4	Template synthesis for the formation of a macrocyclic tetraaza gold(III) complex.	102
3.5	General structure of (a) macrocyclic ligands with quinoxaline subunits, (b) macrocyclic ligands with pyrazine subunits, (c) pseudo-macrocyclic ligands with quinoxaline subunits and (d) an open-chain ligand.	103
3.6	The synthetic route used in the synthesis of quinoxaline-based macrocyclic and pseudo-macrocyclic ligands.	104
3.7	Electrophilic substitution reaction, used to form compound 2 . The inset shows the crude and purified compound 2 .	104
3.8	Acid-catalysed condensation reaction resulting in the formation of an imine bond.	105
3.9	Vilsmeier formylation reaction mechanism.	106
3.10	Protection of primary amines using di-tert-butyl dicarbonate.	107
3.11	Resonance forms of the <i>n</i> -Boc protected amine.	107
3.12	Appel reaction mechanism for the chlorination of an alcohol.	108
3.13	Deprotection reaction to form the hydrochloride salt and solid state reaction to form the corresponding amine.	108
3.14	The synthetic route used in the synthesis of pyrazine-based macrocyclic ligands.	110
3.15	Direct replacement of a nitrile group with a methoxy group.	111
3.16	Condensation reaction to form non-macrocyclic Schiff base ligands.	112
3.17	Synthetic routes for the synthesis of gold(III) Schiff base quinoxaline complexes.	114
3.18	Proposed template pathway for the synthesis of gold(III) complexes.	115

List of Tables

Table	Title	Page
1.1	Summary of some the different classes of chemotherapeutic agents.	7
1.2	Coordination geometries of gold.	18
1.3	IC ₅₀ values of various gold(III) complexes against the human ovarian carcinoma A2780 cell line, both cisplatin sensitive and cisplatin resistant variants.	27
1.4	Stability of complexes of Cu ²⁺ with tetramine ligands in water.	31
1.5	Kinetic data for Cu(II) complexes at 25 °C	32
1.6	Thermodynamic parameters for the formation of 18-crown-6 complexes with metal ions in H ₂ O at 25 °C.	33
1.7	Formation constants of substituted benzo-Crowns with Na(I).	34
1.8	Biological Activity of Cu(II) macrocycles.	41
3.1	Comparison of the ¹ H NMR shifts of 2-hydroxy- and 2-chloro-1,3-diaminopropane dihydro-chloride in D ₂ O.	109
3.2	Ionic radii of selected metal ions.	114
4.1	Reported X-ray crystal structures of bis(pyrrolide-imine) Schiff base ligands.	120
4.2	Average bond lengths and bond angles for previously reported acyclic bis(pyrrolide-imine) Schiff base compounds.	120
4.3	Reported X-ray crystal structure of quinoxaline-based bis(pyrrolide-imine) Schiff base macrocyclic and pseudomacrocyclic ligands.	123
4.4	Average bond lengths and angles for previously reported bis(pyrrolide-imine) Schiff base macrocyclic compounds.	123
4.5	Reported X-ray crystal structure of bis(pyrrolide-imine) Schiff base chelates.	126
4.6	Average bond lengths and bond angles of the coordination sphere of previously reported bis(pyrrolide-imine) Schiff base chelates.	126
4.7	Reported X-ray crystal structures of bis(pyrrolide-imine) Schiff base macrocyclic chelates.	128
4.8	Average bond lengths and angles for previously reported bis(pyrrolide-imine) Schiff base chelates.	128
4.9	Reported X-ray crystal structures of gold(III) macrocyclic complexes.	130
4.10	Average bond lengths and angles of previously reported gold(III) macrocyclic complexes.	131
4.11	Crystallization data for the bis(pyrrolide-imine) Schiff base ligands	133
4.12	Torsion angles (°) of pyrrole rings relative to the quinoxaline moieties.	135
4.13	Maximum deviations (Å) from the 4-atom mean plane defined by the four coordinating N atoms	135
4.14	Average bond lengths and angles for quinoxaline-based bis(pyrrolide-imine) Schiff base ligands.	136
4.15	Hydrogen bond geometry (Å, °) for the quinoxaline-based bis(pyrrolide-imine) Schiff base ligands.	139
4.16	Torsion angles (°) of pyrrole rings relative to the pyrazine moieties.	142
4.17	Maximum deviations (Å) from the four-atom mean plane defined by the four coordinating N atoms of the pyrazine-based macrocycles.	142
4.18	Average bond lengths and angles for pyrazine-based bis(pyrrolide-imine) Schiff base ligands.	143
4.19	Hydrogen bond geometry (Å,°) for the pyrazine bis(pyrrolide-imine) Schiff base macrocycles.	144
4.20	Average bond lengths and angles for the acyclic Schiff base ligand, H ₂ L12.	146
4.21	Hydrogen bond geometry (Å, °) for the acyclic ligand H ₂ L12.	146
4.22	Crystallization data for the bis(pyrrolide-imine) gold (III) Schiff base complexes.	147
4.23	Average bond lengths and bond angles for the gold(III) complexes.	152
4.24	Crystal data and structure refinement details for the Schiff base ligands: H ₂ L2, H ₂ L5, H ₂ L6 and H ₂ L7.	156
4.25	Crystal data and structure refinement details for the Schiff base ligands: H ₂ L8a, H ₂ L8b, H ₂ L8c, H ₂ L9 and H ₂ L12.	157

List of Tables

Table	Title	Page
4.26	Crystal data and structure refinement details for the gold(III) Schiff base complexes: [Au(L1)](PF ₆), [Au(L2)](CF ₃ SO ₃), [Au(L3)](PF ₆), [Au(L10)](AuCl ₄) and [Au(L12)](PF ₆)	158
5.1	Imine stretching vibrations of both the free ligands and gold(III) chelates.	162
5.2	Pyrrole NH stretching bands for the Schiff base ligands.	163
5.3	Summary of the λ _{max} and extinction coefficient values for the absorption bands of the free ligands.	169
5.4	Summary of the λ _{max} and extinction coefficients for the absorption bands of the gold(III) complexes.	171
5.5	¹ H NMR chemical shifts (DMSO- <i>d</i> ₆ , 303 K) for H ₂ L3 and [Au(L3)](PF ₆).	173
5.6	¹³ C NMR chemical shifts (DMSO- <i>d</i> ₆ , 303 K) for H ₂ L3 and [Au(L3)](PF ₆).	173
5.7	¹ H NMR chemical shifts for selected protons of the macrocyclic and pseudomacrocyclic ligands at 303 K in DMSO- <i>d</i> ₆ .	175
5.8	Values of π for various substituents	181
5.9	Summary of the mean log <i>P</i> _{o/w} values for the gold(III) chelates.	183
5.10	Values of π for various substituents of [Au(L1)](PF ₆).	183
5.11	Thermal denaturation data for H ₂ L1, [Au(L1)](PF ₆), [Au(L2)](PF ₆) and [Au(L3)](PF ₆) with human DNA (saliva isolate).	193
5.12	Apparent binding constants of the gold(III) complexes to ctDNA.	196
6.1	Summary of experimental and calculated bond lengths and angles of the bis(pyrrolide-imine) Schiff base ligands.	209
6.2	RMSD values for the least-squares fit of the calculated and X-ray structure of all the tautomers and their relative energies.	211
6.3	Summary of partial Mulliken charges of key atoms for the tautomer B of selected ligands	215
6.4	Comparison of selected experimental and calculated vibrational frequencies for all the tautomers of H ₂ L1.	217
6.5	Comparison of selected experimental and calculated vibrational frequencies for tautomer B of the Schiff base ligands.	218
6.6	Summary of the calculated electronic transitions for the tautomeric forms of H ₂ L1 and the corresponding molecular orbitals	221
6.7	Summary of the calculated electronic transitions for tautomer B of the ligands and the corresponding molecular transitions.	224
6.8	Comparison of experimental and calculated ¹ H NMR data for the tautomeric forms of H ₂ L1.	226
6.9	Comparison of experimental and calculated ¹³ C NMR data of the tautomeric forms of H ₂ L1.	227
6.10	Comparison of experimental and calculated ¹ H and ¹³ C NMR shifts for tautomer B of the Schiff base ligands.	229
6.11	Comparison of the mean bond lengths (Å) and angles (°) of the calculated and experimental structures of the gold(III) chelates: [Au(L1)] ⁺ , [Au(L2)] ⁺ , [Au(L3)] ⁺ , [Au(L10)] ⁺ and [Au(L12)] ⁺ .	232
6.12	Comparison of selected experimental and calculated vibrational frequencies for the bis(pyrrolide-imine) gold(III) chelates presented in this work.	235
6.13	Summary of calculated and experimental electronic transitions for the gold(III) complexes.	238
6.14	Experimental and calculated ¹ H and ¹³ C NMR data for [Au(L1)] ⁺ .	242
6.15	Comparison of experimental and calculated ¹ H NMR data for the gold(III) complexes.	243
6.16	Comparison of experimental and calculated ¹³ C NMR data for the gold(III) complexes.	243
6.17	Intercalation energies of [Au(L3)] ⁺ in the major and minor grooves of a 22 base pair DNA duplex.	248
7.1	Summary of the average cytotoxicity data over sixty human cancer cell lines for [Au(L2)](PF ₆), [Au(L3)](PF ₆), [Au(L6)](PF ₆), [Au(L7)](PF ₆), [Au(L10)](PF ₆) and [Au(L11)](PF ₆) as well as selected commercial cytotoxic agents.	265
7.2	Estimation of the GI ₅₀ values of the compounds selected for a single-dose screen only.	269
7.3	IC ₅₀ values for the cytotoxicity assay in HeLa cells for [Au(L1)](PF ₆), [Au(L2)](PF ₆) and [Au(L3)](PF ₆).	270
7.4	IC ₅₀ values for [Au(L9)](PF ₆) and [Au(L12)](PF ₆) against four human cancer cell lines.	270

List of Tables

Table	Title	Page
7.5	IC ₅₀ values and Hill coefficients determined from dose response curves for TOP1 relaxation assays for [Au(L1)](PF ₆), [Au(L2)](PF ₆), [Au(L3)](PF ₆), [Au(L4)](PF ₆) and [Au(L5)](PF ₆).	278
7.6	IC ₅₀ values and Hill coefficients determined from dose response curves of TOP2 decatanation assays for [Au(L1)](PF ₆), [Au(L2)](PF ₆) and [Au(L3)](PF ₆).	280

Contents

Declaration	II
Acknowledgements	III
Publications	IV
List of Abbreviations	V
Abstract	VIII
List of Figures	X
List of Schemes	XVIII
List of Tables	XIX
CHAPTER ONE: INTRODUCTION	1
1.1 Preface	1
1.2 Introduction to Cancer	2
1.3 Gold: The Noble Metal	17
1.4 Macrocyclic Chemistry	30
1.5 Aims and Objectives	44
1.6 References	48
CHAPTER TWO: EXPERIMENTAL	53
2.1 General Methods	53
2.2 Instrumentation	53
2.3 Synthesis of Ligand Precursors	55
2.4 Synthesis of Ligands	68
2.5 Synthesis of Metal Salt Precursors	81
2.6 Synthesis of Metal Chelates	82
2.7 References	98
CHAPTER THREE: SYNTHESIS	99
3.1 Introduction	99
3.2 Ligand Synthesis	103
3.3 Metallation of Ligands	113
3.4 Summary and Conclusions	116
3.5 References	117
CHAPTER FOUR: X-RAY CRYSTALLOGRAPHY	119
4.1 Introduction	119
4.2 Experimental	132
4.3 X-ray Crystallography of Schiff Base Ligands	133
4.4 X-ray Crystallography of Gold(III) Schiff Base Complexes	147
4.5 Summary of X-ray Data	156
4.6 References	159

CHAPTER FIVE: SPECTROSCOPY	160
5.1 Infrared Spectroscopy	160
5.2 UV/visible Spectroscopy	164
5.3 NMR Spectroscopy	171
5.4 Octanol/Water Partition Coefficients	180
5.5 Glutathione Reduction Stability	185
5.6 DNA Binding Studies	188
5.7 References	199
CHAPTER SIX: COMPUTATIONAL CHEMISTRY	201
6.1 Introduction	201
6.2 Computational Method	207
6.3 Computational Chemistry of Schiff Base Ligands	208
6.4 Computational Chemistry of Bis(Pyrrrolide-Imine) Gold(III) Chelates	230
6.5 Summary and Conclusions of DFT Data	244
6.6 Molecular Mechanics Calculations	245
6.7 References	252
CHAPTER SEVEN: BIOCHEMICAL STUDIES	254
7.1 Introduction	254
7.2 Experimental	257
7.3 Results and Discussion	262
7.4 Conclusions	282
7.5 References	284
CHAPTER EIGHT: CONCLUSIONS AND FUTURE WORK	286
8.1 Conclusions	286
8.2 Future Work	292
8.3 References	297
PATENT	DVD
APPENDIX A: CRYSTALLOGRAPHIC DATA TABLES OF LIGANDS	DVD
APPENDIX B: CRYSTALLOGRAPHIC DATA TABLES OF GOLD(III) COMPLEXES	DVD
APPENDIX C: CRYSTALLOGRAPHIC INFORMATION FILES OF SCHIFF BASE LIGANDS	DVD
APPENDIX D: CRYSTALLOGRAPHIC INFORMATION FILES OF GOLD(III) COMPLEXES	DVD
APPENDIX E: GAUSSIAN JOB FILES AND OUTPUTS	DVD
APPENDIX F: MOLECULAR ORBITAL DIAGRAMS	DVD
APPENDIX G: SP⁴ MOLECULAR MECHANICS FORCE FIELD PARAMETERS	DVD
APPENDIX H: NCI-60 SCREENING DATA	DVD

CHAPTER ONE:

INTRODUCTION

1.1 Preface

Cancer is the second leading cause of death in developing countries and the number one cause of death in developed countries.¹ In 2008, there were an estimated 12.7 million cancer cases reported and 7.6 million cancer related deaths globally with the developing world accounting for 56% of these cases and 64% of all deaths.¹ Breast cancer is the leading cause of cancer death among females, accounting for 14% of all cancer deaths while for males, lung cancer is the leading cause of cancer related death.¹ Economically developing countries are taking increasing strain from cancer deaths due to aging and growing populations.¹

Alarming, these are the cancer statistics nearly four decades after the discovery of one of the leading anti-cancer drugs cis-diamminedichloroplatinum(II), more commonly known as cisplatin.² As most of the currently available chemotherapeutic agents lack the ability to specifically and selectively target cancer cells they induce toxic side effects as well as resistance. The search for new and improved drugs is therefore of the utmost importance. As gold(III) complexes are isoelectronic (d^8) with platinum(II) and form similar tetradentate complexes with the same square-planar geometry as cisplatin,³ they are a logical choice for the next generation of anti-cancer agents.

Gold has been used in medicine since 2500 BC, but its first appearance in modern medicine was in the early 1890's when it was discovered that the gold(I) dicyanide ion had anti-tubercular activity, although it was of little use as it was later found to be very toxic.⁴ Gold(I) thiolate complexes were used as a non-toxic alternative for the treatment of tuberculosis and later arthritis.⁵ Despite the medical history of gold complexes there are problems associated with gold(III) complexes, resulting in a lack of literature when compared to platinum-based compounds. Gold(III) complexes are often difficult to synthesize because gold(III) is readily reduced to gold(I) and gold(0). Gold(III) complexes often precipitate as insoluble $[\text{AuCl}_4]^-$ or $[\text{AuCl}_2]^-$ salts with limited solubility.⁶ Once the complexes are synthesized they are often not stable under physiological conditions and are easily reduced from gold(III) to gold(I) by cellular concentrations of glutathione.⁵ These potential problems can be overcome by choosing strong σ -donor ligands, particularly tetradentate N-donor ligands, which are able to stabilize the gold(III) ion.

The aim of this study is to synthesize bis(pyrrolide-imine) gold(III) Schiff base macrocyclic and pseudo-macrocyclic complexes for use as anti-cancer agents, Figure 1.1. As macrocyclic ligands are more stable than their open-chain analogues, due to the macrocyclic effect,⁷ they should stabilize gold(III) under physiological conditions, a potential pitfall for many anti-cancer agents. This stabilizing effect has been demonstrated with gold(III) tetraaryl porphyrins, which have been shown to be cytotoxic towards a range of human cancer cell lines.⁵ The proposed gold(III) macrocyclic complexes are rigidly planar with an overall positive charge potentially allowing for effective intercalation between DNA base pairs. Intercalation between DNA base pairs can disrupt the enzymes responsible for coiling and uncoiling the DNA, the topoisomerases (TOP). The uncoiling of DNA is required for its replication and transcription, a critical process during cell division.⁸

Disruption of the TOP enzymes and hence the process of DNA replication causes the cell to “commit suicide” via the process of apoptosis. These TOP enzymes are more active in cancer cells as they are rapidly dividing, thus disrupting the TOP enzymes and can lead to selective destruction of cancerous cells over healthy cells. The proposed gold(III) complexes have been designed to act as potential anti-cancer agents by intercalating DNA and disrupting the TOP enzymes.

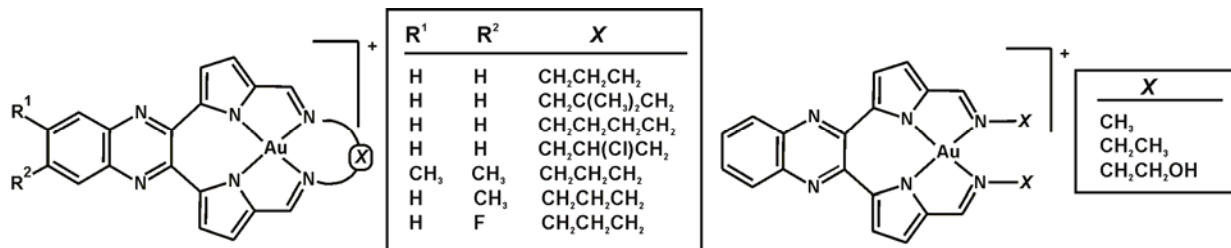


Figure 1.1: General scheme of the proposed gold(III) macrocyclic and pseudo-macrocyclic Schiff base complexes.

This chapter is divided into four main sections. The first section gives an overview of cancer as a disease and the types of drugs that are currently on the market and the mechanism of action of these drugs. The second section gives a description of gold chemistry along with the applications of gold, including the medical applications. The third section gives an overview of macrocycles as ligands and their characteristics as well as applications. The last section consists of the aims and the objectives of this work.

1.2 Introduction to Cancer

1.2.1 Description and Causes of Cancer

Cancer is a disease in which normal cells lose the mechanisms that control growth rate leading to cell proliferation and the formation of a solid mass of cells known as a tumour.⁸⁻¹⁰ When cancerous cells do not invade neighbouring tissues they form benign tumours. The initial tumour that develops, the primary tumour, can become life-threatening if it obstructs vessels or organs. However, the spread of the primary tumour to one or more regions in the body and establishing secondary tumours, a process known as metastasis, is the most common cause of death.⁸⁻¹⁰ Metastasis can occur when tumour cells directly invade blood vessels through thin-walled capillaries or penetrate walls of lymphatic vessels and move to draining lymph nodes. A tumour can also spread across body cavities via organs. It is this ability of cancer to spread to a number of far-reaching sites in the body that makes it such a dangerous disease as it is beyond the reach of local surgery. This, coupled with the fact that there are more than 200 different types of cancer, means it is very difficult to treat as it is not a single disease.⁸⁻¹⁰

Cancer is referred to as a genetic disease that results from changes to a DNA sequence in genes or a structural change due to internal, external or hereditary factors.^{8,10} Internal factors that can result in tumour formation include mutations. The original genes that normally code for proteins involved in control of cell division are called proto-oncogenes. Once they are mutated and no longer fulfill their normal function and the cells become cancerous, these genes are referred to as oncogenes.^{8,10} There are two types of mutations: namely, point mutation and translocation mutation.¹¹ These mutations are illustrated in

Figure 1.2. A point mutation involves the alteration of a single base in a sequence resulting in a new codon and the insertion of the incorrect amino acid into the protein.^{10,11} If the protein is used in cell growth then this could lead to the formation of cancerous cells. A translocation mutation involves an entire segment of DNA being moved from one chromosome to another. Again, if proteins corresponding to these DNA sequences are important for growth control of the cell, then cancerous cells may result.^{10,11}

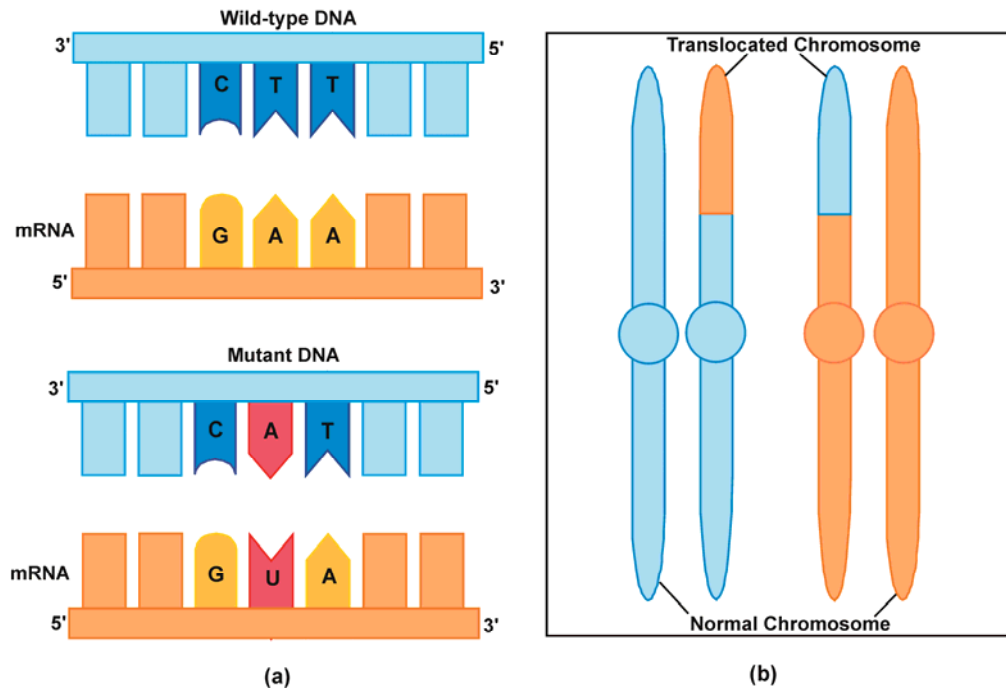


Figure 1.2: Diagram illustrating (a) a point mutation and (b) translocation of genetic material.¹¹

Another internal factor that can cause the formation of cancerous cells is when, during normal DNA replication and repair, DNA is added or lost, leading to the production of defective proteins.⁸ Epigenetic changes are another important internal factor that can influence the formation of cancerous tissue. Epigenetics provides information on how and when genetic information is used and can regulate gene expression without changes to the DNA sequence. Epigenetics influences chromatin regulation, transcriptional repression, chromosome inactivation, DNA repair, and genomic stability.⁸ Epigenetic information can be transmitted in cells through methylation of the C5 position of the pyrimidine cytosine of CpG dinucleotides. It involves two separate single-strand reactions to methylate a double-strand of DNA. In cancerous cells, this DNA methylation pattern has been changed resulting in either hypomethylation, the decrease in methylation of cytosine residues, or hypermethylation, the increase in methylation of these residues.⁸ This disruption in the methylation patterns may lead to suppression of certain growth control genes or over expression of genes both of which can result in the formation of cancerous cells. Chromatin condensation and transcription is controlled by histone acetylation and deacetylation regulated by enzymes known as histone acetyltransferases and histone deacetylases.⁸ The equilibrium between these enzymes can be changed by certain external chemicals such as bromobenzene and butyryl cyclic adenosine monophosphate. A disruption of this equilibrium can result in a change in the cell without changing the DNA sequence, resulting in cancer.⁸

External factors that can cause the formation of tumour cells include: viruses, bacterial infections, chemicals, radioactivity and electromagnetic radiation.⁸ RNA viruses can produce double-stranded viral DNA and when incorporated into the host genome the viral DNA can cause damage to a tumour suppressor gene or insert a completely new gene resulting in the formation of cancerous cells. The mechanism that allows bacterial infections to cause cancer is currently unknown.⁸ Certain chemicals such as aflatoxins, vinyl chloride and polycyclic aromatic hydrocarbons are encountered in the environment through diet and occupation and can lead to cancer.⁸ Exposure to α and β particles can fragment DNA through the formation of free radicals. Ultraviolet radiation and γ or X-rays can also damage DNA. UV radiation does this by causing intrastrand linkage of adjacent pyrimidines which creates distortions in the DNA helix thereby preventing replication and transcription.⁸ γ - and X-rays are higher in energy than UV radiation and thus can penetrate more deeply into tissue causing single and double strand breaks in the DNA. Damage to DNA can result in the formation of cancerous cells.⁸

As described above, cancer results from the modification of the genome of cells due to both internal and external factors. These genetic faults can lead to the following cellular defects which are characteristic of cancerous cells:¹⁰

- Unusual signaling pathways
- Insensitivity to growth-inhibitory signals
- Disruption of the cell cycle
- Evasion of apoptosis
- Unlimited cell division
- Angiogenesis
- Metastasis

Most of these conditions have to be met before a mutated cell can become malignant. These cellular defects are briefly described below as it explains why cancer is so difficult to treat. As many cellular safeguards have been overridden in cancerous tissue it is unlikely that focusing on one specific defect is going to be effective in the treatment of cancer.

One of the cellular defects that occurs in cancerous cells is the disruption of the signaling pathways. Hormones called growth factors give signals to normal cells about whether to grow and divide. These growth factors activate protein kinase receptors in the cell membrane which trigger a signal transduction pathway. This pathway reaches the nucleus initiating transcription of proteins and enzymes needed for growth and division to take place.¹⁰ Cancer cells have some defect in this signaling pathway which causes the cells to constantly multiply.

Another cellular defect is insensitivity to growth-inhibitory signals. Several hormones signal the inhibition of cell growth and division. Insensitivity to these hormones, arising from damage to the genes coding for the receptors of these inhibitory hormones (tumour suppression genes), can increase the risk of a cell becoming cancerous.¹⁰

Disruption of the cell cycle regulation can also lead to cancer. The cell growth cycle involves four phases: G_1 , S, G_2 and M. The cell cycle is illustrated in Figure 1.3(a). In the G_1 phase (gap 1), growth factors signal to the cell to grow in size and prepare to copy its DNA.¹⁰ During the S phase (synthesis) DNA replication takes place.

In the next phase, G_2 (gap 2), the cell prepares for cell division and it is during this phase that any damaged DNA is repaired. During the M phase (mitosis) cell division takes place, producing two cells with a full set of chromosomes.¹⁰ These new cells can either begin the cell cycle again by moving into the G_1 phase or enter the G_0 phase where the cell is dormant. There are various points within the cell cycle where decisions are made to determine whether the cell should continue to the next phase of the cycle.¹⁰ There are also controls which delay the cell cycle if the DNA is damaged. In tumour cells, it is these checkpoints which are defective. Proteins called cyclins and enzymes called cyclin-dependant kinases (CDK's) control the cell cycle with the binding of a cyclin to its kinases, causing the activation of the enzyme, moving the cell cycle to its different phases.¹⁰ Several cancers are associated with overactive kinase cyclins or CDK's leading to the disruption of the normal regulation controls.

The disruption of a cell's apoptotic pathway is another cellular defect that can lead to cancer. Apoptosis is a built-in process where the cell effectively commits suicide to protect the body from abnormal cells.¹⁰ Cancer cells that grow uncontrollably can avoid this process as they have undergone genetic changes. There are two apoptotic pathways; an extrinsic route, where apoptosis is signaled by external factors, or an intrinsic pathway which may be caused by DNA damage.¹⁰ Once apoptosis has been triggered by these factors, signals are sent to mitochondria which have proteins such as cytochrome *c*, which promote apoptosis. The release of cytochrome *c* results in the formation of a large oligomeric protein complex known as apoptosome.¹⁰ The apoptosome in turn activates an enzyme called procaspase 9 which itself activates other caspases. The caspases are protease enzymes and thus destroy the cell's proteins, leading to the destruction of the cells. This apoptotic pathway is shown in Figure 1.3(b). The caspases have a cysteine residue which is an important active site in the catalytic mechanism.¹⁰ As caspases have fatal effects on the cells, there are controls that check that apoptosis does not occur readily. Certain proteins promote apoptosis while others suppress it. This is a complex system and a defect in this system can cause cancer and also has serious consequences for chemotherapeutic drugs as many act by triggering apoptosis.¹⁰

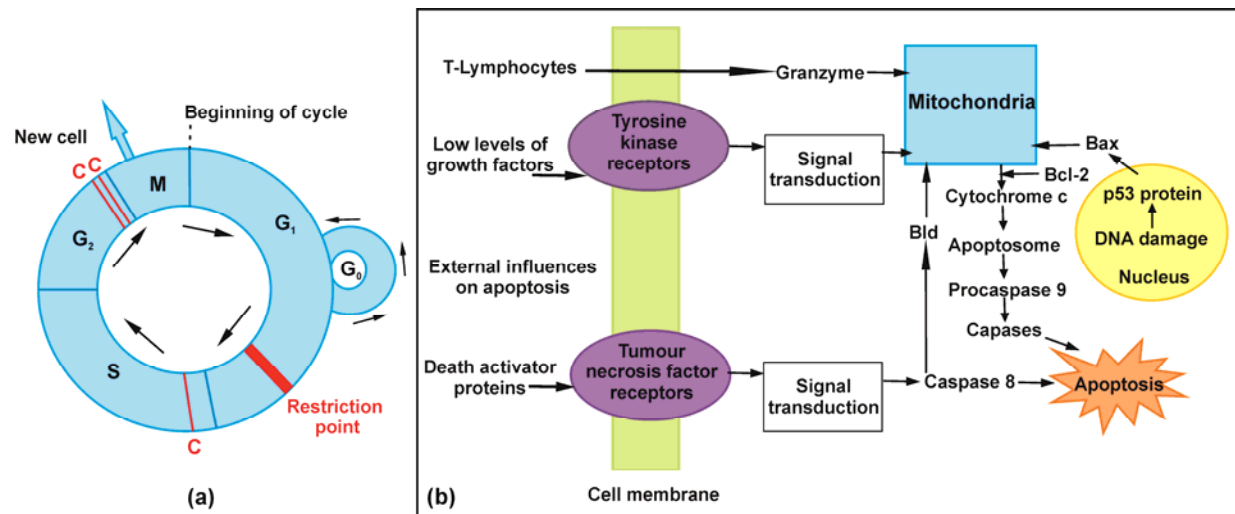


Figure 1.3: (a) The cell cycle where C refers to the various cellular checkpoints, G_1 is the first gap phase, S is the synthesis phase, G_2 is the second gap phase, M is the phase where mitosis occurs and G_0 is the dormant phase.¹⁰ (b) The process of apoptosis.¹⁰

Unlimited cell division is a characteristic of cancer cells with no apparent limit to the number of times they can divide. Telomeres are a polynucleotide region at the 3' ends of chromosomes which effectively control the number of times a cell can divide.¹⁰ A telomere stabilizes and protects the DNA. In normal cells, after each replication process, about 50-100 base pairs are lost from the telomere as DNA polymerase cannot completely replicate the 3' end of chromosomal DNA. When the telomere becomes too short and the DNA becomes unstable, apoptosis is triggered. In cancerous cells an enzyme called telomerase increases the length of the telomere, thus enabling the cells to divide uncontrollably.¹⁰

In order to grow, a tumour needs to have a steady blood supply. To ensure that as the tumour grows it does not become starved of blood, tumour cells release growth factors, which interact with receptors on the cells of nearby blood vessels causing these cells to divide, leading to extension of existing capillaries. This process is known as angiogenesis.¹⁰ Certain chemotherapeutic drugs inhibit angiogenesis and break down abnormal blood vessels.

As mentioned above, not all cancers are life threatening. It is malignant cancers that have the ability to break away from the primary tumour and form secondary tumours elsewhere in the body that can be life threatening.^{8,10} In normal cells, there are cell adhesion molecules ensuring that cells remain with cells of similar character and adhere to the extracellular matrix. If a cell is removed, apoptosis is triggered. Metastasized cancer cells do not contain these cell adhesion molecules and can thus break away from the primary tumour without triggering apoptosis.¹⁰

This section showed the complexity of cancer as a disease and all the various factors that need to be noted when developing anti-cancer drugs or other methods to control the disease. As all these various controls and safeguards are overcome by cancer cells, it shows how difficult it is to treat cancer. The following section gives an overview of the various tactics that have been used to combat cancer.

1.2.2 Treatment of cancer

The strategy used for the treatment of cancer is determined by the nature of the cancer and its stage of development with the option of adopting more than one strategy in the treatment. The main treatments for cancer include: surgery, radiotherapy and chemotherapy, as well as the lesser known treatments such as: photodynamic therapy (PDT), antibody and vaccine related approaches and gene therapy.⁸ Tumours can sometimes be surgically removed if they are small and well defined but additional chemotherapy and radiotherapy is often required for the complete removal of the cancerous cells. Radiotherapy uses X-rays, delivered in a high focus beam to the diseased cells, or radiopharmaceuticals that act as a source of γ rays. Radionuclides in use include ^{60}Co , ^{198}Au and ^{131}I .⁸

Chemotherapy involves the use of drugs to destroy a tumour or at least limit its growth.^{8,10} The advantage of chemotherapy is that the drugs can distribute to most tissues of the body and can kill cells in the process of metastasis. Many anti-cancer drugs do have unpleasant side effects. Traditional anti-cancer drugs are highly toxic, acting on a whole variety of cellular defects.^{8,10} These drugs use the fact that cancerous tissue grows at a rapid rate compared to normal cells and thus will more effectively accumulate the drugs. The problem with this approach is that not all cancerous cells grow quickly and some normal cells grow rapidly resulting in terrible side effects from these drugs. In more recent years, drugs have been developed which target specific abnormalities in the cell, allowing them to have less serious side effects.⁸

The main problem that many anti-cancer drugs face is resistance of cancer cells to the drug. Resistance can be intrinsic, where the tumour is unresponsive to the drug from the beginning of the treatment, or acquired, where a tumour is initially responsive to a drug, but becomes resistant.^{8,10} Acquired resistance is due to the presence of a mixture of drug-sensitive and drug-resistant cells within the tumour. This occurs because cancerous cells are unstable and mutations occur, making some cells resistant. A drug then eliminates all the sensitive cells leading to replication and growth of resistant cells.^{8,10} Resistance may occur by several mechanisms such as decreased uptake of the drug or increased synthesis of the target at which the drug is directed.^{8,10} Cancer cells may also acquire effective efflux pumps over time that block uptake of a drug.

Anti-cancer drugs have a variety of different mechanisms that interfere with tumour cell growth, survival or angiogenesis. The largest group of anti-cancer drugs are those that interact with DNA.^{8,10} They may do this by blocking the synthesis of DNA or by being incorporated into the DNA and then interfering with its function. These drugs can also interact with the DNA through mechanisms of intrastrand or interstrand crosslinking, intercalation between base pairs or interaction in the minor or major grooves.⁸ Drugs such as the antimetabolites affect cell growth by interfering with key biosynthetic pathways while other drugs are classed as hormonal agents and control cell growth by interacting with various hormones. Certain drugs act as vascular targeting agents which prevent angiogenesis by blocking new capillary growth.⁸ Table 1.1 gives a brief description of some of the different classes of chemotherapeutic agents.

Table 1.1: Summary of some the different classes of chemotherapeutic agents.⁸

Drug class	Drug type	Examples	Description
Antimetabolites	• Tetrahydrofolic acid inhibitors (antifolates)	• Methotrexate	These drugs block crucial metabolic pathways essential for cell growth.
	• Purine antimetabolites	• 6-mercaptopurine	
	• Pyrimidine antimetabolites	• 5-fluorouracil	
DNA-interactive agents	• Alkylating Agents	• Dacarbazine	These drugs interfere with DNA processing, leading to cell death, usually through apoptosis.
	• Cross-linking agents	• Cisplatin	
	• Intercalating Agents	• Doxorubicin	
	• Topoisomerase inhibitors	• Topotecan	
	• DNA-cleaving Agents	• Bleomycins	
Antitubulin Agents	• Vinca alkaloids	• Vinblastine	These drugs interfere with the microtubule dynamics in the cells.
	• Taxanes	• Taxol	
Molecularly Targeted Agents	• Kinase inhibitors	• Imatinib	Target a biochemical pathway or protein that is unique to or over expressed in cancer cells.
	• Cell cycle inhibitors	• Flavopiridol	
	• Proteasome inhibitors	• Bortezomib	
	• mTor inhibitors	• Rapamycin	
Hormones	• Anti-estrogens	• Tamoxifen	Cancer cells in some cases can be controlled by hormones.
	• Anti-androgens	• Flutamide	
Biological agents	• Anti-angiogenic agents	• Bevacizumab	Block the ability of tumours to develop new vascular tissue required for growth.
	• Vascular disruptive agents	• Combretastatins	
	• Bioreductive agents	• AQ4N	

The main class of anti-cancer agents of interest to this work is the DNA-interactive agents. The bis(pyrrolide-imine) gold(III) Schiff base macrocyclic complexes have been synthesized with the anticipation that they will exert their cytotoxicity through DNA intercalation and topoisomerase inhibition due to their structural design.

1.2.3 DNA Intercalation

There are five different ways that are frequently reported in which molecules can bind to DNA.¹² They can bind covalently to the DNA bases like cisplatin; this type of binding will be discussed in more detail later. Molecules can also groove bind.^{12,13} Groove binding is where molecules bind into the minor groove or the major groove of the DNA by hydrophobic interactions or by partial intercalation.¹³ Molecules can also bind to the sugar-phosphate backbone of DNA. Intercalators are molecules that partly unwind DNA and π -stack between two base pairs.^{12,13} Once in position, they are held in place by hydrogen bonding and van der Waals forces. Intercalators insert in the major groove of the double helix with the intercalating ligand acting as a new base (Figure 1.4(b) and 1.5(a)). As no bases are removed, the major groove widens.¹³

In addition to these common DNA binding modes, a sixth type of binding mode has been discovered. This binding mode involves the binding of a compound into the central triangular-shaped hydrophobic cavity of the DNA junction.¹² DNA junctions are unique branched structures that consist of several double strands of DNA that converge at a single point with three-way junctions occurring in both RNA and DNA. In DNA these junctions are formed during DNA replication (the replication fork).¹² It has been found that bis(pyridyl-imine) di-iron(II) nanostructures which are formed from three bis(pyridyl-imine) organic strands wrapped around two Fe^{2+} ions, can preferentially bind in the three-way junction and exert highly specific cytotoxic effects.¹² The nanostructures have a high positive charge due to the two Fe^{2+} ions and large hydrophobic surfaces due to the aromatic rings. Both these characteristics enable non-covalent recognition of the DNA junction by the complex. The di-iron(II) compounds are held in position by extensive π -stacking.¹²

In recent times, there has been a drive to produce drugs which are intercalators rather than drugs that bind to DNA directly. DNA intercalators usually have a few key features: they have an electrostatic attraction to the negatively charged phosphate groups of DNA and are planar in geometry, usually consisting of three or four fused aromatic rings.^{8,10,13,14} This gives the compounds the ability to π -stack with the aromatic DNA.¹⁵ As some DNA intercalators have a charged group, it allows the intercalator to form ionic interaction with the negatively charged phosphate backbone of the DNA.¹⁰ Many intercalators also have side chains which have the ability to form hydrogen bonds with the DNA helix.¹⁰

DNA intercalators cause distortions in DNA and can inhibit DNA replication and transcription. Some intercalators affect the topoisomerase enzymes, which are important for forming the supercoils in DNA while others chelate metal ions and produce DNA-cleaving free radicals or interact with the cell membrane.^{8,10}

Traditional DNA intercalators are organic molecules with examples including: doxorubicin, daunorubicin and adriamycin which belong to a group of anti-tumour agents called the anthracyclines.^{8,10} These compounds consist of a planar anthraquinone centre attached to an amino-containing sugar. They approach the DNA via the major groove and intercalate using their planar rings.¹⁰ The charged amino groups allow for interactions with the negatively charged phosphate backbone of the DNA. This amino group is important as studies have

shown that the ring system without this aminosugar has poor activity.¹⁰ Figure 1.4 illustrates the key structural features of daunorubicin as well as daunorubicin intercalated between DNA base pairs. Note how the planar aromatic region sits between the DNA base pairs.

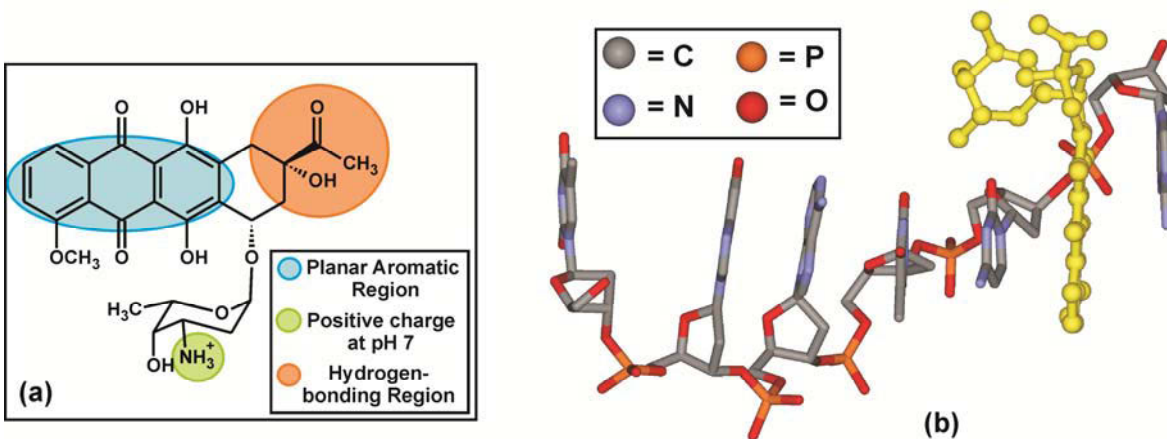


Figure 1.4: (a) Key structural features of daunorubicin that allow for effective DNA intercalation. (b) X-ray crystal structure of daunorubicin (shown in yellow) intercalated between DNA base pairs.¹⁶ Water solvent molecules have been omitted for clarity.

The main problem for many small organic molecules is their lack of solubility in aqueous media. Thus to increase their aqueous solubility the charge of the molecule is often adjusted and the bromide salts of these molecules are often more effective intercalators.¹⁴ The compound dipyrido[3,2-a:2',3'-c]phenazine (dppz) is a successful intercalator, but when converted to the nitrate salt, it has improved solubility.¹⁴

As organic molecules have traditionally been used as DNA intercalators, it is unusual to focus on transition metal DNA binding agents. Most biological transition metals are found at coordination sites in proteins and not as freestanding coordination complexes and cells generally use organic groups for the binding and recognition of DNA.¹³ Although there are few naturally occurring examples of transition metal-binding agents, there are definite advantages of using transition metals to intercalate DNA. Firstly, ligands can be bound to the metal centre, keeping a rigid structure; by substituting the ligands, the recognition properties of the complex may be changed.¹³ Another advantage is that the transition metal centres have photophysical and electrochemical properties that allow the metal complexes to have a wide range of applications from fluorescent markers to electrochemical probes.¹³ These advantages of transition metal DNA binding agents have led to ever increasing interest in this field of research.

In nature there is only one example of a group of transition metal complexes that recognize and bind to DNA; the metalbleomycins.¹³ The bleomycins have a metal-binding region that can coordinate to a variety of metals including Zn(II), Cu(II) and Co(II) with the Fe(II) bleomycin complex being well studied. When the Fe-bleomycin complex is exposed to oxygen and a reducing agent, it becomes activated and can induce both single and double-stranded DNA cleavage.^{10,13,17} Another key feature is their positively charged tail, which allows them to bind through an electrostatic interaction to the negatively charged backbone of the DNA. Figure 1.5(a) shows bleomycin A2 chelated to Co(II) and intercalated between DNA base pairs. Due to their

ability to recognize and bind specific sites in the DNA, bleomycins have been used successfully in the treatment of certain types of cancer.¹⁰

Non-covalent DNA-binding metal complexes share a few important characteristics. All the complexes are kinetically inert, which is important for stability with most of the coordination complexes having a d^6 octahedral or d^8 square-planar geometry. Most of the complexes also have a rigid three-dimensional structure allowing for recognition.¹³ Some examples of synthetic metal-based DNA intercalators include platinum(II) terpyridines and ruthenium(II) dppz complexes, Figure 1.5 (b).^{18,19}

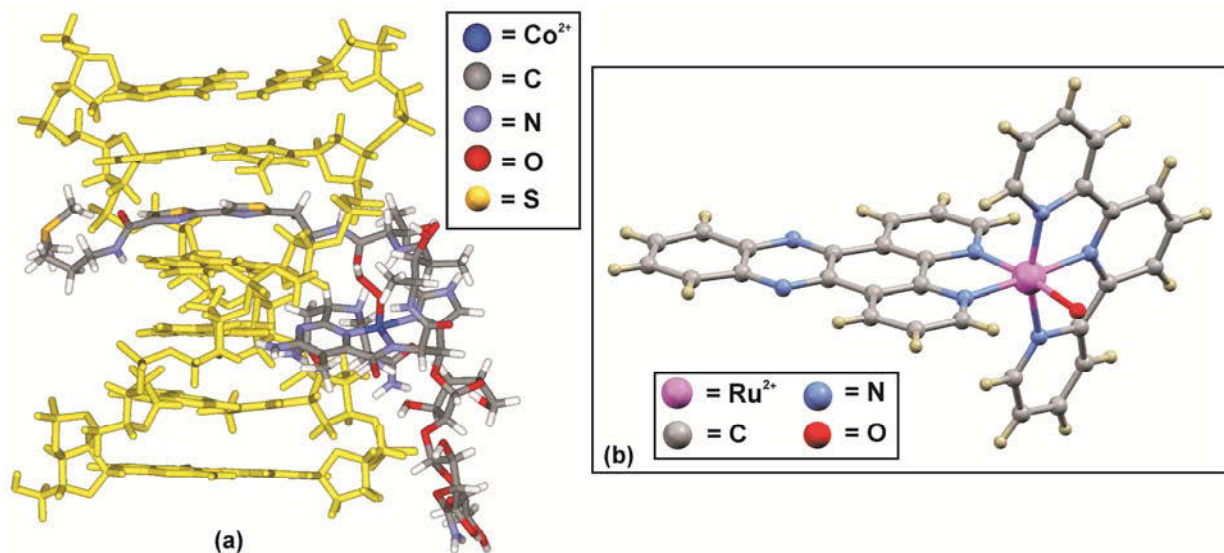


Figure 1.5: X-ray structures of (a) Bleomycin A2 chelated to cobalt and intercalated between DNA base pairs.¹⁷ (b) Ruthenium (dppz).²⁰

The gold(III) complexes presented in this work fulfill the requirements of DNA intercalators. They are macrocyclic complexes with rigid structures and are likely to be stable under biological conditions. The d^8 electronic configuration means the gold(III) ion is rigorously square-planar, thus the chelates have a planar geometry, ideal for intercalation. The conjugated π system should enable interactions between the DNA base pairs with the overall positive charge allowing for interactions with the negatively charged phosphate backbone of the DNA. It is anticipated that the gold(III) complexes will disrupt the functioning of the TOP enzymes through DNA intercalation. The next subsection gives a description of the functioning of the TOP enzymes and mechanisms used to inhibit these enzymes.

1.2.4 DNA Topoisomerases

DNA is an incredibly long polymer with approximately 2 m of DNA squeezed into a cell with a nuclear volume of approximately 10^{-17}m^3 .²¹ Cellular DNA is therefore very highly compacted through the processes of supercoiling, knotting and catenation. DNA can be negatively supercoiled (underwound) when strands cross each other at more than a 10.4 base-pair interval and DNA can be positively supercoiled (overwound) when strands cross each other with a base-pair interval less than 10.4.²¹ DNA is often positively supercoiled upstream of a replication fork and negatively supercoiled downstream of these forks. DNA metabolism

requires the two strands of the duplex to be separated for them to serve as templates for transcription, replication, recombination and repair.²¹

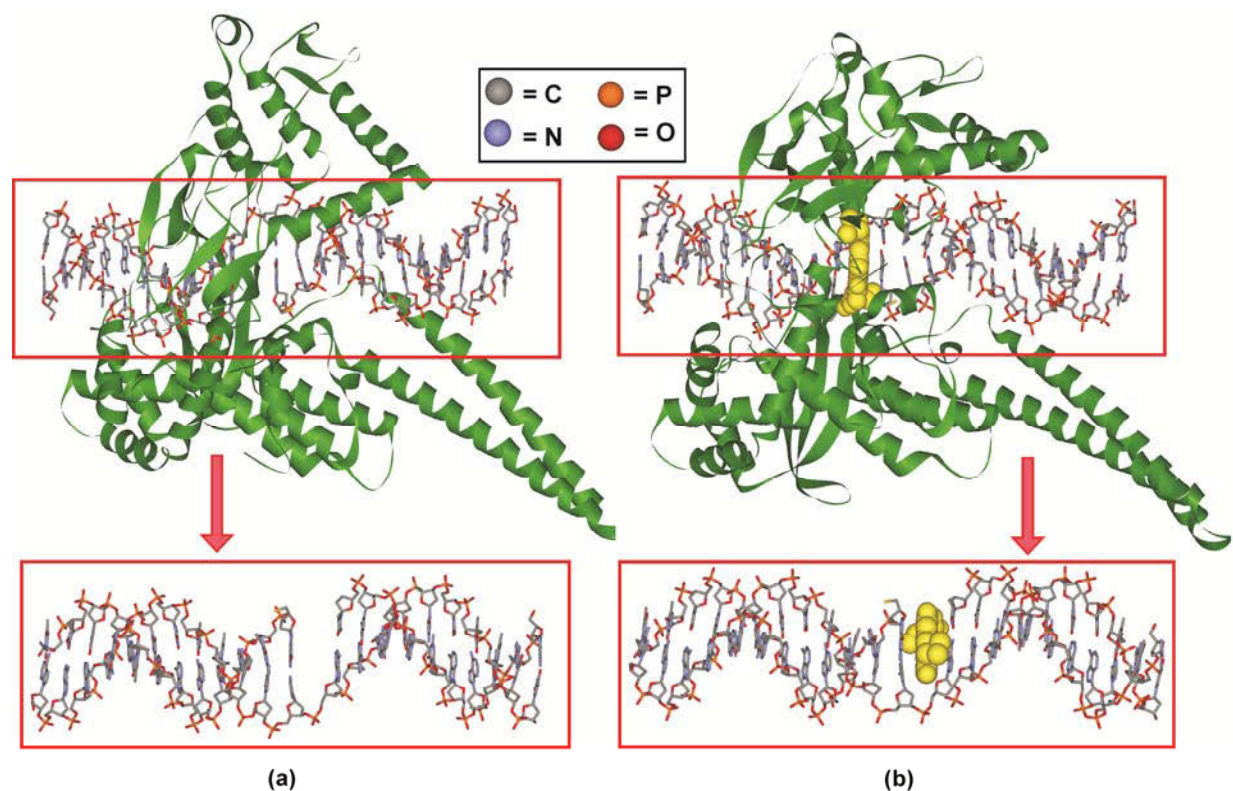
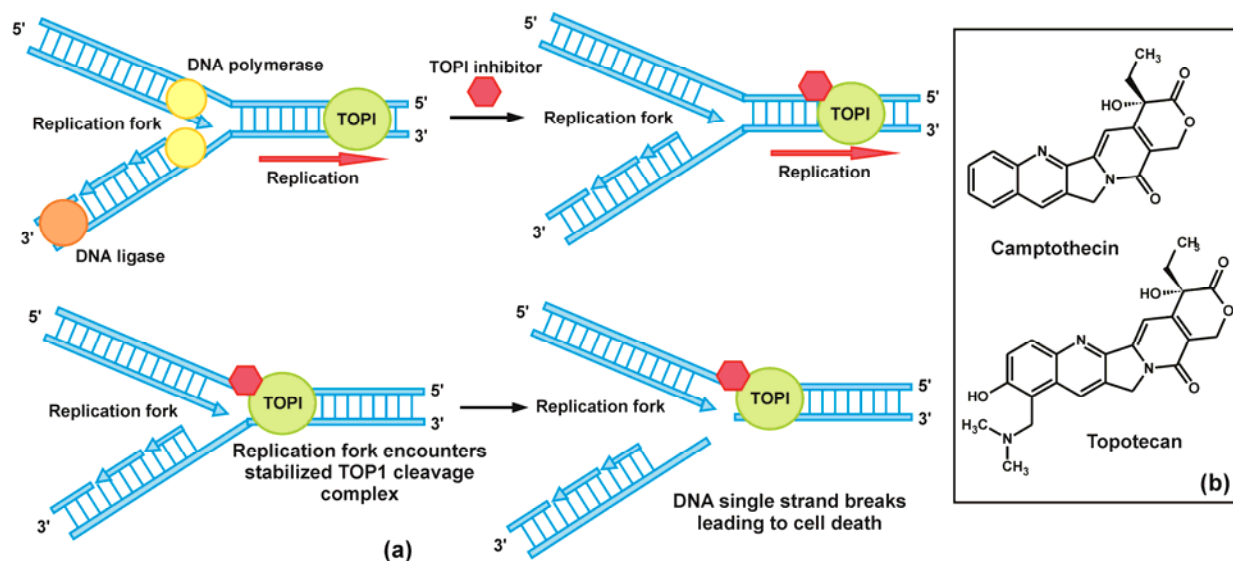
The DNA topoisomerases are a group of enzymes which are responsible for cleavage, annealing and supercoiling of DNA.²¹⁻²⁴ Their most important function is to unwind and wind the supercoiled DNA of the chromosomes to allow replication and transcription to occur. If this unwinding cannot occur then cell death would result as the required proteins could not be synthesized. The TOP enzymes are divided into two types: I and II with both further divided into two classes: TOP1A and 1B as well as TOP2A and 2B.²¹⁻²³ The function of these enzymes and the drugs that can be used to disrupt the enzymes are described below.

TOP I relaxes supercoiled DNA in the absence of an energy cofactor by causing a single-strand nick in the DNA through a reversible transesterification reaction. It does this by forming a clamp around the duplex DNA. The active-site tyrosine of the enzyme acts as a nucleophile and cleaves a single DNA strand. Type IA forms a 5' phosphotyrosyl covalent bond while Type IB forms a bond with the 3' end of the DNA.²¹⁻²⁴ This results in a cleavage complex with a single strand break which allows relaxation of torsional strain, either by allowing the intact strand through the nick or by free rotation of the DNA about the uncleaved strand. Once the DNA is relaxed TOP1 religates the break by reversing its covalent binding. In order for religation to occur the 5' hydroxyl group at the DNA end must be aligned with the tyrosine-DNA phosphodiester bond.²¹⁻²³ The rate of religation is normally much faster than the rate of cleavage and this ensures the concentration of the TOP1 cleavage complex remains low.²¹

It is during the cleavage step and the formation of the cleavage complex that TOP is vulnerable to TOP1 inhibitors. As the religation by TOP1 requires nucleophilic attack of tyrosyl-DNA phosphodiester bond by the free DNA end, there needs to be perfect alignment of the 5' hydroxyl DNA end with the tyrosyl-phosphodiester bond.²¹ Any misalignment prevents religation and leads to accumulation of TOP1 cleavage complexes. TOP1 cleavage complexes accumulate at sites of base mismatches, base oxidation, carcinogenic adducts and pre-existing DNA breaks because of this misalignment. Accumulation of these TOP1 cleavage complexes leads to cell apoptosis.

Drugs such as camptothecin, a naturally occurring cytotoxic alkaloid, binds reversibly to the TOP1 cleavage complexes.²¹ Camptothecin stabilizes the TOP1 enzyme cleavage complex, thereby inhibiting rejoining of the strands. This results in accumulation of TOP1 cleavage complexes. The single strand breaks can be repaired if the drug departs. During the S phase of the cell cycle, if these TOP1 cleavage complexes are still present, they are thought to collide with the replication fork causing an irreversible DNA strand break leading to cell death.^{21,22} Figure 1.6 illustrates the mechanism of action of TOP1 inhibitors. Camptothecin shows selectivity for cancerous cells over normal cells as cancer cells show higher levels of TOP1 than normal cells. Topotecan is a synthetic analogue of camptothecin which has added polar functional groups to improve aqueous solubility and is used for the treatment of ovarian and lung cancer.^{21,22}

Staker *et al.* have reported the X-ray crystal structure of a 70-kDa form of human TOP1 covalently joined to double stranded DNA in the absence and presence of topotecan, Figure 1.7.²⁵ The structures show that Topotecan intercalates at the site of TOP1 DNA cleavage forming base-stacking interactions with both the -1(upstream) and +1 (downstream) base pairs. The planar 5-membered ring system of topotecan are similar to a DNA base pair and topotecan occupies the same space as the +1 base pair in the structure without the drug bound.²⁵



The intercalation site is effectively created by conformation changes of the phosphodiester bond between the +1 and -1 base pairs of the uncleaved strand thus opening up the DNA and does not require rotation of a DNA base out of the helix or breakage of any hydrogen bonds.²⁵ The intercalation site is stabilized by hydrogen bonds and DNA-protein interactions. The intercalation of topotecan extends the distance between the -1 and +1 base from 3.6 Å to 7.2 Å and displaces the reactive 5'OH of the cleaved strand 8 Å further away from the phosphotyrosin residue, thus preventing religation of the strand.²⁵ As the topotecan binding pocket is located within the DNA substrate and can only form after the transesterification reaction, this explains why the drug targets the TOP1 cleavage complex and not the enzyme alone.²⁵

While the TOP1 enzyme relaxes the tension in the DNA supercoiled structure through single strand breaks of the DNA double helix, TOP2 performs the same function but cleaves both strands of the DNA helix.²⁶ TOP2 enzymes are also further divided into two classes IIA and IIB.²⁷ TOP2 binds to DNA where two regions of the double helix are in close proximity. It does this to relieve the tension when the DNA is unraveled. The enzyme binds to one of these helices and the catalytic tyrosine residues nick both strands of the DNA resulting in reversible covalent bonds between the enzyme and the resulting 5' end of each strand.^{10,27} The strands are pulled apart to form a gap through which the intact region of DNA can be passed. Once this is done, the enzyme reseals the strand and departs. This is a simplified outline of the mechanism of TOP2 and is illustrated in Figure 1.8.

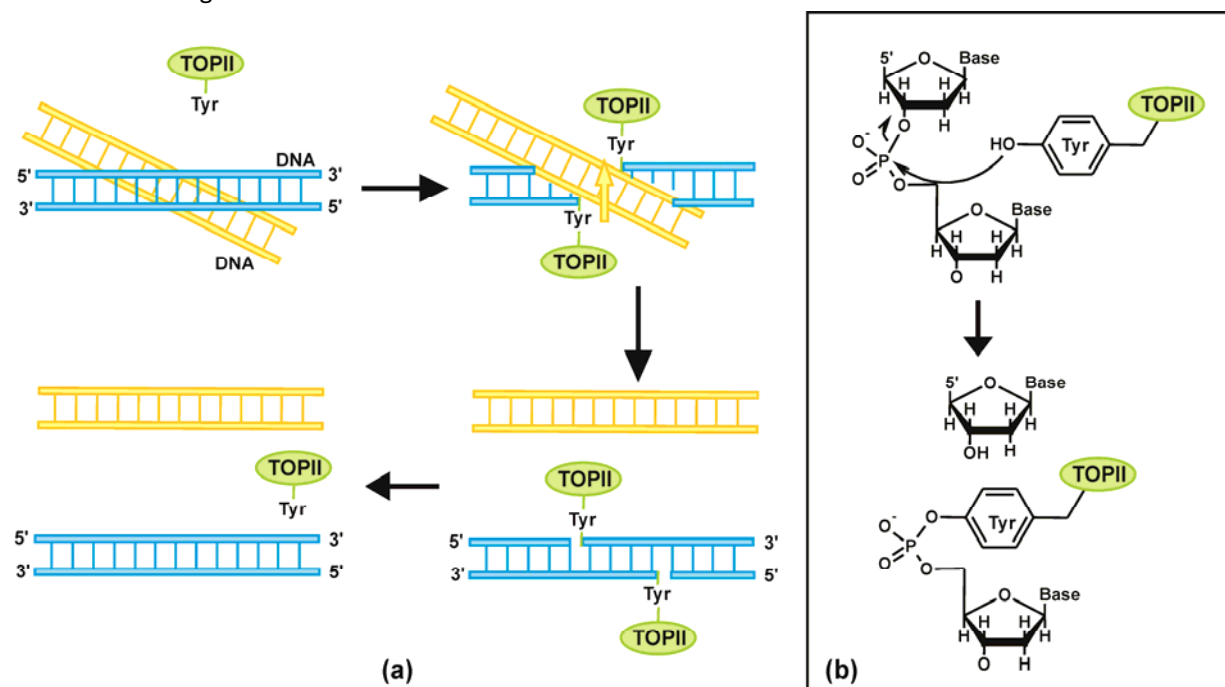


Figure 1.8: (a) Mechanism of action of TOP2. (b) The nicking of the DNA chain by TOP2.¹⁰

In reality the untangling of the strands is more complicated than the process described above. TOP2 promotes the ATP-dependent passage of one DNA segment (the transport or T-segment) through the double-strand break of a second duplex (the gate or G-segment).^{26,27} For type TOP2A, the strand passage is through a 'two-gate mechanism'. TOP2 consist of two ATPase domains which can be closed and opened by reversible dimerization to form the N-gate. On the other side of the enzyme is the carboxy terminal dimerization interface which can also open and close forming the C-gate.²⁷ Between these two gates in the

interior of TOP2 is a third interface: the DNA gate which consists of catalytic tyrosine residues responsible for DNA cleavage and separation. TOP2 also consists of a metal-binding domain called the TOPRIM which is believed to assist formation of the enzyme-DNA intermediate by coordinating magnesium essential for DNA cleavage.²⁷

The 'two-gate mechanism' is depicted in Figure 1.9. The cycle begins with the G-segment of DNA associating with the DNA binding core of TOP2. ATP binding promotes the enzyme capture of a second piece of DNA, the T-segment as well as the dimerization of the ATPase.²⁷ This leads to the closure of the ATPase domains forming the N-gate. This in turn stimulates the cleavage and separation of the G-segment by a nucleophilic attack of catalytic tyrosine residues on the phosphodiester backbone allowing for transport of the T-segment through the break. The G-segment is then religated and the T-segment is removed through the C-gate.²⁷

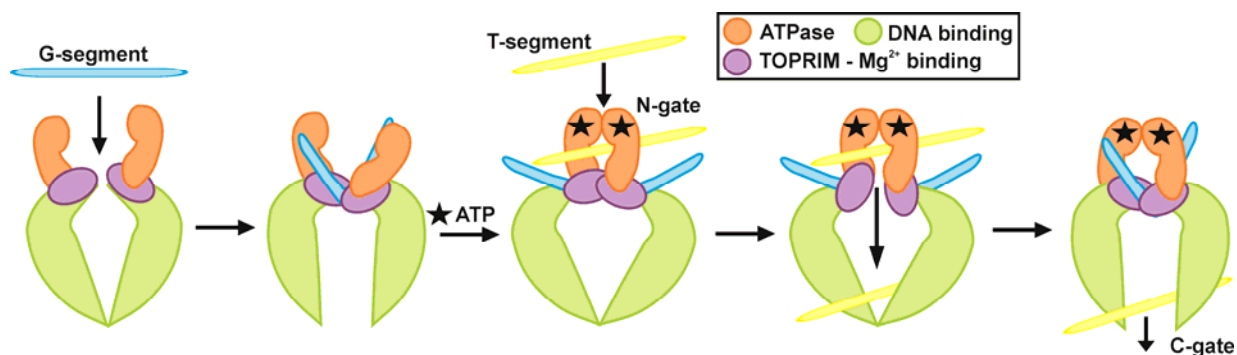


Figure 1.9: Two-gate model for DNA transport in TOP2A.²⁷

There are several commercially available TOP2 inhibitors and poisons for the treatment of cancer. The anthracyclines are a group of drugs that act as DNA intercalators and TOP2 poisons. Some examples are: daunorubicin, doxorubicin and epirubicin.^{8,10} These drugs intercalate DNA at a pyrimidine-purine step with a preference for the cytosine-guanosine (CG) sequence. Once intercalated, the drug stabilizes the DNA-enzyme complex at the point where the enzyme is covalently linked to the nicked DNA. A large number of these stabilized DNA-enzyme complexes result in permanent DNA breaks when replication occurs, triggering apoptosis.^{8,10} Doxorubicin and epirubicin are semi-synthetic compounds which are derived from the natural product daunorubicin. Doxorubicin in particular has been used for the effective treatment of acute non-lymphocytic leukaemia, Hodgkins and non-Hodgkins lymphomas, breast cancer and sarcomas.^{8,10}

The drug etoposide is one of the most effective TOP2 inhibitors known. Etoposide inhibits the ability of TOP2 to reseal cleaved DNA duplexes.⁸ These breaks become lethal during replication and transcription. The drug etoposide is used for the treatment of testicular and small cell lung cancers as well as lymphomas. It acts in the late S/G2 phase of cell cycle, inducing DNA strand breakage.⁸ Although effective chemotherapeutic agents, some of these drugs which interact with and damage DNA have been linked to the onset of secondary tumours.⁸

1.2.5 Platinum(II) based Anti-cancer Agents

An overview of the treatment of cancer would not be complete without mentioning the most famous metal-based anti-cancer agent: cisplatin. Before 1969, testicular cancer patients suffered a high mortality rate.

However, today the prognosis for treatment of testicular cancer is very good.^{2,28,29} This is due to the discovery of the anti-tumour activity of *cis*-diaminedichloroplatinum, commonly known as cisplatin, by Barnett Rosenberg, often referred to as one of the greatest success stories of cancer chemotherapy.²

DNA is the major target of cisplatin.^{2,28,29} Cisplatin predominantly reacts with purine and pyrimidine bases, with binding being dependent on pH. At neutral pH, the platinum prefers the binding sites: N(7) atoms of guanine and adenine, N(3) of cytosine and N(1) of adenine. The guanine N(7) has been shown to be the most likely coordination site for cisplatin. Hydrogen bonding between the O(6) group of guanine and the N-H of cisplatin seems to stabilize binding to the guanine N(7) site.^{2,28,29} The guanine N(7) position is preferred over the adenine N(7) position as it is about 2.3 log units more basic than the corresponding adenine position. It is not likely for binding to take place at the adenine N(1) and the cytosine N(3) sites as they are involved in DNA base pairing and less available for metal binding.^{2,28,29}

Cisplatin, when it binds to DNA, causes the unwinding of the superhelix and shortening of the double helix.²⁹ Cisplatin does this by forming various bifunctional adducts, including intrastrand, interstrand and intermolecular cross-links. The bifunctional intrastrand cross-linking, involves the binding of the platinum(II) complex to two bases within the same strand of DNA and this type of lesion is the major type of adduct found. Intrastrand cross-links between two neighbouring deoxyguanosine residues (GG) make up 65% of all DNA adducts and are shown in Figure 1.10.² About 20% of DNA adducts are formed by intrastrand cross-links at an AG sequence; however, no adducts are formed at a GA sequence. Cross-links between two deoxyguanosine residues separated by a third nucleoside (GNG) make up another 9% of all the DNA adducts formed.² Bifunctional DNA interstrand cross-links involve the binding of platinum(II) complexes to DNA bases on complementary strands. DNA interstrand cross-links have been found between two deoxyguanosine bases; however, these interstrand cross-links only account for less than 1% of the total platinum (II) adducts.² This low level of occurrence is due to the fact that interstrand cross-linking causes a major contortion of the DNA structure and may only occur when an alternate purine is not in close proximity on the same strand. Another type of adduct forms a cross-link between deoxyguanosine and glutathione. Research has shown that the adducts inhibit DNA replication or transcription, but the exact mechanism of toxicity still needs to be determined.²

Although cisplatin is very active against testicular cancer, its overall efficacy is compromised by its toxicity. The drug has many unpleasant side-effects including nephrotoxicity, nausea and vomiting.^{2,28} After treatment of primary tumours with cisplatin, it is relatively common for secondary tumours to be cisplatin resistant. This has led to the synthesis of cisplatin analogues in an attempt to find compounds with the same or greater anti-tumour activity as cisplatin but with fewer associated side-effects. During the attempt to design and synthesize novel platinum(II) anti-cancer drugs, the following factors were determined:³⁰

- Although complexes which hydrolyse quickly can bind efficiently to biomolecules, these reactive platinum(II) complexes can cause severe toxicity due to reactions with proteins.
- Stable, water-soluble platinum complexes are less toxic but their tumour inhibiting properties are also reduced.
- Stable, lipophilic platinum complexes are moved quickly from the blood into the tissues and hence some of the typical side-effects of chemotherapy are reduced.
- Varying the leaving groups alters the toxic side effects.

- Changing the non-leaving amine ligands will produce structurally different adducts with DNA, thereby changing the anti-cancer properties.

This research has led to the synthesis and production of a second generation of compounds such as carboplatin, oxaliplatin and iproplatin.^{28,29} Carboplatin is used to treat ovarian tumours and small lung carcinomas but with fewer side effects than cisplatin. Carboplatin is a myelosuppressive, causing reduced platelet levels in most patients.²⁹ Oxaliplatin is used in the treatment of colorectal cancer, while iproplatin is effective against ovarian cancer and small-cell lung carcinoma.²⁹

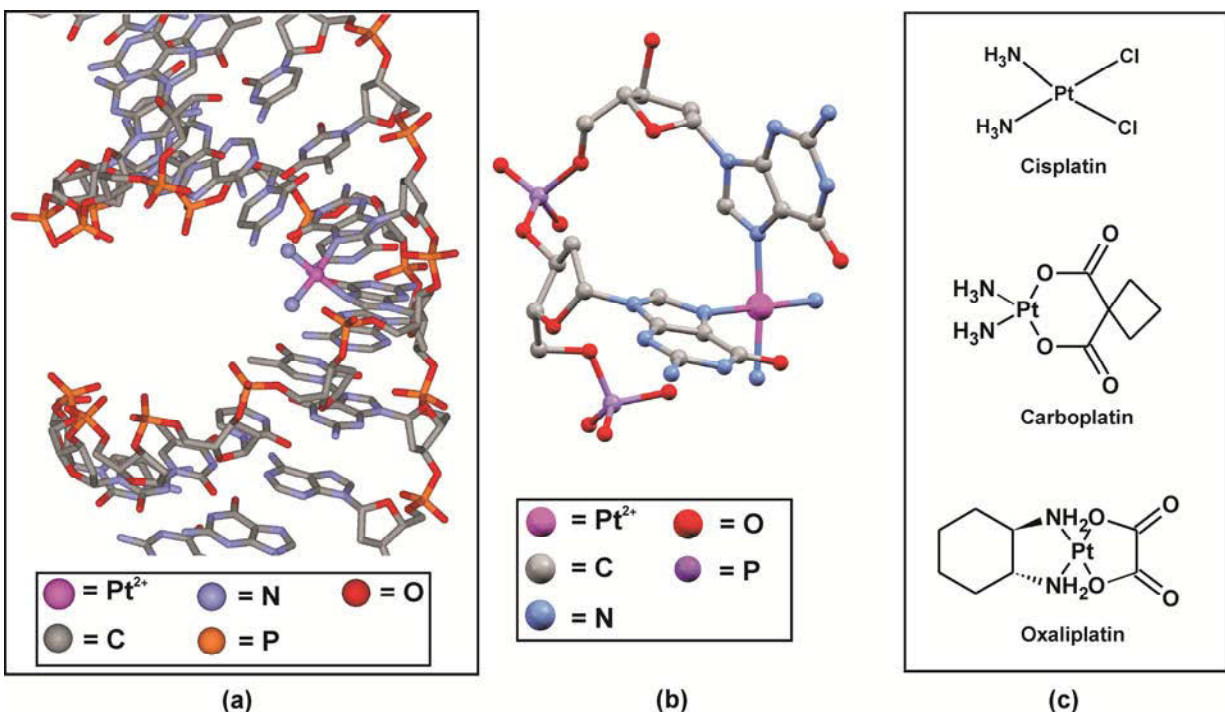


Figure 1.10: (a) X-ray structure of cisplatin forming intrastrand adducts between DNA base pairs.³¹ (b) X-ray structure of cisplatin coordinated to two guanosine residues.³² (c) Structures of cisplatin and the second generation platinum(II) based anti-cancer drugs; carboplatin and oxaliplatin.

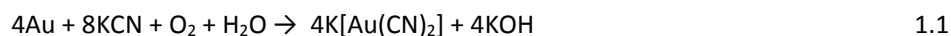
This concludes the section on cancer. To summarize cancer is a difficult disease to treat as cancerous cells have overcome many of the cellular controls and functions. As the cancerous cells are continuously mutating and growing this can lead to resistance of a cancer to a specific drug. Cancer cannot be viewed as a single disease but rather as a number of different diseases. There are many commercially available drugs that function by disrupting different cellular targets with the largest group interacting with DNA. There is an increasing focus on drugs that can intercalate between DNA base pairs and disrupt the TOP enzymes leading to apoptosis of the cell. Although not commonly described, metal-based drugs play an important role in chemotherapy by intercalating DNA or forming DNA adducts such as cisplatin. These metal based drugs are often square-planar with a d^8 electronic configuration and have a very rigid structure. As gold(III) is a d^8 square-planar metal, research has recently focused on gold(III) complexes as anti-cancer agents. The next section further explains the chemistry of gold as well the use of gold in medicine.

1.3 Gold: the Noble Metal

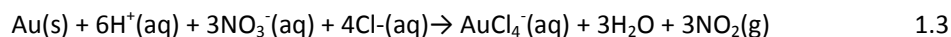
1.3.1 Gold Chemistry

Gold is a soft, yellow, noble metal and occurs in nature almost entirely in its elementary state.^{33,34} The earliest archeological findings of gold date back to 4000 B.C. in Egypt and Mesopotamia while the first legal foundations for the production of gold date back to 1300 B.C.³⁴ In the modern era, the strongest drive forward for gold production came with the discovery of the goldfields of the Witwatersrand in South Africa in 1885. The discovery of these mines raised annual world production from 200 t in 1852 to 500 t in 1904, 700 t in 1907 and 1000 t in 1936 and has presently risen to over 2000 t.³⁴ South Africa has been responsible for 40% of the overall global gold production to date with the United States responsible for 15%, ancient empires about 10%, Russia about 10%, Australia and the Pacific Region about 10% and Canada about 5%.³⁴

During the mining process, the metal is usually concentrated by froth flotation methods. The gold is dissolved in a dilute solution of cyanide in the presence of oxygen to form aurocyanide.^{33,34} The gold is then precipitated out with zinc as shown in Equations 1.1 and 1.2 below.



Gold is the most malleable and ductile of all the metals. Physical properties of gold include a resistance to air, humidity and normal wear. Under normal conditions gold does not react with water, air, oxygen, ozone, nitrogen, fluorine, iodine, sulfur or hydrogen sulfide. Sulfuric acid, nitric acid, hydrochloric acid, hydrofluoric acid and almost all organic acids have no effect on gold. Gold can be dissolved when a hydrohalic acid is combined with an oxidizing agent such as hydrogen peroxide, nitric acid, a halogen or chromic acid.^{33,34} An example of this is the oxidation of gold by aqua regia (a combination of nitric and hydrochloric acid in a 1:3 ratio). The nitric acid oxidizes the metallic gold and a chloride ion subsequently binds and stabilizes the gold(III) ion by forming a coordination complex³⁵, shown by Equation 1.3.



Gold will also dissolve in selenic acid, solutions of alkali metal cyanides in the presence of oxygen or other oxidizing agents or a combination of water and a halogen.³⁴

The electron configuration of gold is $[\text{Xe}] 4f^{14}5d^{10}6s^1$; like copper and silver it has a single *s* electron outside a completed *d*-shell.³³ Despite this similarity in electronic structure and ionization potentials, the chemistry of the metals is not the same. These differences are due to relativistic effects on the 6*s* electron of gold.^{33,36}

Gold has a diverse chemistry as it is able to adopt six oxidation states from (-I) to (III) and (V). All the higher oxidation states are easily reduced to gold(0) forming purple, black or red colloidal gold. In addition to the various oxidation states of gold, it also readily forms metal cluster compounds with both gold and other metal atoms.³³ Table 1.2 describes the coordination geometries of the various oxidation states of gold.

Table 1.2: Coordination geometries of gold.³³

Oxidation State	Coordination number	Geometry
Au (I) d^{10}	2*	Linear
	3	Trigonal
	4	Tetrahedral
Au(II) d^9	4	Square-planar
Au(III) d^8	4*	Square-planar
	5	Trigonal bipyramidal
Au(V) d^6	6	Octahedral
	6	Octahedral

*Most common coordination number

The oxidation states (-I), (II) and (V) are not common for gold. The (-I) oxidation state can be achieved by reducing gold with solvated electrons in liquid ammonia to produce Au^- , which is stable in liquid ammonia.³³

As gold(II) is a d^9 metal, it has an odd electron in the $d(x^2-y^2)$ orbital and therefore has a tendency to disproportionate from gold(II) to gold(I) and gold(III).^{37,38} Mononuclear gold(II) complexes are paramagnetic and can be detected by EPR as they show a hyperfine four line EPR signal.³⁹ Although mononuclear gold(II) complexes have been reported, the formation of gold-gold bonds gives gold(II) complexes additional stability with regard to decomposition.³⁹ Due to this added stability, there are an increasing number of coordination compounds reported with an Au_2^{4+} core. The most prolific of these compounds are those with two equivalent bridges connecting the gold centres forming a cycle, which promotes the formation of a gold-gold bond across the cycle. The double bridges have an important role in holding the gold centres in close proximity to each other to improve the metal-metal bond strength, as shown in Figure 1.11.³⁹ Of these complexes, those containing the bis-ylide ($\text{CH}_2\text{PR}_2\text{CH}_2$) ligands are the most numerous, suggesting that these ligands stabilize the complexes.

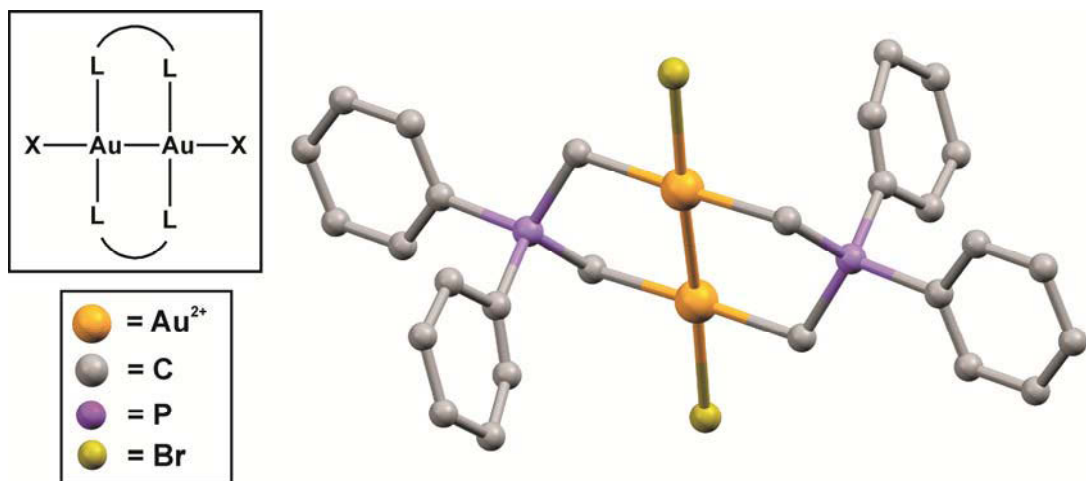
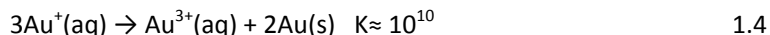


Figure 1.11: X-ray crystal structure of a dinuclear gold(II) complex; Dibromo-bis(μ_2 -diphenyldimethylenephosphoranyl-C,C')-di-gold(II).⁴⁰ The hydrogen atoms have been omitted for clarity.

There are no properly characterized gold(IV) complexes, although the oxidation state is thought to exist under chemically significant conditions.³³ Gold(V) complexes such as AuF_5 and $[\text{AuF}_6]^-$ have a low spin $[\text{Xe}]4f^{14}5d^6$ configuration.³³

The most common oxidation states for gold are (I) and (III) with the most stable oxidation state being (III). Gold(I) compounds often disproportionate to gold(0) and gold(III) as shown in Equation 1.4.³³



The majority of gold(I) complexes are linear and tend to be of the type LAuX where L is a neutral donor such as R_3P or R_2S and X is a halogen or RS. Gold(I) thiolates have been extensively studied.³³ The tendency of gold(I) to display a linear coordination geometry is due to the small energy difference between the filled d orbitals and the unfilled s orbitals which allows for extensive hybridization of the d_{z^2} and s orbitals. These hybrid orbitals formed from the d_{z^2} and s orbitals are orbitals ψ_1 and ψ_2 . The electron pair initially occupies ψ_1 resulting in a circular region of high electron density; ligands are repelled from this region. The region above and below the area of high electron density are themselves low in electron density and thus ligands are attracted to this region. By mixing the ψ_2 with two suitable hybrid p_z orbitals, a linear covalent bond can be formed. This is depicted in Figure 1.12.

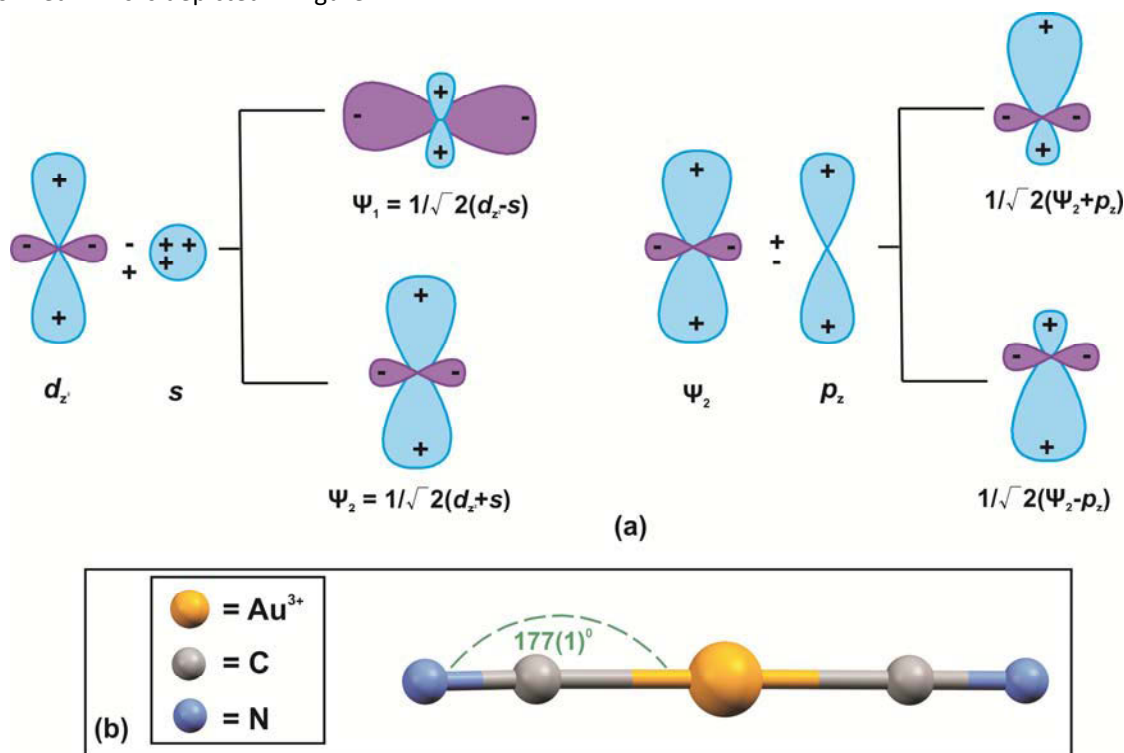


Figure 1.12: (a) The hybrid orbitals ψ_1 and ψ_2 that are formed by the mixing of a d_{z^2} and s orbital as well as the hybrid orbitals formed from the mixing of p_z and ψ_2 .³³ (b) X-ray structure of a linear gold(I) complex; dicyano-gold(I).⁴¹

Gold is capable of forming surprisingly strong Au-Au bonds which are referred to as aurophilic interactions. This allows gold to form metal clusters. As gold(I) has a seemingly closed shell of electrons, gold(I) atoms are not expected to have any affinity for each other.³⁶ However, gold(I) has the greatest aurophilicity due to it having the strongest relativistic contraction, but also due to its low coordination number which results in a lower steric hindrance.³⁶ The low coordination number and linear geometry allows gold(I) complexes to form one-dimensional polymers bridged by gold atoms or macrocycles.

Gold(III) compounds have a $5s^2 2p^6 5d^8$ valence shell, giving it a d^8 electronic configuration. It mainly exhibits a square-planar coordination geometry due to the vacant $d(x^2-y^2)$ orbital. With a strong ligand field the lowering in energy of the dz^2 orbitals is large enough that the electron that was in the $d(x^2-y^2)$ orbital now occupies the dz^2 orbital; this results in the loss of the axial ligands, depicted in Figure 1.13(a). Valence shell electron repulsion (VSEPR) indicates that the dz^2 orbital occupies two coordination sites and thus the donor atoms of the ligands occupy the equatorial plane.⁴² Figure 1.13(b) gives an example of a square-planar gold(III) complex.

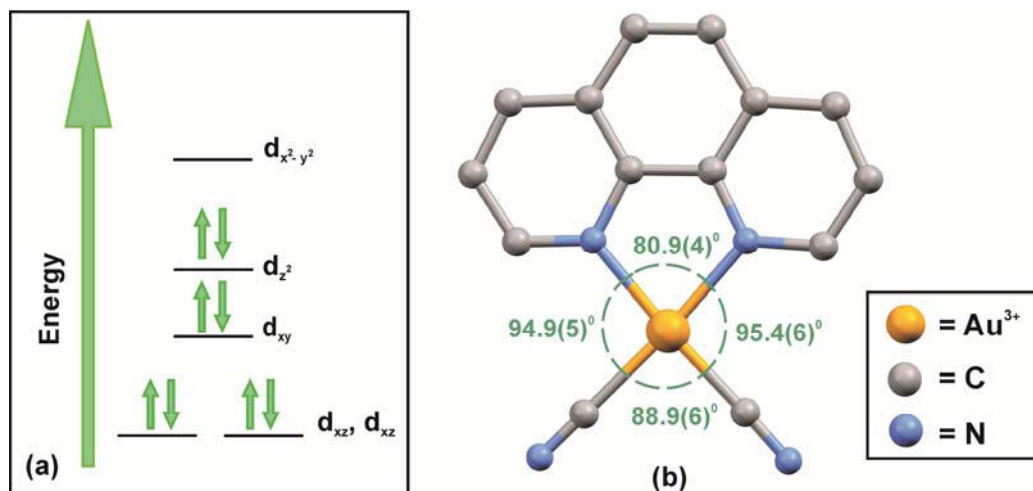


Figure 1.13: (a) Energy level diagram for square-planar gold(III) complexes. (b) X-ray crystal structure of dicyano-(1,10-phenanthroline-*N,N'*)-gold(III), a square-planar gold(III) complex.⁴³ The hydrogen atoms and counter ions were omitted for clarity.

Although the most common geometry is square-planar, five and six coordinate gold(III) complexes are known (Figure 1.14).

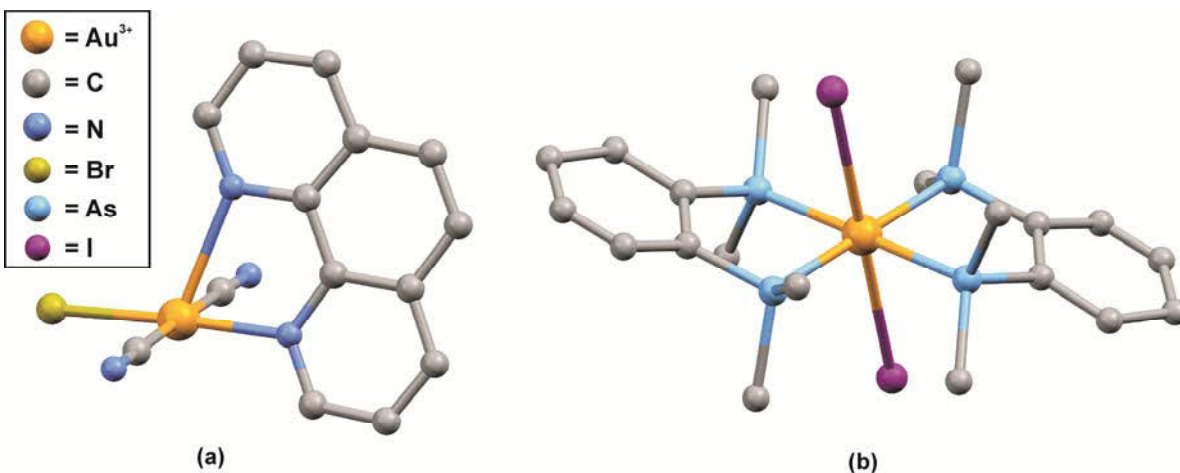


Figure 1.14: X-ray structures of (a) Bromo-dicyano-(1,10-phenanthroline-*N,N'*)-gold(III)⁴⁴ and (b) Di-iodo-bis(*o*-phenylene-bis(dimethylarsine)) gold(III).⁴⁵ These are examples of five and six coordinate gold(III) complexes, respectively. The hydrogen atoms, counterions and solvent molecules have been omitted for clarity.

1.3.2 Applications of Gold Complexes in Organic Chemistry

Although not the focus of this work, gold and gold complexes have a wide range of applications in organic synthesis. Gold-based catalysts have made various organic reactions easily accessible and in recent years there has been increased interest in gold-catalyzed transformations.⁴⁶ Described below are just a few examples of the many applications of gold-based catalysts reported in literature.

Gold can be used in organic chemistry for the selective oxidation of hydrocarbons, which is important for the sustainable exploitation of fossil fuels. Methane can be oxidized to methanol by air at room temperature and atmospheric pressure by gold complexes with a bioflavonoid rutin ligand in water, Figure 1.15.⁴⁷ According to a molecular model, activation of the aliphatic C-H bond occurs upon the oxidative addition to the gold(I) complex. The C-O bond formation is believed to be caused by hydrolysis of the C-H bond. The oxygen is involved in dehydrogenation producing hydrogen peroxide as the by-product.⁴⁷

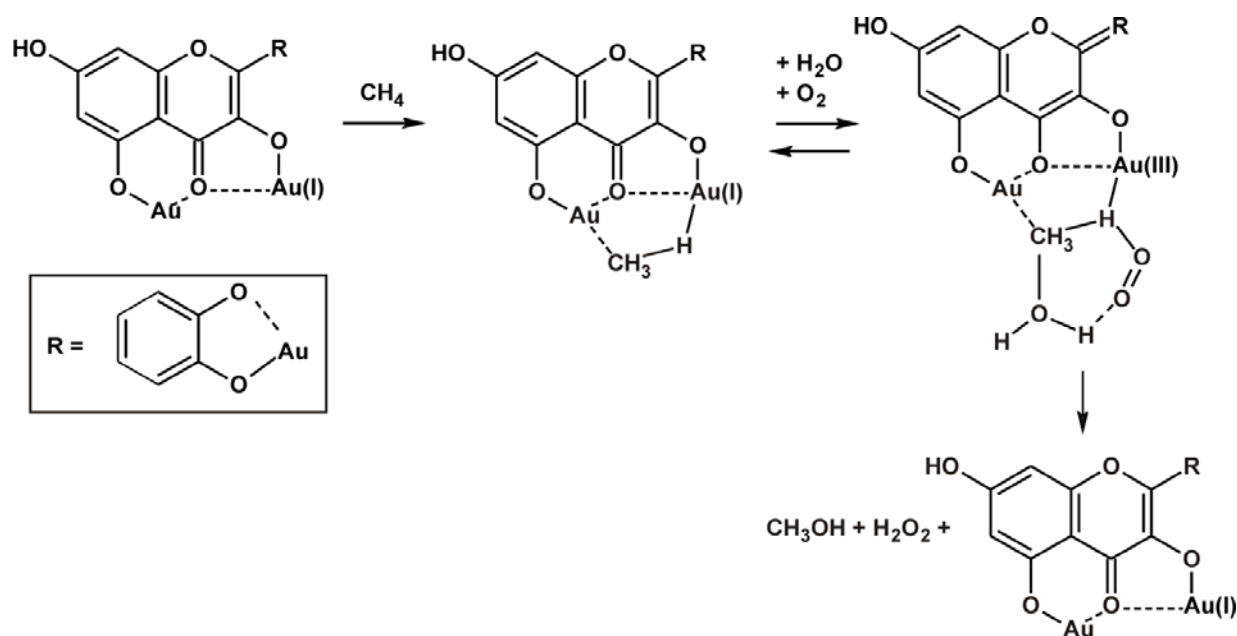


Figure 1.15: Oxidation of methane to methanol using a gold(I)-based catalyst.⁴⁷

Other gold catalysts used for the selective oxidation of hydrocarbons include the use of the heterogeneous gold catalyst, Au/Al₂O₃ which is used to oxidize cyclohexane to cyclohexanol.⁴⁸ Toluene can be oxidized using a bimetallic Au-Pd catalyst, Figure 1.16(a). This catalyst results in 100% conversion of toluene and 90% conversion to benzyl benzoate.⁴⁹ Gold catalysts such as the Au₅₅(PPh₃)₁₂Cl₆ cluster, can promote the aerobic oxidation of styrene in the presence of hydrogen peroxide or organic hydroperoxides as an oxygen chain initiator.⁵⁰ Gold can also catalyze the aerobic oxidation of alcohols as well as the selective oxidation of sugars and carbonyl compounds with catalysts such as AuAl₂O₃, AuZrO₂ and Au/C being used.⁴⁷ These extended gold surfaces and small clusters act as catalysts as they activate molecular oxygen. The catalysts activate the oxygen by absorbing it onto the gold surface. Three modes of O₂ absorption have been found: a weakly interacting end-on mode, a top-bridge-top mode and a bridge-bridge mode (Figure 1.16(b)). The highest

degree of molecular activation is achieved by bridge-bridge conformations, and the lowest activation barriers for O₂ dissociation are obtained for these species.⁴⁷

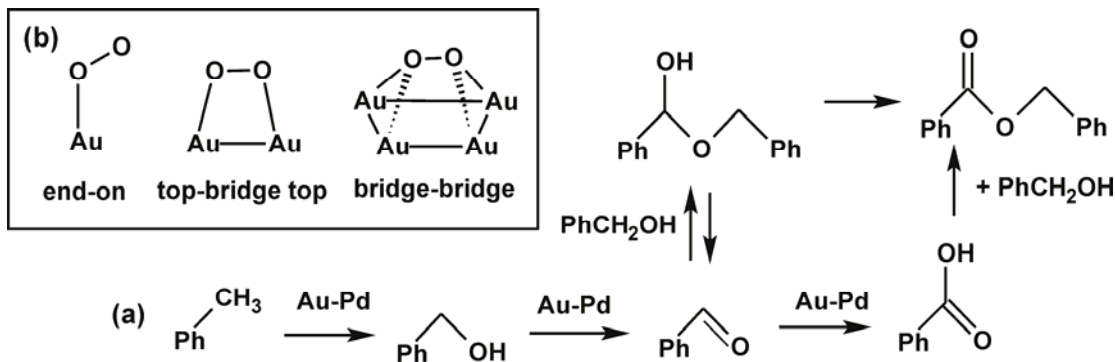


Figure 1.16: (a) Mechanism of toluene oxidation-condensation to benzyl benzoate with Au-Pd catalyst (b) Absorption modes of O₂ on gold.

Gold(I) salts catalyse nucleophilic addition reactions using nitrogen, carbon, oxygen and sulfur nucleophiles; Figure 1.17 (a) and (b). Gold(III) salts are less frequently used in catalysis than gold(I) salts as they have a high chance of forming byproducts due to their high oxidative potentials.⁴⁶ However, a bidentate 2-pyridine carboxylate gold(III) complex has been shown to be a useful catalyst in gold-mediated rearrangement cyclization reactions; Figure 1.17 (c).⁵¹

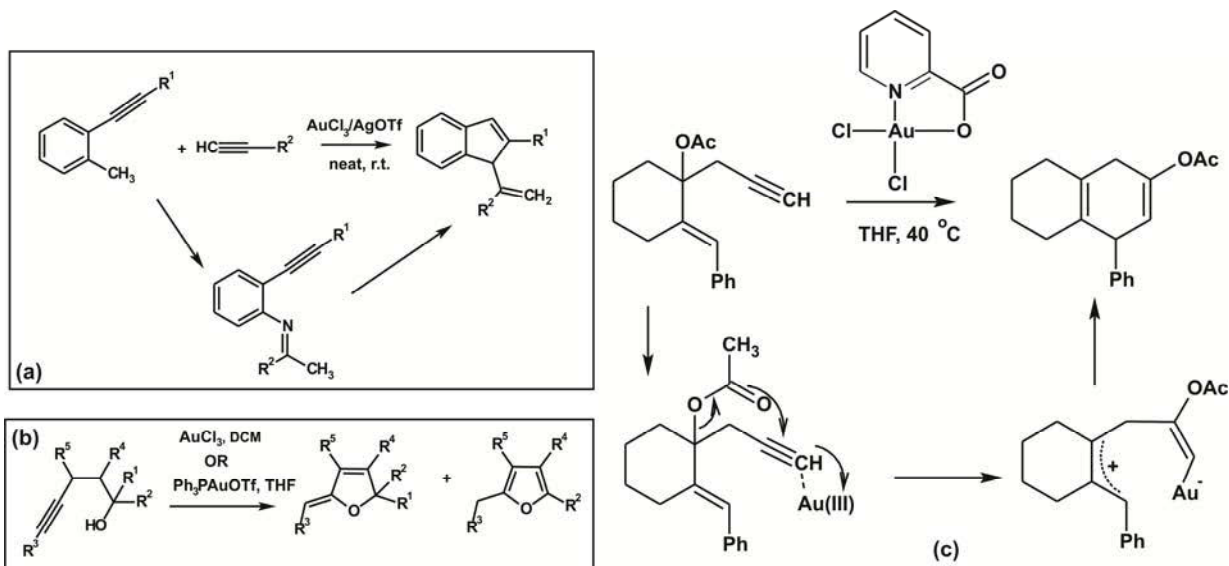


Figure 1.17: (a) Gold(I)-catalyzed nucleophilic addition using a nitrogen nucleophile⁵² (b) Gold(I)-catalyzed nucleophilic addition using an oxygen nucleophile.⁵³ (c) Gold(III)-catalyzed cyclization reaction.⁵¹

1.3.3 Medicinal Applications of Gold

1.3.3.1 Medicinal History of Gold

Gold has been used for its medicinal properties throughout ancient civilization with reports of Indian and Egyptian civilizations exploiting this metal to cure diseases and ward off evil spirits. The earliest medicinal application of gold dates back to 2500 B.C. where the Chinese used gold to treat smallpox, skin ulcers and measles.⁵⁴ At this time gold was associated with immortality and longevity and even today Japanese culture promotes placing thin gold foils into tea and foods as being beneficial to human health.⁵⁵

The first gold complex discovered as a potential therapeutic was gold cyanide $K[Au(I)(CN)_2]$, by bacteriologist Robert Koch in 1890.⁴ This drug was effective against mycobacteria, the causative agent of tuberculosis. Although effective against pulmonary tuberculosis, the drug was toxic and had to be dropped in favour of the less toxic gold(I) thiolate complexes which were also used for the treatment of rheumatoid arthritis. These gold(I) thiolate complexes had been discovered in the 1930s by Jacques Forestier and were being used for the treatment of rheumatoid arthritis, an autoimmune inflammatory disease which leads to erosion of joints, immobility and pain.³ The most effective gold thiolate complexes were aurothiomalate (Myochrysin) and aurothioglucose (Solgonal), Figure 1.18(a) and (b).⁵ Although effective for the treatment of rheumatoid arthritis, the gold accumulates in the kidneys, resulting in nephrotoxicity.⁵⁴ Thus, an important requirement for new therapeutic gold complexes was the ability to be administered in low doses on a daily basis which would in turn reduce the toxicity and improve the therapeutic response of the drug.⁵⁶ With this in mind, the drug, auranofin (Figure 1.18(c)), a triethylphosphine gold(I) complex, was synthesized for the treatment of rheumatoid arthritis. Although this drug can be administered on a daily basis, it does have reduced effectiveness when compared to other drugs.⁵⁵ In general, treatment with gold complexes results in side effects including dermatitis, diarrhea and problems with internal organs such as kidneys and lungs. Thus, gold(I) drugs are used as a last resort for severe cases of rheumatoid arthritis.⁵⁷

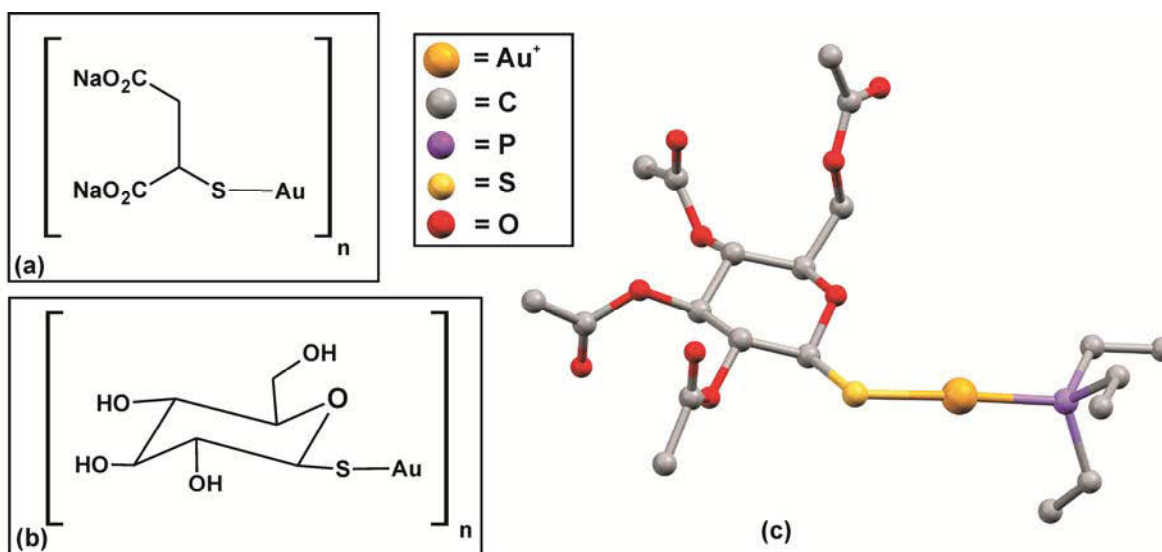


Figure 1.18: Structure of the drugs (a) aurothiomalate and (b) aurothioglucose. (c) X-ray structure of auranofin. Hydrogen atoms have been omitted for clarity.⁵⁸

Since the development of auranofin in 1985, there have been no clinically approved gold-based drugs for any disease.⁵⁵ However, this being said, in the last few decades, gold complexes have been tested against human immunodeficiency virus (HIV) for the treatment of Aids⁵⁹ while there are promising results using gold complexes in the treatment of malaria⁶⁰, Chaga disease⁶¹ and importantly, cancer.⁶² Gold also has application in microsurgery of the ear. Gold is often used in implants that are at risk of infection such as the inner ear as the metal has shown such a high degree of resistance to bacterial colonization.⁵⁵

1.3.3.2 Gold(I) Complexes as Potential Anti-Cancer Drugs

A long-term study indicated that rheumatoid arthritis patients treated with gold-based drugs have no increased risk of developing cancer and actually have a lower malignancy rate.⁶³ This indicated that these gold(I) drugs may actually act as chemotherapeutics and resulted in numerous studies in this area of research. Auranofin and its analogues were shown to be active against melanoma and leukemia cell lines *in vitro* and leukemia cell lines *in vivo*. However, the complexes were inactive against solid tumours.⁶⁴ The main observations from this study are summarized below:

- Lack of efficacy of a drug *in vitro* correlates well with lack of anti-cancer activity.
- Efficacy of a drug *in vitro* does not necessarily correlate to *in vivo* efficacy.
- Antitumour activity *in vivo* is optimized by ligation of gold(I) with a substituted phosphine.

This study led to the development of a series of digold phosphine complexes such as gold(I) 1,2-bis(diphenylphosphine) ethane. These complexes showed *in vitro* and *in vivo* cytotoxicity, and were even active against cisplatin-resistant cell lines.⁶⁵ Unfortunately, these compounds exhibited severe cardiotoxicity in animal studies and thus no further clinical studies took place.

Mechanistic studies indicate that, unlike cisplatin, DNA is not the primary target of gold(I) complexes. Gold(I) complexes act as pro-drugs. A pro-drug is a drug that is administered in an inactive form and is then converted to an active form through either normal metabolic processes or through an external stimulus. Gold(I) drugs are metabolised generating the active species coordinated to a biologically relevant thiol.⁵⁷ For auranofin, the metabolic pathway possibly involves Au-S cleavage and coordination to the albumin from the blood. Further metabolism is believed to involve reduction of the original albumin, coordination of another thiol and oxidation of the phosphine with concomitant Au-P bond cleavage. The result of this is that a gold(I) ion embedded in a ball of protein is delivered to the inflammation site. Several biological targets for auranofin's anti-inflammatory and anti-cancer activities were identified by mechanistic studies. Auranofin has been shown to inhibit DNA, RNA and protein synthesis.⁶⁶ Other studies showed that auranofin can form reactive oxygen species (ROS) in leukemia and ovarian cells.⁶⁷ Auranofin can also inhibit mitochondrial thioredoxin reductase⁶⁸ and cathepsin B.⁶⁹ Inhibition of these targets results in cell death.

1.3.3.3 Gold(III) Complexes as Potential Anti-Cancer Drugs

Gold(III) is an obvious choice of metal for use in chemotherapy as it is isoelectronic and isostructural to platinum(II) possessing the same d^8 electronic configuration and predominantly exhibits a square-planar coordination geometry.⁷⁰ Despite this, gold(III) complexes have not been as well investigated as gold(I) complexes. This is largely due to their high redox potential and poor stability, resulting in reduction of gold(III) to gold(I) and gold(0) under physiological conditions.⁷¹ The breakthrough in gold(III) chemistry came

when it was determined that gold(III) could be sufficiently stabilized using appropriate nitrogen donor multidentate ligands.⁷² The chelating effect and the electron-donating ability of these ligands induce a large stabilization effect for the +3 oxidation state. This led to gold(III) compounds becoming the subject of increasing anti-cancer research.⁵⁵

As gold(III) complexes structurally resemble cisplatin, they were expected to have the same molecular target, DNA. Thus various modeling studies have been performed and show that probable target sites for the gold(III) ion are the N(1), N(7) atoms of adenosine, N(7) or C(6)O of guanosine, N(3) of cytidine and N(3) of thymidine, which are the same binding sites as those of platinum(II).⁷³ Experimental evidence is, however, puzzling, with some research showing clear evidence of direct DNA damage and apoptosis induced by gold(III) complexes while other reports have shown that *in vitro* interactions of some gold(III) complexes with calf thymus DNA are weaker than their platinum analogues.⁵⁵ The inconsistency of the experimental evidence indicates that intracellular DNA might not be the primary or exclusive biological target for gold(III) complexes.⁵⁵ In addition to DNA, mitochondria have been suggested as a major target of gold(III) complexes. These compounds inhibit mitochondrial thioredoxin reductase which influences membrane permeability properties resulting in cell death.⁵⁵ Proteins are also reportedly targets for gold(III) complexes and interactions between gold(III) complexes and model proteins or target proteins have been reported.⁵⁵ Examples of gold(III) complexes tested for anti-cancer activity and their mechanism of action, where known, are reported below.

Gold(III) complexes with Au-N bonds that were tested for their anti-cancer activity are described below. Gold chloride species with pyridine ligands showed good cytotoxic activity although their use is limited as the chloride ligand undergoes hydrolysis in aqueous buffer media.⁷⁴ The bipyridine complexes $[\text{Au}(\text{bipy})(\text{OH})_2][\text{PF}_6]$ and $[\text{Au}(\text{bipy}^{\text{c}}\text{-H})(\text{OH})][\text{PF}_6]$ are both cytotoxic and stable in physiological buffer at 37 °C.⁷⁵ These complexes are shown in Figure 1.19(a).

Gold(III) terpy complexes have shown promising anti-cancer activity. A study has shown that the DNA binding affinity of four gold(III) terpy complexes correlated well with their cytotoxicity in a variety of cancer cell lines suggesting that intracellular DNA is their primary target *in vitro*. Guo *et al.* investigated the possibility of DNA intercalation when they synthesized gold(III) complexes from terpyridine derivatives, Figure 1.19(b), with each complex having different steric and electrostatic effects.⁷⁶ One of the complexes contained a neutral triphenylphosphine moiety, yielding a highly positive chelate while another complex contained a 2-naphthol moiety. The third complex synthesized contained a 2-bromoethanesulfonic moiety which lowered the charge of the complex and improved water solubility. All the complexes exhibited cytotoxic activity with the most highly charged triphenylphosphine complex being the most cytotoxic.⁷⁶ The next most cytotoxic complex was the more water soluble 2-bromoethanesulfonic complex with the bulky 2-naphthol complex being the least cytotoxic. The study showed that the steric and electrostatic effects of the ligands influence the DNA binding affinity of complexes.⁷⁶ Thus the study showed:

- Large steric bulk decreases DNA affinity.
- A higher positive charge on the complex leads to increased DNA affinity.

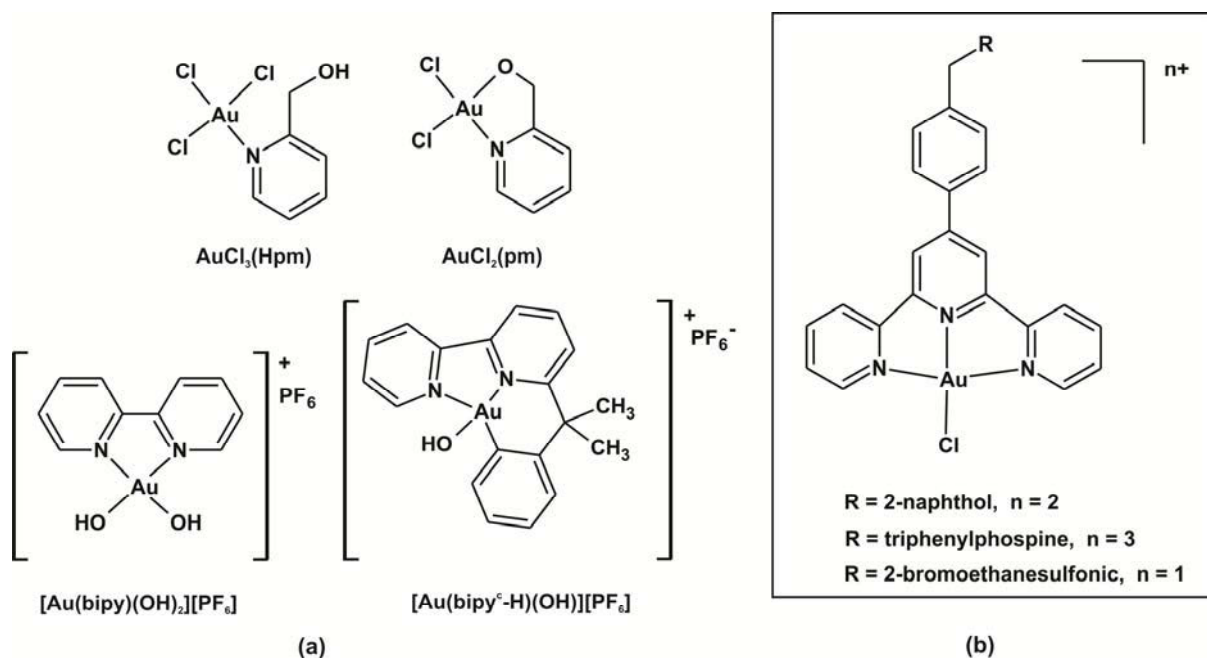


Figure 1.19: (a) Gold(III) complexes with Au-N bonds tested for anti-cancer activity. (b) Gold(III) terpy derivatives.

A study was also done on the *in vivo* activity of the gold(III) complexes shown in Figure 1.20; $[\text{Au}(\text{en})_2]\text{Cl}_3$, $[\text{Au}(\text{dien})\text{Cl}]\text{Cl}_2$, $[\text{Au}(\text{cyclam})](\text{ClO}_4)_2\text{Cl}$, $[\text{Au}(\text{terpy})\text{Cl}]\text{Cl}_2$ and $[\text{Au}(\text{phen})\text{Cl}_2]\text{Cl}$. These complexes were tested against the A2780 ovarian cancer cell line and a cisplatin-resistant variant.^{70,75} All these complexes contained at least two nitrogen atoms directly coordinated to the gold(III) centre which leads to a decrease in the reduction potentials. Table 1.3 contains the IC_{50} values of these gold(III) chelates.

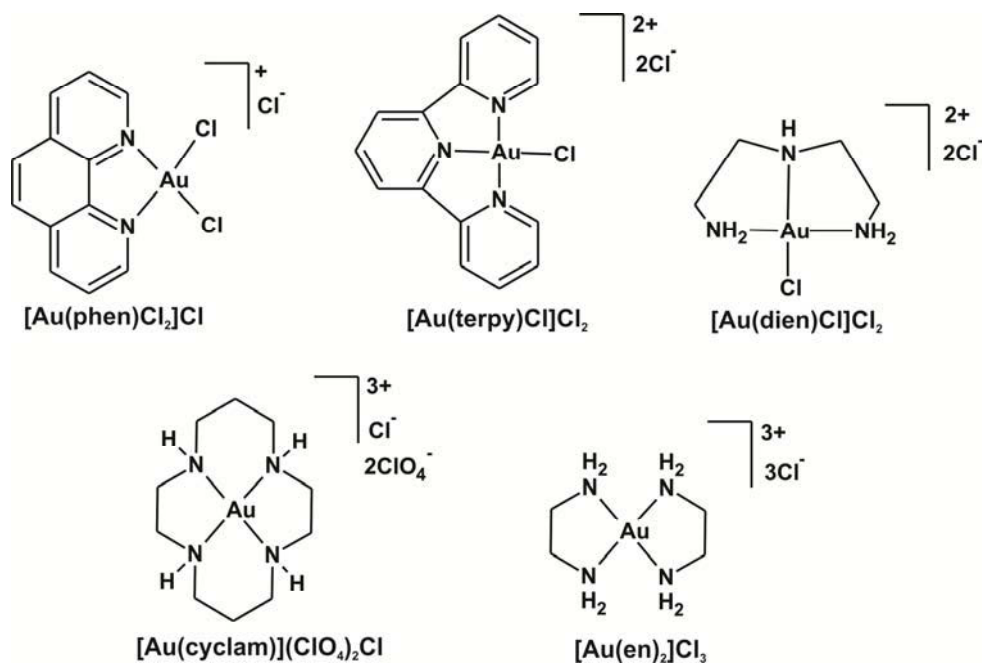


Figure 1.20: Gold(III) chelates tested for anti-cancer activity in a study by Messori and co-workers.⁷⁰

Table 1.3: IC₅₀ values of various gold(III) complexes against the human ovarian carcinoma A2780 cell line, both cisplatin sensitive and cisplatin resistant variants.^{70,75}

Complex	IC ₅₀ (μM) (±SE)	
	A2780/S	A2780/R
[Au(en) ₂]Cl ₃	8.36± 0.77	17.0± 4.24
[Au(dien)Cl]Cl ₂	8.2 ±0.93	18.7± 2.16
[Au(cyclam)](ClO ₄) ₂ Cl	99.0	>120
[Au(terpy)Cl]Cl ₂	0.2	0.37± 0.032
[Au(phen)Cl ₂]Cl	3.8± 1.1	3.49± 0.91

The results from Table 1.3 show that all the investigated complexes, apart from Au(cyclam), are cytotoxic toward the A2780 line with IC₅₀ values falling in the micromolar and sub-micromolar range (from 0.2 to 10 μM) with the three most active complexes being active against the cisplatin-resistant cell line.^{70,75} The relative order of cytotoxicity is: [Au(terpy)Cl]Cl₂ » [Au(phen)Cl₂]Cl > [Au(en)₂]Cl₃, [Au(dien)Cl]Cl₂ » [Au(cyclam)](ClO₄)₂Cl. Interestingly, although the coordination mode of the gold(III) ion is the same in all the complexes, only the two most active complexes, terpy and phen, have ligands with a planar structure. The results also show that the presence of a good leaving group, in this case the chloride ligands, is not an essential requirement for biological activity, as [Au(en)₂]Cl₃ with no gold(III)-bound chlorine ligands was equally as cytotoxic as [Au(dien)Cl]Cl₂ with a gold(III)-coordinated chloride ligand. Other results also showed that [Au(en)₂]Cl₃ and [Au(dien)Cl]Cl₂ are more cytotoxic than the analogous [Pt(en)₂]²⁺ and [Pt(dien)Cl]⁺ compounds with IC₅₀ values of 1684 and 271 μM, respectively against the cell line L1210.⁶⁴ This indicates that gold(III) plays an important role in producing the cytotoxic effect. [Au(cyclam)](ClO₄)₂Cl showed minimal cytotoxicity, which may be due to its low reactivity with the gold(III) ion tightly bound by the macrocycle cage. There is no direct correlation between cytotoxicity and reduction potential. In general, the amine complexes; [Au(en)₂]Cl₃, [Au(dien)Cl]Cl₂ and [Au(cyclam)](ClO₄)₂Cl have reduction potentials in the range of 200 – 600 mV. [Au(cyclam)](ClO₄)₂Cl is the most stable of these complexes owing to the macrocyclic effect. [Au(terpy)Cl]Cl₂ and [Au(phen)Cl₂]Cl are less stable than their amine-coordinated counterparts with reduction potentials of 0.62 and 0.80 V, respectively. In summary, to highlight some of the important findings in this study:

- The gold(III) centre is required for cytotoxicity.
- The presence of good leaving groups is not essential for activity.
- There is no direct correlation between cytotoxicity and reduction potentials.
- Excessive stabilization of the gold(III) centre may lead to loss of activity.

Consequently, although tetradentate ligands have been widely used to stabilize gold(III), the cytotoxicity of most gold(III) tetradentate ligands had been unexplored until the report on promising anti-cancer activity of gold(III) porphyrin compounds in 2003.⁷⁷ An X-ray crystal structure of a gold(III) porphyrin complex is shown in Figure 1.21(a). The porphyrin ligand is dianionic and is a very strong chelator; it has a rigid structure that stabilizes the gold(III) porphyrin complex against reduction, as indicated by the large and negative reduction potentials of the [Au(III) porphyrin]⁺⁰ couple.⁷⁷ These complexes exhibit a 100-fold greater cytotoxicity relative to cisplatin against a number of human cancer cell lines with IC₅₀ values in the range of 0.1–1.5 μM.⁷⁷ The gold(III) porphyrin complex has also shown promising *in vivo* activity against various types of nasopharyngeal carcinoma (NPC) by suppressing tumour growth without observable side-effects. Once treatment with the gold(III) porphyrin complex was terminated, tumour growth resumed.⁷⁸

On comparing the IC_{50} values of a series of substituted gold(III) porphyrin complexes: $[Au(\textit{para}\text{-}Y\text{-}TPP)]Cl$ ($Y=H, Me, OMe, Br$ and Cl), it was determined that the *para*-substituent of the meso-phenyl rings has little effect on the cytotoxicity, Figure 1.21(b).⁷⁷ The gold(III) porphyrin complex exhibits specificity towards cancerous cells as it exhibits at least a 10-fold higher cytotoxicity to cancer cells than normal cells.⁵ It was determined that the gold(III) ions played an important role in the anti-cancer activity of the complexes as the zinc(II) porphyrin complex was at least 100-fold less cytotoxic than the analogous gold(III) complex. The porphyrin ligand is also vital for the cytotoxicity as both $K[AuCl_4]$ and $Bu_4N[AuCl_4]$ are 30-90 times less effective chemotherapeutic agents than the gold(III) porphyrin as the gold(III) ion readily undergoes reduction to colloidal gold(0) under physiological conditions. Che *et al.*^{5,77} propose that the porphyrin stabilizes the gold(III) and the complex acts as a lipophilic planar cation for binding through non-covalent interactions to biological targets.

Che *et al.* determined that the gold(III) porphyrin complex induced cytotoxicity in nasopharyngeal carcinoma (NPC) cells via an apoptotic pathway, Figure 1.21(c). This was determined using confocal microscopy and other techniques. Using these techniques, characteristic apoptotic morphological changes were detected such as: the formation of apoptotic bodies, chromatin condensation and DNA fragmentation.^{77,79} This apoptotic pathway was determined as a mitochondria-mediated pathway.⁷⁹ Functional proteomic studies indicated that there was a change in the expression of several proteins, such as those proteins involved in energy production and cellular redox balance, after treatment with the gold(III) porphyrin complex. Alteration of these proteins indicated that mitochondria may play a role in the gold(III) porphyrin induced apoptosis. Further proof was the quick reduction of the mitochondria membrane potential after treatment with the complex. The complex reduces the membrane potential by activating P38MAPK phosphorylation. The loss of mitochondria membrane potential is linked with the release of cytochrome *c* and apoptosis-inducing factor (AIF) from mitochondria into the cytoplasm, resulting in apoptosis.⁷⁹ Loss of mitochondrial membrane potential is also associated with accumulation of reactive oxygen species (ROS).

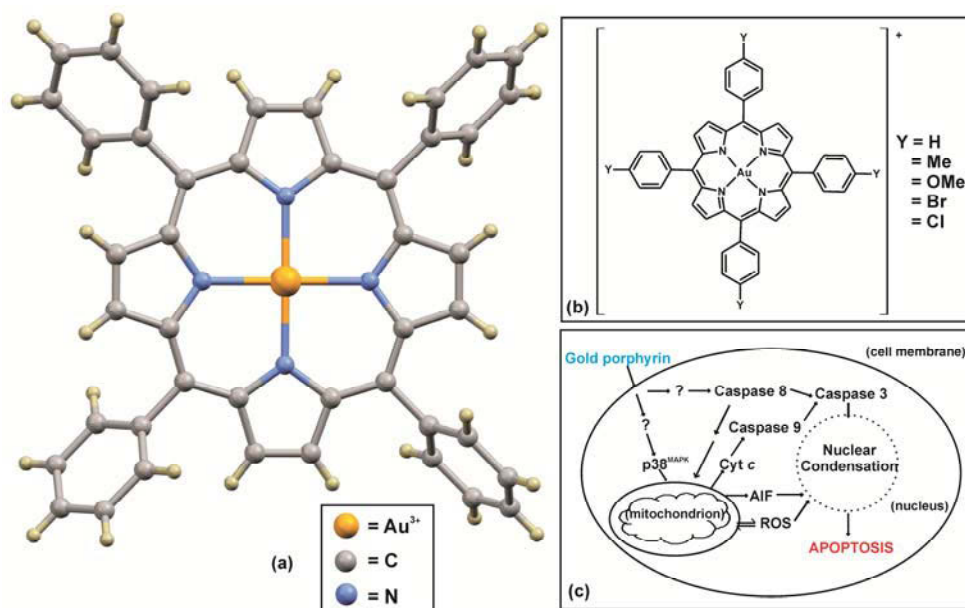


Figure 1.21: (a) X-ray crystal structure of a gold(III) porphyrin, the counterion is omitted for clarity.⁷⁷ (b) Schematic diagram of a gold(III) porphyrin with various substituents in the *para* position of the meso-phenyl rings. (c) Proposed model for the cellular mechanism of gold(III) porphyrin-induced apoptosis in NPC cells.⁵

In our work group a variety of gold(III) bis(pyrrolide-imine) Schiff base complexes have been studied as potential anti-cancer agents, Figure 1.22.⁸⁰ The ligands comprise two pyrrole rings joined by a synthetically variable di(azomethine) linkage. Some of the complexes were highly cytotoxic and in many cases more cytotoxic than cisplatin. These complexes have IC₅₀ values ranging from 9.3 to 30.9 μM.⁸⁰ Experimental evidence showed that these complexes exert their cytotoxicity through topoisomerase II poisoning and inhibition, an unusual dual mode of action.⁸⁰

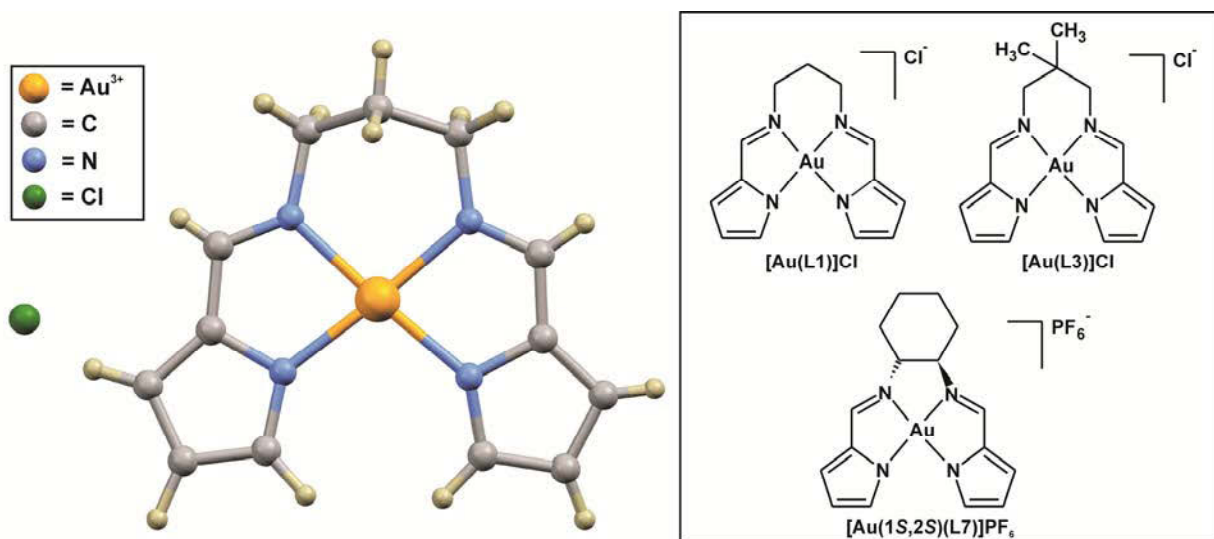


Figure 1.22: X-ray crystal structure of [Au(L1)]Cl and schematic of gold(III)bis(pyrrolide-imine) Schiff base complexes that went through 5-dose screening at the National Cancer Institute (NCI).

Gold(III) complexes with Au-S bonds that have been tested for anti-cancer activity include gold(III) dithiocarbamate complexes with these complexes being more cytotoxic than cisplatin, Figure 1.23(a). They are stable under physiological conditions and have been shown to bind to DNA.⁸¹ These gold(III) dithiocarbamates reportedly stimulate the production of ROS and can modify mitochondrial function, resulting in cell death.⁸²

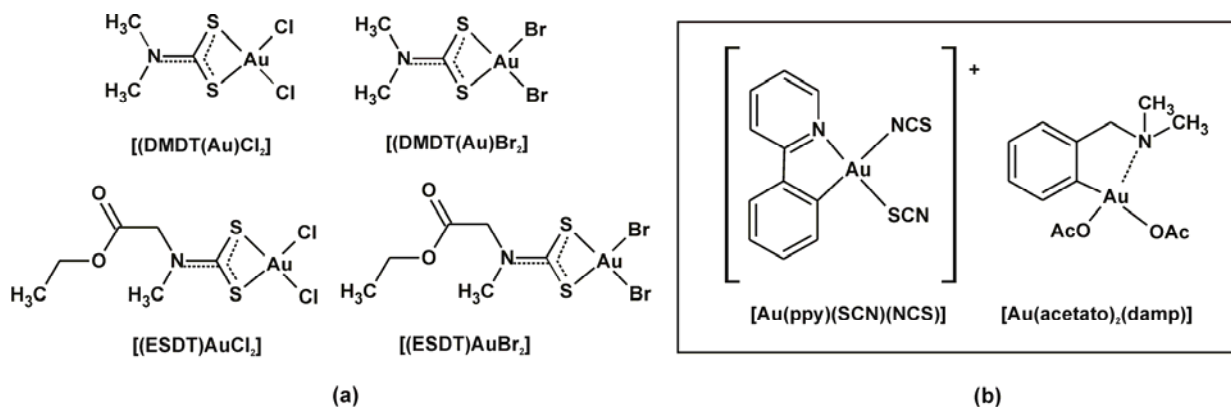


Figure 1.23: Gold(III) complexes with (a) Au-S bonds and (b) Au-C bonds that have been tested for anti-cancer activity.

Gold(III) complexes with Au-C bonds (Figure 1.23(b)) have also shown promising anti-cancer activity with a series of 2-phenylpyridine gold(III) complexes with various thiolate ligands exhibiting greater cytotoxicity than cisplatin *in vitro*.⁸³ Gold(III) complexes with 2-[(dimethylamino)methyl]phenyl (damp) ligand showed promising results both *in vitro* and *in vivo* with activity comparable to that of cisplatin and were equally active against cisplatin-resistant cell lines.⁸⁴ Fricker *et al.* showed that these Au(damp) complexes target proteins and have a preference for S-donor ligands such as glutathione and cysteine, with only limited reactivity against DNA bases.⁶⁴ They report that gold(III) complexes can cleave the di-sulfide bond of cysteine and can oxidize methionine and glycine suggesting that gold(III) can deaminate the amino terminus of peptides and proteins.⁵⁵

In conclusion, this section has described the chemistry of gold as well as the medicinal applications of gold complexes with a focus on gold(III) complexes as anti-cancer agents. Gold(III) forms d^8 square-planar complexes that are isoelectronic and isostructural with platinum(II) with these complexes showing cytotoxicity equal to or greater than that of cisplatin. Although the gold(III) chelates are anticipated to have a different mode of action compared to that of cisplatin, they have been compared as cisplatin is the most widely used metal-based anti-cancer agent. There appears to be no single primary biological target of gold(III) complexes as studies on different compounds have typically reached different conclusions and multiple targets appear to be the norm. It was previously thought that gold(III) was a difficult metal ion to work with as it readily reduces to its elemental state and is unstable under physiological conditions. However, it has been reported that certain ligands can stabilize gold in the +3 oxidation state under physiological conditions. This brings us to our next section: macrocycles. The complexes synthesized in this study are gold(III) macrocyclic complexes with the macrocyclic ligand serving to stabilize the gold(III). This next section gives a description of macrocycles and their importance in coordination and biological chemistry.

1.4 Macrocyclic Chemistry

There has been remarkable growth in the study of macrocycles and their complexation chemistry with a wide variety of metal ions in recent years.⁸⁵ A macrocyclic compound is defined as a cyclic compound with nine or more members (including hetero atoms) and with three or more donor atoms.⁷ This group of compounds encompasses porphyrins, corrins, cyclic polyethers, cryptands, phthalocyanines and other cyclic systems. The interest in macrocycles, especially porphyrins and corrins, is due to their relation to biological macrocyclic systems such as heme, cytochromes, and chlorophyll, and because of their application as dyes.⁷

The study of macrocyclic chemistry has not always been popular and it took a few decades for scientists to realize the importance of this group of compounds. Before 1960 there was little development in the coordination chemistry of macrocyclic compounds while in the early 1960s several independent work groups reported the synthesis of a variety of coordinated macrocyclic complexes.⁸⁶⁻⁸⁸ This led to the publishing of a review article covering the new synthetic approaches of macrocyclic complexes in 1964⁸⁹ which drew attention to the relationship these compounds had to biologically important species and that they may behave as models for important natural products. This led to a rapid expansion in the field of coordination chemistry of macrocyclic complexes; however, there was little variety in the compounds studied resulting in a narrow expansion of the field. The breakthrough in coordination macrocyclic chemistry came in 1967 when Pedersen⁹⁰ reported a new series of macrocyclic compounds which could coordinate metal ions. This series

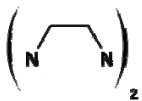
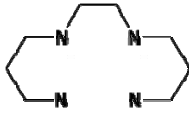
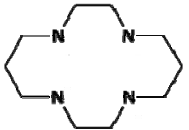
was the cyclic polyethers, otherwise known as the 'crown' compounds. These compounds have a variety of ring sizes, a number of ether oxygens and substituent groups and they could strongly coordinate alkali and alkali earth metals. This led to a broadening of the macrocyclic chemistry field using metal ions and donor atoms not previously investigated. Lehn and co-workers⁹¹ synthesized the first macropolycyclic complexing agents or cryptands shortly after the crown compounds were reported.

This section gives a brief description of the macrocyclic effect, explanation of factors that affect coordination of a macrocyclic ligand to a metal centre and the biological importance of this class of compounds. This information is important in understanding the choice of ligand system for this work.

1.4.1 The Macrocyclic Effect

Cabbiness and Margerum⁹² reported greater stability for the complexes of cyclic ligands compared to similar open-chain ligands and they named this the 'macrocyclic effect'. The authors investigated copper(II) complexes of cyclic tetramine ligands and compared them to their linear analogues. The results showed the cyclic ligands were ten times more stable than the linear counterparts. Similar results have been seen with cyclic polyethers and their open chain analogues. Table 1.4 illustrates the macrocyclic effect with stability of Cu(II) tetramine complexes.

Table 1.4: Stability of complexes of Cu²⁺ with tetramine ligands in water.⁹³

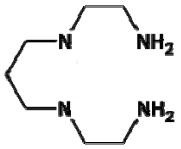
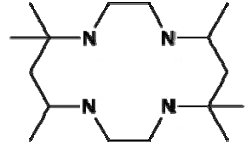
Ligand	log K
	19.7
	20.1
	24.8

It has been established that the chelate effect is of entropic origin.⁹⁴ Although the macrocyclic effect is extrapolated from the chelate effect, there has previously been no agreement as to whether the macrocyclic effect is due to more favourable enthalpy or entropy terms in the reactions. Margerum *et al.*⁹⁵ found the enthalpy term to be responsible for the observed macrocyclic effect when the formation of Ni(II) complexes of cyclam and those of 2,3,2-tet were compared. However, both Paoletti *et al.*^{93,96} and Kodama and Kimura^{97,98} found that the entropy term was the dominant term responsible for the macrocyclic effect using Cu(II) complexes of cyclen and 2,2,2-tet. Paoletti *et al.* later concluded that the relative magnitude of the enthalpy contribution is dependent on the match between cation and ligand cavity sizes for transition metal.⁹⁹ More recently it has been determined that these conflicting reports are dependent on the experimental methods used to determine the thermodynamic parameters, namely: the calorimetric titration method and the use of the temperature variation of the stability constants. It has been found that factors

such as solvation and conformation changes upon bond formation contribute to the enthalpic term, while the number of species present and solvation effects, contribute to the entropic term.^{100,101}

Busch *et al.*¹⁰² attribute the macrocyclic effect to 'multiple juxtapositional fixedness' which is based on the fact that the stability of macrocyclic complexes is due to their slow decomposition rates. Cabbiness and Margerum¹⁰³ reported that the rate of decomposition of the Cu(II) cyclic tetramine complex is much slower than its linear counterpart, as shown in Table 1.5. This low decomposition rate is enough to more than make up for the less favourable formation rate of the cyclic ligand. These results support the hypothesis that open-chained ligands can undergo consecutive S_N1 replacement steps of the nitrogen donors by solvent molecules, beginning at one end of the ligand. In acid media these donor atoms would be readily protonated, hindering complexation. Cyclic ligands, on the other hand, cannot follow the same mechanism because there is no end to the ring and a bimolecular substitution reaction has been proposed. This would involve the distortion of the ligand to weaken and finally break one coordination bond. This leads to enhanced stability even when the metal ion does not fit into the cavity of the macrocycle.

Table 1.5: Kinetic data for Cu(II) complexes at 25 °C¹⁰³

Ligand	Solvent	$k_f (M^{-1}s^{-1})$	$k_d (s^{-1})$
	H ₂ O	8.9×10^4	4.1
	H ₂ O	5.8×10^{-2}	3.6×10^{-7}

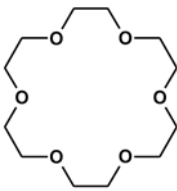
1.4.2 Factors Effecting Coordination of Macrocycles to Metal Ions

1.4.2.1 Relative Sizes of Cation and Ligand Cavity

Investigations involving the coordination of crown ethers to metal centres indicated that the ligands coordinate more strongly to metal ions whose ionic crystal radius best matches the radius of the cavity formed by the ring upon complexation.⁹⁰ It is thought that bond energies between ligand and cation will be greatest when all donor groups can fully contribute. If the cavity is too large the metal ion will fall through or if the ring is too small the metal ion may not fit. X-ray crystallography has been a key technique in these studies and allows the position of atoms to be accurately measured and the best ring cavity size to be calculated.¹⁰⁴

Table 1.6 illustrates that in the case of 18-crown-6, there is increased stability of the complexes of K(I) and Ba(II), where the cavity size matches the metal ion radius. This stability is mainly due to the enthalpy term, which corresponds to the greater electrostatic bond energy for ions that better fit the ligand cavity.¹⁰⁵

Table 1.6: Thermodynamic parameters for the formation of 18-crown-6 complexes with metal ions in H₂O at 25 °C.^{106,107}

Ion	Crown	Dia. M ⁿ⁺ /Dia. cavity	log K	ΔH (kcal mol ⁻¹)	TΔS (kcal mol ⁻¹)
Na ⁺		0.74	0.80	-2.25	-1.16
K ⁺		1.00	2.03	-6.21	-3.40
Rb ⁺		1.08	1.56	-3.82	-1.7
Cs ⁺		1.20	0.99	-3.97	-2.6
Sr ²⁺		0.80	2.72	-3.61	0.1
Ba ²⁺		1.00	3.87	-7.58	-2.30

1.4.2.2 Arrangement of Ligand Binding Sites

Coordination of metal ions may be affected by the arrangement of ligand binding sites. Larger macrocyclic ligands may be able to fold in such a way as to leave no real cavity and even small macrocycles may be fairly flexible. Macrobicyclic ligands have a wider range of selectivity than cyclic polyethers as they are more rigid over a larger range of cavity sizes.

Lehn *et al.*¹⁰⁸ concluded that rigid ligands display peak selectivity and can distinguish between cations which are too small or too large for their cavity. Distortion of a rigid ligand by contraction or by expansion of the cavity leads to destabilization. The authors also determined that flexible ligands exhibit plateau selectivity where the ligands have poor discrimination between metal ions and can accommodate larger metal ions without major variation in binding energy.¹⁰⁸

1.4.2.3 Type and Charge of Cations

The coordination chemistry of macrocycles to alkaline and alkaline earth metal ions has been well studied.⁷ The binding of these metals to macrocyclic ligands has been determined as electrostatic in nature with basic ligand groups distributing themselves evenly over essentially a sphere of positive charge leading to a broad variation in coordination geometry. The size of alkaline and alkaline earth metals affects their complexing ability and characteristics. Smaller ions such as Li(I) are strongly solvated and need more energy to desolvate than larger ions such as Cs(I). However, smaller cations are able to attract and organize ligands more effectively than larger ions. These two effects cause the stabilities of the complexes of the small and large metal ions to be smaller than for those metals of intermediate size. Metal ions in other parts of the periodic table have not been as well studied.⁷

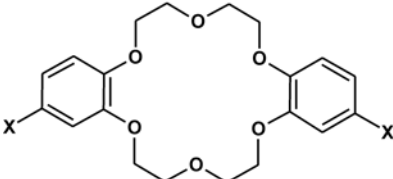
1.4.2.4 Type and Number of Donor Atoms

Electronic effects which influence the binding of metal ions by macrocycles are: charge, polarity, and polarizability of the donor atoms. This means ion pair interactions for negatively charged ligands, ion-dipole and ion-induced interactions for neutral ligands as well as hard-soft acid-base theory all influence chelation of metal ions by macrocyclic ligands.¹⁰⁹ Donor atoms such as nitrogen, phosphorus and sulfur, favour chelation of transition metals while oxygen is a more favourable donor atom for alkaline or alkaline earth metal ions.

1.4.2.5 Substitution on the Macrocyclic Ring

Substitution on the macrocyclic ring can also affect coordination of the macrocycle to metal ions. Schori and Jagur-Grodzinski¹¹⁰ reported that the dinitro derivative of dibenzo-18-crown-6 has less affinity for Na(I) when compared to the unsubstituted ligand in DMF, as shown in Table 1.7. The nitro group is electron-withdrawing and delocalizes electrons from the oxygen atoms. An amino group, on the other hand, is an electron-donating group and will lead to an increase in the stability of a complex. Panell *et al.*¹¹¹ investigated the effect of aromatic substitution on dibenzo-18-crown-6 in dichloromethane. The normal selection for K(I) over Na(I) for this compound was inverted when a strong-electron withdrawing substituent was added. These results suggest that aromatic substituents play a role in determining the selectivity and strength of cation chelation due to their donor basicity. The rate of chelation of tetramines with Cu(II) and Ni(II) in water can also change with a change in the number and position of methyl substituents.¹¹²

Table 1.7: Formation constants of substituted benzo-Crowns with Na(I).¹¹⁰

Crown	X	Log K
	H	2.69
	NH ₂	2.76
	NO ₂	1.99

1.4.2.6 Solvent

Changing the solvent can change the binding properties of ligands as they must compete with the solvent for the cations. Solvents with low solvating ability and dielectric constants will lead to greater complex stability than those that strongly solvate the cations. Changing the solvent may vary the preference of the cation for one macrocycle over another. Friendsdorff reported higher stability constants of cyclic polyethers with metal cations in methanol compared to water.¹¹³ Izatt *et al.*¹⁰⁷ have varied the composition of water/methanol solvent systems when studying the reaction of 18-crown-6 with various cations. They reported that the increased stability of the complex in methanol is explained by the fact that less energy is used in the cation desolvation step in the solvent with a lower dielectric constant.

Complexes of large cations are less affected by solvent than complexes of smaller cations. Thus, large cations should be preferred over smaller cations in strongly solvating solvents as these solvents have a greater affinity for small cations which will lead to destabilization of their chelates.

1.4.3 Biological Importance of Coordinated Macrocycles

Many biologically relevant compounds contain partially unsaturated tetradentate macrocyclic ligands known as the tetrapyrroles.¹¹⁴ These macrocyclic ligands can, in their deprotonated form, bind even labile divalent metal ions. Figure 1.24 illustrates the variety of structures of tetrapyrrole macrocycles.



Figure 1.24: Structures of a variety of tetrapyrrole ligands.¹¹⁵

The complexes described below are among the most common and best known bioinorganic compounds containing tetrapyrrole ligands.

Chlorophyll is the green pigment found in cyanobacteria and chloroplasts of algae and plants and it is essential to the process which allows plants to harvest energy from light: photosynthesis.¹¹⁵ Chlorophyll contains Mg(II) as a central metal ion and a partially hydrogenated and substituted porphyrin ligand system, shown in Figure 1.25. This highly conjugated tetrapyrrole π system has a high absorptivity at both the long and short wavelength regions of the visible spectrum. The partial hydrogenation of the pyrrole rings of the unsaturated porphyrin π system leads to a shift of photon absorption to longer wavelengths. Other open-chain tetrapyrrole molecules work with chlorophyll to ensure that a broad spectral absorption range is covered.¹¹⁶ The Mg(II) ion plays an important role in the spatial orientation of the chlorophyll π chromophores with regard to each other. This is achieved by the coordination of polypeptide side-chain ligands to the two free axial coordination sites at the metal, leading to a high degree of organization.^{117,118} Mg(II) is particularly suited to the chlorophyll system as it is sufficiently naturally abundant, is the correct size and can form hexacoordinate species. Mg(II) is also redox-inactive, which is essential for localizing redox chemistry on the macrocycle ring during the electron transport process of photosynthesis.

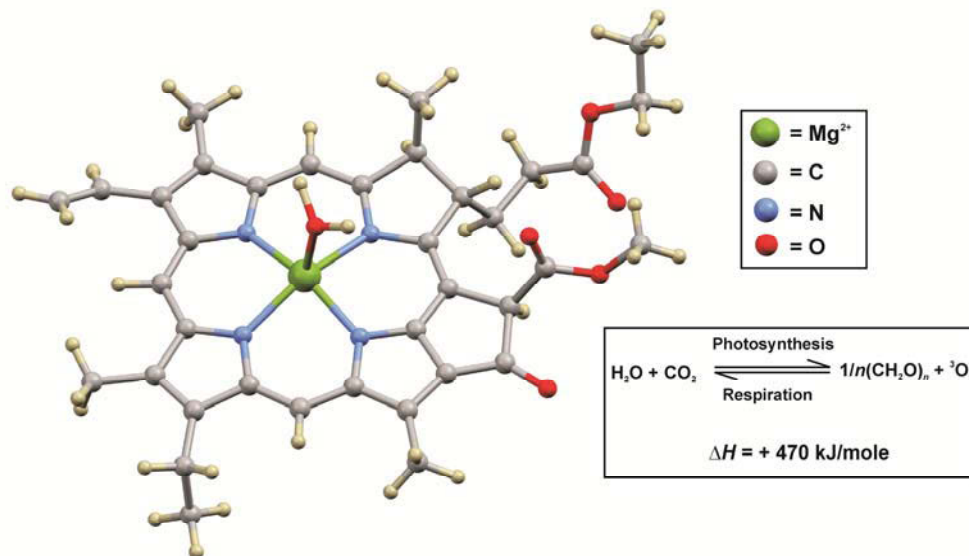


Figure 1.25: X-ray crystal structure of chlorophyll. A single water molecule has been included, the remaining water solvent molecules were omitted for clarity.¹¹⁹

Vitamin B₁₂ or Cobalamin plays an important role in the functioning of the brain and the central nervous system.¹¹⁵ It contains the biochemically rare element cobalt and a partially conjugated corrin π ring system. The complicated structure of vitamin B₁₂, shown in Figure 1.26(a), was eventually elucidated by single crystal X-ray diffraction.¹²⁰ The structure showed that in addition to four of the six coordination sites being occupied by the corrin ligand, that the fifth coordination site was occupied by an N(1)-coordinated 5,6-dimethylbenzimidazole ring. The sixth coordination site is variable and may be a cyano, hydroxyl, methyl or 5'-deoxyadenosine group resulting in different forms of vitamin B₁₂.¹¹⁵ Although, there is an extensive conjugation of π electrons, the macrocycle is not planar, as expected, but rather forms a saddle conformation due to the large metal ion being coordinated by a 15-membered as opposed to a 16-membered macrocycle. Figure 1.26(b) illustrates this saddle effect. It is the reactive Co-C bond that participates in enzyme catalyzed reactions such as isomerases, methyltransferases and dehalogenases giving vitamin B₁₂ its activity.¹¹⁵ Figure 1.26(c) shows the various reductive and oxidative reactions that the complex can undergo.

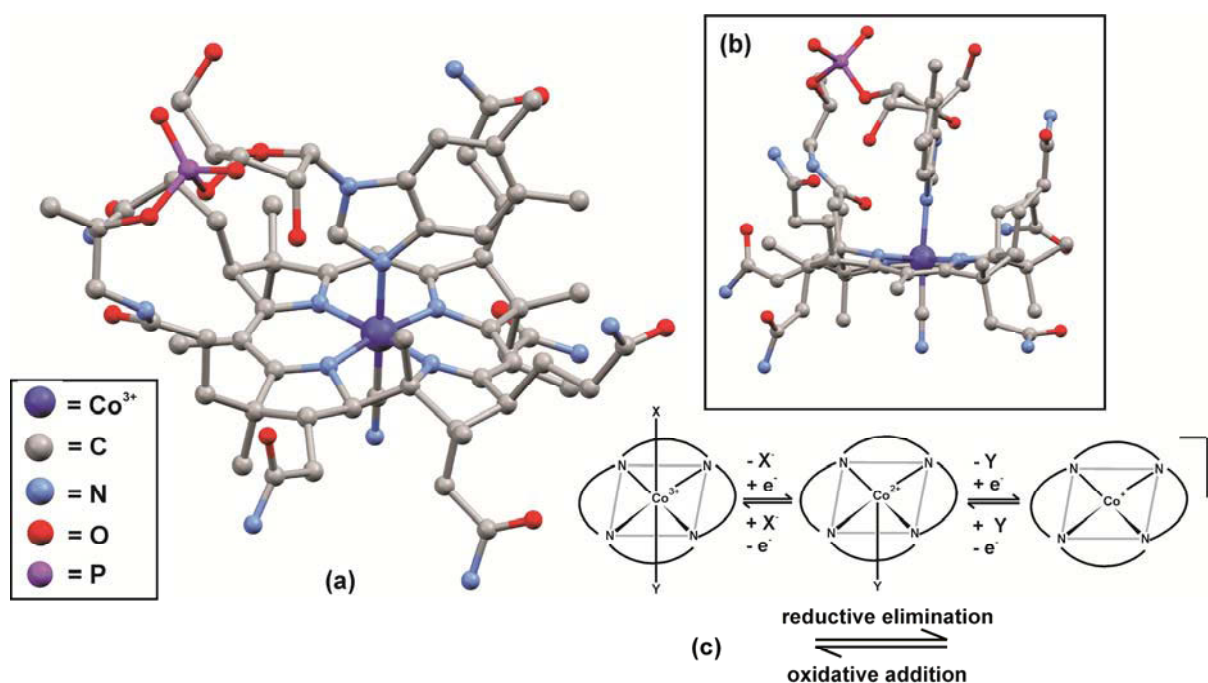


Figure 1.26: (a) X-ray crystal structure of cyanocobalamin (vitamin B12).¹²¹ The hydrogen atoms and solvent molecules are omitted for clarity; (b) Diagram illustrating the saddle conformation of the corrin system and (c) stepwise reduction of the cobalt metal centre with a corresponding decrease in axial ligand coordination.

Another example of a biologically important complex tetrapyrrole system is heme. Heme consists of an iron centre and a porphyrin ligand and is found in hemoglobin, myoglobin, cytochromes and peroxidases.¹¹⁵ Figure 1.27 shows various reactions that the heme centre can undergo in different protein environments.¹¹⁵ Heme plays a significant role in oxygen transport and storage through hemoglobin and myoglobin. Hemoglobin is a tetramer of the monomeric hemoprotein myoglobin. One of the axial coordination sites of the heme in hemoglobin and myoglobin is occupied by a proximal histidine which has the ability to form hydrogen bonds while the other axial site remains free for O₂ coordination. The histidine is important as it is basic in nature, thus preventing protons from weakening the bond between O₂ and the iron centre by acting

as an electrophilic competitor.¹²² Iron-porphyrin complexes such as cytochromes are also involved in a variety of catalytic biochemical processes. Cytochromes are involved in electron transfer in respiration and photosynthesis. There are a variety of cytochromes classed according to their structure and physical properties.¹²³ The cytochromes have different properties depending on axial ligand, coordination environment and the redox potential for $\text{Fe}^{2+}/\text{Fe}^{3+}$ couple.

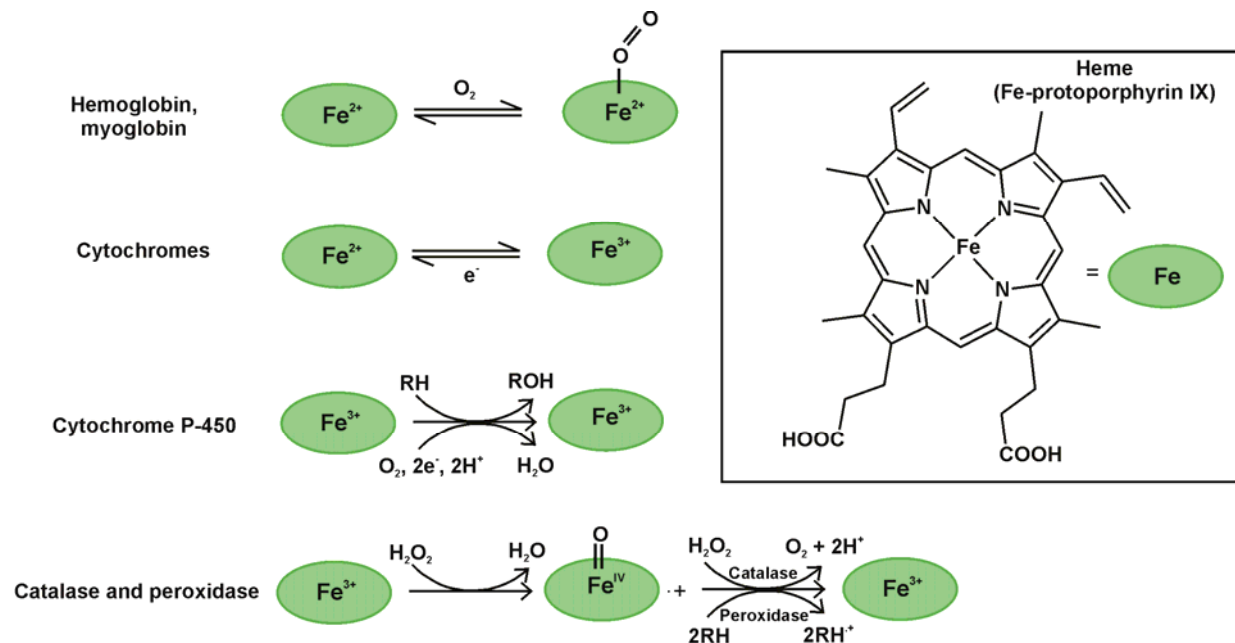


Figure 1.27: Various biological functions of the heme tetrapyrrole complex.

These unique tetrapyrrole bioligands described above have certain characteristics which make them critical to the functioning of biological systems. These characteristics are described below.

The tetrapyrrole ligands have a planar or near planar ring system and are very stable. There is no geometric strain with all bond lengths in the range of 136 -145 pm and bond angles varying between 107-126 °.¹¹⁵ After deprotonation, the ligands are either mono or dicationic, allowing them to bind even labile metal ions.¹¹⁵ As described in previous sections, these macrocyclic complexes are stable as dissociation can only occur in the unlikely event of all metal-to-ligand bonds breaking simultaneously and the metal being ejected.

The selectivity of macrocyclic ligands with regard to the size of the coordinated ion has been discussed in previous sections, but is especially relevant for the tetrapyrroles as they are rigid due to the presence of conjugated double bonds.¹¹⁵ Calculations show that metal ions with a radius of between 60-70 pm are well suited for the cavity of a tetrapyrrole macrocycle; Mg(II), the central ion in chlorophyll has a radius of 72 pm, Co(II) the biologically significant metal ion in cobalmins has a radius of 65 pm and the average Fe(II)/(III) radius is 65 pm.¹²⁴

Another important characteristic of this biologically important class of macrocycles is their extensively conjugated π system, resulting in intense absorption bands in the visible region of the electromagnetic spectrum.¹¹⁵ Narrowing of the π frontier orbital gap, facilitates the uptake and release of electrons by these heterocycles.¹²⁵ Light absorption and redox properties of these macrocycles are important for their roles in photosynthesis and respiration.

Tetrapyrrole macrocycles are tetradentate chelate ligands occupying the equatorial sites of a 6 coordinate metal centre in an octahedral arrangement, leaving two axial coordination sites. These axial sites are essential for stoichiometric or catalytic activation of substrates.¹¹⁵ One of these axial sites is required for substrate binding while the other is required for regulation of catalytic activity. Hemoglobin binds to molecular oxygen, $X=O_2$, which has to be reversibly coordinated for transportation to the tissues. The second axial position, Y, is coordinated to a proximal histidine ligand, as shown in Figure 1.28. Cobalamins have $X = CH_2R$ and homolytic cleavage of the Co-C bonds results in radicals and is affected by changes in the coordination of the sixth ligand, Y.¹¹⁵

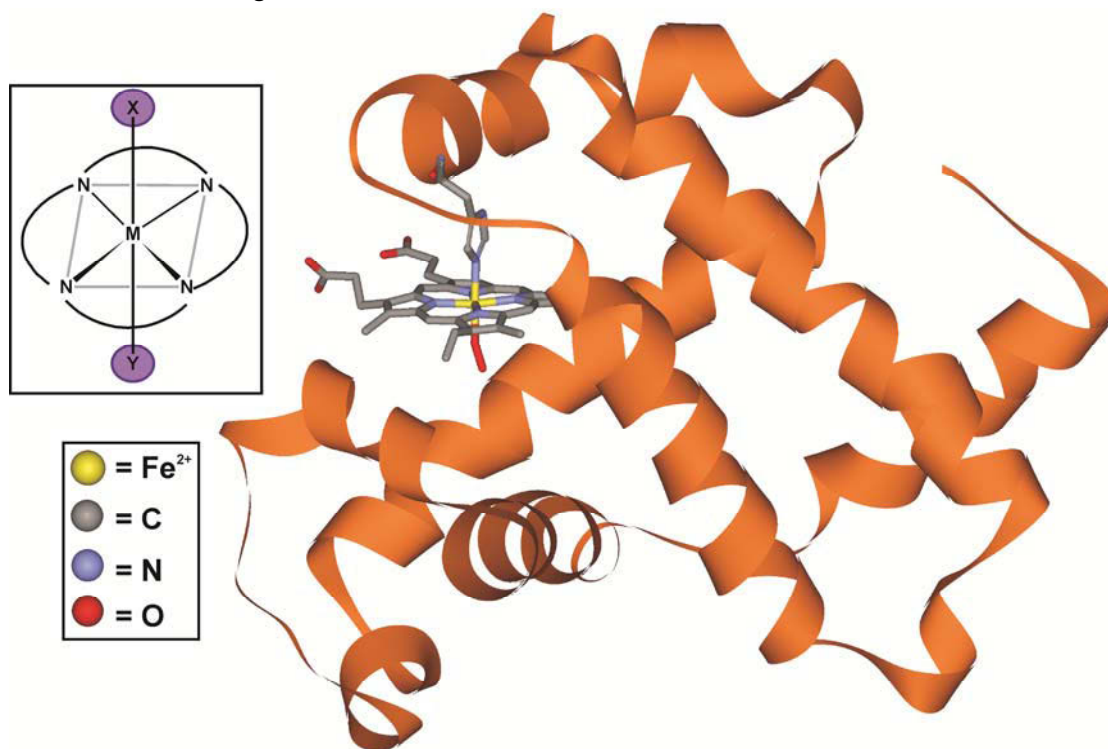


Figure 1.28: Protein structure of one of four subunits of hemoglobin. The water solvent molecules and protein atoms are omitted for clarity.¹²⁶

It is due to these biological macrocyclic systems that widespread interest in macrocyclic chemistry has increased with research focusing on synthetic macrocyclic complexes that can mimic metalloporphyrins and metalocorrins due to their similar structural properties.⁷

1.4.4 Macrocycles in Medicine

Both unchelated and complexed macrocycles have medicinal applications. A few examples are described below to give an indication of the wide variety of biological targets of macrocycles.

Natural product macrocycles have many important pharmacological properties such as good solubility, lipophilicity, metabolic stability and bioavailability.¹²⁷ Natural product macrocycles include a number of therapeutics that are used to: vary immune-system responses, to combat infectious organisms and to treat cancer. Marketed macrocyclic drugs are almost all natural products and have been predominantly used as

anti-infectives. Some of the most important macrocyclic drugs include erythromycin, which acts as an anti-biotic and was originally isolated from *Saccharopolyspora erythraea*; avermectin, which acts as a veterinary anti-parasitic, was isolated from *Streptomyces avermitilis*; amphotericin B is a potent anti-fungal and was isolated from *Streptomyces nodusus*; the anti-tuberculosis compound rifampin was isolated from *Amycolatopsis rifamycinia* and the anti-biotic vancomycin was originally isolated from *Streptomyces orientalis*.¹²⁷ Epothilone B is used as an anti-cancer agent. Figure 1.29 shows the X-ray crystal structures of some of these complex natural product macrocycles. Natural product macrocycles have a high binding affinity for their targets, but also have undesirable side-effects such as toxicity; modifications to overcome these problems are challenging due to the large size and complexity of the molecules.¹²⁸

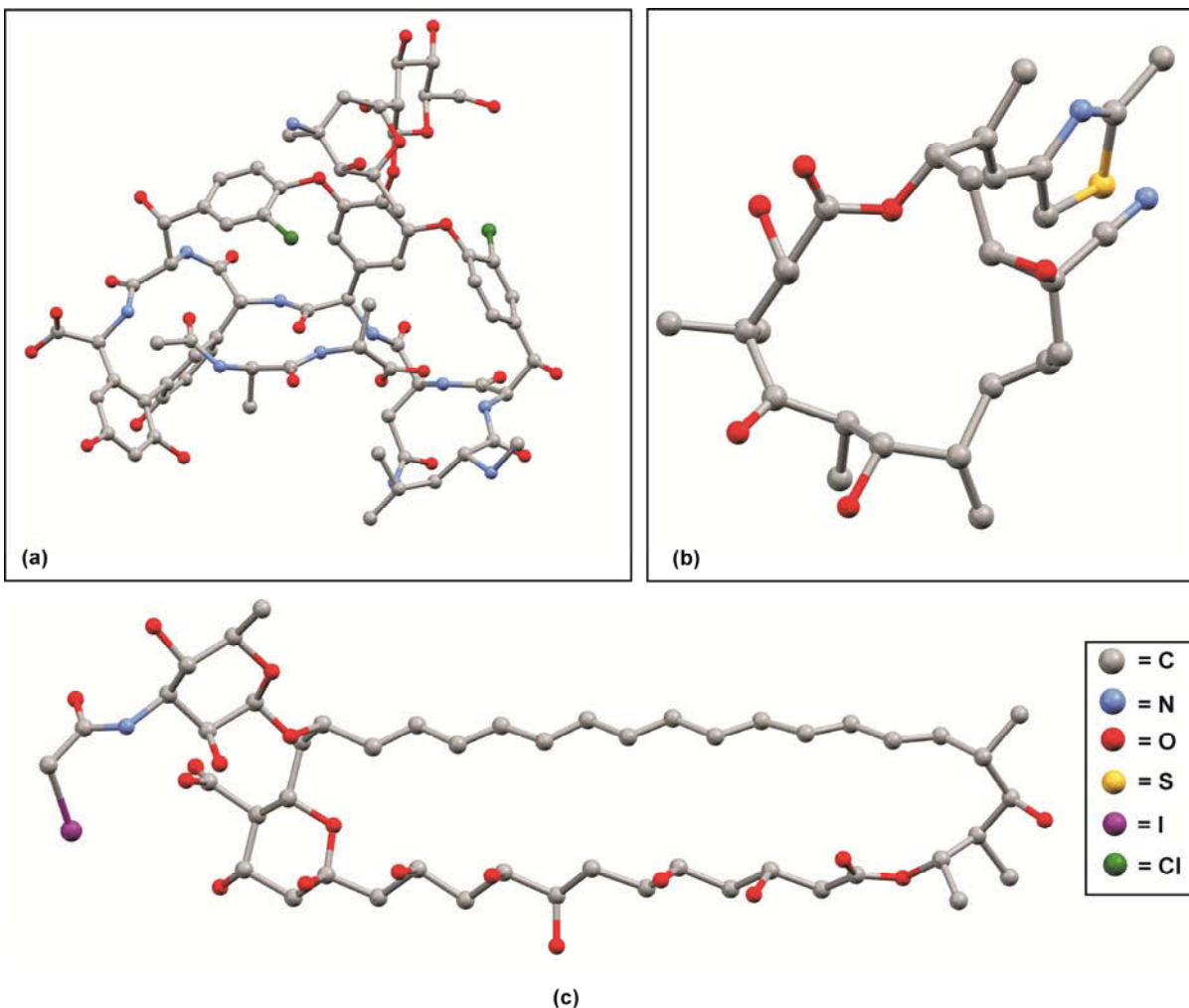


Figure 1.29: Complex structures of natural product macrocycles used in medicine; (a) Vancomycin¹²⁹, used as an anti-biotic (b) Epothilone B¹³⁰, an anti-cancer agent and (c) Amphotericin B¹³¹, an anti-fungal agent. The hydrogen atoms and solvent molecules have been omitted for clarity.

The use of compounds to localize in tumours and as agents to image diseased tissue is important for the study and treatment of both cancer and heart disease. As early as 1924, the localization and fluorescence of porphyrins in tumours was observed.¹³² One of the first macrocyclic systems used as a photodynamic therapy agent for the clinical treatment of tumours was developed in the 1960's.¹³³ This macrocyclic system

was a mixture of hematoporphyrin oligomers known as Photofrin®. The medicinal applications of Photofrin® are hampered due to an unacceptable level of skin phototoxicity. This has led to the development of new photosensitizers in recent years, leading to the discovery of texaphyrin in the late 1980's.^{134,135} The texaphyrins are pentaza Schiff-base porphyrins, Figure 1.30(a), and are known to form stable complexes with many metal ions including trivalent lanthanides.

The gadolinium(III) texaphyrin complex, Xcytrin®, has been widely studied as a potential MRI-detectable anti-cancer agent.^{136,137} The MRI scans show good uptake and retention of the complex in tumours. This complex is undergoing phase III international trials in patients with brain metastases from non-small cell lung cancer.¹³⁸ The lutetium(II) texaphyrin complex, Antrin®, is currently being tested clinically as a photosensitizer for treatment of age-related muscular degeneration, coronary artery disease and cancer.¹³⁹ Both the gadolinium and lutetium compounds produce ROS responsible for their biological activity.¹⁴⁰ The different redox and photophysical properties of the various lanthanide(III) texaphyrin complexes allows for the use of the complexes in a wide range of areas such as photodynamic therapy, direct cancer treatment and in chemotherapy enhancement procedures.

In an effort to improve the efficacy of the texaphyrins, several conjugates are being developed, Figure 1.30(b). These conjugates contain a texaphyrin core linked to various active species including electron deficient species, fluorophores or therapeutic agents with alternate modes of action. This is to deliver the cytotoxins more effectively to cancerous tissue. The diagnostic potential of the complexes could be improved with the addition of a fluorophore. This conjugation could be done through a direct covalent linkage or through solubilizing linkers.¹⁴¹

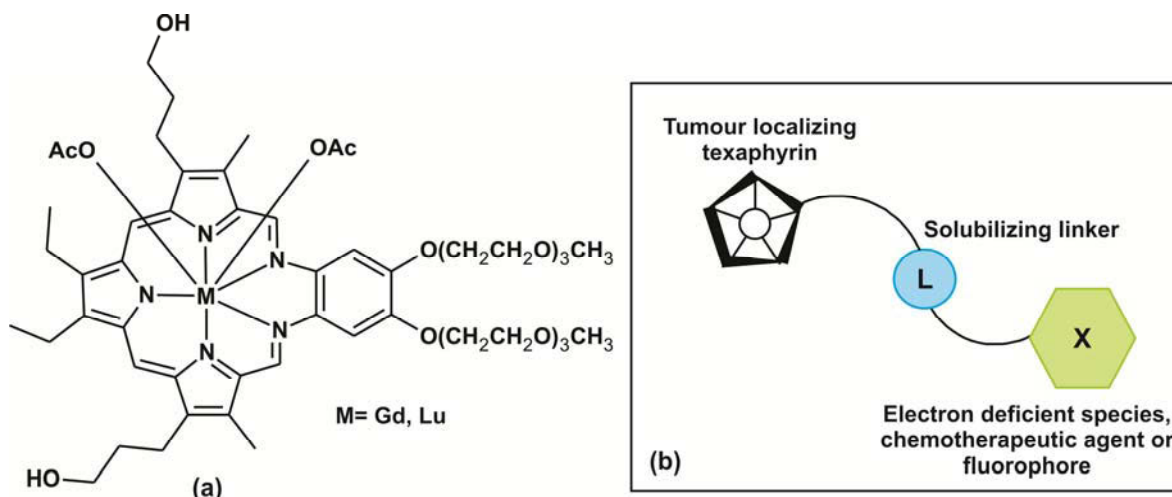


Figure 1.30: (a) Structure of texaphyrin complexes. (b) General approach to conjugate design.¹⁴²

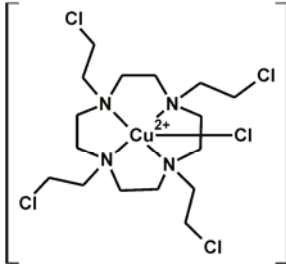
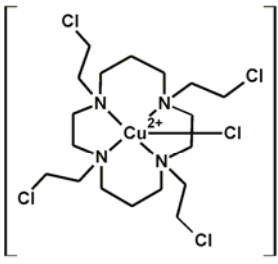
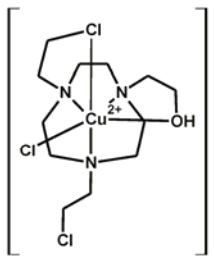
Hypoxia is a condition where the body is deprived of an adequate oxygen supply. Hypoxia in solid tumours is a limiting factor to the success of radiotherapy and chemotherapy, as molecular oxygen is often the requirement for the toxicity of many anti-cancer agents.¹⁴³⁻¹⁴⁵ Chemotherapeutic compounds that target the cell cycle will be less toxic in hypoxic cell as cell growth is significantly reduced due to the lowered oxygen content. Hypoxia promotes metastasis and angiogenesis in tumours.¹⁴⁶ Hypoxia is consistently a tumour-specific condition that can be developed for the selective activation of prodrugs. Prodrugs can be converted to their active form in hypoxic tissue by two different mechanisms. The first mechanism involves using

enzymes such as NADPH-cytochrome P-450 oxidoreductase to convert the prodrugs to a one-electron adduct. The intermediate can then be reoxidized by molecular oxygen in normal tissue, but in the absence of oxygen it can be further converted or fragmented to toxic species.¹⁴⁷ The second method involves using therapeutic ionizing radiation to activate the prodrug.¹⁴⁸

Milbank *et al.*¹⁴⁴ and Chang *et al.*¹⁴³ have explored cobalt(III) and chromium(III) complexes of 8-hydroxyquinoline (8-HQ) and a variety of different ligands at the auxiliary metal coordination positions as potential prodrugs in the treatment of cancer. The ligands included bidentate and tridentate N-donor ligands such as ethylene diamine and diethylene triamine as well as tridentate and tetradentate N-donor macrocyclic ligands such as cyclen (1,4,7,10-tetraazacyclododecane) and tacn (1,4,7-triazacyclononane). These groups showed that the stability of the complex is an important consideration with the bidentate complex less effective than the tridentate complex. Studies have shown a higher efficiency of hypoxia-selective release from complexes using the tetradentate auxiliary ligand when compared to the non-macrocyclic complexes.¹⁴³ With cyclen as the ligand, 8-HQ was efficiently released on exposure to radiation close to the theoretical value for a one-electron reduction of the system.¹⁴⁴

Parker *et al.*¹⁴⁵ have studied copper(II) complexes of cyclen, cyclam and tacn as potential prodrugs activated by hypoxia. They found that low kinetic lability of the complex (before and after reduction) is important to the selectivity of the biological activity. The cyclen complex exhibited the best kinetic stability of the compounds studied and was also the only compound to exhibit reversible redox behavior. This indicates that the compound is sufficiently stable to remain in contact while the other compounds exhibited irreversible redox behavior.¹⁴⁵ Under physiological conditions, stable reduced complexes should remain intact long enough to be reoxidized in the presence of oxygen while less stable complexes may be released too quickly even in aerobic tissue. Table 1.8 summarizes the IC₅₀ values of the complexes in aerobic and anaerobic conditions. The Cu(II)cyclen complex was approximately 24 times more cytotoxic under hypoxic conditions, indicating that it targets hypoxic cells probably through reduction and release of the ligand as shown in Figure 1.31.¹⁴⁵ Macrocycles are very versatile for these studies as thermodynamic and kinetic stabilities can be varied by changing the metal ion, ring size and conformation of the ring formed.

Table 1.8: Biological Activity of Cu(II) macrocycles.

	 + Cl ⁻	 + Cl ⁻	 + PF ₆ ⁻
	Cu(II)cyclen	Cu(II)cyclam	Cu(II)tacn
IC₅₀ (air) μM	54.4±10	10.1±1	8.4±0.7
IC₅₀ (N₂) μM	2.25±0.25	51.3±10	15.9±1
HCR*	24	-	-

*HCR is the hypoxic cytotoxicity ratio; IC₅₀(air)/IC₅₀(N₂).

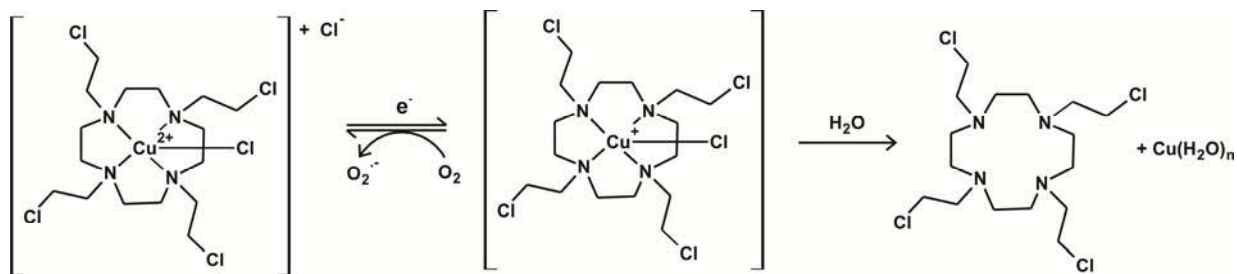


Figure 1.31: Proposed mechanism of action of chemotherapeutic Cu(II) macrocycles in hypoxic cells.

Macrocycles such as cyclam derivatives have shown promising activity against HIV/AIDS. Drug treatment of HIV infection is often associated with post infection, for instance, antiretroviral drugs that inhibit the enzyme essential for HIV replication.¹⁴⁹ Another class of anti-viral agents that has been developed is known as entry inhibitors. These drugs target the preinfection cycle. CD4 is a glycoprotein used by HIV-1 to enter the host cell; by binding to CD4, the virus gains access to the co-receptor CXCR4.¹⁵⁰⁻¹⁵² Interaction with CXCR4 enables the virus to fuse with the cell membrane which allows it to enter the cell where it discharges the viral RNA. Xylylbicyclam is a macrocyclic CXCR4 chemokine antagonist and has reached phase II clinical trials as an entry inhibitor drug against HIV.¹⁴⁹ Ross *et al.* reported that transition-metal complexes of xylylbicyclam show varying levels of anti-HIV activity due to the metal-cyclam geometry and the number of binding site interactions possible.¹⁴⁹ Their studies showed that the varying configuration of the cyclam metal complexes is important for receptor recognition and biological activity. The protein recognition study showed how the affinity of xylylbicyclam for CXCR4 was enhanced further when bound to Ni(II) or Zn(II) with the reported activity of metal xylylbicyclams following the order: Zn(II) > xylylbicyclam ~ Ni(II) > Cu(II) > Co(III).¹⁴⁹ Recognition of metalocyclams such as Zn(II)-xylylbicyclam by the CXCR4 co-receptor is thought to involve a combination of direct coordination to side chains (Asp, Glu), hydrogen-bonding to cyclam NH groups and hydrophobic interactions.

Crown ethers have been tested for biological activity and their interactions with a number of biological molecules have been studied. Crown ethers have been shown to intercalate DNA with an enhancement of the binding strength with the presence of an Na(I) or K(I) cation to interact with the negatively charged phosphate backbone.¹⁵³ Crown ether compounds have also been developed that cleave DNA in the presence of Li(I), Na(I) or K(I) cation leading to an enhancement of the cleavage reaction.¹⁵⁴ These compounds were tested against over 50 cancer cell types and were found to inhibit their growth at concentrations ranging from 1-20 μM . Crown compounds have shown toxicity towards both bacteria and various cancer cell lines.¹⁵⁵

1.4.5 Other Applications of Macrocycles

Macrocycles are a fascinating class of compounds that have a variety of structural and electronic properties that make them ideal candidates for a variety of applications such as: metal ion recognition, solvent extraction and in various sensors. Outlined below is a brief description of a few of the applications of macrocycles and the popular fields within macrocyclic research.

Photochromism is a reversible transformation of a compound between two states leading to different absorption spectra. The transformation in at least one direction is induced by electromagnetic radiation.¹⁵⁶

The widest and most important group of the photochromic systems is based on electrolytic systems¹⁵⁷ while several other photochromic systems are based on *E,Z*-isomerization, cycloaddition reactions and electron or proton transfer. Photochromic macrocyclic compounds undergo conformational change upon the uptake of metal cations resulting in a colouration. As the cation is sensitive to the ligand environment, the binding constant can be controlled.¹⁵⁸ Examples of potential applications of photochromic species include photoswitching extraction of metal cations, optical information storage, photoswitching transport through membranes and nonlinear optical devices.

As discussed in previous sections, macrocycles have structural and electronic features that can be adjusted towards binding a metal ion of interest, resulting in the field of metal ion recognition studies.¹⁵⁹ The number, type and arrangement of the donor atoms present, the macrocyclic ring size, the effect of ring substitution and the number and size of the chelate rings formed can be varied to adjust the selectivity towards specific metal ions.¹⁶⁰ This process changes the electronic and steric properties of the macrocycle and therefore metal ion uptake. The metal ion's ionic radius, oxidation state, overall hardness or softness and typical coordination sphere also play a role in metal ion recognition studies.¹⁶⁰ An example of a metal ion recognition study, Atkinson *et al.*,¹⁶¹ examined the effect of macrocyclic ring substituents on metal ion recognition. In this study the interaction of Co(II), Ni(II), Zn(II), Cd(II) and Pd(II) with N-alkylated O₂N₃ macrocyclic ring systems shows that the presence of N-substituents leads to the formation of weaker complexes. Figure 1.32 illustrates these results. This can be attributed to steric hindrance and electronic effects. This field of research has important applications in a variety of waste management programmes.

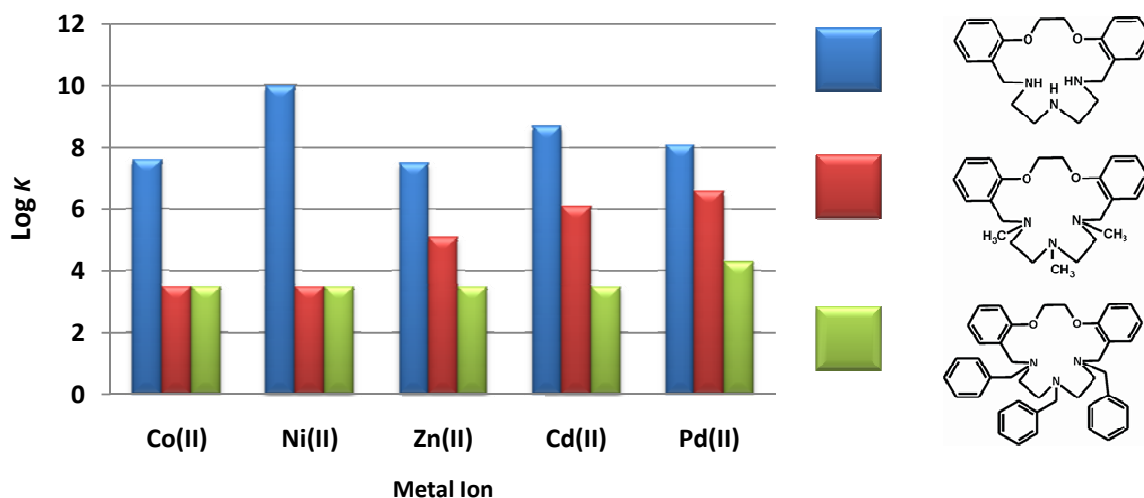


Figure 1.32: The stability constants for a variety of metal N-alkylated macrocyclic complexes.

The treatment of nuclear waste is one of the biggest technical challenges of all time as it requires harsh conditions, high costs and a low tolerance for failure. The need has emerged to remove fission products from waste due to limited disposal space and high disposal costs.¹⁶² The waste mass consists of 10-15 % of metal hydroxide sludge while the bulk is made up of sodium hydroxide, sodium nitrate and other soluble salts while the main radionuclide content consists of ¹³⁷Cs.¹⁶² A breakthrough was made in nuclear waste treatment in 1994 when European researchers reported that calixarene-crown ethers or calixcrowns exhibited sufficiently high selectivity to remove cesium from a 10⁴-10⁶ higher background concentration of sodium leading to the development of the Caustic-Side Solvent Extraction process (CSSX). The calixcrowns

are ideal for the extraction of cesium as they are highly selective, can be stripped with water, have good radiation and chemical stability, are effective at low concentrations and produce little secondary waste.¹⁶²

In conclusion, macrocycles are fascinating ligands with a variety of structural and electronic properties that enable these compounds to be tuned to a variety of different applications. Macrocyclic complexes have been reported in many biologically important systems with many research groups developing complexes to mimic these biological systems. Due to their enhanced stability, stemming from the macrocyclic effect, this class of ligand was chosen to stabilize gold(III) in this work. Drawing on concepts from the above review, macrocyclic complexes of gold(III) should be stable under physiological conditions as dissociation can only occur in the unlikely event of all metal-to-ligand bonds breaking simultaneously.

1.5 Aims and Objectives

The aim of this work is to synthesize a range of bis(pyrrolide-imine) gold(III) macrocyclic, pseudomacrocyclic and open-chain Schiff base complexes as potential anti-cancer agents that exert their cytotoxicity through DNA intercalation and the inhibition of the topoisomerase group of enzymes.

Three ligand types have been synthesized for this work: the first and most important type is a completely macrocyclic ligand, the second is a pseudo-macrocycle and the third is an open-chain tetradentate chelate. All three types consist of two pyrrole rings bridged by a synthetically variable linkage unit. The macrocyclic ligands consist of a pair of pyrrole rings joined through a di(azomethine) linkage on one end and a quinoxaline or pyrazine tail on the other end; this forms a completely closed structure. The pseudomacrocyclic ligands have a pair of pyrrole rings joined at one end by a quinoxaline tail, but instead of a di(azomethine) linkage completing the macrocycle they are left open with methyl and ethyl groups joined to the imine moieties. This group of ligands is referred to as pseudomacrocyclic as the position of the methyl and ethyl chains effectively completes the macrocycle, although there is no formal bond between them. The open-chain macrocycle analogue comprises a pair of pyrrole rings joined by a di(azomethine) linkage on one end and is open on the other end. The structure of the ligands is varied through transformations of the di(azomethine) linkage as well as variation of the quinoxaline tail. As has been previously reported, macrocycles can stabilize metals in comparison to their open chain analogues due to the macrocyclic effect. The macrocyclic, pseudo-macrocyclic and open-chain analogues were synthesized to ascertain whether the increased stability of the macrocyclic system would result in greater cytotoxicity.

In this study, the macrocyclic, pseudomacrocyclic and non-macrocyclic ligands were coordinated to gold(III). Coordination of these ligands results in concomitant deprotonation of the pyrrole NH groups, thus the ligands form tetradentate, N_2N_2' , dianionic ligands. When these ligands are coordinated to gold(III), the complexes carry an overall positive charge. As gold(III) chelates are not always stable under physiological conditions and have been known to readily undergo redox and hydrolysis reactions in solution, these ligands were chosen because they are strong σ -donors and should stabilize the gold(III) ion. The gold(III) complexes synthesized for this study are depicted in Figure 1.33.

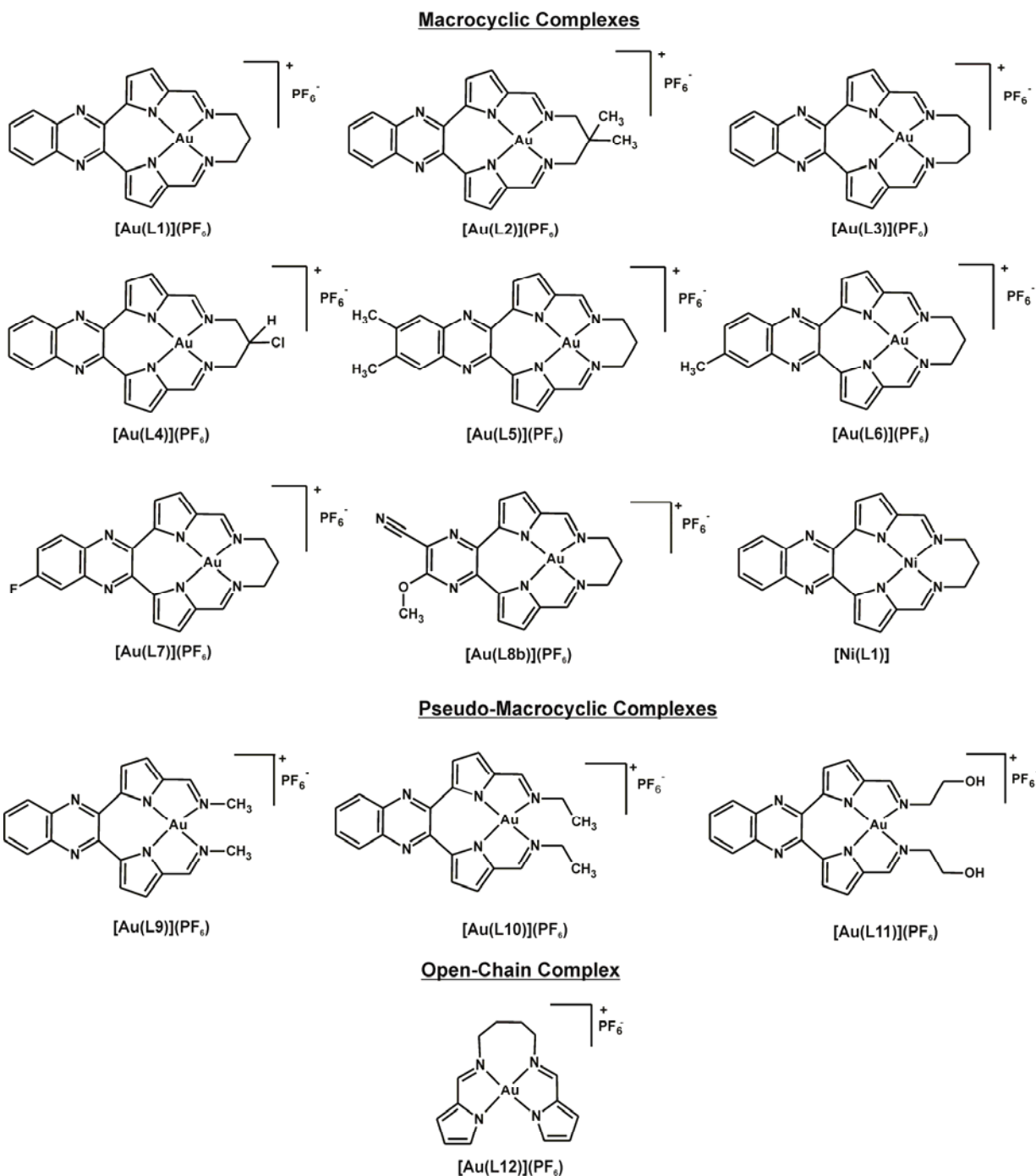


Figure 1.33: Schematic of the gold(III) complexes synthesized in this study.

The bis(pyrrolide-imine) gold(III) Schiff base complexes have been synthesized as DNA intercalators and possess some of the key design features of commercially available DNA intercalators such as daunorubicin. As described previously daunorubicin has a protonated amino group at physiological pH, giving it an overall positive charge which allows for favourable electrostatic interactions with the negatively charged phosphate backbone of DNA. This also increases the solubility of the drug. The complexes also have a planar aromatic region which increases the binding affinity of the drug through π - π interactions with the aromatic DNA base

pairs. Daunorubicin also has a region for hydrogen bonding allowing for hydrogen bonding between the DNA and intercalated drug; this effectively locks the drug into position. These structural features have been built into the synthesized gold(III) complexes. All the gold(III) complexes have an overall positive charge and extended aromaticity. The complex $[\text{Au}(\text{L11})](\text{PF}_6)$ also has a hydrogen bonding region. This is depicted in Figure 1.34.

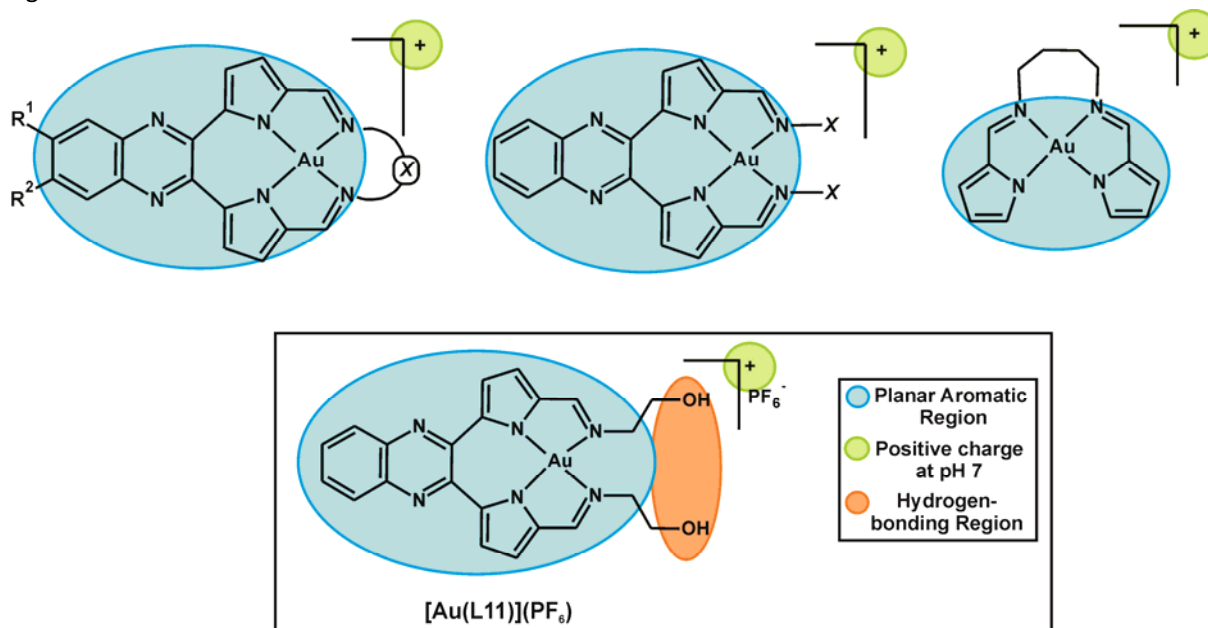


Figure 1.34: Key structural features allowing for potential DNA intercalation.

The complexes were designed to intercalate between DNA base pairs and inhibit or poison the TOP enzymes. Without these enzymes, cell replication and transcription cannot take place and apoptosis will follow. This should affect mainly cancerous cells as these cells are rapidly dividing and thus contain a higher concentration of the enzymes.⁸ Thus, the gold(III) complexes synthesized in this work have been tested as anti-cancer agents and for their ability to inhibit the TOP enzymes.

The main objectives of this work are summarized below:

- To synthesize the proposed macrocyclic, pseudo-macrocyclic and open-chain bis(pyrrolide-imine) Schiff base ligands and to fully characterize these compounds by ^1H and ^{13}C NMR, mass spectrometry (MS), UV/visible and infrared spectroscopy as well as single crystal X-ray crystallography.
- To then use these ligands to synthesize a range of gold(III) bis(pyrrolide-imine) Schiff base complexes. These complexes will be characterized by ^1H and ^{13}C NMR, mass spectrometry (MS), UV/visible and infrared spectroscopy. The complexes will also be studied by X-ray crystallography to determine the exact geometry of the complexes as well as the various interactions of these complexes in the solid state.
- The ligands and complexes will also be studied by the computational method density functional theory (DFT). The results of the simulations will be compared and contrasted with the experimental data to determine their accuracy. The data should provide insight into the spectroscopic and solid-state features of these complexes.

- The affinity of the complexes for calf-thymus DNA will be determined using competitive-binding titrations with ethidium bromide. This should give an indication of the intercalative ability of the complexes for human DNA.
- Other characteristics of the complexes such as the octanol/water partition coefficients will be determined. This will give an indication of the biodistribution of the complexes in the human body. It will also allow for the lipophilicity of the chelates to be tuned so that the chelates can effectively cross the phospholipid bilayer of the cell and reach their cellular target.
- The gold(III) complexes will be screened against sixty different human cancer cell lines by the National Cancer Institute (NCI, USA)^{163,164} to determine their cytotoxicity. This will show any specificity of the gold(III) complexes to specific cancer cell lines. This should show if the structural modifications to the ligands have any effect on the cytotoxicity of the complexes.
- To determine the mode of action through which the gold(III) complexes exert their cytotoxicity via *in vitro* enzyme inhibition assays and gel electrophoresis experiments.

1.6. References

- (1) Organization, W. H. *The Global Burden of Disease: 2004 Update*, World Health Organization, 2008.
- (2) Lippert, B. *Chemistry and Biochemistry of a Leading Anti-cancer Drug*; Wiley-VCH: Weinheim, 1999.
- (3) Kostova, I. *Anticancer Agents Med. Chem.* **2006**, *6*, 19.
- (4) Orvig, C., Abrams, M. J. *Chem. Rev.* **1999**, *99*, 2201.
- (5) Sun, R. W.-Y., Che, C.-M. *Coord. Chem. Rev* **2009**, *253*, 1682.
- (6) Barnholtz, S. L., Lydon, J. D., Huang, G., Venkatesh, M., Barnes, C. L., Ketring, A. R., Jurisson, S. S. *Inorg. Chem.* **2001**, *40*, 972.
- (7) Melson, G. A. *Coordination Chemistry of Macrocyclic Compounds*; Plenum Press: New York, 1979.
- (8) Thurston, D. E. *Chemistry and Pharmacology of Anticancer Drugs*; Taylor & Francis Group: USA, 2007.
- (9) Cairns, J. *Cancer Science and Society*; W. H. Freeman and Company: USA, 1978.
- (10) Patrick, G. L. *An Introduction to Medicinal Chemistry, third edition*; Oxford University Press: New York, 2005.
- (11) Snustad, D. P., Simmons, M. J. *Principles of Genetics, 4th edition*; John Wiley & Sons, Inc.: USA, 2006.
- (12) Oleksi, A., Blanco, A. G., Boer, R., Usón, I., Aymami, J., Rodger, A., Hannon, M. J., Coll, M. *Angew. Chem. Int. Ed.* **2006**, *45*, 1227.
- (13) Zeglis, B. M., Pierre, V. C., Barton, J. K. *Chem. Commun.* **2007**, 4565.
- (14) Phillips, T., Haq, I., Meijer, J. H. M., Adams, H., Soutar, I., Swanson, L., Sykes, M. J., Thomas, J. A. *Biochem.* **2004**, *43*, 13657.
- (15) Wilson, W. D., Streckowski, L., Tanious, F. A., Watson, R. A., Mokrosz, J. L. Streckowska, A., Webster, G. D., Neidle, S. *J. Am. Chem. Soc* **1988**, *110*, 8292.
- (16) Nunn, C. M., Van Meevelt, L., Zhang, S., Moore, M. H., Kennard, O. *J. Mol. Biol.* **1991**, *222*, 167.
- (17) Zhao, C., Xia, C., Mao, Q., Fosterling, H., De Rose, E., Antholine, W. E., Subczynski, W. K., Petering, D. H. *J. Inorg. Biochem.* **2002**, *91*, 259.
- (18) Cummings, S. D. *Coord. Chem. Rev* **2009**, *253*, 1495.
- (19) Chen, L.-M., Liu, J., Chen, J.-C., Tan, C.-P., Shi, S., Zheng, K.-C., Ji, L.-N. *Inorg. Biochem.* **2008**, *102*, 330.
- (20) Gupta, N., Grover, N., Neyhart, G. A., Liang, W., Singh, P., Thorp, H. H. *Angew. Chem. Int. Ed.* **1992**, *31*, 1048.
- (21) Pommier, Y. *Nature Rev.* **2006**, *6*, 789.
- (22) Koster, D. A., Palle, K., Bot, E. S. M., Bjornsti, M.-A., Dekker, N. H. *Nature Lett.* **2007**, *448*, 214.
- (23) Koster, D. A., Croquette, V., Dekker, C., Shuman, S., Dekker, N. H. *Nature Lett.* **2005**, *434*, 671.
- (24) Changela, A., DiGate, R. J., Mondrago, A. *Nature Lett.* **2001**, *411*, 1077.
- (25) Staker, B. L., Hjerrild, K., Freese, M. D., Behnke, C. A., Burgin, A. B., Sterwart, L. *Proc. Natl. Acad. Sci* **2002**, *99*, 15387.
- (26) Strick, T. R., Croquette, V., Bensimon, D. *Nature Lett.* **2000**, 404.
- (27) Dong, K. C., Berger, J. M. *Nature* **2007**, *450*, 1201.
- (28) Sigel, A., Sigel, H. *Metal Ions in Biological Systems*; Marcel Dekker Inc: New York, 1996.
- (29) Hartley, F. R. *Chemistry of the Platinum Group Metals Recent Developments*; Elsevier: Amsterdam, 1991.
- (30) Galanski, M., Keppler, B. K. *Anti-Cancer Agents in Medicinal Chemistry*, 2007; Vol. 7.
- (31) Todd, R. C., Lippard, S. J. *J. Inorg. Biochem.* **2010**, *104*, 902.
- (32) Sherman, S., Gibson, D., Wang A., Lippard, S. *Science* **1985**, *230*, 412.
- (33) Cotton, F. A., Wilkinson, G. W. *Advanced Inorganic Chemistry Fifth Edition*; John Wiley & Sons. Inc.: New York, 1988.
- (34) Renner, H., Schlamp, G., Hollmann, D., Schow, H. M. L., Tews, P., Rothaut, J., Dermann, K., Dler, A. K., Hecht, C., Schlott, M., Drieselmann, R., Peter, C., Schiele, R. In *Ullmanns Encyclopedia of Industrial Chemistry*; Wiley-VCH Verlag GmbH & Co. KGaA: Weinheim, 2012; Vol. 17, p 93.
- (35) Brady, J. E. *General Chemistry: Principles and Structure, 5th Edition*; John Wiley & Sons, Inc.: US, 1990.
- (36) Hutchings, G. J., Brust, M., Schmidbaur, H. *Chem. Soc. Rev.* **2008**, *37*, 1759.

- (37) Grohmann, H., Schmidbaur, H. *Comprehensive Organometallic Chemistry II*; Pergamon Press: Oxford, 1995; Vol. 3.
- (38) Puddephatt, R. J. *Comprehensive Coordination Chemistry*; Pergamon Press: Oxford, 1987; Vol. 5.
- (39) Laguna, A., Laguna, M. *Coord. Chem. Rev* **1999**, *193*, 837.
- (40) Basil, J. D., Murray, H. H., Fackler Junior, J. P., Tocher, J., Mazany, A. M., Trzcinska-Bancroft, B., Knachel, H., Dudis, D., Delord, T. J., Marler, D.O. *J. Am. Chem. Soc* **1985**, *107*, 6908.
- (41) Fourmigue, M., Meziere, C., Canadell, E., Zitoun, D., Bechgaard, K., Auban-Senzier, P. *Adv. Mater.* **1999**, *11*, 766.
- (42) Shriver, D. F., Atkins, P. W. *Inorganic Chemistry, 3rd Edition*; Oxford University Press, 2000.
- (43) Marangoni, G., Pitteri, B., Bertolasi, V., Ferretti, V., Gilli, G. *Dalton Trans.* **1987**, 2235.
- (44) Marangoni, G., Pitteri, B., Bertolasi, V., Gilli, G., Ferrett, V. *Dalton Trans.* **1986**, 1941.
- (45) Duckworth, V. F., Stephenson, N. C. *Inorg. Chem.* **1969**, *8*, 1661.
- (46) Li, Z., Brouwer, C., He, C. *Chem. Rev.* **2008**, *108*, 3239.
- (47) Pina, C. D., Falletta, E., Rossi, M. *Chem. Soc. Rev.* **2012**, *41*, 350.
- (48) Xu, L. X., He, C. H., Zhu, M. Q., Wu, K. J., Lay, Y. L. *Catal. Lett.* **2007**, *118*, 248.
- (49) Kesavan, L., Tiruvalam, R., Ab Rahim, M. H., Izham bin Saiman, M., Enache, D. I., Jenkins, R. L., Dimitratos, N., Lopez-Sanchez, J. A., Taylor, S. H., Knight, D. W., Kiely, C. J., Hutchings, J. G. *J. Science* **2011**, *331*, 195.
- (50) Turner, M., Golovko, V. B., Vaughan, O. P., Abdulkin, P., Berenguer-Marcia, A., Tikhov, M. S., Johnson, B. F., Lambert, R. M. *Nature* **2008**, *454*, 981.
- (51) Hashmi, A. S. K., Weyrauch, J. P., Rudolph, M., Kurpejovic, E. *Angew. Chem. Int. Ed.* **2004**, *43*, 6545.
- (52) Zhang, Y., Donahue, J. P., Li, C.-J. *Org. Lett.* **2007**, *9*, 627.
- (53) Liu, Y., Song, F., Song, Z., Liu, M., Yan, B. *Org. Lett.* **2005**, *7*, 5409.
- (54) Fricker, S. P. *Gold Bull.* **1996**, *29*, 53.
- (55) Milacic, V., Dou, Q. P. *Coord. Chem. Rev* **2009**, *253*, 1649.
- (56) Gottlieb, N. L. *J. Rheumatol. Suppl.* **1982**, *8*, 99.
- (57) Tiekink, E. R. T. *Bioinorg. Chem. Appl.* **2003**, *53*, 1.
- (58) Hill, D. T., Sutton, B. M. *Cryst. Struct. Commun.* **1980**, *9*, 679.
- (59) Okada, T., Patterson, B. K., Ye, S. Q., Gurney, M. E. *Virology* **1993**, *192*, 631.
- (60) Navarro, M., Perez, H., Sanchez-Delgado, R. A. *J. Med. Chem.* **1997**, *40*, 1937.
- (61) Navarro, M., Cisneros-Fajardo, E. J., Lehmann, T., Sanchez-Delgado, R. A., Atencio, R., Silva, P., Lira, R., Urbina, J. A. *Inorg. Chem.* **2001**, *40*, 6879.
- (62) McKeage, M. J., Maharaj, L., Berners-Price, S. J. *Coord. Chem. Rev* **2002**, *232*, 127.
- (63) Fries, J. F., Bloch, D. Spitz, P., Mitchell, D. M. *Am. J. Med.* **1985**, *78*, 39.
- (64) Fricker, S. P., Skerj, R., Cameron, B. R., Mosi, R., Zhu, Y. *Recent Developments in Gold Drugs 2003*; AnorMED Inc: Canada, 2003.
- (65) Sadler, P. J., Sue, R. E. *Met. Based Drugs* **1994**, *1*, 107.
- (66) Mirabelli, C. K., Johnson, R. K., Sung, C. M., Faucette, L., Muirhead, K., Crooke, S. T. *Cancer Res.* **1985**, *45*, 32.
- (67) Kim, I. S., Jin, J. Y., Lee, I. H., Park, S. J. *Br. J. Pharmacol.* **2004**, *142*, 872.
- (68) Gommer, S., Arscott, L. D., Williams Jr, C. H., Schirmer, R. H., Becker, K. *J. Biol. Chem.* **1998**, *273*, 20096.
- (69) Gunatilleke, S. S., Barrios, A. M. *J. Med. Chem.* **2006**, *49*, 3933.
- (70) Messori, L. A., F., Marcon, G., Orioli, P., Fontani, M., Mini, E., Mazzei, T., Carotti, S., O'Connell, T. ZanalloP. *J. Med. Chem.* **2000**, *45*, 3541.
- (71) Shaw, C. F. *Chem. Rev.* **1999**, 99.
- (72) Messori, L., Marcon G., Oriol, P. *Bioinorg. Chem. Appl.* **2003**, *1*, 177.
- (73) Marzano, C., Bettio, F., Baccichetti, F., Trevisan, A., Giovagnini, L., Fregona, D. *Chem. Biol. Interact.* **2004**, *148*, 37.
- (74) Calamai, P. C., S., Guerri, A., Messori, L., Mini, E., Orioli, P., Speroni, G.P. *J. Inorg. Biochem.* **1997**, 103.

- (75) Marcon, G., Carotti, S., Coronello, M., Messori, L., Mini, E., Orioli, P., Mazzei, T., Cinellu, M. A., Minghetti, G. *J. Med. Chem.* **2002**, *45*, 1672.
- (76) Wang, X., Guo, Z. *Dalton Trans.* **2008**, 1521.
- (77) Che, C.-M., Sun, R. W.-Y., Yu, W.-Y., Ko, C.-B., Zhu, N., Sun, H. *Chem. Commun.* **2003**, *14*, 1718.
- (78) To, Y. F., Sun, R. W.-Y., Chen, Y., Chan, V. S.-F., Yu, W.-Y., Tam, P. K.-H., Che, C.-M., Lin C.-L. S., *Int. J. Cancer* **2009**, *124*, 1971.
- (79) Wang, Y., He, Q.-Y., Sun, R. W.-Y., Che, C.-M., Chiu, J.-F. *Cancer Res.* **2005**, *65*, 11553.
- (80) Munro, O. Q., Akerman, K. J., Akerman, M. P. 2011; Vol. WO2011/158176 A2.
- (81) Giovagnini, L., Ronconi, L., Aldinucci, D., Lorenzon, D., Sitran, S., Fregona, D. *J. Med. Chem.* **2005**, *48*, 1588.
- (82) Saggiaro, D., Rigobello, M. P., Paloschi, L., Folda, A., Moggach, S.A., Parsons, S., Roncoini, L., Fregona, D., Bindoli, A. *Chem. Biol.* **2007**, *14*, 1128.
- (83) Fan, D. C., Yang, T., Ranford, J. D., Vittal, J. J., Lee, P.F. *Dalton Trans.* **2003**, 3376.
- (84) Buckley, R. G., Elsome, A. M., Fricker, S. P., Henderson, G. R., Theobald, B. R. C., Parish, R. V., Howe, B. P., Kelland, L. R. *J. Med. Chem.* **1996**, *39*, 5208.
- (85) Sharma, R., Prabhat, R., Singh, R., Pawar, S., Chauhan, A. *J. Am. Chem. Soc.* **2010**, *6*, 559.
- (86) Curtis, N. F. *J. Chem Soc* **1960**, 4409.
- (87) Curtis, N. F. *Coord. Chem. Rev* **1968**, *3*, 3.
- (88) Thompson, M. C., Busch, D. H. *J. Am. Chem. Soc.* **1964**, *86*, 3651.
- (89) Busch, D. H. *Rec. Chem. Prog.* **1964**, *25*, 107.
- (90) Pedersen, C. J. *J. Am. Chem. Soc.* **1967**, *89*, 7017.
- (91) Dietrich, B., Lehn, J.-M., Sauvage, J.-P. *Tetrahedron Lett.* **1969**, 2885, 2889.
- (92) Cabbiness, D. K., Margerum, D. W. *J. Am. Chem. Soc.* **1969**, *91*, 6540.
- (93) Fabbrizzi, L., Paoletti, P., Lever, A. B. P. *Inorg. Chem.* **1976**, *15*, 1502.
- (94) Munro, D. *Chem. Br.* **1977**, *13*, 100.
- (95) Hinz, F. P., Margerum, D. W. *Inorg. Chem.* **1974**, *13*, 2941.
- (96) Paoletti, P., Fabbrizzi, L., Barbucci, R. *Inorg. Chem.* **1973**, *12*, 1961.
- (97) Kodama, M., Kimura, E.J. *Chem. Commun.* **1975**, 326.
- (98) Kodama, M., Kimura, E. *Dalton Trans.* **1976**, 116.
- (99) Anichini, A., Fabbrizzi, L., Paoletti, P., Clay, R. M. *Dalton Trans.* **1978**, 577.
- (100) Bianchi, A., Bologni, L., Dapporto, P., Micheloni, M., Paoletti, P. *Inorg. Chem.* **1984**, *23*, 1201.
- (101) Micheloni, M., Paoletti, P., Sabatini, A. *Dalton Trans.* **1985**, 1169.
- (102) Busch, D. H., Farmery, K., Goedken, V., Katovic, V., Menyk, A. C., Sperati, C. R., Tokel, N. *Adv. Chem. Ser.* **1971**, *100*, 44.
- (103) Cabbiness, D. K., Margerum, D. W. *J. Am. Chem. Soc.* **1970**, *92*, 2151.
- (104) Dalley, N. K. *Synthetic Multidentate Macrocyclic Compounds* Academic Press: New York, 1978.
- (105) Christensen, J. J., Eatough, D. J., Izatt, R. M. *Chem. Revs.* **1974**, *74*, 351.
- (106) Izatt, R. M., Hansen, L. D., Eatough, D. J., Bradshaw, J. S., Christensen, J. J. *Metal-Ligand Interactions in Organic Chemistry and Biochemistry*; B. Pullman and N. Goldbum: Holland, 1977.
- (107) Izatt, R. M., Terry, R. E., Haymore, B. L., Hansen, L. D., Dalley, N. K., Avondet, A. G., Christensen, J. J. *J. Am. Chem. Soc.* **1976**, *98*, 7620.
- (108) Lehn, J. M., Sauvage, J. P. *J. Am. Chem. Soc.* **1975**, *97*, 6700.
- (109) Izatt, R. M., Bradshaw, J. S., Nielsen, S. A., Lamb, J. D., Christensen, J. J. *Chem. Revs.* **1985**, 85.
- (110) Shchori, E., Jagur-Grodzinski, J. *Isr. J. Chem.* **1973**, *11*, 243.
- (111) Midgley, D. *Chem. Soc. Rev.* **1975**, *4*, 549.
- (112) Steinmann, W., Kaden, T. A. *Helv. Chim. Acta.* **1975**, *58*, 1358.
- (113) Frensdorff, H. K. *J. Am. Chem. Soc.* **1971**, *93*, 600.
- (114) Moss, G. P. *Pure Appl. Chem.* **1987**, *59*, 779.
- (115) Kaim W., S., B. *Bioinorganic Chemistry: Inorganic Elements in the Chemistry of Life*; John Wiley & Sons, Inc.: England, 1996.
- (116) Huber, R. *Angew. Chem. Int. Ed.* **1989**, *28*, 848.

- (117) Hunter, C. N., van Grondelle, R., Olsen, J. D. *Trends Biochem. Sci.* **1989**, *14*, 72.
- (118) Zuber, H. *Trends Biochem. Sci.* **1986**, *11*, 414.
- (119) Chow, H. C., Serlin, R., Strouse, C. E. *J. Am. Chem. Soc.* **1975**, *97*, 7230.
- (120) Lenhert, P. G. *Proc. Roy. Soc. A.* **1968**, *303*, 45.
- (121) Krautler, B., Konrat, R., Stuoerich, E., Faber, G., Cruber, K., Kratky, C. *Inorg. Chem.* **1994**, *33*, 4128.
- (122) Perutz, M. F. *Trends Biochem. Sci.* **1989**, *14*, 42.
- (123) Palmer, G., Reedijk, J. *Eur. J. Biochem.* **1991**, *200*, 599.
- (124) Jolly, W. L. *Modern Inorganic Chemistry*; McGraw-Hill: New York, 1984.
- (125) Fuhrhop, J. H. *Angew. Chem. Int. Ed.* **1974**, *15*.
- (126) Shaanan, B. *J. Mol. Biol.* **1983**, *171*, 31.
- (127) Driggers, E. M., Hale, S. P., Lee, J., Terrett, N. K. *Nature Rev.* **2008**, *7*, 608.
- (128) Nghiem, P., Pearson, G., Langley, R.G. *J. Am. Acad. Dermatol.* **2002**, *46*, 228.
- (129) Nitanaï, Y., Kikuchi, T., Kakoi, K., Hanamaki, S., Fujisawa, I., Aoki, K. *J. Mol. Biol.* **2009**, *385*, 1422.
- (130) Reguiero-Ren, A., Leavitt, K., Kim, S.-H., Hoefle, G., Kiffe, M., Gougoutas, J. Z., DiMarco, J. D., Lee, F. Y. F., Fairchild, C. R., Long, B. H., Vite, G. D. *Org. Lett.* **2002**, *4*, 3815.
- (131) Ganis, P., Avitabile, G., Mechlinski, W., Schaffner, C. P. *J. Am. Chem. Soc.* **1971**, *93*, 4560.
- (132) Bonnett, R. *Chemical Aspects of Photodynamic Therapy*; Gordon and Breach Science Publishers: Amsterdam, 2000.
- (133) Sternberg, E. D., Dolphin, D. *Tetrahedron* **1998**, *54*, 4151.
- (134) Paquette, B., Van Lier, J. E. *Photodyn. Ther.* **1992**, 145.
- (135) Sessler, J. L. *J. Am. Chem. Soc.* **1988**, *110*, 5586.
- (136) Sessler, J. L., Miller, R. A. *Biochem. Pharmacol.* **2000**, *59*, 733.
- (137) Carde, P. *J. Clin. Oncol.* **2001**, *19*, 2074.
- (138) Meyers, C. A. *J. Clin. Oncol.* **2004**, *22*, 157.
- (139) Mody, T. D., Sessler, J. L. *J. Porphyrins Phthalocyanines* **2001**, *5*, 134.
- (140) Sessler, J. L. *J. Porphyrins Phthalocyanines* **2001**, *5*, 593.
- (141) Chari, R. V. *J. Adv. Drug Delivery Rev.* **1998**, *31*, 89.
- (142) Wei, W.-H., Fountain, M. E., Sessler, J. L., Magda, D. J., Wang, Z., Miller, R. A. *Texaphyrin Conjugates. Progress towards Second Generation Diagnostic and Therapeutic Agents*; Springer: The Netherlands, 2005.
- (143) Chang, J. Y.-C., Stevenson, R. J., Lu, G.-L., Brothers, P. J., Clark, G. R., Denny, W. A., Ware, D. C. *Dalton Trans.* **2010**, *39*, 11535.
- (144) Milbank, J. B. J., Stevenson, R. J., Ware, D. C., Chang, J. Y. C., Tercel, M., Ahn, G.-O., Wilson, W. R., Denny, W. A. *J. Med. Chem.* **2009**, *52*, 6822.
- (145) Parker, L. L., Lacy, S. M., Farrugia, L. J., Evans, C., Robins, D. J., O'Hare, C. C., Hartley, J. A., Jaffar, M., Stratford, I. J. *J. Med. Chem.* **2004**, *47*, 5683.
- (146) Graeber, T. G., Osmanian, C., Jacks, T., Housman, D. E., Koch, C. J. *Nature* **1996**, *379*, 88.
- (147) Patterson, A. V., Saunders, M. P., Chinje, E. C., Patterson, L. H., Stratford, I. J. *Anti-Cancer Drug Des.* **1998**, *13*, 541.
- (148) Wilson, W. R., Tercel, M., Anderson, R. F., Denny, W. A. *Anti-Cancer Drug Des.* **1998**, *13*, 663.
- (149) Ross, A., Soares, D. C., Covelli, D., Pannecouque, C., Budd, L., Collins, A., Robertson, N., Parsons, S., De Clercq, E., Kennepohl, P., Sadler, P. J. *Inorg. Chem.* **2010**, *49*, 1122.
- (150) Klatzmann, D., Champagne, E., Chamaret, S., Gruest, J., Guetard, D., Hercend, T., Gluckman, J.-C., Montagnier, L. *Nature* **1984**, *312*, 767.
- (151) Dalglish, A. G., Beverley, P. C. L., Clapham, P. R., Crawford, D. H., Greaves, M. F. *Nature* **1984**, *312*, 763.
- (152) Rusconi, S., Moonis, M., Merrill, D. P., Pallai, P. V., Neidhardt, E. A., Singh, S. K., Willis, K. J., Osburne, M. S., Profy, A. T., Jenson, J. C., Hirsch, M. S. *Antimicrob. Agents Chemother.* **1996**, *40*, 234.
- (153) Basak, A., Dugas, H. *Tetrahedron Lett.* **1986**, *27*, 3.
- (154) McPhee, M. M., Kern, J. T. *Biorg. Med. Chem.* **2001**, *9*, 2809.

- (155) Gokel, G. W., Leevy, W. M., Weber, M. E. *Model Systems for Biological Processes*; Springer: The Netherlands, 2005.
- (156) Brown, G. H. *Photochromism*; Wiley-Interscience: New York, 1971.
- (157) Durr, H., Bousas-Laurent, H. *Photochromism: Molecules and Systems*; Elsevier: Amsterdam, 1990.
- (158) Inoue, Y., Gokel, G. W. *Cation Binding by Macrocycles. Complexation of Cationic Species by Crown Ethers*; Marcel Dekker Inc: New York, 1990.
- (159) Lindoy, L. F. *Pure Appl. Chem.* **1989**, *61*, 1575.
- (160) Lindoy, L. F., Meehan, G. V., Vasilescu, I. O., Kim, H. J., Lee, J. E., Lee, S. S. *Coord. Chem. Rev* **2010**, *254*, 1713.
- (161) Atkinson, I. M., Byriel, K. A., Chia, P. S. K., Kennard, C. H. L., Leong, A.J., Lindoy, L. F., Lowe, M. P., Mahendran, S., Smith, G., Wei, G. *Aust. J. Chem.* **1998**, *51*, 985.
- (162) Moyer, B. A., Birdwell, J. F., Bonnesen, P. V., Delmau, L. H. *Use of Macrocycles in Nuclear-Waste Cleanup*; Spinger: The Netherlands, 2005.
- (163) National Cancer Institute; <http://dtp.nci.nih.gov/branches/btb/ivclsp.html> 2012.
- (164) Developmental Therapeutics Programme; <http://dtp.nci.nih.gov> 2012.

CHAPTER TWO:

EXPERIMENTAL

2.1 General Methods

All reactions that require inert conditions were carried out using a double manifold vacuum line, Schlenkware and cannula techniques. All starting materials used in the syntheses were purchased from Aldrich Chemical Company and used as received while organic solvents were purchased from Merck. Dry solvents were prepared using a Pure solvTM MD 7 purification system from Innovative Technologies. Pyrrole was distilled prior to use. Anhydrous *N,N'*-dimethylformamide, 1,2-dichloroethane and pyridine were purchased from Aldrich and used as received. Methylamine and ethylamine were distilled from 40 and 70 wt% aqueous solutions, respectively. Due to the low boiling point of methylamine, it was distilled into methanol and both the methylamine and ethylamine solutions were stored at -4 °C. Metallic gold (99.999%) in the form of gold pellets were provided by Harmony Gold. Aluminium sheets pre-coated with silica gel 60 F254 (Merck) were used for thin layer chromatography. Column ("flash") chromatography was carried out using Merck silica gel 60 according to a previously reported method.¹

2.2 Instrumentation

NMR spectra were recorded with either a Bruker Avance III 500 spectrometer equipped with an Oxford magnet (11.744 T) or an Avance III 400 spectrometer equipped with a Bruker magnet (9.395 T) using either a 5 mm BBOZ probe or a 5 mm TBIZ probe at the following frequencies: ¹H, 500/400 MHz; ¹³C, 125/100 MHz; ³¹P, 202/162 MHz; ¹⁹F, 376 MHz. The spectra were recorded at 30 °C. The chemical shifts are referenced to the solvent and the shifts are reported in ppm with coupling constants calculated from peak separations and measured in Hertz. All NMR experiments were conducted using Bruker Topspin 2.1, patch level 6.² All proton and carbon chemical shifts are quoted relative to the relevant solvent signals (DMSO-*d*₆, ¹H, 2.50 ppm, ¹³C, 39.5 ppm; CDCl₃, ¹H, 7.26 ppm, ¹³C, 77.0 ppm). The proton and carbon NMR spectra of the compounds were assigned with the use of DEPT and 2D COSY and HSQC data.

FTIR spectra were recorded using the Bruker Alpha FTIR spectrometer with ATR platinum Diamond 1 Refl accessory. Spectra were recorded by placing a single crystal on the platform and crushing the crystal between the platform and diamond head. The machine acquired the information in 32 scans with a spectral resolution of 1.0 cm⁻¹. For this study the most relevant portion of the infrared region is in the frequency range 4 000 to 400 cm⁻¹. The abbreviations used in the text refer to intensity of the peaks and are as follows: br, broad; vs, very strong; s, strong; m, medium and w, weak signals.

Electronic spectra were recorded using a Shimadzu UVPC-1800 double beam UV-vis scanning spectrometer (1.0 cm path length sample cell). Spectra were recorded from 800 to 200 nm.

High resolution masses were determined with a Waters Acquity-LCT Premier coupled high performance liquid chromatograph-mass spectrometer (time-of-flight) using electrospray ionization (ESI) in positive mode. All molecular masses reported in this work are high resolution.

The fluorescence spectra were recorded with a photon technologies Int. (PTI) fluorescence spectrometer controlled by Felix 32© version 1.1 software (PTI) at 25.0 ± 0.1 °C. A quartz emission sample cell served as the solution sample holder. Steady state emission spectra were recorded using PTI's XenoFlash™ 300 Hz pulsed light source and gated emission scans with a delay of 95 μ s, an integration window time of 100 μ s and 45 pulses per channel (shots). The detector used was PTI's model 814 Analog/Photon-counting photomultiplier detector.

Elemental analysis of the gold(III) chelates has not been included. The results of these experiments were unreliable due to incomplete pyrolysis of the highly conjugated macrocycles. This conclusion was drawn based on the fact that elemental analysis of the same samples yielded vastly different results even when single crystals of the same sample were analysed. Although not ideal, ¹H NMR and mass spectrometry were used to determine the purity of the bulk material.

For information on experimental X-ray crystallographic details see Chapter Four.

2.3 Synthesis of Ligand Precursors

2.3.1 Synthesis of 1,2-bis(1*H*-pyrrole-2-yl)ethane-1,2-dione

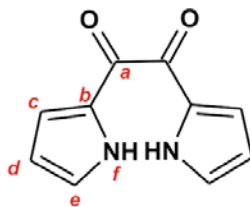


Figure 2.1: Structure of 1,2-bis(1*H*-pyrrole-2-yl)ethane-1,2-dione showing the atom naming scheme.

This compound was prepared according to a previously reported procedure.³ Oxalyl chloride (6.40 g, 0.0500 mol) was added to dry dichloromethane (25 mL) and stirred under an atmosphere of nitrogen. The solution was cooled in an acetone/CO₂ bath to -78 °C and then dry pyridine (10.0 g, 0.120 mol) was added; this led to the formation of a yellow precipitate. The addition of freshly distilled pyrrole (6.70 g, 0.100 mol) in dichloromethane (25 mL) using a canula resulted in the reaction mixture immediately turning from yellow to brown. After stirring the reaction for a further 20 minutes at *c.a.* -60 °C, the reaction was quenched by the addition of hydrochloric acid (5 M, 100 mL). The reaction mixture was filtered to remove any polypyrrole and the organic phase collected using a separating funnel. The aqueous phase was extracted with dichloromethane (3 x 30 mL). The combined organic phases were washed with water (100 mL) and dried over anhydrous magnesium sulfate, filtered and evaporated to dryness to afford a dark green precipitate. The crude product was purified by silica gel column chromatography (dichloromethane eluent, R_f = 0.12) to afford a yellow powder of 1,2-bis(1*H*-pyrrole-2-yl)ethane-1,2-dione (1.61 g, 17% yield).

¹H NMR (500 MHz, DMSO-*d*₆, 303 K) [δ, ppm]: 6.26-6.27 (m, 2H, **d**), 6.89-6.90 (m, 2H, **c**), 7.29-7.30 (m, 2H, **e**), 12.24 (s, 2H, **f**). ¹³C NMR (125 MHz, DMSO-*d*₆, 303 K) [δ, ppm]: 110.92 (**d**), 120.84 (**c**), 128.33 (**e**), 128.57 (**b**), 181.27 (**a**). IR (cm⁻¹): 3273br v(NH-pyrrole), 1613s v(C=O), 1384m v(C=C), 722vs v(C-H wagging). MS: m/z 211.0483 (M + Na⁺).

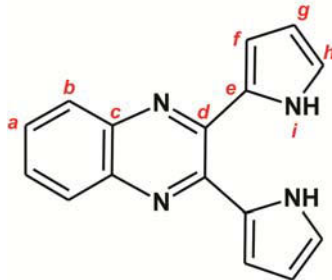
2.3.2 Synthesis of 2,3-di-1*H*-pyrrol-2-ylquinoxaline

Figure 2.2: Structure of 2,3-di-1*H*-pyrrol-2-ylquinoxaline showing the atom naming scheme.

This compound was prepared according to a previously reported procedure.⁴ A solution of 1,2-diaminobenzene (715 mg, 6.62 mmol) in glacial acetic acid (30 mL) was added to 1,2-bis(1*H*-pyrrole-2-yl)ethane-1,2-dione (570 mg, 3.03 mmol) in glacial acetic acid (70 mL) with stirring. The solution was then refluxed under an atmosphere of nitrogen for 90 min before removing the majority of the acetic acid under reduced pressure. The residue was dissolved in a mixture of water (30 mL) and dichloromethane (30 mL). The organic phase was collected and the aqueous phase was extracted with dichloromethane (2 x 20 mL). The combined organic phases were washed with saturated aqueous sodium bicarbonate solution (50 mL), water (50 mL) and brine (50 mL) and dried over anhydrous magnesium sulfate, filtered and evaporated to dryness. The crude product was purified using silica gel column chromatography (dichloromethane eluent, $R_f = 0.46$) and recrystallised from dichloromethane/hexane to afford a yellow crystalline powder of 2,3-di-1*H*-pyrrol-2-ylquinoxaline (0.530 g, 67% yield).

^1H NMR (500 MHz, CDCl_3 , 303 K) [δ , ppm]: 6.27-6.29 (m, 2H, **g**), 6.94-6.95 (m, 2H, **f**), 7.00-7.01 (m, 2H, **h**), 7.58 (dd, $^3J = 6.3$ Hz, $^4J = 3.3$ Hz, 2H, **a**), 7.90 (dd, $^3J = 6.3$ Hz, $^4J = 3.3$ Hz, 2H, **b**), 9.68 (br, 2H, **i**). ^{13}C NMR (125 MHz, CDCl_3 , 303 K) [δ , ppm]: 110.23 (**g**), 113.22 (**f**), 121.46 (**h**), 128.18 (**b**), 129.15 (**a**), 129.20 (**e**), 139.82 (**c**), 143.76 (**d**). IR (cm^{-1}): 3254br $\nu(\text{NH-pyrrole})$, 1513s $\nu(\text{C=N})$, 1403m $\nu(\text{C=C})$, 752vs $\nu(\text{C-H wagging})$. MS: m/z 261.1138 ($\text{M} + \text{H}^+$).

2.3.3 Synthesis of 6,7-dimethyl-2,3-di-1H-pyrrol-2-ylquinoxaline

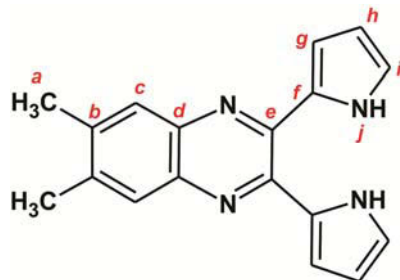


Figure 2.3: Structure of 6,7-dimethyl-2,3-di-1H-pyrrol-2-ylquinoxaline showing the atom naming scheme.

This compound, 6,7-dimethyl-2,3-di-1H-pyrrol-2-ylquinoxaline, was prepared using the same method that was employed to synthesize 2,3-di-1H-pyrrol-2-ylquinoxaline as described above, using 4,5-dimethylbenzene-1,2-diamine (902 mg, 6.62 mmol) as opposed to 1,2-diaminobenzene. The crude product was purified using silica gel column chromatography (dichloromethane eluent, $R_f = 0.46$) and recrystallised from dichloromethane/hexane to afford a yellow crystalline powder of 6,7-dimethyl-2,3-di-1H-pyrrol-2-ylquinoxaline (625 mg, 66% yield).

^1H NMR (500 MHz, $\text{DMSO-}d_6$, 303 K) [δ , ppm]: 2.45 (s, 6H, **a**), 6.10-6.12 (m, 2H, **h**), 6.12-6.14 (m, 2H, **g**), 6.93-6.95 (m, 2H, **i**), 7.71 (s, 2H, **c**), 11.41 (br, 2H, **j**). ^{13}C NMR (125 MHz, $\text{DMSO-}d_6$, 303 K) [δ , ppm]: 20.33 (**a**), 109.21 (**h**), 111.40 (**g**), 121.27 (**i**), 127.56 (**c**), 129.34 (**b**), 138.83 (**f**), 139.67 (**d**), 144.75 (**e**). IR (cm^{-1}): 3261br $\nu(\text{NH-pyrrole})$, 2815w $\nu(\text{CH}_3)$, 1546s $\nu(\text{C=N})$, 1428m $\nu(\text{C=C})$, 722vs $\nu(\text{C-H wagging})$. MS: m/z 289.1450 ($\text{M} + \text{H}^+$).

2.3.4 Synthesis of 6-methyl-2,3-di-1H-pyrrol-2-ylquinoxaline

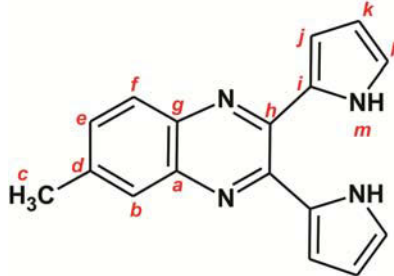


Figure 2.4: Structure of 6-methyl-2,3-di-1H-pyrrol-2-ylquinoxaline showing the atom naming scheme.

A method similar to that used in the synthesis of 2,3-di-1H-pyrrol-2-ylquinoxaline was employed in the synthesis of 6-methyl-2,3-di-1H-pyrrol-2-ylquinoxaline. However, in this case, 3,4-diamino-toluene (808 mg, 6.62 mmol) was used in place of 1,2-diaminobenzene. The crude product was purified using silica gel column chromatography (dichloromethane eluent, $R_f = 0.46$) and recrystallized from dichloromethane/hexane to afford a yellow crystalline powder of 6-methyl-2,3-di-1H-pyrrol-2-ylquinoxaline (565 mg, 68% yield).

^1H NMR: (500 MHz, $\text{DMSO-}d_6$, 303 K) [δ , ppm]: 2.54 (s, 3H, **c**), 6.11-6.12 (m, 2H, **k**), 6.16-6.17 (m, 1H, **j**), 6.18-6.19 (m, 1H, **j**), 6.95-6.97 (m, 2H, **l**), 7.55 (dd, $^3J = 8.5$ Hz, $^4J = 1.8$ Hz, 1H, **e**), 7.72 (br, 1H, **b**), 7.84 (d, $^3J = 8.5$ Hz, 1H, **f**), 11.46 (br, 2H, **m**). ^{13}C NMR: (125 MHz, $\text{DMSO-}d_6$, 303 K) [δ , ppm]: 21.28 (**c**), 108.71 (**k**), 108.82 (**k**), 111.01 (**j**), 111.35 (**j**), 120.85 (**l**), 121.17 (**l**), 126.80 (**b**), 127.59 (**f**), 128.71 (**i**), 131.17 (**e**), 137.78 (**g**), 139.09 (**d**), 139.47 (**a**), 144.29 (**h**), 144.94 (**h**). IR (cm^{-1}): 3200br $\nu(\text{NH-pyrrole})$, 2910w $\nu(\text{CH}_3)$, 1522s $\nu(\text{C=N})$, 1397m $\nu(\text{C=C})$, 728vs $\nu(\text{C-H wagging})$. MS: m/z 275.1301 ($\text{M} + \text{H}^+$).

2.3.5 Synthesis of 6-fluoro-2,3-di-1H-pyrrol-2-ylquinoxaline

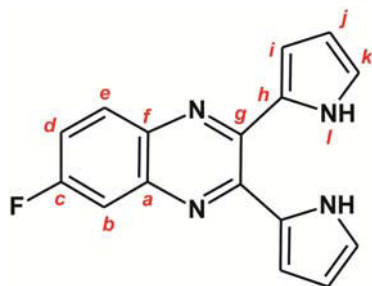


Figure 2.5: Structure of 6-fluoro-2,3-di-1H-pyrrol-2-ylquinoxaline showing the atom naming scheme.

This compound was prepared following a similar method to that used to synthesize 2,3-di-1H-pyrrol-2-ylquinoxaline with 3,4-diaminofluorobenzene (835 mg, 6.62 mmols) being used in place of 1,2-diaminobenzene. The solution was refluxed under an atmosphere of nitrogen for 6 hours as opposed to the 90 min used for the synthesis of 2,3-di-1H-pyrrol-2-ylquinoxaline. Silica gel column chromatography (dichloromethane eluent, $R_f = 0.52$) was used to purify the crude product which was then recrystallized from dichloromethane/hexane resulting in a yellow crystalline powder of 6-fluoro-2,3-di-1H-pyrrol-2-ylquinoxaline (505 mg, 60% yield).

^1H NMR: (500 MHz, $\text{DMSO-}d_6$, 303 K) [δ , ppm]: 6.11-6.15 (m, 2H, **j**), 6.20-6.22 (m, 1H, **i**), 6.27-6.28 (m, 1H, **i**), 6.97-6.98 (m, 1H, **k**), 6.99-7.00 (m, 1H, **k**), 7.61 (dd, $^3J = 8.8$ Hz, $^4J = 2.8$ Hz, 1H, **d**), 7.64 (dd, $^4J = 2.8$ Hz, $^5J = 0.6$ Hz, 1H, **b**), 7.99 (dd, $^3J = 8.8$ Hz, $^5J = 0.6$ Hz, 1H, **e**), 11.50 (s, 1H, **l**), 11.57 (s, 1H, **l**). ^{13}C NMR: (125 MHz, $\text{DMSO-}d_6$, 303 K) [δ , ppm]: 108.79 (**j**), 109.09 (**j**), 111.23 (**b**), 111.31 (**i**), 111.40 (**b**), 112.22 (**h**), 118.64 (**d**), 118.84 (**d**), 121.14 (**k**), 121.97 (**k**), 128.35 (**h**), 128.41 (**h**), 130.29 (**e**), 130.37 (**e**), 136.56 (**a**), 140.02 (**f**), 140.13 (**f**), 144.58 (**g**), 145.70 (**g**), 160.68 (**c**), 162.65 (**c**). ^{19}F NMR: (376 MHz, $\text{DMSO-}d_6$, 303 K) [δ , ppm]: -110.29. IR (cm^{-1}): 3320br v(NH-pyrrole), 1522s v(C=N), 1392m v(C=C), 1230s v(C-F), 738vs v(C-H wagging). MS: m/z 277.0887 ($\text{M} + \text{H}^+$).

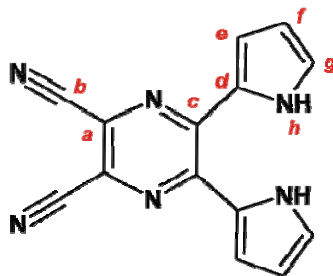
2.3.6 Synthesis of 5,6-di-1*H*-pyrrol-2-ylpyrazine-2,3-dicarbonitrile

Figure 2.6: Structure of 5,6-di-1*H*-pyrrol-2-ylpyrazine-2,3-dicarbonitrile showing the atom naming scheme.

This compound was synthesized according to a previously published procedure.⁵ A solution of 1,2-diaminomaleonitrile (242 mg, 2.20 mmols) in absolute ethanol (20 mL) was added to 1,2-bis(1*H*-pyrrole-2-yl)ethane-1,2-dione (300 mg, 1.60 mmols) in absolute ethanol (30 mL). Boron trifluoride diethyl etherate (454 mg, 3.20 mmols) was added to the reaction mixture and the solution was then refluxed under an atmosphere of nitrogen for 8 hours. The solvent was removed under reduced pressure and the crude product purified using silica gel column chromatography (dichloromethane eluent, $R_f = 0.50$). Recrystallization from dichloromethane/hexane to afford a yellow crystalline powder of 5,6-di-1*H*-pyrrol-2-ylpyrazine-2,3-dicarbonitrile (202 mg, 49% yield).

^1H NMR: (500 MHz, $\text{DMSO-}d_6$, 303 K) [δ , ppm]: 6.19-6.21 (m, 2H, **f**), 6.81-6.83 (m, 2H, **e**), 7.12-7.13 (m, 2H, **g**), 11.90 (br, 2H, **h**). ^{13}C NMR: (125 MHz, $\text{DMSO-}d_6$, 303 K) [δ , ppm]: 110.17 (**f**), 114.50 (**e**), 114.66 (**b**), 125.33 (**g**), 125.99 (**a**), 126.33 (**d**), 143.98 (**c**). IR (cm^{-1}): 3303m $\nu(\text{NH-pyrrole})$, 2243m $\nu(\text{C}\equiv\text{N})$, 1547m $\nu(\text{C}=\text{N})$, 1488s $\nu(\text{C}=\text{C})$, 724vs $\nu(\text{C-H wagging})$. MS: m/z 259.0734 ($\text{M} + \text{H}^+$).

2.3.7 Synthesis of 5,5'-quinoxaline-2,3-diylbis(1H-pyrrole-2-carbaldehyde)

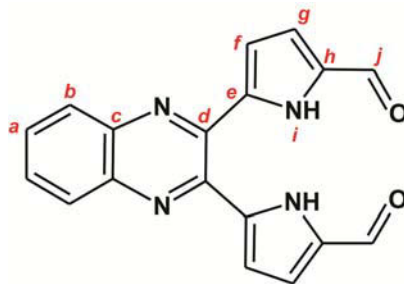


Figure 2.7: Structure of 5,5'-quinoxaline-2,3-diylbis(1H-pyrrole-2-carbaldehyde) showing the atom naming scheme.

This compound was prepared according to a previously reported method.⁴ Under an atmosphere of nitrogen, phosphorus oxychloride (240 μL , 2.57 mmol) was added to *N,N'*-dimethylformamide (454 μL , 5.86 mmol) at 0 $^{\circ}\text{C}$. After stirring the solution for 10 min at room temperature, 1,2-dichloroethane (3 mL) was added. A solution of 2,3-di-1H-pyrrol-2-ylquinoxaline (260 mg, 1.00 mmol) in 1,2-dichloroethane (15 mL) was then added to the reaction mixture over a 10 min period. The reaction mixture was refluxed for 30 min before being cooled to 0 $^{\circ}\text{C}$ whereupon a saturated aqueous solution of sodium acetate (3 mL) was added. The resulting mixture was refluxed for a further 30 min. It was then cooled to room temperature, washed with dichloromethane (3 x 20 mL) and the combined organic phases washed with water (30 mL) and brine (30 mL). The combined organic phases were dried over anhydrous magnesium sulfate, filtered and evaporated to dryness. The crude product was purified using silica gel column chromatography (methanol/dichloromethane (1:100) eluent, $R_f = 0.44$) and recrystallized from dichloromethane/hexane to afford a yellow crystalline powder of 5,5'-quinoxaline-2,3-diylbis(1H-pyrrole-2-carbaldehyde) (250 mg, 79% yield).

^1H NMR (500 MHz, $\text{DMSO-}d_6$, 303 K) [δ , ppm]: 6.16-6.17 (m, 2H, **g**), 7.03-7.04 (m, 2H, **f**), 7.90 (dd, $^3J = 6.4$ Hz, $^4J = 3.4$ Hz, 2H, **a**), 8.14 (dd, $^3J = 6.4$ Hz, $^4J = 3.4$ Hz, 2H, **b**), 9.70 (s, 2H, **j**), 12.66 (s, 2H, **i**). ^{13}C NMR (125 MHz, $\text{DMSO-}d_6$, 303 K) [δ , ppm]: 112.8 (**g**), 118.8 (**f**), 128.6 (**b**), 130.9 (**a**), 134.0 (**h**), 135.4 (**e**), 140.0 (**c**), 144.3 (**d**), 180.3 (**j**). IR (cm^{-1}): 3200 br v(NH-pyrrole), 1634s v(C=O), 1525s v(C=N), 1420m v(C=C), 756vs v(C-H wagging). MS: m/z 339.0860 ($\text{M} + \text{Na}^+$).

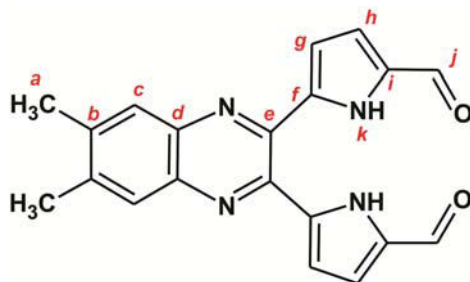
2.3.8 Synthesis of 5,5'-(6,7-dimethylquinoxaline-2,3-diyl)bis(1*H*-pyrrole-2-carbaldehyde)

Figure 2.8: Structure of 5,5'-(6,7-dimethylquinoxaline-2,3-diyl)bis(1*H*-pyrrole-2-carbaldehyde) showing the atom naming scheme.

A similar method was used to synthesize 5,5'-(6-methylquinoxaline-2,3-diyl)bis(1*H*-pyrrole-2-carbaldehyde) as was used to prepare 5,5'-quinoxaline-2,3-diylbis(1*H*-pyrrole-2-carbaldehyde) described above with 6,7-dimethyl-2,3-di-1*H*-pyrrol-2-ylquinoxaline (312 mg, 1.00 mmol) being used in place of 2,3-di-1*H*-pyrrol-2-ylquinoxaline. The crude product was purified using silica gel column chromatography (methanol/dichloromethane eluent, 1:100, $R_f = 0.44$) and recrystallized from dichloromethane/hexane to afford a yellow crystalline powder of 5,5'-(6,7-dimethylquinoxaline-2,3-diyl)bis(1*H*-pyrrole-2-carbaldehyde) (285 mg, 83% yield).

^1H NMR (500 MHz, CDCl_3 , 303 K) [δ , ppm]: 2.49 (s, 6H, **a**), 6.72-6.73 (m, 2H, **h**), 6.94-6.95 (m, 2H, **g**), 7.77 (s, 2H, **c**), 9.62 (s, 2H, **j**), 10.40 (br, 2H, **k**). ^{13}C NMR (125 MHz, CDCl_3 , 303 K) [δ , ppm]: 20.74 (**a**), 113.86 (**h**), 120.98 (**g**), 128.00 (**c**), 133.95 (**i**), 135.68 (**f**), 139.85 (**d**), 141.74 (**b**), 142.23 (**e**), 179.69 (**j**). IR (cm^{-1}): 3165br $\nu(\text{NH-pyrrole})$, 2850w $\nu(\text{CH}_3)$, 1651s $\nu(\text{C=O})$, 1547m $\nu(\text{C=N})$, 1485m (C=C), 752m $\nu(\text{CH wagging})$. MS: m/z 367.1176 ($\text{M} + \text{H}^+$).

2.3.9 Synthesis of 5,5'-(6-methylquinoxaline-2,3-diyl)bis(1H-pyrrole-2-carbaldehyde)

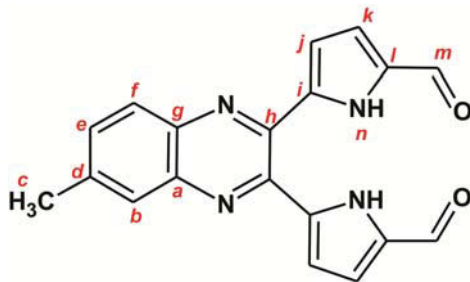


Figure 2.9: Structure of 5,5'-(6-methylquinoxaline-2,3-diyl)bis(1H-pyrrole-2-carbaldehyde) showing the atom naming scheme.

The compound 5,5'-(6-methylquinoxaline-2,3-diyl)bis(1H-pyrrole-2-carbaldehyde) was synthesized following the method used to synthesize 5,5'-quinoxaline-2,3-diylbis(1H-pyrrole-2-carbaldehyde) with 6-methyl-2,3-di-1H-pyrrol-2-ylquinoxaline (274 mg, 1.00 mmol) used in place of 2,3-di-1H-pyrrol-2-ylquinoxaline. The crude product was purified using silica gel column chromatography (methanol/dichloromethane eluent, 1:100, $R_f = 0.40$) and evaporation of the solvent afforded a brown powder of 5,5'-(6-methylquinoxaline-2,3-diyl)bis(1H-pyrrole-2-carbaldehyde) (280 mg, 85% yield).

^1H NMR (500 MHz, CDCl_3 , 303 K) [δ , ppm]: 2.60 (s, 3H, **c**), 6.13-6.15 (m, 2H, **k**), 6.702-7.05 (m, 2H, **j**), 7.75 (dd, $^3J = 8.6$ Hz, $^4J = 1.9$ Hz, 1H, **e**), 7.91 (br, 1H, **b**), 8.03 (d, $^3J = 8.6$ Hz, 1H, **f**), 9.68 (s, 1H, **n**), 9.69 (s, 1H, **n**) 12.60 (s, 2H, **m**). ^{13}C NMR (125 MHz, CDCl_3 , 303 K) [δ , ppm]: 21.39 (**d**), 112.56 (**j**), 112.67 (**k**), 118.84 (**j**), 127.27 (**b**), 128.17 (**f**), 133.09 (**e**), 133.90 (**l**), 133.95 (**l**), 135.55 (**i**), 135.57 (**i**), 138.50 (**a**), 140.08 (**g**), 141.23 (**c**), 143.47 (**h**), 144.19 (**h**) 180.26 (**m**). IR (cm^{-1}): 3179br v(NH-pyrrole), 2920 v(CH_3), 1632s v($\text{C}=\text{O}$), 1500m v($\text{C}=\text{N}$), 1425m v($\text{C}=\text{C}$), 752m v(CH_3 wagging). MS: m/z 329.1042 ($\text{M} + \text{H}^+$).

2.3.10 Synthesis of 5,5'-(6-fluoroquinoxaline-2,3-diyl)bis(1H-pyrrole-2-carbaldehyde)

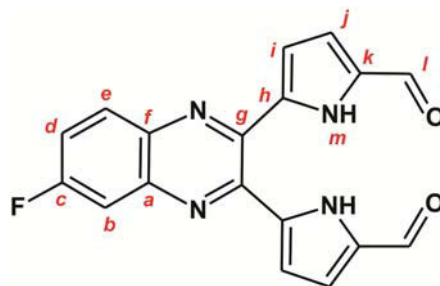


Figure 2.10: Structure of 5,5'-(6-fluoroquinoxaline-2,3-diyl)bis(1H-pyrrole-2-carbaldehyde) showing the atom naming scheme.

This compound was synthesized using a similar method to that used to synthesize 5,5'-quinoxaline-2,3-diylbis(1H-pyrrole-2-carbaldehyde). However, for this synthesis 6-fluoro-2,3-di-1H-pyrrol-2-ylquinoxaline (277 mg, 1.00 mmol) was used in place of 2,3-di-1H-pyrrol-2-ylquinoxaline. Silica gel column chromatography (methanol/dichloromethane eluent, 1:100, $R_f = 0.52$) was used to purify the crude material and resulting in a yellow crystalline powder of 5,5'-(6-fluoroquinoxaline-2,3-diyl)bis(1H-pyrrole-2-carbaldehyde) (199 mg, 60% yield).

^1H NMR: (500 MHz, $\text{DMSO-}d_6$, 303 K) [δ , ppm]: 6.13-6.14 (m, 1H, **j**), 6.19-6.20 (m, 1H, **j**), 7.02-7.03 (m, 1H, **i**), 7.04-7.05 (m, 1H, **i**), 7.83 (dd, $^3J = 9.2$ Hz, $^4J = 2.7$ Hz, 1H, **d**), 7.89 (d, $^4J = 2.7$ Hz, 1H, **b**), 8.21 (d, $^3J = 9.2$ Hz, 1H, **e**), 9.67 (s, 1H, **l**), 9.70 (s, 1H, **l**), 12.65 (s, 1H, **m**), 12.68 (s, 1H, **m**). ^{13}C NMR: (125 MHz, $\text{DMSO-}d_6$, 303 K) [δ , ppm]: 111.93 (**b**), 112.10 (**b**), 112.74 (**j**), 113.09 (**j**), 118.77 (**i**), 118.97 (**i**), 120.92 (**d**), 121.13 (**d**), 131.18 (**e**), 131.26 (**e**), 134.01 (**k**), 134.24 (**k**), 134.99 (**h**), 135.22 (**h**), 137.33 (**a**), 140.72 (**f**), 140.83 (**f**), 143.85 (**g**), 145.08 (**g**), 161.57 (**c**), 163.56 (**c**), 180.31 (**l**), 180.45 (**l**). ^{19}F NMR: (376 MHz, $\text{DMSO-}d_6$, 303 K) [δ , ppm]: -107.2. IR (cm^{-1}): 3207br v(NH-pyrrole), 1615s v(C=O), 1498m v(C=N), 1430m v(C=C), 1192s v(C-F), 789m v(C-H wagging). MS: m/z 333.0791 ($\text{M} + \text{H}^+$).

2.3.11 Synthesis of 5,6-bis(5-formyl-1H-pyrrol-2-yl)pyrazine-2,3-dicarbonitrile

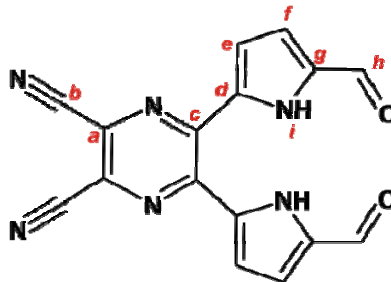


Figure 2.11: Structure of 5,6-bis(5-formyl-1H-pyrrol-2-yl)pyrazine-2,3-dicarbonitrile showing the atom naming scheme.

This compound was synthesized using the same method as that used to synthesize 5,5'-quinoxaline-2,3-diylbis(1H-pyrrole-2-carbaldehyde) with 5,6-di-1H-pyrrol-2-ylpyrazine-2,3-dicarbonitrile (260 mg, 1.00 mmol) used in place of 2,3-di-1H-pyrrol-2-ylquinoxaline. The reaction mixture was also refluxed for 1 hour as opposed to the 30 min used for the synthesis of the former. The crude compound was purified using silica gel column chromatography (methanol/dichloromethane eluent, 1:100, $R_f = 0.40$) and recrystallised from dichloromethane/hexane resulting in a yellow powder of 5,6-bis(5-formyl-1H-pyrrol-2-yl)pyrazine-2,3-dicarbonitrile (125 mg, 40% yield).

^1H NMR: (500 MHz, $\text{DMSO-}d_6$, 303 K) [δ , ppm]: 6.48 (dd, $^3J = 3.9$ Hz, $^4J = 2.2$ Hz, 2H, **f**), 7.04 (dd, $^3J = 3.9$ Hz, $^4J = 2.2$ Hz, 2H, **e**), 9.73 (s, 2H, **h**), 13.02 (s, 2H, **i**). ^{13}C NMR: (125 MHz, $\text{DMSO-}d_6$, 303 K) [δ , ppm]: 114.06 (**b**), 114.89 (**f**), 118.34 (**e**), 128.98 (**a**), 132.21 (**d**), 135.80 (**g**), 144.69 (**c**), 180.99 (**h**). IR (cm^{-1}): 3265br v(NH-pyrrole), 2235m v(C \equiv N), 1659vs v(C=O), 1544m v(C=N), 1436m v(C=C), 796vs v(C-H wagging). MS: m/z 315.0628 (M + H $^+$).

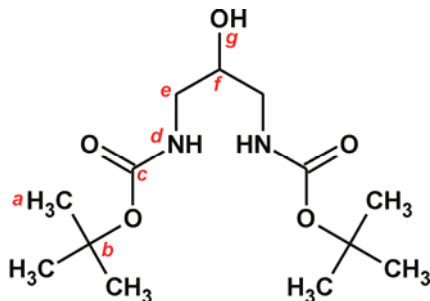
2.3.12 Synthesis of 2,2,12,12-*t*-methyl-3,11-dioxo-4,10-dioxa-5,9-diazatridecan-7-ol (*N,N'*-di-*t*-boc-2-hydroxy-1,3-diaminopropane)

Figure 2.12: Structure of 2,2,12,12-*t*-methyl-3,11-dioxo-4,10-dioxa-5,9-diazatridecan-7-ol (*N,N'*-di-*t*-boc-2-hydroxy-1,3-diaminopropane) showing the atom naming scheme.

Sodium hydrogencarbonate (8.30 g, 99.0 mmol) was dissolved in a 1:1 acetonitrile:water mixture (190 mL) and the solution cooled to 4 °C in an ice bath. 1,3-diamino-2-hydroxypropane (2.50 g, 27.0 mmol) and di-*tert*-butyldicarbonate (12.8 g, 59.0 mmol) were dissolved in the same solvent system (65 mL) and were added to the cooled sodium hydrogencarbonate solution and stirred on ice for 2 hours. The reaction was heated to room temperature and stirred overnight. The acetonitrile was removed by rotary evaporation and the protected amine was extracted into DCM (3 x 75 mL portions). The organic portions were combined, dried over sodium carbonate, and evaporated to dryness by rotary evaporation. The resulting oil was recrystallized from diethylether/hexane, giving colourless crystals (7.20 g, 91% yield).

^1H NMR (400 MHz, CDCl_3 , 303 K) [δ , ppm]: 1.45 (s, 18H, **a**), 3.20 (m, 4H, **e**), 3.75 (m, 2H, **f**, **g**), 5.20 (br, 2H, **d**).
 ^{13}C NMR (100 MHz, CDCl_3 , 303 K) [δ , ppm]: 28.55 (**a**), 43.75 (**b**), 71.07 (**e**), 79.87 (**f**), 157.24 (**c**). IR (cm^{-1}): 3316br $\nu(\text{OH and NH})$, 2971m $\nu(\text{CH}_3 \text{ and CH})$, 2930m $\nu(\text{CH}_3 \text{ and CH})$, 1681s $\nu(\text{C=O})$.

2.3.13 Synthesis of 2-chloro-1,3-diaminopropane dihydrochloride

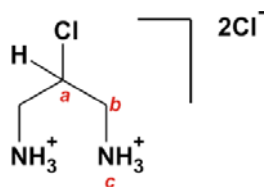


Figure 2.13: Structure of 2-chloro-1,3-diaminopropane dihydrochloride showing the atom naming scheme.

N,N'-di-*t*-*boc*-2-hydroxy-1,3-diaminopropane (1.00 g, 3.50 mmol) and triphenylphosphine (1.50 g, 5.72 mmol) were dissolved in dry chloroform (15 mL) and carbon tetrachloride (35 mL). This solution was refluxed for 5 hours; the solvents were then removed under reduced pressure by rotary evaporation. The resulting oil was dissolved in diethylether to precipitate the OPPh_3 and the resulting suspension centrifuged to remove the insoluble OPPh_3 . The diethyl ether was removed by rotary evaporation and the resulting oil dissolved in methanolic HCl (1.25 M, 30 mL) and stirred overnight. The 2-chloro-1,3-diaminopropane dihydrochloride was precipitated as a white powder by the addition of dichloromethane. The powder was stored over P_2O_5 (304 mg, 49% yield).

^1H NMR (400 MHz, D_2O , 303 K) [δ , ppm]: 3.34 (dd, $^3J = 16.7$ Hz, $^3J = 3.8$ Hz, 2H, **b**), 3.57 (dd, $^3J = 13.9$ Hz $^3J = 3.3$ Hz, 2H, **b**), 4.58 (m, 1H, **a**). ^{13}C NMR (100 MHz, D_2O , 303 K) [δ , ppm]: 42.95 (**b**), 54.94 (**a**).

2.4 Synthesis of Ligands

2.4.1 Synthesis of 12,13-dihydro-14*H*-6,9:17,20-diepipimino[1,6]diazacyclo-heptadecino [12,13- β]quinoxalinato (H_2L1)

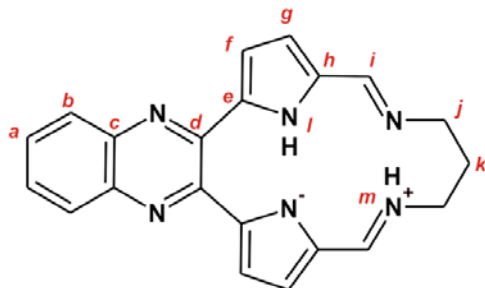


Figure 2.14: Structure of 12,13-dihydro-14*H*-6,9:17,20-diepipimino[1,6]diazacyclo-heptadecino [12,13- β]quinoxalinato showing the atom numbering scheme.

This ligand was synthesized according to a previously described method.⁴ Triethylamine (80 μ l) was added to 5,5'-quinoxaline-2,3-diylbis(1*H*-pyrrole-2-carbaldehyde) (63.4 mg, 0.200 mmol) in dry methanol (40 mL) and the reaction was stirred under reflux for 30 min. After this time, 1,3-diaminopropane (15.0 mg, 0.200 mmol) in dry methanol (2 mL) was added dropwise to the solution which was then refluxed for an additional 2 hours during which time the product precipitated from the solution as an orange solid (48.0 mg, 68% yield).

¹H NMR (500 MHz, DMSO-*d*₆, 303 K) [δ , ppm]: 2.06 (br, 2H, **k**), 4.02 (br, 4H, **j**), 6.98 (d, ³*J* = 3.8 Hz, 2H, **g**), 7.43 (d, ³*J* = 3.8 Hz, 2H, **f**), 7.76 (dd, ³*J* = 6.4 Hz, ⁴*J* = 3.3 Hz, 2H, **a**), 8.00 (dd, ³*J* = 6.4 Hz, ⁴*J* = 3.3 Hz, 2H, **b**), 8.24 (s, 1H, **i**), 8.26 (s, 1H, **i**), 12.21 (br, 1H, **m**), 17.71 (s, 1H, **l**). ¹³C NMR (125 MHz, DMSO-*d*₆, 303 K) [δ , ppm]: 30.80 (**k**), 54.51 (**j**), 116.79 (**f**), 120.96 (**g**), 128.21 (**b**), 129.62 (**a**), 131.51 (**h**), 139.48 (**c**), 143.63 (**d**), 143.77 (**e**), 151.67 (**i**). IR (cm⁻¹): 2836br ν (NH-pyrrole), 1642s ν (C=N), 1600s ν (C=N), 1465m ν (C=C), 770s (C-H wagging). UV-vis (CH₂Cl₂) λ_{\max} [nm] (ϵ /M⁻¹ cm⁻¹): 335 (37 595), 428 (19 508). MS: *m/z* 355.1668 (M + H⁺).

2.4.2 Synthesis of 12,14-dihydro-13,13-dimethyl-6,9:17,20-diepimino[1,6]diazacyclohepta decino[12,13- β]quinoxalinato (H₂L2)

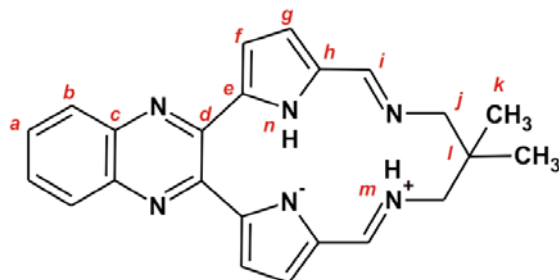


Figure 2.15: Structure of 12,14-dihydro-13,13-dimethyl-6,9:17,20-diepimino[1,6]diazacycloheptadecino-[12,13- β]quinoxalinato showing the atom numbering scheme.

This compound was synthesized using the same method as that employed in the preparation of H₂L1, using 1,3-diamino-2,2-dimethylpropane (20.5 mg, 0.200 mmol) as the bridging diamine. The product precipitated from the reaction mixture as an orange solid (55.0 mg, 72% yield). A crystal suitable for X-ray crystallography was grown by slow evaporation from dichloromethane.

¹H NMR (500 MHz, DMSO-*d*₆, 303 K) [δ , ppm]: 1.00 (s, 6H, **k**), 3.79 (br, 4H, **j**), 6.98 (d, ³*J* = 3.7 Hz, 2H, **g**), 7.40 (d, ³*J* = 3.7 Hz, 2H, **f**), 7.77 (dd, ³*J* = 6.4 Hz, ⁴*J* = 3.3 Hz, 2H, **a**), 8.01 (dd, ³*J* = 6.4 Hz, ⁴*J* = 3.3 Hz, 2H, **b**), 8.19 (s, 1H, **i**), 8.20 (s, 1H, **i**), 12.13 (br, 1H, **m**), 17.75 (s, 1H, **n**). ¹³C NMR (125 MHz, DMSO-*d*₆, 303 K) [δ , ppm]: 24.01 (**l**), 37.74 (**k**), 65.12 (**j**), 116.83 (**f**), 120.97 (**g**), 128.25 (**b**), 129.68 (**a**), 131.42 (**h**), 139.52 (**c**), 143.69 (**d**), 143.90 (**e**), 152.20 (**i**). IR (cm⁻¹): 2819 br v(NH-pyrrole), 1643s v(C=N), 1601s v(C=N), 1466m (C=C), 767s v(C-H wagging). UV-vis (CH₂Cl₂) λ_{\max} [nm] (ϵ /M⁻¹ cm⁻¹): 334 (35 140), 427 (18 407). MS: *m/z* 383.1987 (M + H⁺).

2.4.3 Synthesis of 12,13,14,15-tetrahydro-6,9:18,21-diepimino[1,6]diazacycloctadecino[12,13-β]quinoxalinato (H₂L3)

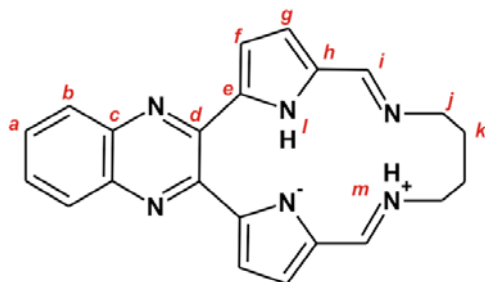


Figure 2.16: Structure of 12,13,14,15-tetrahydro-6,9:18,21-diepimino[1,6]diazacyclooctadecino[12,13-β]quinoxalinato showing the atom numbering scheme.

The method employed for the synthesis of this ligand is similar to the method used to synthesize H₂L1. The diamine; 1,4-diaminobutane (17.6 mg, 0.200 mmol) was used in place of 1,3-diaminopropane. The product, H₂L3, precipitated from the reaction mixture as a brown, micro-crystalline powder (56.0 mg, 76% yield).

¹H NMR (500 MHz, DMSO-*d*₆, 303 K) [δ, ppm]: 1.96 (br, 4H, **k**), 3.77 (br, 4H, **j**), 7.00 (d, ³J = 3.7 Hz, 2H, **g**), 7.49 (d, ³J = 3.7 Hz, 2H, **f**), 7.75 (dd, ³J = 6.4 Hz, ⁴J = 3.3 Hz, 2H, **a**), 7.99 (dd, ³J = 6.4 Hz, ⁴J = 3.3 Hz, 2H, **b**), 8.27 (br, 2H, **i**), 11.24 (br, 1H, **m**), 18.38 (s, 1H, **l**). ¹³C NMR (125 MHz, DMSO-*d*₆, 303 K) [δ, ppm]: 27.85 (**k**), 54.84 (**j**), 116.81 (**f**), 122.60 (**g**), 128.19 (**b**), 129.65 (**a**), 131.02 (**h**), 139.53 (**c**), 143.56 (**d**), 144.22 (**e**), 153.10 (**l**). IR (cm⁻¹): 2842br ν(NH-pyrrole), 1642s ν(C=N), 1606s ν(C=N), 1302s (C=C), 757s ν(C-H wagging). UV-vis (CH₂Cl₂) λ_{max} [nm] (ε/M⁻¹ cm⁻¹): 333 (34 493), 346 (35 636), 421 (17 726). MS: m/z 369.1824 (M + H⁺).

2.4.4 Synthesis of 12,13-dihydro-14*H*-6,9:17,20-diepipimino[1,6]diazacyclo-heptadecino [12,13- β] -6,7-dimethylquinoxalinato (H_2L5)

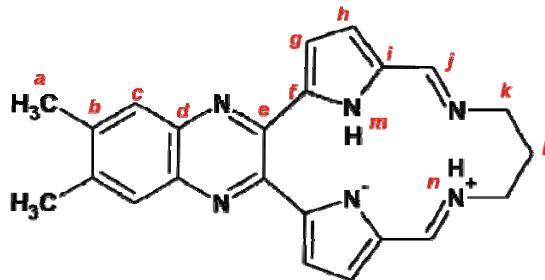


Figure 2.17: Structure of 12,13-dihydro-14*H*-6,9:17,20-diepipimino[1,6]diazacyclo-heptadecino[12,13- β]-6,7-dimethylquinoxalinato showing the atom naming scheme.

A method similar to that used to prepare H_2L1 was employed in the synthesis of H_2L5 . In this synthesis 5,5'-(6,7-dimethylquinoxaline-2,3-diyl)bis(1*H*-pyrrole-2-carbaldehyde) (69.0 mg, 0.200 mmol) was used in place of 5,5'-quinoxaline-2,3-diylbis(1*H*-pyrrole-2-carbaldehyde). An orange powder of H_2L5 (55.0 mg, 72% yield) precipitated from the reaction mixture. A crystal suitable for X-ray crystallography was grown by slow liquid diffusion of hexane into a tetrahydrofuran solution of the compound.

1H NMR (500 MHz, $DMSO-d_6$, 303 K) [δ , ppm]: 2.05 (br, 2H, *l*), 2.47 (s, 6H, *a*), 4.01 (br, 4H, *k*), 6.97 (d, $^3J = 3.8$ Hz, 2H, *h*), 7.38 (d, $^3J = 3.8$ Hz, 2H, *g*), 7.78 (s, 2H, *c*), 8.22 (s, 1H, *j*), 8.23 (s, 1H, *j*), 12.15 (br, 1H, *n*), 17.64 (s, 1H, *m*). ^{13}C NMR (125 MHz, d_6 , 303 K) [δ , ppm]: 19.82 (*a*), 30.91 (*l*), 54.48 (*k*), 116.39 (*g*), 120.97 (*h*), 127.11 (*c*), 131.25 (*i*), 138.53 (*d*), 140.08 (*b*), 142.94 (*e*), 144.04 (*f*), 151.44 (*j*). IR (cm^{-1}): 2835br ν (NH-pyrrole), 1650s ν (C=N), 1631s ν (C=N), 1438m ν (C=C), 769m ν (C-H wagging). UV-vis (CH_2Cl_2) λ_{max} [nm] ($\epsilon/M^{-1} cm^{-1}$): 338 (45 856), 430 (23 996). MS: m/z 383.1982 ($M + H^+$).

2.4.5 Synthesis of 12,13-dihydro-14*H*-6,9:17,20-diepipimino[1,6]diazacyclo-heptadecino[12,13β]6-methylquinoxalino (H₂L6)

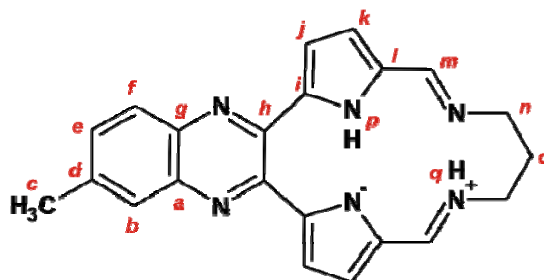


Figure 2.18: Structure of 12,13-dihydro-14*H*-6,9:17,20-diepipimino[1,6]diazacyclo-heptadecino[12,13β]6-methylquinoxalino showing the atom naming scheme.

This compound was synthesized using a similar method to that described for the preparation of H₂L1 with 5,5'-(6-methylquinoxaline-2,3-diyl)bis(1*H*-pyrrole-2-carbaldehyde) (69.8 mg, 0.200 mmols) used in place of 5,5'-quinoxaline-2,3-diylbis(1*H*-pyrrole-2-carbaldehyde). This affords a brown crystalline product of H₂L6 (55.0 mg, 75% yield). A crystal suitable for X-ray crystallography was grown by diffusion of hexane into tetrahydrofuran containing the compound.

¹H NMR (500 MHz, DMSO-*d*₆, 303 K) [δ, ppm]: 2.06 (br, 2H, **o**), 2.56 (s, 3H, **c**), 4.02 (t, ³*J* = 5.0 Hz, 4H, **n**), 6.97-6.98 (m, 2H, **k**), 7.39-7.40 (m, 2H, **j**), 7.60 (dd, ³*J* = 8.5 Hz, ⁴*J* = 1.8 Hz, 1H, **e**), 7.80 (s, 1H, **b**), 7.90 (d, ³*J* = 8.5 Hz, 1H, **f**), 8.24 (br, 2H, **m**), 12.18 (br, 1H, **q**), 17.67 (s, 1H, **p**). ¹³C NMR: (125 MHz, DMSO-*d*₆, 303 K) [δ, ppm]: 21.33 (**c**), 30.87 (**o**), 54.42 (**n**), 54.61 (**n**), 116.57 (**j**), 116.63 (**j**), 120.87 (**k**), 121.09 (**k**), 126.92 (**b**), 127.85 (**f**), 131.36 (**l**), 131.43 (**l**), 131.96 (**e**), 138.01 (**g**), 139.57 (**d**), 139.80 (**a**), 143.04 (**h**), 143.65 (**i**), 144.04 (**h**), 151.53 (**m**), 151.61 (**m**). IR (cm⁻¹): 2845br ν(NH-pyrrole), 1647s ν(C=N), 1610s ν(C=N), 1436m ν(C=C), 774s (C-H wagging). UV-vis (CH₂Cl₂) λ_{max} [nm] (ε/M⁻¹ cm⁻¹): 336 (36 962), 430 (19 002). MS: *m/z* 369.1824 (M + H⁺).

2.4.6 Synthesis of 12,13-dihydro-14*H*-6,9:17,20-diepipimino[1,6]diazacyclo-heptadecino [12,13 β] 6-fluoroquinoxalinato (H_2L7)

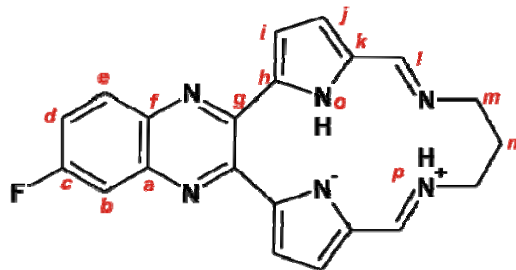


Figure 2.19: Structure of 12,13-dihydro-14*H*-6,9:17,20-diepipimino[1,6]diazacyclo-heptadecino [12,13 β] 6-fluoroquinoxalinato showing the atom naming scheme.

The method used to synthesize this compound was similar to that used to prepare H_2L1 . In this case, 5,5'-(6-fluoroquinoxaline-2,3-diyl)bis(1*H*-pyrrole-2-carbaldehyde) (70.0 mg, 0.200 mmols) was used instead of 2,3-bis(5'-formylpyrrol-2'-yl)quinoxaline. This reaction resulted in the formation of a brown solid of H_2L7 (48.0 mg, 65% yield). A crystal suitable for X-ray crystallography was grown by slow liquid diffusion of hexane into a tetrahydrofuran solution of the compound.

1H NMR (500 MHz, $DMSO-d_6$, 303 K) [δ , ppm]: 2.05 (br, 2H, **n**), 4.03 (br, 4H, **m**), 6.97-7.00 (m, 2H, **j**), 7.41 (d, $^3J = 3.8$ Hz, 1H, **i**), 7.43 (d, $^3J = 3.8$ Hz, 1H, **i**), 7.65-7.69 (m, 1H, **d**), 7.70-7.75 (m, 1H, **b**), 8.04-8.08 (m, 1H, **e**), 8.22-8.24 (m, 2H, **l**), 12.24 (br, 1H, **p**), 17.72 (s, 1H, **o**). ^{13}C NMR (125 MHz, $DMSO-d_6$, 303 K) [δ , ppm]: 30.78 (**n**), 54.31 (**m**), 54.75 (**m**), 111.27 (**b**), 111.44 (**b**), 116.82 (**i**), 117.04 (**i**), 119.75 (**d**), 119.95 (**d**), 120.73 (**j**), 121.24 (**j**), 130.72 (**e**), 130.75 (**e**), 131.52 (**k**), 131.78 (**k**), 136.85 (**a**), 142.80 (**f**), 143.34 (**f**), 143.81 (**g**), 144.33 (**h**), 151.72 (**l**), 157.86 (**l**), 161.86 (**c**). ^{19}F NMR: (376 MHz, $DMSO-d_6$, 303 K) [δ , ppm]: -109.5. IR (cm^{-1}): 2837br v(NH-pyrrole), 1640s v(C=N), 1599s v(C=N), 1462m v(C=C), 1296s v(C-F), 767vs v(C-H wagging). UV-vis (CH_2Cl_2) λ_{max} [nm] 332 (37 622), 430 (19 345). ($\epsilon/M^{-1} cm^{-1}$): MS: m/z 373.1569 ($M + H^+$).

2.4.7 Synthesis of 12,13-dihydro-14*H*-6,9:17,20-diepipino[1,6]diazacyclo-heptadecino-pyrazine-2,3-dicarbonitrile (H₂L8a)

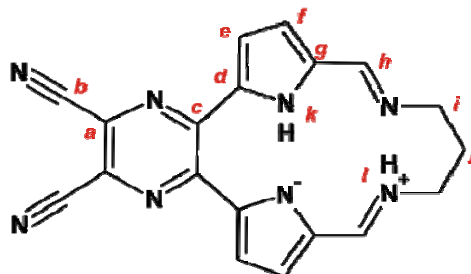


Figure 2.20: Structure of 12,13-dihydro-14*H*-6,9:17,20-diepipino[1,6]diazacyclo-heptadecino-pyrazine-2,3-dicarbonitrile showing the atom naming scheme.

To a solution of 5,6-bis(5-formyl-1*H*-pyrrol-2-yl)pyrazine-2,3-dicarbonitrile (63.0 mg, 0.170 mmols) in methanol, 1,3-diaminopropane (14.0 mg, 0.180 mmols) was added; the solution immediately turned from yellow to red. Silica gel column chromatography (dichloromethane eluent) was used to purify the product. Evaporation of the eluent afforded a red powder of H₂L8a (32.0 mg, 60% yield). A crystal suitable for X-ray crystallography was grown by slow liquid diffusion of diethyl ether into a solution of H₂L8a in *N,N'*-dimethylformamide.

¹H NMR (500 MHz, DMSO-*d*₆, 303 K) [δ, ppm]: 2.12 (br, 2H, *j*), 4.08 (br, 4H, *i*), 7.06 (dd, ³*J* = 3.9 Hz, ⁴*J* = 0.8 Hz, 2H, *f*), 7.37 (dd, ³*J* = 3.9 Hz, ⁴*J* = 0.8 Hz, 2H, *e*), 8.40 (s, 1H, *h*), 8.41 (s, 1H, *h*), 12.51 (br, 1H, *l*), 17.56 (s, 1H, *k*). ¹³C NMR (125 MHz, DMSO-*d*₆, 303 K) [δ, ppm]: 31.51 (*j*), 55.15 (*i*), 115.16 (*b*), 119.37 (*e*), 121.88 (*f*), 127.72 (*a*), 133.66 (*g*), 141.00 (*d*), 143.44 (*c*), 153.13 (*h*). IR (cm⁻¹): 2846br ν(NH-pyrrole), 2227m ν(C≡N), 1645s ν(C=N), 1630s ν(C=N), 1479m (C=C), 769s ν(C-H wagging). UV-vis (DMSO) λ_{max} [nm] (ε/M⁻¹ cm⁻¹): 323 (26 102), 379 (31 697), 476 (19 189). MS: *m/z* 353.1262 (M + H⁺).

2.4.8 Synthesis of 12,13-dihydro-14*H*-6,9:17,20-diepipino[1,6]diazacyclo-heptadecino-pyrazine-3-methoxy-2-carbonitrile (H₂L8b)

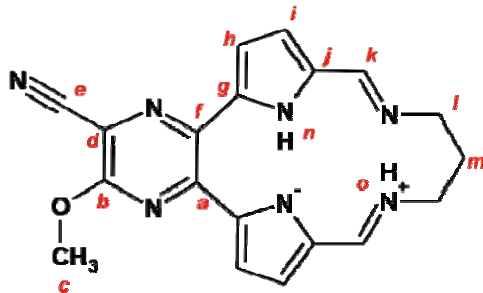


Figure 2.21: Structure of 12,13-dihydro-14*H*-6,9:17,20-diepipino[1,6]diazacyclo-heptadecino-pyrazine-3-methoxy-2-carbonitrile showing the atom naming scheme.

Triethylamine (80 μ l) was added to a solution of 5,6-bis(5-formyl-1*H*-pyrrol-2-yl)pyrazine-2,3-dicarbonitrile (63.0 mg, 0.170 mmols) in dry methanol (30 mL) and the solution refluxed for 30 minutes. A solution of 1,3-diaminopropane (14.0 mg, 0.180 mmols) in dry methanol (2 mL) was added to the reaction vessel which was then refluxed for a further 2 hours; during this time the solution turned from orange to dark red. The solvent was removed under reduced pressure and silica gel column chromatography (dichloromethane eluent, $R_f = 0.60$) was used to purify the crude material resulting in a red powder of H₂L8b (23.0 mg, 38% yield). A crystal suitable for X-ray crystallography was grown by slow liquid diffusion of hexane into a dichloromethane solution of the compound.

¹H NMR (500 MHz, DMSO-*d*₆, 303 K) [δ , ppm]: 2.09 (br, 2H, *m*), 4.04 (br, 4H, *l*), 4.14 (s, 3H, *c*), 6.99 (dd, ³*J* = 3.8 Hz, ⁴*J* = 1.3 Hz, 1H, *i*), 7.03 (dd, ³*J* = 3.8 Hz, ⁴*J* = 0.7 Hz, 1H, *i*), 7.13 (dd, ³*J* = 3.8 Hz, ⁴*J* = 0.7 Hz, 1H, *h*), 7.43 (dd, ³*J* = 3.8 Hz, ⁴*J* = 1.3 Hz, 1H, *h*), 8.21-8.22 (m, 1H, *k*), 8.34-8.35 (m, 1H, *k*), 12.19 (br, 1H, *o*), 17.37 (s, 1H, *n*). ¹³C NMR (125 MHz, DMSO-*d*₆, 303 K) [δ , ppm]: 31.25 (*m*), 53.09 (*l*), 54.29 (*c*), 55.72 (*l*), 112.89 (*d*), 115.11 (*e*), 115.86 (*h*), 117.99 (*h*), 119.61 (*i*), 122.65 (*i*), 130.60 (*j*), 132.66 (*j*), 136.63 (*a*), 139.14 (*g*), 141.61 (*f*), 144.48 (*i*), 150.94 (*k*), 151.86 (*k*), 156.59 (*b*). IR (cm⁻¹): 2833br v(NH-pyrrole), 2217m v(C≡N), 1642s v(C=N), 1625s v(C=N), 1285s v(C-O), 1451m v(C=C), m764s (C-H wagging). UV-vis (CH₂Cl₂) λ_{max} [nm] (ϵ /M⁻¹ cm⁻¹): 322 (27 131), 364 (22 149), 423 (15 285). MS: *m/z* 358.1411 (M + H⁺).

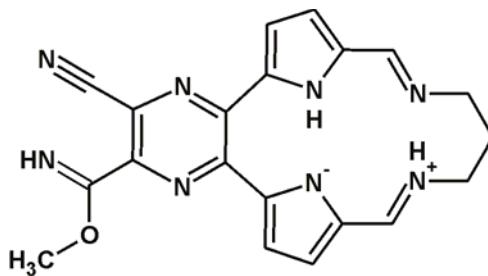
2.4.9 Synthesis of 12,13-dihydro-14H-6,9:17,20-diepipino[1,6]diazacyclo-heptadecino-methyl-3-cyanopyrazine-2-carboxidoate (H₂L8c)

Figure 2.22: Structure of 12,13-dihydro-14H-6,9:17,20-diepipino[1,6]diazacyclo-heptadecino-methyl-3-cyanopyrazine-2-carboxidoate showing the atom naming scheme.

A second red band was collected from the silica gel column chromatography (dichloromethane eluent, $R_f = 0.65$) from the reaction mixture of H₂L8b above. Evaporation of the eluent afforded the product as a red powder of H₂L8c (5.00 mg, 7% yield) as determined by X-ray crystallography. A crystal suitable for X-ray crystallography was grown by evaporation of the dichloromethane solution containing the compound. The compound was not isolated in sufficient yield to fully characterize it using NMR, IR and UV-visible spectroscopy as was done for the other compounds.

2.4.10 Synthesis of *N,N'*-{quinoxaline-2,3-diylbis[1*H*-pyrrole-5,2-diyl(*E*)methylidene]} dimethanamine (**H₂L9**)

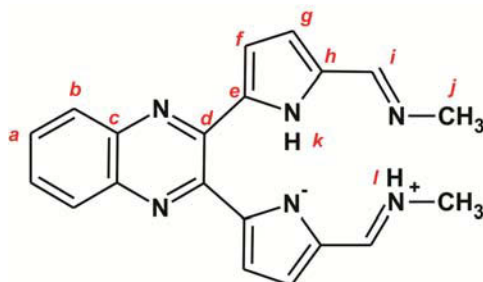


Figure 2.23: Structure of *N,N'*-{quinoxaline-2,3-diylbis[1*H*-pyrrole-5,2-diyl(*E*)methylidene]} dimethanamine showing the atom naming scheme.

Methylamine (29.0 mg, 0.950 mmols) in methanol was added to a solution of 5,5'-quinoxaline-2,3-diylbis(1*H*-pyrrole-2-carbaldehyde) (60.0 mg, 0.190 mmols) in methanol. The solution immediately turned from yellow in colour to orange and was left to stir for 2 hours. After this time the solvent was removed under reduced pressure to afford a red crystalline product of **H₂L9** (60.0 mg, 92% yield). A crystal suitable for X-ray crystallography was grown by slow liquid diffusion of hexane into a dichloromethane solution of the product.

¹H NMR (500 MHz, DMSO-*d*₆, 303 K) [δ, ppm]: 3.42 (s, 6H, **j**), 6.18 (br, 2H, **g**), 6.63 (br, 2H, **f**), 7.77 (dd, ³*J* = 6.3 Hz, ⁴*J* = 3.3 Hz, 2H, **a**), 8.02 (dd, ³*J* = 6.3 Hz, ⁴*J* = 3.3 Hz, 2H, **b**), 8.24 (s, 2H, **i**), 11.40 (br, 1H, **l**). ¹³C NMR (125 MHz, DMSO-*d*₆, 303 K) [δ, ppm]: 47.31 (**j**), 112.54 (**g**), 112.63 (**f**), 128.22 (**b**), 129.79 (**a**), 131.77 (**h**), 139.65 (**c**), 143.56 (**e**), 144.51 (**d**), 153.0 (**i**). IR (cm⁻¹): 2830br v(NH-pyrrole), 1650s v(C=N), 1635s v(C=N), 1462m (C=C), 765vs v(C-H wagging). UV-vis (CH₂Cl₂) λ_{max} [nm] (ε/M⁻¹ cm⁻¹): 269 (11 824), 287 (12 289), 317 (16 981), 356 (14 704), 372 (14 787), 420 (10 189). MS: *m/z* 343.1676 (M + H⁺).

2.4.11 Synthesis of N,N' -{quinoxaline-2,3-diylbis[1*H*-pyrrole-5,2-diyl(*E*)methylidene]} diethanamine (H₂L10)

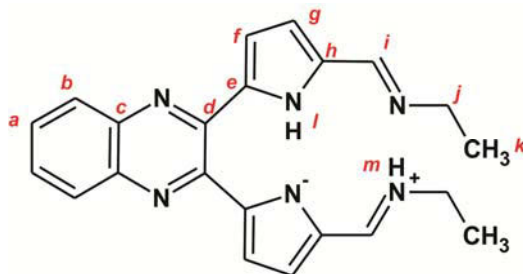


Figure 2.24: Structure of N,N' -{quinoxaline-2,3-diylbis[1*H*-pyrrole-5,2-diyl(*E*)methylidene]}diethanamine showing the atom naming scheme.

The compound H₂L10 was synthesized using a similar method used to prepare H₂L9 with ethylamine (34.0 mg, 0.750 mmols) used in place of methylamine. This yielded a yellow powder of H₂L10 (63.0 mg, 90% yield).

¹H NMR (500 MHz, DMSO-*d*₆, 303 K) [δ, ppm]: 1.21 (t, ³*J* = 7.2 Hz, 6H, **k**), 3.55 (q, ³*J* = 7.0 Hz, 4H, **j**), 6.28 (br, 2H, **g**), 6.61 (br, 2H, **f**), 7.77 (dd, ³*J* = 6.3 Hz, ⁴*J* = 3.4 Hz, 2H, **a**), 8.03 (dd, ³*J* = 6.3 Hz, ⁴*J* = 3.4 Hz, 2H, **b**), 8.25 (s, 2H, **i**) 11.41 (br, 1H, **m**). ¹³C NMR (125 MHz, DMSO-*d*₆, 303 K) [δ, ppm]: 16.44 (**k**), 54.81 (**j**), 112.63 (**g**), 128.22 (**b**), 129.80 (**a**), 132.27 (**h**), 139.36 (**c**), 139.66 (**e**), 144.65 (**d**), 151.50 (**i**). IR (cm⁻¹): 2835br v(NH-pyrrole), 1643s v(C=N), 1633s v(C=N), 1309m (C=C), 754s v(C-H wagging). UV-vis (CH₂Cl₂) λ_{max} [nm] (ε/M⁻¹ cm⁻¹): 270 (17 967), 288 (19 131), 318 (26 900), 344 (25 403), 371 (23 166), 420 (16 718). MS: m/z 371.1989 (M + H⁺).

2.4.12 Synthesis of {quinoxaline-2,3-diylbis[1*H*-pyrrole-5,2-diyl(*E*)methylidene nitrilo]}diethanol (H₂L11)

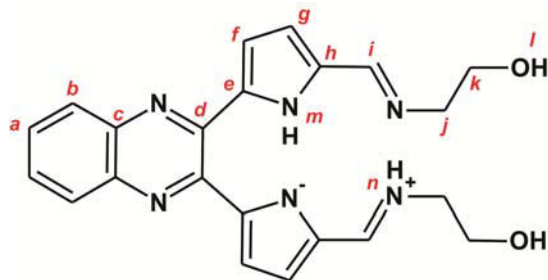


Figure 2.25: Structure of {quinoxaline-2,3-diylbis[1*H*-pyrrole-5,2-diyl(*E*)methylidene nitrilo]}diethanol showing the atom naming scheme.

The dialdehyde 5,5'-quinoxaline-2,3-diylbis(1*H*-pyrrole-2-carbaldehyde) (60.0 mg, 0.190 mmols) was ground together with ethanolamine (46.0 mg, 0.760 mmols) in a solid state reaction using a pestle and mortar. The yellow powder turned to a green paste. This paste was washed with water and dried in an oven at 100 °C for 4 hours yielding a yellow powder of H₂L11 (68.0 mg, 89% yield).

¹H NMR (500 MHz, DMSO-*d*₆, 303 K) [δ, ppm]: 3.60-3.63 (m, 8H, **j,k**), 4.62 (br, 2H, **l**), 6.25 (br, 2H, **g**), 6.61 (br, 2H, **f**), 7.77-7.79 (m, 2H, **a**), 8.02-8.04 (m, 2H, **b**), 8.21 (s, 2H, **i**), 11.71 (br, 1H, **n**). ¹³C NMR (125 MHz, DMSO-*d*₆, 303 K) [δ, ppm]: 60.89 (**j,k**), 62.83 (**j,k**), 112.53 (**f**), 112.61 (**g**), 129.83 (**b**), 132.34 (**h**), 139.71 (**c**), 144.63 (**d**), 152.80 (**i**). IR (cm⁻¹): 3300s, br v(O-H), 2831br v(NH-pyrrole), 1632s v(C=N), 1488m v(C=C), 762vs (C-H wagging). UV-vis (CH₂Cl₂) λ_{max} [nm] (ε/M⁻¹ cm⁻¹): 268 (12 130), 288 (12 069), 318 (17 097), 373 (17 195), 421 (10 222). MS: m/z 403.1885 (M + H⁺).

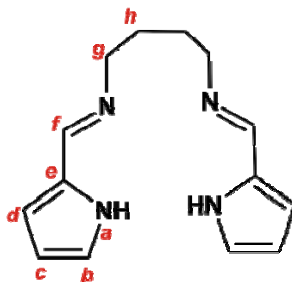
2.4.13 Synthesis of *N,N'*-bis[(1E)-1H-pyrrol-2-ylmethylene]butane-1,4-diamine (H_2L12)

Figure 2.26: Structure of *N,N'*-bis[(1E)-1H-pyrrol-2-ylmethylene]butane-1,4-diamine showing the atom naming scheme.

A solution of 1,4-diaminobutane (139 mg, 1.58 mmols) in methanol (10 mL) was added to a solution of pyrrole-2-carboxaldehyde (300 mg, 3.15 mmols) in methanol (20 mL). The yellow solution was refluxed for 2 hours over which time a pink precipitate formed. This precipitate was filtered and air-dried to produce a pink micro-crystalline powder of H_2L12 (335 mg, 87% yield). A crystal suitable for X-ray crystallography was grown by slow liquid diffusion of hexane into a tetrahydrofuran solution of the compound.

1H NMR (500 MHz, $DMSO-d_6$, 303 K) [δ , ppm]: 1.98 (br, 4H, **h**), 3.48 (br, 4H, **g**), 6.08 (t, $^3J = 3.0$ Hz, 2H, **c**), 6.40 (dd, $^3J = 3.5$ Hz, $^4J = 1.5$ Hz, 2H, **d**), 6.83 (br, 2H, **b**), 8.05 (s, 2H, **f**), 11.31 (br, 2H, **a**). ^{13}C NMR (125 MHz, $DMSO-d_6$, 303 K) [δ , ppm]: 28.47 (**h**), 60.06 (**g**), 108.68 (**c**), 113.06 (**d**), 121.77 (**b**), 129.99 (**e**), 151.47 (**f**). IR (cm^{-1}): 2926br ν (NH-pyrrole), 1641s ν (C=N), 1421s ν (C=C), 725s ν (C-H wagging). UV-vis (CH_2Cl_2) λ_{max} [nm] ($\epsilon/M^{-1}cm^{-1}$): 287 (25 058). MS: 243.1610 m/z ($M + H^+$).

2.5 Synthesis of Metal Salt Precursors

2.5.1 Synthesis of tetrachloroauric acid tetrahydrate (H[AuCl₄] \cdot 4H₂O)

Gold pellets (200 mg, 1.01 mmol) were added to aqua regia (HCl_{Conc}:HNO_{3Conc} 1:3) (10 mL) and stirred with mild heating over a period of 18 hours until the gold had dissolved producing hydrogen tetrachloroaurate(III), as shown by Equation 2.5.1.



This product was washed with 35% hydrochloric acid which was removed by heating the solution. Deionized water was then added to the gold (III) solution to remove all traces of hydrochloric and nitric acid used in the digestion of the gold pellets. The deionized water was removed by heating to leave a concentrated solution of hydrogen tetrachloroaurate(III). This process of washing with deionized water was repeated until the vapours evolved were no longer acidic, as shown by litmus paper. Evaporation of the water affords a yellow powder of hydrogen tetrachloroaurate(III) tetrahydrate (400 mg, 96% yield) which was dried under vacuum and stored under nitrogen.

2.5.2 Synthesis of *tert*-Butylammonium Tetrachloroaurate(III)

Hydrogen tetrachloroaurate(III) tetrahydrate (406 mg, 0.980 mmol) was dissolved in deionized water (15 mL) and *tert*-butylammonium hydrogen sulfate (340 mg, 1.01 mmol) added to the solution. This resulted in the formation of a lipophilic gold(III) salt, *tert*-butylammonium tetrachloroaurate(III), which immediately precipitated as a bright yellow powder as shown in Equation 2.5.2.



The *tert*-butylammonium tetrachloroaurate was extracted into chloroform and dried over anhydrous magnesium sulfate. The solvent was removed by rotary evaporation under reduced pressure yielding a yellow crystalline solid of *tert*-butylammonium tetrachloroaurate(III) (560 mg, 95% yield), which was stored under nitrogen.

2.6 Synthesis of Metal Chelates

2.6.1 Synthesis of [12,13-dihydro-14*H*-6,9:17,20-diepipimino[1,6]diazacyclo-heptadecino [12,13- β] quinoxalinato]gold(III) hexafluorophosphate(V) [Au(L1)](PF₆)

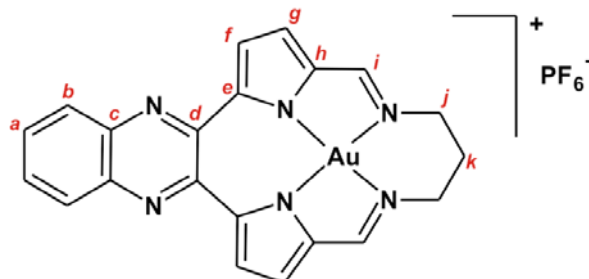


Figure 2.27: Structure of [12,13-dihydro-14*H*-6,9:17,20-diepipimino[1,6]diazacyclo-heptadecino[12,13- β] quinoxalinato]gold(III) hexafluorophosphate(V), showing the atom numbering scheme.

The ligand, H₂L1 (75.0 mg, 0.210 mmols), was dissolved in dichloromethane (20 mL) and a mixture of *tert*-butylammonium tetrachloroaurate (80.0 mg, 0.140 mmols) and *tert*-butylammonium hexafluorophosphate(V) (160 mg, 0.410 mmols) in dichloromethane (15 mL) was added dropwise. The solution was heated to reflux for 16 hours. Over this time a precipitate formed which was filtered, washed with dichloromethane and dried to afford a brick-red powder of [AuL1](PF₆) (44.0 mg, 37% yield). Crystals of suitable quality for X-ray diffraction were grown by vapour diffusion of diethylether into a benzonitrile solution of [Au(L1)](PF₆).

¹H NMR (400 MHz, DMSO-*d*₆, 303 K) [δ , ppm]: 2.42 (br, 2H, **k**), 3.94 (br, 4H, **j**), 7.25 (d, ³*J* = 4.4 Hz, 2H, **g**), 7.81 (d, ³*J* = 4.4 Hz, 2H, **f**), 7.94 (dd, ³*J* = 6.4 Hz, ⁴*J* = 3.3 Hz, 2H, **a**), 8.06 (dd, ³*J* = 6.4 Hz, ⁴*J* = 3.3 Hz, 2H, **b**), 8.73 (s, 2H, **i**); ¹³C NMR (100 MHz, DMSO-*d*₆, 303 K) [δ , ppm]: 33.81 (**k**), 51.27 (**j**), 118.76 (**f**), 122.46 (**g**), 128.48 (**b**), 131.69 (**a**), 135.53 (**d**), 138.99 (**h**), 139.35 (**c**), 147.54 (**e**), 163.05 (**i**); ³¹P NMR (162 MHz, DMSO-*d*₆, 303 K) [δ , ppm]: -144.18, (PF₆); ¹⁹F NMR (376 MHz, DMSO-*d*₆, 303 K) [δ , ppm]: -71.11, -69.23 (PF₆); IR (cm⁻¹): 2954w ν (CH₂), 1572s ν (C=N), 1400m ν (C=C), 832vs ν (PF₆), 760s ν (C-H wagging); UV-vis (CH₃CN) λ_{\max} [nm] (ϵ /M⁻¹ cm⁻¹): 246 (23 346), 309 (30 077), 346 (18 001), 373 (15 237), 455 (12 041);); MS: m/z 549.1104 (M⁺).

2.6.2 Synthesis of [12,14-dihydro-13,13-dimethyl-6,9:17,20-diepipimino[1,6]diazacyclo-heptadecino-[12,13-β]quinoxalinato]gold(III) hexafluorophosphate(V) [Au(L2)](PF₆)

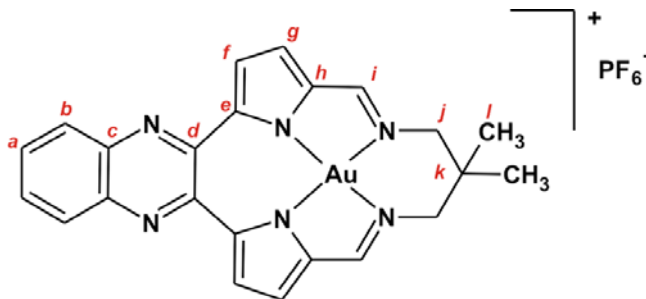


Figure 2.28: Structure of [12,14-dihydro-13,13-dimethyl-6,9:17,20-diepipimino[1,6]diazacyclo-heptadecino-[12,13-β]quinoxalinato]-gold(III) hexafluorophosphate(V), showing the atom numbering scheme.

Attempt 1: Metallation of Ligand

Tert-butylammonium tetrachloroaurate (80.0 mg, 0.138 mmols) and *tert*-butylammonium hexafluorophosphate(V) (160 mg, 0.414 mmols) were dissolved in dichloromethane (15 mL) and added dropwise to a solution of H₂L2 (106 mg, 0.276 mmols) in dichloromethane (20 mL). The reaction mixture was refluxed for 16 hours. Over this time the solution changed from orange to dark red, but no precipitate had formed. On further analysis, metallation of the ligand could not be confirmed.

Attempt 2: Template method

Tert-butylammonium tetrachloroaurate (100 mg, 0.172 mmols) was dissolved in dichloromethane (20 mL) and 2,3-bis(5'-formylpyrrol-2'-yl)quinoxaline (54.0 mg, 0.172 mmols) in dichloromethane (10 mL) was added drop-wise to the gold(III) solution. The solution was heated to reflux for 90 min before adding 1,3-diamino-2,2-dimethylpropane (18.0 mg, 0.172 mmols). A yellow solid immediately precipitated out of solution. The reaction mixture was refluxed for a further 30 min and then triethylamine (35.0 mg, 0.344 mmols) was added. The reaction mixture was refluxed for an additional hour before the orange precipitate was isolated and dried. This precipitate was dissolved in methanol and a saturated solution of ammonium hexafluorophosphate(V) was added to precipitate out the hexafluorophosphate(V) salt of the gold complex. The precipitate was filtered and dried to afford an orange powder of [Au(L2)](PF₆) (45.0 mg, 36% yield).

¹H NMR (500 MHz, DMSO-*d*₆, 303 K) [δ, ppm]: 1.19 (s, 6H, *l*), 3.72 (s, 4H, *j*), 7.44 (d, ³J = 4.4 Hz, 2H, *g*), 7.98 (dd, ³J = 6.4 Hz, ⁴J = 3.4 Hz, 2H, *a*), 7.99 (d, ³J = 4.4 Hz, 2H, *f*), 8.18 (dd, ³J = 6.4 Hz, ⁴J = 3.4 Hz, 2H, *b*), 8.83 (s, 2H, *i*); ¹³C NMR (125 MHz, DMSO-*d*₆, 303 K) [δ, ppm]: 23.09 (*l*), 43.05 (*k*), 61.57 (*j*), 119.35 (*f*), 123.39 (*g*), 129.08 (*b*), 132.31 (*a*), 136.73 (*d*), 139.67 (*h*), 140.03 (*c*), 148.43 (*e*), 164.56 (*i*); ³¹P NMR (162 MHz, DMSO-*d*₆, 303 K) [δ, ppm]: -144.19 (PF₆); ¹⁹F NMR (376 MHz, DMSO-*d*₆, 303 K) [δ, ppm]: -71.14, -69.25 (PF₆); IR (cm⁻¹): 2965w ν(CH₂,CH₃), 1569s ν(C=N), 1405m ν(C=C), 835s ν(PF₆), 768s (C-H wagging). UV-vis (CH₃CN) λ_{max} [nm] (ε/M⁻¹ cm⁻¹): 230 (17 642), 249 (14 463), 309 (16 131), 348 (8 795), 375 (8 680), 458 (6 640), 481 (6 360); MS: m/z 577.1416 (M⁺).

2.6.3 Synthesis of [12,14-dihydro-13,13-dimethyl-6,9:17,20-diepipimino[1,6]diazacyclo-heptadecino-[12,13-β]quinoxalinato]gold(III)trifluoromethanesulfonate [Au(L2)](CF₃SO₃)

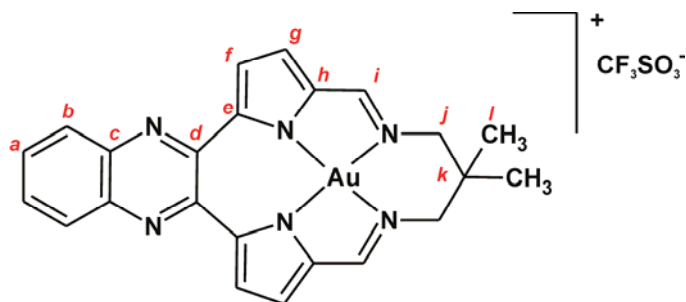


Figure 2.29: Structure of [12,14-dihydro-13,13-dimethyl-6,9:17,20-diepipimino[1,6]diazacyclo-heptadecino-[12,13-β]quinoxalinato]gold(III) trifluoromethanesulfonate.

A solution of 2,3-bis(5'-formylpyrrol-2'-yl)quinoxaline (54.0 mg, 0.172 mmols) in dichloromethane (10 mL) was added to *tert*-butylammonium tetrachloroaurate (100 mg, 0.172 mmols) in dichloromethane (20 mL) and the solution refluxed for 90 min. 1,3-Diamino-2,2-dimethylpropane (18.0 mg, 0.172 mmols) was added to the reaction mixture and a yellow solid immediately precipitated out of solution. The reaction mixture was refluxed for a further 30 min after which triethylamine (35.0 mg, 0.344 mmols) was added. An orange precipitate was isolated and dried after the reaction mixture had been refluxed for 1 hour. The orange precipitate was dissolved in methanol and a saturated, aqueous solution of lithium trifluoromethanesulfonate was added. This resulted in the precipitation of the trifluoromethanesulfonate salt of the gold(III) complex. The precipitate was filtered and dried to afford an orange powder of [Au(L2)](CF₃SO₃) (48.0 mg, 38% yield). Crystals of suitable quality for X-ray diffraction were grown by vapour diffusion of diethylether into an acetonitrile solution of the product.

¹H NMR (500 MHz, DMSO-*d*₆, 303 K) [δ, ppm]: 1.19 (s, 6H, *l*), 3.71 (s, 4H, *j*), 7.47 (d, ³*J* = 4.4 Hz, 2H, *f*), 7.97-7.99 (dd, ⁴*J* = 3.3 Hz, ³*J* = 6.5 Hz, 2H, *a*), 8.02 (d, ³*J* = 4.4 Hz, 2H, *g*), 8.19-8.21 (dd, ⁴*J* = 3.4 Hz, ³*J* = 6.4 Hz, 2H, *b*), 8.85 (s, 2H, *i*). (125 MHz, DMSO-*d*₆, 303 K) [δ, ppm]: 23.10 (*l*), 42.51 (*k*), 61.05 (*j*), 118.85 (*g*), 122.88 (*f*), 128.55 (*b*), 131.78 (*a*), 136.29 (*d*), 139.18 (*h*), 139.52 (*c*), 147.94 (*e*), 164.07 (*i*). ¹⁹F NMR (377 MHz, DMSO-*d*₆, 303 K) [δ, ppm]: -77.74 (s, 3F, 99% ¹²CF₃SO₃⁻), -77.87 (d, ¹*J*_{FC} = 322 Hz, 1% ¹³CF₃SO₃⁻). IR (cm⁻¹): 2953 (w), 2922 (m), 2852 (m), 1570 (s), 1470 (m), 1406 (w), 1338 (m), 1258 (s), 1235 (s), 1144 (m), 1104 (m), 1027 (s), 841 (w), 788 (w), 767 (w), 664 (w), 635 (s), 572 (w), 516 (m), 432 (m). MS: *m/z* 577.1413 (M⁺).

2.6.4 Synthesis of [12,13,14,15-tetrahydro-6,9:18,21-diepipimino[1,6]diazacycloctadecino [12,13- β]quinoxalinato]-gold(III) hexafluorophosphate [Au(L3)](PF₆)

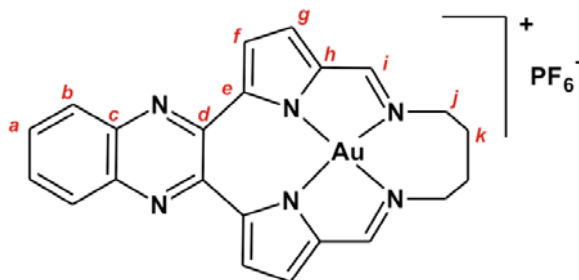


Figure 2.30: Structure of [12,13,14,15-tetrahydro-6,9:18,21-diepipimino[1,6]diazacycloctadecino[12,13 β]quinoxalinato]gold(III) hexafluorophosphate(V), showing the atom naming scheme.

This complex was synthesized using the same template method as that was used to prepare [Au(L2)](PF₆) with 1,4-diamino-butane (15.2 mg, 0.172 mmols) used in place of 1,3-diamino-2,2-dimethylpropane. This reaction afforded a brown powder of [Au(L3)](PF₆) (20.0 mg, 16% yield).

¹H NMR (500 MHz, DMSO-*d*₆, 303 K) [δ , ppm]: 2.04 (br, 4H, **k**), 4.31 (br, 4H, **j**), 7.45 (d, ³*J* = 4.4 Hz, 2H, **g**), 7.96 (dd, ³*J* = 6.4 Hz, ⁴*J* = 3.3 Hz, 2H, **a**), 8.06 (d, ³*J* = 4.4 Hz, 2H, **f**), 8.18 (dd, ³*J* = 6.4 Hz, ⁴*J* = 3.3 Hz, 2H, **b**), 8.74 (s, 2H, **i**); ¹³C NMR(125 MHz, DMSO-*d*₆, 303 K) [δ , ppm]: 23.68 (**k**), 55.41 (**j**), 118.92 (**f**), 122.26 (**g**), 128.52 (**b**), 131.69 (**a**), 135.69 (**d**), 139.64 (**h**), 139.72 (**c**), 147.92 (**e**), 164.83 (**i**); ³¹P NMR (162 MHz, DMSO *d*₆, 303 K) [δ , ppm]: -144.19 (PF₆); ¹⁹F NMR (376 MHz, DMSO *d*₆, 303 K) [δ , ppm]: -71.13, -69.25 (PF₆); IR (cm⁻¹): 2955w ν (CH₂), 590s ν (C=N), 1400m ν (C=C), 829vs ν (PF₆), 796s (C-H wagging); UV-vis (CH₃CN) λ_{\max} [nm] (ϵ /M⁻¹ cm⁻¹): 244 (16 439), 306 (19 364), 347 (13 712), 370 (13 425), 449 (9 825); MS: m/z 563.1265 (M⁺).

2.6.5 Synthesis of [13-chloro-12,14-dihydro-6,9:17,20-diepipimino-[1,6]-diazacyclohepta-decino-[12,13-β]quinoxalinato]gold(III) hexafluorophosphate(V) [Au(L4)](PF₆)

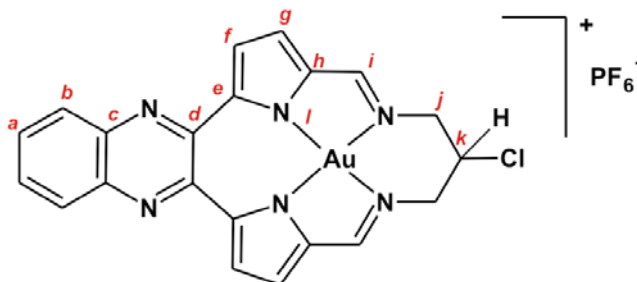


Figure 2.31: Structure of [13-chloro-12,14-dihydro-6,9:17,20-diepipimino-[1,6]-diazacycloheptadecino-[12,13-β]-quinoxalinato]gold(III) hexafluorophosphate(V).

To a solution of *tert*-butylammonium tetrachloroaurate (100 mg, 0.172 mmols) in dichloromethane (20 mL), 2,3-bis(5'-formylpyrrol-2'-yl)quinoxaline (54.0 mg, 0.172 mmols) in dichloromethane (10 mL) was added drop-wise before refluxing the reaction mixture for 90 min. 2-chloro-1,3-diaminopropane dihydrochloride (32.0 mg, 0.172 mmols) was ground together with sodium carbonate (36.0 mg, 0.344 mmols) in a mortar with a pestle until a paste formed. Ethanol was added to extract the amine and the solution filtered to remove the sodium chloride. The ethanolic solution of the amine was added to the gold(III) solution which was refluxed for a further 30 min before triethylamine (35.0 mg, 0.344 mmols) was added. The solution turned a deep orange colour and was refluxed for an additional hour. A saturated aqueous solution of ammonium hexafluorophosphate(V) was added to the reaction solution which was left undisturbed overnight. A precipitate formed and was filtered and dried to give a red powder of [Au(L4)](PF₆) (7.0 mg, 6% yield).

¹H NMR (500 MHz, DMSO-*d*₆, 303 K) [δ, ppm]: 4.25 (dd, ³J = 14.3, ³J = 4.3 Hz, 2H, **j**), 4.43 (d, ³J = 14.3 Hz, 2H, **j**), 5.38 (s, 1H, **k**), 7.50 (d, ³J = 4.3 Hz, 2H, **g**), 7.97 (dd, ³J = 6.4 Hz, ⁴J = 3.3 Hz, 2H, **a**), 8.02 (d, ³J = 4.3 Hz, 2H, **f**), 8.17 (dd, ³J = 6.4 Hz, ⁴J = 3.3 Hz, 2H, **b**), 8.95 (s, 2H, **i**). ¹³C NMR (125 MHz, DMSO-*d*₆, 303 K) [δ, ppm]: 56.06 (**k**), 61.50 (**j**), 119.78 (**f**), 124.03 (**g**), 129.10 (**b**), 132.43 (**a**), 136.61 (**d**), 139.50 (**h**), 140.05 (**c**), 149.20 (**e**), 165.18 (**i**). ³¹P NMR (162 MHz, DMSO-*d*₆, 303 K) [δ, ppm]: -144.19 (PF₆); ¹⁹F NMR (376 MHz, DMSO-*d*₆, 303 K) [δ, ppm]: -71.13, -69.24 (PF₆). IR (cm⁻¹): 2963w v(CH₂), 1569s v(C=N), 1400 m v(C=C), 828vs v(PF₆), 785s v(C-Cl). UV-vis (CH₃CN) λ_{max} [nm] (ε/M⁻¹ cm⁻¹): 246 (21 525), 308 (26 968), 348 (15 730), 376 (16 424), 455 (12 038), 481 (11 542). MS: m/z 583.0717 (M⁺).

2.6.6 Synthesis of [12,13-dihydro-14*H*-6,9:17,20-diepipimino[1,6]diazacyclo-heptadecino [12,13- β]-6,7-dimethylquinoxalinato]gold(III)hexafluorophosphate(V) [Au(L5)](PF₆)

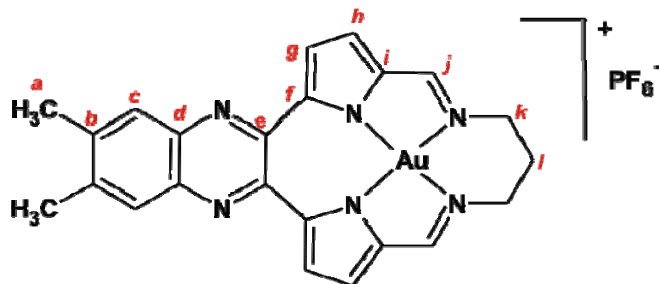


Figure 2.32: Structure of [12,13-dihydro-14*H*-6,9:17,20-diepipimino[1,6]diazacyclo-heptadecino[12,13- β]-6,7-dimethylquinoxalinato]-gold(III) hexafluorophosphate(V), showing the atom naming scheme.

This complex was prepared by the same method used for [Au(L1)](PF₆) with H₂L5 (80.0 mg, 0.210 mmols) used in place of H₂L1 to give a red powder of [Au(L5)](PF₆) (23.0 mg, 23% yield).

¹H NMR: (500 MHz, DMSO-*d*₆, 303 K) [δ , ppm]: 2.42 (br, 2H, *l*), 2.57 (s, 6H, *a*), 3.95 (br, 4H, *k*), 7.40 (d, ³*J* = 4.4 Hz, 2H, *h*), 7.91 (s, 2H, *c*), 7.93 (d, ³*J* = 4.4 Hz, 2H, *g*), 8.83 (s, 2H, *j*). ¹³C NMR (125 MHz, DMSO-*d*₆, 303 K) [δ , ppm]: 20.06 (*a*), 33.91 (*l*), 51.32 (*k*), 118.48 (*g*), 122.63 (*h*), 127.03 (*c*), 135.05 (*e*), 138.70 (*i*), 138.87 (*d*), 143.41 (*b*), 148.62 (*f*), 163.48 (*j*). ³¹P NMR (162 MHz, DMSO-*d*₆, 303 K) [δ , ppm]: -144.19 (PF₆); ¹⁹F NMR (376 MHz, DMSO-*d*₆, 303 K) [δ , ppm]: -71.14, -69.25 (PF₆); IR (cm⁻¹): 2955br v(CH₂, CH₃), 1573s v(C=N), 1396 m v(C=C), 830vs v(PF₆), 795s v(C-H wagging). UV-vis (CH₃CN) λ_{\max} [nm] (ϵ /M⁻¹ cm⁻¹): 248 (25 332), 316 (33 978), 350 (21 241), 378 (18 569), 457 (15 356), 484 (14 097). MS: m/z 577.1425 (M⁺).

2.6.7 Synthesis of [12,13-dihydro-14*H*-6,9:17,20-diepipimino[1,6]diazacyclo-heptadecino [12,13β]6-methylquinoxalinato]gold(III) hexafluorophosphate(V) [Au(L6)](PF₆)

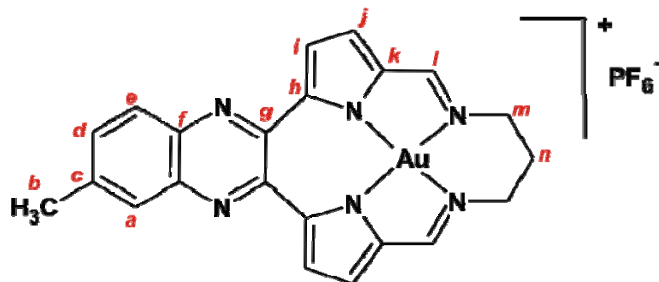


Figure 2.33: Structure of [12,13-dihydro-14*H*-6,9:17,20-diepipimino[1,6]diazacyclo-heptadecino[12,13β]6-methylquinoxalinato]gold(III) hexafluorophosphate(V), showing the atom naming scheme.

This compound was synthesized using a similar method to that which was used to prepare [Au(L1)](PF₆) with H₂L6 (77.0 mg, 0.210 mmols) being used as the ligand. The reaction resulted in a red precipitate of [Au(L6)](PF₆) (28.0 mg, 28% yield).

¹H NMR: (500 MHz, DMSO-*d*₆, 303 K) [δ, ppm]: 2.43 (br, 2H, *n*), 2.65 (s, 3H, *b*), 3.97 (t, ³*J* = 4.3 Hz, 4H, *m*), 7.44 (d, ³*J* = 4.4 Hz, 2H, *j*), 7.82 (dd, ³*J* = 8.6 Hz, ⁴*J* = 1.8 Hz, 1H, *d*), 7.96 (s, 1H, *a*), 7.99 (dd, ³*J* = 4.4 Hz, *J* = 1.3 Hz, 2H, *i*), 8.08 (d, ³*J* = 8.6 Hz, 1H, *e*), 8.86 (s, 1H, *l*), 8.87 (s, 1H, *l*). ¹³C NMR: (125 MHz, DMSO-*d*₆, 303 K) [δ, ppm]: 21.55 (*b*), 33.85 (*n*), 51.37 (*m*), 118.62 (*i*), 118.75 (*i*), 122.65 (*j*), 126.88 (*a*), 128.08 (*e*), 134.26 (*d*), 135.22 (*g*), 135.92 (*g*), 138.20 (*f*), 139.03 (*k*), 139.15 (*k*), 139.63 (*f*), 142.36 (*c*), 147.89 (*h*), 147.95 (*h*), 163.12 (*l*), 163.24 (*l*); ³¹P NMR (162 MHz, DMSO-*d*₆, 303 K) [δ, ppm]: -144.19 (PF₆); ¹⁹F NMR (376 MHz, DMSO-*d*₆, 303 K) [δ, ppm]: -71.14, -69.20 (PF₆). IR (cm⁻¹): 2955br v(CH₂, CH₃), 1573s v(C=N), 1335m v(C=C), 830vs (PF₆). UV-vis (CH₃CN) λ_{max} [nm] (ε/M⁻¹ cm⁻¹): 247 (20 185), 310 (25 593), 348 (15 984), 375 (14 312), 457 (11 183), 482 (10 411). MS: m/z 563.1252 (M⁺).

2.6.8 Synthesis of [12,13-dihydro-14*H*-6,9:17,20-diepipimino[1,6]diazacyclo-heptadecino [12,13β]6-fluoroquinoxalinato]gold(III) hexafluorophosphate(V) [Au(L7)](PF₆)

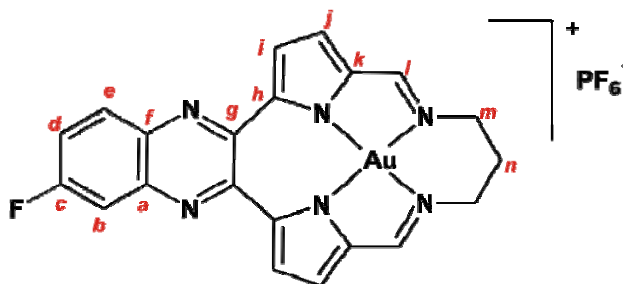


Figure 2.34: Structure of [12,13-dihydro-14*H*-6,9:17,20-diepipimino[1,6]diazacyclo-heptadecino[12,13β]6-fluoroquinoxalinato]gold(III) hexafluorophosphate(V), showing the atom naming scheme.

This compound was prepared using the same method that was used to prepare [Au(L1)](PF₆). The ligand H₂L7 (78.0 mg, 0.210 mmols) was used in this synthesis. During the reaction, a red precipitate of the crude product formed; this was recrystallized from acetonitrile/diethylether which afforded a red powder of [Au(L7)](PF₆) (23.0 mg, 23% yield).

¹H NMR: (500 MHz, DMSO-*d*₆, 303 K) [δ, ppm]: 2.43 (br, 2H, *n*), 3.96 (br, 4H, *m*), 7.37-7.39 (m, 2H, *j*), 7.89-7.94 (m, 4H, *i, d, b*), 8.21-8.24 (m, 1H, *e*), 8.83 (s, 1H, *l*), 8.85 (s, 1H, *l*) ¹³C NMR: (125 MHz, DMSO-*d*₆, 303 K) [δ, ppm]: 33.80 (*n*), 51.38 (*m*), 51.43 (*m*), 111.38 (*b*), 111.57 (*b*), 122.57 (*d*), 122.64 (*j*), 131.23 (*e*), 131.40 (*e*), 135.42 (*a*), 136.53 (*f*), 137.06 (*f*), 139.16 (*k*), 139.49 (*k*), 140.08 (*g*), 140.21 (*g*), 147.29 (*h*), 147.52 (*h*), 162.19 (*c*), 163.29 (*l*), 163.50 (*l*); ³¹P NMR (162 MHz, DMSO-*d*₆, 303 K) [δ, ppm]: -144.19 (PF₆); ¹⁹F NMR (376 MHz, DMSO-*d*₆, 303 K) [δ, ppm]: -105.57 (F), -71.12, -69.24 (PF₆); IR (cm⁻¹): 2958w ν(CH₂), 1618s ν(C=N), 1397m ν(C=C), 1334s ν(C-F), 822vs ν(PF₆), 797s ν(C-H wagging). UV-vis (CH₃CN) λ_{max} [nm] (ε/M⁻¹ cm⁻¹): 245 (29 786), 309 (38 130), 347 (21 781), 371 (18 083), 458 (15 542). MS: m/z 567.0998 (M⁺).

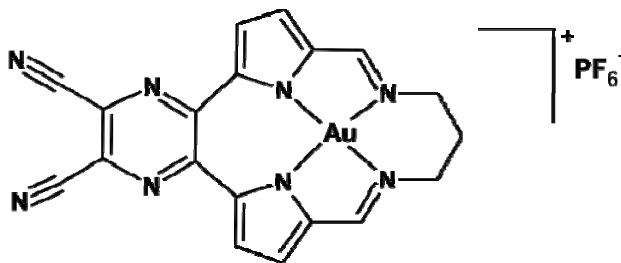
2.6.9 Attempted Synthesis of [12,13-dihydro-14H-6,9:17,20-diepipimino[1,6]diazacyclo-heptadecino-pyrazine-2,3-dicarbonitrile]gold(III)hexafluorophosphate(V) [Au(L8a)](PF₆)

Figure 2.35: Structure of [12,13-dihydro-14H-6,9:17,20-diepipimino[1,6]diazacyclo-heptadecino-pyrazine-2,3-dicarbonitrile]gold(III)hexafluorophosphate(V).

The ligand, H₂L8a (74.0 mg, 0.210 mmols), was dissolved in dichloromethane (20 mL) and a mixture of *tert*-butylammonium tetrachloroaurate (80.0 mg, 0.140 mmols) and *tert*-butylammonium hexafluorophosphate (160 mg, 0.410 mmols) in dichloromethane and ethanol (15 mL) was added dropwise. The solution was heated to reflux for 120 hours. The solution did not change colour and no precipitate formed. The solution was analyzed and no chelation of the metal ion could be detected.

2.6.10 Synthesis of [12,13-dihydro-14*H*-6,9:17,20-diepipino[1,6]diazacyclo-heptadecino-pyrazine-3-methoxy-2-carbonitrile]gold(III)hexafluorophosphate(V) [Au(L8b)](PF₆)

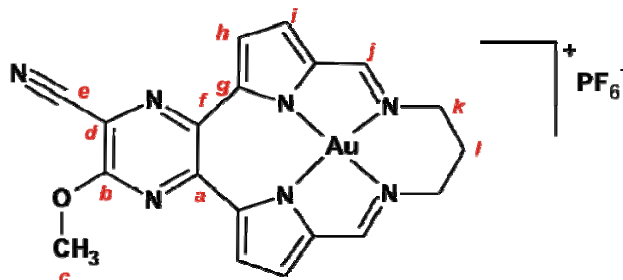


Figure 2.36: Structure of [12,13-dihydro-14*H*-6,9:17,20-diepipino[1,6]diazacyclo-heptadecino-pyrazine-3-methoxy-2-carbonitrile]gold(III) hexafluorophosphate(V), showing the atom naming scheme.

The synthesis of this complex follows the same procedure used for the synthesis of [Au(L1)](PF₆). The ligand used in this reaction is H₂L8b (75.0 mg, 0.210 mmols). The only variation is that the reaction mixture was refluxed for 72 hours before a red precipitate formed. This precipitate was collected by filtration and dried, affording a red powder of [Au(L8b)](PF₆) (8.0 mg, 8% yield).

¹H NMR: (500 MHz, DMSO-*d*₆, 303 K) [δ, ppm]: 2.09 (br, 2H, *l*), 2.85 (br, 4H, *k*), 4.23 (s, 3H, *c*), 7.51 (d, ³*J* = 4.5 Hz, 1H, *i*), 7.52 (d, ³*J* = 4.4 Hz, 1H, *i*), 7.70 (d, ³*J* = 4.5 Hz, 1H, *h*), 8.01 (d, ³*J* = 4.5 Hz, 1H, *h*), 8.93 (s, 1H, *j*), 9.05 (s, 1H, *j*). ³¹P NMR (162 MHz, DMSO-*d*₆, 303 K) [δ, ppm]: -144.20 (PF₆); ¹⁹F NMR (376 MHz, DMSO-*d*₆, 303 K) [δ, ppm]: -71.13, -69.25 (PF₆); IR (cm⁻¹): 2955br v(CH₂), 2230m v(C≡N), 1566s v(C=N), 1458m v(C=C), 1290s v(C-O), 833vs v(PF₆), 786s v(C-H wagging). UV-vis (CH₃CN) λ_{max} [nm] (ε/M⁻¹ cm⁻¹): 248 (18 414), 304 (30 104), 369 (29 338), 451 (15 845). MS: m/z 554.1000 (M⁺).

2.6.11 Synthesis of $[N,N'\text{-}\{quinoxaline\text{-}2,3\text{-}diylbis\{pyrrole\text{-}5,2\text{-}diyl(E)methylidene\}\}dimethanamine]gold(III) hexafluorophosphate(V) [Au(L9)](PF_6)$

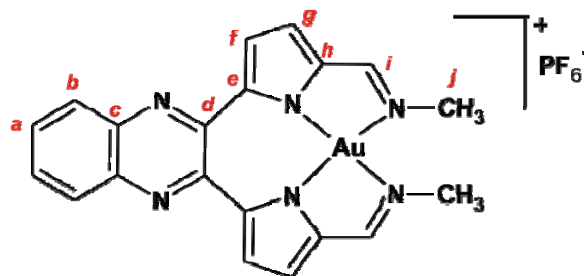


Figure 2.37: Structure of $[N,N'\text{-}\{quinoxaline\text{-}2,3\text{-}diylbis\{pyrrole\text{-}5,2\text{-}diyl(E)methylidene\}\}dimethanamine]gold(III) hexafluorophosphate(V)$, showing the atom naming scheme.

The gold(III) salt, *tert*-butylammonium tetrachloroaurate (92.0 mg, 0.160 mmols) and *tert*-butylammonium hexafluorophosphate(V) (160 mg, 0.410 mmols) in dichloromethane (15 mL) were slowly added to a solution of the ligand H₂L9 (65.0 mg, 0.190 mmols) in DCM/ethanol (50:50). The solution was refluxed for 30 min during which time the solution went dark red and a brown precipitate formed. The precipitate was collected by filtration and dried affording a brown powder of $[Au(L9)](PF_6)$ (48.0 mg, 44% yield).

¹H NMR (500 MHz, DMSO-*d*₆, 303 K) [δ , ppm]: 3.89 (s, 6H, *j*), 7.33 (d, ³*J* = 4.4 Hz, 2H, *g*), 7.90 (d, ³*J* = 4.4 Hz, 2H, *f*), 7.94 (dd, ³*J* = 6.5 Hz, ⁴*J* = 3.4 Hz, 2H, *a*), 8.11 (dd, ³*J* = 6.5 Hz, ⁴*J* = 3.4 Hz, 2H, *b*), 8.61 (s, 2H, *i*). ¹³C NMR (125 MHz, DMSO-*d*₆, 303 K) [δ , ppm]: 47.95 (*j*), 118.85 (*f*), 121.86 (*g*), 128.50 (*b*), 131.65 (*a*), 135.60 (*d*), 139.31 (*h*), 139.80 (*c*), 148.13 (*e*), 166.35 (*i*); ³¹P NMR (162 MHz, DMSO-*d*₆, 303 K) [δ , ppm]: -144.19, (PF₆); ¹⁹F NMR (376 MHz, DMSO-*d*₆, 303 K) [δ , ppm]: -71.13, -69.25 (PF₆); IR (cm⁻¹): 2966br ν (CH₂, CH₃), 1602s ν (C=N), 1360m ν (C=C), 812vs ν (PF₆), 755s ν (C-H wagging). UV-vis (CH₃CN) λ_{max} [nm] ($\epsilon/M^{-1} cm^{-1}$): 244 (23 006), 302 (25 543), 345 (19 045), 368 (17 580), 448 (14 281). MS: *m/z* 537.1111 (M⁺).

2.6.12 Synthesis of $[N,N'\text{-}\{quinoxaline\text{-}2,3\text{-}diylbis[1H\text{-}pyrrole\text{-}5,2\text{-}diyl(E)methylidene]\}diethanamine]gold(III) \text{ hexafluorophosphate(V) } [Au(L10)](PF_6)$

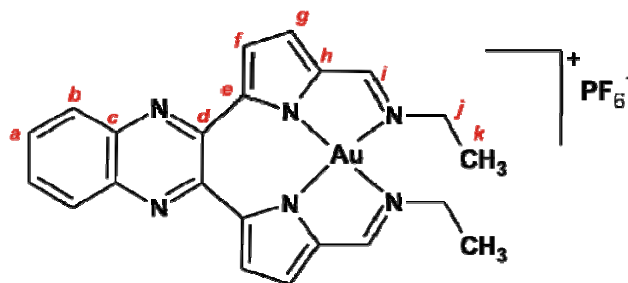


Figure 2.38: Structure of $[N,N'\text{-}\{quinoxaline\text{-}2,3\text{-}diylbis[1H\text{-}pyrrole\text{-}5,2\text{-}diyl(E)methylidene]\}diethanamine]gold(III) \text{ hexafluorophosphate(V) } [Au(L10)](PF_6)$, showing the atom naming scheme.

This complex was synthesized using the same method as that used to synthesize $[Au(L9)](PF_6)$. The ligand H_2L10 (70.0 mg, 0.190 mmols) was used in place of the methyl analogue. This reaction resulted in a brown powder of $[Au(L10)](PF_6)$ (45.0 mg, 39% yield).

1H NMR (500 MHz, $DMSO-d_6$, 303 K) [δ , ppm]: 1.49 (t, $^3J = 7.0$ Hz, 6H, **k**), 4.07 (q, $^3J = 7.0$ Hz, 4H, **j**), 7.44 (d, $^3J = 4.4$ Hz, 2H, **g**), 7.95 (dd, $^3J = 6.5$ Hz, $^4J = 3.4$ Hz, 2H, **a**), 7.97 (d, $^3J = 4.4$ Hz, 2H, **f**), 8.17 (dd, $^3J = 6.5$ Hz, $^4J = 3.4$ Hz, 2H, **b**), 8.70 (s, 2H, **i**). ^{13}C NMR (125 MHz, $DMSO-d_6$, 303 K) [δ , ppm]: 16.65 (**k**), 52.79 (**j**), 118.95 (**f**), 122.24 (**g**), 128.55 (**b**), 131.69 (**a**), 136.19 (**d**), 139.99 (**h**), 140.05 (**c**), 148.36 (**e**), 165.85 (**i**). ^{31}P NMR (162 MHz, $DMSO-d_6$, 303 K) [δ , ppm]: -144.18 (PF_6); ^{19}F NMR (376 MHz, $DMSO-d_6$, 303 K) [δ , ppm]: -71.14, -69.25 (PF_6); IR (cm^{-1}): 2965br v(CH_2 , CH_3), 1597s v($C=N$), 1363m v($C=C$), 833vs v(PF_6), 755s v($C-H$ wagging). UV-vis (CH_3CN) λ_{max} [nm] ($\epsilon/M^{-1}cm^{-1}$): 245 (29 211), 304 (30 762), 346 (23 090), 370 (21 764), 449 (18 094). MS: m/z 565.1426 (M^+).

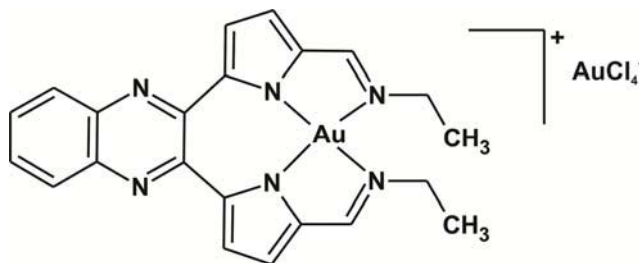
2.6.13 Synthesis of $[N,N'\text{-}\{quinoxaline\text{-}2,3\text{-}diylbis[1H\text{-}pyrrole\text{-}5,2\text{-}diyl(E)methylidene]\}diethanamine]gold(III) tetrachloroaurate [Au(L10)](AuCl_4)$ 

Figure 2.39: Structure of $[N,N'\text{-}\{quinoxaline\text{-}2,3\text{-}diylbis[1H\text{-}pyrrole\text{-}5,2\text{-}diyl(E)methylidene]\}diethanamine]gold(III) tetrachloroaurate$.

To the ligand, H₂L10 (70.0 mg, 0.190 mmols), dissolved in dichloromethane (20 mL) a solution of *tert*-butylammonium tetrachloroaurate (80.0 mg, 0.140 mmols) in dichloromethane and ethanol (15 mL) was added dropwise. The solution was heated to reflux for 1 hour. A brown precipitate formed which was dissolved in acetonitrile and layered with diethylether. This resulted in single crystals of $[AuL(10)](AuCl_4)$ suitable for X-ray crystallography.

2.6.14 Synthesis of [{quinoxaline-2,3-diylbis[pyrrole-5,2-diyl(*E*)methylidene]nitri]gold(III) hexafluorophosphate(V) [Au(L11)](PF₆)

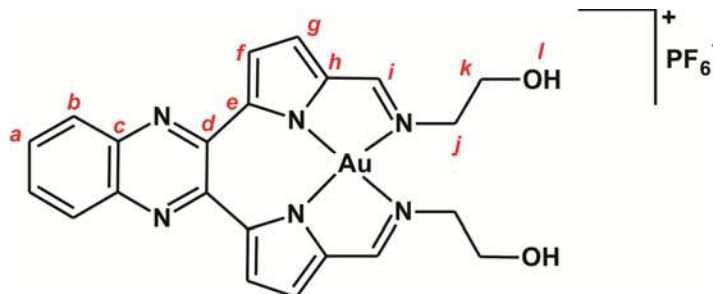


Figure 2.40: Structure of [{quinoxaline-2,3-diylbis[pyrrole-5,2-diyl(*E*)methylidene]nitri]gold(III) hexafluorophosphate(V), showing the atom numbering scheme.

A similar method to that used to synthesize [Au(L9)](PF₆) was employed to prepare this metal chelate, using H₂L11 in place of the methylene analogue. The reaction afforded a brown powder of [Au(L11)](PF₆) (38.0 mg, 32% yield).

¹H NMR: (500 MHz, DMSO-*d*₆, 303 K) [δ, ppm]: 3.81 (q, ³J = 4.9 Hz, 4H, **k**), 4.08 (t, ³J = 4.7 Hz, 4H, **j**), 5.19 (t, ³J = 5.6 Hz, 2H, **l**), 7.49 (d, ³J = 4.4 Hz, 2H, **g**), 7.95 (dd, ³J = 6.4 Hz, ⁴J = 3.4 Hz, 2H, **a**), 7.98 (d, ³J = 4.4 Hz, 2H, **f**), 8.18 (dd, ³J = 6.4 Hz, ⁴J = 3.4 Hz, 2H, **b**), 8.62 (s, 2H, **i**). ¹³C NMR (125 MHz, DMSO-*d*₆, 303 K) [δ, ppm]: 60.01 (**k**), 60.18 (**j**), 119.12 (**f**), 122.59 (**g**), 128.58 (**b**), 131.75 (**a**), 136.18 (**d**), 139.84 (**h**), 140.03 (**c**), 148.44 (**e**), 167.41 (**i**). ³¹P NMR (162 MHz, DMSO-*d*₆, 303 K) [δ, ppm]: -144.18 (PF₆); ¹⁹F NMR (376 MHz, DMSO-*d*₆, 303 K) [δ, ppm]: -71.13, -69.25 (PF₆); IR (cm⁻¹): 3275br ν(O-H), 2968w ν(CH₂), 1597s ν(C=N), 1400m ν(C=C), 833vs ν(PF₆), 777s ν(C-H wagging). UV-vis (DMSO) λ_{max} [nm] (ε/M⁻¹ cm⁻¹): 302 (23 313), 339 (20 649), 423 (11 282), 454 (12 691). MS: m/z 597.1318 (M⁺).

2.6.15 Synthesis of *N,N'*-bis[(1*E*)-1H-pyrrol-2-ylmethylene]butane-1,4-diamine gold(III) hexafluorophosphate(V) [Au(L12)](PF₆)

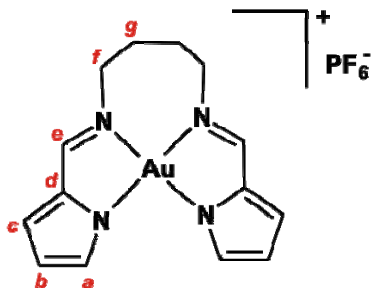


Figure 2.41: Structure of *N,N'*-bis[(1*E*)-1H-pyrrol-2-ylmethylene]butane-1,4-diamine gold(III) hexafluorophosphate(V), showing the atom numbering scheme.

The ligand, H₂L12 (200 mg, 0.850 mmols), was dissolved in ethanol (10 mL) and a mixture of *tert*-butylammonium tetrachloroaurate (100 mg, 0.170 mmols) and *tert*-butylammonium hexafluorophosphate (160 mg, 0.410 mmols) in dichloromethane (15 mL) was added dropwise. The solution was refluxed for 1 hour until a red precipitate formed. The precipitate was filtered and air dried to afford a red powder of [Au(L12)](PF₆) (41.0 mg, 41% yield).

¹H NMR: (500 MHz, DMSO-*d*₆, 303 K) [δ, ppm]: 1.95 (br, 4H, **g**), 4.11 (br, 4H, **f**), 6.45 (dd, ³*J* = 4.1 Hz, ³*J* = 2.3, 2H, **b**), 7.06 (dd, ³*J* = 4.1 Hz, ⁴*J* = 2.3 Hz, 2H, **c**), 7.73 (br, 2H, **a**), 8.28 (s, 2H, **e**). ¹³C NMR (125 MHz, DMSO-*d*₆, 303 K) [δ, ppm]: 23.80 (**g**), 55.21 (**f**), 111.95 (**b**), 121.96 (**c**), 136.26 (**d**), 137.68 (**a**), 164.91 (**e**). ³¹P NMR (162 MHz, DMSO-*d*₆, 303 K) [δ, ppm]: -144.19 (PF₆); ¹⁹F NMR (376 MHz, DMSO-*d*₆, 303 K) [δ, ppm]: -71.14, -69.25 (PF₆). IR (cm⁻¹): 2967w ν(CH₂), 1585s ν(C=N), 1441m ν(C=C), 826vs ν(PF₆), 744s ν(C-H wagging). UV-vis (CH₃CN) λ_{max} [nm] (ε/M⁻¹ cm⁻¹): 284 (14 488), 372 (11 051). MS: 437.1045 m/z (M⁺).

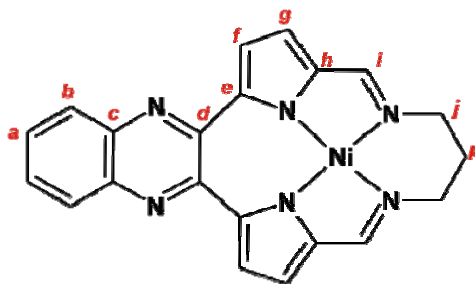
2.6.16 Synthesis of [12,13-dihydro-14*H*-6,9:17,20-diepipimino[1,6]diazacyclo-heptadecino [12,13- β]quinoxalinato]nickel(II) [Ni(L1)]

Figure 2.42: Structure of [12,13-dihydro-14*H*-6,9:17,20-diepipimino[1,6]diazacyclo-heptadecino[12,13- β]quinoxalinato]nickel(II), showing the atom numbering scheme.

The synthesis of this complex has been previously described.⁴ A solution of nickel(II) nitrate hexahydrate (58.0 mg, 0.200 mmol) in methanol (20 mL) was added to a mixture of the ligand, H₂L1 (69.0 mg, 0.200 mmol) in methanol (10 mL). The reaction mixture was left stirring at room temperature for 16 hours before the solvent was removed under reduced pressure to afford a red precipitate. The crude product was purified by silica gel column chromatography (dichloromethane eluent) and recrystallized from DCM:hexane to afford purple crystals of Ni(L1) (35.0 mg, 43% yield).

¹H NMR: (500 MHz, CDCl₃, 303 K) [δ , ppm]: 2.06 (br, 2H, *k*), 3.45 (t, ³*J* = 5.0 Hz 4H, *j*), 6.98 (d, ³*J* = 4.1 Hz, 2H, *f*), 7.66 (s, 2H, *i*), 7.8 (dd, ³*J* = 6.4 Hz, ⁴*J* = 3.4 Hz, 2H, *a*), 7.87 (d, ³*J* = 4.1 Hz, 2H, *g*), 8.10 (dd, ³*J* = 6.4 Hz, ⁴*J* = 3.4 Hz, 2H, *b*). ¹³C NMR: (125 MHz, CDCl₃, 298 K) [δ , ppm]: 31.28 (*k*), 53.44 (*j*), 117.61 (*f*), 120.17 (*g*), 128.32 (*b*), 129.13 (*a*), 139.82 (*c*), 141.93 (*h*), 148.81 (*e*), 150.04(*d*), 159.63 (*i*). MS: *m/z* 411.0860 (M+H)⁺.

2.7 References

- (1) Still, W. C., Kahn, M., Mitra, A. *J. Org. Chem.* **1978**, *43*, 2923.
- (2) Bruker Topspin 2.1(pl6) from Bruker BioSpin
- (3) Black, C. B., Andrioletti, B., Try, A. C., Ruiperez, C., Sessler J. L. *J. Am. Chem. Soc.* **1999**, *121*, 10438.
- (4) Wang, L., Zhu, X.-J., Wong, W.-Y., Guo, J.-P., Wong, W.-K., Li, Z.-Y. *Dalton Trans.* **2005**, 3235.
- (5) Ghosh, T., Maiya, B. G., Wong, M. W. *J. Phys. Chem. A.* **2004**, *108*, 11249.

CHAPTER THREE:

SYNTHESIS

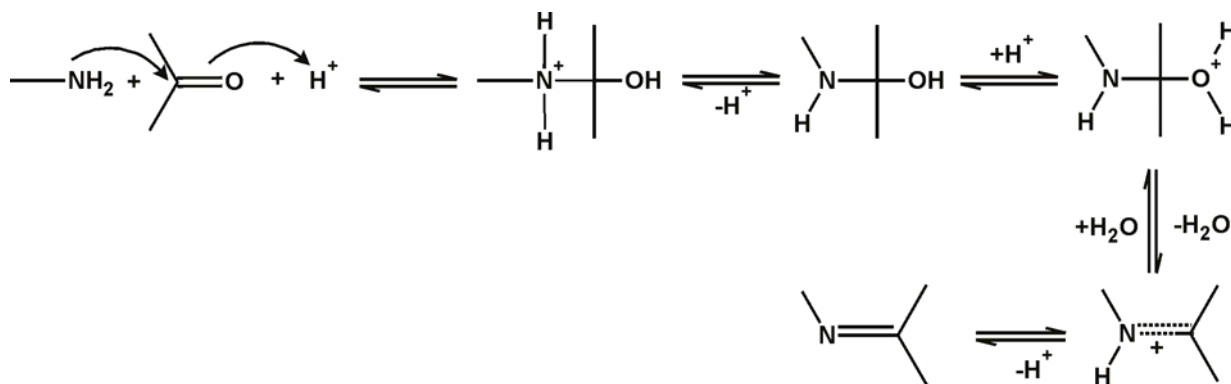
3.1 Introduction

There are three types of Schiff base ligands that have been synthesized for this work:

- Macrocyclic: further divided into quinoxaline and pyrazine derived macrocycles
- Pseudomacrocyclic
- Acyclic

These Schiff base ligands have all been successfully coordinated to gold(III).

Acyclic tetradentate bis(pyrrolide-imine) Schiff base ligands bridged by variable di-(azomethine) units have been well studied.¹⁻³ These compounds are formed by the condensation reactions of carbonyl compounds with primary amines; the reaction was discovered in 1864 by Hugo Schiff.⁴ This acid-catalyzed reaction made it possible to synthesize a wide variety of azomethines.⁵ The classical Schiff condensation using carbonyl compounds and primary amines as starting materials occurs in high yields and the mechanism is well understood, with each step in the reaction being reversible, Scheme 3.1.⁵



Scheme 3.1: Mechanism of condensation of carbonyl compounds with primary amines.

Coordination of metal ions to tetradentate bis(pyrrolide-imine) Schiff base ligands occurs with concomitant deprotonation of the two pyrrole NH atoms to afford a dianionic ligand which is capable of stabilizing metals in high oxidation states. These ligands react with metals to give four-coordinate complexes with a metal: ligand ratio of 1:1.^{6,7} When flexible alkyl bridging units are used, a linear configuration, which is capable of forming binuclear complexes is adopted and several examples of such complexes are known.⁸ Studies suggest that ligands of this nature are well suited to chelation of octahedral and square-planar metals such as Mn(II), Ni(II), Pd(II), Co(III) and Fe(III).^{6,9-13} This indicates that the square-planar gold(III) ion should be stabilized by these σ -donor Schiff base ligands.

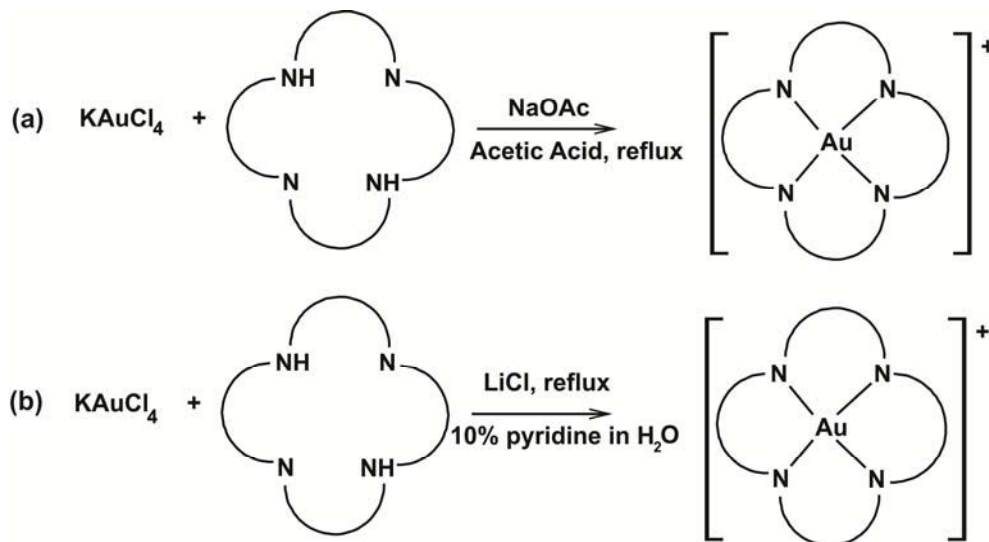
In order to further stabilize the gold(III) ion, macrocyclic Schiff base ligands were synthesized. In general the methods for the synthesis of macrocyclic compounds fall into three categories¹⁴⁻¹⁸:

- Synthesis involving complexation reactions
- *In situ* synthesis
- Synthesis involving modification of the macrocyclic ligand and/or metal ion

Procedures from more than one category may be used to synthesize a compound.

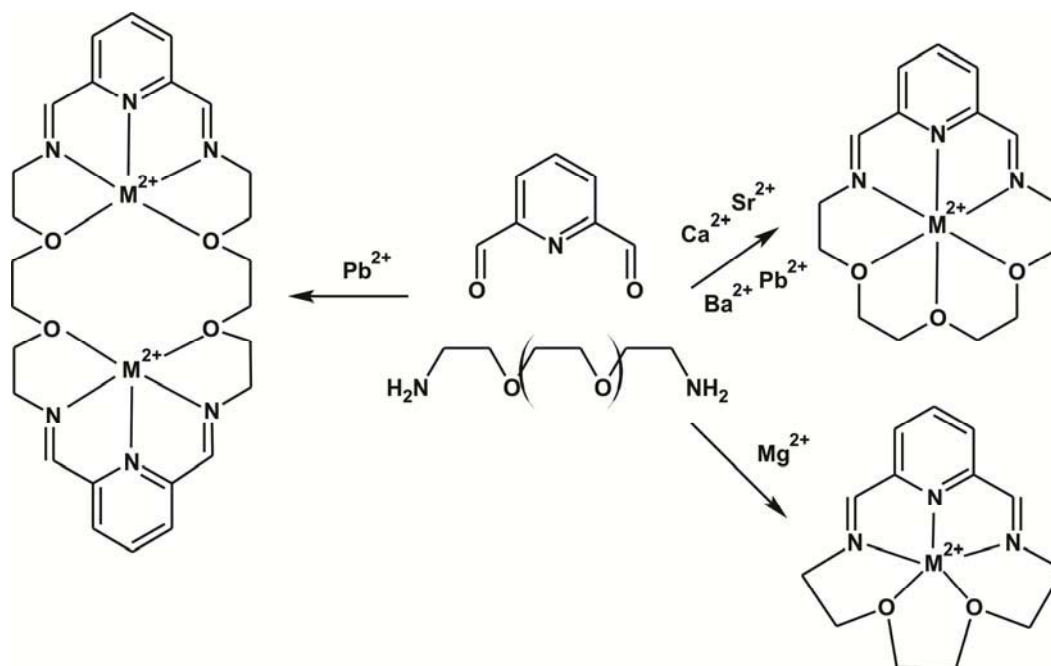
The first category involves a complexation reaction between a macrocyclic ligand and the metal ion in solution.¹⁹ This approach has many advantages in that the macrocyclic ligand may be isolated, purified and characterized before further reaction which should result in a complexation reaction that is relatively free from side reactions and impurities.¹⁹ This approach also allows for the physical properties of the macrocyclic ligand to be compared with the complex to determine if the complexation reaction was successful. A disadvantage of this technique is that synthesis of the macrocycle often results in low yield of the desired product.¹⁹ This complexation reaction is commonly used for the synthesis of cyclic tetramines, crown ethers and macrobicyclic ligands.¹⁹

This technique was used to synthesize a few of the gold(III) macrocycles reported in this thesis. This method is also widely employed for the synthesis of gold(III) porphyrins.¹⁹ These compounds are prepared by the treatment of KAuCl_4 with the free-base porphyrin in the presence of sodium acetate in acetic acid, Scheme 3.2(a), while aqueous-soluble gold(III) porphyrin compounds are obtained using 10% aqueous pyridine as the solvent, Scheme 3.2(b).²⁰ Metallation occurs with deprotonation of the N-H groups producing a dianionic ligand. The reversible redox couples of the gold(III) porphyrin system reveals that no demetallation of the gold(III) porphyrin takes place upon electrochemical reduction, indicating the high stability of this system.²⁰



Scheme 3.2: Synthetic methods for the synthesis of (a) non-aqueous soluble and (b) aqueous-soluble gold(III) porphyrin complexes.

The second category of macrocyclic complex formation involves the synthesis of the macrocyclic ligand around a metal ion, which acts as a scaffold. The influence that the metal ion has on a reaction has been described by Busch as the 'template effect'.^{21,22} Two template effects have been reported: kinetic and thermodynamic template effects. The kinetic template effect occurs when the metal ion controls the steric path of a stepwise reaction as opposed to the thermodynamic template effect where the metal ion disrupts the equilibrium in an organic system to produce the metal complex.¹⁹ Most *in situ* macrocyclic syntheses involve a condensation reaction between the reactants in the presence of a metal ion to produce a macrocyclic ligand. An example of this type of synthesis is the reaction between 1,3-propane-diamine and 2,3-butanedione in the presence of iron(II), nickel(II), or cobalt(II) salts.^{23,24} The size of the cation used as a template is important in directing the synthetic pathway in Schiff base systems.²⁵ For example: of the alkaline earth metal cations, only magnesium can form the pentadentate [1+1] macrocycle, but it cannot form the hexadentate [1+1] macrocycle which can be synthesized only in the presence of the larger cations: calcium, strontium, barium and lead(II), Scheme 3.3.²⁵

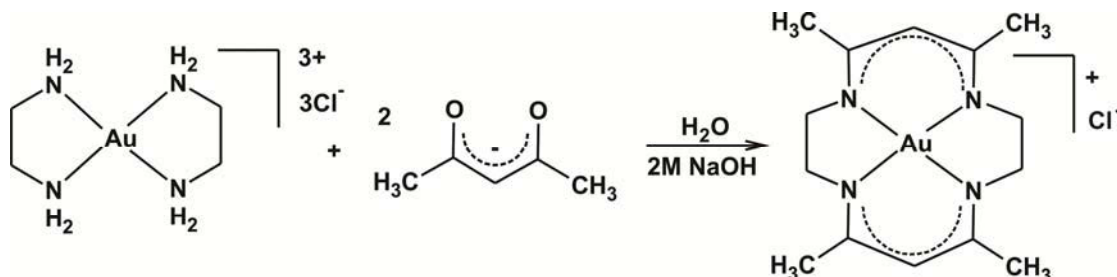


Scheme 3.3: Template synthesis of Schiff base macrocycles in the presence of main group metal ions.²⁵

An advantage of the template method is that it leads to improved yields as a result of reduction in side reactions such as polymerizations. In some cases the macrocyclic ligand may be unstable and may only be synthesized in the presence of a metal ion and produced as the metal complex.¹⁹ By using a metal ion with certain steric properties, the desired product may be selectively synthesized. However, a significant disadvantage of template cyclizations is that removal of the metal ion from the macrocycle is not always possible. *In situ* reactions may be used for the synthesis of some porphyrins and corrins.¹⁹

The template method was used to synthesize some of the proposed gold(III) complexes. Gold(III) has seldom been used as a template for the synthesis of macrocyclic complexes as colloidal gold or gold oxide is often formed during the reaction.²⁶ However, there are reports that describe gold(III) as a good metal template for the condensation of diketones and amines.^{27,28} The reaction of $[\text{Au}(\text{en})_2]\text{Cl}_3$ in water at pH 9-10 with a two-fold molar excess of 2,4-pentanedione at 25 °C for 2 hours results in the formation of a β -diimine chelate,

Scheme 3.4.²⁷ This reaction occurs because amine complexes of gold(III) are acidic due to the high polarizing power of the cation. Chelating amines have even lower pK_a values; $[\text{Au}(\text{en})_2]^{3+}$ has a pK_a of about 6.5 (ethylene diamine has a pK_a of 7.56).²⁷ Thus $[\text{Au}(\text{en})_2]^{3+}$ has nucleophilic coordinated amides present even at neutral pH. These tetraaza gold(III) complexes are remarkably stable to acid and base with the complex remaining unchanged in 1M HCl or 1M NaOH for at least three days with no decomposition.²⁷



Scheme 3.4: Template synthesis for the formation of a macrocyclic tetraaza gold(III) complex.^{27,28}

The third category of macrocyclic complex formation involves the adjustment of the ligand and/or the metal ion in the macrocyclic complex. The most extensively studied reactions are those involving oxidative dehydrogenation²⁹ while reactions involving oxidation and reduction of the metal ion have also been widely investigated with macrocyclic ligands shown to stabilize a wide range of oxidation states.³⁰⁻³² This method was not used in the synthesis of the proposed gold(III) chelates.

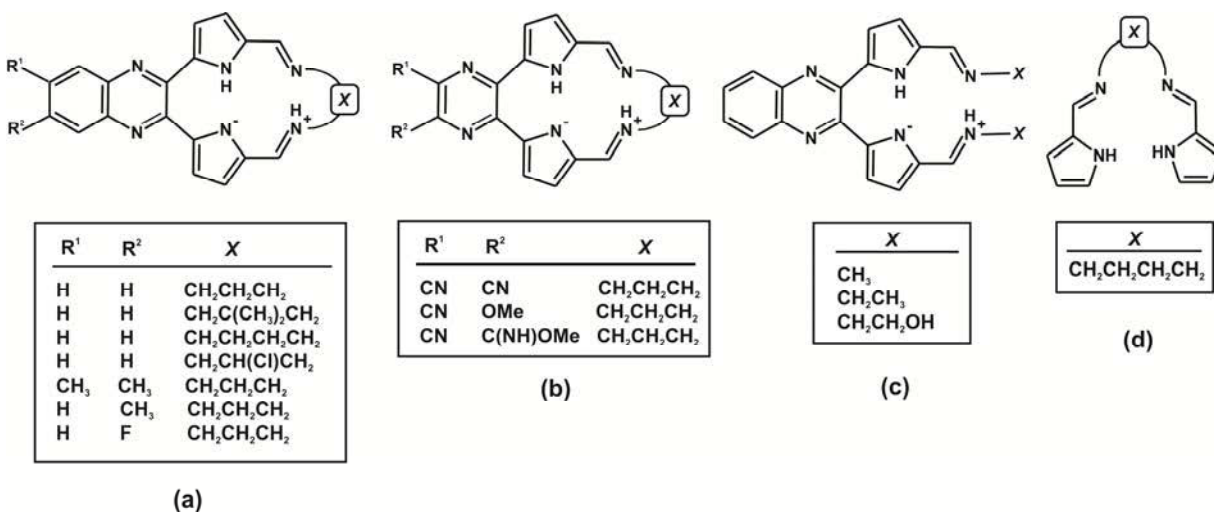
The macrocyclic Schiff base compounds synthesized in this work contain a quinoxaline subunit with either a 3 or 4 carbon di(azomethine) linkage, Scheme 3.5(a). A complex with a pyrazine subunit has also been synthesized, Scheme 3.5(b). Two of the quinoxaline ligands described in this work have been previously reported.³³ Wang *et al.* developed these compounds as a new class of fluorescent sensors for mercury(II), a heavy metal ion pollutant. Complexation of the compound to mercury(II) results in changes in the fluorescence intensity and absorption spectra. The dipyrrolylquinoxaline groups act as the fluorophore with the pyrrole and imine groups acting as the recognition site.³³ An X-ray structure of these rigid compounds coordinated to nickel(II), shows the nickel ion bound to two N atoms from the deprotonated pyrroles and two N atoms from the adjacent imine groups yielding a square-planar geometry at the nickel centre.³³ The bulk of the macrocyclic ligands described in this work are derivatives of these previously reported ligands. There is no previous literature relating to gold(III) coordinated to this type of ligand.

The other class of ligands described in this work incorporates open-chain dipyrrolylquinoxaline pseudo-macrocyclic Schiff base derivatives, Scheme 3.5(c). Limited examples of these ligands have been previously described, but the pseudomacrocyclic ligands reported in this work are all novel compounds.³⁴ The previously reported derivatives contain a dipyrrolylquinoxaline subunit with methoxyaniline or aniline moieties attached to the imine groups as opposed to a bridging system. These compounds form 1:1 metal:ligand complexes with Zn(II), Cd(II), Hg(II) and Cu(II) ions. These complexes carry no overall charge as the ligands are dianionic.³⁴ There are no reports of these compounds coordinated to gold(III).

A single open-chain Schiff base ligand has also been synthesized in this work, Scheme 3.5(d). This ligand contains two bis (pyrrolide-imine) units and a butyl linkage unit. Similar compounds have been described in

literature with a variation of the bridging unit. Our work group has described the successful chelation of this class of Schiff base ligands to gold(III).³⁵ The complex synthesized in this work is novel.

Thus, although two of the ligands synthesized in this work are known, the remainder are novel and many of the synthetic procedures are novel adaptations of reported synthetic methods. All the gold(III) chelates prepared in this work are novel and have been synthesized either by direct metallation of the free-ligand or by template methods.



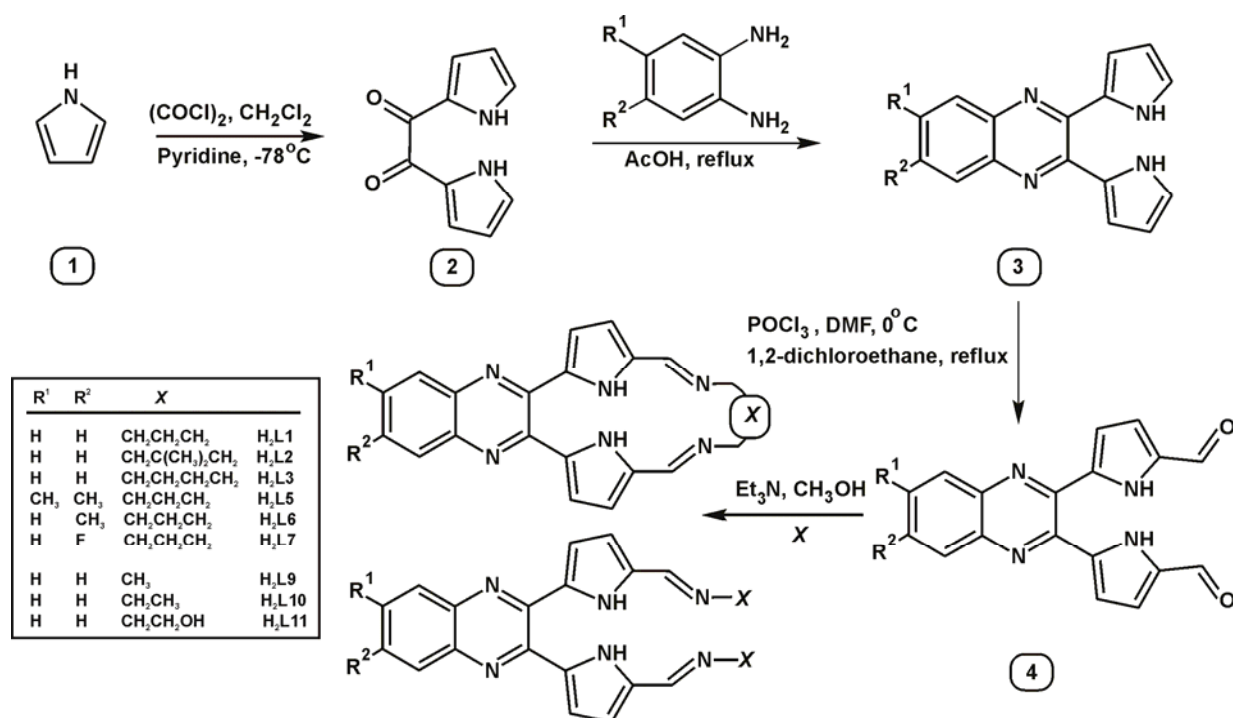
Scheme 3.5: General structure of (a) macrocyclic ligands with quinoxaline subunits, (b) macrocyclic ligands with pyrazine subunits, (c) pseudomacrocyclic ligands with quinoxaline subunits and (d) an open-chain ligand.

The overall goal of this research is to develop gold(III) bis(pyrrolide-imine) Schiff base complexes that will act as DNA intercalators and inhibit topoisomerase enzymes. In order to achieve this goal, reliable techniques had to be developed to synthesize tetradentate N-donor ligands that would stabilize the gold in the +3 oxidation state. This Chapter describes the synthetic techniques used to produce these ligands and gold(III) complexes.

3.2 Ligand Synthesis

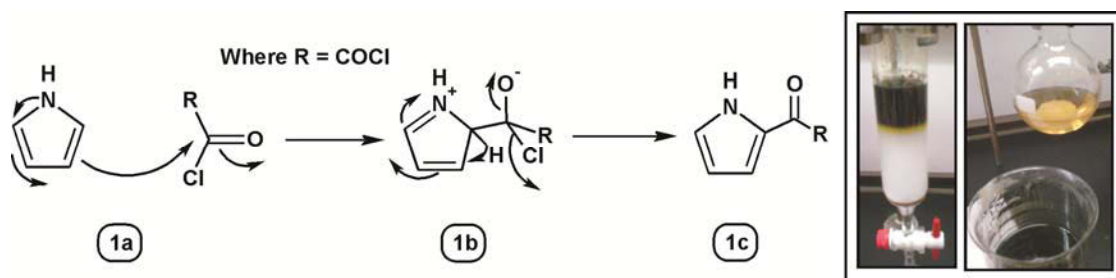
3.2.1 Synthesis of Quinoxaline Macrocyclic and Pseudomacrocyclic Schiff base Ligands

The macrocyclic and pseudomacrocyclic ligands were synthesized in a four-step synthetic route as shown in Scheme 3.5. The complexes were synthesized by two different routes. One involving the reaction of the free ligand with the metal salt and the other a template reaction. The complex synthesis involving a template reaction followed the same pathway in Scheme 3.6 up to the synthesis of 2,3-bis(5'-formylpyrrol-2'-yl)quinoxaline; **4**. This template complexation reaction will be further discussed later in this Chapter. Described below are the reaction mechanisms for the synthesis of the metal-free macrocyclic and pseudomacrocyclic ligands.



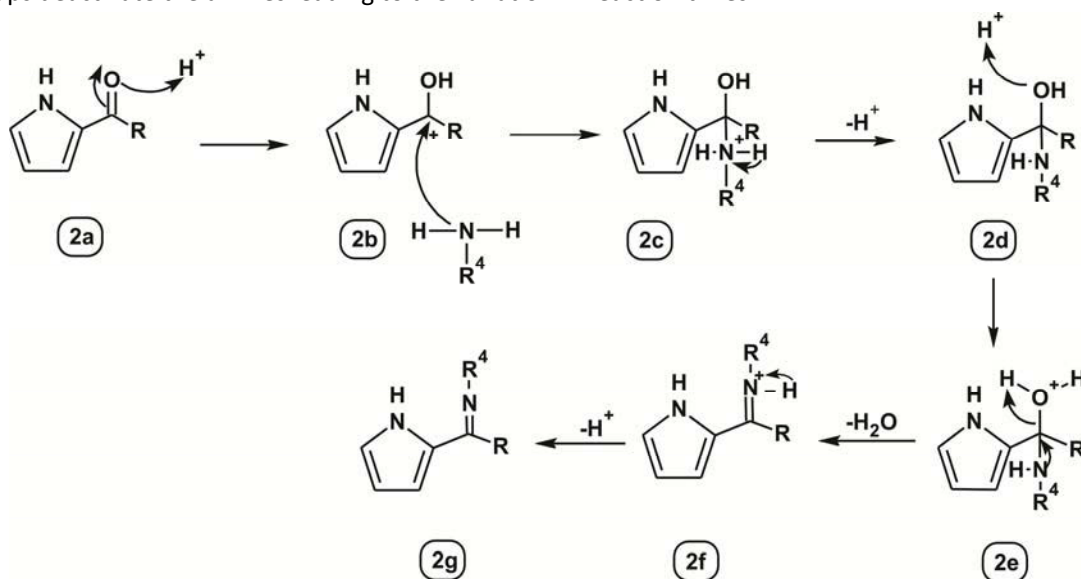
Scheme 3.6: The synthetic route used in the synthesis of quinoxaline-based macrocyclic and pseudo-macrocylic ligands.

The first step in the synthesis of the macrocycles involved the formation of the precursor, 1,2-bis(1*H*-pyrrole-2-yl)ethane-1,2-dione, **2**. In this first step, oxalyl chloride was reacted with pyrrole, **1**, in the presence of the base pyridine. The reaction was done under inert conditions with dry solvents as oxalyl chloride reacts violently with water. This reaction involves an electrophilic substitution, as shown in Scheme 3.7. This substitution takes place by an initial electrophilic addition of oxalyl chloride to pyrrole, **1a**, followed by proton loss to regenerate the aromatic ring, **1b**. As two equivalents of pyrrole are added relative to oxalyl chloride, the electrophilic substitution reaction occurs twice to form **2**. There is a preference for substitution at the α -position of the pyrrole ring. The intermediate formed by the electrophilic addition at the α -position of the pyrrole ring is stabilized by charge delocalization to a higher degree than the intermediate that would be formed by addition at the β -position of the pyrrole ring. After extraction and purification, **2** is obtained as a yellow powder in a 17% yield, comparable to that reported in literature.³⁶ Yields are low due to side reactions such as the formation of polypyrroles. The photographs to the right of scheme 3.6 show the black crude product which is columned to produce the pure yellow 1,2-bis(1*H*-pyrrole-2-yl)ethane-1,2-dione, **2**.



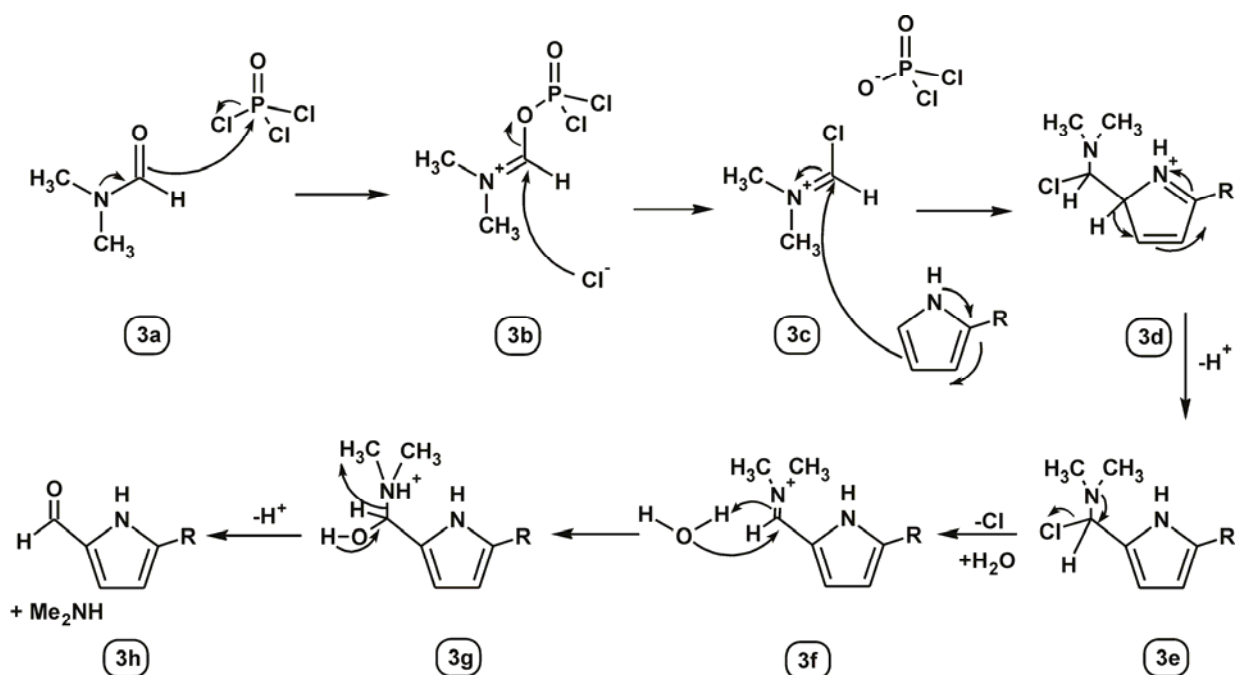
Scheme 3.7: Electrophilic substitution reaction, used to form compound **2**. The inset shows the crude and purified compound **2**.

The next step in the synthesis of the macrocyclic ligands is the formation of 1,2-bis(1*H*-pyrrole-2-yl)quinoxaline, **3**. This reaction involves the addition of the relevant phenylenediamine to the diketone, **2**, using an acid catalyst. Scheme 3.8 shows a simplified version of the reaction. The mechanism begins by forming a bond between a proton from the acid catalyst and the carbonyl group, **2a**. The lone pair of electrons on the primary amine then attacks the electron deficient carbon atom, forming a new bond, **2b**. The hydroxyl group forms a bond to a second proton and is ejected from the molecule in the form of water, **2c-e**. This in turn leads to the formation of an imine bond through the loss of the amine proton, **2e-f**. As the phenylenediamine contains two amine groups, imine bond formation occurs twice, resulting in a heterocyclic ring. The di-imine bond formation is driven forward in part by the high stability of the resulting heterocyclic ring. Compound **3**, 1,2-bis(1*H*-pyrrole-2-yl)quinoxaline, is isolated as a yellow powder in a 67% yield. The reaction yields were higher and the reaction times considerably shorter for the derivatives of phenylenediamine which possessed electron donating groups, such as the methyl groups. The electron withdrawing fluorine and cyanide functional groups lead to an increase in reaction times and a decrease in reaction yields. The electron donating groups serve to activate the amines while the electron withdrawing groups deactivate the amines leading to the variation in reaction times.



Scheme 3.8: Acid-catalysed condensation reaction resulting in the formation of an imine bond.

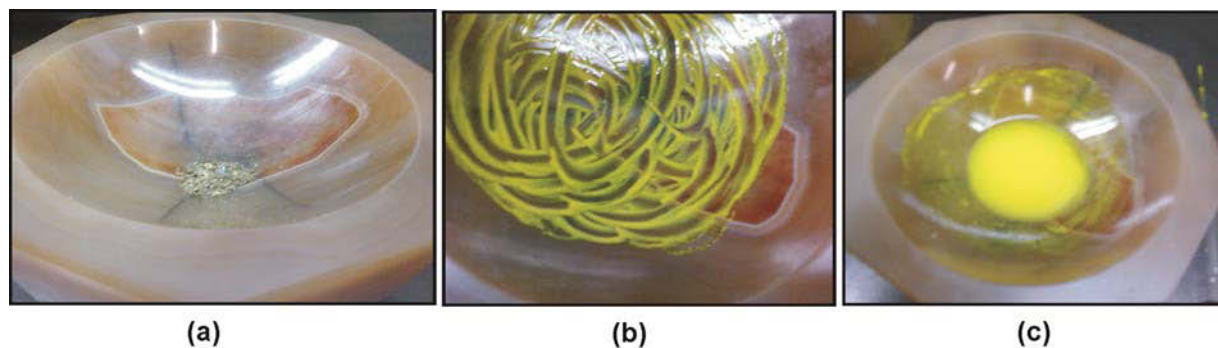
The third step in the macrocycle synthesis is the formation of 2,3-bis(5'-formylpyrrol-2'-yl)quinoxaline, **4**. This was achieved via a Vilsmeier formylation reaction during which phosphorus oxychloride and *N,N*-dimethylformamide and compound **3** were reacted (Scheme 3.9). The reaction was performed under inert conditions owing to the sensitivity of phosphorous oxychloride. The reaction of DMF with phosphorous oxychloride, **3a-b**, gives a substituted chloroiminium ion known as the Vilsmeier reagent. The Vilsmeier reagent then undergoes an electrophilic substitution reaction with the aromatic compound **3**, as shown by **3c-e**. This leads to the formation of an iminium ion which is hydrolyzed to give the desired aldehyde, **3f-h**, when an aqueous solution of sodium acetate is added to the system. The reaction resulted in a yellow powder of 2,3-bis(5'-formylpyrrol-2'-yl)quinoxaline **4** in a 79% yield.



Scheme 3.9: Vilsmeier formylation reaction mechanism.

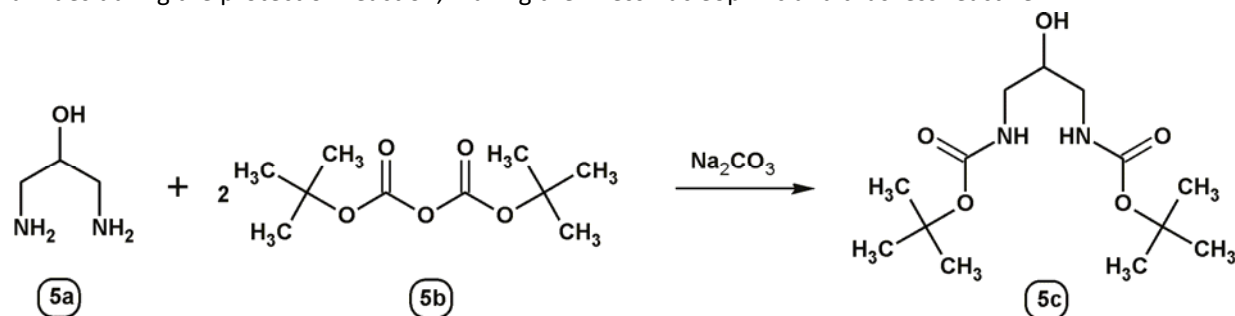
The last step in the macrocycle formation involves refluxing 2,3-bis(5'-formylpyrrol-2'-yl)quinoxaline, **4**, in methanol with triethylamine followed by the addition of the appropriate amine. In the case of the macrocycles, one equivalent of a diamine was added to bridge the compound while in the case of the pseudomacrocycles two equivalents of a monoamine were added. A condensation reaction between the carbonyl groups of **4** and the amine groups yields imine bonds. In this case imine bond formation is catalysed by the base triethylamine as opposed to an acid. Yields of the ligands varied from 65% to 92% depending on the nature of the substituents.

As the ligand $\text{H}_2\text{L11}$ is soluble in methanol, refluxing the reagents in methanol was not the most efficient pathway to synthesize this ligand; instead a solid-state reaction was used. One equivalent of 2,3-bis(5'-formylpyrrol-2'-yl)quinoxaline, **4**, (Figure 3.1(a)) and an excess of ethanolamine were ground together with a mortar and pestle forming a yellow paste (Figure 3.1(b)). Water is then added to wash off the excess ethanolamine (Figure 3.1(c)); the product is insoluble in water. The ligand product was isolated by centrifugation and dried by heating, yielding $\text{H}_2\text{L11}$ as a clean yellow powder in 89 % yield.

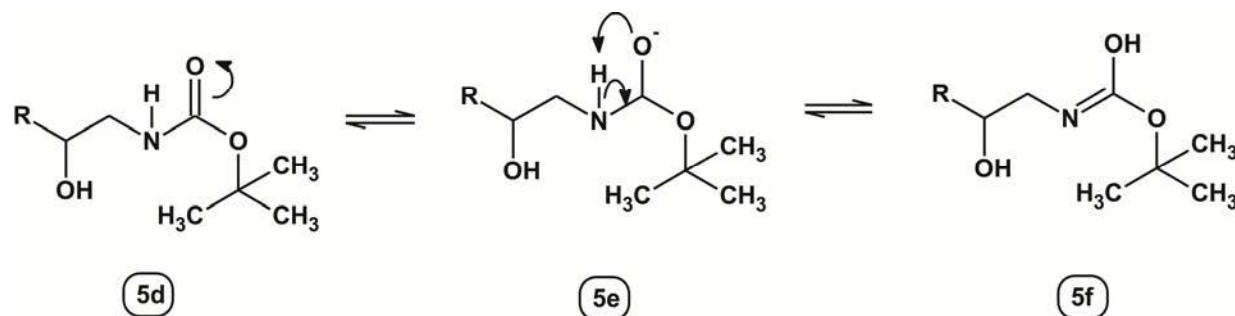
Figure 3.1: Solid-state reaction for the synthesis of $\text{H}_2\text{L11}$.

3.2.1.1 Synthesis of 2-chloro-1,3-diaminopropane

For the synthesis of the quinoxaline-based complex, $[\text{Au}(\text{L}4)](\text{PF}_6)$, the bridging unit 2-chloro-1,3-diaminopropane had to be produced from 1,3-diamino-2-propanol. The alcohol group on the second carbon lends itself well to derivatization. As primary amines ($\text{p}K_{\text{a}} = 10\text{--}11$)³⁷ are more reactive than secondary alcohols ($\text{p}K_{\text{a}} = 16.5$)³⁷, the amine groups were protected with di-*tert*-butyl dicarbonate (Boc_2O) before the conversion of the alcohol to the chlorine, Scheme 3.10. The primary amines are converted to secondary amides during the protection reaction, making them less nucleophilic and thus less reactive.

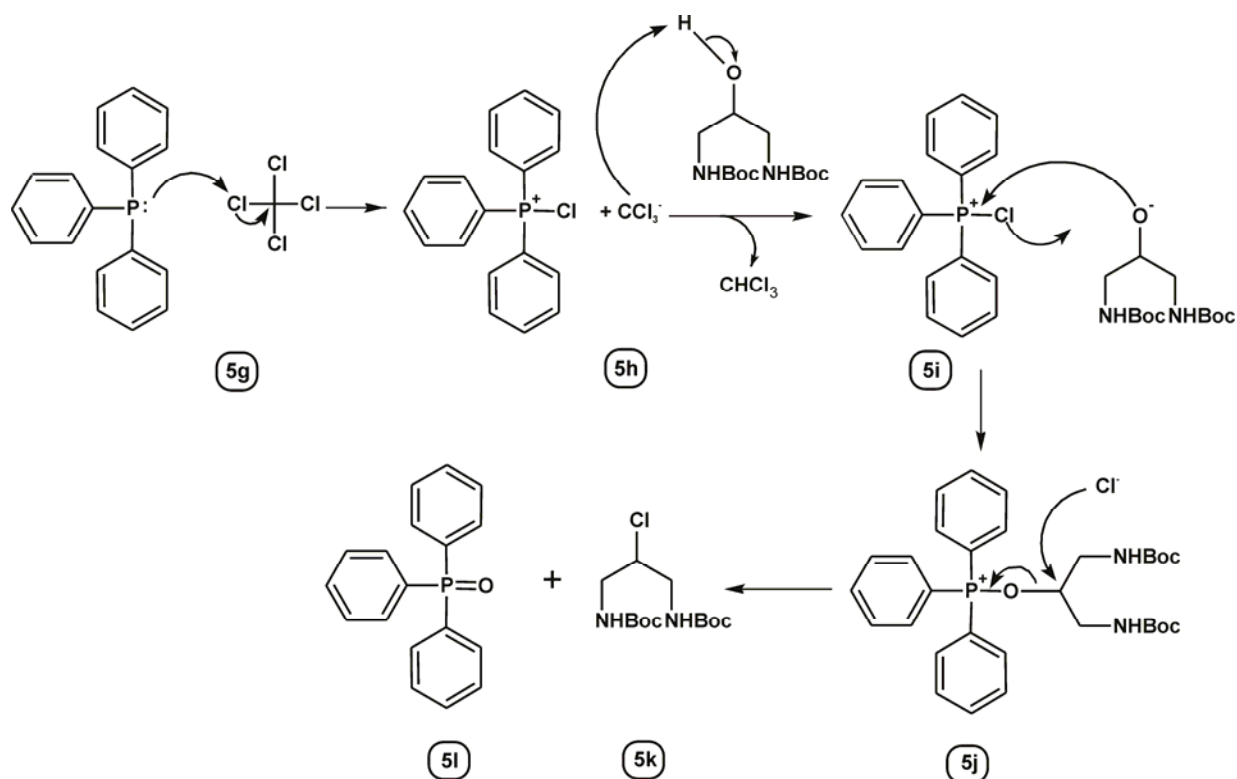
Scheme 3.10: Protection of primary amines using di-*tert*-butyl dicarbonate.

The amide bond that is formed has different resonance forms, Scheme 3.11. The resonance forms show that there is protonation of the oxygen with deprotonation of the amine, rendering it inactive. The alcohol functional group on the second position of the bridge can then be derivatized.

Scheme 3.11: Resonance forms of the *n*-Boc protected amine.

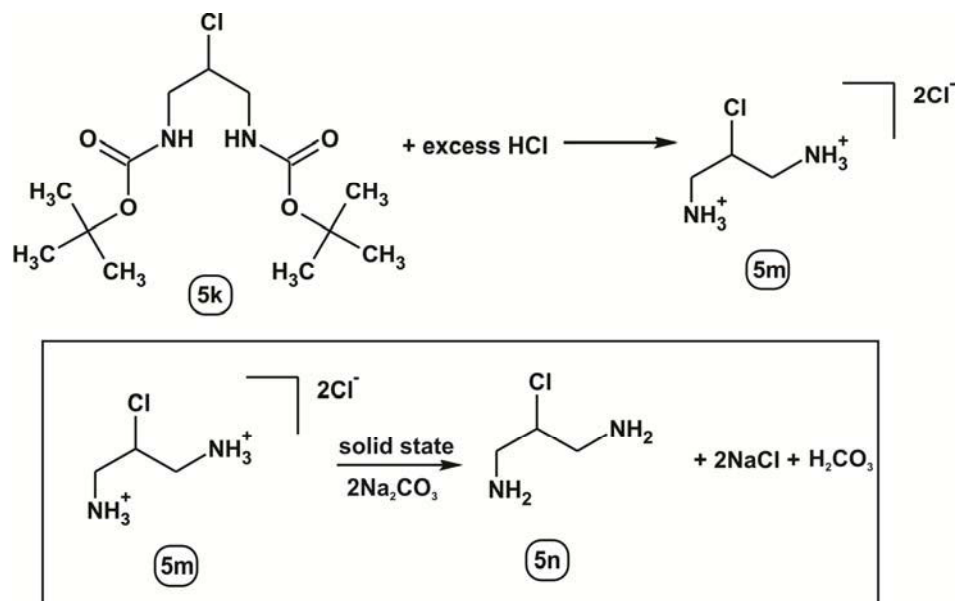
The Appel reaction was used to convert the alcohol functional group of the *n*-Boc-protected 1,3-diamino-2-propanol into an alkyl chloride using triphenylphosphine and carbon tetrachloride, Scheme 3.12.³⁸

The first step of the Appel reaction is the formation of the phosphonium salt, 5h. The protected alcohol is then deprotonated leading to the formation of chloroform and an alkoxide ion pair, 5i. A nucleophilic substitution reaction by the alkoxide on the phosphonium salt yields 5j. The halide reacts with the primary alcohol in an $\text{S}_{\text{N}}2$ process to form the alkyl halide 5k and triphenylphosphine oxide, 5l. An $\text{S}_{\text{N}}2$ reaction can potentially lead to a racemic mixture of products; however, in this case the carbon is not chiral or prochiral and therefore only a single product will result.



Scheme 3.12: Appel reaction mechanism for the chlorination of an alcohol.

The chloro-compound is then deprotected through a reaction with HCl. This leaves the product as a hydrochloride salt, 2-chloro-1,3-diaminopropane dihydrochloride, **5m** (Scheme 3.13).



Scheme 3.13: Deprotection reaction to form the hydrochloride salt and solid state reaction to form the corresponding amine.

In order to reduce the possibility of acid-catalyzed decomposition reactions, the hydrochloride salt was converted to the corresponding primary amine before the condensation reaction with the aldehyde. As primary amines are water-soluble, traditional solvent extraction techniques with aqueous base could not be used to obtain the desired product. The hydrochloride salt was converted to the amine using a solid state reaction. The acid RNH_3^+ is relatively weak ($\text{pK}_a = 11$)³⁷ and requires a moderately strong base to remove the proton. Thus sodium carbonate was ground with the hydrochloride, **5m**, (Scheme 3.13) until a paste formed. The resulting 2-chloro-1,3-diaminopropane, **5n**, was extracted into ethanol and then used in the gold(III) template reaction.

Determining whether the conversion from the alcohol to the alkyl chloride has been successful is not an easy task as NMR experiments for covalently bound chlorine atoms are unreliable as the spectral window is large. The ^1H NMR shifts of 2-chloro-1,3-diaminopropane dihydrochloride and 1,3-diamino-2-propanol dihydrochloride were compared (Table 3.1) and show a clear downfield shift for the equivalent protons in the alkyl chloride analogue. This is consistent with the deshielding effect of the chlorine atom when compared to the alcohol group.

Table 3.1: Comparison of the ^1H NMR shifts of 2-hydroxy- and 2-chloro-1,3-diaminopropane dihydrochloride in D_2O . X represents either OH or Cl for the respective compounds.

	^1H NMR Shift (ppm)	
	$\text{NH}_2\text{CH}_2\text{CH}(\text{OH})\text{CH}_2\text{NH}_2 \cdot 2\text{HCl}$	$\text{NH}_2\text{CH}_2\text{CH}(\text{Cl})\text{CH}_2\text{NH}_2 \cdot 2\text{HCl}$
$\text{CH}_2\text{CHXCH}_2$	3.02	3.34
$\text{CH}_2\text{CHXCH}_2$	3.23	3.57
$\text{CH}_2\text{CHXCH}_2$	4.18	4.58

The Beilstein test³⁹, a qualitative test to determine the presence of a halide in a compound, was also performed. This test exploits the fact that when copper halides are burned, a green flame is observed. The test was performed by heating a clean piece of copper wire in a Bunsen burner flame to form a copper(II) oxide coating.³⁹ The copper wire was then dipped in the test compound and then again placed into the flame. As the Beilstein test for the chlorinated amine resulted in a green flame, it indicated that the chlorination had been successful.

The mass spectrometry data for the complex $[\text{Au}(\text{L4})](\text{PF}_6)$ (Figure 3.2) also indicates that the chlorination was successful. The data shows an actual mass $583.0717 \text{ g mol}^{-1}$, which is in good agreement with the calculated molar mass of $583.8036 \text{ g mol}^{-1}$. There is another peak at $585.0697 \text{ g mol}^{-1}$ which also is indicative of a chlorine atom as chlorine has two isotopes; ^{35}Cl and ^{37}Cl .

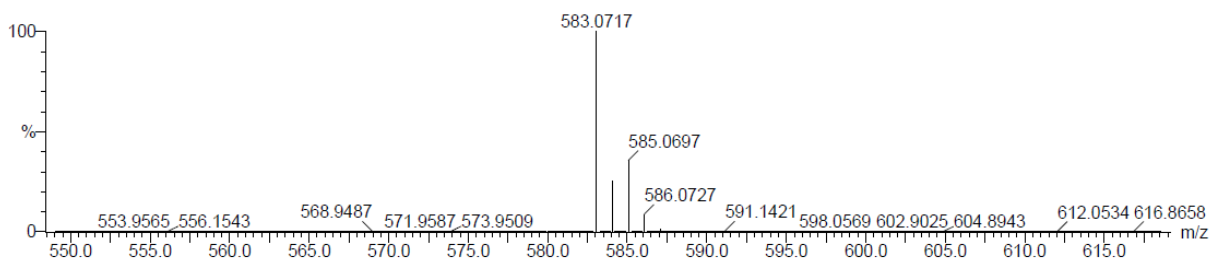
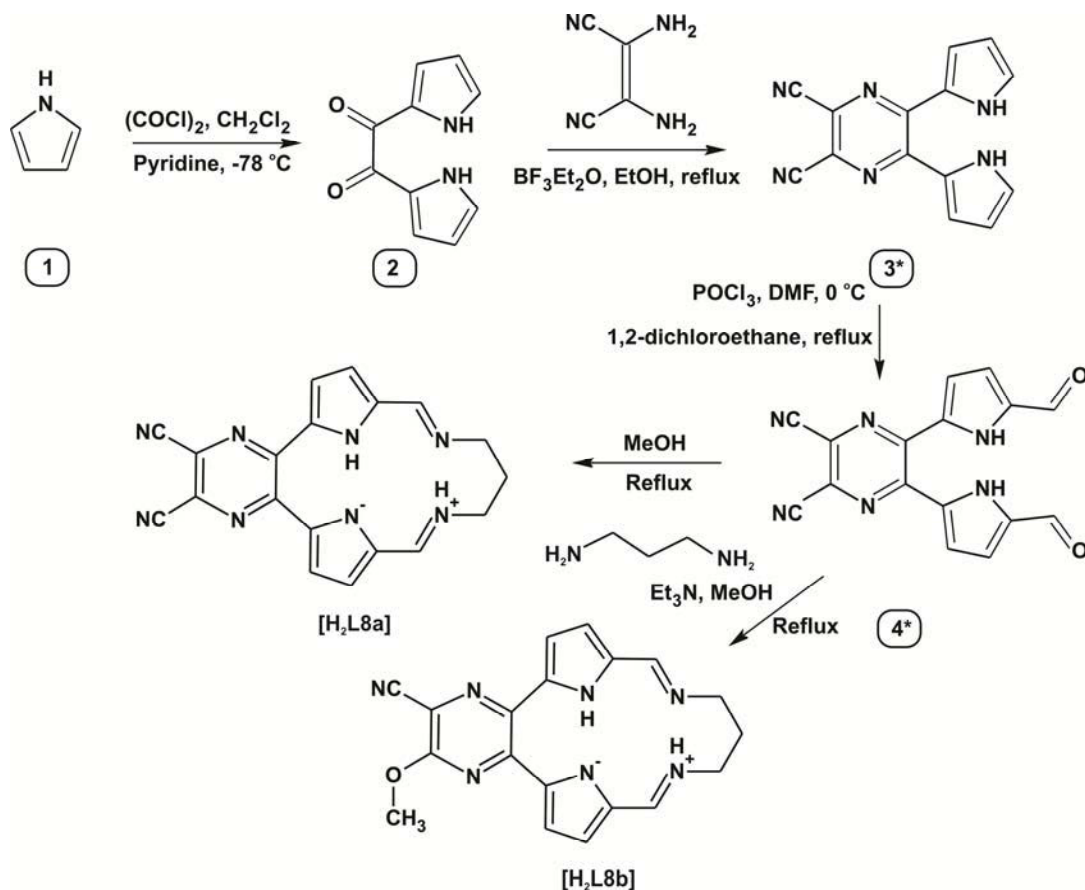


Figure 3.2: High resolution mass spectrum of $[\text{Au}(\text{L4})](\text{PF}_6)$.

3.2.2 Synthesis of Pyrazine Macrocylic Schiff base Ligands

The pyrazine-based macrocyclic ligands H₂L8a and H₂L8b were synthesized following similar reaction steps to those for the quinoxaline macrocycles, Scheme 3.14.



Scheme 3.14: The synthetic route used in the synthesis of pyrazine-based macrocyclic ligands.

The first step of the reaction to form 1,2-bis(1H-pyrrole-2-yl)ethane-1,2-dione, **2**, is depicted in Scheme 3.6. The second step of the reaction to form **3*** has been previously reported.^{40,41} This is a condensation reaction between 1,2-diaminomaleonitrile and **2** to form 6-di-1H-pyrrol-2-ylpyrazine-2,3-dicarbonitrile, **3***; a similar condensation reaction is depicted in Scheme 3.7. As the nitrile groups are strongly electron withdrawing, the amine groups of the diaminomaleonitrile are less nucleophilic and thus less reactive than other primary amines. Consequently, boron trifluoride diethyl etherate is used to catalyse the reaction and the solution is refluxed over a longer period of time: 8 hours. The third step is a Vilsmeier formylation reaction to form 5,6-bis(5-formyl-1H-pyrrol-2-yl)pyrazine-2,3-dicarbonitrile, **4***, similar to the reaction depicted in Scheme 3.9.

By using different reaction conditions in the final step of the reaction, two ligands, H₂L8a and H₂L8b, are synthesized. Triethylamine in the presence of methanol appears to catalyze the substitution of a single nitrile group for a methoxy group. This reaction was unexpected as the desired reaction product was H₂L8a. Two column fractions were collected (DCM eluent): the first was H₂L8b. It was identified that H₂L8b had formed rather than H₂L8a by the presence of a peak at 4.14 ppm in the ¹H NMR spectrum corresponding to the

methoxy group. As the compound was asymmetrical all the proton peaks for the compound were split. An X-ray crystal structure of H₂L8b was also obtained to further verify the structure of the product. The second column fraction was shown by X-ray crystallography to be a monoimidate, H₂L8c, shown in Figure 3.3. This was a minor product of the reaction (<5% yield) and thus has little potential as a ligand.

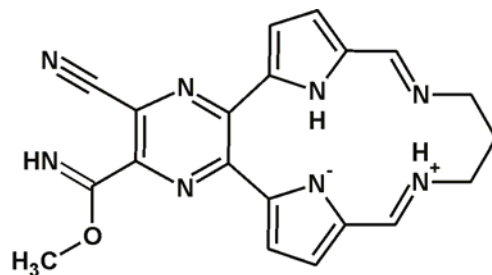
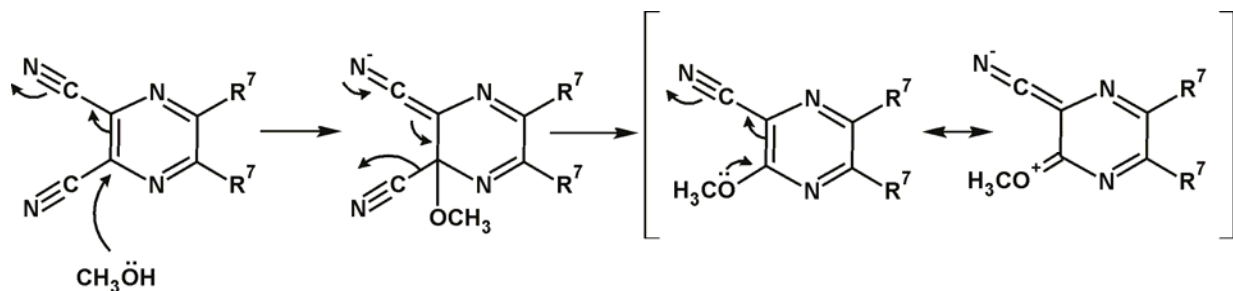


Figure 3.3: Structure of monoimidate, H₂L8c, formed during the reaction involving triethylamine.

Kojima *et al.* report a similar result when refluxing pyrazine-2,3-dicarbonitrile and methanol in a polar aprotic solvent (DMF) in the presence of triethylamine as a catalyst for 16 hours.⁴² This reaction produced 3-methoxy-2-carbonitrile in a 30% yield. The selectivity of the substitution reaction can be attributed to the electron-donating nature of the methoxy group which deactivates the adjacent positions toward further nucleophilic attack.⁴³ Kojima *et al.* also found that the reaction of pyrazine-2,3-dicarbonitrile with a catalytic amount of sodium methoxide at room temperature could give the di-imidate product. They also reported that reacting 5,6-diphenylene-2,3-dicarbonitrile with methanol and aqueous sodium hydroxide yielded the monoimidate product. They further attempted to determine whether the imidate was an intermediate in the synthesis of the alkoxy compounds. They did this by further reacting the imidate under the same reaction conditions to determine if the alkoxy compound could be formed. As the alkoxy compound was only formed in very low yields (<4%), they concluded that the imidate was not a viable intermediate for the main substitution reaction. Also, as a di-imidate forms from the pyrazine-2,3-dicarbonitrile starting material, but only one nitrile group is replaced in the substitution reaction, they further concluded that it could not be an intermediate. They suggested that the mechanism takes place by direct replacement of a nitrile group with an alkoxy group, as shown in Scheme 3.15.

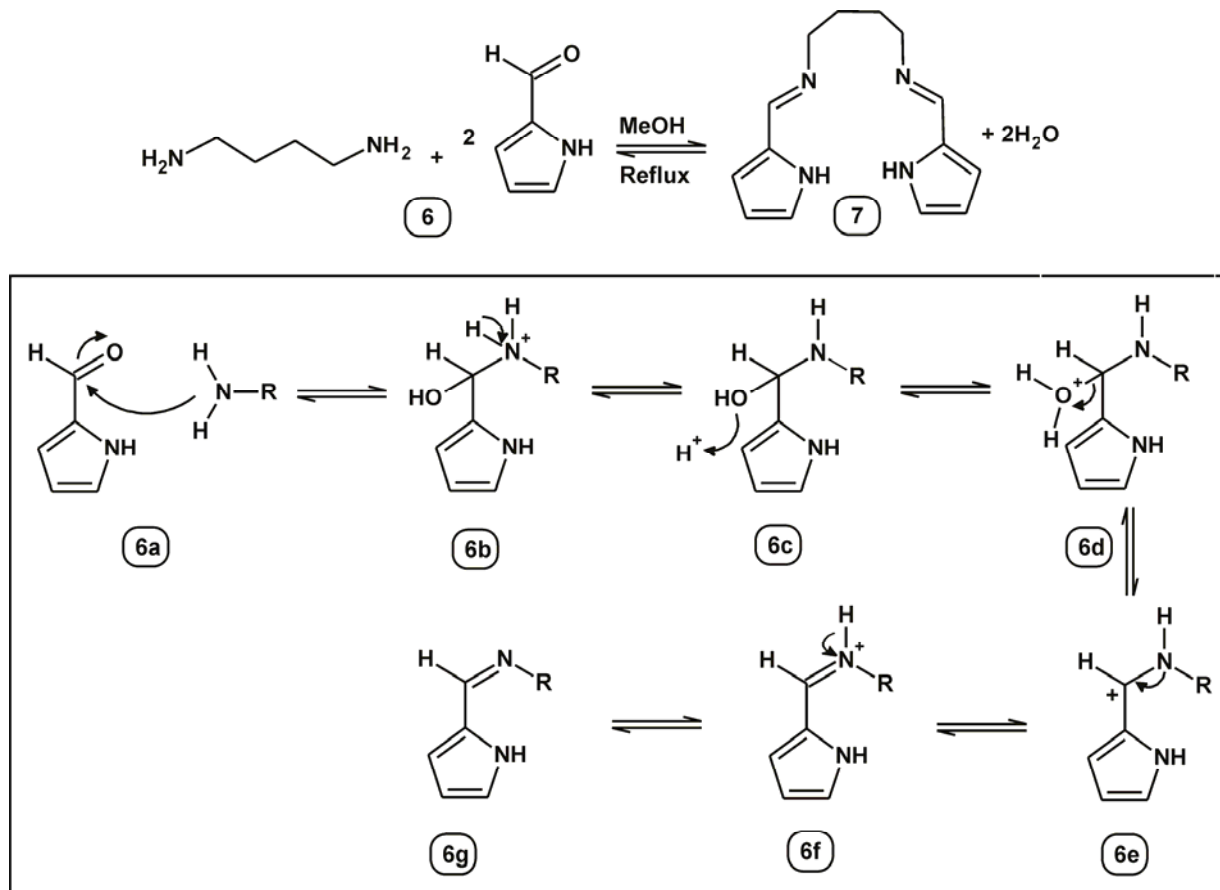


Scheme 3.15: Direct replacement of a nitrile group with a methoxy group.

The ligand, H₂L8a, was synthesised in the absence of triethylamine. The aldehyde, **4***, was condensed with 1,3-diaminopropane in methanol. This product was identified by the symmetrical nature of the ¹H NMR spectrum as well as by MS and X-ray crystallography.

3.2.3 Synthesis of Non-Macrocyclic Schiff base Ligands

The synthesis of the non-macrocyclic Schiff base ligand H₂L12 involved a simple condensation reaction between 1,4-butanediamine and pyrrole-2-carboxaldehyde with the formation of water as a by-product, Scheme 3.16.



Scheme 3.16: Condensation reaction to form non-macrocyclic Schiff base ligands.

Primary amines add to aldehydes to give imine bonds. The stability of the imine bond is mainly dependent on the substituents attached to the carbonyl carbon and nitrogen atom. An aryl group attached to one of these atoms will result in a more stable compound.³⁷

The synthetic method for the synthesis of H₂L12 is based upon that used by Jing-Wen Ran *et al.* for a similar ethylene bridged Schiff base.¹¹ Franceschi *et al.* have reported an additional synthetic method for the synthesis of benzene-bridged Schiff base ligands.⁸ This method involved stirring reagents in dichloromethane at room temperature for 48 hours. This method offered no advantage to the chosen method and the reaction is considerably slower. The potentially problematic addition of only a single pyrrole-2-carboxaldehyde has been reported,⁴⁴ but in this case it was not an issue with both mass spectrometry and X-ray crystallography showing the addition of two pyrrole-2-carboxaldehyde units.

3.3 Metallation of Ligands

3.3.1 Gold(III) Salts

There are many different types of gold(III) salts that can be used as a source of gold(III) ions. Some of these include: $\text{Na}[\text{AuCl}_4]$, $\text{H}[\text{AuCl}_4]$ and $[\text{Bu}_4\text{N}][\text{AuCl}_4]$. Metallation by refluxing the free ligand with sodium tetrachloroaurate is the most widely reported method in literature.^{13,45} It is, however, common with this method to get an $[\text{AuCl}_4]^-$ or an $[\text{AuCl}_2]^-$ counter ion, instead of the desired chloride anion.^{10,12,26,45} These gold counter-ions lead to the complex having limited solubility, making it difficult to characterize. It is also inefficient to generate a complex with a gold-based anion as effectively only half the moles of gold in the reaction are forming the desired chelate.

Hydrogen tetrachloroaurate has also been reported as an effective source of gold(III) ions for chelation by N donor ligands,^{10,13,45,46} although the success of this salt has been argued. Some articles suggest that this salt is favoured as it lowers the pH of the solution which assists ligand chelation to gold(III).^{10,46} Other articles suggest that the lower pH interferes with the complexation as the pyrrole nitrogen atoms are less likely to be deprotonated under acidic condition, which is required for chelation.¹⁰

Previously in our work group, attempts have been made to metallate Schiff base ligands using both $\text{Na}[\text{AuCl}_4]$ and $\text{H}[\text{AuCl}_4]$ at different temperatures and using different solvents.⁴⁷ These reactions were unsuccessful, resulting in the formation of a black precipitate, likely to be Au_2O_3 and colloidal gold.

Barnholtz *et al.* reported the use of the $\text{Na}[\text{AuCl}_4]$, $\text{H}[\text{AuCl}_4]$, $[\text{Bu}_4\text{N}][\text{AuCl}_4]$ salts separately to synthesize gold(III) Schiff base complexes and concluded that the synthesis was much more efficient starting from the $[\text{Bu}_4\text{N}][\text{AuCl}_4]$ salt.¹⁰ They reported that the reaction with this salt requires the presence of a hexafluorophosphate(V) salt and ethanol to proceed and the reaction would not occur in the absence of either reagent. These reagents appear to facilitate breaking up the $[\text{Bu}_4\text{N}][\text{AuCl}_4]$ ion pair.¹⁰

Thus, the salt $[\text{Bu}_4\text{N}][\text{AuCl}_4]$ was chosen as the source of gold(III) ions for the proposed gold(III) complexes. This gold(III) salt is lipophilic and is only soluble in non-polar organic solvents. This is useful, as the gold(III) chelates are only soluble in polar organic solvents and thus the product precipitates out of solution leaving any unreacted starting materials in solution.

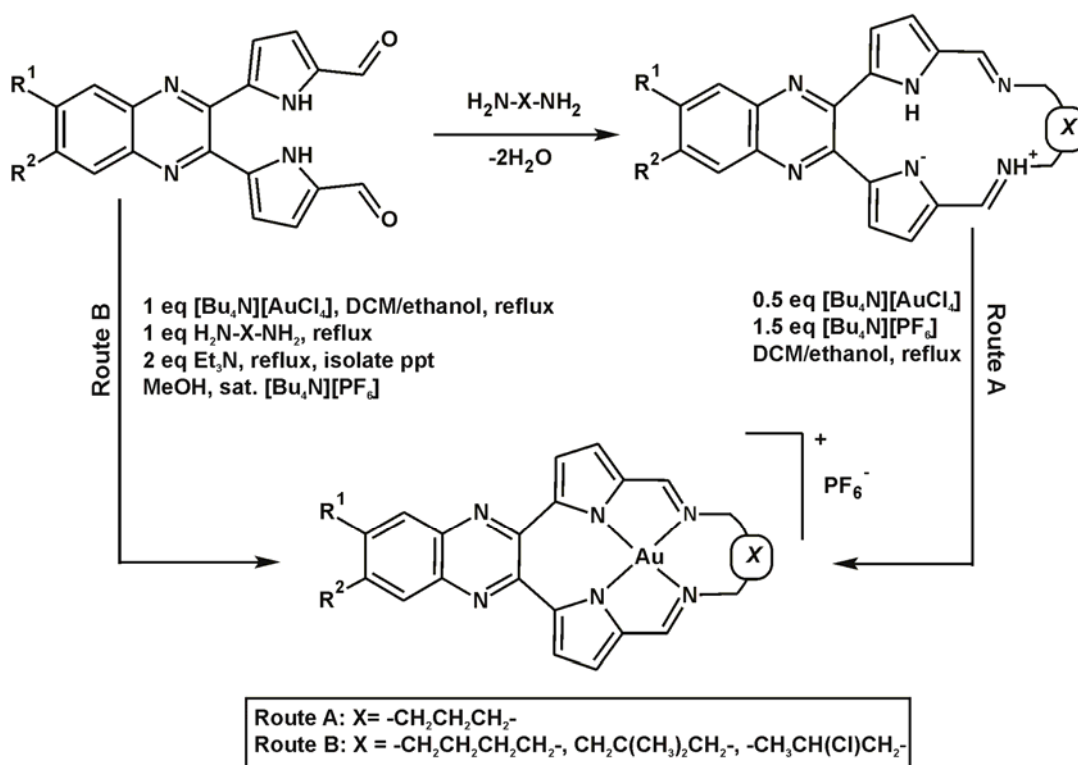
3.3.2 Formation of Gold(III) Quinoxaline Macrocylic Complexes

As described in Chapter One (Section 1.4.2.1), macrocyclic ligands coordinate more strongly to metal ions with an ionic radius that best matches the macrocyclic cavity.¹⁹ The ligands $\text{H}_2\text{L1}$ and $\text{H}_2\text{L3}$ have been previously synthesized and coordinated to nickel(II).³³ The reaction is fairly quick with a reflux time of 30 minutes. This indicates that nickel(II) has a suitable ionic radius, 0.63 Å, (Table 3.2) to interact with the macrocyclic cavity. This could suggest that gold(III) has a potentially unsuitable ionic radius; 0.82 Å. However, Wang *et al.* reported that these ligands are able to chelate mercury(II), which has virtually the same ionic radius as gold(III) (Table 3.2).³³ Thus, gold(III) was reacted with the macrocyclic ligands, but for an extended period to ensure complete complexation.

Table 3.2: Ionic radii of selected metal ions.⁴⁸

Metal	C.N	Ionic Radius(Å)
Ni(II)	4 (square-planar)	0.63
Hg(II)	2	0.83
	4	1.10
	6	1.16
Au(III)	4 (square-planar)	0.82

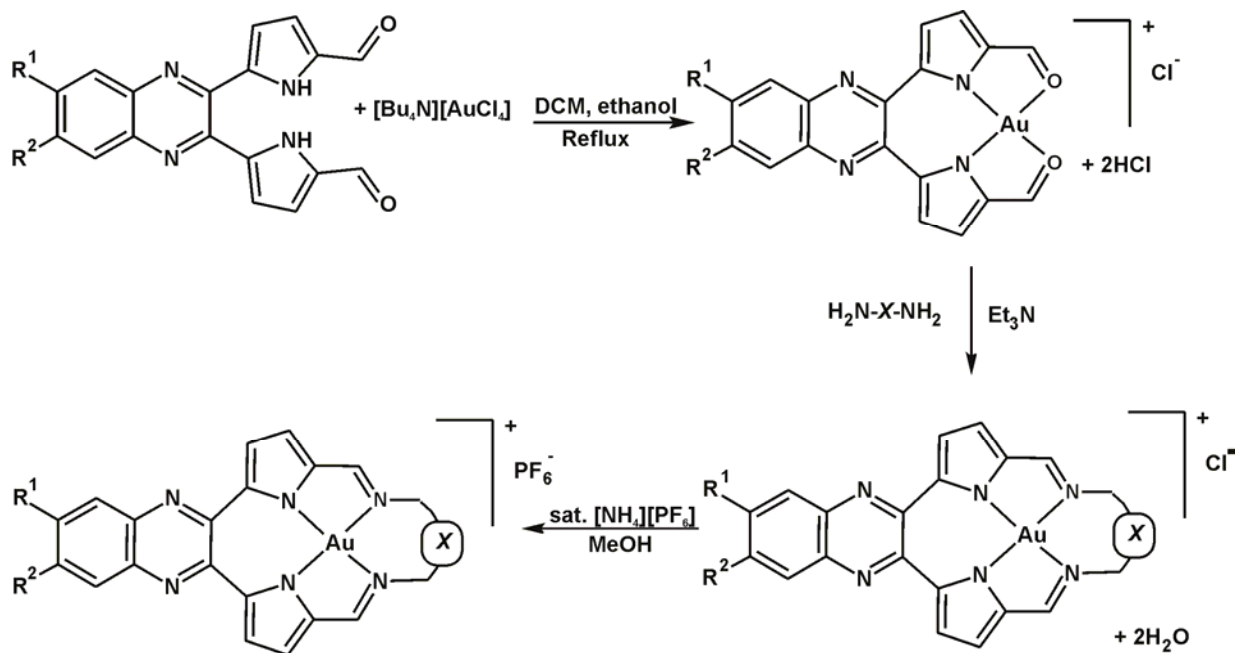
As depicted in Scheme 3.17, two metallation routes were used for the synthesis of the quinoxaline macrocyclic ligands.



Scheme 3.17: Synthetic routes for the synthesis of gold(III) Schiff base quinoxaline complexes.

The first and more conventional method of metallation involves direct metallation of a preformed macrocycle (Route A). This method involved refluxing the gold *tert*-butyl ammonium salt with the macrocycle in DCM/ethanol in the presence of *tert*-butyl ammonium hexafluorophosphate(V) for 16 hours. The length of reflux time is relatively long to ensure that the slightly unfavourable reaction (owing to the large ionic radius of gold(III)) can take place. The synthesis also involves a metathesis reaction as the initial counter ion is a chloride ion, but it is substituted for hexafluorophosphate(V). Hexafluorophosphate(V) is a useful counterion as it has a relatively large volume and can aid in crystallisation. Chloride or hexafluorophosphate(V) anions are preferred as the compounds are intended to be chemotherapeutics and these anions are non-toxic.⁴⁹ This direct method employing the lipophilic gold(III) salt, [Bu₄N][AuCl₄], allows for a clean synthesis of the polar complexes. Route A could only be used to synthesize complexes with an unsubstituted propyl bridging unit; numerous attempts using this method under various conditions inexplicably failed to afford the derivatized gold(III) complexes.

To synthesise the derivatized gold(III) complexes an alternative template method had to be employed (Route B). Scheme 3.18 gives a proposed pathway for the template reaction. This template method entails reacting the aldehyde, 2,3-bis(5'-formylpyrrol-2'-yl)quinoxaline, **4**, with *tert*-butylammonium tetrachloroaurate leading to the formation of an anionic gold (III) species. This anionic gold(III) species remains in solution. The addition of the bridging amine along with triethylamine, results in the formation of a yellow precipitate. The yellow precipitate is the desired gold(III) macrocycle with a chloride counter ion, which is formed by a condensation reaction. This product is isolated and dissolved in methanol; any undissolved gold oxide and gold colloid is filtered off. The product is precipitated out of solution by the addition of ammonium hexafluorophosphate(V) yielding the gold(III) macrocycle with a hexafluorophosphate(V) counter ion. The necessity of the metathesis reaction is two-fold: firstly to clean the reaction mixture and secondly to aid in crystallisation. For $[\text{Au}(\text{L2b})]^+$, lithium trifluoromethanesulfonate was used for the metathesis as opposed to ammonium hexafluorophosphate(V) giving a $[\text{CF}_3\text{SO}_3]^-$ counter ion. In this instance, the larger counter ion yielded larger crystals. Although Route B is faster than Route A, Route B results in lower reaction yields than Route A, likely due to unwanted side reactions.



Scheme 3.18: Proposed template pathway for the synthesis of gold(III) complexes.

3.3.3 Formation of Gold(III) Quinoxaline Pseudo Macrocylic, Pyrazine Macrocylic and Acyclic Complexes

The pseudo-macrocylic, pyrazine macrocylic and acyclic complexes were synthesized by direct metallation of the free ligand. For the pseudo macrocylic ligands and the acyclic complexes, the ligand was added to a solution of *tert*-butylammonium tetrachloroaurate and *tert*-butylammonium hexafluorophosphate(V) in DCM/ethanol. The reaction mixtures were refluxed for 30 min to 1 hour during which time a precipitate formed. The reaction times are much shorter as the metal does not have to fit into a rigid cavity; the yields are also higher for these, reactions *ca.* 40%.

The attempted synthesis of the macrocyclic pyrazine complexes was carried out in a similar manner, but over a much longer period of time. The dicyanopyrazine ligand, H₂L8a, was refluxed for 5 days in the presence of gold(III). The reaction mixture was analyzed and only the starting materials were detected. Thus, the synthesis of [Au(L8a)]⁺ was unsuccessful. The strongly withdrawing nature of the nitrile groups deactivate the ligand, making it a weaker σ -donor and reducing its ability to chelate gold(III). The ligand, H₂L8b, contains only one deactivating group, meaning it can more effectively stabilize the metal ion. Using similar reaction conditions the complex precipitated out of solution after 3 days of refluxing, although yield of this reaction is very poor (8%).

3.4 Summary and Conclusions

In conclusion, ten novel Schiff base ligands and twelve novel gold(III) Schiff base complexes were synthesized. The quinoxaline macrocyclic and pseudo-macrocyclic ligands as well as the pyrazine macrocyclic ligands were synthesized in a four-step reaction pathway involving the following key steps electrophilic substitution, condensation and Vilsmeier formylation reactions. These ligand synthesis reactions were fairly high yielding on the whole. Most of the complexes could be synthesized by metallation of the free ligands with gold(III); however, macrocyclic ligands with substituted and extended bridging groups had to be synthesized by template-directed reactions. The metallation reactions were, in general, low yielding with the template-directed reactions giving the lowest yields. Notwithstanding this, the template-directed synthesis of bridge-substituted gold(III) macrocycles offered the only route to a broader range of compounds.

3.4 References

- (1) Jones, C. J., McCleverty, J. A. *J. Chem. Soc. A* **1971**, 1052.
- (2) Weber, J. H. *Inorg. Chem.* **1967**, *6*, 258.
- (3) Van Stein, G. C., Van Koten, G., Passenier, H., Steinebach, O., Vrieze, K. *Inorg. Chim. Acta* **1984**, *89*, 79.
- (4) Schiff, H. *Annalen* **1864**, *131*, 118.
- (5) Borisova, N. E., Reshetova, M. D., Ustynyuk, Y. A. *Chem. Rev.* **2007**, 107.
- (6) Bacchi, A., Carcelli, M., Gabba, L., Ianelli, S., Pelagatti, P., Pelizzi, G., Rogolino, D. *Inorg. Chim. Acta* **2003**, *342*, 229.
- (7) Allen, F. H. *Acta Cryst.* **2002**, *B58*, 380.
- (8) Franceschi, F., Guillemot, G., Solari, E., Floriani, C., Re, N., Birkedal, H., Pattison, P. *Chem. Eur. J.* **2001**, *7*, 1468.
- (9) Munro, O. Q., Camp, G. L. *Acta Cryst.* **2003**, *C59*, o672.
- (10) Barnholtz, S. L., Lydon, J. D., Huang, G., Venkatesh, M., Barnes, C. L., Ketring, A. R., Jurisson, S. S. *Inorg. Chem.* **2001**, *40*, 972.
- (11) van den Ancker, T. R., Cave, G. W. V., Raston, C. L. *Green Chem.* **2006**, *8*, 50.
- (12) Bourrosh, P., Bologa, O., Simonov, Y., Gerbeleu, N., Lipkowski, J., Gdaniec, M. *Inorg. Chim. Acta* **2006**, *359*, 721.
- (13) Block, B. P., Bailer, J. C. *J. Am. Chem. Soc.* **1951**, *73*, 4722.
- (14) Busch, D. H., Farmery, K., Goedken, V., Katovic, V., Menyk, A. C., Sperati, C. R., Tokel, N. *Adv. Chem. Ser.* **1971**, *100*, 44.
- (15) Busch, D. H. *Helv. Chim. Acta.* **1967**, *50*, 174.
- (16) Busch, D. H. *Science* **1971**, *171*, 241.
- (17) Christensen, J. J., Hill, J. O., Izatt, R. M. *Science* **1971**, *174*, 459.
- (18) Black, D. C., Hartahorn, A. J. *Coord. Chem. Rev.* **1972**, *9*, 219.
- (19) Melson, G. A. *Coordination Chemistry of Macrocyclic Compounds*; Plenum Press: New York, 1979.
- (20) Sun, R. W.-Y., Che, C.-M. *Coord. Chem. Rev.* **2009**, *253*, 1682.
- (21) Thompson, M. C., Busch, D. H. *J. Am. Chem. Soc.* **1964**, *86*, 3651.
- (22) Busch, D. H. *Rec. Chem. Prog.* **1964**, *25*, 107.
- (23) D. A. Baldwin, R. M. P., D. W. Reichgott, and N. J. Rose *J. Am. Chem. Soc.* **1973**, *95*, 5152.
- (24) Jackals, S. C., Farmery, K., Barefield, E. K., Rose, N.J., Busch, D. H. *Inorg. Chem.* **1972**, *11*, 2893.
- (25) Guerriero, P., Tamburini, S., Vigato, P. A. *Coord. Chem. Rev.* **1995**, *139*, 17.
- (26) Suh, M. P., Kim, I. S., Shim, B. Y., Hong, D., Yoon, T.-S. *Inorg. Chem.* **1996**, *35*, 3595.
- (27) Kim, J.-H., Everett, G. W., Jr. *Inorg. Chem.* **1979**, *18*, 3145.
- (28) Kim, J.-H., Everett, G. W., Jr. *Inorg. Chem.* **1981**, *20*, 853.
- (29) Curtis, N. F. *Coord. Chem. Rev.* **1968**, *3*, 3.
- (30) Olson, D. C., Vasilevskis, J. *Inorg. Chem.* **1969**, *8*, 1611.
- (31) Olson, D. C., Vasilevskis, J. *Inorg. Chem.* **1971**, *10*, 463.
- (32) Olson, D. C., Vasilevskis, J. *Inorg. Chem.* **1972**, *11*, 980.
- (33) Wang, L., Zhu, X.-J., Wong, W.-Y., Guo, J.-P., Wong, W.-K., Li, Z.-Y. *Dalton Trans.* **2005**, 3235.
- (34) Hu, Y., Li, Q.-Q., Li, H., Guo, Q.-N., Lu, Y.-G., Li, Z.-Y. *Dalton Trans.* **2010**, *39*, 11344.
- (35) Munro, O. Q., Akerman, K. J., Akerman, M. P. 2011; Vol. WO2011/158176 A2.
- (36) Black, C. B., Andrioletti, B., Try, A. C., Ruiperez, C., Sessler J. L. *J. Am. Chem. Soc.* **1999**, *121*, 10438.
- (37) March, J. *Advanced Organic Chemistry*; Wiley-Interscience.
- (38) Appel, R. *Angew. Chem. Int. Ed.* **1975**, *14*, 801.
- (39) Beilstein, F. *Ber. Dtsch. Chem. Ges.* **1872**, *5*, 8416.
- (40) Ghosh, T., Maiya, B. G., Wong, M. W. *J. Phys. Chem. A.* **2004**, *108*, 11249.
- (41) Sessler, J. L., Dan Pantos, G. Katayev, E., Lynch, V. M. *Org. Lett.* **2003**, *5*, 4141.
- (42) Kojima, T., Nagasaki, F. *J. Heterocyclic Chem.* **1980**, *17*, 455.

- (43) Chang, T.-H., Wu, B.-R., Chiang, M. Y., Liao, S.-C., Ong, C. W., Hsu, H.-F., Lin, S. Y. *Org. Lett.* **2005**, *7*, 4075.
- (44) Munro, O. Q., Strydom, S. D., Grimmer, C. D. *New J. Chem.* **2004**, *28*, 34.
- (45) Best, S. L., Chattopadhyay, T. K., Djuran, M. I., Palmer, R. A., Sadler, P. J., Sóvágó, I., Varnagy, K. *Dalton Trans.* **1997**, 2587.
- (46) Gonzalez-Arellano, C., Corma, A., Iglesias M., Sanchez, F. *Chem. Commun.* **2005**, 1990.
- (47) Akerman, M. P., University of KwaZulu Natal, 2011.
- (48) Cotton, F. A., Wilkinson, G. W. *Advanced Inorganic Chemistry Fifth Edition*; John Wiley & Sons. Inc.: New York, 1988.
- (49) Che, C.-M., Sun, R. W.-Y., Yu, W.-Y., Ko, C.-B., Zhu, N., Sun, H. *Chem. Commun.* **2003**, *14*, 1718.

CHAPTER FOUR:

X-RAY CRYSTALLOGRAPHY

4.1 Introduction

The main objective of the X-ray crystallography experiments described in this Chapter was to determine the solid state structures of the novel gold(III) bis(pyrrolide-imine) Schiff base complexes. This would provide insight into the nature of the solid state interactions of these systems and would therefore provide valuable information as to whether or not these systems are likely to be effective DNA intercalators. This work would also serve to expand the limited available literature relating to tetradentate gold(III) chelates.

The first section of this Chapter is a review of previously reported X-ray crystal structures relating to this work. This includes a review of acyclic bis(pyrrolide-imine) ligands with a structure similar to the macrocyclic ligands reported in this work. The structures of two macrocyclic ligands that have been previously reported and were synthesized in this work are also discussed. This section also includes a comparison of acyclic bis(pyrrolide-imine) chelates with a variety of metal centres as well as a discussion on the structures of gold(III) macrocyclic and porphyrin structures found in the literature. This review section is important as it serves as a comparison for the experimental data and shows the properties and characteristics of similar compounds. The second section of this Chapter is a discussion of the experimental X-ray data obtained during this research. In this section, the structures of the ligands and gold(III) chelates are compared in the solid state and important structural and supramolecular properties of the molecules are discussed.

4.1.1 Previously Reported Bis(pyrrolide-Imine) Schiff Base Ligands

In this work eight macrocyclic, three pseudomacrocyclic, and one acyclic bis(pyrrolide-imine) ligand have been synthesized. A survey of the published X-ray structures related to the Schiff base ligands was conducted using the Cambridge Structural Database (CSD).¹ This survey showed that only two of the eight macrocyclic ligands have been previously reported and only synthetic derivatives of the other bis(pyrrolide-imine) acyclic and pseudomacrocyclic ligands have been reported.

The CSD data for the reported compounds, similar in structure to the proposed acyclic Schiff base ligand, are shown in Table 4.1. The structures of the compounds listed in the Table below are similar to H₂L12 but also have the same basic framework as the bis(pyrrolide-imine) macrocyclic ligands synthesized in this work. The reported X-ray structures have the same acyclic bis(pyrrolide-imine) structure but differ from H₂L12 in their di(azomethine) linkage unit. The compound *N,N'*-bis[(1*E*)-1*H*-pyrrol-2-ylmethylene]propane-1,3-diamine has a three carbon bis(imine) linkage while *N,N'*-bis[(1*E*)-1*H*-pyrrol-2-ylmethyl-ene]benzene-1,2-diamine has a phenylene bridging unit. Two different enantiomers of a cyclohexyl bridged unit have also been reported.

Table 4.1: Reported X-ray crystal structures of bis(pyrrrolide-imine) Schiff base ligands.

CSD Ref. Code ¹	Compound Name	Lit. Reference
EMIHEN	<i>N,N'</i> -bis[(1 <i>E</i>)-1 <i>H</i> -pyrrol-2-ylmethylene]propane-1,3-diamine	2
TETZIC	<i>N,N'</i> -bis[(1 <i>E</i>)-1 <i>H</i> -pyrrol-2-ylmethylene]benzene-1,2-diamine	3
DAZXOS/GIHJOX	(1 <i>R</i> ,2 <i>R</i>)- <i>N,N'</i> -bis[(1 <i>E</i>)-1 <i>H</i> -pyrrol-2-ylmethylene]cyclohexane-1,2-diamine	4,5
XUVQAG	(1 <i>S</i> ,2 <i>S</i>)- <i>N,N'</i> -bis[(1 <i>E</i>)-1 <i>H</i> -pyrrol-2-ylmethylene]cyclohexane-1,2-diamine	4-6

Average bond lengths and angles for these reported compounds are given in Table 4.2. These mean distances and angles for the compounds are all very similar, as expected. The average imine bond length is 1.279 Å and the average bond lengths for a pyrrole ring are 1.372 Å (C_{α} -N), 1.375 Å (C_{α} - C_{β}) and 1.412 Å (C_{β} - C_{β}) as reported by Allen *et al.*⁷ The bond lengths given in Table 4.2 are similar to these standard values.

Table 4.2: Average bond lengths and bond angles for previously reported acyclic bis(pyrrrolide-imine) Schiff base compounds.

	EMIHEN	TETZIC (molecule B)	DAZXOS	XUVQAG
Bond Length (Å)				
$C=N_{\text{imine}}$	1.280(1)	1.278(1)	1.279(1)	1.276(1)
$C_{\alpha}-N_{\text{pyrrole}}$	1.373(7)	1.369(7)	1.370(6)	1.360(8)
$C_{\alpha}-C_{\beta}$	1.384(5)	1.378(6)	1.381(5)	1.370(7)
$C_{\beta}-C_{\beta}$	1.413(4)	1.414(2)	1.409(1)	1.395(4)
$C_{\alpha}-(C=N_{\text{imine}})$	1.446(1)	1.441(4)	1.446(1)	1.442(3)
Bond Angle (°)				
$C_{\alpha}-N_{\text{pyrrole}}-C_{\alpha}$	109.0(1)	109.6(6)	109.2(1)	109.7(1)
$C=N_{\text{imine}}-C$	116.9(1)	118.3(6)	117.2(1)	117.4(2)

These previously reported acyclic compounds all exhibit the same hydrogen-bonding motif; however, they do not have the same supramolecular structure as the variable di(azomethine) linkages result in different degrees of conformational freedom. Two independent studies^{2,8} published in 2003 showed that the pyrrole-imine functional combination, Figure 4.1(a), is a useful supramolecular synthon comprising a strong H-bond donor (pyrrole N-H group) and a strong H-bond acceptor (imine nitrogen). Efficient self-recognition or self-assembly through complementary hydrogen bonding in this type of system is now known to lead to either dimerization in the case of mono(pyrrole) derivatives (Figure 4.1(b)) and bis(pyrrole) derivatives with a rigid linker or polymerization in the case of bis(pyrrole) derivatives with flexible linkers (Figure 4.1(c)).³ A brief outline on these reported compounds is given below for comparison with the novel structures that will be discussed later.

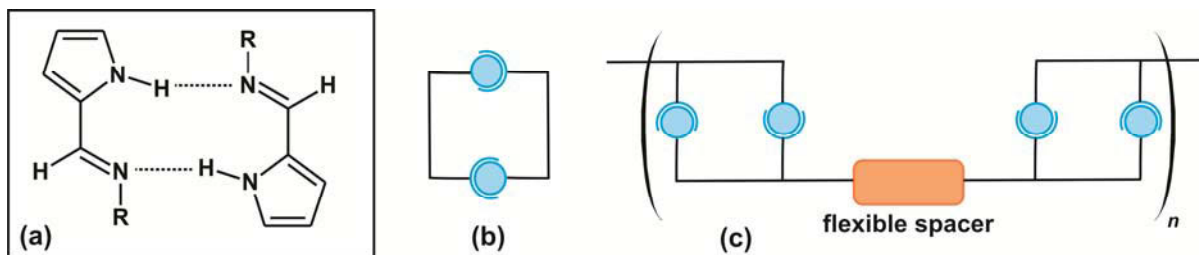


Figure 4.1: (a) Hydrogen bonding motif consisting of a pyrrole NH and imine N. (b) Schematic diagram showing complementary hydrogen bonding in a mono(pyrrrolide-imine) derivative. (c) Complementary hydrogen bonding in a bis(pyrrrolide-imine) system with a flexible linker.

The compound, *N,N'*-bis[(1*E*)-1*H*-pyrrol-2-ylmethylene]propane-1,3-diamine (CSD ref: EMIHEN), Figure 4.2(a) and (b), crystallized in the orthorhombic space group *Pccn*, with eight molecules in the unit cell ($Z = 8$). The X-ray crystal structure shows that the geometry about both imine bonds is *trans*. This conformation is preferred as the *cis* isomer would lead to unfavourable interactions between the pyrrole C_{α} -H groups and the methylene groups of the propyl bridge.² As the compound has six torsional degrees of freedom, there are potentially many possible stable conformations for this molecule. In the crystal structure, the molecule favours an all-staggered conformation for the methylene groups of the propyl chain and a *trans* configuration for the two pyrrole rings.² This conformation is favoured as it allows for stabilizing hydrogen bonds to form. The pyrrole NH groups act as hydrogen bond donors and the imine N groups act as hydrogen bond acceptors. This pair of functional groups allows for the 'recognition' of the complementary motif in a neighbouring molecule.² As there are two hydrogen-bonding motifs at opposite ends of the molecule, a one-dimensional hydrogen-bonded chain is formed, Figure 4.2(c). The hydrogen bonding forms stable ten-membered rings with the pairs of hydrogen-bonding motifs not lying in the same plane, resulting in a twist of the ten-membered rings.² This twisting possibly minimizes the unfavourable steric contacts between the pyrrole C_{α} -H group of one molecule and the methylene group of the neighbouring molecule.² The formation of hydrogen bonds between neighbouring molecules leads to a 'ladder' structure where each step is laterally displaced from the preceding step.

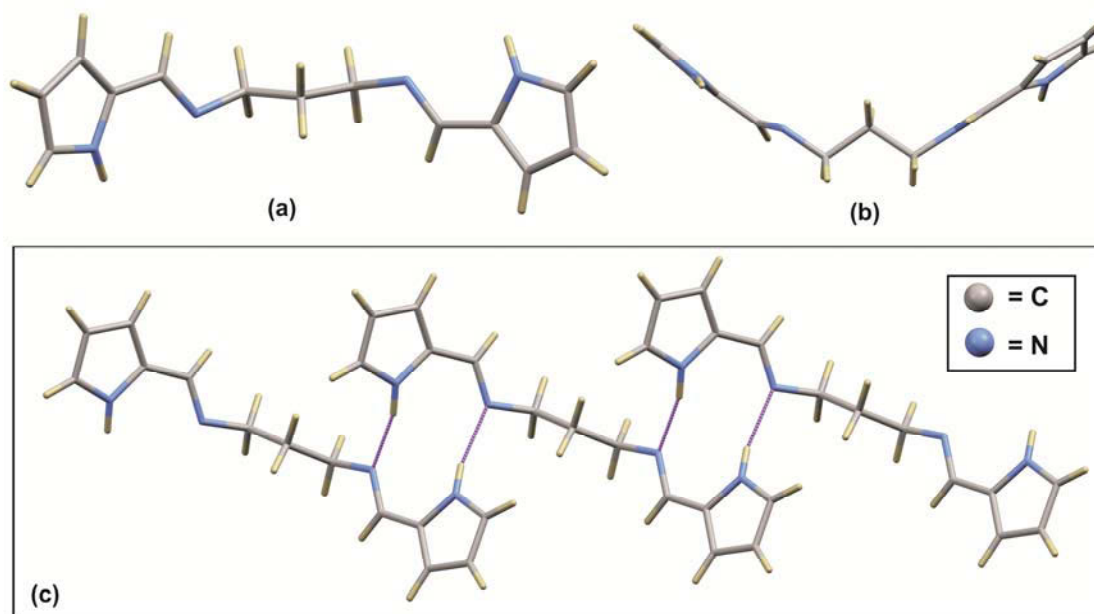


Figure 4.2: (a) X-ray structure of *N,N'*-bis[(1*E*)-1*H*-pyrrol-2-ylmethylene]propane-1,3-diamine. (b) Side view illustrating W-shaped conformation of the molecule. (c) Repeating unit of an infinite one-dimensional hydrogen-bonded chain.

The compound, *N,N'*-bis[(1*E*)-1*H*-pyrrol-2-ylmethylene]benzene-1,2-diamine (CSD ref: TETZIC) (Figure 4.3(a)), crystallized in the monoclinic spacegroup *C2/c* with 24 molecules in the unit cell. Each asymmetric unit contained two full molecules, arranged in a dimer formation, and two half molecules. The compound does not adopt a planar conformation as would be expected due to the rigidity of the aromatic bridge and extended π -conjugation throughout the molecule. The angle between the mean plane of one pyrrole group and the adjacent pyrrole group of the same molecule is $35.98(4)^\circ$.³ AM1 calculations have shown that non-bonded repulsion between the two pyrrole NH groups in the planar conformer are responsible for the strain-

relieving twisted conformation.³ There are complementary hydrogen bonds between the pyrrole NH groups of one molecule and the imine nitrogen atoms of the other to lock the two C-shaped structures almost perpendicularly together in a tight dimer, Figure 4.3(b).

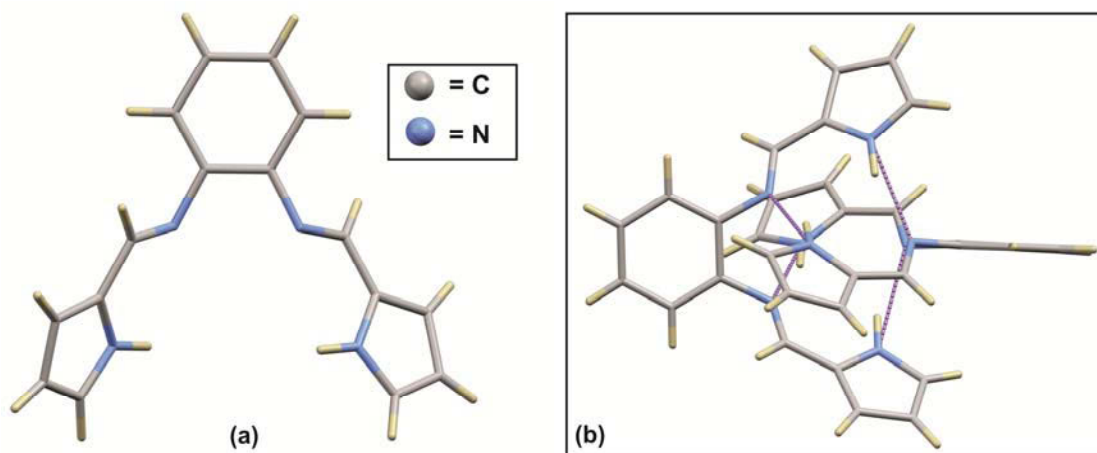


Figure 4.3: (a) X-ray crystal structure of *N,N'*-bis[(1*E*)-1*H*-pyrrol-2-ylmethylene]benzene-1,2-diamine. (b) Hydrogen-bonded dimer structure supported by complementary hydrogen bonding between the pyrrole NH and imine N atom.

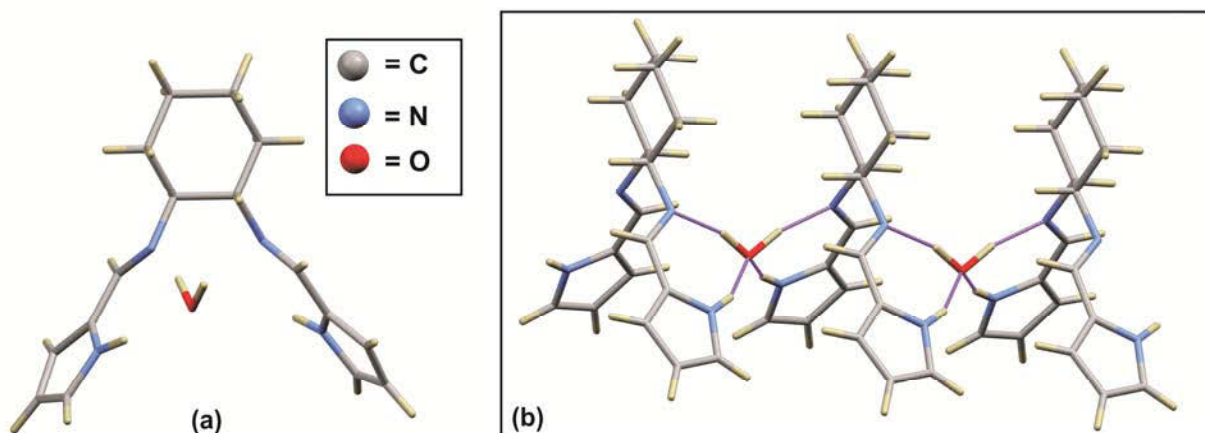


Figure 4.4: (a) X-ray crystal structure of (1*S*,2*S*)-*N,N'*-bis[(1*E*)-1*H*-pyrrol-2-ylmethylene]cyclohexane-1,2-diamine monohydrate showing the water solvent molecule.⁶ (b) One dimensional polymer formed by water molecules bridging Schiff base ligands.

The different enantiomers of the cyclohexyl-bridged bis(pyrrolide-imine) Schiff base analogue have also been reported. The (1*S*,2*S*) enantiomer (CSD ref: XUVQAG), Figure 4.4(a), shows a hydrogen-bonded water molecule in all three reported structures. The pyrrole NH of the compound, acts as a hydrogen bond donor and the water O acts as the hydrogen bond acceptor. The same water molecule also acts as a hydrogen bond donor compound while the compound's imine N acts as the hydrogen bond acceptor. The water molecule serves to link adjacent compounds through hydrogen bonding, forming an infinite one-dimensional hydrogen-bonded chain⁴⁻⁶ (Figure 4.4 (b)). The (1*R*,2*R*) enantiomer has been shown to crystallize in different space groups with different crystal packing dependent on the crystallization conditions. Wang *et al.*⁵

crystallized this enantiomer in the orthorhombic spacegroup $P2_12_12$ with $Z = 2$ (CSD ref: GIHJOX). The crystal structure also contained a water solvent molecule in the lattice and thus has a very similar supramolecular structure to that described above for the (1*S*,2*S*) enantiomer. Van den Ancker *et al.*⁴ crystallized the racemic mixture of the (1*R*,2*R*) and (1*S*,2*S*) enantiomers in the achiral monoclinic spacegroup $C2/c$ with 4 molecules in the unit cell ($Z = 4$) (CSD ref: DAZXOS). The pyrrole NH of one molecule acts as hydrogen bond donor while the imine N of an adjacent molecule acts as a hydrogen bond acceptor. As the imine and pyrrole moieties are *trans* to each other they form an infinite, one-dimensional hydrogen-bonded chain.

A survey of the CSD showed that two of the quinoxaline-based macrocyclic ligands synthesized in this work have been previously reported. A quinoxaline-based pseudomacrocyclic ligand similar in structure to the pseudomacrocyclic ligands: H₂L9, H₂L10 and H₂L11 reported in this work, has also been previously reported. The CSD data for these reported ligands is summarized in Table 4.3.

Table 4.3: Reported X-ray crystal structure of quinoxaline-based bis(pyrrolide-imine) Schiff base macrocyclic and pseudomacrocyclic ligands.

CSD Ref. Code ¹	Compound Name	Lit. Reference
KAVXIP	11,12,13,14-tetrahydro-9,6-azeno-17,20-epimino[1,5]diazacycloheptadecino [11,12-b]quinoxaline (H ₂ L1)	9
KAVXEL	12,13,14,15-tetrahydro-11H-9,6-azeno-18,21-epimino[1,6]diazacyclooctadecino[12,13-b]quinoxaline (H ₂ L3)	9
781633*	<i>N,N'</i> -((5,5'-(Quinoxaline-2,3-diyl))bis(1 <i>H</i> -pyrrole-5,2-diyl))bis(methanylylidene))bis(4-methoxyaniline)	10

*CIF file obtained from publication text

Table 4.4 gives the average bond lengths and angles for these reported compounds. The macrocyclic and pseudomacrocyclic compounds have very similar structures. The compounds all contain the same quinoxaline bridge unit and bis(pyrrolide-imine) moieties. The macrocyclic ligands, however, have di(azomethine) linkage units; H₂L1 has a propyl (three-carbon) bridging unit and H₂L3 has a butyl (four-carbon) bridging unit. The pseudomacrocyclic complex, *N,N'*-((5,5'-(Quinoxaline-2,3-diyl))bis(1*H*-pyrrole-5,2-diyl))bis(methanylylidene))bis(4-methoxyaniline), does not have a closed bridging system but rather has methoxyaniline moieties attached to the imine groups. These compounds have similar bond lengths and angles. These reported Schiff bases also have bond distances and angles in good agreement with their acyclic analogues (Table 4.2).

Table 4.4: Average bond lengths and angles for previously reported bis(pyrrolide-imine) Schiff base macrocyclic compounds.

	KAVXIP	KAVXEL	781633
		Bond Lengths (Å)	
C=N _{imine}	1.288(3)	1.283(8)	1.275(3)
C _α -N _{pyrrole}	1.359(8)	1.361(6)	1.358(3)
C _α -C _β	1.400(8)	1.380(6)	1.380(3)
C _β -C _β	1.371(3)	1.375(7)	1.389(3)
C _α -(C=N _{imine})	1.412(8)	1.408(7)	1.432(3)
		Bond Angles (°)	
C _α -N _{pyrrole} -C _α	108.0(4)	108.0(3)	110.5(1)
C=N _{imine} -C	123.8(8)	121.1(5)	120.8(2)

The ligand H₂L1 (CSD ref: KAVXIP), crystallized in the monoclinic space group $P2_1/c$ with $Z = 4$ (Figure 4.5(a)). H₂L3 (CSD ref: KAVXEL), crystallized in the orthorhombic space group $Pca2_1$ with $Z = 8$ (Figure 4.5(b)). The X-ray crystal structures of both compounds, which are expected to be completely planar due to the extended aromaticity, exhibit a slightly domed conformation. The pyrrole rings are both canted relative to the quinoxaline group, Figure 4.5(c). Porphyrin molecules, which show similar extended aromaticity to the compounds reported here, can also exhibit a domed conformation.¹¹ This perhaps suggests that highly conjugated aromatic systems are not necessarily inflexible and planar.

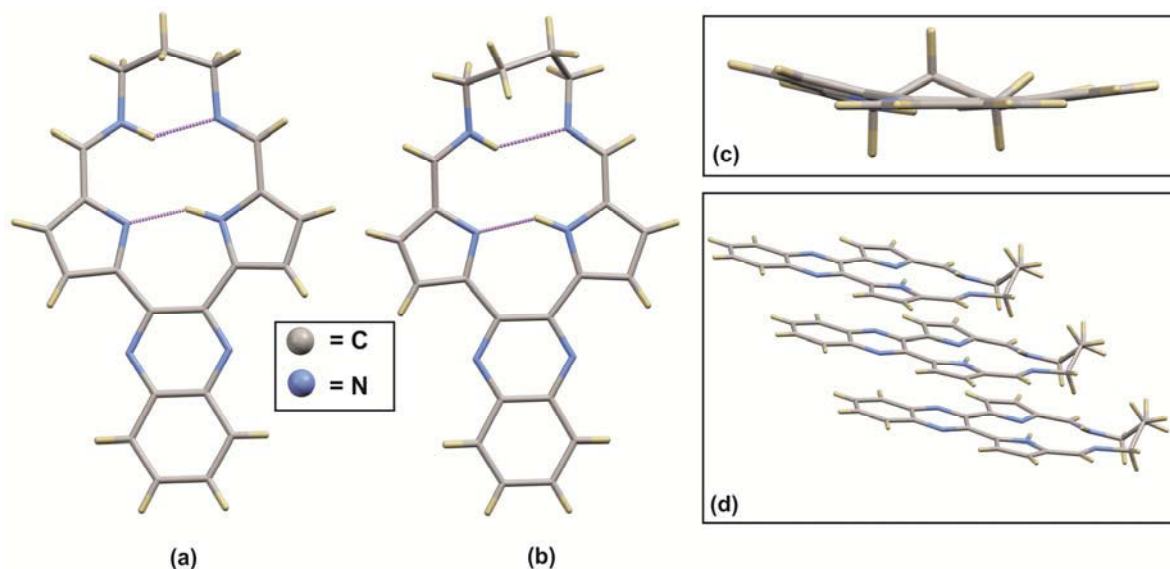


Figure 4.5: X-ray crystal structures of (a) H₂L1 and (b) H₂L3 showing intra-molecular hydrogen bonds.⁹ (c) Side view of H₂L1 showing the out-of-plane twisting of the pyrrole rings. (d) π - π stacking of H₂L3 molecules.

One of the most notable features of both compounds is that in the solid state, contrary to expectation, both pyrrole N atoms are not protonated. Interestingly, the X-ray data showed that one pyrrole N atom and the diagonally opposite imine N atom were protonated. This is in stark contrast to non-macrocyclic Schiff base compounds described above which show both hydrogen atoms located on the pyrrole N atoms.²⁻⁶ Wang *et al.*⁹ reported that this is one possible tautomer of the compound with other resonance forms existing where the hydrogen atoms may be located on the pyrrole N atoms or on the other pyrrole and imine N atoms. This will be further discussed at a later stage.

Both these compounds exhibit two intramolecular hydrogen bonds. The first hydrogen bond has the pyrrole NH acting as the hydrogen bond donor and the opposite pyrrole N atom acting as the hydrogen bond acceptor. The second hydrogen bond comprises the imine NH acting as the hydrogen bond donor and the opposite imine N atom acting as the hydrogen bond acceptor. The hydrogen bonds are considerably shorter than the sum of the van der Waals radii, although this short bond length is not necessarily indicative of bond strength as the length of the bonds is governed by the geometry of the macrocycle and not by the strength of the interaction. The compound H₂L3 also exhibits π - π interactions, Figure 4.5(d), with the imine groups of one molecule interacting with the pyrrole rings of an adjacent molecule as well as overlap of the quinoxaline tails. This is an important consideration as it means this compound is predisposed to π -stacking, an important aspect of DNA intercalators.

The compound, N,N' -((5,5'-(quinoxaline-2,3-diyl)bis(1H-pyrrole-5,2-diyl))bis(methanylylidene))bis(4-methoxyaniline) (781633), crystallized in the monoclinic spacegroup $P2_1/c$ with $Z = 4$. The asymmetric unit is the methanol monosolvate of the compound, Figure 4.6. The compound has adopted a linear configuration. It is referred to as a pseudomacrocyclic ligand because, although, it is linear when it is a free ligand, when it complexes a metal ion through the two pyrrole-imine moieties it takes the appearance of a macrocyclic complex. The molecule is non-planar with the two arms twisting out of the quinoxaline plane with torsion angles of 33.2° and 11.6° between the pyrrole rings and quinoxaline plane.¹⁰ The X-ray crystal structure shows that the geometry about both imine bonds is *trans* with both pyrrole moieties facing outwards. This configuration possibly minimizes the unfavourable steric contacts between the two bulky methoxy arms of the compound. There is hydrogen bonding between the methanol solvent molecule and the compound with the methanol OH acting as the hydrogen bond donor and the imine N acting as the hydrogen bond acceptor. The same methanol O also acts as a hydrogen bond acceptor while the pyrrole NH of the same arm acts as the hydrogen bond donor. This hydrogen bonding pattern yields a closed, seven-membered hydrogen-bonded ring. Similar to the acyclic Schiff base ligands, this compound has both hydrogen atoms located on the pyrrole N atoms.

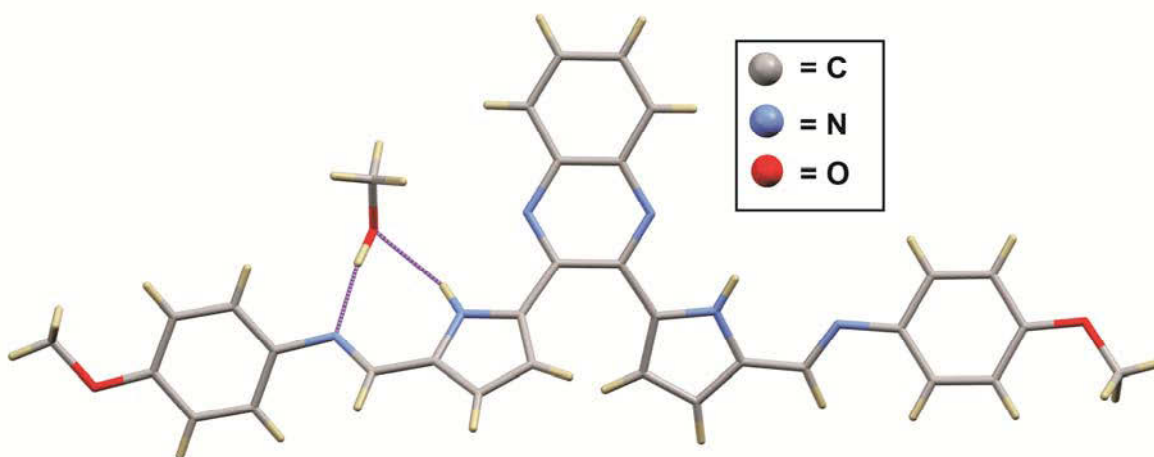


Figure 4.6: X-ray crystal structure of N,N' -((5,5'-(quinoxaline-2,3-diyl)bis(1H-pyrrole-5,2-diyl))bis(methanylylidene))bis(4-methoxyaniline) showing hydrogen bonding to the methanol solvent molecule.

4.1.2 Previously Reported Bis(pyrrolide-Imine) Metal Chelates

A survey of the published X-ray structures relating to the gold(III) chelates synthesized in this work using the CSD was conducted.¹ The survey showed that the two bis(pyrrolide-imine) macrocyclic ligands previously discussed, H_2L1 and H_2L3 , have been coordinated to nickel(II). The survey also showed that acyclic Schiff base ligands similar in structure to H_2L12 , have been coordinated to various metal centres. The pseudomacrocyclic ligand described above has also reportedly been coordinated to copper(II). None of the ligands described in this work have, however, reportedly been chelated to gold(III). A study of the structural features of other d^8 metals such as palladium(II) and nickel(II) chelated to similar Schiff base ligands could prove relevant to this work and was therefore also conducted. The CSD data for the Schiff base chelates is summarized in Table 4.5. Table 4.6 gives the average bond distances and angles for these reported metal chelates.

Table 4.5: Reported X-ray crystal structure of bis(pyrrolide-imine) Schiff base chelates.

CSD Ref. Code ¹	Compound Name	Lit. Reference
GEPPEX	(1,2-bis(1H-pyrrol-2-ylmethyleneamino) ethane-N,N',N'',N''')-iron(II)	12
MAGJEK	(1,3-bis(2-Pyrrolylmethyleneamino) propane)-copper(II)	13
NACRAK	Dipyridine-(N,N'-bis(2-pyrrolylmethylene)propane-1,3-diamine)-cobalt(III) pyridinetrichloro-cobalt	14
VIDKAV	(N,N'-bis(Pyrrol-2-ylmethylene) cyclohexane-1,2-diamine-N,N',N'',N''')-nickel(II)	6
XUVQEK	(N,N'-(1,2-Cyclohexylene)-bis(pyrrole-2-ylmethyleneamine))-palladium(II)	6
XUVQIO	(N,N'-1,3-Propylene-bis(pyrrole-2-ylmethyleneamine))-palladium(II)	6

Table 4.6: Average bond lengths and bond angles of the coordination sphere of previously reported bis(pyrrolide-imine) Schiff base chelates.

	GEPPEX	VIDKAV	XUVQEK	MAJEK	NACRAK	XUVQIO
Metal	Fe(II)	Ni(II)	Pd(II)	Cu(II)	Co(III)	Pd(II)
Bridging group	Ethyl	Cyclohexyl			Propyl	
	Bond Length (Å)					
M–N_{imine}	1.837(4)	1.850(5)	1.960(3)	1.980(7)	1.95(1)	2.006(5)
M–N_{pyrrole}	1.876(4)	1.887(5)	2.046(3)	1.948(7)	1.92(1)	2.011(5)
	Bond Angles (°)					
N_{imine}–M–N_{pyrrole}	84.5(2)	84.4(2)	81.2(1)	82.6(3)	83.6(4)	80.7(2)
N_{imine}–M–N_{imine}	84.5 (2)	84.5(2)	83.9(1)	92.7(3)	92.3(5)	95.3(2)
N_{pyrrole}–M–N_{pyrrole}	106.4(1)	106.5(2)	114.0(1)	101.9(3)	100.5(4)	103.1(2)

The iron(II) compound with the ethyl bridging unit (CSD ref: GEPPEX), Figure 4.7(a), as well as the nickel(II) and palladium(II) (Figure 4.7(b)) complexes with the cyclohexyl bridge (CSD ref: VIDKAV and XUVQEK) have shorter M–N_{imine} distances than M–N_{pyrrole} distances due to the restricted ligand binding site size imposed by the two-carbon bridge. As the chelates have a short bridge, they correspondingly have smaller N_{imine}–M–N_{imine} bite angles. As there is no bridge across the pyrrole moieties the N_{pyrrole}–M–N_{pyrrole} angle is fairly large, allowing the metal to sit more comfortably in the coordination sphere. These complexes show a characteristic out of plane twisting of the di(azomethine) linkage, Figure 4.7(c). This twisting is to accommodate the metal ion in the coordination site. Although the bridge is twisted the pyrrole heterocycles are planar with the coordination geometry around the metal ion being nominally square-planar.

The acyclic propyl-bridged bis(pyrrolide-imine) Schiff base ligand, *N,N'*-bis[(1*E*)-1*H*-pyrrol-2-ylmethylene]propane-1,3-diamine was chelated to the metals copper(II) (CSD ref: MAGJEK), cobalt(III) (CSD ref: NACRAK), and palladium(II) (CSD ref: XUVQIO), Figure 4.8(a). The M–N_{pyrrole} and M–N_{imine} bond distances are similar lengths within each complex. As the three-carbon propylene bridge is larger than the two-carbon ethylene bridge, the N_{imine}–M–N_{imine} bite angle is correspondingly larger. The metal ion in both cases exhibits a nominally square-planar coordination geometry. The ligand is relatively planar in the extended aromatic region, including the pyrrole ring and imine bond; however, the central carbon of the propyl bridge sits out-of-plane (Figure 4.8(b)). The propyl-bridged copper(II) complex (MAGJEK) exhibits Cu⋯π interactions between the copper(II) ion of one chelate and the π system of the pyrrole ring of an adjacent chelate. This leads to a domed configuration of the ligand. The palladium complex (XUVQIO) also exhibits a domed ligand with π–π interactions between the imine moiety of one molecule and the pyrrole moiety of an adjacent

molecule (Figure 4.8(c)). This is interesting to note as it suggests that these molecules have the ability to π -stack which is a crucial property of DNA intercalators.

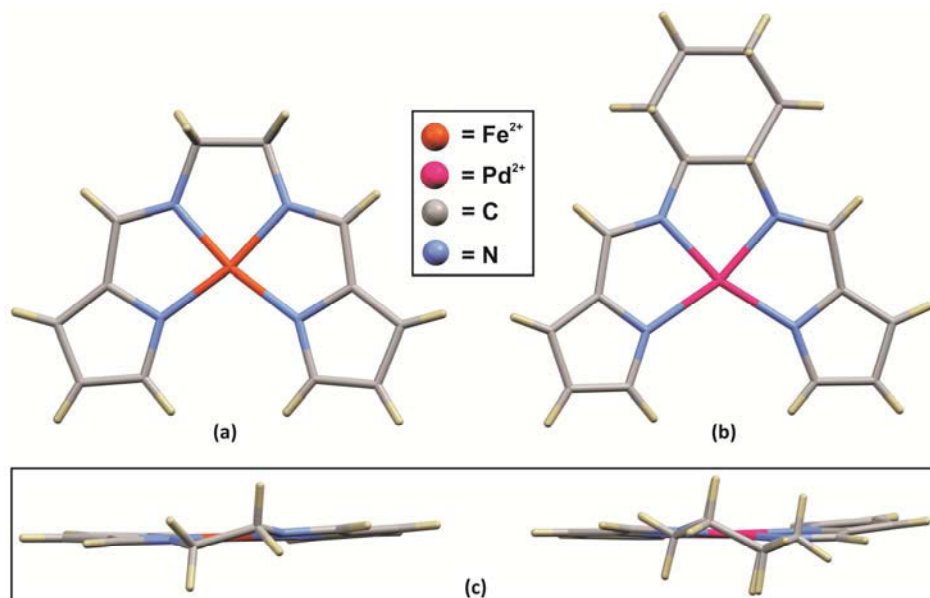


Figure 4.7: X-ray crystal structures of (a) (1,2-bis(pyrrol-2-ylmethyleneamino) ethane- N,N',N'',N''')-iron(II) and (b) (N,N' -(1,2-cyclohexylene)-bis(pyrrol-2-ylmethyleneamino))-palladium(II). (c) Front view of the iron(II) and palladium(II) complexes showing the twisting of the bridge.

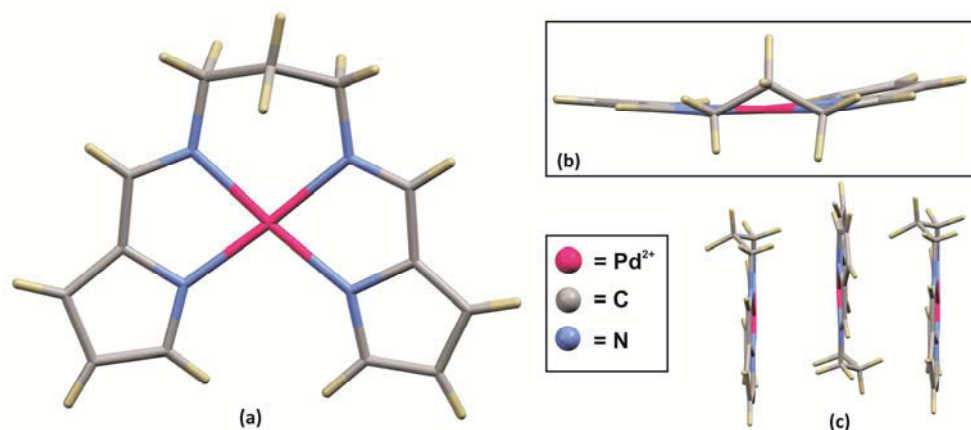


Figure 4.8: (a) X-ray structure of (N,N' -1,3-propylene-bis(pyrrole-2-ylmethyleneamine))-palladium(II). (b) Front view of the palladium(II) complex showing the out-of-plane nature of the central methylene carbon atom of the propyl bridge. (c) π - π stacking of the palladium(II) complex.

The two bis(pyrrolide-imine) Schiff base macrocyclic structures described above, H_2L1 and H_2L3 , have been coordinated to nickel(II) and the X-ray crystal structures elucidated. The nickel(II) complex of H_2L1 has been synthesized in this work as a d^8 square-planar analogue of the gold(III) complexes to ascertain the necessity of the gold(III) ion for cytotoxicity. The pseudomacrocyclic ligand, N,N' -((5,5'-(quinoxaline-2,3-diyl)bis(1H-pyrrole-5,2-diyl))bis(methan-ylidene))bis(4-methoxyaniline), described above has been reported coordinated to copper(II). Table 4.7 summarizes the CSD data and Table 4.8 summarizes the bond lengths and angles of the complexes.

Table 4.7: Reported X-ray crystal structures of bis(pyrrrolide-imine) Schiff base macrocyclic chelates.

CSD Ref. Code ¹	Compound Name	Lit. Reference
KAVXAH	(12,13-dihydro-14H-6,9:17,20-diepipimino[1,6]diazacycloheptadecino [12,13-b]quinoxalinato)-nickel(II) dichloromethane solvate	9
KAVWUA	(12,13,14,15-tetrahydro-6,9:18,21-diepipimino[1,6]diazacyclooctadecino [12,13-b]quinoxalinato)-nickel(II)	9
781632*	<i>N,N'</i> -((5,5'-(Quinoxaline-2,3-diyl)bis(1H-pyrrole-5,2-diyl))bis(methanylylidene))bis(4-methoxyaniline)-copper(II)	10

*Obtained from publication text

Table 4.8: Average bond lengths and angles for previously reported bis(pyrrrolide-imine) Schiff base chelates.

	KAVXAH	KAVWUA	781632
		Bond Lengths (Å)	
M–N_{imine}	1.887(5)	1.918(5)	2.047(3)
M–N_{pyrrole}	1.880(4)	1.878(4)	1.958(3)
		Bond Angles (°)	
N_{imine}–M–N_{pyrrole}	85.3(2)	85.0(2)	84.0(9)
N_{imine}–M–N_{imine}	93.3(2)	95.1(2)	99.1(1)
N_{pyrrole}–M–N_{pyrrole}	96.1(2)	95.4(2)	92.8(1)

The propyl-bridged nickel(II) Schiff base macrocyclic chelate (CSD ref: KAVXAH), has similar M–N_{imine} and M–N_{pyrrole} bond distances while the butyl-bridged Schiff base nickel(II) macrocyclic chelate (CSD ref: KAVWUA), has a longer M–N_{imine} bond length than M–N_{pyrrole} bond length. This is due to the longer (four-carbon) bridge forcing the imine N atoms further apart than for the three carbon bridges. The acyclic Schiff base complexes with shorter (two-carbon) bridges have shorter M–N_{imine} bond lengths than M–N_{pyrrole} bond lengths (Table 4.6). Both complexes have N_{imine}–M–N_{imine} bond angles similar to those reported for the acyclic Schiff base complexes with the butyl bridged complex subtending a slightly larger angle. Due to the quinoxaline bridge linking the pyrrole moieties, the N_{pyrrole}–M–N_{pyrrole} bond angles for both complexes are smaller than those of the open-ended acyclic ligands.

The pseudomacrocyclic complex *N,N'*-((5,5'-(quinoxaline-2,3-diyl)bis(1H-pyrrole-5,2-diyl))bis(methanylylidene))bis(4-methoxyaniline)-copper(II) (781632) has M–N_{pyrrole} bonds shorter than the M–N_{imine} bonds in the complex. As there is no di(azomethine) bridging linkage, this compound has a large N_{imine}–M–N_{imine} bond angle relative to the macrocyclic Schiff base complexes. However, as the quinoxaline moiety bridges the pyrrole groups the N_{pyrrole}–M–N_{pyrrole} angle is much smaller than other Schiff base complexes without bridged pyrrole rings.

The propyl-bridged Schiff base nickel(II) macrocyclic chelate Figure 4.9(a), crystallized in the monoclinic spacegroup $P2_1/c$ with $Z = 8$. The asymmetric unit consists of two metal chelates as the DCM solvate. The propyl-bridged chelate has an almost square-planar metal centre with both molecules in the asymmetric unit exhibiting a similar structure. The nickel(II) ion is positioned only 0.020(1) Å above the 4-atom mean plane defined by the four coordinating nitrogen atoms in molecule B. The ligand itself is not completely planar, Figure 4.9(c), the 10-atom mean plane of the quinoxalone tail of molecule B is canted out of the 5-atom mean plane defined by the four coordinating nitrogen atoms and the metal ion by 18.8(2)°. The pyrrole rings are also twisted out of the 5 atom mean plane with the C_β of one pyrrole ring exhibiting the largest out-of-plane deviation, sitting 0.212(2) Å below the mean plane. The central methylene carbon atom is puckered

and sits 0.714(1) Å above the 5 atom mean plane. This puckering is necessary to allow the bridge to adopt a nearly ideal bond angle for an sp^3 hybridized carbon atom, 109.5°.

The butyl-bridged macrocyclic nickel(II) Schiff base chelate, Figure 4.9(b), crystallized in the orthorhombic spacegroup $P2_12_12_1$ with $Z=12$. The three molecules in the asymmetric unit of the butyl chelate are all different in structure, Figure 4.9 (d). All three molecules have a nominally square-planar metal centre with molecule C exhibiting the greatest deviation with the nickel(II) ion positioned 0.032(1) Å above the four-atom mean plane defined by the four coordinating nitrogen atoms. Molecule A, like the propyl bridged chelate, has both the quinoxaline tail and pyrrole moieties canted out-of-plane of the molecule. Molecule B has the quinoxaline tail in the plane of the molecule and the pyrrole ring only slightly out of the plane. Molecule C also has the quinoxaline tail and pyrrole moieties twisted slightly out-of-plane. In all three molecules the four-carbon bridge is twisted out-of-plane. The M–N_{imine} bonds have to sit out of the plane of the molecule in order to coordinate. All the molecules exhibit M– π stacking, Figure 4.9(e).

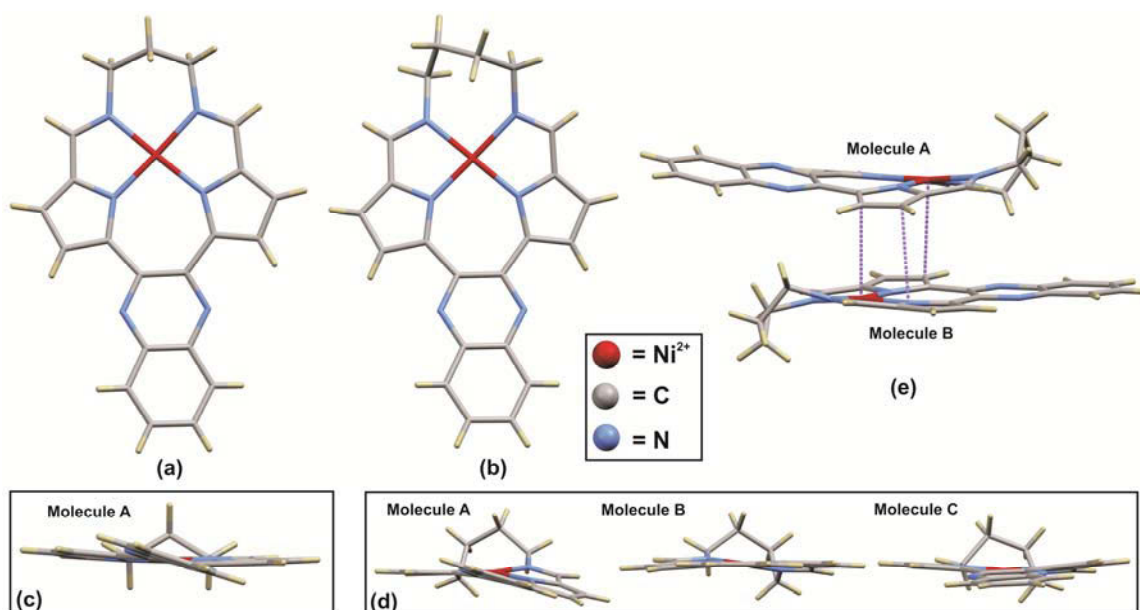


Figure 4.9: X-ray crystal structures of (a) (12,13-dihydro-6,9:17,20-diepimino[1,6]diazacyclo-heptadeceno[12,13-b]quinoxalinato)-nickel(II) and (b) (12,13,14,15-tetrahydro-6,9:18,21-diepimino[1,6] diazacyclooctadeceno[12,13-b]quinoxalinato)-nickel(II) (c) “Front view” of molecule A of the propyl-bridged macrocyclic Ni(II) chelate showing the canted quinoxaline tail and puckered propyl bridge. Molecule B shows a similar deviation from planarity. (d) “Front view” of the different molecules in the asymmetric unit of the butyl-bridged macrocyclic Ni(II) chelate. (e) M– π stacking between molecules A and B of the butyl-bridged chelate.

The pseudomacrocyclic complex N,N' -((5,5'-(quinoxaline-2,3-diyl)bis(1*H*-pyrrole-5,2-diyl))bis(methanylylidene))bis(4-methoxyaniline)-copper(II) crystallized in the triclinic spacegroup $P-1$ with four molecules in the unit cell, Figure 4.10(a); the asymmetric unit contains two molecules. These molecules both experience the same deviations from planarity with the copper(II) atom positioned 0.056(1) Å above the four-atom mean plan defined by the four coordinating nitrogen atoms of molecule A. Both molecules are domed with the pyrrole rings canted above the plane of the metal and the quinoxaline ring canted below the plane, Figure 4.10(b). The two methoxy-aniline arms are almost parallel to each other and make an angle of

59.6(3)° and 68.8(4)° relative to the plane of the coordination sphere for molecule A. These complexes are referred to as pseudomacrocyclic complexes; the spacefilling diagram in Figure 4.10(c) shows that the electron density of the ligand completely encloses the metal ion, similar to a true macrocycle.

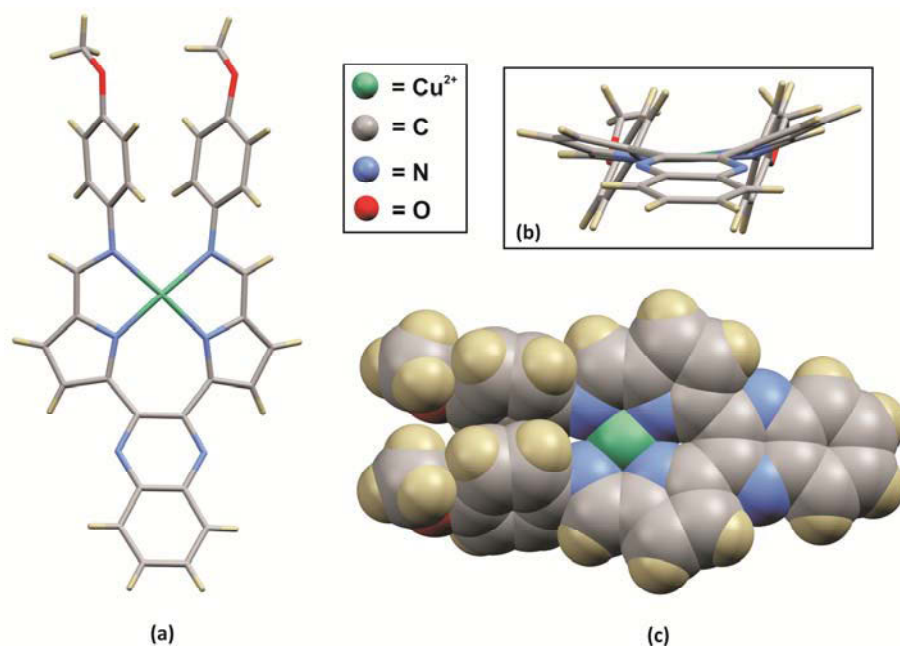


Figure 4.10: (a) X-ray crystal structure of *N,N'*-((5,5'-(quinoxaline-2,3-diyl)bis(1H-pyrrole-5,2-diyl))bis(methanylylidene))bis(4-methoxyaniline)-copper(II). (b) Back view of the copper(II) complex(II) showing the domed nature of the pyrrole moieties. (c) Space-fill diagram of the copper(II) complex, illustrating why it is referred to as a pseudomacrocycle.

4.1.2 Previously Reported X-ray Crystal Structures of Gold(III) Chelates

The CSD¹ showed that a few relevant macrocyclic gold(III) complexes have been reported. These include the gold(III) porphyrins and macrocyclic gold(III) cyclam complexes. A summary of these compounds is given in Table 4.9.

Table 4.9: Reported X-ray crystal structures of gold(III) macrocyclic complexes.

CSD Ref. Code ¹	Compound Name	Lit. Reference
AZEGIV	(5,7,12,14-Tetramethyl-1,4,8,11-tetraaza-4,6,11,13-tetraene)-gold(III) bromide	15
DOKDIR	(5,10,15,20-tetraphenyl-7-aza-22-carbaporphyrinato)-gold(III) dichloromethane solvate	16
ILIWIJ	(5,10,15,20-Tetraphenylporphyrinato)-gold(III) perchlorate	11
REXNIR	(<i>cis</i> -6,13-Dimethyl-6,13-dinitro-1,4,8,11-tetra-azacyclotetradecan-1-ido)-gold(III) diperchlorate	17
TAKPIF	(6,13-Dichloro-5,7,12,14-tetramethyl-1,4,8,11-tetraazacyclotetradeca-4,6,11,13-tetraene)-gold(III) perchlorate	18
TEMMED	Dichloro-(1,8-bis(hydroxyethyl)-1,3,6,8,10,13-hexa-azacyclotetradecane- <i>N,N',N'',N'''</i>)-gold(III) tetrachloro-gold(III)	19
TITGIN	(6,13-Dibromo-5,7,12,14-tetramethyl-1,4,8,11-tetra-aza-4,6,11,13-tetraenato)-gold(III) perchlorate	20

Table 4.10: Average bond lengths and angles of previously reported gold(III) macrocyclic complexes.

	AZEGIV	REXNER	TAKPIF	TEMMED	TITGIN	DOKDIR	ILIWIJ	
Type of macrocycle:			Cyclam			Porphyrin		
			Bond Lengths (Å)					
Au–N _{imine}	1.981(6)	N/A	1.975(3)	N/A	1.985(3)	N/A	N/A	
Au–N _{pyrrole}	N/A	N/A	N/A	N/A	N/A	2.04(1)	2.033(6)	
Au–N _{amine}	N/A	2.05(2)	N/A	2.05(1)	N/A	N/A	N/A	
			Bond Angles (°)					
N–Au–N (2) [*]	84.4(8)	83.8(9)	85.3(5)	85.2(3)	85.9(3)	N/A	N/A	
N–Au–N (3) [#]	95.6(8)	96.1(9)	94.7(5)	94.7(3)	94.1(3)	90.3(4)	90.0(1)	

* Refers to the two carbon bridge linking the N atoms.

Refers to the three carbon bridge linking the N atoms.

The reported cyclam macrocyclic chelates (Figure 4.11 (a) and (b)) are linked by ethylene bridges and 1,3-dimethyl-propylene bridges *trans* to each other. The two-carbon bridge forms a five-membered chelate ring about the gold(III) ion while the three-carbon bridge forms a six-membered ring about the gold(III) ion. The compounds have varying substituents on the 2' position of the propylene bridge. Some of the cyclam chelates have imine nitrogen atoms whilst others have amine nitrogen atoms. The Au–N_{imine} bond lengths for the cyclam macrocycles are shorter than the Au–N_{amine} bond lengths. The cyclam chelates have more accurate N–Au–N bond angles between the two-carbon bridges than the three carbon bridges, which is due to the constrained bite angle of the ligand induced by the shorter bridge. The porphyrin complexes have longer Au–N_{pyrrole} bond lengths than the corresponding Au–N_{imine} bond distances of the gold(III) cyclam chelates. The porphyrin complexes feature near perfect square-planar coordination geometry with almost four identical N–Au–N bond angles and Au–N bond lengths. These bond lengths are consistent with comparable bond lengths reported in literature where the mean Au–N bond length is 1.928–2.216 Å.²¹

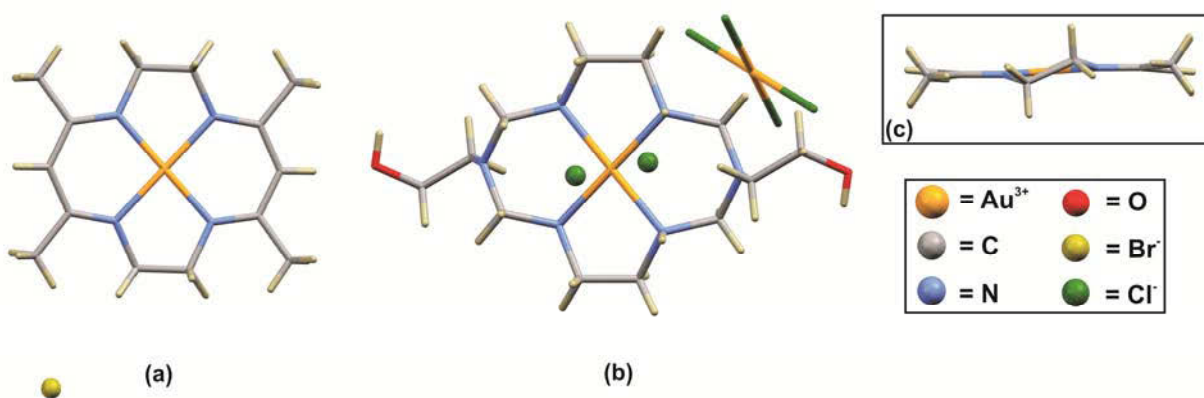


Figure 4.11: X-ray crystal structures of (a) (5,7,12,14-tetramethyl-1,4,8,11-tetraaza-4,6,11,13-tetraene)-gold(III) bromide and (b) dichloro-(1,8-bis(hydroxyethyl)-1,3,6,8,10,13-hexa-azacyclotetradecane-*N,N',N'',N'''*)-gold(III) tetrachloro-gold(III). (c) “Side view” of (5,7,12,14-tetramethyl-1,4,8,11-tetraaza-4,6,11,13-tetraene)-gold(III) bromide showing the slight twist in the ethylene bridging group and overall planar nature of the ligand.

The cyclam gold(III) macrocycles reported show a square-planar, four-coordinate gold(III) ion. The gold(III) ion is positioned in the plane defined by the four coordinating atoms of the ligand. Only the complex (*cis*-6,13-dimethyl-6,13-dinitro-1,4,8,11-tetra-azacyclotetradecan-1-ido)-gold(III) diperchlorate (CSD ref: REXNER) exhibits a gold(III) ion positioned out of the mean plane by 0.056(2) Å. The complexes all have ethylene

bridges twisted out of the plane to allow the carbon atoms to adopt a reasonable angle for sp^3 hybridized carbon atoms (Figure 4.11(c)).

As mentioned above, the gold(III) porphyrins are also rigorously square-planar with the gold(III) positioned in the plane defined by the four coordinating atoms. This is due to the rigid scaffold of the porphyrin ligand. Although the ligands are conjugated, the ligand is not completely planar, but slightly domed. The peripheral phenylene rings are twisted out of the plane of the ligand, having a torsion angle of up to 62° relative to the rest of the ligand, a common feature of tetraphenyl porphyrins.

The gold(III) chelates reported in the CSD¹ almost exclusively exhibit square-planar coordination geometry. This reflects the large crystal field stabilization energy associated with a $5d^8$ electronic configuration and a vacant $5d(x^2-y^2)$ orbital.

4.2 Experimental

X-ray diffraction data for H₂L2, H₂L5, H₂L6, H₂L7, H₂L8a, H₂L8b, H₂L9, H₂L12, [Au(L1)](PF₆), [Au(L2)](CF₃SO₃) and [Au(L12)](PF₆) were recorded on an Oxford Diffraction Xcalibur2 CCD 4-circle diffractometer equipped with an Oxford instruments Cryojet operating at 120(2) K, unless otherwise specified. The data were collected with Mo $K\alpha$ ($\lambda = 0.71073 \text{ \AA}$) radiation at a crystal-to-detector distance of 50 mm using Ω scans at $\theta = 29.389^\circ$ with 5-30 s exposures taken at 2.00 kW X-ray power with 0.75° frame widths using the programme CrysAlis CCD Version 170.²² The data were reduced with the programme CrysAlis RED Version 170²² using outlier rejection, scan speed scaling, as well as standard Lorentz and polarisation correction factors. A semi-empirical multi-scan absorption correction was applied to all data.²³

X-ray diffraction data for [Au(L10)](AuCl₄) and H₂L8c were recorded on a Bruker Apex Duo while the data for [Au(L3)](PF₆) were recorded on a Bruker X8 Proteum. Both machines are equipped with an Oxford Instruments Cryojet operating at 100(2) K and an Incoatec μ S microsource operating at 30 W power. In the case of [Au(L10)](AuCl₄) Mo $K\alpha$ ($\lambda = 0.71073 \text{ \AA}$) radiation at a crystal-to-detector distance of 50 mm was used while for [Au(L3)](PF₆), and H₂L8c Cu $K\alpha$ ($\lambda = 1.54178 \text{ \AA}$) radiation at a crystal-to-detector distance of 60 mm was used. The data were collected using Ω and ϕ scans with exposure times between 5 and 60 s using 0.50° frame widths using the programme APEX2.²⁴ The data were reduced with the programme SAINT²⁴ using outlier rejection, scan speed scaling, as well as standard Lorentz and polarisation correction factors. A SADABS semi-empirical multi-scan absorption correction was applied to the data.²⁴

Unless otherwise stated, direct methods (SHELXS-97, WinGX1.8)^{25,26} were used to solve all structures. PLATON's SQUEEZE²⁷ algorithm was used to remove disordered solvent from H₂L5 and [Au(L2)](CF₃SO₃). All non-hydrogen atoms were located in the difference density map and refined anisotropically with SHELXL-97.²⁵ All carbon-bound hydrogen atoms in the structures were included as idealised contributors. Their positions were calculated using a standard riding model (SHELXL-97)²⁵ with C-H(aromatic) distances of 0.95 \AA and $U_{iso} = 1.2 U_{eq}$, C-H(methylene) distances of 0.99 \AA and $U_{iso} = 1.2 U_{eq}$ and C-H(methyl) distances of 0.96 \AA and $U_{iso} = 1.5 U_{eq}$. The hydrogen atoms of all heteroatoms were located in the difference density map and were refined isotropically. All diagrams were generated using Mercury 2.4²⁸ and POV-ray.²⁹

Atomic coordinates, crystal data and crystal refinement tables as well as the IUCR³⁰ CIF check report are available for all free ligand structures in **Appendix A**. Full crystallographic data tables for the free ligands can

be found in **Appendix C**. In the case of the gold(III) chelates there is residual electron density in the density map (in the range of 0.288 to 3.719 e Å⁻³). These peaks are located near the gold(III) ion (within 1 Å) and are the result of the strong absorption effects of the heavy metal ion. Atomic coordinates, crystal data and crystal refinement tables as well as the IUCR³⁰ CIF check report for all metal chelates are available in **Appendix B**. Full crystallographic data tables for the metal chelates can be found in **Appendix D**. For details on how the crystals were grown see Chapter Two: Experimental. The author solved all crystal structures except [Au(L3)](PF₆), which was solved by Bruker, Germany.

4.3 X-ray Crystallography of Schiff Base Ligands

The X-ray crystal data were collected for the following ligands: H₂L2, H₂L5, H₂L6, H₂L7, H₂L8a, H₂L8b, H₂L8c, H₂L9 and H₂L12. Table 4.11 gives the space group that the compounds crystallized in as well as the number of molecules in the asymmetric unit and unit cell. For more crystallization data for these compounds see Table 4.24 and Table 4.25.

Table 4.11: Crystallization data for the bis(pyrrolide-imine) Schiff base ligands

	Crystal System	Spacegroup	Temperature (K)	No. molecules in asymmetric unit	Z
H ₂ L2	Monoclinic	<i>P2₁/c</i>	120(2)	1	4
H ₂ L5	Monoclinic	<i>C2/c</i>	120(2)	1	8
H ₂ L6	Monoclinic	<i>C2/c</i>	296(2)	1 and 1/2 water solvate	8
H ₂ L7	Monoclinic	<i>P2₁/c</i>	120(2)	1	4
H ₂ L8a	Orthorhombic	<i>P2₁2₁2₁</i>	120(2)	2	8
H ₂ L8b	Orthorhombic	<i>Pna2₁</i>	100(2)	1	4
H ₂ L8c	Monoclinic	<i>P2₁/c</i>	100(2)	1	4
H ₂ L9	Monoclinic	<i>P2₁/c</i>	120(2)	1	4
H ₂ L12	Monoclinic	<i>C2/c</i>	120(2)	1/2	4

Although essentially the ligands are very similar in structure, for ease of discussion they will be divided into groups. These groups are divided by the structure of the ligands and are as follows: quinoxaline-based, pyrazine-based and acyclic ligands.

The ligands: H₂L2, H₂L5, H₂L6, H₂L7 and H₂L9 are all quinoxaline-based ligands (see Figure 4.12). H₂L2 has two methyl groups on the second carbon atom of the three-carbon di(azomethine) linkage and an unsubstituted quinoxaline tail. Compounds H₂L5, H₂L6 and H₂L7 all have derivatized quinoxaline tails, dimethyl, methyl and fluorine groups, respectively; and all three have a three-carbon di(azomethine) linkage unit. H₂L9 is a pseudomacrocyclic compound with no di(azomethine) linkage unit, but rather a methyl group bound to each imine moiety.

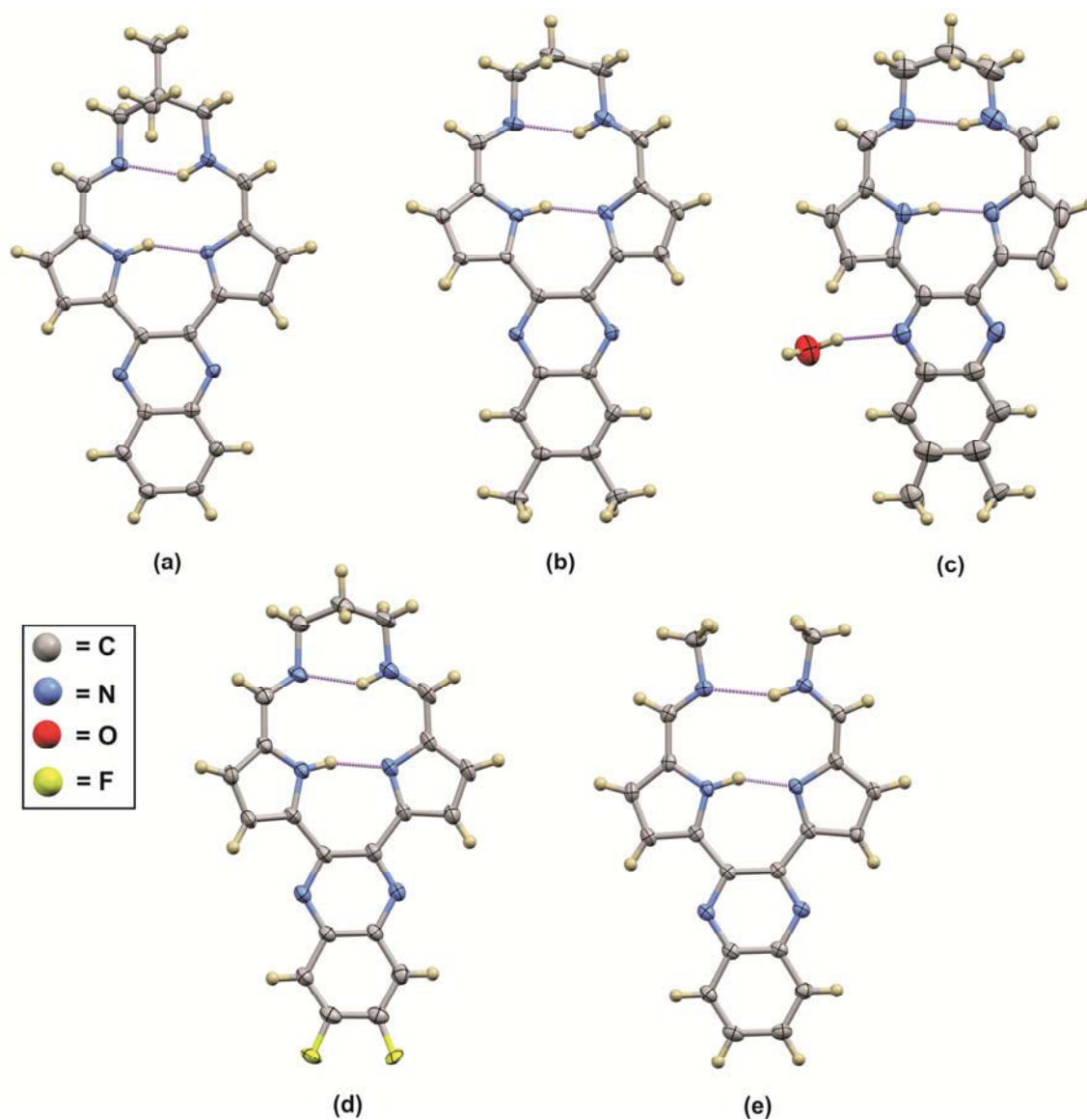


Figure 4.12: Thermal ellipsoid plots of (a) H₂L₂, (b) H₂L₅, (c) H₂L₆ (with 50:50 site occupancy of the methyl substituent), (d) H₂L₇ (with 80:20 site occupancy of the fluorine substituent) and H₂L₉ showing 50% probability surfaces. Hydrogen atoms have been rendered as spheres of arbitrary radius. Hydrogen-bonding has been indicated by broken purple tubes.

In the case of both H₂L₆ and H₂L₇, the asymmetric ligands, two possible orientations can exist in the solid state. If the diamine bridge is fixed as a point of reference then it is possible for the functional groups to be on either the left or the right hand side of the molecules. Therefore, when the molecules crystallize we see positional disorder caused by the crystallisation process and close packing in the lattice. The asymmetric unit therefore shows a functional group on both the left and right hand sides with the sum of the site occupancy factors equal to one. The site occupancy factors for each position were allowed to refine freely. In the case of H₂L₆ there is a 50/50 site occupancy factor and for H₂L₇ there is an 80/20 site occupancy factor.

The X-ray structures of the compounds are expected to be planar due to the extended aromaticity. However, these compounds all exhibit a slightly domed configuration with the pyrrole rings both canted relative to the quinoxaline tail, Figure 4.13. This doming effect is also observed in other highly conjugated π -systems such as gold(III) porphyrins as discussed above.¹¹ Table 4.12 lists the torsion angles of the two pyrrole rings with respect to the quinoxaline tail. Table 4.13 lists the maximum deviations from the four atom mean plane defined by the central N atoms. The compounds with the substituted quinoxaline rings experience the greatest deviation from planarity with the pyrrole rings of H₂L5 and H₂L6 having the greatest torsion angles relative to the quinoxaline ring. These two ligands also have both quinoxaline rings bent significantly below the plane of the molecule. The distance between the four atom mean plane through the central N atoms of the molecule and the quinoxaline C atom at the point of greatest deviation is 1.308(3) Å and 1.500(3)Å for H₂L5 and H₂L6, respectively. These distances are much greater than those measured for H₂L2, H₂L7 and H₂L9. This out-of-plane distortion is seemingly to accommodate the larger steric bulk of the methyl groups compared to the hydrogen atoms of the unsubstituted quinoxaline rings. The lower steric bulk of the hydrogen atoms means that the planar molecules are able to pack closely in the lattice. The same is not true for the methyl substituted molecules which have to distort from planarity to get a close-packed structure. The pseudomacrocyclic ligand, H₂L9, is more planar when compared to the true macrocycles. This is attributed to the higher degrees of freedom associated with the pseudomacrocyclic compared to the genuine macrocycle. The central methylene C atom for all the ligands is characteristically raised out of the four atom mean plane. This deviation is necessary for the atom to attain the ideal bond angle for an sp³ hybridised carbon atom and is a common feature of bis(pyrrolide-imine) Schiff base ligands and metal chelates with three-carbon di(azomethine) linkages.^{6,9}

Table 4.12: Torsion angles (°) of pyrrole rings relative to the quinoxaline moieties.

	H ₂ L2	H ₂ L5	H ₂ L6	H ₂ L7	H ₂ L9
C–C–C _α –N	9.1(1)	28.7(2)	-31.2(3)	15.5(2)	8.4(2)
C–C–C _α –N(H)	-11.2(1)	-27.7(2)	29.0(3)	-7.8(2)	-4.5(2)

Table 4.13: Maximum deviations (Å) from the 4-atom mean plane defined by the four coordinating N atoms.

	H ₂ L2	H ₂ L5	H ₂ L6	H ₂ L7	H ₂ L9
NH pyrrole ring (C _β)	0.578(2)	0.927(3)	0.970(3)	0.562(2)	0.065(1)
N pyrrole ring (C _β)	0.131(1)	0.597(2)	0.648(2)	0.299(3)	0.432(2)
Quinoxaline ring	0.637(2)	1.308(3)	1.500(3)	0.153(2)	0.135(2)
Central methylene C of bridge	0.649(2)	0.823(3)	0.826(2)	0.755(2)	N/A

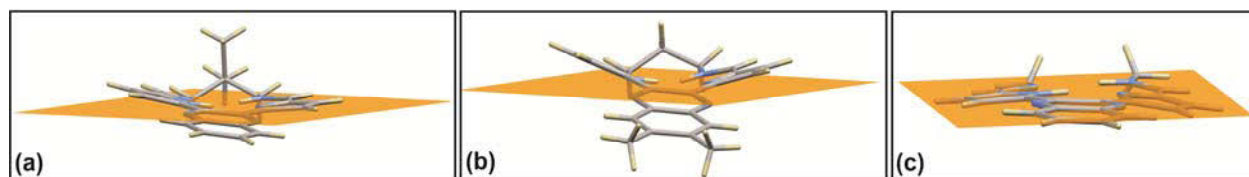

 Figure 4.13: Diagrams showing the four atom mean plane defined by the four coordinating N atoms for (a) H₂L2, (b) H₂L5 and (c) H₂L9 to illustrate the varying extent of doming of the molecule.

Table 4.14 gives the average bond lengths and bond angles for the quinoxaline-based ligands. All these bond lengths and bond angles are similar for all the free ligands. The imine bond distances for all the compounds are similar to the standard imine bond length (1.279 Å). Interestingly the C_α–C_β bond lengths (1.404-1.413 Å)

for the pyrrole rings are longer than the standard value of 1.375 Å while the C_β-C_β bond lengths (1.375-1.386 Å) are shorter than the standard value of 1.412 Å.⁷ This suggests delocalisation of electron density over the pyrrole ring. The C=N_{imine}-C bond angle is very similar for all the macrocyclic ligands as they all have a three carbon di(azomethine) linkage. The pseudomacrocyclic ligand, H₂L9, has a smaller C=N_{imine}-C bond angle, 118.9(1)°, than the macrocyclic compounds. As this bond angle is not determined by the length of the di(azomethine) linkage, it is able to adopt an angle which more closely approaches the ideal angle for an sp² hybridised N atom, i.e. 120°.

Table 4.14: Average bond lengths and angles for quinoxaline-based bis(pyrrolide-imine) Schiff base ligands.

	H ₂ L2	H ₂ L5	H ₂ L6	H ₂ L7	H ₂ L9
	Bond Lengths (Å)				
C=N _{imine}	1.297(4)	1.285(3)	1.289(4)	1.289(3)	1.291(2)
C _α -N _{pyrrole}	1.364(4)	1.363(3)	1.362(4)	1.363(3)	1.363(2)
C _α -C _β	1.413(4)	1.404(3)	1.406(5)	1.408(3)	1.406(2)
C _β -C _β	1.386(4)	1.380(2)	1.375(4)	1.376(3)	1.379(2)
C _α -(C=N _{imine})	1.416(4)	1.417(2)	1.411(3)	1.413(3)	1.415(2)
	Bond Angles (°)				
C _α -N _{pyrrole} -C _α	107.4(2)	107.9(1)	108.0(2)	107.3(2)	107.7(1)
C=N _{imine} -C	123.9(2)	123.0(1)	123.0(3)	123.7(2)	118.9(1)

An interesting feature of these compounds is that the pyrrole N atoms are not both protonated in the solid state. The X-ray data shows, in the form of a peak of electron density, that one pyrrole N atom and the diagonally opposite imine N atom are protonated. This is in contrast to the acyclic Schiff base compounds which usually show both hydrogen atoms located on the pyrrole N atoms.^{2,3} As described above, in the acyclic Schiff base systems, the molecules adopt a linear configuration when the bis(imine) linkage is a flexible aromatic carbon chain such as a propyl group. This configuration ensures minimum steric strain and consequently the highly basic pyrrolide nitrogen atoms are protonated. The reported macrocyclic compounds are rigid and cannot adopt this linear configuration and thus protonation of both pyrrolide N atoms would lead to considerable non-bonded repulsion. Thus, the configuration with the diagonally opposite N atoms protonated is favoured as the steric strain is minimized. This same trend has been observed for the previously reported and structurally similar bis(pyrrolide-imine) macrocyclic compounds, H₂L1 and H₂L3, described above. It has been reported that this is only one possible tautomer with other resonance forms existing where the hydrogen atoms may be located on the pyrrole N atoms or on the other pyrrole and imine N atoms. The symmetric ligands have four possible tautomeric forms, Figure 4.14(a) while the asymmetric ligands have more possible tautomeric forms 4.14(b).

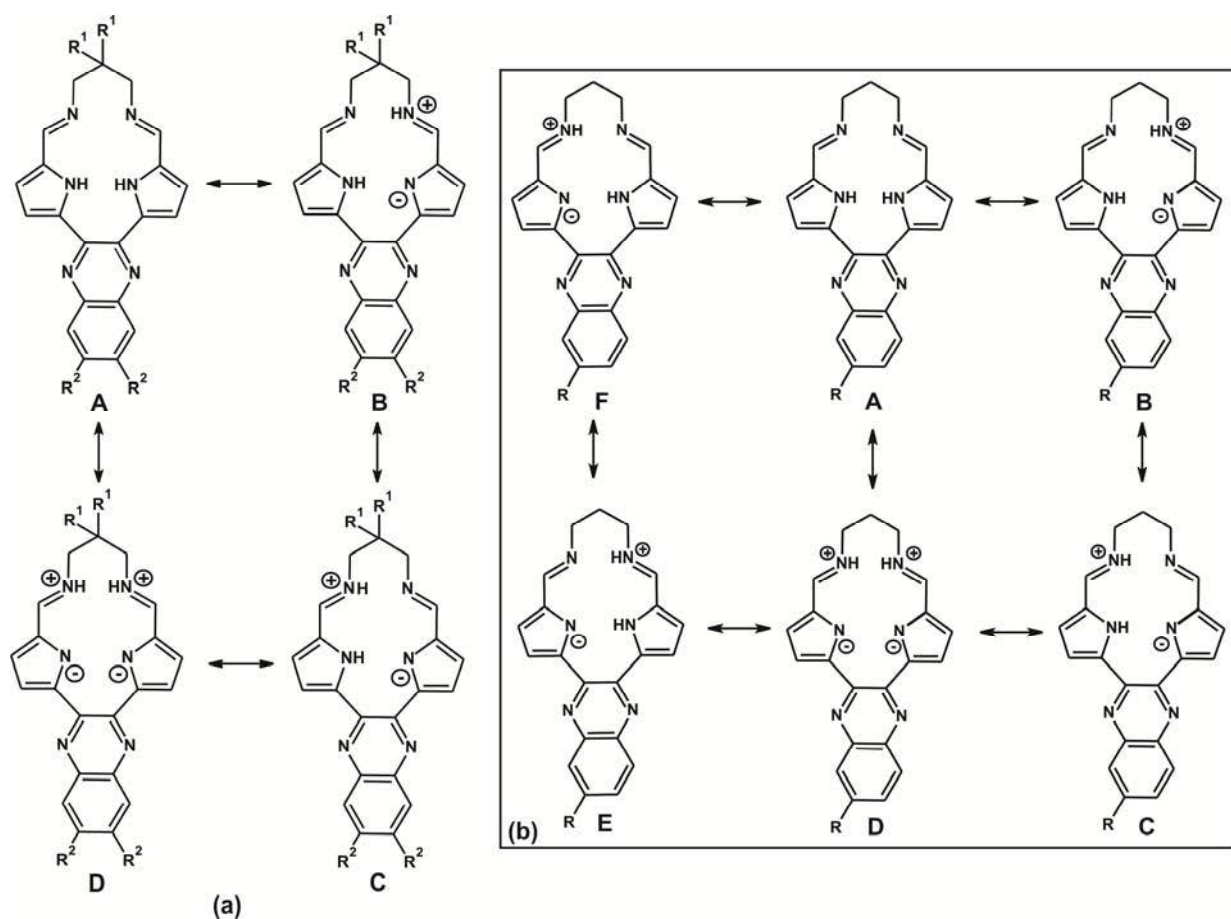


Figure 4.14: Tautomeric forms of (a) symmetric and (b) asymmetric macrocyclic ligands.

Similarly, the pseudomacrocyclic ligand, H₂L9, has one pyrrole N atom and the diagonally opposite imine N atom protonated in the solid state. This is interesting as the similar pseudomacrocyclic ligand, *N,N'*-((5,5'-(quinoxaline-2,3-diyl)bis(1H-pyrrole-5,2-diyl))bis(methanylylidene))bis(4-methoxyaniline), described in the review section above, has both pyrrole N atoms protonated. The reported pseudomacrocyclic ligand adopts a T-shaped configuration (Figure 4.5) with the methoxyaniline groups extending in opposite directions. This configuration relieves any potential steric strain which could be incurred by the bulky methoxyaniline groups. Similar to the acyclic Schiff base ligands with flexible linkers, there is minimal steric strain incurred by the protonation of both pyrrole nitrogen atoms and thus that is the preferred configuration. The structure, H₂L9, does not have bulky methoxyaniline arms, but smaller methyl arms. As a consequence, H₂L9 does not adopt a linear configuration, but rather a more compact, closed configuration: a true pseudomacrocyclic. The spacefilling diagram in Figure 4.15 shows the atoms rendered at their van der Waals radii and shows that the coordination sphere is effectively closed, as in a true macrocycle. This configuration is therefore more similar to that of the genuine macrocycles with all four nitrogen atoms in close proximity; thus the lowest energy tautomer (See Chapter Six: Computation Chemistry) with diagonally opposite N atoms protonated is adopted. The resulting hydrogen bond between the protonated and deprotonated imine N atoms (allowed by the situation with diagonally opposite pyrrole and imine N atoms protonated) will have a large stabilizing effect and is likely a strong driving force for the pseudomacrocyclic to adopt this closed configuration.

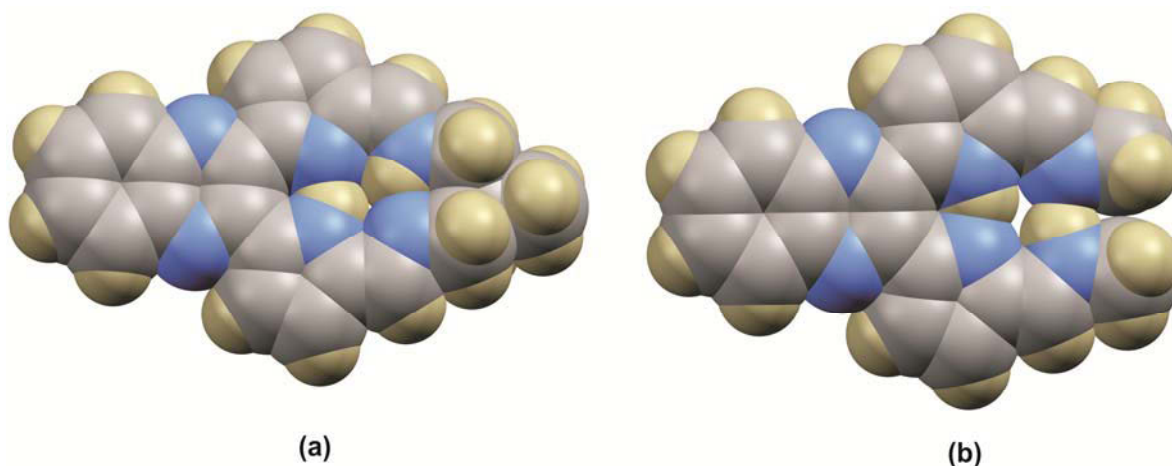


Figure 4.15: Spacefilling diagram, with atoms rendered at their van der Waals radii, of (a) a genuine macrocycle, H₂L₂, and (b) the pseudomacrocycle H₂L₉ showing how the coordination sphere is effectively closed by electron density from the methyl groups.

Tautomerism in macrocyclic ligands has been previously described. The NH-tautomerism of porphyrins and related compounds has been well studied due to the major role that these compounds play in biological processes such as redox reactions and photosynthesis.³¹⁻³³ NH-tautomerism can significantly change the electronic and photophysical properties of these structures. Research has shown that the ratio of NH-tautomers that exist at equilibrium is dependent on several factors such as solvent and temperature.³² The tautomerism of porphyrins was first explored by Storm and Teklu^{34,35} who determined that there is usually rapid transformation between the different tautomers of porphyrins as each tautomer exhibits similar stability.³⁶ The N-confused porphyrin is one of the porphyrin isomers with an inverted ring; consequently there are three core N atoms and one N atom on the periphery of the molecule. This results in the tautomers of this compound having noticeably different structures and stabilities. DFT calculations indicate that the structure where two core N atoms are protonated is the most stable tautomeric form.³⁶ Chapter Six contains a detailed computational study of the tautomers described above.

All the quinoxaline-based compounds show two intramolecular hydrogen bonds, Figure 4.12. The first hydrogen bond has the pyrrole N-H acting as the hydrogen bond donor and the opposite pyrrole N atom acting as the hydrogen bond acceptor. The second hydrogen bond comprises the imine N-H acting as the hydrogen bond donor and the opposite imine N atom acting as the hydrogen bond acceptor. The hydrogen bonds are considerably shorter than the sum of the van der Waals radii, although this short bond length is not necessarily indicative of bond strength as the length of the bonds is governed by the geometry of the macrocycle and not by the strength of the interaction. Table 4.15 gives the hydrogen bond geometries. This same configuration is observed for H₂L₉; the stabilizing effect of the hydrogen bonds is likely one of the major driving forces for adopting its closed, compact configuration.

Table 4.15: Hydrogen bond geometry (Å, °) for the quinoxaline-based bis(pyrrolide-imine) Schiff base ligands.

<i>D</i> – <i>H</i> ··· <i>A</i>	<i>D</i> – <i>H</i>	<i>H</i> ··· <i>A</i>	<i>D</i> ··· <i>A</i>	<i>D</i> – <i>H</i> ··· <i>A</i>
H₂L2				
N_{imine}–H···N_{imine}	0.90(2)	1.96(3)	2.715(4)	140(2)
N_{pyrrole}–H···N_{pyrrole}	0.92(3)	1.82(3)	2.647(3)	148(3)
H₂L5				
N_{imine}–H···N_{imine}	0.88(3)	1.96(3)	2.712(3)	142(2)
N_{pyrrole}–H···N_{pyrrole}	0.89(3)	1.78(3)	2.625(2)	157(2)
H₂L6				
N_{imine}–H···N_{imine}	0.92(6)	1.86(6)	2.713(4)	153(5)
N_{pyrrole}–H···N_{pyrrole}	0.92(5)	1.77(5)	2.622(4)	153(4)
O_w–H–N_{quinoxaline}	1.00(6)	2.04(6)	3.026(3)	167(4)
H₂L7				
N_{imine}–H···N_{imine}	0.88(1)	1.93(2)	2.700(3)	145(2)
N_{pyrrole}–H···N_{pyrrole}	0.89(2)	1.77(2)	2.630(3)	161(2)
H₂L9				
N_{imine}–H···N_{imine}	0.92(2)	2.08(2)	2.943(2)	156(1)
N_{pyrrole}–H···N_{pyrrole}	0.96(2)	1.70(2)	2.595(2)	154(2)

Very few true intermolecular hydrogen bonds are observed for any of the compounds. This is due to the fact that there are no suitable hydrogen bond donor or acceptor groups positioned on the outside of the molecules. The lone pair of electrons on the quinoxaline N atoms are not in a suitable orientation to act as hydrogen bond acceptors. An exception to this is H₂L6, which has a water molecule hydrogen-bonded to the quinoxaline N atom. This is possible as the water molecule is sufficiently small to position itself in a suitable orientation for the equatorially positioned lone pair of electrons on the quinoxaline N atom to act as a hydrogen bond acceptor. Described below are other intermolecular interactions observed in the quinoxaline-based free ligands.

The compound H₂L2 forms π -stacked dimers. The molecules in this dimer sit in a head-to-tail configuration and are slipped relative to each other such that the quinoxaline ring and pyrrole moieties of one molecule overlap with the quinoxaline and pyrrole moieties of the adjacent molecule. The 26-atom mean plane of one molecule (plane through all non-hydrogen atoms, excluding the central bridging carbon) is displaced by 3.37(1) Å from the 26-atom mean plane of the adjacent molecule. This is a relatively short interaction, comparing favourably with the interplanar spacing of graphite, 3.35 Å³⁷, and is therefore likely to be a moderately strong interaction.

The compound H₂L5 and H₂L6 both form π -stacked dimers with favourable π -interactions between the quinoxaline tails of adjacent molecules. The molecules in the dimer also adopt a head-to-tail configuration and are slipped relative to each other with quinoxaline rings of both molecules overlapping. The 10-atom mean planes defined by the non-hydrogen atoms of the two quinoxaline groups are separated by a distance of 3.43(3) Å for both H₂L5 and H₂L6. The distance between the π -systems is longer than that observed for H₂L2. This is attributed to the added steric bulk of the methyl groups which prevent the molecules approaching as closely.

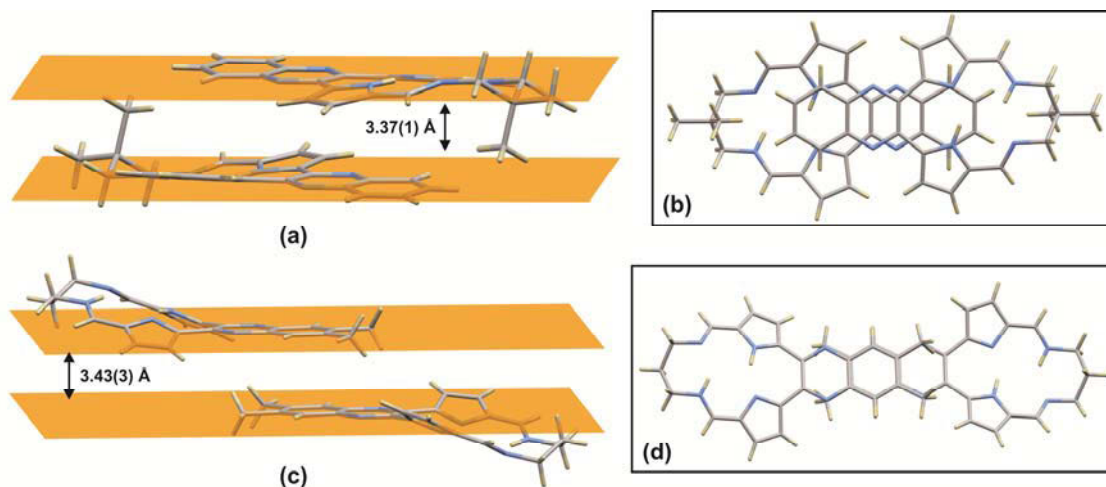


Figure 4.16: (a) Side view of H₂L2 showing the interplanar spacing between the 26-atom mean planes of two adjacent π -stacked molecules. (b) Top view of the π -stacked dimer of H₂L2 showing the π interactions of the quinoxaline and pyrrole rings. (c) Side view of H₂L5 showing the interplanar spacing between the 10-atom mean plane defined by the quinoxaline group of one molecule and the quinoxaline group of an adjacent, π -stacked molecule. (d) Top view of the π -stacked dimer of H₂L5 showing the π interactions between the quinoxaline rings of adjacent molecules. H₂L6 shows similar interactions.

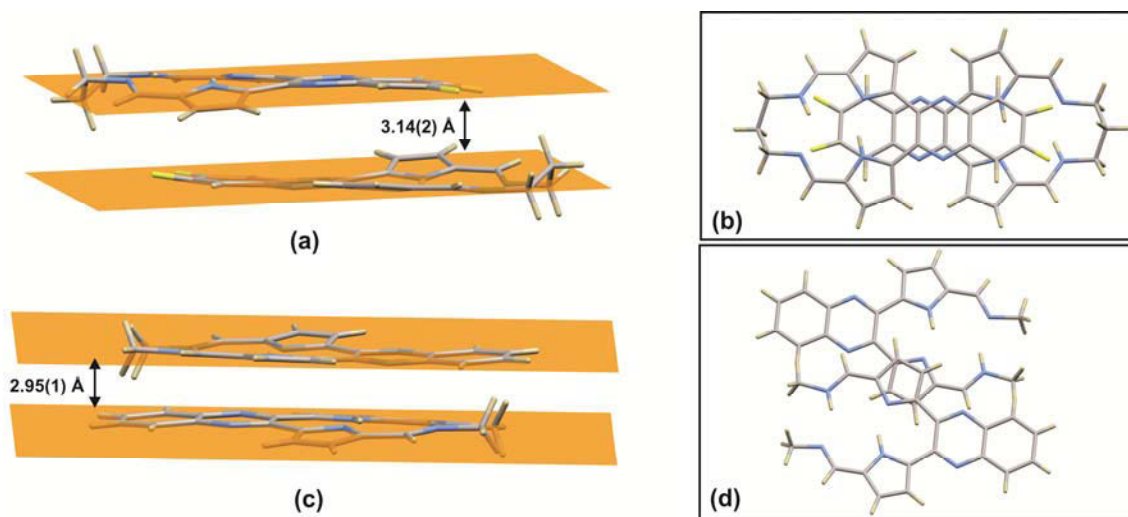


Figure 4.17: (a) Side view of H₂L7 showing the interplanar spacing between the 28-atom mean plane of one molecule and the mean plane of an adjacent π -stacked molecule. (b) Top view of the π -stacked dimer of H₂L7 showing the π interactions of the quinoxaline and pyrrole rings. (c) Side view of H₂L9 showing the interplanar spacing between the 26-atom mean plane of one molecule and the mean plane of an adjacent π -stacked molecule. (d) Top view of the π -stacked dimer of H₂L9 showing the nature of the slipped configuration and the resulting π interactions between the pyrrole rings of adjacent molecules.

The compound H₂L7 exhibits an electrostatic interaction between the fluorine group on the quinoxaline tail of one molecule and the central methylene group of the propylene bridge of an adjacent molecule. The

distance between the C–H and the F is 2.619(5) Å and is likely a moderate to weak interaction as it is only marginally shorter than the sum of the van der Waal's radii. This compound also forms π -stacked dimers with the molecules in the dimer adopting a head-to-tail configuration. The molecules are slipped relative to each other such that the quinoxaline ring and pyrrole moieties of one molecule overlap with the quinoxaline and pyrrole moieties of the adjacent molecule. The 28-atom mean plane (comprising all non-hydrogen atoms except that of the central bridging carbon) of one molecule sits 3.14(2) Å above the equivalent 28-atom mean plane of the adjacent molecule. This is a very short interaction and therefore is likely to be strong. This short interaction is likely due to the more planar nature of the ligand, compared to the other quinoxaline-based ligands, allowing the molecules to stack more closely.

The pseudomacrocylic ligand, H₂L9 similarly forms head-to-tail, π -stacked dimers with favourable π -interactions between the quinoxaline rings and pyrrole-imine moieties of adjacent molecules. The molecules are slipped relative to each other such that a single pyrrole-imine moiety of one molecule overlaps with the quinoxaline ring of the adjacent molecule. The 26-atom mean plane of one molecule is displaced by 2.95(1) Å relative to the equivalent 26-atom mean plane of the adjacent molecule. As this is a very short interplanar spacing it would suggest that the interaction is likely to be strong.

The compounds H₂L8a, H₂L8b and H₂L8c are all macrocyclic bis(pyrrolide-imine) pyrazine-based Schiff base compounds and differ only by the functional groups attached to the pyrazine moieties, Figure 4.18. H₂L8a has nitrile groups attached to the terminal carbon atoms of the pyrazine tail while H₂L8b has a nitrile group and a methoxy group attached. H₂L8c has a nitrile group and an imidoate moiety attached to the pyrazine tail. All three compounds have a three-carbon di(azomethine) linkage unit.

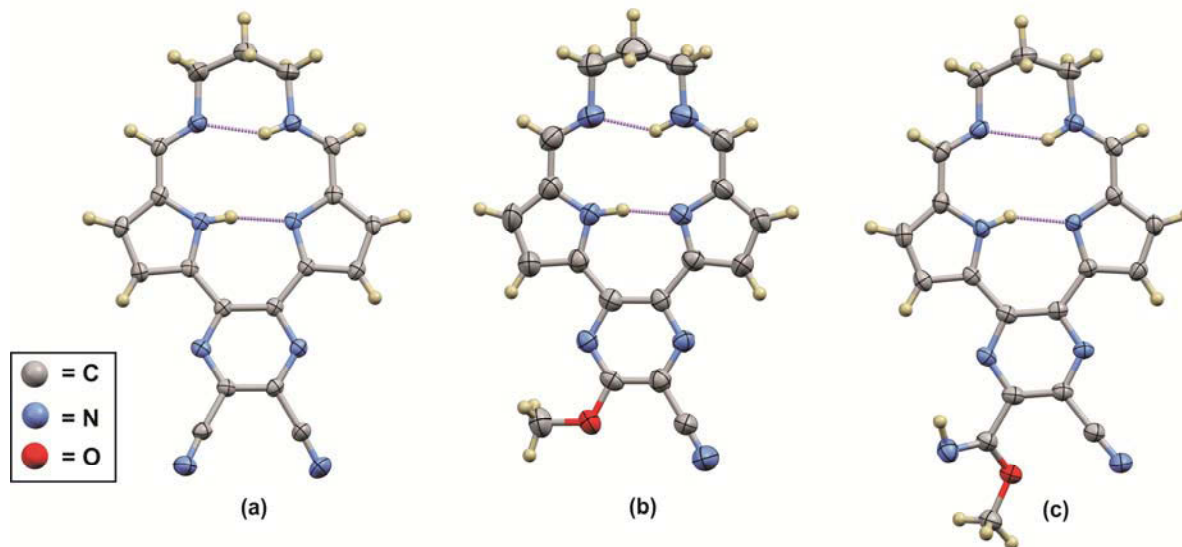


Figure 4.18: Thermal ellipsoid plots of (a) H₂L8a (b) H₂L8b (c) H₂L8c showing 50% probability surfaces, hydrogen atoms have been rendered as spheres of arbitrary radius. Intramolecular hydrogen bonding has been indicated by broken purple tubes.

These compounds also exhibit a domed conformation with both pyrrole rings canted relative to the pyrazine tail, Figure 4.19(a)-(c). Table 4.16 lists the torsion angles of the pyrrole rings relative to the pyrazine rings and Table 4.17 lists the maximum deviation for the different moieties of the molecules from the four-atom mean plane defined by the four coordinating N atoms. The pyrazine-based compounds adopt a more planar

geometry than the quinoxaline-based derivatives. This may be due to the less bulky pyrazine moiety. H₂L8a has two molecules in the asymmetric unit: A and B. Molecule B has the pyrrole C_β atom of the deprotonated pyrrole ring displaced by 0.124(2) Å above the 4-atom mean plane, defined by the four coordinating N atoms, while molecule B has the equivalent atom positioned 0.134(2) Å above the plane. The more pronounced difference is shown by the displacement of the pyrrole C_β atom of the protonated ring from the four-atom mean plane. This distance is 0.240(2) Å for molecule A and 0.016(2) Å for molecule B. The pyrazine ring of molecule B is only displaced by 0.043(2) Å above the four-atom mean plane at its point of maximum deviation from planarity while molecule B has its pyrazine ring displaced by 0.360(2) Å. This indicates that molecule B is more planar than molecule A. The difference in the geometry of the molecules is illustrated by a least squares fit of the two molecules, Figure 4.19(d). The RMSD for the fit is 0.202 Å.²⁸ This difference may be due to the π-stacking interactions exhibited by this compound with one molecule bending to allow the molecules in the asymmetric unit to pack closely. The other compounds H₂L8b and H₂L8c are also relatively planar although molecule B of H₂L8a is the most planar of all the compounds. As molecule H₂L8c has the bulkiest substituent group, it is, as expected, the least planar of these pyrazine-based compounds. The four-atom mean plane of the bulky imidate group subtends an angle of 32.8° relative to the rest of the molecule. All the compounds have the central methylene carbon of the three-carbon bridge significantly raised out of the plane of the molecule, consistent with other molecules with the same bis(imine) linkage.

Table 4.16: Torsion angles (°) of pyrrole rings relative to the pyrazine moieties.

	H ₂ L8a (A)	H ₂ L8a (B)	H ₂ L8b	H ₂ L8c
C–C–C _α –N	-4.6(6)	-3.0(6)	-0.3(9)	-2.0(3)
C–C–C _α –N(H)	8.5(6)	0.2(6)	1.8(9)	1.6(3)

Table 4.17: Maximum deviations (Å) from the four-atom mean plane defined by the four coordinating N atoms of the pyrazine-based macrocycles.

	H ₂ L8a (A)	H ₂ L8(B)	H ₂ L8b	H ₂ L8c
NH pyrrole ring (C _β)	0.240(2)	0.016(2)	0.173(1)	0.168(1)
N pyrrole ring (C _β)	0.134(2)	0.124(2)	0.023(1)	0.070(1)
Pyrazine ring	0.360(2)	0.043(2)	0.208(1)	0.256(1)
Central methylene C of bridge	0.720(2)	0.535(2)	0.637(1)	0.686(1)

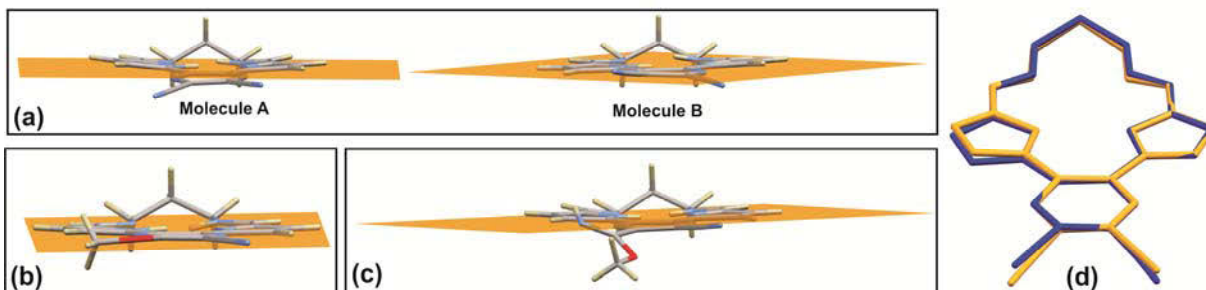


Figure 4.19: Diagrams showing the four-atom mean plane defined by the four coordinating N atoms for (a) H₂L8a, (b) H₂L8b and (c) H₂L8c to illustrate the varying extent of doming of the molecule. (d) Least squares fit of molecules A and B of H₂L8a. Molecule A is shown in yellow and molecule B is shown in blue. RMSD = 0.202 Å.

Table 4.18 gives the average bond lengths and bond angles for the pyrazine-based ligands. These bond lengths and bond angles compare favourably with those of the quinoxaline-based ligands (Table 4.14). The $C_{\alpha}-C_{\beta}$ bond lengths for the pyrrole rings of these compounds are longer than the standard value (1.375 Å)⁷ while the $C_{\beta}-C_{\beta}$ bond lengths are shorter than the standard value (1.412 Å)⁷ indicating delocalisation of electron density over the pyrrole ring. The compounds have $C\equiv N$ bond lengths of 1.120-1.140 Å which are similar to the standard $C\equiv N$ bond length of 1.136 Å.⁷ The compounds also have $C-C\equiv N$ bond angles of 176.5-177.7°. These bond distances and angles highlight the sp hybridization of the nitrile carbon atom. Compounds H₂L8b and H₂L8c have O-CH₃ bond distances of 1.423(6) Å and 1.433(3) Å, respectively. These values are in good agreement with the standard value for O-CH₃ bonds of 1.426 Å.⁷ Compound H₂L8c has a C=NH imidoate bond distance of 1.252(2) Å; this bond length highlights the double-bond character.

Table 4.18: Average bond lengths and angles for pyrazine-based bis(pyrrolide-imine) Schiff base ligands.

	H ₂ L8a	H ₂ L8b	H ₂ L8c
		Bond Lengths (Å)	
C=N _{imine}	1.283(5)	1.293(9)	1.282(3)
C _α -N _{pyrrole}	1.360(5)	1.365(7)	1.361(3)
C _α -C _β	1.409(6)	1.400(9)	1.409(3)
C _β -C _β	1.372(6)	1.381(9)	1.373(3)
C _α -(C=N _{imine})	1.421(6)	1.412(9)	1.423(3)
C≡N	1.140(6)	1.120(9)	1.138(3)
O-CH ₃	N/A	1.423(6)	1.433(3)
C=NH	N/A	N/A	1.252(4)
		Bond Angles (°)	
C _α -N _{pyrrole} -C _α	107.7(3)	107.8(4)	108.1(2)
C=N _{imine} -C	124.1(4)	123.3(6)	124.2(2)
C-C≡N	177.7(5)	179.2(7)	176.5(2)
C-O-C	N/A	118.4(5)	115.7(2)

These pyrazine-based macrocycles, like the quinoxaline analogues, do not have both pyrrole N atoms protonated in the solid state, but have one pyrrole N atom and the diagonally opposite imine N atom protonated. As described above, this configuration is favoured as it minimizes non-bonded repulsion between the two protons. Four possible tautomers exist for the symmetric H₂L8a ligand with the hydrogen atoms located on the pyrrole N atoms or on the other pyrrole and imine N atoms as well as on both imine N atoms. Figure 4.14(a) above shows the position of the hydrogen atoms for the different tautomers of symmetric quinoxaline-based macrocycles. The same possible arrangements of hydrogen atoms depicted in Figure 4.14(a) can be applied to the pyrazine-based compounds. The asymmetric ligands, H₂L8b and H₂L8c, can adopt more tautomeric forms than the symmetrical ligands. Figure 4.14(b) above depicts these forms for the quinoxaline-based ligands.

All the pyrazine-based compounds show two intramolecular hydrogen bonds. The first hydrogen bond has the pyrrole N-H acting as the hydrogen bond donor and the opposite pyrrole N atom acting as the hydrogen bond acceptor. The second hydrogen bond comprises the imine N-H acting as the hydrogen bond donor and the opposite imine N atom acting as the hydrogen bond acceptor. The hydrogen bonds are considerably shorter than the sum of the van der Waals radii. The compound H₂L8c has an intermolecular hydrogen bond with the imidate N-H acting as the hydrogen bond donor and the pyrrole N of an adjacent molecule acting as the hydrogen bond acceptor. This bond is predicted to be a fairly weak interaction as the bond is not shorter than the sum of the van der Waal's radii. Table 4.19 gives the hydrogen bond geometries.

Table 4.19: Hydrogen bond geometry (\AA , $^\circ$) for the pyrazine bis(pyrrolide-imine) Schiff base macrocycles.

$D-H\cdots A$	$D-H$	$H\cdots A$	$D\cdots A$	$D-H\cdots A$
H₂L8a				
$N_{\text{imine}}-H\cdots N_{\text{imine}}$	0.88(5)	1.966(3)	2.91(5)	141(6)
$N_{\text{pyrrole}}-H\cdots N_{\text{pyrrole}}$	0.88(4)	1.81(6)	2.633(4)	157(6)
H₂L8b				
$N_{\text{imine}}-H\cdots N_{\text{imine}}$	0.94(5)	1.90(5)	2.681(7)	139(6)
$N_{\text{pyrrole}}-H\cdots N_{\text{pyrrole}}$	0.95(4)	1.68(3)	2.612(5)	167(2)
H₂L8c				
$N_{\text{imine}}-H\cdots N_{\text{imine}}$	0.880(2)	1.960(2)	2.693(3)	139.8(1)
$N_{\text{pyrrole}}-H\cdots N_{\text{pyrrole}}$	0.880(2)	1.811(2)	2.615(2)	150.9(1)
$N_{\text{imidoate}}-H-N_{\text{pyrrole}}$	0.98(4)	2.70(5)	3.292(3)	128(3)

Compound H₂L8a forms a one-dimensional π -stacked column co-linear with the a -axis. The adjacent molecules in the column are rotated by approximately 120° relative to one another, Figure 4.20(a). The pyrrole ring of one molecule overlaps with the pyrazine ring of the adjacent molecule. The interplanar distance between the molecules is approximately 3.3 \AA . This is a relatively short distance and indicates that the interaction is moderately strong.

Compound H₂L8b forms a one-dimensional π -stacked column co-linear with the a -axis with π interactions between the pyrrole moiety of one molecule and the pyrazine ring of another molecule, Figure 4.20(b). These molecules are parallel, but slipped relative to each other. The interplanar distance between the molecules is approximately 3.4 \AA .

The compound H₂L8c forms head-to-tail π -stacked dimers with favourable π -interactions between the pyrrole ring of one molecule and the pyrazine ring of an adjacent molecule, Figure 4.20(c) and (d). The dimer structure is further stabilized by the intermolecular hydrogen bond between the imidoate N–H and the pyrrole N of an adjacent molecule. The interplanar spacing between the 22-atom mean planes of the molecules defined by all non-hydrogen atoms excluding the central carbon of the bridging unit and the pyrazine substituent is $3.28(4) \text{ \AA}$. This is a relatively short distance and indicates the interaction is moderately strong.

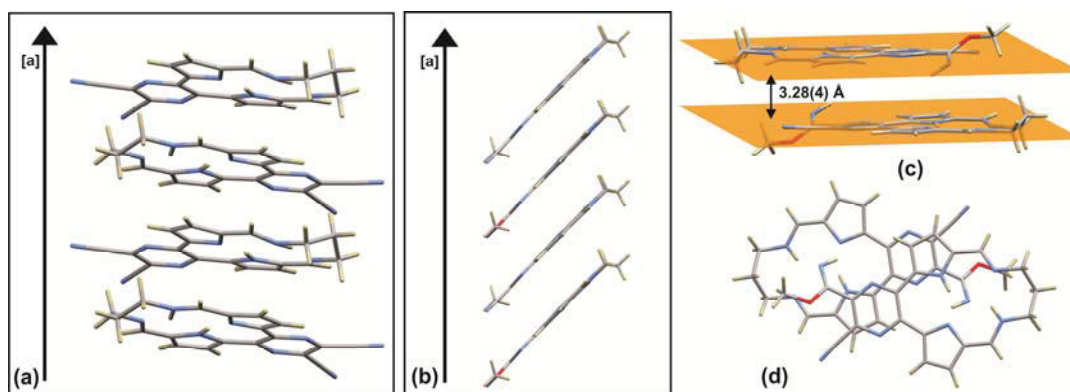


Figure 4.20: One-dimensional hydrogen-bonded chain adopted by (a) H₂L8a and (b) H₂L8b running co-linear to the a -axis. (c) Side view of H₂L8c showing the interplanar spacing between the 22-atom mean plane of one molecule and the mean plane of an adjacent π -stacked molecule. (d) Top view of the π -stacked dimer of H₂L8c showing the π interactions of the pyrazine and pyrrole rings.

The ligand, H₂L12, is an acyclic bis(pyrrolide-imine) Schiff base ligand with a four carbon di(azomethine) linkage unit, Figure 4.21(a). The X-ray structure of this compound is very similar to that of the previously reported compound *N,N'*-bis[(1*E*)-1*H*-pyrrol-2-ylmethylene]propane-1,3-diamine, (the propyl-bridged analogue of H₂L12) described in the review section above. The ligand crystallized in the monoclinic space group *C2/c*. As this is a *C*-centred unit cell, it contains one additional lattice point, i.e. 2 lattice points as opposed to one, which is observed for the equivalent primitive lattice. Therefore the unit cell contains eight asymmetric units as opposed to the four of the primitive analogue. Since the structure has *Z* = 4, but eight asymmetric units in the unit cell, each asymmetric unit contains a half molecule. This is possible as the ligand molecule is located on a special position with a centre of inversion at the midpoint of the butyl bridge; the two halves of the molecule are related by inversion symmetry.

H₂L12 adopts a linear configuration with a *trans* geometry about both imine bonds. As reported for the propyl-bridged analogue, the *trans* conformation is preferred as the *cis* isomer would lead to unfavourable interactions between the pyrrole α -CH groups and the methylene groups of the bridge.² The molecule favours an all-staggered conformation for the methylene groups of the butyl chain and a *trans* configuration for the two pyrrole rings.

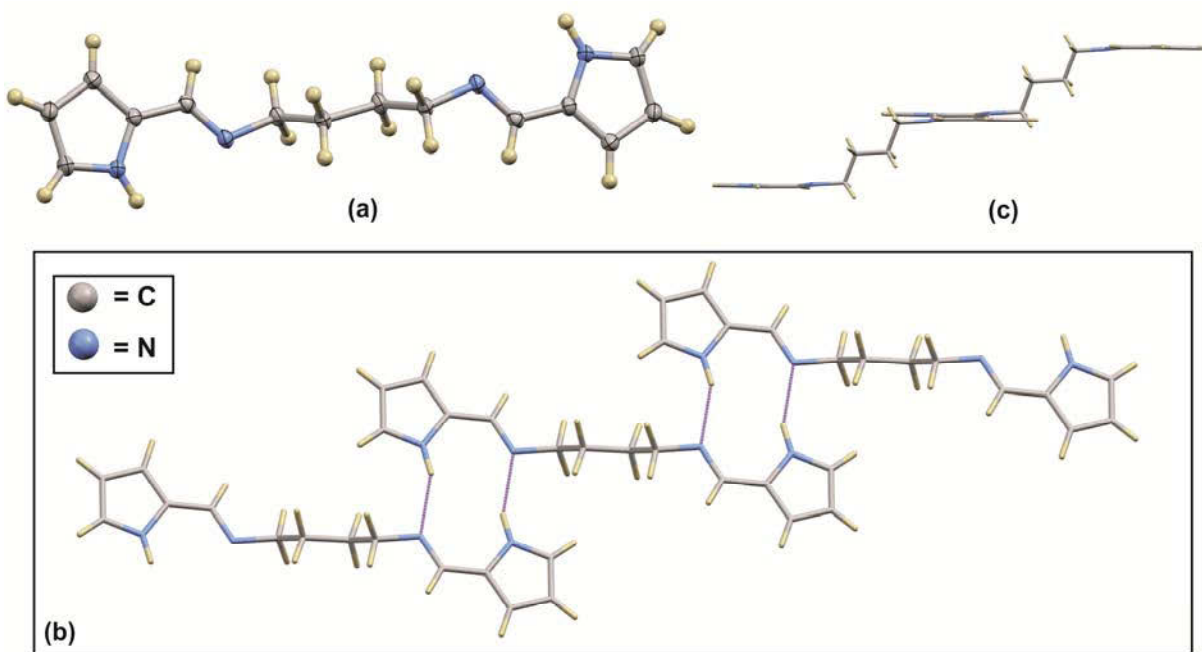


Figure 4.21: (a) Thermal ellipsoid plot of H₂L12 showing 50% probability surfaces, hydrogen atoms have been rendered as spheres of arbitrary radius. (b) Infinite, one-dimensional hydrogen-bonded chain adopted by H₂L12. (c) Side view of two hydrogen-bonded molecules showing the relative planarity of the ten-membered hydrogen bonding ring.

Table 4.20 gives the bond distances and angles for H₂L12. The C=N_{imine} bond distance of 1.277 Å is similar to the standard bond distances for these types of bonds. The pyrrole C_α-C_β bond length of 1.380(2) Å and the C_β-C_β bond length of 1.413(1) Å are similar to the standard bond lengths of 1.375 Å and 1.412 Å, respectively for these types of bonds.⁷ These differ from the quinoxaline- and pyrazine-based macrocycles which have longer pyrrole C_α-C_β bonds and shorter C_β-C_β bond lengths than the standard values. This suggests that there is less delocalization of electron density in H₂L12 compared to the more highly conjugated quinoxaline

and pyrazine macrocycles. All the bond lengths and bond angles reported in Table 4.20 compare favourably with similar, previously reported, acyclic bis(pyrrolide-imine) Schiff base ligands.²⁻⁶

Table 4.20: Average bond lengths and angles for the acyclic Schiff base ligand, H₂L12.

H ₂ L12	
	Bond Lengths (Å)
C=N _{imine}	1.277(1)
C _α -N _{pyrrole}	1.369(1)
C _α -C _β	1.380(2)
C _β -C _β	1.413(1)
C _α -(C=N _{imine})	1.443(1)
	Bond Angles (°)
C _α -N _{pyrrole} -C _α	109.0(1)
C=N _{imine} -C	113.2(1)

This compound exhibits a supramolecular structure similar to that of the propyl analogue.² A one-dimensional, hydrogen-bonded chain is formed as the result of a self-recognising motif. This motif consists of the pyrrole NH groups (acting as hydrogen bond donors) and the imine N groups (acting as hydrogen bond acceptors). As there is a hydrogen-bonding motif on each end of the molecule, a one-dimensional polymeric chain is formed, Figure 4.21(b). Table 4.21 lists the hydrogen bond lengths and bond angles. Although the chain is stabilized by two hydrogen bonds they are related by inversion symmetry and therefore have the same geometric parameters. The hydrogen bond is considerably shorter than the sum of the van der Waals radii, suggesting that it is a relatively strong interaction.

Table 4.21: Hydrogen bond geometry (Å, °) for the acyclic ligand H₂L12.

D-H...A	D-H	H...A	D...A	D-H...A
H ₂ L12				
N _{pyrrole} -H...N _{imine}	0.93(1)	2.11(1)	2.968(2)	154(1)

The hydrogen bonding network in this system is characterized by the formation of stable, ten-membered rings. This ten-membered ring lies almost planar and is not twisted as the pairs of hydrogen-bonding motifs lie in the same plane, Figure 4.21(c). This is not true for the propyl analogue which has a twisted ten-membered ring as the hydrogen-bonding motifs do not lie in the same plane.² This twist was reportedly to minimize the unfavourable steric contacts between the pyrrole α-CH group of one molecule and the methylene group of the neighbouring molecule.² As the butyl group is longer than the propyl group the pyrrole α-CH group is further from the methylene groups of the bridge of the neighbouring molecules and twisting is not necessary. Similar to the propyl analogue, the formation of hydrogen bonds in H₂L12 between adjacent molecules also leads to a 'ladder' structure where each step is laterally displaced from the preceding step.

The seemingly predictable nature of this structural motif in the formation of hydrogen-bonded networks suggests that it would be a useful synthon in supramolecular chemistry. The benzene-bridged derivative, *N,N'*-bis[(1*E*)-1*H*-pyrrol-2-ylmethylene]benzene-1,2-diamine, has already been used in creating nanoscale molecular structures such as nanowires, nanotubes and nanospheres based on this motif.³⁸

4.4 X-ray Crystallography of Schiff base Gold(III) Complexes

The X-ray crystal data were collected for the following gold(III) complexes: [Au(L1)](PF₆), [Au(L2)](CF₃SO₃), [Au(L3)](PF₆), [Au(L10)](AuCl₄) and [Au(L12)](PF₆). The triflate and tetrachloroaurate counterions were used to aid in crystallization of the complexes [Au(L2)] and [Au(L10)], respectively. A search of the CSD¹ showed that none of these gold(III) complexes have been previously studied by X-ray crystallography. Table 4.22 gives the space group the compounds crystallized in, as well as the number of molecules in the asymmetric unit and unit cell. For more crystallization data for these complexes see Table 4.26.

Table 4.22: Crystallization data for the bis(pyrrrolide-imine) gold (III) Schiff base complexes.

	Crystal System	Spacegroup	Temperature (K)	No. molecules in asymmetric unit	Z
[Au(L1)](PF ₆)	Monoclinic	<i>P2/c</i>	173(2)	1	4
[Au(L2)](CF ₃ SO ₃)	Monoclinic	<i>Cc</i>	120(2)	2	8
[Au(L3)](PF ₆)	Orthorhombic	<i>P nac1</i>	100(2)	6 and 7 acetonitrile solvates	24
[Au(L10)](AuCl ₄)	Monoclinic	<i>C2/c</i>	100(2)	1/2	4
[Au(L12)](PF ₆)	Monoclinic	<i>P2₁/n</i>	120(2)	1	4

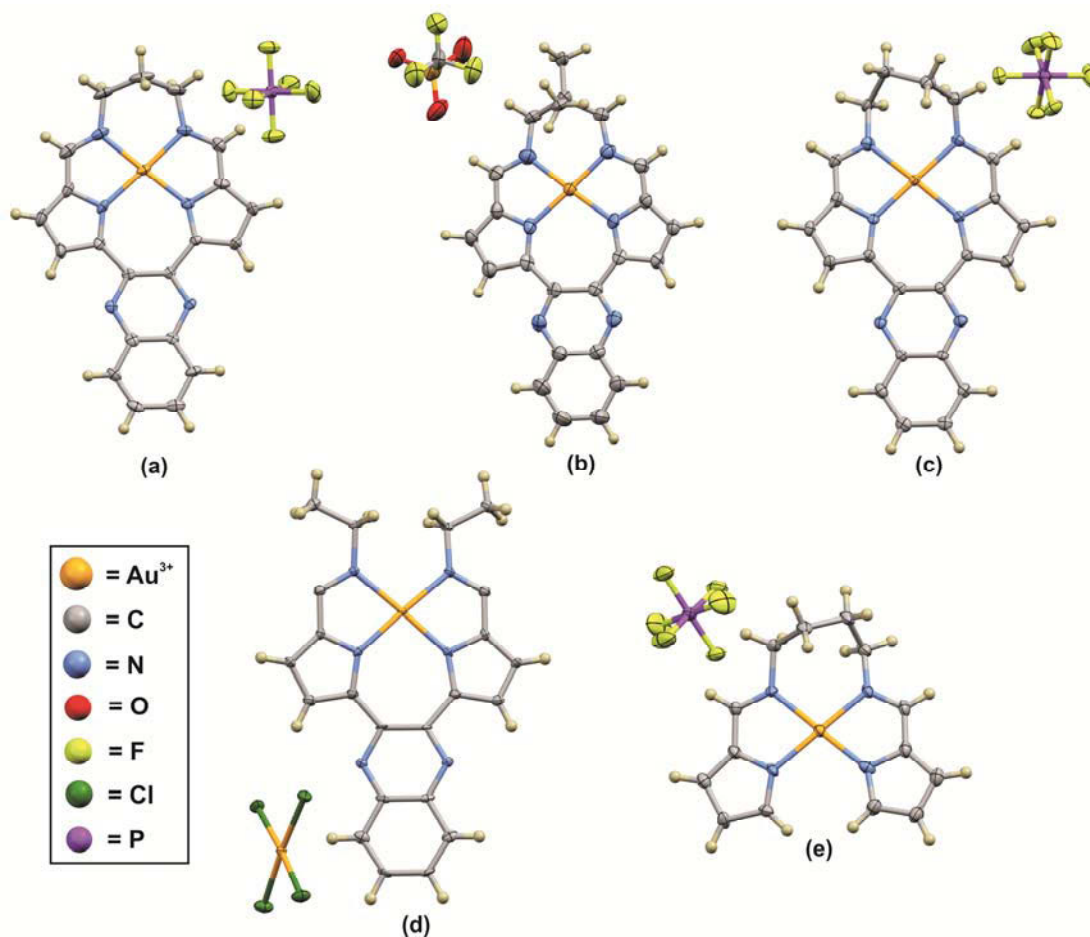


Figure 4.22: Thermal ellipsoid plots showing a single molecule of the asymmetric unit of (a) [Au(L1)](PF₆), (b) [Au(L2)](CF₃SO₃) (c) [Au(L3)](PF₆) (d) [Au(L10)](AuCl₄) and (e) [Au(L12)](PF₆) showing 50% probability surfaces; hydrogen atoms have been rendered as spheres of arbitrary radius.

The complexes: $[\text{Au}(\text{L1})](\text{PF}_6)$, $[\text{Au}(\text{L2})](\text{CF}_3\text{SO}_3)$ and $[\text{Au}(\text{L3})](\text{PF}_6)$ all have quinoxaline-based macrocyclic ligands. They differ in structure by the length and substituents of their di(azomethine) linkage. The complex $[\text{Au}(\text{L1})](\text{PF}_6)$ has a propyl (three-carbon) linkage unit while $[\text{Au}(\text{L2})](\text{CF}_3\text{SO}_3)$ has a 2,2-dimethyl propyl bridge. $[\text{Au}(\text{L3})](\text{PF}_6)$ has a butyl (four-carbon) bridge. The complex, $[\text{Au}(\text{L10})](\text{AuCl}_4)$, is a quinoxaline-based pseudomacrocyclic complex with ethyl moieties attached to the imine N atoms. $[\text{Au}(\text{L12})](\text{PF}_6)$ is an acyclic complex with a butyl (four-carbon) di(azomethine) unit. The X-ray structures for the five gold(III) complexes all show the gold(III) ion chelated to the two imine N atoms and the pyrrole N atoms. All of the protonated nitrogen atoms of the free ligands have been deprotonated to allow for the metal ion chelation. Figure 4.22 shows the X-ray crystal structures of a single molecule in the asymmetric unit of each gold(III) complex.

The coordination of the gold(III) ion by the propyl-bridged ligands, $[\text{Au}(\text{L1})](\text{PF}_6)$ and $[\text{Au}(\text{L2})](\text{CF}_3\text{SO}_3)$, results in the formation of two five-membered chelate rings as well as a six- and seven-membered chelate ring. The two five-membered rings, consisting of the imine and pyrrole nitrogen atoms, as well as the two adjoining carbon atoms, are both planar. The six-membered chelate ring is puckered with the central methylene group of the propyl bridge raised above the mean plane of the molecule. The seven-membered ring consists of the pyrrole N atoms and the carbon atoms of the quinoxaline ring. This seven-membered ring approaches planarity. The butyl-bridged macrocyclic complex, $[\text{Au}(\text{L3})](\text{PF}_6)$, forms the same two planar five-membered chelate rings, but also two seven-membered chelate rings. In this case the seven-membered ring formed by the bridging unit is twisted out of the plane of the molecule. The pseudomacrocyclic, $[\text{Au}(\text{L10})](\text{AuCl}_4)$, and acyclic complex, $[\text{Au}(\text{L12})](\text{PF}_6)$, also have the two five-membered chelate rings but only one seven-membered chelate ring. In the case of the acyclic complex, $[\text{Au}(\text{L12})](\text{PF}_6)$, it has a puckered seven-membered chelate ring formed by the bridging unit while the pseudomacrocyclic complex only has a planar seven-membered ring formed by the quinoxaline tail.

All the gold(III) complexes deviate from planarity to varying extents. The out-of-plane displacements of the rings may be the result of π - π interactions between two neighbouring molecules positioned in close proximity and in a co-planar orientation. The complex, $[\text{Au}(\text{L1})](\text{PF}_6)$, exhibits a domed configuration with the pyrrole- β carbon atoms exhibiting a large deviation from the 5-atom mean plane defined by the four coordinating nitrogen atoms and the gold(III) ion. The maximum pyrrole deviation is 0.279(1) Å. Similarly the quinoxaline carbon atom shows a maximum deviation of 0.185(1) Å. The central methylene carbon is raised 0.692(1) Å above the same 5-atom mean plane. A summary of the displacement of atoms above and below the mean plane is presented in Figure 4.23(a) and (b).

Both molecules A and B of $[\text{Au}(\text{L2})](\text{CF}_3\text{SO}_3)$ exhibit slight deviations from planarity. Molecule A exhibits a domed configuration. Molecule B does not exhibit doming, rather the quinoxaline tail shows a slight rotation out-of-plane of the pyrrole-imine moiety. The terminal quinoxaline carbon atoms of molecule A show a maximum deviation of 0.246(1) Å below the 5-atom mean plane, defined by the four coordinating nitrogen atoms and the gold(III) ion, while the maximum displacement from planarity in molecule B is exhibited by a quinoxaline C atom with a maximum shift of 0.288 Å above the 5-atom mean plane. Similarly the central carbon atom of the bridge of molecule A exhibits a maximum deviation of 0.514(1) Å from the 5-atom mean plane while molecule B exhibits a deviation of 0.535(1) Å, Figure 4.23(c) and (d). Although molecules A and B appear to have quite different geometries, a least squares fit of molecules A and B of $[\text{Au}(\text{L2})](\text{CF}_3\text{SO}_3)$ shows these molecules to have an RMSD value of 0.0948 Å, Figure 4.23(e), indicating that they are in fact very similar.

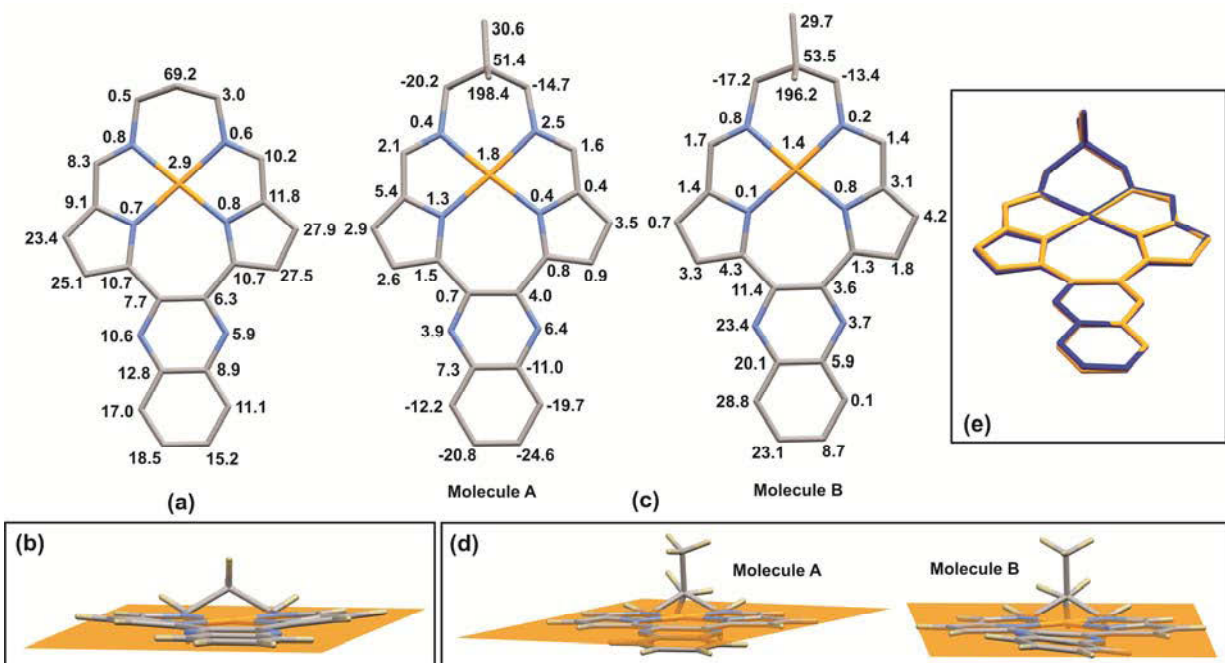


Figure 4.23: (a) Mean plane diagram for $[\text{Au}(\text{L1})](\text{PF}_6)$ showing the perpendicular displacement of each non-H atom (in units of pm) from the five-atom mean plane defined by the four coordinating nitrogen atoms and the gold(III) ion. (b) “Back view” of $[\text{Au}(\text{L1})](\text{PF}_6)$ showing the deviation from the five atom mean plane. (c) Mean plane diagram for both molecules in the asymmetric unit of $[\text{Au}(\text{L2})](\text{CF}_3\text{SO}_3)$ showing the perpendicular displacement of each non-H atom (in units of pm) from the five-atom mean plane defined by the four coordinating nitrogen atoms and the gold(III) atom. (d) “Back view” of both molecules of $[\text{Au}(\text{L2})](\text{CF}_3\text{SO}_3)$ showing the deviations from the five atom mean plane. (e) Least squares fit of molecules A and B of $[\text{Au}(\text{L2})](\text{CF}_3\text{SO}_3)$. Molecule A is shown in yellow and molecule B is shown in blue, RMSD = 0.0948 Å.

All six molecules in the asymmetric unit of $[\text{Au}(\text{L3})](\text{PF}_6)$ exhibit varying degrees of the same distortion from planarity with one pyrrole ring sitting above the plane and the other below the plane. The quinoxaline ring has also been twisted out-of-plane to varying extents. Molecule B has the most planar quinoxaline ring with an angle of $1.80(1)^\circ$ subtended by the 5-atom mean plane defined by the four coordinating nitrogen atoms and the gold(III) ion and the ten atom mean plane defined by the non-hydrogen atoms of the quinoxaline tail. Molecule D has the greatest twist in the quinoxaline ring with the respect to the 5-atom mean plane with an angle of $13.53(1)^\circ$. A slight displacement of the gold(III) ion from the plane defined by the four coordinating nitrogen atoms is observed for all six molecules. The displacement of the gold(III) ion from the four-atom mean plane ranges from $0.001(1)$ Å to $0.019(1)$ for molecules A and F, respectively. The butyl bridge is twisted to a similar extent in all the molecules with the carbon atoms sitting above and below the mean plane. A summary of the displacement of atoms above and below the mean plane for all the molecules in the asymmetric unit of $[\text{Au}(\text{L3})](\text{PF}_6)$ is presented in Figure 4.24(a) and (b).

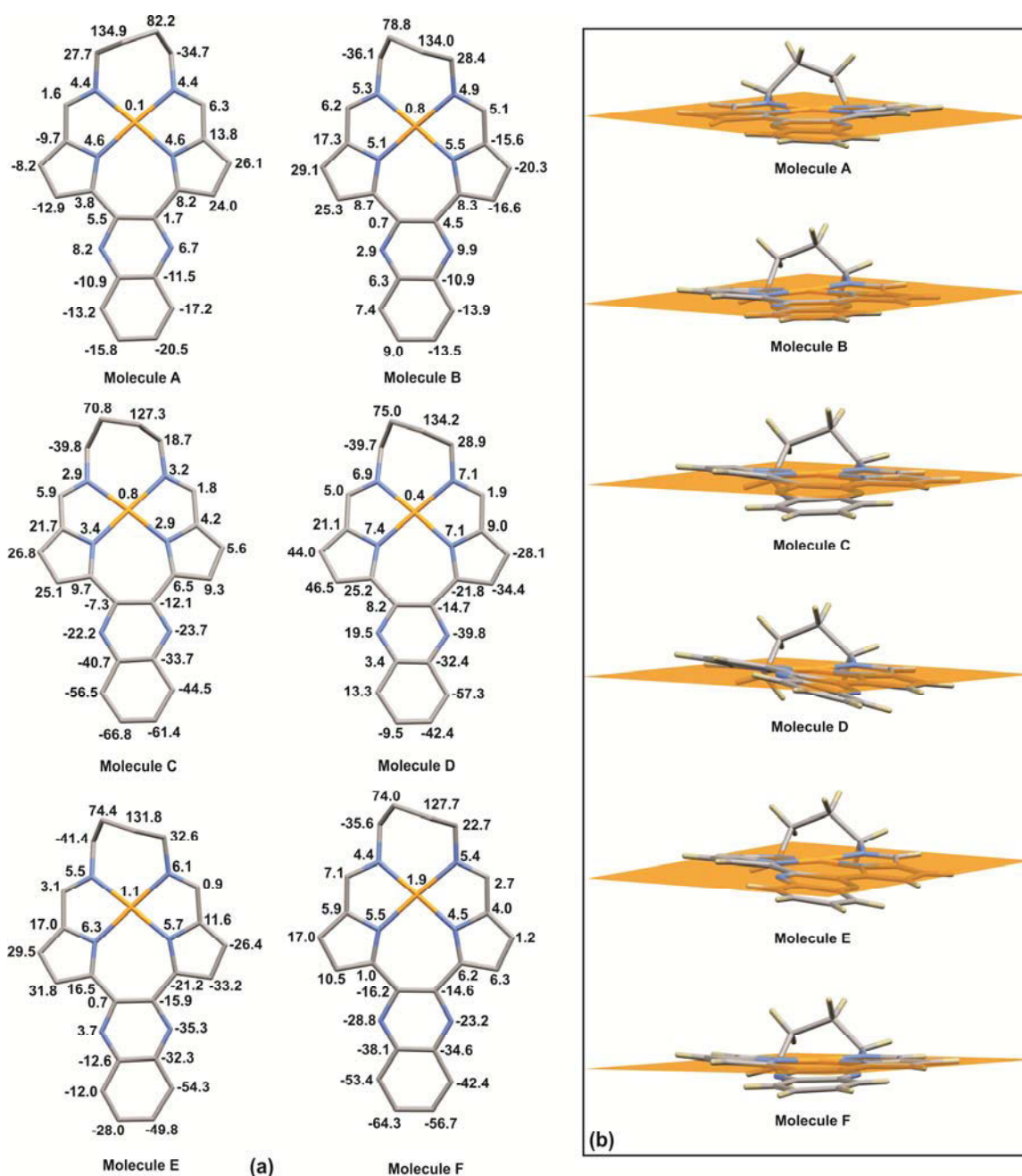


Figure 4.24: (a) Mean plane diagrams of all the molecules in the asymmetric unit of $[\text{Au}(\text{L3})](\text{PF}_6)$ showing the perpendicular displacement of each non-H atom (in units of pm) from the five-atom mean plane defined by the four coordinating nitrogen atoms and the gold(III) atom. (b) "Back view" of all the molecules in the asymmetric unit of $[\text{Au}(\text{L3})](\text{PF}_6)$ showing the deviations from the five-atom mean plane.

The compound $[\text{Au}(\text{L10})](\text{AuCl}_4)$ crystallized with a half chelate molecule and a half anion in the asymmetric unit. The two halves of the molecule are related by a crystallographically-imposed two-fold rotation axis which runs through the gold(III) ion of the chelate and anion and bisects the quinoxaline tail of the chelate. The X-ray data show that the gold(III) ion sits in the four-atom mean plane defined by the coordinating

nitrogen atoms. The molecule is relatively planar with just a slight twist of the quinoxaline tail relative to the pyrrole-imine moiety. The twist results in one pyrrole ring and half the quinoxaline ring sit below the plane defined by the coordination sphere while the other pyrrole ring and half the quinoxaline ring sitting above the plane. The quinoxaline ring is twisted out-of-plane by an angle of $12.65(1)^\circ$. The greatest deviation from the mean-plane by an atom of the quinoxaline tail is $0.328(1)$ Å. The pyrrole atom that exhibits the maximum deviation from the 5-atom mean plane is the β -carbon which is displaced by $0.229(1)$ Å from the mean plane. Figure 4.25 (a) and (c) illustrate these deviations from planarity.

The complex $[\text{Au}(\text{L12})](\text{PF}_6)$ also deviates from planarity as one pyrrole ring is displaced below the plane defined by the coordinating nitrogen atoms and gold(III) ion while the other pyrrole ring sits above the plane. The butyl bridge is buckled such that it sits both above and below the plane, Figure 4.25(b) and (d).

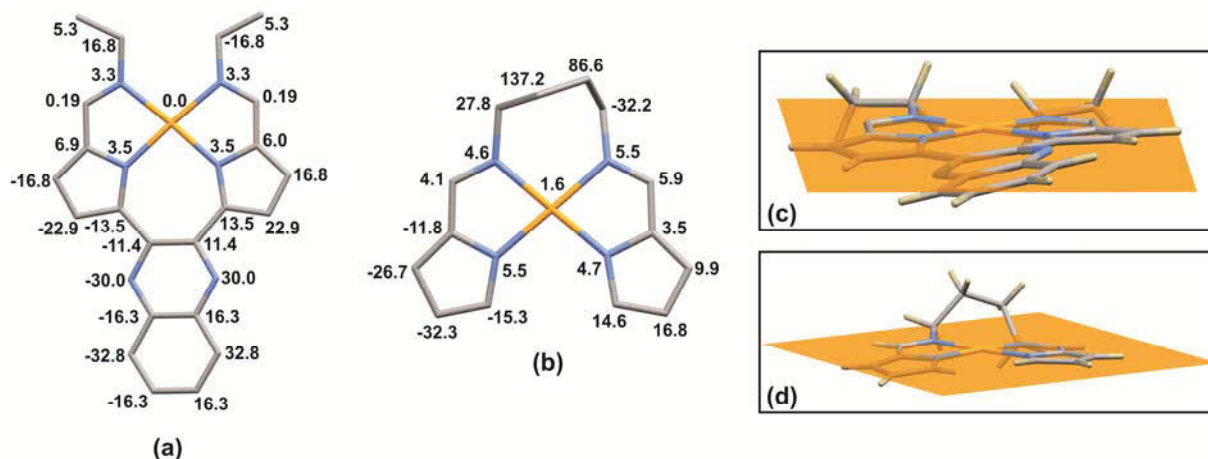


Figure 4.25: (a) Mean plane diagram of (a) $[\text{Au}(\text{L10})](\text{AuCl}_4)$ and (b) $[\text{Au}(\text{L12})](\text{PF}_6)$ showing the perpendicular displacement of each non-H atom (in units of pm) from the five-atom mean plane defined by the four coordinating nitrogen atoms and the gold(III) ion. (c) "Back view" of $[\text{Au}(\text{L10})](\text{AuCl}_4)$ and (d) "back view" of $[\text{Au}(\text{L12})](\text{PF}_6)$ illustrating the deviations from the five-atom mean planes.

The coordination geometry about the gold(III) ion is nominally square-planar in all cases. This is illustrated by the $\text{N}-\text{Au}-\text{N}$ bond angles for the complexes which are approaching 90° as well as the $\text{Au}-\text{N}$ distances which are all approximately equal and fall in the range of 1.98 - 2.06 Å. The average $\text{Au}-\text{N}_{\text{pyrrole}}$ distance for the gold(III) complexes is $1.98(3)$ Å while the $\text{Au}-\text{N}_{\text{imine}}$ bond distances average $2.03(6)$ Å. These bond distances are consistent with comparable $\text{Au}-\text{N}$ bond distances reported in literature, which fall in the range of 1.928 - 2.216 Å.³⁷ The average $\text{N}_{\text{pyrrole}}-\text{Au}-\text{N}_{\text{pyrrole}}$ and $\text{N}_{\text{imine}}-\text{Au}-\text{N}_{\text{imine}}$ bond angle for the propyl-bridged systems, $[\text{Au}(\text{L1})](\text{PF}_6)$ and $[\text{Au}(\text{L2})](\text{CF}_3\text{SO}_3)$, are $99.6(8)^\circ$ and $96.5(5)^\circ$ respectively. The equivalent bond angles for the butyl-bridged macrocyclic complex, $[\text{Au}(\text{L3})](\text{PF}_6)$, average $97.1(9)^\circ$ and $99.2(6)^\circ$, respectively. The butyl-bridged acyclic complex, $[\text{Au}(\text{L12})](\text{PF}_6)$, has $\text{N}_{\text{pyrrole}}-\text{Au}-\text{N}_{\text{pyrrole}}$ and $\text{N}_{\text{imine}}-\text{Au}-\text{N}_{\text{imine}}$ bond angles of $99.8(2)^\circ$ and $98.8(2)^\circ$, respectively. Both of the butyl-bridged complexes have larger $\text{N}_{\text{imine}}-\text{Au}-\text{N}_{\text{imine}}$ bond angles than the propyl-bridged complexes. This is expected as the longer bridge forces the imine N atoms further apart thus changing the bite angle of the ligand. This effect is also observed in the magnitude of the $\text{C}=\text{N}_{\text{imine}}-\text{C}$ angle. $[\text{Au}(\text{L3})](\text{PF}_6)$ and $[\text{Au}(\text{L12})](\text{PF}_6)$ have angles of $121(2)^\circ$ and $120.3(5)^\circ$, respectively, which are smaller than the average angle for the three-carbon bridged complexes of $124.1(5)^\circ$. The nickel(II) analogues of complexes $[\text{Au}(\text{L1})](\text{PF}_6)$ and $[\text{Au}(\text{L3})](\text{PF}_6)$ have been previously reported. They also show a larger

$N_{\text{imine}}\text{-Ni-}N_{\text{imine}}$ distance of $95.1(2)^\circ$ degrees for the butyl-bridged complex as opposed to the propyl-bridged complex which has an angle of $93.3(2)^\circ$, Table 4.8. The pseudomacrocyclic complex $[\text{Au}(\text{L10})](\text{AuCl}_4)$ has $N_{\text{pyrrole}}\text{-Au-}N_{\text{pyrrole}}$ and $N_{\text{imine}}\text{-Au-}N_{\text{imine}}$ bond angles of $95.8(3)^\circ$ and $101.2(3)^\circ$. As this complex has no di(azomethine) bridging unit restricting the angle, it exhibits the largest $N_{\text{imine}}\text{-Au-}N_{\text{imine}}$ bond angle. To accommodate this larger angle, it has a smallest $N_{\text{pyrrole}}\text{-Au-}N_{\text{pyrrole}}$ angle. Table 4.23 summarizes these bond lengths and angles.

Table 4.23: Average bond lengths and bond angles for the gold(III) complexes.

	$[\text{Au}(\text{L1})](\text{PF}_6)$	$[\text{Au}(\text{L2})](\text{CF}_3\text{SO}_3)$	$[\text{Au}(\text{L3})](\text{PF}_6)$	$[\text{Au}(\text{L10})](\text{AuCl}_4)$	$[\text{Au}(\text{L12})](\text{PF}_6)$
Bond Lengths (Å)					
Au-N_{pyrrole}	1.99(1)	1.98(1)	1.98(1)	1.987(6)	1.994(6)
Au-N_{imine}	2.01(1)	2.00(1)	2.02(2)	2.059(7)	2.043(4)
C=N_{imine}	1.31(1)	1.32(5)	1.30(3)	1.30(1)	1.313(8)
Bond Angles (°)					
$N_{\text{pyrrole}}\text{-Au-}N_{\text{pyrrole}}$	99.2(2)	100.2(2)	97.1(8)	95.8(3)	99.8(2)
<i>cis</i>-$N_{\text{pyrrole}}\text{-Au-}N_{\text{imine}}$	81.8(1)	81.7(1)	81.9(8)	81.5(3)	80.8(2)
<i>trans</i>-$N_{\text{pyrrole}}\text{-Au-}N_{\text{imine}}$	177.7(1)	177.8(7)	177(1)	176.7(3)	177.1(2)
$N_{\text{imine}}\text{-Au-}N_{\text{imine}}$	97.2(2)	96.4(6)	99.2(4)	101.2(3)	98.8(2)
$C_\alpha\text{-}N_{\text{pyrrole}}\text{-}C_\alpha$	108.5(1)	110(2)	108(1)	107.5(6)	107.4(5)
C=$N_{\text{imine}}\text{-}C$	124.1(5)	124(2)	121(2)	121.3(6)	120.3(5)

As with the ligands, few true intermolecular hydrogen bonds are observed for any of the complexes. This is due to the fact that there are no suitable hydrogen bond donor or acceptor groups positioned on the outside of the molecules. Although devoid of true hydrogen bonds the complexes exhibit several weak electrostatic interactions. As the molecules are relatively planar they all exhibit π and $\text{Au}\cdots\pi$ interactions. These interactions are described below.

The complex, $[\text{Au}(\text{L1})](\text{PF}_6)$ has a single ion pair in the asymmetric unit. The adjacent cationic molecules form head-to-tail (inverted) π -stacked dimers related by crystallographically imposed inversion symmetry with a mean plane separation (MPS) of $3.43(1) \text{ \AA}$, and an $\text{Au}\cdots\text{Au}$ separation of $7.328(2) \text{ \AA}$. There are cation to π interactions with a short distance of $3.302(5) \text{ \AA}$ between C=C of the benzene moieties and gold(III) ions of adjacent molecules indicating potential for cation- π -stacking with DNA base pairs. Figure 4.26(a) and (b) illustrates the π -stacking interactions of the complex. Figure 4.26 (b) shows that the complexes stack closely together. The dimers are further stabilized by electrostatic interactions between a methylene H atom and a fluorine atom of the hexafluorophosphate(V) anion. The same fluorine atom has electrostatic interactions with the quinoxaline C-H of the adjacent molecule, bridging the dimers. These interactions are shorter than the sum of the van der Waals radii by approximately 0.1 \AA . Although bond length does not necessarily correlate linearly with bond strength, due to packing constraints in the lattice, it is likely that these short bonds are moderate in strength.

The asymmetric unit of $[\text{Au}(\text{L2})](\text{CF}_3\text{SO}_3)$ consists of two cations and the corresponding triflate anions. Unlike $[\text{Au}(\text{L1})](\text{PF}_6)$, $[\text{Au}(\text{L2})](\text{CF}_3\text{SO}_3)$ does not stack head-to tail but rather in an oblique fashion where the one molecule is rotated by approximately 65° relative to the adjacent molecule. This change in configuration may be due to the added steric bulk of the dimethyl groups leading to a disruption in $\text{Au}\cdots\pi$ stacking. This configuration allows the cations to sit closer with an $\text{Au}\cdots\text{Au}$ separation of $5.124(1) \text{ \AA}$. There is $\pi\cdots\pi$ stacking

of the quinoxaline rings and the pyrrole rings of an adjacent molecule with an approximate separation of 3.35(2)-3.39(2) Å. Figure 4.26(c) and (d) illustrate the π -stacking interactions of the complex. The dimers of molecules A and B are linked by stabilizing electrostatic interactions. There are electrostatic interactions between the imine hydrogen atoms of both molecules A and B and an oxygen atom of the same triflate anion. The H \cdots O bond length is 2.486 Å and 2.248 Å for molecules A and B, respectively. In addition to these, there is also an electrostatic interaction between the methylene H-atom of molecule A and a triflate oxygen, with an H \cdots O bond length of 2.598 Å.

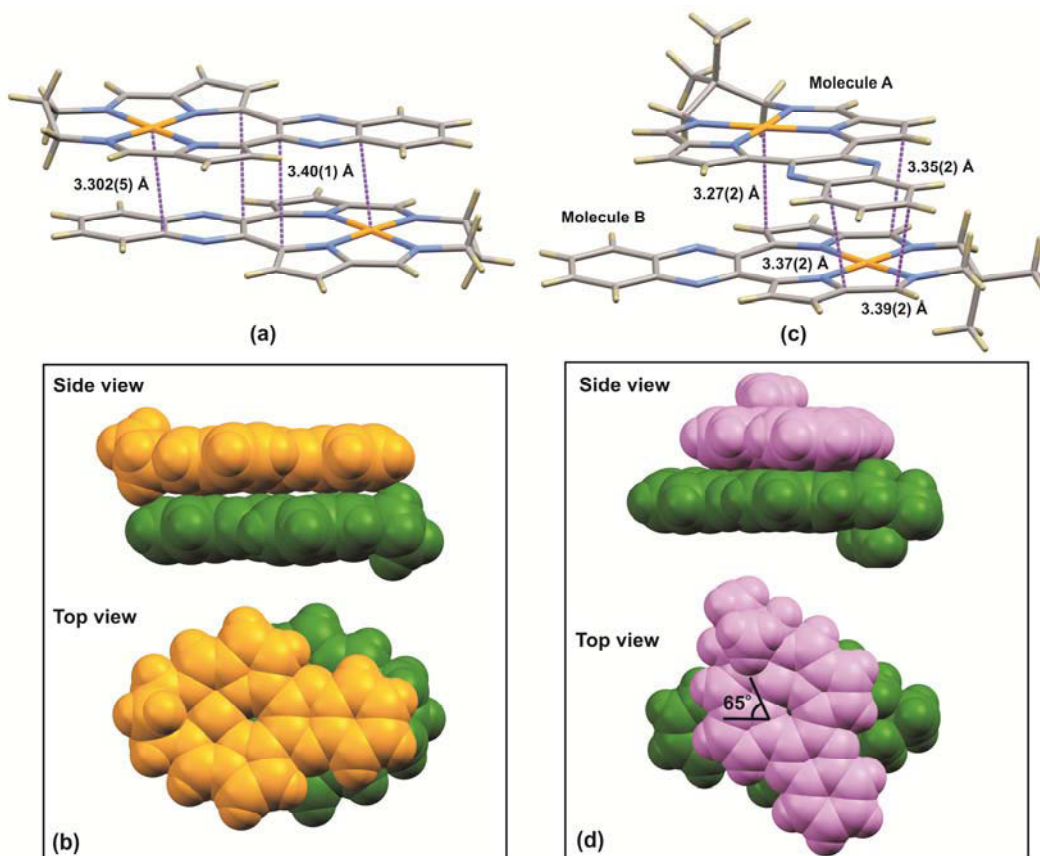


Figure 4.26: (a) View of the π - π dimers formed by the cations of compound $[\text{Au}(\text{L1})](\text{PF}_6)$ in the crystalline solid state. (b) Space-filling structure diagrams (van der Waals radii) of $[\text{Au}(\text{L1})](\text{PF}_6)$ viewed perpendicular and down the axis normal to the cation's 5-atom mean plane. (c) π - π dimers formed by the cation of compound $[\text{Au}(\text{L2})](\text{CF}_3\text{SO}_3)$ in the crystalline solid state. (d) Space-filling structure diagram (van der Waals radii) of $[\text{Au}(\text{L2})](\text{CF}_3\text{SO}_3)$.

The asymmetric unit of $[\text{Au}(\text{L3})](\text{PF}_6)$ contains six ion pairs and seven acetonitrile molecules. There are two distinct types of stacking in this crystal. These two different types of stacking are shown in Figure 4.27(a) and (b). The first type is similar to that of $[\text{Au}(\text{L1})](\text{PF}_6)$ where the molecules stack in a head-to-tail configuration. This type of stacking is adopted by Molecules A and B in the asymmetric unit. There are Au- π interactions between the C=C double bonds of the benzene moieties and the Au(III) ions, with a relatively short distance of 3.36(1) Å. There are also π -interactions between the pyrrole rings of one molecule and the quinoxaline rings of another with a distance of 3.39(1) Å separating the pyrrole C $_{\alpha}$ and the quinoxaline ring. The gold(III) atoms sit further apart with an Au \cdots Au separation of 9.368(7). The molecules form π -stacked columns which are co-linear with the b -axis. These π stacked columns are further stabilized by electrostatic interactions

between the hexafluorophosphate(V) fluorine atom and the quinoxaline C–H of molecule A. The same hexafluorophosphate(V) counterion also has electrostatic interactions with the imine CH and methylene proton of the bridge of molecule B, linking the two molecules.

The other type of stacking is an oblique configuration, more similar to that of $[\text{Au}(\text{L}2)](\text{CF}_3\text{SO}_3)$; however, in this case the molecules are rotated by an angle of approximately 112° relative to one another. Molecules C and D as well as E and F adopt this configuration. Molecule C and D have similar interactions to that of molecules E and F and thus only the interactions adopted by molecules E and F are discussed. Molecules E and F form π -stacked dimers with Au– π interactions between the Au(III) cation of one molecule and the pyrrole ring of another molecule. The gold(III) cation of molecule E interacts with the C_α of the pyrrole moiety of molecule F with an Au– C_α length of $3.25(1) \text{ \AA}$. The gold(III) cation of molecule F interacts with the C_β of the pyrrole moiety of molecule E with an Au– C_β length of $3.35(1) \text{ \AA}$. There is also a π – π interaction between the quinoxaline rings of adjacent molecules with a bond distance of $3.38(2) \text{ \AA}$. As the butyl bridges are facing away from each other, the molecules are able to approach closely with an Au...Au separation of $5.289(1) \text{ \AA}$. The molecules of the dimer are also linked by electrostatic interactions from the hexafluorophosphate(V) F atom and the imine C–H of molecule E. The same counterion also has an electrostatic interaction from an F atom to a methylene C–H of the butyl bridge of molecule F.

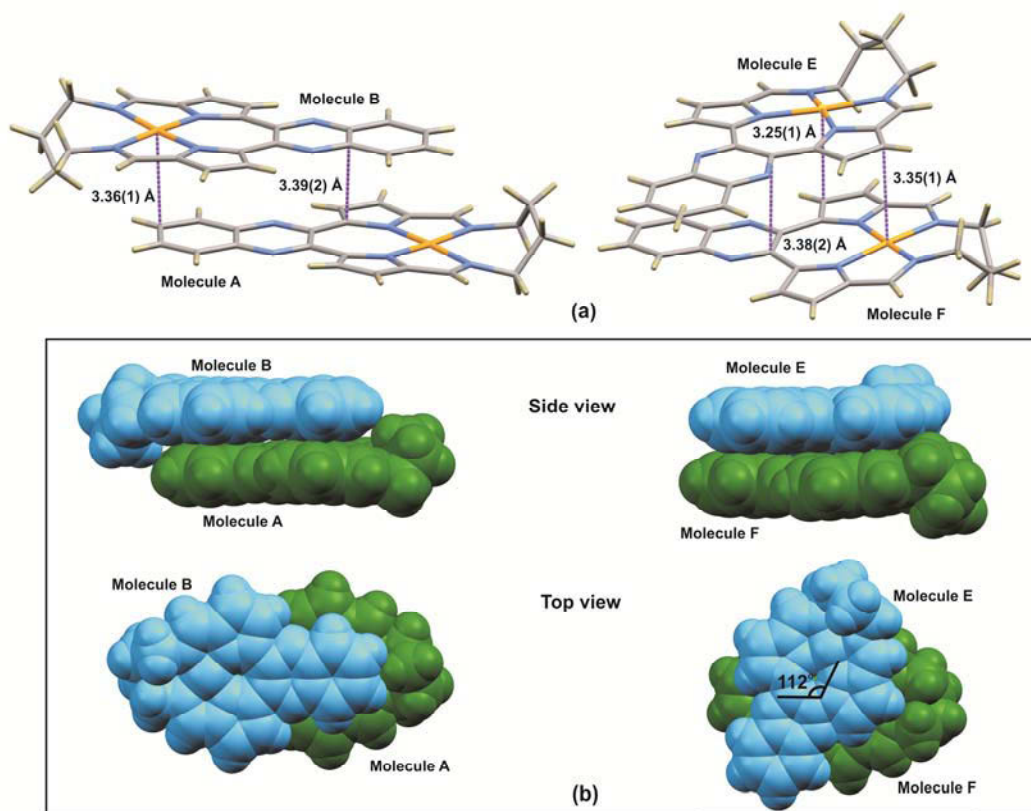


Figure 4.27: (a) View of the different π -stacking orientations formed by molecules A and B and molecules E and F of $[\text{Au}(\text{L}3)](\text{PF}_6)$ in the crystalline solid state. Molecules C and D exhibit similar stacking to molecules E and F. (b) Space-filling structure diagrams (van der Waals radii) of molecules A and B and molecule E and F of $[\text{Au}(\text{L}3)](\text{PF}_6)$ viewed perpendicular and down the axis normal to the cation's 5-atom mean plane.

The asymmetric unit of $[\text{Au}(\text{L10})](\text{AuCl}_4)$ has one ion pair. The adjacent molecules form head-to-tail π -stacked columns co-linear with the c -axis. The molecules in the column are slipped from each other such that there is overlap of the quinoxaline and pyrrole rings of one molecule with the quinoxaline and pyrrole rings of the adjacent molecule, Figure 4.28(a) and (b). There is an $\text{Au}\cdots\text{Au}$ separation of 6.879(1) Å. There are also electrostatic interactions between the tetrachloroaurate counterion and the C–H of the quinoxaline ring. There is an interplanar spacing of 3.505 Å between the 5-atom mean planes of the molecule defined by the four coordinating nitrogen atoms and the gold(III) ion.

The asymmetric unit of $[\text{Au}(\text{L12})](\text{PF}_6)$ contains a half-molecule. The molecules form head-to-tail π -stacked dimers with the imine and pyrrole moieties of the molecules overlapping. There is a short $\text{Au}\cdots\text{Au}$ distance of 3.681(2) Å between the molecules and an interplanar spacing of 3.416(1) Å between the planes of the molecules. The π interactions of the complex are summarized in Figure 4.28 (c) and (d). The π -stacked dimer is further stabilised by electrostatic interactions between the F atom of the counterion and the imine C–H atoms of one molecule. The same counterion also has electrostatic interactions with the pyrrole $\text{C}_\beta\text{--H}$ of an adjacent molecule.

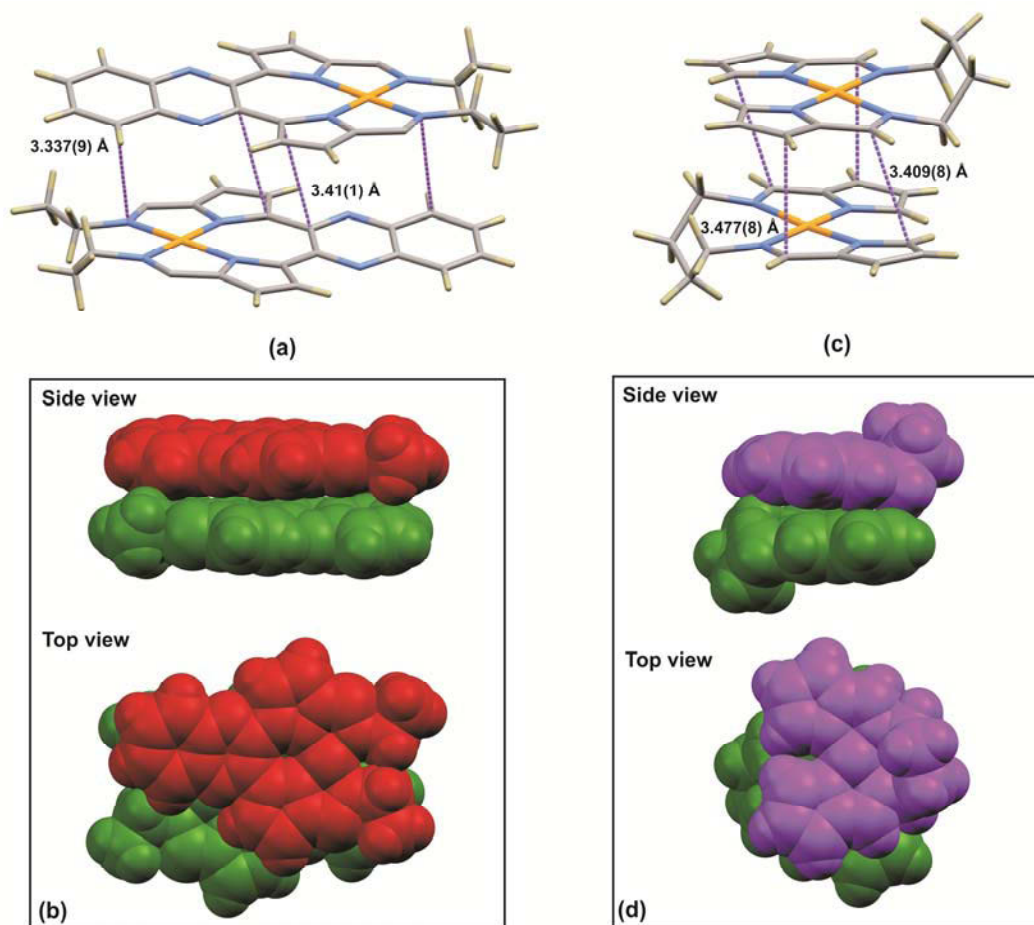


Figure 4.28: (a) View of the different π -stacking and orientations formed by $[\text{Au}(\text{L10})](\text{AuCl}_4)$ in the crystalline solid state. (b) Space-filling structure diagrams (van der Waals radii) of $[\text{Au}(\text{L10})](\text{AuCl}_4)$ viewed perpendicular and down the axis normal to the cation's 5-atom mean plane. (c) View of the π - π dimers formed by the cation of compound $[\text{Au}(\text{L12})](\text{PF}_6)$ in the crystalline solid state. (d) Space-filling structure diagrams (van der Waals radii) of $[\text{Au}(\text{L12})](\text{PF}_6)$.

In conclusion, the X-ray structure determinations reported here have been important in determining the solid state structures of the novel gold(III) bis(pyrrolide-imine) Schiff base complexes. The gold(III) ion coordinates, as would be expected, to the pyrrole and imine nitrogen atoms of the ligand and has a nominally square-planar coordination sphere. The gold(III) complexes show small deviations from planarity, similar to gold(III) porphyrins¹¹, although in general the complexes are approaching planarity with the exception of the bis(imine) linkage which sits out-of-plane of the complexes. It is important that these complexes are nearly planar as they have been designed as DNA intercalators. These planar aromatic regions of the ligand have the potential to enhance intercalation between the DNA base pairs. The gold(III) complexes have been shown to readily form π - π interactions as well as Au- π interactions which is important for potential DNA intercalation as these interactions will stabilize the DNA-drug conjugate.

4.5 Summary of X-ray Data

4.5.1 X-ray Data for Schiff Base Ligands

Table 4.24: Crystal data and structure refinement details for Schiff base ligands: H₂L2, H₂L5, H₂L6 and H₂L7.

Crystal Data	H ₂ L2	H ₂ L5	H ₂ L6	H ₂ L7
Formula	C ₂₃ H ₂₂ N ₆	C ₂₃ H ₂₂ N ₆	C ₂₂ H ₁₉ N ₆ ,HO _{0.5}	C ₂₁ H ₁₆ FN ₆
Cell Setting	Monoclinic	Monoclinic	Monoclinic	Monoclinic
Space Group	<i>P2₁/c</i>	<i>C2/c</i>	<i>C2/c</i>	<i>P2₁/c</i>
M _r (g mol ⁻¹)	382.47	382.47	376.44	371.40
a / Å	9.170(5)	31.645(5)	31.219(5)	9.396(5)
b / Å	11.244(5)	7.749(4)	7.724(4)	10.667(5)
c / Å	18.720(6)	19.067(5)	19.098(5)	17.165(6)
α / °	90	90	90	90
β / °	96.718(5)	123.596(5)	125.403(5)	90.254(5)
γ / °	90	90	90	90
T/K	120(2)	120(2)	120(2)	120(2)
Z	4	8	8	4
V / Å ³	1916.0(14)	3895(3)	3754(3)	1720.4(13)
ρ / g cm ⁻³	1.325	1.305	1.332	1.434
F(000)	808	1616	1584	772
μ / mm ⁻¹	0.083	0.081	0.085	0.098
Crystal Dim. / mm	0.55 x 0.30 x 0.05	0.50 x 0.30 x 0.10	0.45 x 0.45 x 0.10	0.30 x 0.30 x 0.15
Radiation M _o K _α	0.71073 Å			
Total Data collected	13312	13929	13380	10797
Unique Data	3693	3841	3700	2331
R _{int}	0.108	0.038	0.039	0.085
Refinement Method	Full-matrix least-squares on F ²			
Final R indices	R ₁ = 0.058	R ₁ = 0.038	R ₁ = 0.055	R ₁ = 0.061
[>2σ(I)]	wR ₂ = 0.113	wR ₂ = 0.085	wR ₂ = 0.153	wR ₂ = 0.127
Final R indices	R ₁ = 0.126	R ₁ = 0.058	R ₁ = 0.081	R ₁ = 0.137
[all data]	wR ₂ = 0.131	wR ₂ = 0.089	wR ₂ = 0.162	wR ₂ = 0.144
Δρ _{max} , Δρ _{min} (e Å ⁻³)	0.52, -0.28	0.24, -0.30	1.06, -0.34	0.29, -0.34

Table 4.25: Crystal data and structure refinement details for the Schiff base ligands: H₂L8a, H₂L8b, H₂L8c, H₂L9 and H₂L12.

Crystal Data	H ₂ L8a	H ₂ L8b	H ₂ L8c	H ₂ L9	H ₂ L12
Formula	C ₁₉ H ₁₄ N ₈	C ₁₉ H ₁₇ N ₇ O	C ₂₀ H ₁₈ N ₈ O	C ₂₀ H ₁₈ N ₆	C ₁₄ H ₁₈ N ₄
Cell Setting	Orthorhombic	Orthorhombic	Monoclinic	Monoclinic	Monoclinic
Space Group	<i>P</i> 2 ₁ 2 ₁ 2 ₁	<i>P</i> na2 ₁	<i>P</i> 2 ₁ / <i>c</i>	<i>P</i> 2 ₁ / <i>c</i>	<i>C</i> 2/ <i>c</i>
M_r (g mol⁻¹)	354.38	359.40	386.42	342.40	242.32
a / Å	6.9450(3)	9.792(3)	8.8718(2)	9.174(4)	18.140(5)
b / Å	19.387(1)	17.151(6)	20.4106(3)	17.089(5)	5.129(4)
c / Å	24.018(1)	10.407(4)	10.0909(2)	11.072(5)	14.310(5)
α / °	90	90	90	90	90
β / °	90	90	98.344(1)	108.624(5)	102.177(5)
γ / °	90	90	90	90	90
T/K	296(2)	100(2)	100(2)	120(2)	120(2)
Z	8	4	4	4	4
V / Å³	3233.7(3)	1747(1)	1807.91(6)	1645(1)	1301(1)
ρ / g cm⁻³	1.420	1.366	1.420	1.383	1.237
F(000)	1472.0	752	808	720	520
μ / mm⁻¹	0.095	0.091	0.774	0.087	0.077
Crystal Dim. / mm	0.25 x 0.07 x 0.03	0.35 x 0.30 x 0.15	0.15 x 0.15 x 0.05	0.40 x 0.30 x 0.10	0.50 x 0.29 x 0.22
Radiation	Mo K _α 0.71073 Å		Cu K _α 1.54178 Å	Mo K _α 0.71073 Å	
Total Data collected	10797	7081	11955	12114	6311
Unique Data	5271	1671	3279	3248	2095
R_{int}	0.085	0.042	0.019	0.041	0.026
Refinement Method	Full-matrix least-squares on F ²				
Final R indices [I > 2σ(I)]	R ₁ = 0.061 wR ₂ = 0.127	R ₁ = 0.059 wR ₂ = 0.160	R ₁ = 0.056 wR ₂ = 0.150	R ₁ = 0.039 wR ₂ = 0.091	R ₁ = 0.043 wR ₂ = 0.119
Final R indices [all data]	R ₁ = 0.137 wR ₂ = 0.144	R ₁ = 0.082 wR ₂ = 0.176	R ₁ = 0.060 wR ₂ = 0.153	R ₁ = 0.054 wR ₂ = 0.95	R ₁ = 0.052 wR ₂ = 0.123
Δρ_{max}, Δρ_{min} (e Å⁻³)	0.40, -0.31	0.40, -0.21	0.53, -0.32	0.16, -0.29	0.22, -0.35

4.5.2 X-ray Data for Gold(III) Complexes

Table 4.26: Crystal data and structure refinement details for the gold(III) Schiff base complexes:

 [Au(L1)](PF₆), [Au(L2)](CF₃SO₃), [Au(L3)](PF₆), [Au(L10)](AuCl₄) and [Au(L12)](PF₆)

Crystal Data	[Au(L1)](PF ₆)	[Au(L2)](CF ₃ SO ₃)	[Au(L3)](PF ₆)	[Au(L10)](AuCl ₄)	[Au(L12)](PF ₆)
Formula	C ₂₁ H ₁₆ AuN ₆ F ₆ P	C ₂₃ H ₂₀ AuN ₆ , CF ₃ O ₃ S	C ₂₂ H ₁₈ AuN ₆ , F ₆ P, C ₂ H ₃ N	C ₂₂ H ₁₈ AuN ₆ , AuCl ₄	C ₁₄ N ₁₆ AuN ₄ , F ₆ P
Cell Setting	Monoclinic	Monoclinic	Orthorhombic	Monoclinic	Monoclinic
Space Group	<i>P2/c</i>	<i>Cc</i>	<i>Pna2₁</i>	<i>C2/c</i>	<i>P2₁/n</i>
M_r (g mol⁻¹)	694.33	726.49	749.41	902.16	582.24
a / Å	16.473(5)	17.092(5)	43.902(1)	9.467(1)	8.293(5)
b / Å	6.980(5)	25.520(5)	6.7597(2)	31.073(4)	10.903(5)
c / Å	18.804(5)	13.625(5)	48.896(1)	8.352(1)	19.024(6)
α / °	90	90	90	90	90
β / °	105.675(5)	119.057(5)	90	103.831(3)	96.808(5)
γ / °	90	90	90	90	90
T/K	173(2)	120(2)	100(2)	100(2)	120(2)
Z	4	8	24	4	4
V / Å³	2082(1)	5195(3)	14510.8(7)	2385.7(6)	1708(1)
ρ / g cm⁻³	2.215	1.8528	2.058	2.512	2.264
F(000)	1328	2816	8688	1672	1104
μ / mm⁻¹	7.223	5.804	12.760	12.758	8.775
Crystal Dim. / mm	0.50 x 0.02 x 0.01	0.3 x 0.1 x 0.07	0.12 x 0.02 x 0.02	0.10 x 0.05 x 0.01	0.45 x 0.20 x 0.15
Radiation	M _o K _α 0.71073 Å		Cu K _α 1.54178 Å		M _o K _α 0.71073 Å
Total Data collected	14581	19009	101016	9729	16330
Unique Data	4010	7804	24413	2871	5430
R_{int}	0.060	0.074	0.098	0.029	0.040
Refinement Method	Full-matrix least-squares on F ²				
Final R indices	R ₁ = 0.032	R ₁ = 0.065	R ₁ = 0.052	R ₁ = 0.034	R ₁ = 0.036
[I > 2σ(I)]	wR ₂ = 0.070	wR ₂ = 0.160	wR ₂ = 0.107	wR ₂ = 0.102	wR ₂ = 0.085
Final R indices	R ₁ = 0.45	R ₁ = 0.090	R ₁ = 0.068	R ₁ = 0.042	R ₁ = 0.058
[all data]	wR ₂ = 0.073	wR ₂ = 0.170	wR ₂ = 0.113	wR ₂ = 0.111	wR ₂ = 0.085
Δρ_{max}, Δρ_{min} (e Å⁻³)	2.28, -1.45	2.74, -1.65	2.02, -2.00	3.72, -1.56	3.06, -2.76

4.6 References

- (1) Cambridge Crystallographic Data Centre *12 Union Rd, Cambridge CB21EZ, UK* **2010**.
- (2) Munro, O. Q., Camp, G. L. *Acta Cryst.* **2003**, C59, o672.
- (3) Munro, O. Q., Strydom, S. D., Grimmer, C. D. *Chem. Eur. J.* **2006**, 12, 7987.
- (4) van den Ancker, T. R., Cave, G. W. V., Raston, C. L. *Green Chem.* **2006**, 8, 50.
- (5) Wang, Y., Fu, H., Shen, F., Sheng, X., Peng, A., Gu, Z., Ma, H., Shi Ma, J., Yao, J. *Inorg. Chem.* **2007**, 46, 3548.
- (6) Bacchi, A., Carcelli, M., Gabba, L., Ianelli, S., Pelagatti, P., Pelizzi, G., Rogolino, D. *Inorg. Chim. Acta* **2003**, 342, 229.
- (7) Allen, F. H., Kennard, O., Watson, D. G. *Perkin Trans. II* **1987**, S1.
- (8) Wu, Z., Chen, Q., Xiong, S., Xin, B., Zhao, Z., Jiang, L., Ma, J. S. *Angew. Chem. Int. Ed.* **2003**, 42, 3271.
- (9) Wang, L., Zhu, X.-J., Wong, W.-Y., Guo, J.-P., Wong, W.-K., Li, Z.-Y. *Dalton Trans.* **2005**, 3235.
- (10) Hu, Y., Li, Q.-Q., Li, H., Guo, Q.-N., Lu, Y.-G., Li, Z.-Y. *Dalton Trans.* **2010**, 39, 11344.
- (11) Che, C.-M., Sun, R. W.-Y., Yu, W.-Y., Ko, C.-B., Zhu, N., Sun, H. *Chem. Commun.* **2003**, 14, 1718.
- (12) Chen, J. M., Ruan, W. J., Gao, F., Zhang Y. H., Zhu, Z. A. *Acta Cryst.* **2007**, E63, m1546.
- (13) Yang, L., Chen, Q., Li, Y., Xiong, S., Li, G., Shi Ma, J. *Eur. J. Inorg. Chem.* **2004**, 1478.
- (14) Mueller-Westerhoff, U., Rheingold, A. L., Allen, M. B. *Private Commun.* **1996**.
- (15) Glinskaya, L. A., Afanas'eva, V.A., Klevtsova, R.F. *Zh.Strukt.Khim.(Russ.)(J.Struct.Chem.)* **2004**, 45, 129.
- (16) Toganoh, M., Niino, T., Furuta, H. *Chem. Commun.* **2008**.
- (17) Rossignoli, M., Bernhardt, P.V., Lawrance, G. A., Maeder, M. *Dalton Trans.* **1997**.
- (18) Afanas'eva, V. A., Glinskaya, L. A., Klevtsova, R. F., Mironov, I. V., Sheludyakova, L. A., Tkachev, S. V. *Zh.Strukt.Khim.(Russ.)(J.Struct.Chem.)* **2003**, 44, 83.
- (19) Suh, M. P., Kim, I. S., Shim, B. Y., Hong, D., Yoon, T.-S. *Inorg. Chem.* **1996**, 35, 3595.
- (20) Afanas'eva, V. A., Glinskaya, L.A., Klevtsova, R.F., Mironov, N.V., Sheludyakova, L.A. *Zh.Strukt.Khim.(Russ.)(J.Struct.Chem.)* **2007**, 48, 296.
- (21) Barnholtz, S. L., Lydon, J. D., Huang, G., Venkatesh, M., Barnes, C. L., Ketring, A. R., Jurisson, S. S. *Inorg. Chem.* **2001**, 40, 972.
- (22) CrysAlis CCD and CrysAlis RED Version 170 *Oxford Diffraction Ltd., Abingdon, UK* **2002**.
- (23) Blessing, R. H. *Acta Cryst.* **1995**, A51.
- (24) Bruker AXS Inc Madison, Wisconsin, USA., 2010.
- (25) Sheldrick, G. M. University of Göttingen, Germany, 1997.
- (26) Farrugia, L. J. *J. Appl. Crystallogr.* **1999**, 32.
- (27) Spek, A. L. *Acta Cryst.* **2009**, D65.
- (28) Mercury Version 2.4 *Cambridge Crystallographic Data Centre: Cambridge, UK* **2010**.
- (29) Cason, C. J. *POV-RAY for Windows*; Persistence of Vision Raytracer Pty. Ltd.; Australia, 2002.
- (30) International Union of Crystallography; Vol. 2013.
- (31) Maity, D. K., Bell, R. L., Truong, T. N. *J. Am. Chem. Soc* **2000**, 122.
- (32) Toganoh, M., Yamamoto, T., Hihara, T., Akimaru, H., Furuta, H. *Org. Biomol. Chem* **2012**, 10, 4367.
- (33) Wacker, P., Dahms, K., Senge, M. O., Kleinpeter, E. *J. Org. Chem.* **2008**, 73, 2182.
- (34) Storm, C. B., Teklu, Y. *J. Am. Chem. Soc* **1972**, 94.
- (35) Storm, C. B., Teklu, Y., Sokoloski, E. *Ann. N. Y. Acad. Sci.* **1973**, 206.
- (36) Scipioni, R., Boero, M., Richards, G. J., Hill, J. P., Ohno, T., Mori, T., Ariga, K. *J. Chem. Theory Comput.* **2010**, 6, 517.
- (37) Shriver, D. F., Atkins, P. W. *Inorganic Chemistry, 3rd Edition*; Oxford University Press, 2000.
- (38) Wang, Y., Fu, H., Peng, A., Zhao, Y., Ma, J., Ma, Y., Yao, J. *Chem. Commun.* **2007**, 1623.

CHAPTER FIVE:

SPECTROSCOPY

5.1 Infrared Spectroscopy

5.1.1 Introduction

Almost all compounds containing covalent bonds absorb various frequencies of electromagnetic radiation in the infrared (IR) region of the electromagnetic spectrum. For chemical purposes the most relevant portion of the IR region is the vibrational section which extends from about 4000 to 400 cm^{-1} .¹ The internal molecular energy of a molecule can be divided into three additive components: the rotation of the molecule, the vibrations of each atom in the molecule and the movement of the electrons in the molecule (Equation 5.1).²

$$E_{\text{total}} = E_{\text{el}} + E_{\text{vib}} + E_{\text{rot}} \quad 5.1$$

The vibrational transitions occur at frequencies within the IR range and so it is only the vibrational transitions that are observed in the IR spectrum.¹ The simplest modes of vibrational motion in a molecule that are infrared active are the stretching and bending modes. In general, asymmetric stretching vibrations occur at higher frequencies than symmetric stretching frequencies and stretching vibrations occur at higher frequencies than bending vibrations.¹ Figure 5.1(a) illustrates the different types of stretching and bending vibrations.

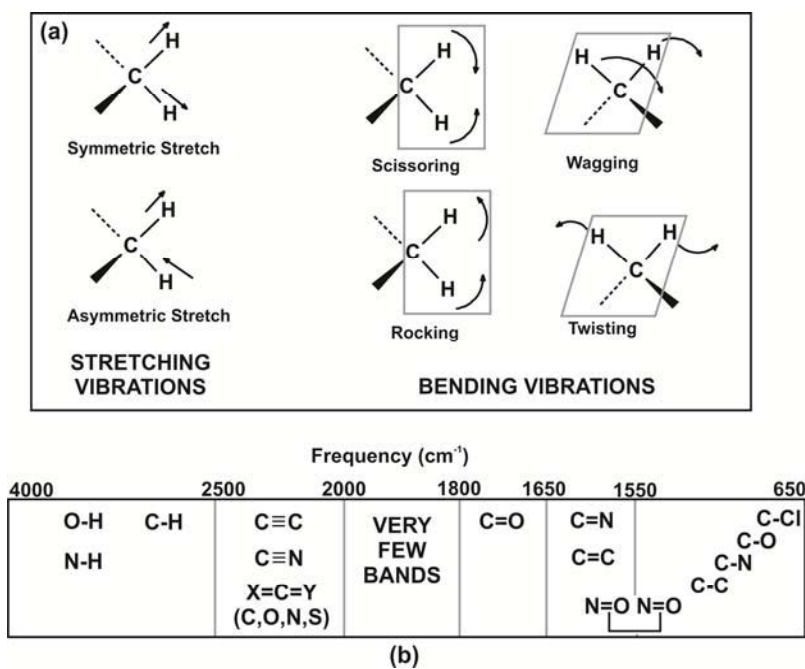


Figure 5.1: (a) Different modes of stretching and bending vibrational motion. (b) The approximate regions of the electromagnetic spectrum at which various bonds resonate (stretching vibrations only).

When molecules absorb IR radiation they are excited to a higher energy state. In the absorption process, those frequencies of IR radiation that match the vibrational frequencies of the molecule are absorbed.¹ The energy absorbed serves to increase the amplitude of the vibrational motions of the bonds in the molecule. Not all bonds in a molecule are capable of absorbing IR energy, even if the frequency of the radiation exactly matches that of the bond motion.^{1,3} Only those bonds that have a change of dipole moment due to a vibration are capable of absorbing infrared radiation.^{1,3,4}

No two molecules of different structure have the same infrared spectrum, as every bond has a different natural frequency of vibration.^{1,4,5} Even the same bond in different compounds will be in two slightly different environments. IR spectroscopy can thus be used as a fingerprinting tool to determine if two compounds are identical. Another application of IR spectroscopy is to determine structural information about a molecule.^{1,4,5} This is possible since most functional groups absorb in a specific narrow region of the infrared spectrum, Figure 5.1(b).

The Schiff base ligands reported in this work exhibit characteristic absorption bands. These include a pyrrole $\nu(\text{NH})$ stretching vibration in the region of $3500\text{--}3300\text{ cm}^{-1}$ and a $\nu(\text{C}=\text{N})$ band which is a strong and distinct band and occurs in the region $1690\text{--}1640\text{ cm}^{-1}$ in the free ligands.¹ When chelation to the gold(III) ion occurs, the pyrrole $\nu(\text{NH})$ band disappears and the $\nu(\text{C}=\text{N})$ band shifts to lower wavenumbers.⁶ The rest of the ligand bands will only show small changes upon chelation to the gold(III) ion.⁷ The substituents on the quinoxaline and pyrazine tails as well as the bis(pyrrolide-imine) bridging units will also show characteristic shifts. The hexafluorophosphate(V) anion will give a strong absorption in the region $800\text{--}900\text{ cm}^{-1}$ due to the P-F stretch.

The main objective of IR spectroscopy within the context of this thesis is to help characterize the bis(pyrrolide-imine) Schiff base ligands and the chelated gold(III) complexes. Comparisons can be made between the spectra of the free ligands and gold(III) chelates to determine the effects of chelation on the spectral properties of the ligands.

5.1.2 IR Spectroscopy: Results and Discussion

The most significant band in the IR spectrum of a Schiff base is that of the imine ($\text{C}=\text{N}$) group which is generally in the range of $1690\text{--}1600\text{ cm}^{-1}$.¹ This band also undergoes the largest spectral shift when the ligand is chelated to the gold(III).^{6,7} Table 5.1 summarizes the frequencies of the absorption bands for the imine groups for both the ligands and the gold(III) complexes.

The X-ray crystallographic structures (Chapter Four) of the macrocyclic ligands showed that both pyrrole N atoms are not protonated in the solid state, but rather one pyrrole N atom and the diagonally opposite imine N atom are protonated. As IR spectroscopy was used as a solid state technique in this instance, the macrocyclic ligands are most likely still in the same tautomeric form as shown in the X-ray structure. The IR spectrum also suggests that this is the case as there are two distinct imine stretching vibrations in the typical region for $\text{C}=\text{N}$ imine bonds in the IR spectrum for some of the compounds. This would be expected for this tautomer as the imine $\text{C}=\text{N}$ bonds are no longer equivalent with only one imine band expected in the IR spectrum for the symmetric tautomer where both pyrrole N atoms are protonated.

The pseudomacrocyclic ligand, H₂L11, appears to have only one imine band, but this band is very broad so there may well be two peaks that have overlapped. This ligand also may have both pyrrole N atoms protonated as the analogous ligand, *N,N'*-((5,5'-(Quinoxaline-2,3-diyl)bis(1H-pyrrole-5,2-diyl))bis(methanylylidene))bis(4-methoxyaniline),⁸ reviewed in Chapter Four which has methoxyaniline substituents attached to imine groups, is of this tautomeric form. This previously reported ligand adopts a T-shaped configuration to relieve any steric strain imposed by the bulky methoxy aniline groups. This less strained configuration allows both pyrrole N atoms to be protonated. The ligand H₂L11 may adopt a similar configuration as it has fairly bulky alcohol chains.

The acyclic ligand, H₂L12, has a linear configuration due to the flexible carbon chain linking the two bis(pyrrolide-imine) units. This linear configuration ensures minimum steric strain and correspondingly the X-ray crystal structure (Chapter Four) shows that both pyrrole N atoms are protonated. This leads to only one imine band in the IR spectrum.

Table 5.1: Imine stretching vibrations of both the free ligands and gold(III) chelates.

Schiff base ligand	Free ligand / cm ⁻¹		Gold(III) chelate /cm ⁻¹
H ₂ L1	1642	1600	1572
H ₂ L2	1643	1601	1569
H ₂ L3	1642	1606	1590
H ₂ L4	N/A	N/A	1569
H ₂ L5	1650	1631	1573
H ₂ L6	1647	1610	1573
H ₂ L7	1640	1599	1618
H ₂ L8a	1645	1630	N/A
H ₂ L8b	1642	1625	1566
H ₂ L9	1650	1635	1602
H ₂ L10	1643	1633	1597
H ₂ L11	1632	N/A	1597
H ₂ L12	1641	N/A	1585

The splitting of the imine bands observed for the macrocyclic and some of the pseudomacrocyclic ligands disappears to become one band when the ligand is chelated to gold(III). When metal chelation occurs, there is concomitant deprotonation of the coordinating N-atoms and the complex has a symmetric coordination sphere. Table 5.1 also illustrates the characteristic shift of the imine stretch to lower wavenumbers associated with metal chelation.^{6,7} The shift to lower wavenumbers is attributed to a minor weakening of the imine bond upon metal chelation as the metal draws electron density towards itself. As a bond weakens the stretching frequency correspondingly decreases. Although the gold(III) chelate imine frequency was lower than for the ligands, no relationship was observed between the chelated and free ligand imine stretching vibrations i.e. ligands with lower imine frequencies do not result in chelates with lower imine frequencies.

Molecular simulations (Chapter Six) predict that in the tautomeric form observed in the solid state, with diagonally opposite pyrrole and imine N atoms protonated, there should be a band at approximately 3200 cm⁻¹ that corresponds to the imine NH stretch. It is not possible to determine from the experimental IR data whether this band is in fact present as the pyrrole NH stretch is also predicted in this region and is a fairly broad band. This pyrrole NH peak disappears on chelation of the ligand to the gold(III) ion. The frequencies of the pyrrole NH stretching vibration are given in Table 5.2 below.

The frequencies of the pyrrole NH stretching band are slightly lower than the bands reported for secondary amines which are in the region of $3500\text{-}3300\text{ cm}^{-1}$.² Hydrogen bonding can lower the force constant of the NH and thus lower the frequency of the absorption band.⁹ The macrocyclic and pseudomacrocyclic ligands have been shown by X-ray crystallography to exhibit intramolecular hydrogen bonding while the acyclic ligand is involved in intermolecular hydrogen bonding, explaining the discrepancy.

Table 5.2: Pyrrole NH stretching bands for the Schiff base ligands.

Schiff base ligand	$\delta(\text{NH, pyrrole}) / \text{cm}^{-1}$
H ₂ L1	2836
H ₂ L2	2819
H ₂ L3	2842
H ₂ L4	N/A
H ₂ L5	2835
H ₂ L6	2845
H ₂ L7	2837
H ₂ L8a	2846
H ₂ L8b	2830
H ₂ L9	2830
H ₂ L10	2835
H ₂ L11	2831
H ₂ L12	2929

A comparison of the IR spectra of H₂L1 and [Au(L1)](PF₆) in Figure 5.2 highlight the characteristic features of these compounds that have been discussed above. There is no notable band in the region $3500\text{-}3000\text{ cm}^{-1}$ in the spectrum of the gold(III) complex which could correlate to an NH stretch which is present in the ligand spectrum. This is consistent with chelation of the metal ion with deprotonation of the N atoms. The ligand spectrum contains two C=N stretches indicating that an asymmetric tautomer may be present. There is only one C=N stretch in the gold(III) spectrum indicating that the coordination sphere is symmetrical. There is a shift to lower frequency for the C=N stretch from 1642 and 1600 in the ligand to 1572 cm^{-1} in the complex. The spectrum of the gold(III) chelate also shows the presence of a hexafluorophosphate(V) counterion with a strong P-F stretch at 832 cm^{-1} .

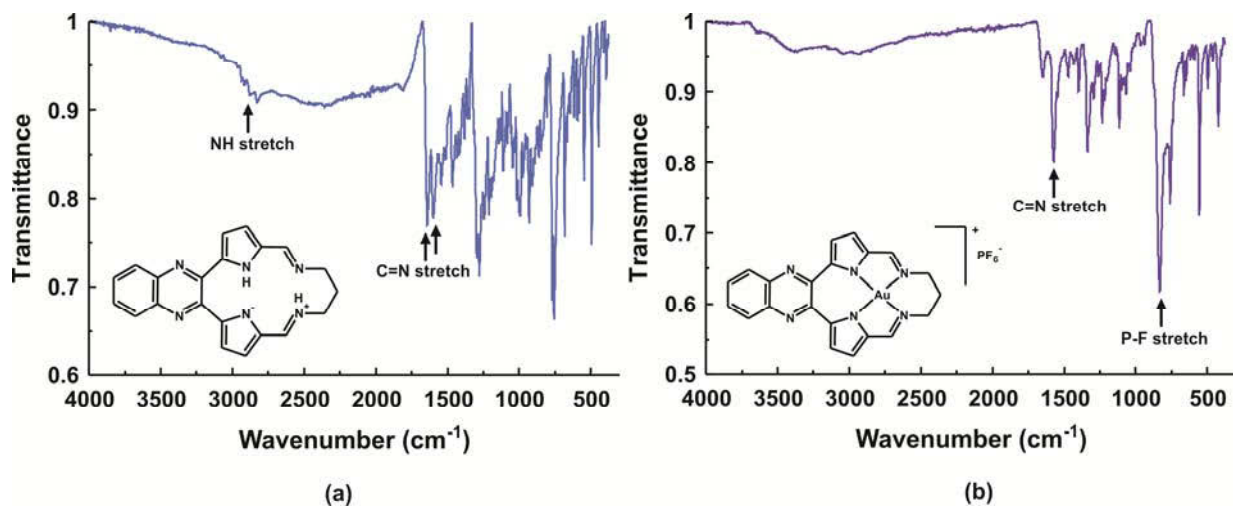


Figure 5.2: IR spectrum of (a) H₂L1 and (b) [Au(L1)](PF₆).

The complex $[\text{Au}(\text{L4})](\text{PF}_6)$ has a chlorine group attached to the central carbon of the three-carbon bis(pyrrolide-imine) bridging unit. This is reflected in the IR spectrum with a peak in the region of 765 cm^{-1} which falls in the standard range of $780\text{-}550\text{ cm}^{-1}$ for this type of bond.¹ The ligand, $\text{H}_2\text{L7}$, and complex $[\text{Au}(\text{L7})](\text{PF}_6)$ have a fluorine substituent attached to the quinoxaline tail. This results in C-F stretching bands in the IR spectrum at 1296 cm^{-1} for $\text{H}_2\text{L7}$ and 1334 cm^{-1} for $[\text{Au}(\text{L7})](\text{PF}_6)$ which fall in the standard range $1400\text{-}1000\text{ cm}^{-1}$ for this vibrational mode.¹

The ligands $\text{H}_2\text{L8a}$ and $\text{H}_2\text{L8b}$ and the complex $[\text{Au}(\text{L8b})](\text{PF}_6)$ show the presence of the $\text{C}\equiv\text{N}$ stretching bands at 2227 cm^{-1} , 2217 cm^{-1} and 2230 cm^{-1} , respectively. These values are close to the reported $\text{C}\equiv\text{N}$ stretching range of $2260\text{ to }2240\text{ cm}^{-1}$.¹ Nitrile bonds, in conjugation with double bonds or aromatic ring, tend to resonate at lower frequencies, which is the case here as the nitrile groups are substituents on conjugated pyrazine rings.¹ There are few functional groups that resonate in this region and it is therefore likely that this band is due to the nitrile functional group. The aromatic nature of the nitrile group in the compounds is responsible for the absorption band being intense.¹ The ligand $\text{H}_2\text{L8b}$ and the complex $[\text{Au}(\text{L8b})](\text{PF}_6)$ also have methoxy groups attached to the pyrazine ring. This C-O stretch is observed in the spectra at 1285 cm^{-1} for $\text{H}_2\text{L8b}$ as a strong band and at 1290 cm^{-1} for $[\text{Au}(\text{L8b})](\text{PF}_6)$. The standard frequency for a C-O stretch is in the range $1300\text{-}1000\text{ cm}^{-1}$.¹ Figure 5.3(a) illustrates these key vibrational modes for $\text{H}_2\text{L8b}$.

The ligand, $\text{H}_2\text{L11}$, and the complex, $[\text{Au}(\text{L11})](\text{PF}_6)$, show the presence of OH stretching bands at 3300 and 3275 cm^{-1} , respectively. Reportedly, a broadening of the OH stretching vibration is observed for intermolecular hydrogen bonding in the range from $3400\text{ to }3300\text{ cm}^{-1}$.^{1,2} Both these compounds also show C-O stretching bands in the standard region of $1300\text{ to }1000\text{ cm}^{-1}$. $\text{H}_2\text{L11}$ has a C-O band at 1098 cm^{-1} and $[\text{Au}(\text{L11})](\text{PF}_6)$ has a C-O stretch at 1051 cm^{-1} . These are aliphatic C-O bonds and thus the values are closer to 1000 cm^{-1} ; aromatic C-O bonds would be nearer to 1300 cm^{-1} . Figure 5.3(b) shows the IR spectrum of $\text{H}_2\text{L11}$.¹

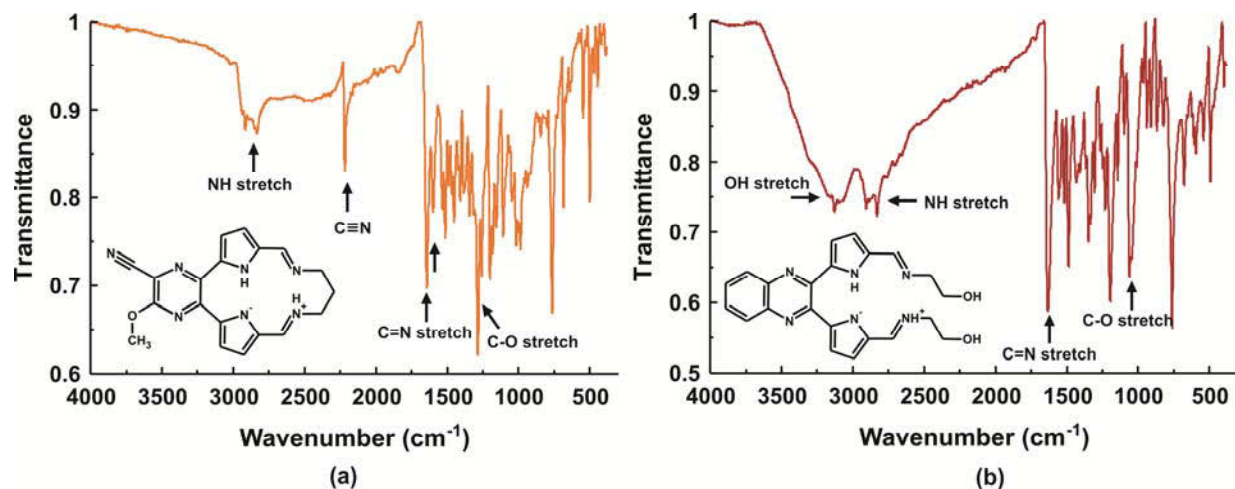


Figure 5.3: IR spectrum of (a) $\text{H}_2\text{L8b}$ and (b) $\text{H}_2\text{L11}$ highlighting selected resonance frequencies.

5.2 UV/Visible Spectroscopy

5.2.1 Introduction

Molecules can absorb well-defined amounts of energy to increase their vibration and rotational energy as well as to increase the energy of their electrons (Equation 5.1).⁴ The energy changes involved to excite electrons are greater than the energy changes involved in vibration and rotation and correspond to radiation in the ultraviolet (200-400 nm) and visible (400-750 nm) regions of the electromagnetic spectrum.⁴

When energy is absorbed by molecules or atoms, they move from the low energy ground state to the higher energy excited state. The electromagnetic radiation that is absorbed has energy exactly equal to the energy difference between the excited and ground states.¹ In UV/visible spectroscopy, when a molecule absorbs energy, an electron is promoted from an occupied orbital to an unoccupied orbital of greater energy. The most probable transition is from the highest occupied molecular orbital (HOMO) to the lowest unoccupied molecular orbital (LUMO).¹ For most molecules, the lowest energy occupied orbitals are the σ orbitals corresponding to σ bonds. The π orbitals lie at higher energy levels and orbitals that hold unshared electron pairs, the non-bonding (n) orbitals, are at even higher energies. The unoccupied or antibonding orbital (π^* and σ^*) are the highest energy orbitals.¹ In compounds other than alkanes, electrons can undergo several possible transitions of different energies, Figure 5.4(a). The energy required to move from the HOMO to the LUMO is less than the energy required to bring about a transition from a lower energy level to the LUMO. Not all transitions that appear possible are observed. Certain restrictions, called the selection rules, give rise to forbidden transitions.¹

In inorganic chemistry the majority of metal chelates exhibit charge-transfer bands. These transitions can either be from a predominantly metal-based molecular orbital to a predominantly ligand-based molecular orbital giving a metal-to-ligand charge transfer (MLCT) band.¹⁰ The inverse is also possible where charge transfer from a ligand MO to a metal-based MO occurs; ligand to metal charge transfer (LMCT). The latter is more relevant for gold(III) chelates as the highly oxidised metal centre is not able to transfer electron density to a ligand-based MO.¹⁰ Another possible transition in metal chelates is a d-d transition where an electron jumps from one d-orbital of a metal to another. This is possible since the d-orbitals are not all degenerate. The extent of the d-orbital splitting is dependent on the metal, its oxidation state and the coordinated ligands.¹⁰

Electronic energy levels in aromatic molecules are more complicated than those depicted in Figure 5.4 (a). Using benzene as an example, the UV/vis spectrum contains three $\pi \rightarrow \pi^*$ bands.¹¹ It would be predicted that four transitions are possible, but as each transition has the same energy, only one band would be observed in the UV/vis spectrum. However, due to electron-electron repulsion and symmetry, the actual energy states are modified with three electronic transitions taking place. Two of these bands are referred to as primary bands and are at 184 and 202 nm while the third band is referred to as the secondary band and is at approximately 260 nm.¹¹ As one of the primary bands is at about 180 nm it is not observed on standard spectrophotometers. Substitution on the ring can cause a bathochromic (shift to longer wavelength) and hyperchromic (increase in intensity) shifts, but these shifts are difficult to predict.¹

The nuclei that the electrons hold together in bonds play an important role in determining which wavelengths of radiation are absorbed.¹ The nuclei determine the strength with which the electrons are bound and influence the energy spacing between ground and excited states. The energy of a transition and the wavelength of radiation absorbed are properties of groups of atoms called chromophores rather than the electrons themselves.¹

UV absorption occurs over a wide range of wavelengths because molecules usually have many excited modes of vibration and rotation.¹ The energy levels for these vibrational and rotational states are quite closely spaced corresponding to smaller energy differences than those of electronic levels. The rotational and vibrational levels are thus superimposed on the electronic levels and a molecule may undergo electronic and vibrational-rotation excitation at the same time, Figure 5.4(b). As there are so many possible transitions differing from each other by only a very small amount, these transitions are recorded as a broad band by UV/vis spectrometers.¹

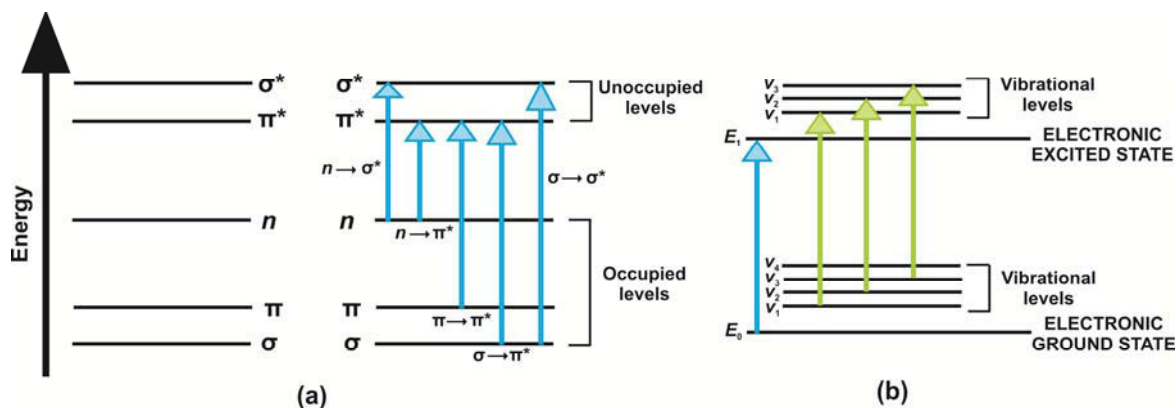


Figure 5.4: (a) Electronic energy levels and transitions. (b) Electronic and vibrational transitions superimposed (rotational levels have been omitted for clarity).¹

In a UV/visible spectrophotometer, light from a continuous light source is passed through a monochromator (a prism, grating or even a filter) to select a single wavelength.¹²⁻¹⁶ Light of the desired wavelength with an intensity, I_0 , hits a sample in a cell called a cuvette of length, L . The intensity of the beam exiting the sample is I where $I \leq I_0$ as the sample absorbs the light.¹²⁻¹⁶ In a double-beam spectrophotometer, light passes alternately through the sample and reference cuvettes. Using a reference cuvette containing pure solvent is important as it compensates for absorption due to the cuvette and solvent or light scattering.¹²⁻¹⁶ A double-beam spectrophotometer, as shown in Figure 5.5, alternates between cuvettes by using a chopper which is a motor that rotates a mirror into and out of the light path. When the chopper is not deflecting the beam, the light passes through the sample and the detector measures the intensity; however, when the chopper deflects the beam through the reference cuvette, the detector reads the reference value.¹²⁻¹⁶ The beam is chopped several times per second.

A spectrophotometer can measure the transmittance, T , which is defined as the fraction of the original light passing through the sample.¹²⁻¹⁶

$$T = \frac{I}{I_0} \quad 5.2$$

However, absorbance is a more useful quantity and can be easily converted to from transmittance.¹²⁻¹⁶

$$A = \log\left(\frac{I_0}{I}\right) = -\log T \quad 5.3$$

Absorbance is important because according to Beer's law given in Equation 5.4, it is directly proportional to the concentration of the sample:

$$A = \varepsilon \times c \times L \quad 5.4$$

Where A is the absorbance (it is dimensionless), c is the concentration of the sample (in units mol dm^{-3}), L is the pathlength (with units of cm) and ε is the extinction coefficient (with the units $\text{M}^{-1}\text{cm}^{-1}$).¹²⁻¹⁶ From this equation the extinction coefficient can be easily calculated.

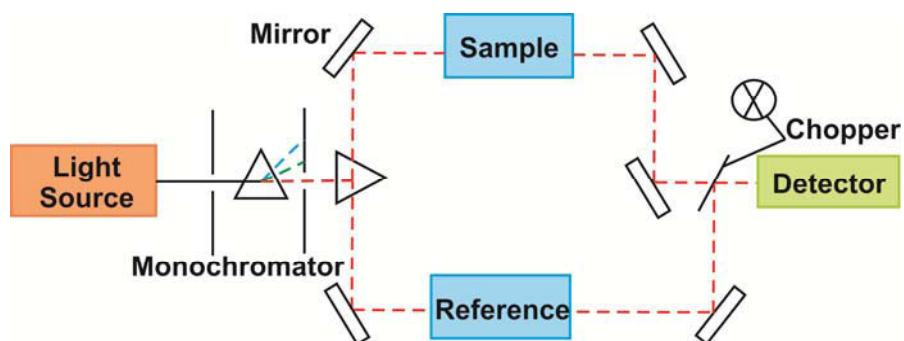


Figure 5.5: Schematic diagram of a double-beam UV/Vis spectrophotometer.¹⁶

The UV/visible spectra of the quinoxaline-based macrocycles and pseudomacrocycles are expected to be dominated by $\pi \rightarrow \pi^*$ transitions due to the aromatic quinoxaline and pyrazine rings, pyrrole rings and imine bonds. For alkanes the only possible transitions are $\sigma \rightarrow \sigma^*$.¹ These transitions are at such high energy that the wavelengths of UV light required are not accessible experimentally with standard spectrometers. Alcohols, ethers, nitriles and amines all have $n \rightarrow \sigma^*$ transitions at 175-200 nm which are also out of the range of standard spectrometers.¹ Thus the UV/visible spectra will be unaffected by the alkyl di(azomethine) bridge and substituents on the quinoxaline and pyrazine tails unless these substituents significantly modulate the HOMO-LUMO gap for the $\pi \rightarrow \pi^*$ transitions. The spectra for the gold(III) complexes are expected to have ligand-to-metal charge-transfer bands in the near UV or visible regions and $\pi \rightarrow \pi^*$ transitions at higher wavelengths.

The distinctive UV/visible spectra of the dipyrrolylquinoxaline-based ligands and complexes means that they have found applications as sensors for detecting mercury(II) and other toxic metal ions.¹⁷ Heavy metals can be easily chelated and detected in organic solvents, but it is difficult to chelate heavy metals in an aqueous environment with few reported complexes selectively detecting mercury(II) in aqueous solution. Quinoxaline-based ligands undergo a change in the electronic density of the chromophore on complexation with metal ions such as mercury(II) resulting in significant changes in the fluorescence intensity and absorption spectra.¹⁷ The presence of mercury(II) ions can be detected by a decrease in absorbance of the peak at ca. 309 nm of these dipyrrolylquinoxaline-based compounds. Dipyrrolylquinoxaline derivatives have also found applications as anion receptors.¹⁷

In this work UV/visible spectroscopy was used to determine the types of transitions occurring in the free ligands and metal complexes as well as to determine the extinction coefficients of the absorption bands. This

information coupled with IR spectroscopy and NMR spectroscopy was used to gain invaluable structural information.

5.2.2 UV/visible Spectroscopy: Results and Discussion

The ligands and complexes synthesized in this work have large aromatic chromophores and extended conjugation, resulting in complex absorption spectra. The electronic spectra of the macrocyclic H_2L1 and the gold(III) complex, $[Au(L1)](PF_6)$, as well as the spectra of the pseudomacrocycle, H_2L10 , and the gold(III) complex, $[Au(L10)](PF_6)$ are given as representative examples of the UV/vis spectra in Figure 5.6.

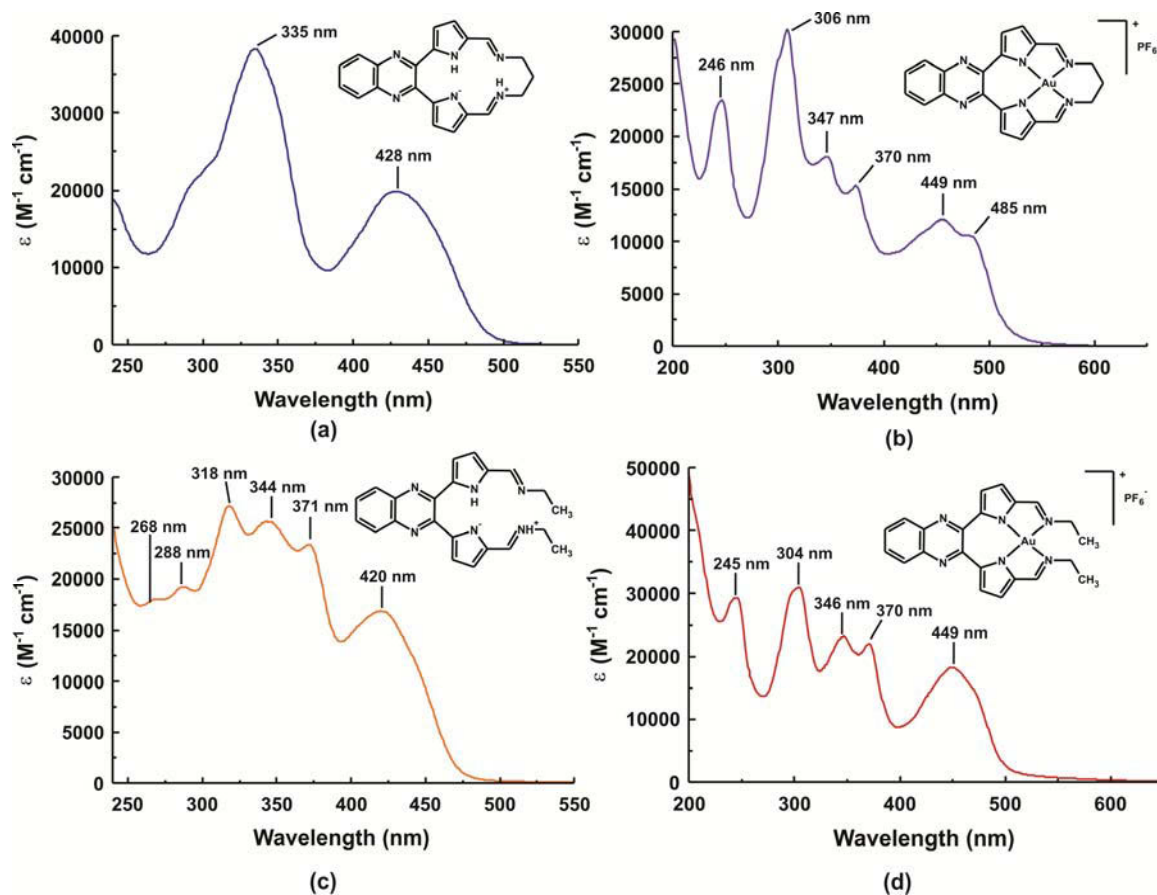


Figure 5.6: Electronic spectra of (a) H_2L1 in chloroform, (b) $[Au(L1)](PF_6)$ in acetonitrile, (c) H_2L10 in chloroform and (d) $[Au(L10)](PF_6)$ in acetonitrile.

The spectrum of H_2L10 has more bands in its electronic spectrum than H_2L1 , although the basic shape of the spectra are the same. Both spectra contain a broad band at *ca.* 420 nm, H_2L1 also contains a broad band at *ca.* 335 nm with a shoulder at *ca.* 300 nm while the spectrum of H_2L10 is more resolved with three bands in the region of 344 nm and two bands at *ca.* 280 nm. The intensity of the broad band in the spectrum of H_2L1 at *ca.* 420 nm is $1.95 \times 10^4 M^{-1} cm^{-1}$ while the same band in H_2L10 has a similar intensity of $1.67 \times 10^4 M^{-1} cm^{-1}$. The band at 335 nm in H_2L1 has a high intensity of $3.76 \times 10^4 M^{-1} cm^{-1}$ while H_2L10 has less intense bands ranging from $1.79 \times 10^4 M^{-1} cm^{-1}$ to $2.69 \times 10^4 M^{-1} cm^{-1}$. All the quinoxaline macrocyclic ligands have very similar electronic spectra to H_2L1 while the pseudomacroyclic ligands have spectra similar to those of H_2L10 . Substitution on the quinoxaline ring appears to make little difference to the electronic spectra with H_2L5 ,

H₂L6 and H₂L7 all having absorption bands at almost identical wavelengths with the most highly substituted ligand, H₂L5, having the most intense bands. The electronic spectrum of the pyrazine macrocyclic ligand that was recorded in chloroform showed similar bands to those described for H₂L1 with a broad band at 423 nm and two peaks at 364 nm and 322 nm. The acyclic ligand H₂L12 does not have large aromatic chromophores and hence has a more simple absorption spectrum with one very intense band at 287 nm ($\epsilon = 2.50 \times 10^4 \text{ M}^{-1} \text{ cm}^{-1}$) and a weaker band at 427 nm ($\epsilon = 17.7 \text{ M}^{-1} \text{ cm}^{-1}$). Table 5.3 lists the λ_{max} values for the ligands and the corresponding extinction coefficients.

Table 5.3: Summary of the λ_{max} and extinction coefficient values for the absorption bands of the free ligands.

	Solv.	$\lambda_{\text{max}}/\text{nm}$ ($\epsilon/\text{M}^{-1} \text{ cm}^{-1}$)	$\lambda_{\text{max}}/\text{nm}$ ($\epsilon/\text{M}^{-1} \text{ cm}^{-1}$)	$\lambda_{\text{max}}/\text{nm}$ ($\epsilon/\text{M}^{-1} \text{ cm}^{-1}$)	$\lambda_{\text{max}}/\text{nm}$ ($\epsilon/\text{M}^{-1} \text{ cm}^{-1}$)	$\lambda_{\text{max}}/\text{nm}$ ($\epsilon/\text{M}^{-1} \text{ cm}^{-1}$)	$\lambda_{\text{max}}/\text{nm}$ ($\epsilon/\text{M}^{-1} \text{ cm}^{-1}$)
H ₂ L1	CH ₃ Cl	335 (3.76×10^4)	428 (1.95×10^4)				
H ₂ L2	CH ₃ Cl	334 (3.51×10^4)	427 (1.84×10^4)				
H ₂ L3	CH ₃ Cl	333 (3.45×10^4)	346 (3.56×10^4)	421 (1.77×10^4)			
H ₂ L5	CH ₃ Cl	338 (4.58×10^4)	430 (2.40×10^4)				
H ₂ L6	CH ₃ Cl	336 (3.69×10^4)	430 (1.90×10^4)				
H ₂ L7	CH ₃ Cl	332 (3.76×10^4)	430 (1.93×10^4)				
H ₂ L8a	DMSO	323 (2.6×10^4)	379 (3.17×10^4)	476 (1.92×10^4)			
H ₂ L8b	CH ₃ Cl	322 (2.71×10^4)	364 (2.21×10^4)	423 (1.52×10^4)			
H ₂ L9	CH ₃ Cl	269 (1.18×10^4)	287 (1.22×10^4)	317 (1.69×10^4)	356 (1.47×10^4)	372 (1.47×10^4)	420 (1.02×10^4)
H ₂ L10	CH ₃ Cl	270 (1.79×10^4)	288 (1.91×10^4)	318 (2.69×10^4)	344 (2.54×10^4)	371 (2.31×10^4)	420 (1.67×10^4)
H ₂ L11	CH ₃ Cl	268 (1.21×10^4)	288 (1.20×10^4)	318 (1.70×10^4)	358 (1.57×10^4)	373 (1.72×10^4)	421 (1.02×10^4)
H ₂ L12	CH ₃ Cl	287 (2.50×10^4)	427 (17.7)				

Density functional theory simulations were used to predict the transitions of the UV/visible spectra. The simulations gave results that were in good agreement with the experimental electronic spectra of the ligands and will be further discussed in Chapter Six. As expected, the spectra of the ligands are completely dominated by $\pi \rightarrow \pi^*$ transitions with all the bands in the UV/vis spectra of the macrocyclic and pseudomacrocyclic ligands being of this type. The simulations did indicate that although the bands and shoulders at *ca.* 280 nm of all the macrocyclic and pseudomacrocyclic ligands show dominant $\pi \rightarrow \pi^*$ transitions, they do also contain a small amount of $\sigma \rightarrow \pi^*$ character. It was originally predicted, due to their shape and decreasing intensity, that the three peaks at *ca.* 344 nm in the UV/vis spectrum of the pseudomacrocycles were due to vibronic progression. However, this was proved not to be the case as the computational calculations, which can only predict electronic transitions, showed the presence of these peaks.

Compounds containing both conjugated π systems and unshared electron pairs, such as the ligands reported in this work, are expected to show the absorption bands due to the following electronic transitions: low intensity $n \rightarrow \pi^*$ bands at longer wavelengths and high intensity $\pi \rightarrow \pi^*$ bands at shorter wavelengths. As described the $\pi \rightarrow \pi^*$ bands were easily identifiable for all the ligands; however, in the case of the macrocycles and pseudomacrocycles the $n \rightarrow \pi^*$ band could not be experimentally identified and may be obscured by the stronger $\pi \rightarrow \pi^*$ bands. In the case of the acyclic ligand, H₂L12, the $n \rightarrow \pi^*$ was observed at 427 nm and could be confidently assigned due to its minimal extinction coefficient. A high intensity $\pi \rightarrow \pi^*$ band at 287 nm was also observed.

The quinoxaline-based macrocyclic and pseudomacrocyclic gold(III) complexes have very similar electronic spectra, Figure 5.5. The spectrum of [Au(L1)](PF₆) has two low intensity bands at ca. 460 nm while [Au(L10)](PF₆) has one broad band at 449 nm. The rest of the bands are similar with both complexes having bands at approximately 370 nm, 347 nm, 305 nm and 245 nm. The intensity of the bands ranges from 1×10^4 to $3 \times 10^4 \text{ M}^{-1} \text{ cm}^{-1}$ for these bands. The electronic spectra of the complexes are different to those of the ligands with an increase in the number of bands observed in the metal complex spectra indicating that metallation has been successful. Substitution on the quinoxaline ring appears to have made little difference to the electronic spectra of the complexes, as was the case with the ligands. The pyrazine-based macrocyclic complex has fewer, broader peaks, but at very similar shifts to the quinoxaline-based macrocycles. The acyclic complex, [Au(L12)](PF₆) has two bands at 284 nm and 372 nm. Table 5.4 lists the λ_{max} values for the gold(III) complexes and the corresponding extinction coefficients.

DFT simulations of the gold(III) complexes did not predict accurate electronic spectra when compared to the experimental spectra of the complexes. The simulations showed fewer peaks with no peaks below 330 nm. Some bands differed greatly in intensity and shift. DFT simulations showed that all the bands had $\pi \rightarrow \pi^*$, $\pi \rightarrow \sigma^*$ and ligand-to-metal charge-transfer (LMCT) character. This will be discussed further in Chapter Six.

As the simulations were not very accurate, literature was used to explain the observed electronic spectra. Since gold(III) is an oxidizing metal ion, low energy LMCT transitions are an important feature of the spectra.¹⁸ Metal-to-ligand charge-transfer (MLCT) bands are not observed in electronic spectra owing to the lack of reducing properties of gold(III).¹⁸ It is reported that LMCT transitions are observed in the visible region of the spectrum when the metal is in a high oxidation state and the ligands contain non-bonding orbitals.¹⁰ Some gold(III) complexes in acetonitrile are reported to have LMCT transitions in the near UV region of the spectrum or with more reducing ligands in the visible region.¹⁸ The spectra of [Au(III)(dbbpy)(tdt)]⁺ and [Au(III)(η^2 -C, N-ppy)(tdt)] in chloroform with dbbpy = dibutyl-2,2'-bipyridyl, η^2 -C,N-ppy- = O-C-deprotonated 2-phenylpyridine and tdt²⁻ = 4-toluene-1,2-dithiolate, display fairly intense absorption in the visible region at $\lambda_{\text{max}} = 440 \text{ nm}$ and 408 nm , respectively.¹⁹ These bands can be attributed to tdt²⁻ to Au(III) LMCT.¹⁹ Other pyridyl- and isoquinolyl-amido Au(III) chelates have spectra characterised by more intense $\pi \rightarrow \pi^*$ bands between 270 and 330 nm and multiple, weaker LMCT bands in the region 330-600 nm.²⁰

Using this information, the bands in the region 450 to 480 nm of the reported complexes are most likely LMCT bands with the more intense bands below 400 nm due to $\pi \rightarrow \pi^*$ transitions and $\pi \rightarrow \sigma^*$ transitions. The acyclic ligand has a $\pi \rightarrow \pi^*$ transition at 284 nm and $\pi \rightarrow \sigma^*$ transition at 372 nm as determined from similar gold(III) complexes.²¹

Table 5.4: Summary of the λ_{\max} and extinction coefficients for the absorption bands of the gold(III) complexes.

	Solv.	λ_{\max}/nm ($\epsilon/\text{M}^{-1}\text{cm}^{-1}$)	λ_{\max}/nm ($\epsilon/\text{M}^{-1}\text{cm}^{-1}$)	λ_{\max}/nm ($\epsilon/\text{M}^{-1}\text{cm}^{-1}$)	λ_{\max}/nm ($\epsilon/\text{M}^{-1}\text{cm}^{-1}$)	λ_{\max}/nm ($\epsilon/\text{M}^{-1}\text{cm}^{-1}$)	λ_{\max}/nm ($\epsilon/\text{M}^{-1}\text{cm}^{-1}$)	λ_{\max}/nm ($\epsilon/\text{M}^{-1}\text{cm}^{-1}$)
[Au(L1)]	CH ₃ CN	246 (2.33×10^4)	309 (3.01×10^4)	346 (1.80×10^4)	373 (1.52×10^4)	455 (1.20×10^4)	485 (1.04×10^4)	
[Au(L2)]	CH ₃ CN	230 (1.76×10^4)	249 (1.44×10^4)	309 (1.61×10^4)	348 (8.79×10^3)	375 (8.68×10^3)	458 (6.64×10^3)	481 (6.34×10^3)
[Au(L3)]	CH ₃ CN	244 (1.64×10^4)	306 (1.94×10^4)	347 (1.37×10^4)	370 (1.34×10^4)	449 (9.82×10^3)	485 (1.04×10^4)	
[Au(L4)]	CH ₃ CN	246 (2.15×10^4)	308 (2.69×10^4)	348 (1.37×10^4)	376 (1.64×10^4)	455 (1.20×10^4)	481 (1.15×10^4)	
[Au(L5)]	CH ₃ CN	248 (2.53×10^4)	316 (3.39×10^4)	350 (2.12×10^4)	378 (1.85×10^4)	457 (1.54×10^4)	484 (1.41×10^4)	
[Au(L6)]	CH ₃ CN	247 (2.02×10^4)	310 (2.56×10^4)	348 (1.60×10^4)	375 (1.43×10^4)	457 (1.11×10^4)	484 (1.04×10^4)	
[Au(L7)]	CH ₃ CN	245 (2.98×10^4)	309 (3.81×10^4)	347 (2.18×10^4)	371 (1.8×10^4)	458 (1.54×10^4)	484 (1.24×10^4)	
[Au(L8b)]	CH ₃ CN	248 (1.84×10^4)	304 (3.01×10^4)	369 (2.93×10^4)	451 (1.58×10^4)			
[Au(L9)]	CH ₃ CN	244 (2.30×10^4)	302 (2.55×10^4)	345 (1.90×10^4)	368 (1.75×10^4)	448 (1.43×10^4)		
[Au(L10)]	CH ₃ CN	245 (2.92×10^4)	304 (3.08×10^4)	346 (2.31×10^4)	370 (2.18×10^4)	449 (1.81×10^4)		
[Au(L11)]	DMSO	302 (2.33×10^4)	339 (2.06×10^4)	423 (1.12×10^4)	454 (1.27×10^4)			
[Au(L12)]	CH ₃ CN	284 (1.45×10^4)	372 (1.10×10^4)					

5.3 NMR Spectroscopy

5.3.1 Introduction

Nuclear magnetic resonance (NMR) is an important spectroscopic method that gives information about the number of magnetically distinct atoms being studied. Many atomic nuclei have a property called spin and the nuclei behave as if they were spinning.^{1,22,23} The most common nuclei that possess spin include ¹H, ²H, ¹³C, ¹⁴N, ¹⁷O and ¹⁹F. For each nucleus with spin the number of allowed spin states it may adopt is quantized and is determined by its nuclear spin quantum number.^{1,22,23} A proton has two spin states for its nucleus; +½ and -½. Spin states are not of equal energy in an applied magnetic field because the nucleus is a charged particle and any moving charge generates a magnetic field of its own.^{1,22,23} The nucleus has a magnetic moment, μ , generated by its charge and spin. A hydrogen nucleus may have a clockwise or anticlockwise spin and the nuclear magnetic moments are either aligned with the applied field or opposed to it. NMR works when nuclei aligned with an applied field are induced to absorb energy and change their spin with respect to the applied field.^{1,22,23} The energy absorbed is quantized and the energy absorbed must equal the energy difference between the two states. This energy difference is due to the strength of the applied magnetic field.

There are specific field strengths and frequencies at which nuclei absorb energy and make spin transitions. Not all protons in a molecule absorb energy at exactly the same frequency. This is because the protons in a

molecule are surrounded by electrons and exist in slightly different magnetic environments from one another.¹ In an applied magnetic field the valence shell electrons begin to circulate and this generates a counter magnetic field that opposes the applied magnetic field. Thus each proton is shielded from the applied magnetic field to an extent depending on the electron density surrounding it.¹ Each proton in a molecule is in a slightly different chemical environment and consequently has a slightly different amount of electronic shielding, which results in a slightly different resonance frequency and thus chemical shift.¹

A pulsed Fourier Transform instrument works by giving a sample a burst of energy or pulse that excites all the magnetic nuclei in the molecule at the same time.¹ When the pulse is discontinued the excited nuclei relax and return to their original spin state. As each excited state relaxes, it emits electromagnetic radiation. As a molecule contains many different nuclei, many different frequencies of electromagnetic radiation are emitted simultaneously.¹ The emission is called a free-induction decay (FID) signal. Usually a mathematical method called Fourier Transform (FT) analysis is used to extract individual frequencies to produce the NMR spectrum.

The compounds reported in this work have been studied by ¹H and ¹³C NMR as well as ¹⁹F and ³¹P NMR where applicable. The ¹H and ¹³C NMR spectra of the free ligands and the gold(III) complexes are expected to be similar. The main difference is that the gold(III) spectrum should not contain any NH signals in the ¹H NMR spectrum and the remaining peaks should experience a downfield shift when compared to the free ligand. This is due to the deshielding that the carbon and hydrogen nuclei of the gold(III) complexes experience as the electron withdrawing effects of the gold(III) cation reduce the valence electron density around the carbon and proton nuclei. These electrons can no longer shield the nuclei from the applied magnetic field and they experience a downfield shift. The deshielding effect should be felt by the nuclei closest to the gold(III) cation with the deshielding effect reducing as the distance from the gold(III) cation increases.

Although the gold(III) ion is diamagnetic, ¹⁹⁷Au NMR is not possible.⁷ This is due to the fact that the nucleus is quadrupolar (I = 3/2) and it has a large quadrupole moment and low gyromagnetic ratio, making the frequency of the gold(III) nucleus beyond the range of most NMR spectrometers.⁷ Only the most symmetrical gold(III) compounds can exhibit a ¹⁹⁷Au NMR signal sharp enough to be observed at high concentrations and even then only with specialised NMR spectrometers.

The main objective of NMR spectroscopy is in this work to fully characterize the ligands and gold(III) Schiff base complexes and to provide important structural information on these compounds. It also allows the effects of metal chelation to be determined by comparison of the free ligand and gold(III) spectra. Both 1D (¹H, ¹³C and DEPT) and 2D NMR (COSY, HSQC and HMBC) spectra were used to elucidate the structure of the ligands and gold(III) chelates.

5.3.2 NMR Spectroscopy: Results and Discussion

Chelation of the gold(III) ion to the Schiff base ligands resulted in a downfield shift in the ¹H NMR spectra of the gold(III) complexes relative to the free ligand spectra. A summary of the chemical shifts from the ¹H NMR spectra of the ligand, H₂L3, and the gold(III) complex, [Au(L3)](PF₆), is given in Table 5.5. The spectra of both compounds are shown in Figure 5.7.

Table 5.5: ^1H NMR chemical shifts (DMSO- d_6 , 303 K) for $\text{H}_2\text{L3}$ and $[\text{Au}(\text{L3})](\text{PF}_6)$.

	Proton	$\text{H}_2\text{L3}$ (ppm)	$[\text{Au}(\text{L3})](\text{PF}_6)$ (ppm)
Butyl bridge	$-\text{CH}_2\text{CH}_2\text{CH}_2\text{CH}_2-$ (<i>k</i>)*	1.96	2.04
Butyl bridge	$-\text{CH}_2\text{CH}_2\text{CH}_2\text{CH}_2-$ (<i>j</i>)	3.77	4.31
Pyrrole	$-\text{CH}=\text{C}=\text{N}_{\text{imine}}-$ (<i>g</i>)-	7.00	7.45
Pyrrole	$\text{CH}=\text{C}=\text{N}_{\text{quinoxaline}}-$ (<i>f</i>)	7.49	8.06
Quinoxaline	$-\text{CH}=\text{CH}-\text{C}-$ (<i>a</i>)	7.75	7.96
Quinoxaline	$-\text{CH}-\text{C}-\text{N}-$ (<i>b</i>)	7.99	8.18
Imine	$-\text{CH}=\text{N}_{\text{imine}}-$ (<i>i</i>)	8.27	8.74
Imine	$-\text{NH}$ (<i>m</i>)	11.24	N/A
Pyrrole	$-\text{NH}$ (<i>l</i>)	18.38	N/A

*Diagram showing the labelling scheme is available in Figure 5.7.

A comparison of the ^1H NMR chemical shifts of $\text{H}_2\text{L3}$ and $[\text{Au}(\text{L3})](\text{PF}_6)$ shows a significant downfield shift for the signals of the gold(III) chelate. The pyrrole and imine protons experience the greatest deshielding upon chelation to the gold(III) ion and hence show the largest downfield shift. The quinoxaline and butyl di(azomethine) bridging proton show the smallest deshielding effect as they are furthest from the gold(III) cation. This is clearly evident as the pyrrole protons in the ligand spectra sit upfield to the quinoxaline protons, but in the complex the pyrrole protons are deshielded to a greater effect than the quinoxaline rings such that the peak of one of the pyrrole protons now is positioned between the peaks of the quinoxaline protons. All the ligands and complexes exhibit similar spectra with the same deshielding effect. The ^1H NMR spectra are in agreement with the reported NMR spectra of previously reported bis(pyrrolide-imine) metal chelates.^{6,24}

A comparison of the chemical shifts for the ^{13}C NMR spectra of the complex of $\text{H}_2\text{L3}$ and $[\text{Au}(\text{L3})](\text{PF}_6)$ is shown in Table 5.6.

Table 5.6: ^{13}C NMR chemical shifts (DMSO- d_6 , 303 K) for $\text{H}_2\text{L3}$ and $[\text{Au}(\text{L3})](\text{PF}_6)$.

	Carbon	$\text{H}_2\text{L3}$ (ppm)	$[\text{Au}(\text{L3})](\text{PF}_6)$ (ppm)
Butyl bridge	$-\text{CH}_2\text{CH}_2\text{CH}_2\text{CH}_2-$ (<i>k</i>)*	27.85	23.68
Butyl bridge	$-\text{CH}_2\text{CH}_2\text{CH}_2\text{CH}_2-$ (<i>j</i>)	54.84	55.41
Pyrrole	$-\text{CH}=\text{C}=\text{N}_{\text{quinoxaline}}-$ (<i>f</i>)	116.81	118.92
Pyrrole	$-\text{CH}=\text{C}=\text{N}_{\text{imine}}-$ (<i>g</i>)	122.60	122.26
Quinoxaline	$-\text{CH}-\text{C}-\text{N}-$ (<i>b</i>)	128.19	128.52
Quinoxaline	$-\text{CH}=\text{CH}-\text{C}-$ (<i>a</i>)	129.65	131.69
Pyrrole	$-\text{C}_{\text{imine}}-\text{C}-\text{CH}$ (<i>h</i>)	131.02	139.64
Quinoxaline	$-\text{C}-\text{N}_{\text{quinoxaline}}=\text{C}-$ (<i>c</i>)	139.53	139.72
Quinoxaline	$-\text{N}_{\text{quinoxaline}}=\text{C}-\text{C}_{\text{pyrrole}}-$ (<i>d</i>)	143.56	135.69
Pyrrole	$-\text{C}_{\text{quinoxaline}}-\text{C}=\text{CH}-$ (<i>e</i>)	144.22	147.92
Imine	$-\text{CH}=\text{N}_{\text{imine}}-$ (<i>i</i>)	153.10	164.83

*Diagram showing the labelling scheme is available in Figure 5.7.

The comparative data in Table 5.6 shows that only the imine carbon atom experiences a significant downfield shift upon chelation to the gold(III) cation with the closer pyrrole α -carbon atoms experiencing a similar, although less pronounced, downfield shift. The pyrrole β -carbon atoms, quinoxaline and bridging carbon atoms do not show significant changes in their chemical shifts upon chelation to the gold(III) ion as they are further removed from the gold(III) cation. Full spectral assignments for the ligands and the gold(III) chelates are given in Chapter Two.

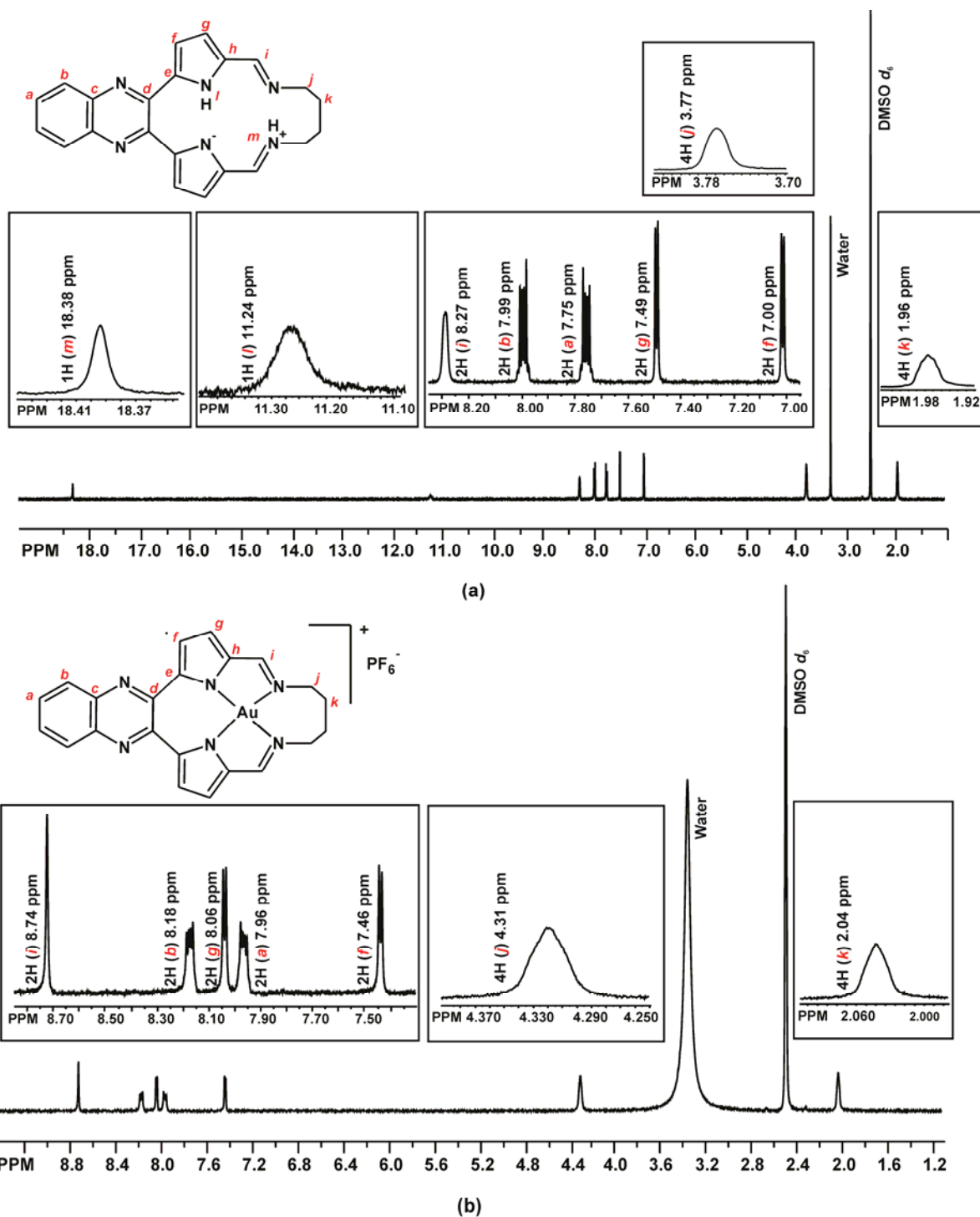


Figure 5.7: ^1H spectrum of (a) H_2L_3 and (b) $[\text{Au}(\text{L}_3)](\text{PF}_6)$ in $\text{DMSO}-d_6$ at 303 K showing the spectral assignments.

As described in Chapter Four, the macrocyclic ligands show that both pyrrole N atoms are not protonated in the solid state, but rather one pyrrole N atom and the diagonally opposite imine N atom are protonated. The same tautomer also appears to be favoured in solution as the NMR spectra for the ligands show a peak at *ca.* 11 ppm corresponding to a single imine N-H and another peak at *ca.* 18 ppm corresponding to a pyrrole N-H

proton. The shift of these protons is interesting as pyrrole N-H peaks are usually around 11 ppm. The assignment of these protons was done based on density functional theory calculations (Chapter Six) which clearly show that the pyrrole N-H proton is positioned more downfield than the imine N-H proton. Both these peaks are not present in the ^1H NMR spectra of the gold(III) complexes as there is concomitant deprotonation of the nitrogen atoms for gold(III) chelation to occur. The pseudomacrocyclic ligands do not have the imine N-H peak which indicates that they may be in the tautomeric form where both pyrrole nitrogen atoms are protonated. This is possibly true as the pseudomacrocyclic ligands have a greater degree of freedom than the macrocyclic ligands and the intramolecular hydrogen bonding effects in the pseudomacrocycles may be overcome in solution. However, the pyrrole NH signal in these compounds only corresponds to a single proton which may indicate that there is potentially proton exchange with water and the imine N-H thus obscuring the peak.

Another interesting observation from the ^1H NMR spectra of the macrocycles and pseudomacrocycles is that the imine CH peak in the spectra are either single broad peaks corresponding to two protons or there are two peaks each correlating to a single proton (spectra recorded at 303 K). This indicates that the two imine protons are not equivalent which would be the case if the compounds were asymmetric, as they are in the tautomeric form with the diagonally opposite pyrrole N and imine N atoms protonated. These data suggest that the tautomeric form, which dominates the solid state, similarly dominates the solution state. Table 5.7 lists the imine CH and NH shifts as well as the pyrrole NH shifts for the macrocyclic and pseudomacrocyclic ligands.

Table 5.7: ^1H NMR chemical shifts for selected protons of the macrocyclic and pseudomacrocyclic ligands at 303 K in $\text{DMSO-}d_6$.

Ligand	Imine CH (ppm)	Imine NH (ppm)	Pyrrole NH (ppm)
H ₂ L1	8.26 (2H)	12.21 (1H)	17.71 (1H)
H ₂ L2	8.19 (1H), 8.20 (1H)	12.13 (1H)	17.75 (1H)
H ₂ L3	8.27 (2H)	11.24 (1H)	18.38 (1H)
H ₂ L5	8.22 (1H), 8.23 (1H)	12.15 (1H)	17.64 (1H)
H ₂ L6	8.24 (2H)	12.18 (1H)	17.67 (1H)
H ₂ L7	8.22 (1H), 8.24 (1H)	12.24 (1H)	17.72 (1H)
H ₂ L8a	8.40 (1H), 8.41 (1H)	12.51 (1H)	17.56 (1H)
H ₂ L8b	8.34 (1H), 8.35 (1H)	12.19 (1H)	17.37 (1H)
H ₂ L9	8.24 (2H)	11.40 (1H)	
H ₂ L10	8.25 (2H)	11.41 (1H)	
H ₂ L11	8.21 (2H)	11.71 (1H)	

When the spectrum of H₂L3 is recorded at 223 K, the imine CH manifests as two single peaks, each of which integrate to one proton. At lower temperatures the movement or exchange of the NH protons is reduced and thus two peaks are observed. At lower temperatures the timescale of the proton exchange is reduced and becomes more comparable to the timescale of the NMR experiment thus two distinct resonances can be detected using NMR spectroscopy. The sample was then heated at 10 K intervals and spectra recorded at each temperature. As the sample is heated, the two peaks merge into a single peak which integrates to two protons. The temperature at which the two peaks merge to become one peak, where slow and fast exchange meet, is known as the coalescence temperature (T_c).²³ The coalescence temperature for the imine CH peaks of H₂L3 is 238 K. At 303 K the peak is a broad peak but on heating to 323 K the peak becomes sharp because at higher temperatures the rate of proton exchange has greatly increased. As the NMR spectra are

recorded at 303 K, the peak observed is a single broad peak but on cooling to 238 K the rate of proton exchange is reduced and the peak separates out to form two peaks. Figure 5.8(a) shows the stacked ^1H NMR spectra for $\text{H}_2\text{L3}$ in deuterated chloroform over a range of temperatures.

The pyrazine-based macrocyclic ligand, $\text{H}_2\text{L8a}$, exhibits two peaks. Integration of these peaks shows they correspond to a single proton each at 303 K. On heating the sample, the separate peaks coalesce, becoming one at 358 K. The same peak becomes sharper as the rate of exchange increases when the temperature is increased to 393 K. Figure 5.8(b) shows the stacked ^1H NMR spectra for $\text{H}_2\text{L8a}$ in deuterated DMF over a range of temperatures. The coalescence temperature for $\text{H}_2\text{L8a}$ is much higher than that for $\text{H}_2\text{L3}$, indicating that the proton movement or exchange is much faster in $\text{H}_2\text{L3}$ and the sample needs to be cooled to greater temperatures to slow the exchange. The imine NH and pyrrole NH peaks were also monitored as the temperature was increased for $\text{H}_2\text{L8a}$ to determine if the peaks would coalesce to become a single peak by increasing the speed of the proton exchange. Neither peak, however, showed any significant shift within the experimental temperature range.

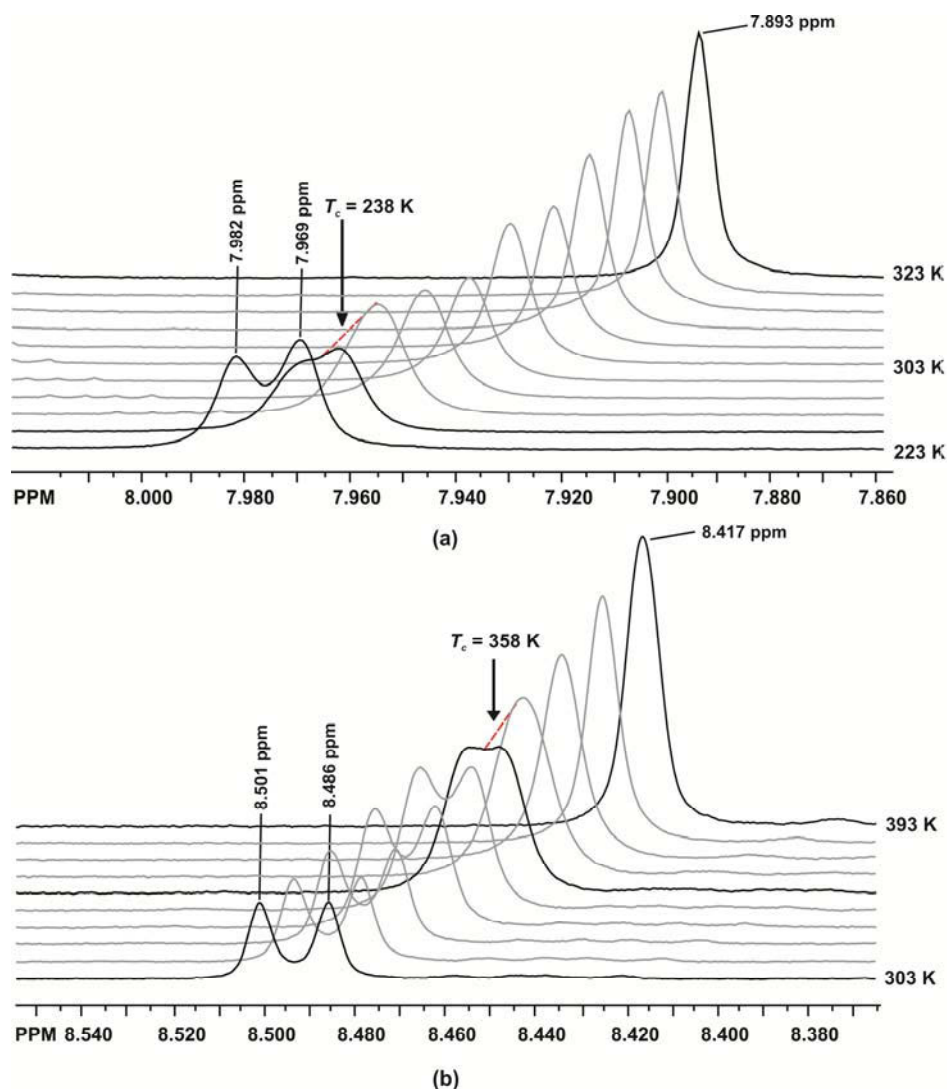


Figure 5.8: Stacked ^1H NMR spectra of the imine CH for (a) $\text{H}_2\text{L3}$ in chloroform and (b) $\text{H}_2\text{L8a}$ in DMF.

The NH tautomerism in porphyrins has been well studied by NMR spectroscopy and the mechanism by which the tautomers interconvert has been the subject of numerous studies.^{25,26} Two mechanisms of interconversion have been proposed: proton transfer either occurring by two single proton shifts via a *cis* intermediate or a simultaneous two proton shift. Limach and co-workers have determined, through variable temperature NMR and ¹⁵N NMR, that the proton transfer mechanism is via two single proton shifts.²⁷ Similar studies need to be carried out on our ligand system as part of the future work in order to determine the mechanism of proton transfer in these compounds.

Most of the ligands and gold(III) complexes are symmetric with the protons and carbon atoms on each side of the molecule in equivalent chemical environments. This results in a single signal for two equivalent protons in the NMR spectra. The quinoxaline-based macrocycles, H₂L6, H₂L7, and complexes, [Au(L6)](PF₆) and [Au(L7)](PF₆) are asymmetric as they contain either a methyl or a fluorine substituent on the quinoxaline tail. This results in splitting of the ¹H and ¹³C signals of the atoms on either side of the compound. The splitting effect is most evident in the quinoxaline protons and carbon atoms as there is a signal for each proton and carbon in this region. The pyrrole rings and three-carbon di(azomethine) bridge are further removed from the substituent and as such are not as affected by the asymmetric environment of the tail region. In the spectra of H₂L6 and [Au(L6)](PF₆), where the methyl substituent is neither strongly electron-withdrawing or electron donating, the splitting effect is minimal, even on the quinoxaline ring as although the peaks are split the difference in the chemical shifts is marginal. The methyl substituted compounds still have two peaks corresponding to two protons each for the pyrrole rings; however, these peaks have many coupling constants and appear as multiplets instead of doublets as in the spectra of the symmetrical compounds. The electron-withdrawing effect of the fluorine substituent in the spectra of H₂L7 and [Au(L7)](PF₆) has a greater influence on the splitting of the peaks with the pyrrole peaks also being in both the ¹H and ¹³C NMR spectra.

In an attempt to synthesize the pyrazine-based ligand, H₂L8a, the ligand H₂L8b was produced. It was determined by NMR spectroscopy that H₂L8b had been synthesized instead of H₂L8a. The spectra shown in Figure 5.9 clearly indicate an asymmetric ligand, H₂L8b, while the spectrum of H₂L8a shows a symmetric ligand. For every one pyrrole C-H peak obtained in the spectrum for H₂L8a, there are two peaks in the spectrum of H₂L8b highlighting the asymmetric nature of the ligand. There is also an extra peak present in the spectrum of H₂L8b at 4.14 ppm corresponding to three protons. As a typical methyl group resonates between 0.7-1.3 ppm,¹ it was determined that the methyl group had to be attached to a deshielding atom such as oxygen. Methoxy groups generally have shifts in the region 3.2-3.8 ppm¹ and thus this peak was determined to be due to a methoxy substituent. This was confirmed by single crystal X-ray diffraction (Chapter Four).

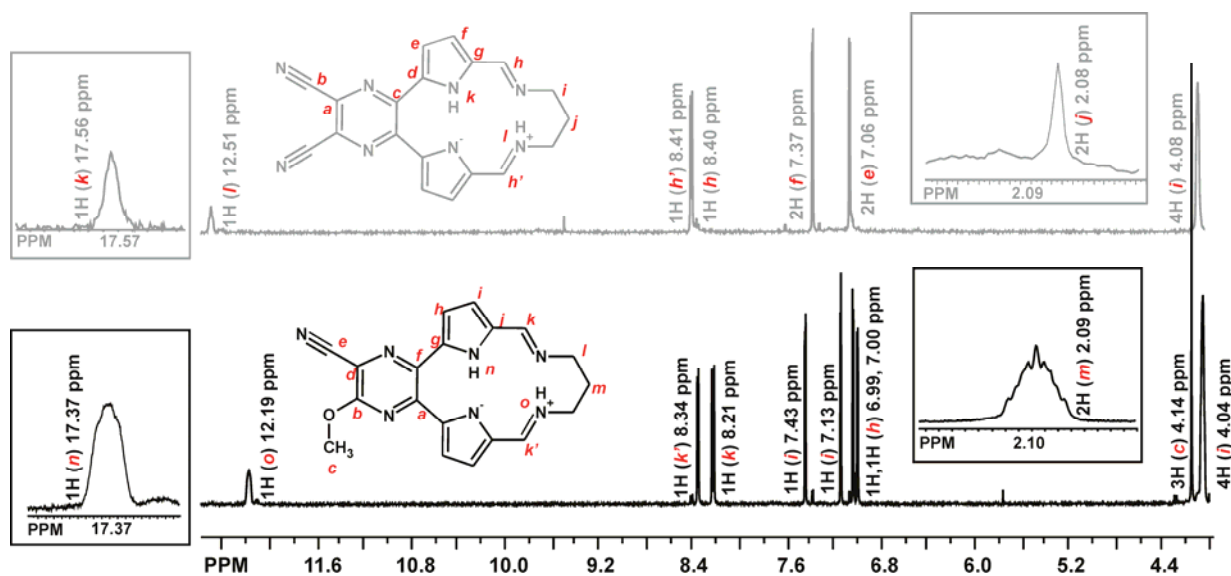


Figure 5.9: Section of the ^1H NMR spectra of $\text{H}_2\text{L}8\text{a}$ (grey) and $\text{H}_2\text{L}8\text{b}$ (black) in $\text{DMSO-}d_6$ at 303 K.

As discussed in Chapter Three, it is difficult to prove whether a chlorination reaction is successful as ^{37}Cl NMR is unreliable. To verify the successful synthesis of the chloro-substituted gold(III) complex, $[\text{Au}(\text{L}4)](\text{PF}_6)$, experiments were performed to determine the chemical shifts of ^{35}Cl and ^{37}Cl in the molecule. This was unsuccessful due to the quadrupolar nature of ^{35}Cl and ^{37}Cl (spin 3/2) as well as the poor sensitivity of 0.0047 and 0.0027, respectively relative to ^1H .²⁸ The poor sensitivity and wide spectral window for covalent chlorine NMR resulted in no signal being detected. However, the ^1H NMR shifts of the chlorinated dihydrochloride salt of the amine, suggested that the chlorination was successful when the proton chemical shifts were compared with the shifts of the alcohol substituted diamine which would have been synthesized if the reaction had not been successful, Figure 5.10.

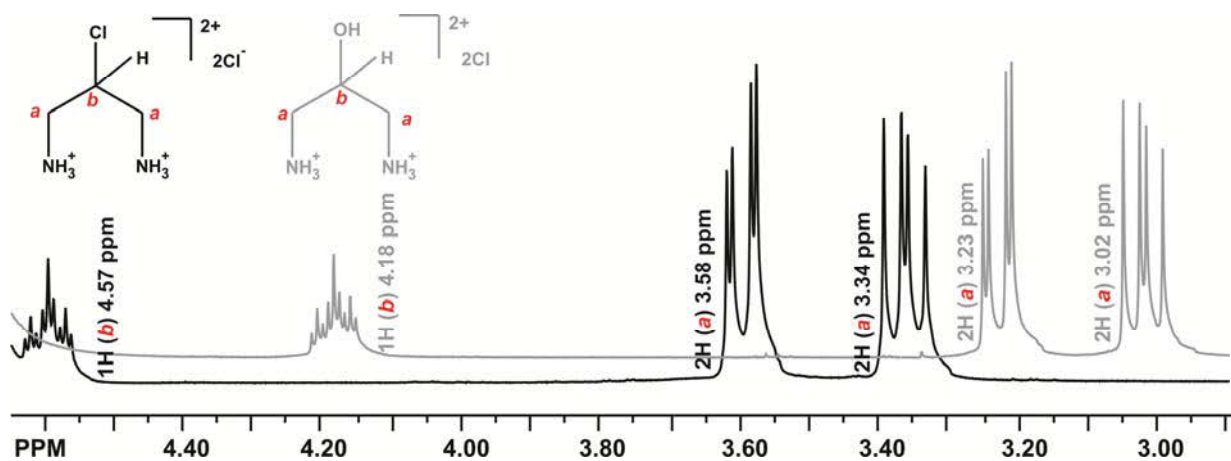


Figure 5.10: Overlay of the ^1H NMR spectra of 2-chloro- and 2-hydroxy-1,3-diaminopropane dihydrochloride, shown in black and grey respectively, in D_2O at 303 K.

The spectra in Figure 5.10 clearly show a downfield shift of the protons of the chloro-substituted amine when compared to the equivalent protons on the alcohol analogue. This is due to the deshielding effect of

the chlorine group compared to the alcohol functional group. Based on the ^1H NMR shifts and the supporting mass spectrometry data, it was concluded that the chlorination reaction was successful.

The gold(III) complex $[\text{Au}(\text{L4})](\text{PF}_6)$ with the chlorine functional group on the central carbon of the alkyl bridge has some interesting signals in the ^1H NMR spectrum. The methylene protons adjacent to the chloro functional group on the di(azomethine) linkage are not all in an equivalent environment and thus the chemical shifts of the protons are not all the same. Although the molecule appears symmetrical, the DFT optimized structures of the complex shown in Figure 5.11(a) and (b) indicate that the di(azomethine) linkage is not planar and the functional group, whether in the axial or equatorial position, approaches some protons more closely than others. DFT calculations (Chapter Six) show that the protons closest to the chlorine functional group are more deshielded by the functional group and thus resonate further downfield. The axial orientation of the chlorine atom is energetically more favourable, this is discussed further in Chapter Six (section 6.4.1). The hydrogen atoms closest to the chlorine atom (in the axial position) resonate further downfield, refer to Figure 5.11. The hydrogen atoms which are further displaced from the chlorine resonate further upfield. This difference is attributed to the deshielding effect of the chlorine atom; the further the hydrogen atoms are from the chlorine atom the more they are shielded. It is also interesting to note that the downfield protons manifest as a doublet while the upfield hydrogen atoms appear as a doublet of doublets.

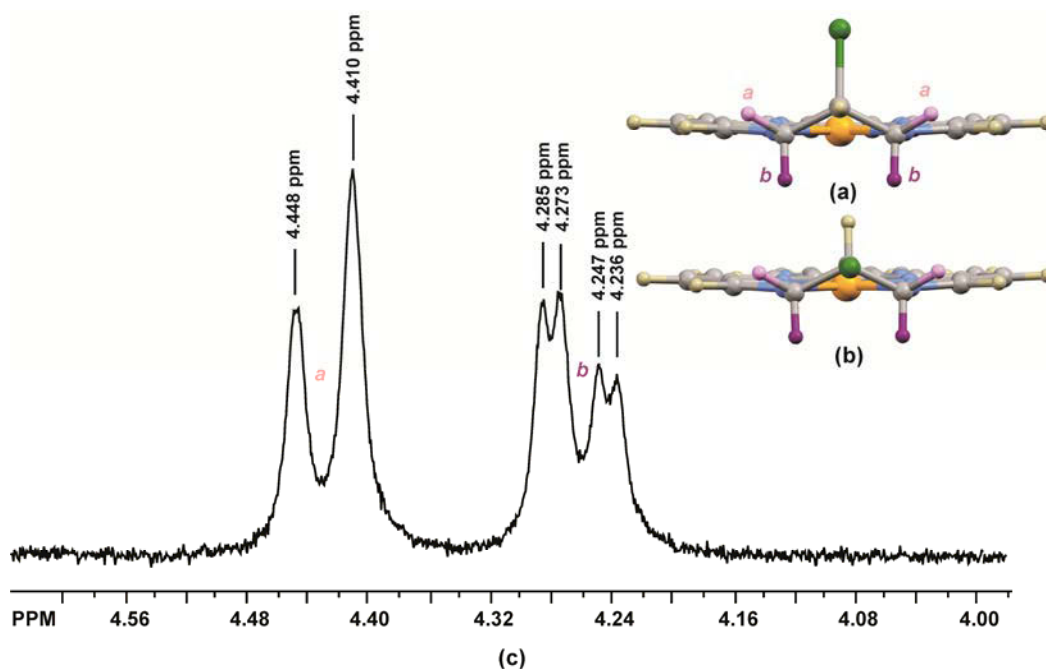


Figure 5.11: DFT optimised structures of $[\text{Au}(\text{L4})](\text{PF}_6)$ with the chlorine substituent in the (a) axial and (b) equatorial positions. The protons closest to the chlorine substituent are shown in pink and are more deshielded than the protons shown in purple. (c) ^1H NMR spectrum of $[\text{Au}(\text{L4})](\text{PF}_6)$ in $\text{DMSO}-d_6$ at 303 K showing the chemical shifts of the methylene protons on the di(azomethine) linkage adjacent to the chlorine substituent.

In conclusion, the IR, UV/visible and NMR data have been important in determining the structures of the free ligands and the gold(III) complexes. The data obtained for the macrocyclic ligands indicated that these compounds are likely in the tautomeric form where the pyrrole N and diagonally opposite imine N atoms are

protonated in both the solid state and the solution state. Comparison of the IR and NMR spectra for the ligands and gold(III) complexes clearly show that metal chelation was successful as the signals for the NH protons were no longer present in the spectra of the gold(III) chelates. The gold(III) chelate NMR and IR spectra were also shifted relative to the corresponding ligand.

5.4 Octanol/Water Partition Coefficients

5.4.1 Introduction

The ability of a compound to cross biological membranes is a prerequisite for any drug, especially orally ingested drugs which move from the intestine to the bloodstream and then the tumour cell.²⁹ The ability of a potential drug candidate to cross these barriers until it binds to the target and induces the desired response is often described by the octanol/water partition coefficient.

Octanol/water partition coefficients ($\log P_{o/w}$) are a measure of the hydrophobicity or hydrophilicity of a substance and can give an indication of a compound's biodistribution.³⁰ This is a key parameter in structure-activity relationship studies.³⁰ The octanol/water partition coefficient is the ratio of the concentration of the compound in octanol to that in water. This ratio is most commonly determined with the shake flask method.³⁰

Octanol/water partition coefficients are used as a biomodel as octanol has a similar structure to phospholipids that make up biological membranes as it has a hydrophobic tail (eight-carbon alkyl chain) and a hydrophilic head (alcohol group). Hydrophobic molecules will prefer to dissolve in the octanol layer and will have a high octanol/water partition coefficient.^{29,31,32} Blood serum is mostly made up of water; hence the use of water in the biphasic partition coefficient determination. Hydrophilic molecules will prefer the aqueous layer and have a low octanol/water partition coefficient.^{29,31,32} Thus, if a compound has a high hydrophilicity, it will not move across the cell membrane by passive transport.

The hydrophobic nature of a drug is crucial as it determines how easily it will move across cell membranes, the extent of important hydrophobic interactions in enzyme-ligand interaction, drug-receptor interaction, aggregation of surfactants, coagulation and detergency.³³ Hydrophobic interactions are favoured thermodynamically because of the increase in entropy of the water molecules that accompanies its association with non-polar molecules, which squeeze out water. Hydrophobicity affects drug absorption, bioavailability, hydrophobic drug-receptor interactions, metabolism of molecules and their toxicity.³³

It is generally found that an increase in the hydrophobicity of a compound will also lead to an increase in biological activity.³¹ This is attributed to the fact that drugs have to cross cell membranes to reach their target. Even if no barriers have to be crossed such as in *in vitro* studies, the drug has to interact with a target such as an enzyme or receptor where the binding site is usually hydrophobic.³¹ This might imply that increasing the partition coefficient should increase the biological activity indefinitely but this does not happen. The drug may become so hydrophobic that it is poorly soluble in aqueous media or it may become trapped in lipid deposits and never reach the intended site. Hydrophobic drugs are also often more susceptible to metabolism and elimination.³¹

Various substituents can make a contribution to hydrophobicity and this contribution is known as the hydrophobicity constant (π) and is a measure of how hydrophobic a substituent is relative to hydrogen.^{31,32} A positive hydrophobicity constant indicates that a substituent is more hydrophobic than hydrogen while a negative value indicates that the substituent is less hydrophobic.^{31,32} The hydrophobicity constants for a range of substituents on hexane and benzene are shown in Table 5.8.

Table 5.8: Values of π for various substituents³¹

Group	CH ₃	t-Bu	OH	OCH ₃	CF ₃	Cl	Br	F
π (aliphatic substituents)	0.50	1.68	-1.16	0.47	1.07	0.39	0.60	-0.17
π (aromatic substituents)	0.52	1.68	-0.67	-0.02	1.16	0.71	0.86	0.14

These values are only accurate for the compounds from which they were derived, but can be used as approximations when studying other compounds.^{31,32} In general, the introduction of methyl groups usually increases the hydrophobicity of the compound and reduces its water solubility, improving the rate at which transfer across the biological membrane occurs, but it can make release from the biological membrane more difficult.^{31,32} The incorporation of halogen atoms into compounds results in compounds which are also more hydrophobic and less water soluble. These compounds have improved penetration of lipid membranes, but have an undesirable tendency to accumulate in lipid tissue.^{31,32} The introduction of hydroxyl groups should result in a structure which is less hydrophobic.^{31,32}

As the hydrophobic nature of a drug is crucial to how easily it crosses cell membranes and may also be important in drug-receptor interactions, it is important to determine the $\log P_{o/w}$ for the gold(III) chelates. Even minor changes of substituents on a drug may have a significant impact on its hydrophobicity and therefore biological activity. Therefore, it is important to predict this physical property quantitatively.

5.4.2 Experimental Methods

The method used for the determination of $\log P_{o/w}$ was the 'shake-flask' method. This is the most labour intensive, but most accurate method for partition coefficient determination.^{30,33} Another method for determining $\log P_{o/w}$ values involves using high performance liquid chromatography (HPLC) and is based on retention times in the column and comparing data with a library of compounds with known $\log P_{o/w}$ values. Although this method is quicker it is likely to be inaccurate for the reported compounds as they are novel and are not structurally similar to literature compounds.³⁴

The 'shake-flask' method requires the use of water-saturated octanol and octanol-saturated water to ensure there is no artificial carry over between the two phases during the experiment.^{30,33} Solutions of water-saturated octanol and octanol-saturated water were prepared by shaking high purity octanol ($\geq 99\%$) with ultra-pure water (18.0 M Ω cm⁻¹ resistivity). The layers were allowed to equilibrate over a period of 24 hours before they were centrifuged and collected separately. These solvents were used for all further partition coefficient determinations.

Although compounds were soluble in octanol, they were not sufficiently soluble in pure water to permit the determination of their aqueous phase molar absorptivities (extinction coefficients) from the Beer-Lambert law. However, since the spectra of dilute aqueous solutions of the complexes matched those in pure acetonitrile, particularly around 300 nm, molar absorptivities were determined for the gold(III) chelates in

pure acetonitrile in order to calculate the concentrations of the compounds from their 300 nm absorbance values in dilute aqueous solution. Beer-Lambert law plots were determined for each complex in acetonitrile by monitoring the absorption spectrum in a 1.0 cm pathlength cuvette from 200 to 800 nm with increasing concentration of the complex. The extinction coefficient at the wavelength of maximum absorbance (or wavelength of interest) was calculated using Equation 5.4.

A solution of each complex in water-saturated octanol ($\sim 2 \times 10^{-5}$ M; the partition coefficient is independent of concentration and therefore the exact concentration is not important) was shaken with an equal volume of octanol-saturated water and allowed to settle for 1 hour before the two phases were separated. The absorption spectrum of each phase was recorded and the concentration of the gold(III) complex determined using the measured absorption and molar absorptivity at 300 nm. The octanol/water partition coefficients were then calculated using Equation 5.5:

$$\log P_{o/w} = \log \left(\frac{[\text{Au(III)complex}]_{\text{octanol}}}{[\text{Au(III)complex}]_{\text{water}}} \right) \quad 5.5$$

All partition coefficients were determined in duplicate and the reported results are a mean value.

5.4.3 Results and Discussion of Octanol/Water Partition Coefficients

The UV/visible absorption spectra for the octanol and water layers of $[\text{Au(L1)}](\text{PF}_6)$ as well as the Beer-Lambert plot in acetonitrile at 300 nm are shown in Figure 5.12(a). The slope of the Beer-Lambert plot gives the extinction coefficients of the complex at that wavelength. The extinction coefficients were used to calculate the concentration of the complex in each phase after equilibrium had been reached. Using the concentrations in each phase the $\log P_{o/w}$ value for each chelate was calculated using Equation 5.5. The $\log P_{o/w}$ values for the chelates are given in Table 5.9.

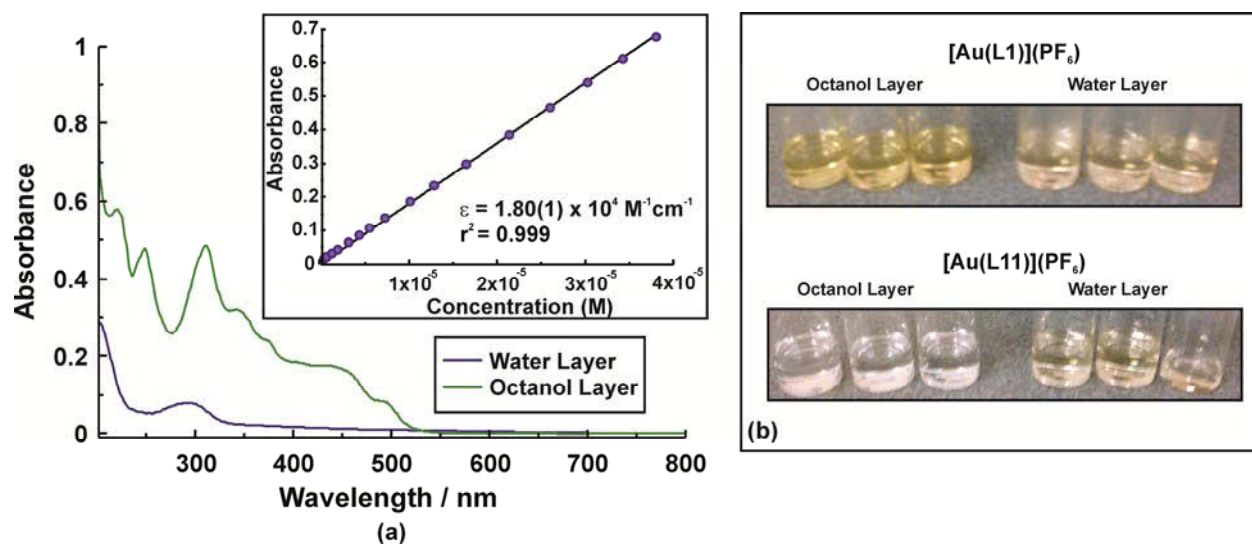


Figure 5.12: (a) UV/visible spectra of the octanol and water layers containing $[\text{Au(L1)}](\text{PF}_6)$ at 298 K. Inset is the Beer-Lambert plot for $[\text{Au(L1)}](\text{PF}_6)$ in acetonitrile at 300 nm. (b) Photographs of the octanol and water layers of $[\text{Au(L1)}](\text{PF}_6)$ and $[\text{Au(L11)}](\text{PF}_6)$.

Table 5.9: Summary of the mean $\log P_{o/w}$ values for the gold(III) chelates.

Complex	$\log P_{o/w}$
[Au(L1)](PF ₆)	0.77(3)
[Au(L2)](PF ₆)	1.01(4)
[Au(L3)](PF ₆)	0.88(4)
[Au(L4)](PF ₆)	1.06(5)
[Au(L5)](PF ₆)	1.02(2)
[Au(L6)](PF ₆)	1.03(9)
[Au(L7)](PF ₆)	1.34(8)
[Au(L8b)](PF ₆)	1.04(3)
[Au(L9)](PF ₆)	1.29(4)
[Au(L10)](PF ₆)	1.468(3)
[Au(L11)](PF ₆)	0.578(1)
[Au(L12)](PF ₆)	-0.58(1)

All the macrocyclic and pseudomacrocyclic chelates have a high affinity for octanol with $\log P_{o/w}$ values ranging from 0.578(1) for [Au(L11)](PF₆) to 1.468(3) for [Au(L10)](PF₆). Figure 5.12(b) shows that there is a higher concentration of [Au(L1)](PF₆) in the octanol layer as opposed to the water. This large positive $\log P_{o/w}$ indicates that the complexes should move readily from the blood serum to the cell membrane. This result is expected as the complexes consist of a large organic ligand as well as a bulky hexafluorophosphate(V) counterion which will lead to increased hydrophobicity.

Upon examination of the data obtained for the quinoxaline-based macrocycles, it was evident that small changes in the substituents can have a large effect on the hydrophobicity of the chelates. The hydrophobicity constant (π) relative to [Au(L1)](PF₆), the reference macrocycle which contains no substituents on the quinoxaline tail or the di(azomethine) linkage, was calculated for the substituted quinoxaline-based macrocycles using Equation 5.6.^{31,32}

$$\pi = \log P_x - \log P_H \quad 5.6$$

where P_H is the partition coefficient of the standard compound and P_x is the partition coefficient for the standard compound with an added functional group. Table 5.10 summarizes the π values for the substituted quinoxaline-based gold(III) chelates.

Table 5.10: Values of π for various substituents of [Au(L1)](PF₆).

	Aliphatic substituent	Aromatic substituent	π
[Au(L2)](PF ₆)	(CH ₃) ₂		0.24
[Au(L4)](PF ₆)	Cl		0.29
[Au(L5)](PF ₆)		(CH ₃) ₂	0.25
[Au(L6)](PF ₆)		CH ₃	0.26
[Au(L7)](PF ₆)		F	0.57

All the substituents raise the hydrophobicity of the complexes as illustrated by the positive hydrophobicity constants. These substituents all increase the size of the organic ligand and therefore increase the hydrophobicity. The complex [Au(L2)](PF₆) has two methyl groups attached to the di(azomethine) linkage while the complex [Au(L5)](PF₆) has two methyl groups attached to the quinoxaline tail. Both these complexes have fairly similar π values of 0.24 and 0.25, respectively, indicating that addition of the methyl substituents to the aliphatic or aromatic regions makes little difference to the $\log P_{o/w}$ value of a complex. A

similar result has been reported for benzene and hexane (Table 5.6). The addition of only one methyl group to the quinoxaline ring in the complex $[\text{Au}(\text{L6})](\text{PF}_6)$ does not result in a large difference in the $\log P_{o/w}$ value when compared to $[\text{Au}(\text{L5})](\text{PF}_6)$ with the two methyl groups attached to the quinoxaline tail.

The complexes with halogen substituents make the greatest difference in the $\log P_{o/w}$ value. The addition of chlorine functional groups to molecules designed as β -tryptase inhibitors, for the treatment of asthma has been found to markedly increase the efficacy of the drugs.³⁵ In the development of μ and κ opioid analgesics, the addition of a chlorine functional group has been shown to increase hydrophobicity and subsequently efficacy of a range of compounds.³⁶ $[\text{Au}(\text{L7})](\text{PF}_6)$ which has a fluorine group attached to the quinoxaline ring, has the largest π value of 0.57. This value is even greater than the value observed for $[\text{Au}(\text{L4})](\text{PF}_6)$ which has a chlorine atom attached to the di(azomethine) bridge. The general trend shown by the data in Table 5.8 for the substituents on benzene and hexane was that the substituents attached to aromatic moieties contributed more to hydrophobicity than those attached to aliphatic groups. Other groups obtained similar results. Monterio *et al.* studied the $\log P_{o/w}$ of *ortho*-halogenated tetraporphyrins with sulphamide substituents. The $\log P_{o/w}$ values increased from 2.23(5) to 2.53(8) when the chlorine atom in the *ortho*-position of the tetrapyrrole ring is replaced by the less polarisable fluorine atom.³⁰

The quinoxaline-based macrocycle, $[\text{Au}(\text{L3})](\text{PF}_6)$, has a four-carbon di(azomethine) linkage while $[\text{Au}(\text{L1})](\text{PF}_6)$ has a three-carbon linkage. Larger alkyl chains are expected to result in higher hydrophobicity. This is illustrated by the larger $\log P_{o/w}$ value for $[\text{Au}(\text{L3})](\text{PF}_6)$ of 0.88(4) compared to 0.77(3) for $[\text{Au}(\text{L1})](\text{PF}_6)$.

Similarly, the effect of functional group changes on hydrophobicity is observed for the pseudomacrocycles. The complex $[\text{Au}(\text{L9})](\text{PF}_6)$ has methyl groups attached to the imine moieties of the complex while $[\text{Au}(\text{L10})](\text{PF}_6)$ has ethyl chains attached to the imine moieties. This increase in organic bulk results in an increase in the $\log P_{o/w}$ value from 1.29(4) to 1.468(3) for $[\text{Au}(\text{L9})](\text{PF}_6)$ and $[\text{Au}(\text{L10})](\text{PF}_6)$, respectively. It is reported that increasing the size of the alkyl group reaches a point where it reduces the water solubility to an impractical level and consequently most substituents are restricted to methyl and ethyl groups.³² Although $[\text{Au}(\text{L11})](\text{PF}_6)$ also contains a two-carbon alkyl chain, it has a much lower $\log P_{o/w}$ value of 0.578(1) than either $[\text{Au}(\text{L9})](\text{PF}_6)$ or $[\text{Au}(\text{L10})](\text{PF}_6)$. This is because it also contains a hydroxyl group at the end of the chain. Hydroxyl groups are known to lead to an increase in the hydrophilic nature of a compound, as shown in Table 5.8 for benzene and hexane compounds.

The macrocyclic ligand $[\text{Au}(\text{L3})](\text{PF}_6)$ and the pseudomacrocyclic complex $[\text{Au}(\text{L10})](\text{PF}_6)$ can be compared as they contain the same number of carbon atoms attached to the imine groups. It is interesting to note that although these complexes contain almost the identical numbers and types of atoms, the arrangement of these atoms makes a large difference to the $\log P_{o/w}$ value. $[\text{Au}(\text{L3})](\text{PF}_6)$ has a closed structure with a butyl di(azomethine) linkage and a $\log P_{o/w}$ value of 0.88(4). $[\text{Au}(\text{L10})](\text{PF}_6)$ has an open structure with ethyl groups attached to the imine moieties (equivalent in terms of number of carbon atoms to a butyl bridge) and a much higher $\log P_{o/w}$ value of 1.468(3). Seemingly the increased molecular volume of $[\text{Au}(\text{L10})](\text{PF}_6)$ relative to $[\text{Au}(\text{L3})](\text{PF}_6)$ leads to a large increase in hydrophobicity.

The acyclic complex $[\text{Au}(\text{L12})](\text{PF}_6)$ has a large and negative $\log P_{o/w}$ value of -0.58(1). Figure 5.12(b) shows that the complex is in a higher concentration in the water layer as opposed to the octanol layer. This shows that this compound is more likely to be found in the blood serum as opposed to the cell membrane. This

complex is lacking the quinoxaline group which increases the hydrophobicity of the macrocyclic and pseudomacrocyclic complexes relative to the acyclic complex.

The hydrophobicity of commercially available drugs varies from as low as -1.71 for amoxicillin to as high as 6.03 for chlorprothixene.³⁰ The anticancer agent doxorubicin has a log $P_{o/w}$ value of 0.65. A set of $[M(dppe)_2]^+$ complexes where $M = Au(I), Ag(I)$ and $Cu(I)$ has been patented for their efficacy as anti-cancer agents.³⁷ The $[Au(dppe)_2]^+$ complex has a high partition coefficient of 25.5 and also exhibits severe hepatotoxicity and shows the least selectivity to cancer cell lines. The hydrophobicity of the compounds was tuned by exchanging some of the phenyl rings.³⁷ This changed the partition coefficient to between 0.017 and 0.178 which enhanced the selectivity of the complexes.³⁷ The vast majority of drugs are hydrophobic as they are mostly organic drugs. It is generally found that increasing the hydrophobicity of a compound will also lead to an increase in biological activity which is due to the fact that drugs have to cross cell membranes to reach their target. However, increasing the partition coefficient does not increase the biological activity indefinitely.³¹

In conclusion, as the macrocyclic and pseudomacrocyclic complexes are largely organic they are hydrophobic. This is important, as it means that the drugs should be able to cross cell membranes and reach their target. It was also shown that the hydrophobicity of the chelates could be tuned through small changes in the structures of the compounds. Commercially available drugs such as doxorubicin are also hydrophobic. So the hydrophobicity of these metal chelates suggests that they might well be able to effectively reach their intended cellular target: DNA.

5.5 Glutathione Reduction Stability

5.5.1 Introduction

Glutathione is a tripeptide considered to be essential to living cells.³⁸ Glutathione contains a thiol group which can play a role in electron transfer.³⁹ Glutathione can be found in reduced (GSH) and oxidized (GSSG) forms. Glutathione in its reduced form is a simple tripeptide consisting of ι -glutamic acid, ι -cysteine and glycine. The oxidized form has two GSH molecules joined together as the thiol groups of cysteine are oxidized to form a disulfide bridge.³⁹ The structure of glutathione in its reduced and oxidized state is shown in Figure 5.13. In the reduced state the thiol group of cysteine is able to donate an electron to other unstable molecules such as reactive oxygen. By donating an electron and with the aid of glutathione peroxidase, glutathione becomes reactive and two oxidized glutathione molecules react to form the disulfide species (GSSG), Equation 5.7.³⁹



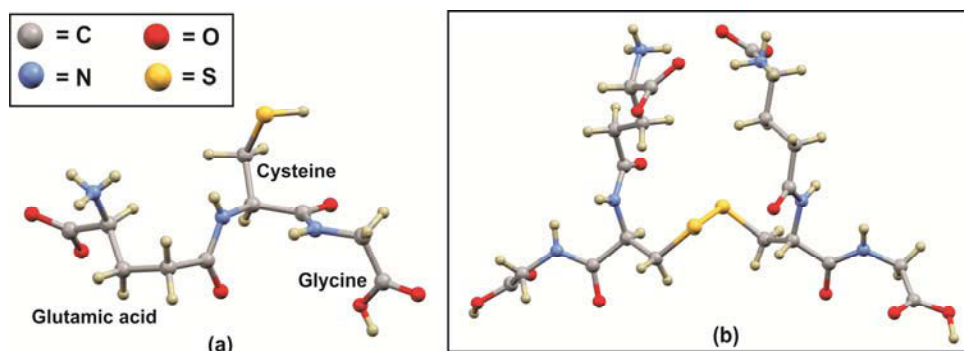


Figure 5.13: X-ray Crystal structures of the (a) reduced (GSH) form⁴⁰ and the (b) oxidized (GSSG) form of glutathione.⁴¹ The solvent molecules in (b) have been omitted for clarity.

In healthy cells 90% of the total glutathione is in the reduced form, while less than 10% exists in the oxidized form (GSSG). An increase in the ratio is indicative of oxidative stress.³⁹ Glutathione is produced in all organs, especially in the liver, lungs, heart and brain and is found intracellularly in a concentration of 0.5 to 10 mM with the plasma only containing micromolar concentrations.⁴² Glutathione levels will decrease with age in animals and are different at certain times of the day.³⁹

Glutathione has multiple functions: it neutralises free radicals and reactive oxygen compounds and it maintains exogenous antioxidants such as vitamins C and E in their active forms and glutathione removes many foreign compounds.³⁹ Glutathione is essential for the functioning of the immune system and plays an important role in metabolic and biochemical reactions such as DNA synthesis and repair, protein synthesis, amino acid transport and enzyme activation.³⁹

The coordination chemistry of GSH is of interest as it is capable of binding strongly to a metal centre thus decreasing the activity of a metal-based drug or even eliminating the compound from the cell.⁴² GSH has eight potential binding sites, two carboxylic acid groups, an amino group, a sulfhydryl group and two amide moieties. All the binding sites cannot be simultaneously coordinated to a single metal ion due to the geometry of the molecule. The coordination chemistry of GSH is therefore characterized by the formation of protonated and polynuclear complexes.³⁸

Glutathione is generally regarded as the strongest reducing agent in the mammalian system.⁴³ An increase in GSH levels in cells protects them from oxidative stress as well as antitumour agents such as cisplatin. In the case of cisplatin, GSH-adducts are formed and actively removed from the cell.⁴² For inorganic compounds such as the proposed gold(III) chelates to be effective chemotherapeutic agents they need to be stable against reduction and elimination by glutathione. Thus the objective of this study was to determine the stability of the complexes to glutathione and the rate at which they decompose.

There are many factors that influence the rate of a reaction such as concentration, ionic strength, pH, solvent, temperature and pressure.⁴⁴ Controlling these factors and ensuring the reactions are done under pseudo first order conditions should ensure reliable results.

5.5.2 Experimental Methods

The kinetic experiments were performed using glutathione concentrations in the range of 50-150 μM . The concentration of the $[\text{Au}(\text{L1})](\text{PF}_6)$ was fixed in all the experiments at 39 μM . The concentration of GSH in various body tissues ranges from 1 – 10 mM.³⁹ However, for performing kinetics experiments the ratio of glutathione to the gold(III) chelate is an important parameter and owing to the limited solubility of the gold(III) chelates in aqueous media only low concentrations can be prepared. Correspondingly lower than cellular concentrations of GSH were used in the experiments. The experiments were performed at 310 K to mimic the mammalian cellular environment. A 25 mM ionic strength Tris-HCl buffer, pH = 7.0 was prepared (buffer preparation described in Section 5.6.2. The buffer for this experiment was prepared at 310 K). A solution of glutathione of the desired concentration in a DMSO/Tris-HCl buffer solvent system was prepared and an aliquot of the gold(III) chelate in DMSO was added giving a solution with a final composition of 15% DMSO and 85% Tris-HCl buffer. The stability of the chelate in the presence of glutathione was determined by measuring the absorbance of the chelate as a function of time.

5.5.3 Results and Discussion: Glutathione Stability

The experimental data that were collected did not show a decay of the LMCT band of the metal chelates, which would be indicative of reductive demetallation of the complexes. What was observed was a slow decay of all of the peaks in the UV/vis spectrum and a corresponding shift in the baseline (Figure 5.14). These data suggest that the complexes gradually precipitated out of solution over a period of 120 hours. The compounds are not very aqueous soluble, as shown by the octanol/water partition coefficients. The reactions were done in 15% DMSO in order to help keep the complexes in solution. Even at this percentage of DMSO, precipitation over time was observed. The complexes were also dissolved in a 20% DMSO and 80% Tris-HCl buffer solution, but the glutathione would not dissolve in this mixture. On close inspection of the cuvette, it was noted that a fine precipitate, corresponding to the complex, was clearly visible. The precipitation resulted in a change in the baseline of the spectrum as well as inconsistent movement of the bands over time. To confirm that precipitation was being observed, not reductive demetallation, additional experiments were performed with the same concentration of the metal complex, but in the absence of the GSH, these experiments showed a similar shift in the baseline. This suggests that the spectral changes can indeed be attributed to precipitation.

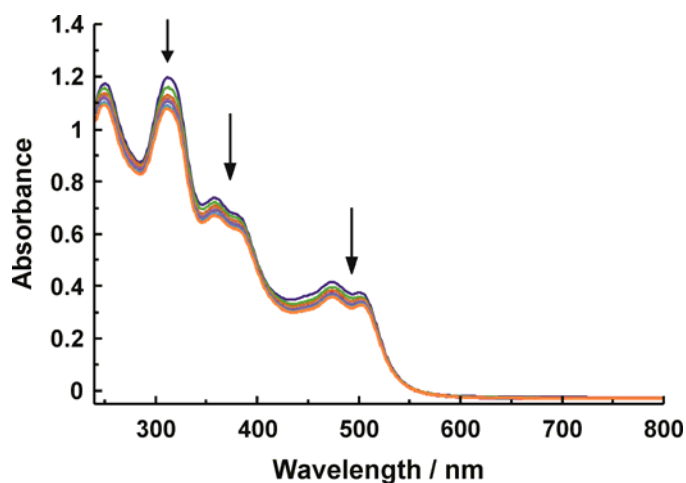


Figure 5.14: Spectral changes in the UV/visible spectrum of 39 μM $[\text{Au}(\text{L1})](\text{PF}_6)$ in the presence of 50 μM GSH at 37 $^\circ\text{C}$ in 15% DMSO 85% 25 mM TRIS-HCl buffer (pH = 7.00). The spectrum was recorded over 24 hours at one hour intervals. The arrows indicate the spectral changes.

Although no reliable rate constant could be measured from the experiments, they did indicate that the complexes are likely stable to glutathione reduction. Literature experiments, where the glutathione has reduced the metal centre, show isosbestic points as the LMCT bands decrease and the $\pi \rightarrow \pi^*$ bands, due to the ligand, increase in intensity.²¹ The resulting spectrum after glutathione reduction should be that of the ligand. For these gold(III) complexes there are no isosbestic points and eventually after 120 hours the absorbance spectrum disappears almost completely. The gold(III) complexes precipitate out of solution over a long period of time. The complex left in solution during this time does not appear to be affected by glutathione reduction as there are no peaks due to the ligand present.

In general, the gold(III) ion can be readily reduced to the more stable gold(I) ion or even metallic gold(0) under the *in vivo* reducing conditions, characteristic of the mammalian environment.⁴⁵ The coordination of a ligand which is a strong σ -donor ligand that can stabilize the gold(III) ion under physiological conditions is therefore critical if gold(III) is to be used in the treatment of cancer.⁴⁵

Although gold(III) is readily reduced, the proposed complexes were predicted to be stable to glutathione reduction as they contain macrocyclic ligands. As discussed in Chapter One there is a greater stability of cyclic ligands compared to open-chain ligands due to the 'macrocyclic effect'.⁴⁶ The 'macrocyclic effect' is due to 'multiple juxtapositional fixedness' which states that the stability of macrocyclic complexes is due to their slow decomposition rates.⁴⁷ Open-chain ligands can undergo consecutive S_N1 replacement steps of the nitrogen donors by solvent molecules, beginning at one end of the ligand. Macrocyclic ligands on the other hand cannot follow the same mechanism because there is no end to the ring; a bimolecular substitution reaction has been proposed for macrocyclic complexes. This would involve the distortion of the ligand to weaken and finally break one coordination bond.⁴⁸

There are few, if any, kinetic studies in the literature data related to the reduction of metal chelates by GSH. The gold(III) porphyrins which are similar macrocyclic structures have also proven stable under physiological conditions.⁴⁵ The acyclic gold(III) Schiff base complexes [Au(salen)]Cl show signs of slow decomposition under similar conditions.⁴⁵ Despite this decomposition, the [Au(salen)]Cl complex is cytotoxic with IC_{50} values in the range 10-30 μ M indicating that a susceptibility to reduction over time does not necessarily preclude them from acting as chemotherapeutic agents.⁴⁵

In conclusion, stability is an important factor in the design of new pharmaceuticals. As far as inorganic compounds are concerned, this mostly implies stability towards glutathione. The macrocyclic complexes were tested for reduction by glutathione, but as the complexes precipitated out of solution no rate constant could be measured. However, the complexes appear to be stable to glutathione reduction over time with the spectra indicating that only precipitation occurs over time rather than precipitation and reduction. The stability of the complexes is due to the macrocyclic ligands that stabilize the gold(III) ion.

5.6 DNA Binding Studies

5.6.1 Introduction

The gold(III) complexes were designed to act as chemotherapeutic agents. Their intended mode of action through which they would exert their cytotoxicity is through DNA intercalation and topoisomerase inhibition

and poisoning. There are several methods for inhibiting the topoisomerase (TOP) enzymes, but as this class of compounds is planar and aromatic, the anticipated method is DNA intercalation. Intercalating compounds insert themselves between the nuclear bases of the DNA helix and can cause distortions in the DNA helix. The intercalating agents prevent the religation of the DNA after the formation of the TOP-DNA covalent adduct. An increase in the concentration of TOP-DNA covalent complexes results in apoptosis of the cell. Classical DNA intercalators include EB (an antimicrobial agent), proflavine and aminoacridine (dyes), doxorubicin (chemotherapeutic drug) and daunomycin and actinomycin (antibiotics).⁴⁹

There are many different techniques that can be used to study the binding of the complexes to DNA. One such technique is viscosity studies. When a compound intercalates between base pairs, the DNA helix must lengthen as the base pairs have to separate to accommodate the compound which leads to an increase in viscosity.⁵⁰⁻⁵² A partial or non-classical intercalating compound could bend the DNA, reducing its effective length as well as its viscosity. Compounds that bind exclusively in the DNA grooves, typically cause less pronounced changes or no changes in the viscosity.⁵⁰⁻⁵² Circular dichroism is another technique that is useful in diagnosing the changes in DNA morphology during drug-DNA interaction. It is sensitive to the base-stacking and stabilizing of the DNA.⁵⁰ Neither of these techniques could be explored due to lack of equipment, but other spectroscopic methods were applied.

Another technique for analyzing DNA binding is thermal DNA denaturation studies. This technique was implemented in this work. The melting temperature (T_m) studies are used in predicting the nature of the binding and relative binding strength of metal complexes to DNA.^{50,51} These studies involve denaturation of the DNA. The most important contribution to DNA helix stability is the stacking of the bases on top of one another. In order to denature DNA the stacking energies need to be overcome.⁵³ In general stacking energies are less for pyrimidine/purine steps and for A:T rich regions. The most common method to denature DNA is to heat the DNA at a temperature above its melting point.⁵³ When the temperature in solution is increased, the double stranded DNA gradually dissociates into its constituent single strands. The unstacking of the DNA base pairs can be monitored using spectroscopy.⁵³

An increase in the melting temperature, T_m , when a compound intercalates between the DNA base pairs indicates that there is increased stabilization of the double helix due to the intercalation.^{50,51} The main classes of non-covalent interactions that can play a role in the binding of drugs to DNA are: hydrogen bonds, van der Waal's forces and hydrophobic interactions. In the intercalation process, a planar aromatic compound is inserted between two adjacent DNA base pairs in the DNA helix.⁵⁴ In minor groove binding a compound binds in the minor groove of the DNA without inducing significant structural changes in the DNA. While the DNA/drug conjugate formed by intercalation is stabilized by hydrophobic interactions and van der Waals forces, the conjugate formed by minor groove binding is stabilized mainly by hydrophobic interactions.⁵⁴ Thus an intercalated compound should increase the stability of the DNA, resulting in an increase in T_m in comparison to minor groove binders.

Fluorescence competitive binding DNA titrations were used to determine the affinity of the gold(III) macrocycles for calf thymus DNA (ctDNA). When ethidium bromide (EB) is intercalated between DNA base pairs, this leads to a significant increase in fluorescence emission.^{52,55} With the addition of a second DNA binding molecule, the emission intensity should decrease as the complex replaces EB and/or accepts the excited state electron from EB through a photoelectron transfer mechanism.^{55,56} This technique alone does not confirm the mode of DNA interaction, but does indicate the potential for DNA intercalation. This

technique was chosen instead of typical DNA titrations where aliquots of DNA are added to the complex in solution and the absorbance spectrum is recorded after each addition due to solubility issues. The fluorescence titrations are more sensitive and thus lower concentrations of the complexes could be used in the study.

As DNA is the anticipated cellular target of the gold(III) complexes, the interactions the complexes have with DNA are of great importance for the development of the complexes as chemotherapeutic agents. Also varying the location of the substituents on the ligands can create some interesting differences in configuration and electron distribution of the metal complexes which could result in different DNA binding modes and affinities.

5.6.2 Experimental

a. Thermal DNA denaturation studies

The DNA denaturation experiments were performed by Dr. Watson in the Department of Biochemistry at the University of KwaZulu-Natal and the method is included here for completeness.

The drugs were added post-PCR and pre-melt. PCR reactions were made using a master mix, appropriate primers (to amplify a portion of the ACTN3 gene) and DNA extracted from human saliva as template. The primer concentrations are about 200 nM each and the template DNA was *ca* 7 ng/ μ L. The total volume for each reaction was 20 μ L. The cyber-green fluorescent dye was added to the DNA.

Post-PCR the run was paused and drugs were added. A five-fold serial dilution, in DMSO, was performed for each drug. 1 μ L of drug was added to each reaction. In addition no template (NTC) and no drug controls (NDC, DMSO only) were included.

The denaturation studies were run on the Rotor-Gene 6000 real-time PCR machine with 5-plex fluorescence channels and high resolution melt application from Corbett Research. The software used to analyze the data was the Rotor-Gene 6000 series software 1.7.

b. Fluorescence competitive binding DNA titrations

The ctDNA was purchased from Sigma Aldrich as the high purity, highly polymerised sodium salt. A solution of ctDNA in the above buffer gave an absorbance ratio (A_{260 nm}/A_{280 nm}) of 1.9:1, indicating that the DNA was sufficiently free of protein and can be used without further purification.⁵⁷ The concentration of ctDNA, per base pair (bp), was determined spectroscopically at 260 nm using an extinction coefficient of 13 200 bp M⁻¹ cm⁻¹.

Ultrapure water (resistivity = 18 M Ω cm⁻¹) was used to prepare 25 mM Tris-HCl buffer. The required quantity of Tris-HCl was dissolved in ultrapure water. The pH was then adjusted to 7.0 with 1 M HCl and the buffer was brought to the desired volume.

Aliquots of stock solutions of the gold(III) complexes were dissolved in DMSO and added to solutions containing 15 μ M ctDNA base pairs and 15 μ M EB in 15% DMSO 25mM Tris-HCl buffer (pH 7.0) to give final

complex concentrations ranging from 0 to 200 μM . All samples were excited at 500 nm and emission was recorded between 530 and 800 nm. The apparent binding constants were calculated using Equation 5.8:

$$K_{\text{app}} = \frac{K_{\text{EB}}[\text{EB}]}{[\text{complex}]} \quad 5.8$$

Where K_{EB} is the binding constant of EB to ctDNA, $[\text{EB}]$ is the molar concentration of EB, K_{app} is the apparent binding constant of the complex to ctDNA and $[\text{complex}]$ is the concentration of the complex (C_{50}) that causes 50% quenching of the initial EB fluorescence, I_0 , as determined from a non-linear least-squares fit of the change in EB emission at 614 nm, $f(x)$, with the concentration of the metal chelate, x , to Equation 5.9:

$$f(x) = \frac{I_0 \times C_{50}}{x + C_{50}} \quad 5.9$$

K_{EB} was determined beforehand in an independent experiment in the buffer system of choice using a standard ctDNA absorption spectroscopy titration as described below. The concentration of EB was fixed at 4.36×10^{-5} M in 15% pH 7.0 DMSO-TrisHCl buffer at 25 °C in a 1.0 cm path length quartz cuvette. Aliquots (5-200 μL) of a concentrated ctDNA stock solution were added and the absorption spectra recorded in the 700-200 nm spectral region after a 10 minute incubation period. Absorbance values at 492 nm were corrected for dilution prior to fitting the optical density data to Equation 5.10:⁵⁰

$$(\varepsilon_a - \varepsilon_f)/(\varepsilon_b - \varepsilon_f) = \left(b - (b^2 - 2K_a^2 C_t [\text{DNA}]/s)^{\frac{1}{2}} \right) / 2K_a C_t \quad 5.10$$

Where
$$b = 1 + K_b C_t + K_b [\text{DNA}]/2s \quad 5.11$$

and where $[\text{DNA}]$ is the concentration of ctDNA base pairs, ε_a is the molar absorptivity of the band at a given $[\text{DNA}]$, ε_f is the molar absorptivity of the free EB, ε_b is the molar absorptivity of the fully intercalated EB, K_b is the equilibrium binding constant, C_t is the concentration of the EB and s is the binding site size (number of nucleotides per EB). The binding constant of EB, K_{EB} , to ctDNA under these specific solution conditions was $3.04(1.1) \times 10^6 \text{ M}^{-1}$ (bp).

For details of the spectrometers used for this section, see: Chapter Two.

5.6.3 Results and Discussion: DNA Binding

a. DNA Denaturation Study

The DNA melting curves for $\text{H}_2\text{L1}$ and $[\text{Au}(\text{L1})](\text{PF}_6)$ are shown in Figure 5.15. The temperature at which the DNA melts when there is no compound present is 82.87 °C and this is referred to as the no drug control (NDC). When the DNA sample is heated, the fluorescence intensity decreases until all the DNA has been converted to single-stranded DNA and then remains constant on further heating. In order to determine the melting point, a new graph of the first derivative of the fluorescence with respect to temperature is plotted against temperature. To determine the effect that the compounds would have on the denaturation of the DNA, the concentration of the compound was systematically increased and the fluorescence spectrum

recorded. Table 5.11 lists the T_m for various concentrations of H_2L1 , $[Au(L1)](PF_6)$, $[Au(L2)](PF_6)$, and $[Au(L3)](PF_6)$.

The free ligand H_2L1 has little effect on the T_m of the DNA over the concentration range. Higher concentrations of the ligands were used compared with the complexes. However, there was only a slight change in T_m of the DNA. The greatest change in the melting temperature was at an H_2L1 concentration of $26.5 \mu M$ where ΔT_m is $0.43 \text{ }^\circ C$. However, this may be an outlier because at an even higher concentration of $135 \mu M$, ΔT_m is only $0.08 \text{ }^\circ C$. These results indicate that H_2L1 does not interact with the DNA.

The gold(III) complexes all cause an increase in the melting temperature of the DNA at increased concentrations. At concentrations of approx $50 \mu M$, the T_m could not be measured as the fluorescence spectra changed to give flat lines. At a concentration of $2.04 \mu M$, $[Au(L1)](PF_6)$ increases the melting temperature of the DNA by $1.13 \text{ }^\circ C$ and at $10.1 \mu M$ $[Au(L2)](PF_6)$ increases the temperature by $1.65 \text{ }^\circ C$. These results indicate that the complexes are interacting with the DNA and stabilizing it due to increased intermolecular interactions which leads to an increase in T_m .

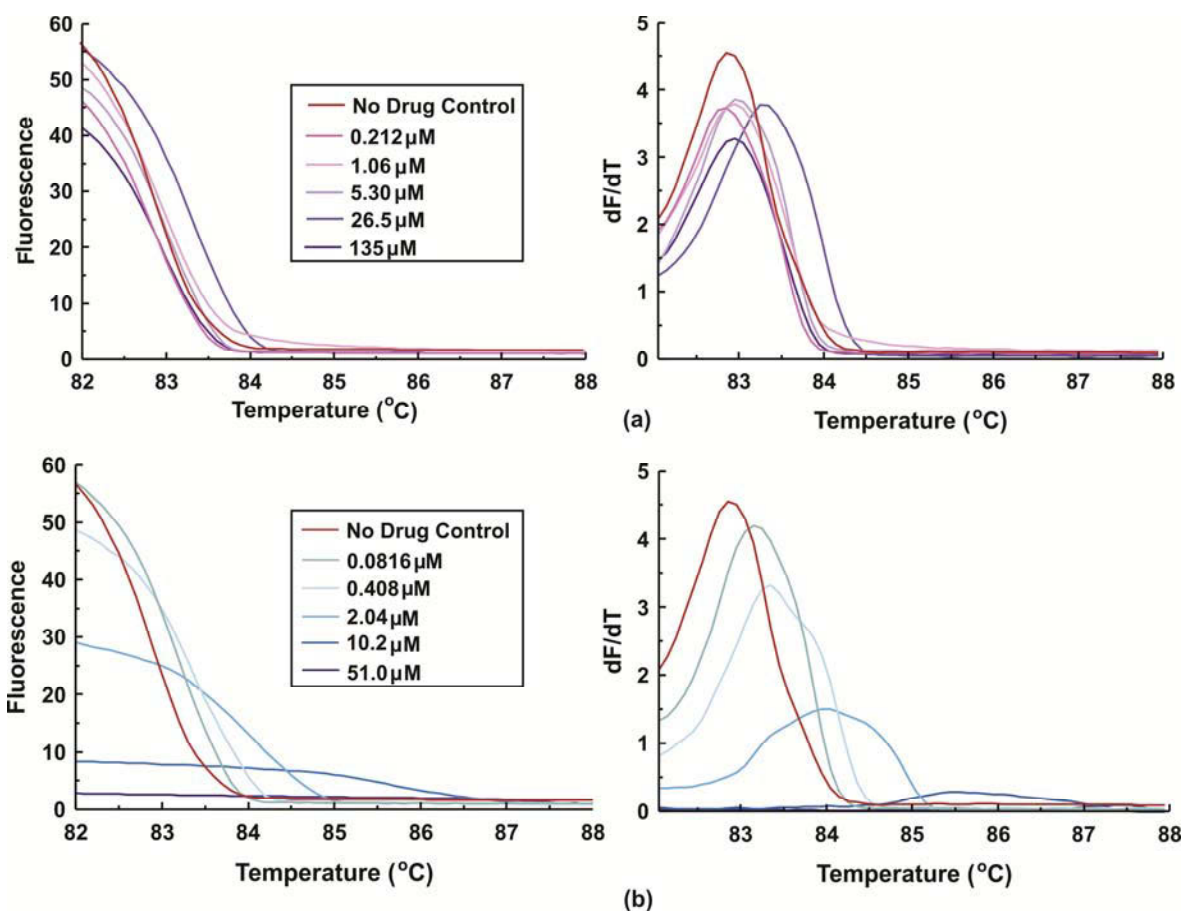


Figure 5.15: Melting point curves of DNA in the absence and presence of increasing concentrations of (a) H_2L1 and (b) $[Au(L1)](PF_6)$.

Table 5.11: Thermal denaturation data for H₂L1, [Au(L1)](PF₆), [Au(L2)](PF₆) and [Au(L3)](PF₆) with human DNA (saliva isolate).

H ₂ L1						
	NDC	0.212 μM	1.06 μM	5.30 μM	26.5 μM	135 μM
T_m (°C)	82.87	82.82	82.95	82.98	83.30	82.95
ΔT_m (°C)	N/A	-0.05	0.08	0.11	0.43	0.08
[Au(L1)](PF ₆)						
	NDC	0.0816 μM	0.408 μM	2.04 μM	10.2 μM	51.0 μM
T_m (°C)	82.87	83.17	83.33	84.00	*	*
ΔT_m (°C)	N/A	0.30	0.46	1.13	*	*
[Au(L2)](PF ₆)						
	NDC	0.0808 μM	0.404 μM	2.02 μM	10.1 μM	50.5 μM
T_m (°C)	82.87	83.20	83.40	83.37	84.52	*
ΔT_m (°C)	N/A	0.33	0.53	0.50	1.65	*
[Au(L3)](PF ₆)						
	NDC	0.0832 μM	0.416 μM	2.08 μM	10.4 μM	52.0 μM
T_m (°C)	82.87	83.05	83.17	83.35	84.02	*
ΔT_m (°C)	N/A	0.18	0.30	0.48	1.15	*

*Graph becomes a flat line

According to previous reports, the interaction of intercalators with DNA generally results in a considerable increase in T_m .⁵⁰ Low T_m values with increases between 1-3 °C generally indicate a non-classical binding mode.⁵¹ A range of [Ru(L)₄(dppz)]²⁺ complexes where L = imidazole, 1-methylimidazole and dppz = dipyrido[3,2-a:2'3'-c]phenazine] have been used in DNA denaturation studies.⁵⁰ These complexes showed an increase in the melting temperature of between 7 and 12 °C for ctDNA.⁵⁰ This indicates that the dppz ligand strongly intercalates between the DNA base pairs. In order to verify these results, viscosity studies were performed on the complexes. These studies showed that the relative viscosity of the DNA increases steadily with increasing concentration of the complexes.⁵⁰ This further verified that the complexes were intercalating between the base pairs as an increase in viscosity results from an increase in the length of the DNA through intercalation. Another study involving [Co(pic)₂(NN)] complexes where pic = picolate, NN = dipyrido[3,2-d:2'3'-f]quinoxaline (dpq) or dppz, also used thermal DNA denaturation studies in the determination of the binding mode.⁵¹ The only complex that showed an intercalative binding mode was [Co(pic)₂(dppz)] with a ΔT_m value of 4.4 °C while the complex [Co(pic)₂dpq] was believed to bind by a non-classical binding mode with a ΔT_m of 1.7 °C.⁵¹ Viscosity studies were done to verify the results. Both compounds were shown to increase the viscosity of the DNA. Thus, although the DNA denaturation studies suggested that [Co(pic)₂dpq] used a non-classical binding mode, the viscosity indicated that it was a DNA intercalator.⁵¹

As the proposed gold(III) complexes only increase the DNA melting temperature by *ca.* 1.1 °C, this could potentially indicate that the complexes bind only partially to the DNA or by a non-classical binding mode. However, this study cannot be reliably compared to previously reported cases as ctDNA was used in other cases while in these studies human saliva DNA was used. The melting point of a given piece of DNA will depend on factors such as length of the DNA strand; shorter pieces of DNA will melt more readily. The base composition of the DNA is also a factor; DNA containing more A:T rich regions melt more easily. Finally, the composition of the buffer used also influences the melting point of the DNA.⁵³ These factors can make the DNA more or less resistant to denaturation which could change the magnitude of T_m when a complex is bound to the DNA. Further studies such as viscosity measurements need to be done as, although the thermal

DNA denaturation study may indicate a non-classical binding mode, a viscosity study will give more conclusive results.

These are only preliminary studies with the only reliable information obtained from these experiments being that the complexes do interact with the DNA in some manner while the free ligand does not appear to interact with the DNA. This indicates that the gold(III) ion is important for interaction with the DNA. In order to make reliable comparisons, the same type of DNA needs to be used as that used in reported studies and preferably the experiments need to be done on a piece of DNA where the sequence is known.

b. Competitive Binding Fluorescence Studies

Fluorescence competitive binding DNA titrations were done to determine the affinity of the gold(III) macrocycles for ctDNA. On the addition of increasing concentrations of the complexes to the solution of EB and DNA there was quenching of the initial EB-DNA emission intensity by *ca.* 75 % (Figure 5.16). This indicates that the complexes bind efficiently and out-compete the EB for binding sites on the DNA. The apparent binding constant (K_{app}) of the complexes was determined using Equation 5.8. This equation requires the concentration of the complex at 50% reduction in emission intensity. This is determined from a non-linear least-squares fit of the change in EB emission at 614 nm with increasing concentration of the metal chelate, Equation 5.9 and Figure 5.16.

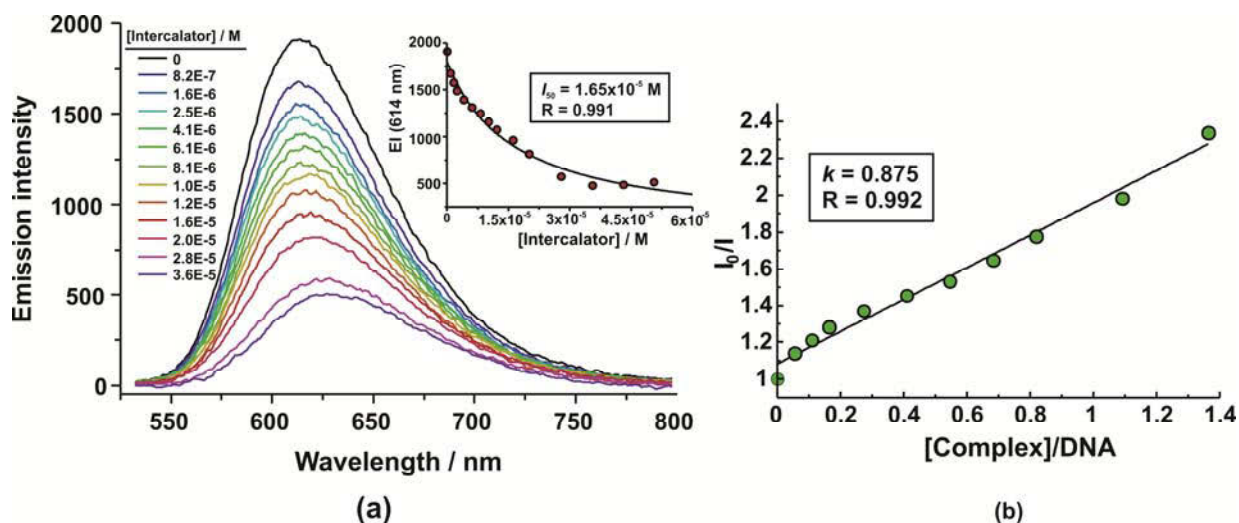


Figure 5.16: (a) Displacement of ctDNA-intercalated EB by $[\text{Au}(\text{L}1)](\text{PF}_6)$ ($T = 25^\circ\text{C}$, 15% DMSO-TRIS buffer, pH 7.0). Inset is a least-squares fit of the change in EB emission at 614 nm with increasing concentration of the metal chelate to determine concentration of the complex at 50% reduction in emission. (b) Stern-Volmer plot for $[\text{Au}(\text{L}1)](\text{PF}_6)$.

Knowledge of the binding constant of EB (K_{EB}) to the ctDNA under the specific conditions of the experiment (15% DMSO TRIS buffer, pH 7.0 and 25°C) is required for Equation 5.8 to determine K_{app} for the complexes. A DNA titration was performed with EB under the experimental conditions used for the competitive binding fluorescence titrations. For this experiment the absorbance of an EB solution was recorded in the presence of increasing concentrations of ctDNA. The binding constant of EB to DNA was calculated using Equations

5.10 and 5.11. The binding constant of EB to ctDNA under these specific solution conditions was $3.04(1.1) \times 10^6 \text{ M}^{-1}$ (bp). The absorbance titration of EB with increasing concentrations of ctDNA is shown in Figure 5.17. This technique could not be used to determine the binding constants of the complexes due to the poor solubility and thus only an apparent binding constant could be determined by competitive binding titrations.

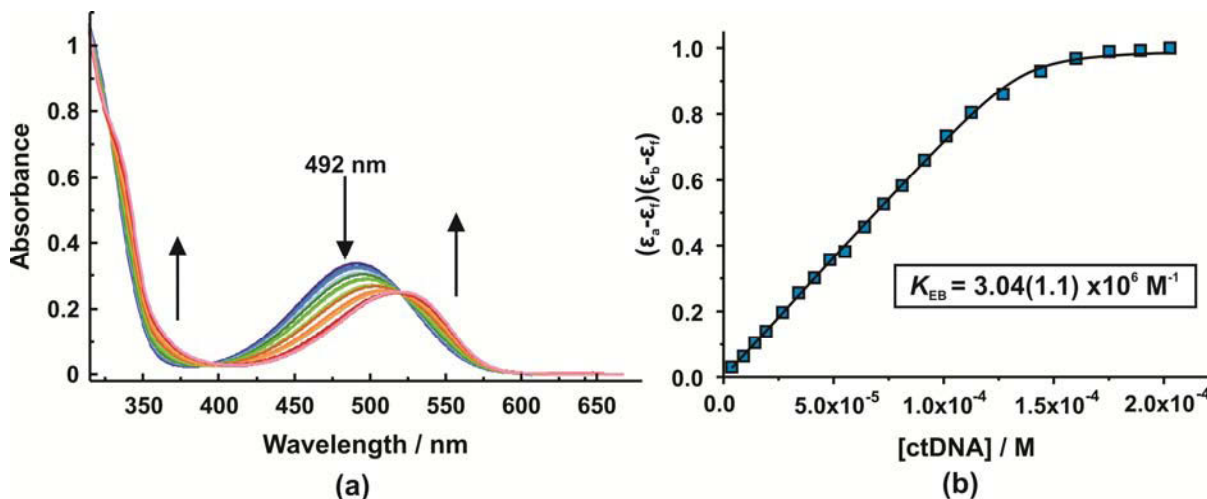


Figure 5.17: (a) Absorbance plot of EB with increasing concentrations of ctDNA. The arrows indicate spectral changes. (b) Non-linear fit for the titration of EB with ctDNA at 492 nm in pH 7.0, 15% DMSO TRIS-HCl buffer at 25 °C.

Using this information K_{app} values for the different complexes were calculated and are listed in Table 5.12. The K_{app} values of the complexes range from $1.20 \times 10^6 \text{ M}^{-1}$ for $[\text{Au}(\text{L}3)](\text{PF}_6)$ to $4.91 \times 10^6 \text{ M}^{-1}$ for $[\text{Au}(\text{L}7)](\text{PF}_6)$ for the macrocyclic complexes. The pseudomacrocyclic complexes have even higher binding constants ranging from $2.85 \times 10^6 \text{ M}^{-1}$ for $[\text{Au}(\text{L}10)](\text{PF}_6)$ to $6.61 \times 10^6 \text{ M}^{-1}$ for $[\text{Au}(\text{L}11)](\text{PF}_6)$.

When compared to the binding affinity of EB ($3.04(1.1) \times 10^6 \text{ M}^{-1}$) which is considered a strong DNA intercalator, the gold(III) macrocyclic and pseudomacrocyclic complexes have a relatively high affinity for DNA.⁵² The competitive binding fluorescence studies were also done for a Cu(II) phenanthroline complex. From this study the K_{app} value for the complex was determined as $5.1 \times 10^6 \text{ M}^{-1}$ indicating the interaction with the DNA is strong.⁵² Similar studies were done on Ru(dppz) complexes where the binding constants were in the range of $1.1 - 5.0 \times 10^6 \text{ M}^{-1}$, again indicative of strong DNA binders.⁵⁰ A Co(dppz) complex had a binding constant of $8.3 \times 10^5 \text{ M}^{-1}$ which is also considered to be a strong interaction.⁵¹ As the K_{app} values (binding constants) for the gold(III) complexes are similar to those previously reported, it shows that the complexes do have a high affinity for ctDNA.

This strong affinity is due to the planar complexes having extended aromaticity, which would allow for favourable π - π interactions with the aromatic DNA base pairs. The acyclic complex, $[\text{Au}(\text{L}12)](\text{PF}_6)$, which does not have the quinoxaline tail for π - π stacking has a considerably lower binding constant of $4.88 \times 10^5 \text{ M}^{-1}$.

Table 5.12: Apparent binding constants of the gold(III) complexes to ctDNA.

Complex	I_{50}^* / M	K_{app} / M^{-1}
[Au(L1)](PF ₆)	$1.65(12) \times 10^{-5}$	2.76×10^6
[Au(L2)](PF ₆)	$2.98(20) \times 10^{-5}$	1.49×10^6
[Au(L3)](PF ₆)	$3.67(29) \times 10^{-5}$	1.20×10^6
[Au(L4)](PF ₆)	$1.67(17) \times 10^{-5}$	2.62×10^6
[Au(L5)](PF ₆)	$1.56(11) \times 10^{-5}$	2.81×10^6
[Au(L6)](PF ₆)	$1.33(10) \times 10^{-5}$	3.41×10^6
[Au(L7)](PF ₆)	$9.23(90) \times 10^{-6}$	4.91×10^6
[Au(L8b)](PF ₆)	$1.54(10) \times 10^{-5}$	2.82×10^6
[Au(L9)](PF ₆)	$1.09(13) \times 10^{-5}$	3.96×10^6
[Au(L10)](PF ₆)	$1.58(15) \times 10^{-5}$	2.85×10^6
[Au(L11)](PF ₆)	$6.66(43) \times 10^{-6}$	6.61×10^6
[Au(L12)](PF ₆)	$8.29(73) \times 10^{-5}$	4.88×10^5

*This is the concentration of the complex at 50% reduction in emission intensity.

In a separate study on the binding affinity of [Pt(terpy)X]⁺ (where X is an anion) complexes it has been reported that the magnitude of the binding constant ($3.3 \times 10^3 - 1.8 \times 10^7 M^{-1}$) depends heavily on factors such as: size and steric effects, hydrogen-bonding capability and charge of the complexes.⁴⁹ In a separate study, four gold(III) complexes were synthesized from terpy derivatives, incorporating factors that affect their steric and electrostatic properties.⁵⁸ For the complexes with the same positive charge, the complex with the greater steric bulk had a lower DNA binding affinity.⁵⁸ Complexes which had a higher positive charge led to enhanced binding affinity. As a whole the electrostatic effect appears to have the greatest impact on the interaction. Low steric hindrance and high positive charge enhanced the binding affinity of the complexes to DNA.⁵⁸

The steric bulk of the di(azomethine) bridging groups of the gold(III) macrocyclic complexes does appear to have an effect on the binding affinities in this study. The quinoxaline macrocyclic complexes with the least sterically hindered bridge systems, [Au(L1)](PF₆), [Au(L5)](PF₆), [Au(L6)](PF₆) and [Au(L7)](PF₆) have larger binding affinities than those complexes with bulkier bridging units, [Au(L2)](PF₆), [Au(L3)](PF₆), [Au(L4)](PF₆). The complex with the fluorine atom substituent on the quinoxaline ring, [Au(L7)](PF₆) has the highest binding constant of the macrocyclic complexes. The fluorine atom seemingly serves to enhance electrostatic interactions between the DNA double helix and the complexes.

The drugs were designed in two separate phases; the first phase consisted of the macrocyclic complexes. The second phase consisted of the pseudomacrocyclic gold(III) complexes which were designed for enhanced binding affinity to the ctDNA. The pseudomacrocyclic complexes were designed after observations were made from the three-dimensional plot of the binding constants of [Au(L1)](PF₆), [Au(L2)](PF₆), [Au(L3)](PF₆), [Au(L4)](PF₆) and [Au(L5)](PF₆) as a function of bridge volume and the partition coefficient, Figure 5.18. It was evident from this plot that the binding constant increases with increasing drug hydrophobicity and decreasing bulk of the bridging unit. This meant that by decreasing the bridge volume of the complex and increasing the hydrophobicity of the complexes, the apparent binding constant could be increased. This led to the design of the pseudomacrocyclic, [Au(L9)](PF₆), which only contains methyl groups attached to the imine moieties, thus shortening the bridge length. This complex had an increased hydrophobicity of 1.29(4) (Table 5.9) as well as an increased binding constant of $3.96 \times 10^6 M^{-1}$ when compared to the bulk of the quinoxaline complexes. The pseudomacrocyclic complex [Au(L10)](PF₆) has ethyl groups attached to the imine moieties. This complex has a higher hydrophobicity of 1.468(3), but a lower

binding constant of $2.85 \times 10^6 \text{ M}^{-1}$ due to the added steric bulk of the ethyl groups. The pseudomacrocyclic complex $[\text{Au}(\text{L11})](\text{PF}_6)$ does not follow the trend that increased hydrophobicity and decreased bridge volume will increase the binding constant of the complexes. This complex has bulky ethanol groups attached to the imine moieties and a lower hydrophobicity of 0.578(1), but also has the largest binding constant of $6.61 \times 10^6 \text{ M}^{-1}$. This is attributed to the fact that the hydroxyl groups of the complex can form hydrogen bonds with the DNA enhancing the binding affinity.

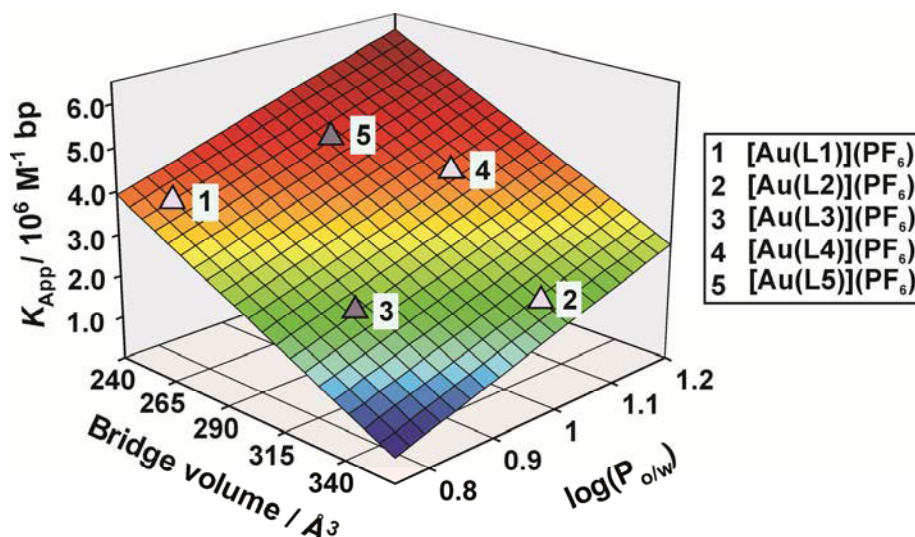


Figure 5.18: Graph of the ctDNA affinity constant (K_{app} , 298 K) of $[\text{Au}(\text{L1})](\text{PF}_6)$, $[\text{Au}(\text{L2})](\text{PF}_6)$, $[\text{Au}(\text{L3})](\text{PF}_6)$, $[\text{Au}(\text{L4})](\text{PF}_6)$ and $[\text{Au}(\text{L5})](\text{PF}_6)$ as a function of the steric bulk of the macrocycle's hydrocarbon bridge and the hydrophobicity of the complete Au^{3+} cation, $\log(P_{o/w})$. The 3D surface is the best-fit bivariate linear regression function to the data.

The complex $[\text{Au}(\text{L12})](\text{PF}_6)$ was designed to determine if the quinoxaline tail was an important feature for binding to the DNA. As this complex has a binding constant which is an order of magnitude lower than the complexes with the quinoxaline tail, it is clear that the extended aromaticity of the quinoxaline moieties which leads to favourable π - π interactions with the DNA bases is important to enhance the DNA binding affinity.

As the complexes all cause a reduction in EB-DNA emission intensity, this suggests that the complexes efficiently compete with EB for intercalative binding sites. This implies that the complexes do indeed intercalate between the DNA base pairs. The fluorescence quenching of the EB bound to DNA by the complexes is in agreement with the classic Stern-Volmer equation at lower concentrations of the complexes, Equation 5.12:

$$I_0 / I_f = 1 + kr \quad 5.12$$

Where I_0 and I_f are the emission intensity in the absence and presence, respectively, of the compound, k is the Stern-Volmer quenching constant and r is the ratio of the total concentration of the compound to that of the DNA. Figure 5.16 shows the linear Stern-Volmer plot of $[\text{Au}(\text{L1})](\text{PF}_6)$. The k value of $[\text{Au}(\text{L1})](\text{PF}_6)$ was calculated as 0.875 which again suggests a strong interaction between the complex and DNA.

A competitive binding study was attempted for the free ligand, H₂L1. However, after the addition of 2.1×10^{-5} M of the compound to the EB-DNA solution, the macrocycle precipitated out of solution. It must be noted that there was no significant decrease in the emission intensity with increasing additions before the compound precipitated out of solution. This indicates the free macrocycle may not intercalate DNA base pairs and that the gold(III) ion is important for interaction with the DNA base pairs.

In conclusion, the competitive binding fluorescence studies have shown that the macrocyclic and pseudomacrocyclic complexes interact strongly with ctDNA. The complex [Au(L11)](PF₆) has the largest k_{app} value as it has the alcohol functional groups which can hydrogen bond with the DNA base pairs or sugar-phosphate units. The quinoxaline moiety is also important for effective DNA intercalation as the acyclic [Au(L12)](PF₆), which does not contain the quinoxaline ring system, has the lowest k_{app} value. Steric and electrostatic factors can affect the DNA binding constant. The ligand H₂L1 does not appear to interact with the DNA, indicating that the gold(III) ion is also essential for DNA interaction. This technique indicates that DNA intercalation is the mode of action as the complexes displace the EB by intercalating between the base pairs.

5.7 References

- (1) Pavia, D. L., Lampman, G. M., Kriz, G. S., Vyvyan, J. R. *Introduction to Spectroscopy, 4th edition*; Brooks/Cole: USA, 2009.
- (2) Silverstein, R. M., Webster, F. X. *Spectrometric Identification of Organic Compounds, 6th Edition*; John Wiley and Sons, 1998.
- (3) Nakanishi, K., Solomon, P. H. *Infrared Absorption Spectroscopy, 2nd Edition*; Holden-Day: San Francisco, 1977.
- (4) Duckett, S., Gilbert, B. *Foundations of Spectroscopy*; Oxford University Press: USA, 2001.
- (5) Gunzler, H., Gremlich, H.-U. *IR Spectroscopy An Introduction*; Wiley-VCH Verlag GmbH: Germany, 2002.
- (6) Bacchi, A., Carcelli, M., Gabba, L., Ianelli, S., Pelagatti, P., Pelizzi, G., Rogolino, D. *Inorg. Chim. Acta* **2003**, *342*, 229.
- (7) Sadler, P. J., Sue, R. E. *Met. Based Drugs* **1994**, *1*, 107.
- (8) Hu, Y., Li, Q.-Q., Li, H., Guo, Q.-N., Lu, Y.-G., Li, Z.-Y. *Dalton Trans.* **2010**, *39*, 11344.
- (9) Munro, O. Q., Strydom, S. D., Grimmer, C. D. *New J. Chem.* **2004**, *28*, 34.
- (10) Shriver, D. F., Atkins, P. W. *Inorganic Chemistry, 3rd Edition*; Oxford University Press, 2000.
- (11) Petruska, J. *J. Chem. Phys.* **1961**, *34*.
- (12) Harris, D. C. *Quantitative Chemical Analysis*; W. H. Freeman and Company: San Francisco, 1982.
- (13) Wilkins, R. G. *Kinetics and Mechanism of Reactions of Transition Metal Complexes, 2nd Edition*; VCH Verlagsgesellschaft mbH: Weinheim, 1991.
- (14) Willard, H. H., Merritt, L. L. Jr., Dean, J. A., Settle, F.A. Jr. *Instrumental Methods of Analysis, 7th edition*; Wadsworth Publishing Company: California, 1988.
- (15) Skoog, D. A., West, D. M. *Principles of Instrumental Analysis, 2nd Edition*; Saunders College: USA, 1980.
- (16) Bauer, H. H., Christian, G. D., O'Reilly, J. E. *Instrumental Analysis*; Allyn and Bacon, Inc.: Boston, 1978.
- (17) Wang, L., Zhu, X.-J., Wong, W.-Y., Guo, J.-P., Wong, W.-K., Li, Z.-Y. *Dalton Trans.* **2005**, 3235.
- (18) Vogler, A., Kunkely, H. *Coord. Chem. Rev.* **2001**.
- (19) Paw, W. C., S. D., Mansour, M. A., Cennick, W. B., Geiger, D. K., Eisenberg, R. *Coord. Chem. Rev.* **1998**, *171*, 125.
- (20) Wilson, C. R., Fagenson, A. M., Ruangpradit, W., Muller, M. T., Munro, O. Q. *Inorg. Chem.* **2013**, *52*, 7889.
- (21) Akerman, M. P., University of KwaZulu Natal, 2011.
- (22) Parish, R. V. *NMR, NQR, EPR, and Mossbauer Spectroscopy in Inorganic Chemistry*; Ellis Horwood Limited: Great Britain, 1990.
- (23) Sanders, J. K. M., Hunter, B. K. *Modern NMR Spectroscopy A Guide for Chemists*; Oxford University Press: Great Britain, 1989.
- (24) Yang, L., Chen, Q., Li, Y., Xiong, S., Li, G., Shi Ma, J. *Eur. J. Inorg. Chem.* **2004**, 1478.
- (25) Kay, L. E., Gardner, K. H. *Curr. Opin. Struct. Biol.* **1997**, *7*.
- (26) Garret, D. S., Seok, Y. J., Liao, D. I., Peterofsky, A., Gronenborn, A. M., Clore, G. M. *Biochem.* **1997**, *36*.
- (27) Ubbink, M., Ejdebaeck, M., Karlsson, B. G., Bendall, D. S. *Structure* **1998**, *6*, 323.
- (28) Foris, A. *Magn. Reson. Chem.* **2000**, *38*.
- (29) Rudnev, A. V., Foteeva, L. S., Kowol, C., Berger, R., Jakupec, M. A., Arion, V. B., Timerbaev, A. R., Keppler, B. K. *J. Inorg. Biochem.* **2006**, *100*.
- (30) Monteiro, C. J. P., Pereira, M. M., Pinto, S. M. A., Simões, A. V.C., Sa', G. F.F., Arnaut, L. G., Formosinho, S. J., Simões, S., Wyatt, M. F. *Tetrahedron* **2008**, *64*.
- (31) Patrick, G. L. *An Introduction to Medicinal Chemistry, third edition*; Oxford University Press: New York, 2005.
- (32) Thomas, G. *Medicinal Chemistry An Introduction*; John Wiley & Sons, Ltd: USA, 2002.
- (33) Ghasemi, J., Saaidpour, S. *Anal. Chim. Acta.* **2007**, *604*, 99.
- (34) Valko, K. *J. Chromatogr.* **2003**.

- (35) Miyazaki, Y., Kato, Y., Manabe, T., Shimada, H., Mizuno, M., Egusa, T., Ohkouchi, M., Shiromizu, I., Matsusue, T., Yamamoto, I. *Biorg. Med. Chem.* **2006**.
- (36) Clark, C. R., Halfpenny, P. R., Hill, R. G., Horwell, D. C., Hughes, J., Jarvis, T. C., Rees, D. C., Schofield, D. *J. Med. Chem.* **1988**, 31, 831.
- (37) Berners-Price, S. J., Bowen, R. J, Parsons, P. G. 1996; Vol. C07F 9/58 A61K 31/675.
- (38) El-Ayaan, U., Linert, W. *J. Coord. Chem.* **2002**, 55.
- (39) Halliwell, B., Halliwell, J. M. C. *Free Radicals in Biology and Medicine, 2nd edition*; Claren Press: Oxford, 1989.
- (40) Gorbitz, C. H. *Acta Chem. Scand. B.* **1987**, 41.
- (41) Jelsch, C., Didierjean, C. *Acta Cryst.* **1999**, C55, 1538.
- (42) Schluga, P., Hartinger, C. G., Egger, A., Reisner, E., Galanski, M., Jakupec, M. A., Keppler, B. K. *Dalton Trans.* **2006**, 1796.
- (43) Barnholtz, S. L., Lydon, J. D., Huang, G., Venkatesh, M., Barnes, C. L., Ketring, A. R., Jurisson, S. S. *Inorg. Chem.* **2001**, 40, 972.
- (44) Espenson, J. H. *Chemical Kinetics and Reaction Mechanisms, 2nd Edition*; McGraw-Hill: New York, 1995.
- (45) Sun, R. W.-Y., Che, C.-M. *Coord. Chem. Rev.* **2009**, 253, 1682.
- (46) Cabbiness, D. K., Margerum, D. W. *J. Am. Chem. Soc.* **1969**, 91, 6540.
- (47) Busch, D. H., Farmery, K., Goedken, V., Katovic, V., Melnyk, A. C., Sperati, C. R., Tokel, N. *Advan. Chem. Ser.* **1971**, 100, 44.
- (48) Melson, G. A. *Coordination Chemistry of Macrocyclic Compounds*; Plenum Press: New York, 1979.
- (49) Cummings, S. D. *Coord. Chem. Rev.* **2009**, 253, 1495.
- (50) Chen, L.-M., Liu, J., Chen, J.-C., Tan, C.-P., Shi, S., Zheng, K.-C., Ji, L.-N. *Inorg. Biochem.* **2008**, 102, 330.
- (51) Kawade, V. A., Kumbhar, A. A., Kumbhar, A. S., N`ather, C., Erxleben, A., Sonawaned, U. B., Joshid, R. *Dalton Trans.* **2011**, 40.
- (52) Garcia-Gimenez, J. L., Gonzalez-Alvarez, M., Liu-Gonzalez, M., Macias, B., Borrás, J, Alzuet, G. *J. Inorg. Biochem.* **2009**, 103.
- (53) Ussey, D. W. In *Academic Press; Analysis*, C. f. B. S., Ed.; Academic Press: 2001.
- (54) Shahabadi, N., Heidari, L. *Spectrochimica Acta A* **2012**, 97.
- (55) Selvakumar, B., Rajendiran, V., Uma, P., Maheswari, H., Stoeckli-Evans, M., Palaniandavar, J. *J. Inorg. Biochem.* **2006**, 100, 316.
- (56) Baguley, B. C., Le Bret, M. *Biochem.* **1984**, 23.
- (57) Liu, X., Li, J., Li, H., Zheng, K., Chao, H., Ji, L. *J. Inorg. Biochem.* **2005**, 99, 2372.
- (58) Wang, X., Guo, Z. *Dalton Trans.* **2008**, 1521.

CHAPTER SIX:

COMPUTATIONAL CHEMISTRY

6.1 Introduction

Computational chemistry is a powerful tool that can give information on the molecular geometry of compounds which includes the shape, bond lengths and bond angles of molecules. It can also give important information on the energies of molecules, the transition states and the chemical reactivity of molecules. IR, UV and NMR spectra can all be calculated using this technique.¹⁻⁴

There are a number of different computational methods available:

- Molecular mechanics is based on a model of a molecule as a collection of balls (atoms) held together by springs (bonds). This is a fast technique, requiring minimal computational power and allows for the optimization of large molecules like steroids quickly.^{1,2}
- *Ab Initio* calculations are based on approximate solutions of the Schrödinger equation, which describes how electrons in a molecule behave, and gives an energy and wavefunction. A wavefunction is a mathematical function that can be used to calculate the electron distribution. As the Schrödinger equation cannot be solved for any molecule with more than one electron, approximations need to be used. This technique is based only on physical theory and the calculations are relatively slow.^{1,2}
- Semi-empirical calculations are also based on approximate solutions of the Schrödinger equation, but use experimental values for solving the equation (parametrization). Semi-empirical calculations are slower than molecular mechanics calculations, but faster than *ab initio* calculations.^{1,2}
- Density Functional Theory (DFT) is also based on the Schrödinger equation; however, it does not calculate a wavefunction, but rather derives the electron distribution directly. These calculations are faster than *ab initio*, but slower than semi-empirical calculations.^{1,2}
- Molecular dynamics calculations study molecules in motion.^{1,2}

In general, *ab initio* and DFT calculations enable novel molecules of theoretical interest to be studied, provided they are not too big. Semi-empirical methods can be applied to fairly large molecules while molecular mechanics can be used to calculate geometries of very large molecules such as proteins and nucleic acids.¹ DFT was chosen as the method to study the ligand systems as well as the gold(III) complexes as DFT is the method of choice for geometry and energy calculations of transition metal compounds for which conventional *ab initio* calculations often give poor results.¹ DFT is also known to give reasonable IR frequencies and the time-dependent DFT and NMR calculations are often precise.¹

Both *ab initio* and the semi-empirical approaches calculate a wavefunction.¹⁻⁴ However, a wavefunction is not a measurable feature of a molecule or atom and whose physical meaning is controversial. DFT is not based on a wavefunction, but rather on the electron probability density function or simply the electron density.^{1,2} The electron density, ρ , is measurable by techniques such as X-ray diffraction or electron diffraction. The electron density is a function of position only, just three variables (x , y , z), while the

wavefunction of an n -electron molecule is a function of $4n$ variables, three spatial coordinates and one spin coordinate, for each electron. No matter how big the molecule may be, the electron density remains a function of just three variables.^{1,2} Thus, the electron density function is better than the wavefunction in that it is measurable and it can be mathematically determined.

DFT calculations on molecules are based on the Kohn-Sham approach^{1,2}, which is reliant on two theorems published by Hohenberg and Kohn in 1964. The first Hohenberg-Kohn theorem states that all the properties of a molecule in a ground electronic state are determined by the ground state electron density function $\rho_0(x,y,z)$ i.e., given $\rho_0(x,y,z)$ any ground state property such as E_0 can be calculated.^{1,2} This is represented in Equation 6.1:

$$\rho_0(x,y,z) \rightarrow E_0 \quad 6.1$$

The relationship in Equation 6.1 means that E_0 is a functional of $\rho_0(x,y,z)$. A function is a rule that transforms a number into another (or the same number). A functional is a rule that transforms a function into a number. Thus, the first Hohenberg-Kohn theorem states that any ground state property of a molecule is a functional of the ground state electron density.^{1,2} This can be expressed as Equation 6.2 for energy:

$$E_0 = F[\rho_0] = E[\rho_0] \quad 6.2$$

This first theorem is merely an existence theorem in that it states that a functional F exists, but does not explain how to find it. This is a major problem with DFT. The significance of this theorem lies in the fact that it shows there is in principle a way to calculate molecular properties from electron density.^{1,2}

The second Hohenberg-Kohn theorem is the DFT analogue of the wavefunction variation theorem. It states that any trial electron density function will give an energy higher than (or equal to) the true ground state energy.^{1,2} In DFT molecular calculations, the electronic energy from the trial electron density is the energy of the electron moving under the potential of the atomic nuclei. The second theorem can be stated as in Equation 6.3:

$$E_v[\rho_t] \geq E_0[\rho_0] \quad 6.3$$

Where ρ_t is a trial electronic density, E_v is the electronic energy of the nuclear potential and $E_0[\rho_0]$ is the true ground state energy corresponding to the true electronic density ρ_0 . The trial density must satisfy the conditions in Equation 6.4:

$$\int \rho_t(r) dr = n \quad 6.4$$

Where r is the position vector of the point coordinates (x,y,z) and n is the number of electrons in the molecule. This theorem suggests that any value of the molecular energy that is calculated from the Kohn-Sham equation will be greater than or equal to the true energy.^{1,2}

The Kohn-Sham equations are the basis of current molecular DFT calculations. If an accurate molecular electron density function ρ and the correct energy functional were known, then the electron density

function could be converted straight to the electron density.^{1,2} Unfortunately, an accurate ρ and correct energy functional are not known. The Kohn–Sham approach takes into account these two problems. The basic ideas behind the Kohn–Sham approach is to express the molecular energy as a sum of terms, with only one relatively small term involving the unknown functional and to use an initial guess of the electron density ρ in the Kohn–Sham equations to calculate an initial guess of the orbitals and energy levels.^{1,2} This initial guess is then used to refine these orbital and energy levels. The final Kohn–Sham orbitals are used to calculate an electron density that can be used to calculate the energy.^{1,2}

The strategy is to separate the electronic energy of a molecule into portions which can be calculated accurately without using DFT. The ground state electronic energy of a molecule is the sum of electron kinetic energies, the nucleus–attraction potential energies and the electron–electron repulsion potential energies,^{1,2} Equation 6.5.

$$E = T[\rho] + V_{Ne}[\rho] + V_{ee}[\rho] \quad 6.5$$

The key to Kohn–Sham theory is that it calculates the kinetic energy under the assumption of non-interacting electrons.^{1,2} For a non-interacting system the Slater determinant which is composed of molecular orbitals, ϕ_i , is used, the exact kinetic energy is given by Equation 6.6.

$$T_s = \sum_{i=1}^{N_{elec}} \left\langle \phi_i \left| -\frac{1}{2} \nabla^2 \right| \phi_i \right\rangle \quad 6.6$$

The subscript S denotes that the kinetic energy is calculated from the Slater determinant. This is an approximation to the real kinetic energy as it is for non-interacting electrons. In reality the electrons are interacting and this does not provide the total kinetic energy.^{1,2} The difference between the exact kinetic energy and that calculated by assuming non-interacting orbitals is small. The remaining kinetic energy is absorbed into an exchange–correlation term; the general DFT energy expression is given in Equation 6.7.

$$E_{DFT}[\rho] = T_s[\rho] + E_{Ne}[\rho] + J[\rho] + E_{xc}[\rho] \quad 6.7$$

Where $J[\rho]$ is the coulomb part of the electron–electron repulsion potential energy. By equating E_{DFT} to the exact energy for the real system given in Equation 6.5, the term E_{xc} (exchange–correlation energy) can be defined as the part that remains after subtraction of the non-interacting kinetic energy and the E_{Ne} and J potential energy terms.^{1,2} Essentially, E_{xc} is the difference in the true system and the idealized non-interacting system and is expressed in Equation 6.8.

$$E_{xc}[\rho] = (T[\rho] - T_s[\rho]) + (E_{ee}[\rho] - J[\rho]) \quad 6.8$$

This exchange–correlation functional is the only unknown term in the expression of DFT energy and this approximation is the main problem with DFT. From the energy equation, the Kohn–Sham equations can be derived. The molecular orbitals of the Kohn–Sham equations are expanded with basis functions; matrix methods are used to refine the energy and to get a set of molecular orbitals.^{1,2}

Deriving a good functional is a major challenge in density functional theory. A good functional handles not only exchange and correlation error, but also self repulsion and kinetic errors.^{1,2} The functional is normally tackled as an exchange term and a correlation term. The functionals used are: local density approximation (LDA), local spin density approximation (LSDA), Generalized gradient approximation (GGA) or gradient corrected functional, Meta-GGA (MGGA), Hybrid GGA or adiabatic connection methods (ACM methods), hybrid meta GGA (hybrid MGGA) methods and 'fully' non-local theory.^{1,2}

The accuracy of a DFT calculation depends on the size of the basis set and the density functional used. The gradient-corrected functional (GGA), PBEPBE (Perdew, Burke and Ernzerhof)^{5,6} was used for the DFT calculations for the gold(III) complexes. The hybrid GGA (HGGA) functional, B3LYP (Becke three parameter Lee-Yang-Parr)^{7,8} was used for the ligands. These functionals utilize both the electron density and its gradient. Gradient corrected functionals, especially hybrid functionals, give good to excellent geometries and fairly good reaction energies.⁹ The functional B3LYP is one of the most successful functionals in terms of overall performance.^{1,2}

The basis set is the set of atomic functions that describes the number and type of atomic orbitals considered in the calculation for a particular atom or molecule.¹⁰ Essentially it is the region in space that each electron is restricted to. For a basis set to be complete it would need to include an infinite number of functions, but as this is not possible for practical applications, a restricted basis set has to be used. The size of the basis sets that are logically possible are therefore limited by available computational power.¹⁰ The fewer the number of restrictions on the position of each electron, the more accurate the prediction of the molecular orbitals; however, this will also lead to increased computational time.¹⁰

The basis set used for the ligands was 6-311G(d,p) while the effective core potential basis LANL2DZ (Los Alamos National Laboratory 2-double-zeta) was used for the gold(III) chelates. The basis set 6-311G(d,p) is restricted to atoms from H-Kr, but is considered to give more accurate results than the broader basis set 3-21G, which could also be used as it is applicable to atoms in the range H-Xe.⁹ Although computational time using the basis set 6-311G will be greater than 3-21G, it should give a more accurate result. The basis set 6-311G(d,p) applies fewer restrictions to the calculations than 3-21G.⁹ The 6-311G(d,p) basis set uses different components to make up the set. The 6-311G basis is used for the first-row atoms, H and He, and the McLean-Chandler (12s, 9p) basis set for the second-row atoms, Li-Ne.^{11,12} Single first polarization and diffuse functions (d,p) have been included in the basis set to increase their accuracy.

The basis set LANL2DZ^{13,14} can be used for atoms in the range H, Li-Ba, La-Bi and is therefore applicable for the gold(III) chelates. This basis uses effective core potentials (ECP) to deal with atoms in the second row of the periodic table and beyond to the heavier atoms.⁹ The core electrons of an atom are only slightly affected by their chemical environment and primarily shield the nuclei and provide an effective field for the electrons. ECPs replace the atomic core electrons in the calculations where the atomic cores are inactive, reducing the number of electrons involved in calculation involving heavy elements.⁹ This allows for accuracy to be maintained while computational time is reduced. The LANL2DZ basis set applies the D95V (Dunning/Huzinaga valence double zeta)¹⁵ basis set on the first row elements and the Los Alamos ECP plus double zeta on Na-La, Hf-Bi.^{13,14} The double zeta type basis implies that the basis set of all basis functions are double which allows for a better description of the fact that the electron distribution is not the same in different directions.⁹

Solvent effects on the NMR and electronic spectra are determined by placing the molecule in a solvent continuum.⁹ The molecule is placed in a field with the same dielectric constant as the solvent with no solvent molecules explicitly included in the calculations.⁹ This results in a reduced computational time for the calculation, while taking into account solvent effects.

The objective of the computational calculations is to perform geometry optimizations, NMR, vibrational frequency and electronic transition analyses on the synthesized ligands and the gold(III) complexes. This will allow for a comparison of the calculated data with the experimental data and to determine the correlation and calculated values. The calculations can be used to broaden the understanding of the chemistry of both the ligands and gold(III) chelates.

6.1.1 Previous Computational Studies on Schiff base and macrocyclic ligands

A literature review showed that computational studies have been done on two acyclic ligands which have the same basic framework as the bis(pyrrolide-imine) macrocyclic ligands reported in this work. The reported structures have the same acyclic bis(pyrrolide-imine) structure but differ from H₂L12 in their di(azomethine) linkage unit. The compound *N,N'*-bis[(1*E*)-1*H*-pyrrol-2-ylmethylene]propane-1,3-diamine has a three carbon bis(imine) linkage while *N,N'*-bis[(1*E*)-1*H*-pyrrol-2-ylmethyl-ene]benzene-1,2-diamine has a phenylene bridging unit. The X-ray crystal structures and solid state interactions for these compounds have also been discussed in Chapter Four.

The X-ray structure of *N,N'*-bis[(1*E*)-1*H*-pyrrol-2-ylmethylene]propane-1,3-diamine showed that the compound in the solid state forms a one-dimensional hydrogen-bonded chain with the pyrrole N-H acting as the hydrogen bond donor and the imine N atom as the hydrogen bond acceptor.¹⁶ The monomer structure of *N,N'*-bis[(1*E*)-1*H*-pyrrol-2-ylmethylene]propane-1,3-diamine as well as its hydrogen-bonded trimer and pentamer supramolecular analogues were studied by gas-phase quantum chemical AM1 calculations. The aim of this study was to quantify the electrostatics of the intermolecular hydrogen-bonding interaction. As the calculations involved up to five interacting monomers, *ab initio* or DFT calculations, would take too long.¹⁶ Thus the semi-empirical valence-electron method, AM1 was used.¹⁷ The AM1 calculations readily explained the complementary hydrogen-bonded network. The pyrrole NH proton had the most positive fractional charge while the imine N atom was the most negative atom relative to the rest of the molecule.¹⁶ This data showed in electrostatic terms that the hydrogen-bonded network observed in the X-ray crystal structure is stable. A least square (RMS) fit of the experimental X-ray and calculated structures of the hydrogen-bonded trimers was also plotted. The RMSD value for the calculated and experimental structures is 0.460 Å with the pyrrole rings showing the most deviation.¹⁶ This is due to the fact that the molecules in the lattice are more closely packed than the molecules in the gas phase.¹⁶

The X-ray crystal structure of *N,N'*-bis[(1*E*)-1*H*-pyrrol-2-ylmethyl-ene]benzene-1,2-diamine showed that the compound is not planar as would be expected due to the rigidity of the aromatic bridge and extended π conjugation throughout the molecule.¹⁸ AM1 calculations were run on this compound to explain the deviation in planarity. Different conformers of the compound were calculated to determine the lowest energy structure. The calculations showed that the planar structure is the highest energy conformation of the ligand.¹⁸ Non-bonded repulsion between the two pyrrole NH groups in the planar conformation is responsible for the strain-relieving twisted conformation.¹⁸ The RMS fits for the calculated and experimental structures were plotted and the RMSD value for the overlay was 0.661 Å, indicating that the structures are in fairly good agreement.¹⁸ The calculations for this compound also showed that the pyrrole NH hydrogen atom

has the most positive fractional charge, while the imine type nitrogen atom is the most negative atom relative to the rest of the molecule.¹⁸

As described in Chapter Four, the proposed macrocyclic ligands exhibit NH tautomerism. NH tautomerism is also an important phenomenon in porphyrins.¹⁹ Normally, the tautomerism of porphyrins occurs rapidly among the four nitrogen atoms in the core and computational calculations have been important in showing that each tautomer has a similar stability.²⁰ The N-confused porphyrin (NCP) is a porphyrin isomer with an inverted pyrrole ring and contains three core nitrogen atoms and one peripheral nitrogen atom.²⁰ An NCP possesses an asymmetrical structure, unlike regular porphyrins, resulting in the presence of six tautomeric forms. These tautomers can be categorized into two groups: type A is when the N-confused pyrrole ring takes on an imino form and type B is when the pyrrole ring takes on the amino form, Figure 6.1.¹⁹ The different tautomer types of the N-confused tetraaryl porphyrin (NCTPP) were calculated at the B3LYP/6-311G** level of theory. The type A tautomer was calculated as the lowest energy tautomer while type B was 4.94 kcal mol⁻¹ higher in energy.¹⁹ A typical tetraaryl porphyrin is usually 12.29 kcal mol⁻¹ lower in energy than type A of the N-confused tetraaryl porphyrin. Structures were also calculated for N-alkylated NCTPP at the B3LYP/6-311G** level of theory. Through N-alkylation NH tautomerism is prevented and the porphyrin can be fixed as one type of tautomer. Again the type B tautomer was shown to be less stable than type A by 13-15 kcal mol⁻¹.¹⁹ The large difference is attributed to the fact that no intramolecular hydrogen bonding can take place in type B.¹⁹

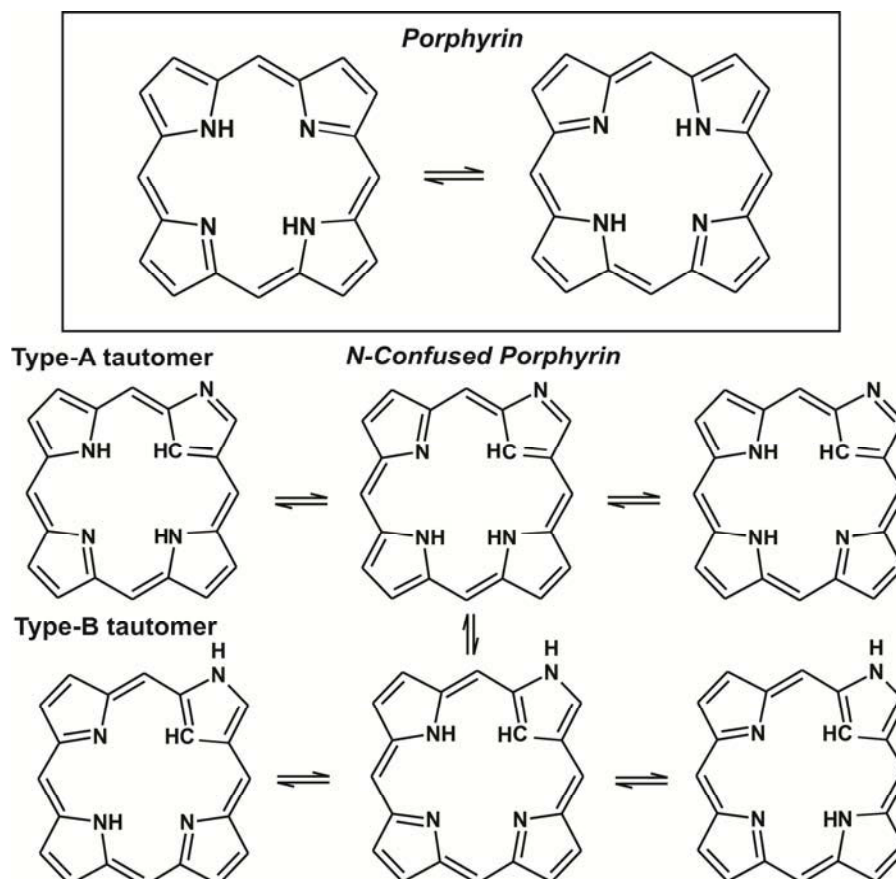


Figure 6.1: NH-tautomerism in porphyrins and N-confused porphyrins.

Molecular simulations can also give important information on the geometry of the porphyrins and how this affects the NH tautomerism. The non-planar saddled 2,3,7,8,12,13,17,18-octaethyl-5,10,15,20-Tetraphenyl porphyrin has a higher activation barrier than porphine while the ruffled 5,10,15,20-tetra-(tert-butyl)porphyrin has a lower barrier.^{21,22} It was calculated that in the latter case that the lower barrier was a result of the out of plane ruffled conformation of the porphyrin core, leading to a decreased distance between the two inner nitrogen atoms. It was also calculated that there is a strong reduction in the N-N distance in the transition state of the proton-hopping process in planar porphine.²³

Thus, molecular simulations can give important insight into the structure of compounds and can be used to explain some of the interactions seen in the solid state. As described with the porphyrins, computational chemistry can be used to understand the tautomerism in compounds as well as to calculate their most stable structures.

6.1.2 Previous Computational Studies of Relevant Metal chelates

The proposed gold(III) chelates are novel structures and there are no examples of computational work on them or any closely related structure in the literature. Computational work has been done on the nickel(II) chelate of *N,N'*-bis[(1*E*)-1*H*-pyrrol-2-ylmethyl-ene]benzene-1,2-diamine.²⁴ The calculations made use of the ZINDO-SOS method and focused on the calculation of second order molecular optical non-linearities²⁴ which are not relevant to this work.

There are reports of DFT simulations that have been performed on gold(III) chelates.²⁵⁻²⁸ The most widely employed functional was B3LYP with the basis set LANL2DZ. These are the same conditions that have been used in the calculations of the synthesized gold(III) chelates. Literature shows that the results obtained from this functional depend on the similarities between the test molecules and the molecules that were used to train the hybrid functional.²⁹

The calculations obtained from these reports were mainly geometry optimizations with the results in good agreement with the experimental data.²⁵⁻²⁸ Mulliken charges were also calculated for the chelates and these values appear to be sensible when compared to experimentally observed results.³⁰ The lack of calculated NMR shifts reported in the computational work of gold(III) chelates may be due to the use of ECPs in the LANL2DZ basis set. This basis set does not take into account the core electrons of the gold(III) ion and the calculated values may be unreliable. Gold is also not a nucleus easily observed by experimental NMR.

6.2 Computational Method

The DFT calculations were all performed with Gaussian 09W.³¹ The X-ray structure coordinates were not used as the input structures for the geometry optimizations, the input structures were created using GaussView version 5.09.³² The geometry optimizations were done at the B3LYP/6-311G(d,p) level of theory for the ligands and at the PBEPBE/LANL2DZ level of theory for the gold(III) complexes. The results of the calculations were analyzed using GaussView version 5.09.³² Symmetry constraints were placed on tautomer 3 of all the macrocyclic and pseudomacrocyclic ligands; the N-H bond distance was fixed at 1.040 Å. The NMR calculations were performed using the GIAO method at the same level of theory used for the geometry optimizations. Frequency calculations were performed on all compounds, both as free ligands and gold(III) chelates. The ¹H and ¹³C NMR chemical shifts were determined by comparisons with the ¹H and ¹³C NMR

isotropic shift computed for TMS at the same level of theory as that used for the calculations. The electronic spectral data were calculated using the TD-SCF method solving for 30 excited states. The collection of Gaussian job files can be found in **Appendix E**. Least-squares fits of the geometry optimized and experimental structures were performed using Mercury 2.4.³³

6.3 Computational Chemistry of Schiff Base Ligands

6.3.1 Geometry optimization results

Geometry optimization calculations were performed on all bis(pyrrolide-imine) ligands synthesized in this work using the B3LYP hybrid functional and the basis set 6-311G(d,p). As discussed in Chapter Four, there are four possible tautomers of the symmetric macrocyclic ligands where the hydrogen atoms may be located on the different pyrrole and imine N atoms. The asymmetric ligands have even more possible tautomeric forms (Chapter Four, Figure 4.15). The geometry optimized structures were calculated for all four possible tautomers for the symmetric ligands and all six possible tautomeric forms for the asymmetric ligands. Table 6.1 gives a comparison of the bond distances, angles and torsion angles for the experimental and geometry optimized tautomeric forms. The experimental and calculated structures were compared by fitting non-linear least-squares regression fit of the two structures for all the tautomers. The root-mean square deviation can be obtained from this plot, giving a mathematical means for comparing the structures. The RMS plots for the tautomeric forms of H₂L2, H₂L7 and H₂L9 and corresponding RMSD values are shown in Figure 6.2. The RMSD values for the rest of the ligands are given in Table 6.2. No negative eigen values were observed for any of the frequency calculations, indicating that the optimized structures were true minima on the global potential energy surface.

In general terms, the geometry optimized structures are in good agreement with the solid state structures. It must be considered that the calculated structures are in the gas phase and are completely free of any intermolecular interactions, while the solid state structures are influenced by these interactions. Each tautomeric form has a different geometry and therefore gives a different RMSD value. The X-ray structure of H₂L2 (Chapter Four, Figure 4.12) shows that the molecule is almost planar with the pyrrole rings both slightly canted relative to the quinoxaline ring. The geometry optimized structure of tautomer A (both hydrogen atoms positioned on the pyrrole N atoms) of H₂L2 is non-planar with one pyrrole ring and imine moiety twisted above the plane of the quinoxaline ring while the other pyrrole ring and imine moiety is below the plane. This deviation from planarity can mainly be seen in the torsion angle of the pyrrole rings relative to the quinoxaline ring. These torsion angles for the calculated structures are 39.3° for the one pyrrole ring and 7.6° for the other pyrrole ring of tautomer A while the X-ray structure has torsion angles of 9.1(1)° and -11.2(1)°. The out of plane twist of the pyrrole and imine moieties of tautomer A causes the propyl di(azomethine) linkage to twist out of the plane of the quinoxaline ring. This configuration of tautomer A is due to the non-bonded repulsion of the pyrrole N–H atoms. The two pyrrole rings twist away from one another to minimize the repulsion forces between the pyrrole N–H atoms. As the X-ray structure has one pyrrole N atom and the diagonally opposite imine N atom protonated there are minimal repulsion effects and the molecule is relatively planar. The difference in structures leads to a fairly large RMSD value of 0.601 Å for the X-ray crystal structure and tautomer A.

The geometry optimized structure of tautomer B has the hydrogen atoms positioned on the same N atoms as the X-ray structure. Consequently, both structures are very similar with the geometry optimized structure

also relatively planar with both pyrrole rings canted slightly relative to the quinoxaline tail. This is reflected in a small RMSD value of 0.098 Å. This indicates that the calculations are in good agreement with the experimental data.

Table 6.1: Summary of experimental and calculated bond lengths and angles of the bis(pyrrolide-imine) Schiff base ligands.

	C-C-C _α -N _{pyrr} torsion (°)	C=N _{imine} -C-N torsion (°)	C=N _{imine} -C angle (°)	C=N length (Å)
H₂L2				
Experimental	9.1(1), -11.2(1)	4.2(4), -1.4(4)	123.9(2)	1.297(4)
Tautomer A	39.3, 7.6	6.3, -1.7	119.1	1.274
Tautomer B	9.2, -11.4	4.7, -2.1	124.4	1.302
Tautomer C	5.5, -5.6	1.8, -3.3	124.2	1.299
Tautomer D	17.7, -48.7	-3.4, -5.1	125.1	1.347
H₂L5				
Experimental	28.7(2), -27.7(2)	2.3(3), -2.8(3)	123.0(1)	1.285(3)
Tautomer A	38.4, 10.2	6.7, 0.1	118.9	1.274
Tautomer B	8.7, -10.3	4.1, -1.2	124.5	1.302
Tautomer C	5.0, -5.4	1.1, -2.7	124.1	1.300
Tautomer D	-11.7, -33.5	-3.0, -3.7	124.6	1.346
H₂L6				
Experimental	29.0(3), -31.2(3)	3.5(4), -1.8(4)	123.0	1.289(4)
Tautomer A	10.4, 37.3	6.8, 0.1	118.8	1.274
Tautomer B	8.4, -10.3	4.2, -1.1	124.5	1.301
Tautomer C	5.1, -5.3	1.3, -2.7	124.1	1.300
Tautomer D	-11.8, -32.9	-3.1, -3.6	124.6	1.346
Tautomer E	-5.3, -5.5	3.3, -1.1	124.2	1.300
Tautomer F	8.9, -10.8	4.1, -1.3	124.4	1.301
H₂L7				
Experimental	15.5(2), -7.8(2)	3.3(3), -3.7(3)	123.7(2)	1.289(3)
Tautomer A	38.4, 9.4	6.5, -0.1	119.0	1.274
Tautomer B	8.3, -10.2	4.3, -1.2	124.5	1.301
Tautomer C	5.3, -5.4	1.2, -2.6	124.0	1.299
Tautomer D	49.0, -49.4	5.9, -5.9	126.0	1.344
Tautomer E	5.2, -5.1	3.0, -1.2	124.1	1.300
Tautomer F	10.6, -8.9	1.3, -4.1	124.4	1.300
H₂L8a				
Experimental	8.5(6), -4.6(6)	2.6(6), 2.1(6)	124.1(4)	1.289(5)
Tautomer A	-9.5, -26.5	1.7, -7.5	119.1	1.273
Tautomer B	6.2, -4.9	1.4, -3.9	124.5	1.298
Tautomer C	3.8, -3.2	1.3, -2.9	124.1	1.300
Tautomer D	-8.4, -26.1	-3.2, -3.8	125.1	1.340
H₂L8b				
Experimental	1.8(9), -0.3(9)	-0.3(9), -1.0(9)	123.3(6)	1.293(9)
Tautomer A	-13.6, -27.9	0.9, -7.8	119.1	1.273
Tautomer B	5.4, -6.9,	4.3, -1.2	124.6	1.300
Tautomer C	3.8, -3.8	1.1, -2.4	124.0	1.300
Tautomer D	-12.1, -29.1	-2.4, -4.3	124.8	1.344
Tautomer E	3.6, -3.8	3.3, -1.1	124.3	1.299
Tautomer F	7.4, -6.4	1.1, -3.2	124.1	1.300

Table 6.1 continued...

	C-C-C _α -N _{pyrr} torsion (°)	C=N _{imine} -C-N torsion (°)	C=N _{imine} -C angle (°)	C=N length (Å)
H₂L9				
Experimental	8.4(2), -4.5(2)	-0.7(2), -2.7(2)	118.9(1)	1.291(2)
Tautomer A	29.2, 29.2	0.7, 0.7	118.4	1.274
Tautomer B	0.02, -0.004	0.02, -0.02	119.5	1.305
Tautomer C	0.002, 0.007	0.01, -0.007	118.9	1.304
Tautomer D	32.0, 32.0	-1.6, -1.6	125.8	1.337
H₂L12				
Experimental		-3.1(1), -3.1(1)	113.2(1)	1.277(1)
Calculated		0.083, -0.083	118.5	1.275

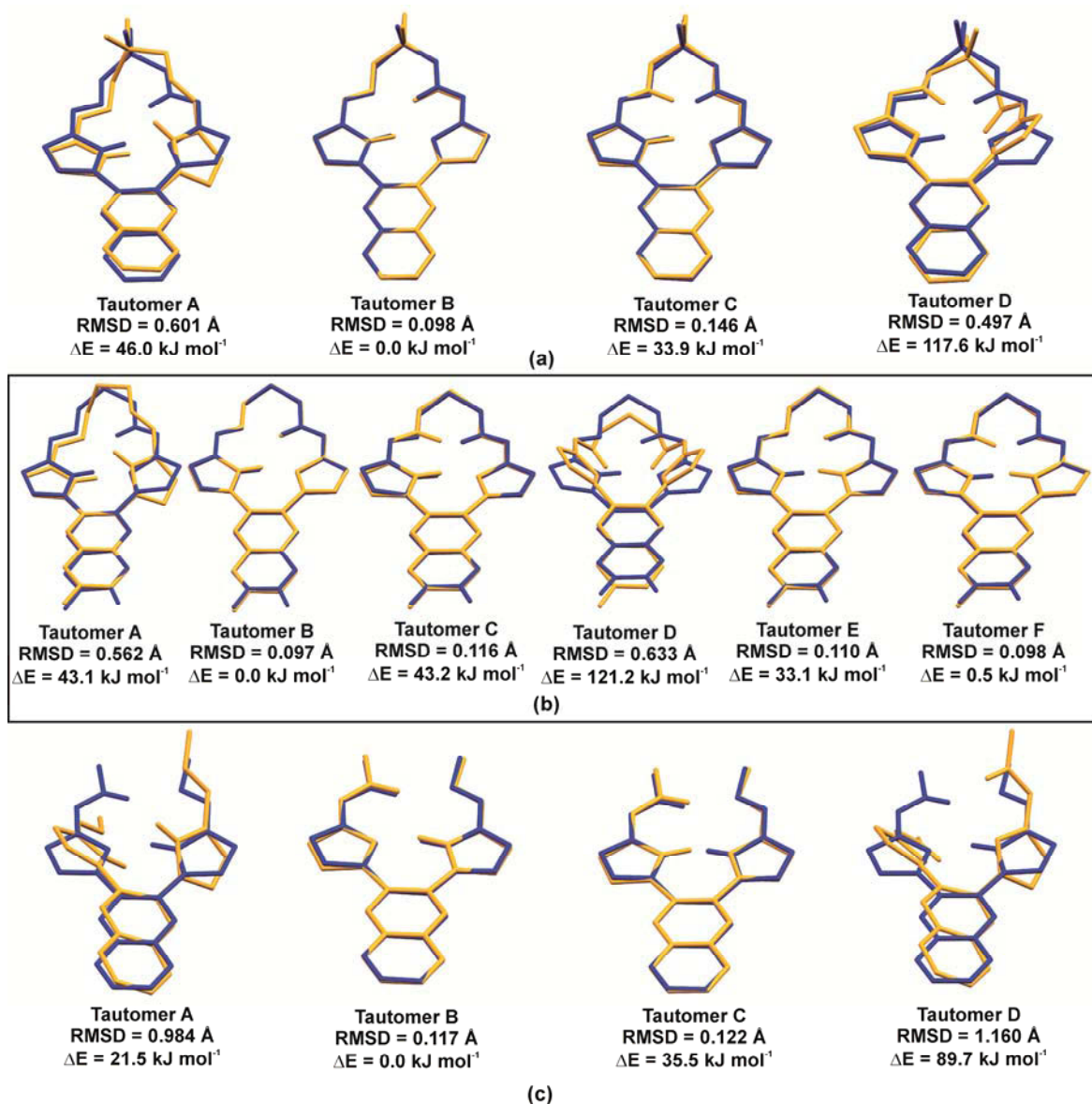


Figure 6.2: Least-squares fit of the non-H atoms of the DFT calculated (yellow) and the X-ray crystal structures (blue) of all the tautomers of (a) H₂L2, (b) H₂L7 and (c) H₂L9. The RMSD values and the relative energies of each tautomer are indicated on the diagram. The pyrrole and imine NH atoms have been included only to show the tautomeric form.

Table 6.2: RMSD values for the least-squares fit of the calculated and X-ray structure of all the tautomers and their relative energies.

	RMSD (Å)	E (kJ mol ⁻¹)	Δ E(kJ mol ⁻¹)
H₂L2			
Tautomer A	0.601	-3.199127x10 ⁶	46.0
Tautomer B	0.098	-3.199172x10 ⁶	0.0
Tautomer C	0.146	-3.199139x10 ⁶	33.9
Tautomer D	0.497	-3.199056x10 ⁶	117.6
H₂L5			
Tautomer A	0.729	-3.199147x10 ⁶	41.9
Tautomer B	0.275	-3.199189x10 ⁶	0.0
Tautomer C	0.338	-3.199155x10 ⁶	34.2
Tautomer D	0.798	-3.199082x10 ⁶	107.0
H₂L6			
Tautomer A	0.804	-3.095891x10 ⁶	44.9
Tautomer B	0.321	-3.095936x10 ⁶	0.0
Tautomer C	0.374	-3.095901x10 ⁶	34.7
Tautomer D	0.751	-3.095829x10 ⁶	106.8
Tautomer E	0.379	-3.095890x10 ⁶	45.3
Tautomer F	0.304	-3.095936x10 ⁶	0.2
H₂L7			
Tautomer A	0.562	-3.253254x10 ⁶	43.1
Tautomer B	0.097	-3.253297x10 ⁶	0.0
Tautomer C	0.116	-3.253254x10 ⁶	43.2
Tautomer D	0.633	-3.253176x10 ⁶	121.2
Tautomer E	0.110	-3.253264x10 ⁶	33.1
Tautomer F	0.098	-3.253297x10 ⁶	0.5
H₂L8a			
Tautomer A	0.534	-3.073595x10 ⁶	50.0
Tautomer B	0.131	-3.073645x10 ⁶	0.0
Tautomer C	0.125	-3.073617x10 ⁶	28.5
Tautomer D	0.592	-3.073537x10 ⁶	107.9
H₂L8b			
Tautomer A	0.493	-3.132171x10 ⁶	49.9
Tautomer B	0.116	-3.132221x10 ⁶	0.0
Tautomer C	0.0968	-3.132180x10 ⁶	40.4
Tautomer D	0.553	-3.132110x10 ⁶	110.9
Tautomer E	0.0862	-3.132218x10 ⁶	23.0
Tautomer F	0.129		2.9
H₂L9			
Tautomer A	0.984	-2.892538x10 ⁶	21.5
Tautomer B	0.117	-2.892604x10 ⁶	0.0
Tautomer C	0.122	-2.892569x10 ⁶	35.5
Tautomer D	1.160	-2.892515x10 ⁶	89.7
H₂L12			
Calculated	0.195		

The geometry optimized structure of tautomer C has a hydrogen atom positioned on a pyrrole N atom and the other located on the adjacent imine N atom. The N–H bond distance in this geometry-optimized structure had to be fixed at 1.040 Å, otherwise the pyrrole N–H would migrate to the adjacent pyrrole N

atom during the optimization process to give tautomer B. Figure 6.3 shows the movement of the hydrogen atom from the 4N pyrrole atom of H₂L2 to the 14N pyrrole atom when the N–H bond length is not fixed. This Figure is an overlay of the increasing bond length between 4N and 28H and decreasing bond length between 14N and 28H with increasing optimization steps as the bond is broken and the hydrogen atom migrates to 14N. There is minimal steric strain in the fixed structure of tautomer C as there is limited non-bonded repulsion between the NH hydrogen atoms in the structure. As a consequence this structure is the most planar of the four tautomers with small torsion angles of 5.5 and -5.6 ° for the pyrrole rings relative to the quinoxaline ring. The RMSD value is 0.147 Å indicating that the X-ray structure and the experimental data correlate well.

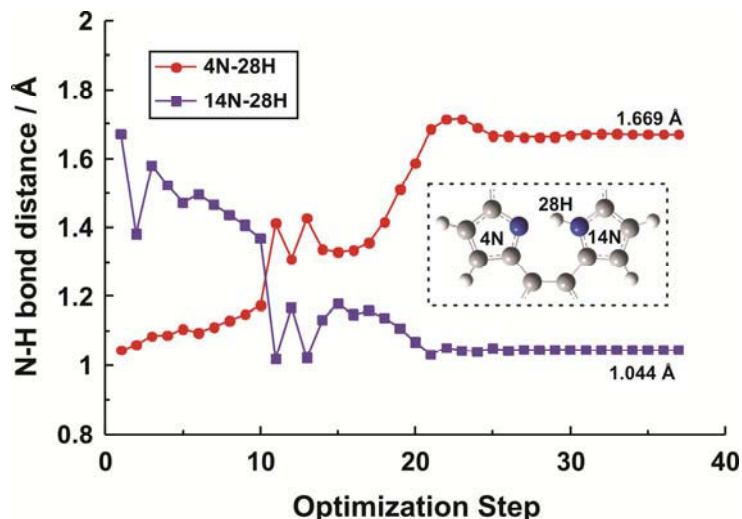


Figure 6.3: Change in selected N–H bond lengths with increasing optimization steps of tautomer C of H₂L2 with no restrictions on the bond lengths.

Tautomer D has both NH hydrogens positioned on the imine N atoms. The geometry optimized structure shows that this tautomer is non-planar due to steric strain and non-bonded repulsion. In order to relieve the strain of the close proximity of the imine N–H atoms, the pyrrole and imine moieties are twisted out of the plane of the quinoxaline ring. The one pyrrole ring is twisted by a much greater distance than the other to ensure maximum separation of the imine N–H atoms. This is reflected in the large torsion angles of 17.7 and -48.7° for the pyrrole rings relative to the quinoxaline ring. This difference in the twisting of the pyrrole and imine moieties when compared to the relatively planar X-ray structure is reflected in the relatively large RMSD value of 0.497 Å. This calculated structure also has an imine bond length of 1.347 Å which is larger than the experimental imine bond length of 1.297(4) Å and the standard imine bond length of 1.279 Å.³⁴ This larger value indicates that this bond also has some single bond character and that there is electron delocalization over the imine bonds.

Tautomer B has the lowest RMD value of all the tautomers, showing that it is the most similar in structure to the experimental X-ray crystal structure. It is also the most stable tautomer as it has the lowest energy. For H₂L2, tautomer D is the highest energy tautomer and is 117.6 kJmol⁻¹ higher in energy than tautomer B. Tautomer A is 46.0 kJ mol⁻¹ and tautomer C is 33.9 kJ mol⁻¹ higher in energy than tautomer B. The relative energies for the rest of the geometry optimized tautomers for the other macrocyclic and pseudomacrocyclic ligands are given in Table 6.2. The Boltzmann's distribution equation, Equation 6.1, can be used to calculate the relative populations of each tautomeric state:

$$\frac{N_B}{N_A} = e^{\frac{-\Delta E}{kT}}$$

6.9

Where N_B and N_A are the relative populations of states B and A respectively, ΔE is the energy difference of the two states in Joules, T is the temperature in Kelvin and k is Boltzmann's distribution constant. It was calculated for H₂L2 that for every one molecule of the tautomeric form A there are 1.15×10^8 molecules in tautomeric form B while for every one molecule there is of the tautomeric form C there are 8.91×10^5 molecules in tautomeric form B. Also for every molecule of the tautomeric form D there are 4.22×10^{20} molecules in the tautomeric form B. This indicates that the tautomeric form B is by far the most dominant tautomeric form.

The asymmetric ligands, H₂L6, H₂L7 and H₂L8b, have six tautomeric forms. The X-ray structure of H₂L7 is relatively planar with a slight doming of the pyrrole rings. For H₂L7, the geometry optimized structure of the tautomeric form A experiences the same non-bonded repulsions as discussed for tautomer A of H₂L2. This leads to a twisted configuration to relieve the steric strain resulting in a high RMSD value of 0.562 Å. Tautomers B and F are very similar as they both have diagonally opposite pyrrole and imine N-atoms protonated. The only difference is if the fluoro group is used as a reference on the left-hand side of a molecule, then tautomer B has the left pyrrole and right imine N atoms protonated while tautomer F has the right pyrrole and left imine N atoms protonated. Both these tautomers are fairly planar with slightly canted pyrrole rings relative to the quinoxaline tail and both have very similar geometries to the X-ray structure. Tautomer B has an RMSD of 0.097 Å and tautomer F has a value of 0.098 Å. Tautomers C and E are also very similar in structure as they both have a pyrrole N atom and the adjacent imine atom protonated. Again if the fluoro group is used as a reference on the left-hand side of a molecule, then tautomer C has the left hand imine and pyrrole N atoms protonated and tautomer E has the right hand moieties protonated. Both these tautomers are planar and similar in structure to the X-ray structure with RMSD values of 0.116 and 0.110 Å for tautomers C and E, respectively. The geometry optimized structure of tautomer D has both imine N atoms protonated and the structure exhibits the same strain relieving twist as tautomer D of H₂L2. This twist results in difference in the orientation of the experimental and calculated structures with an RMSD value of 0.633 Å.

Tautomers B and F have the lowest RMSD values and are the most similar to the experimental X-ray structure. Tautomer B is the lowest energy structure while tautomer F is only 0.5 kJ mol⁻¹ higher in energy for H₂L7. There is also a nearly equal distribution between these two tautomers; for every one molecule of tautomer F, there are 1.22 molecules of tautomer B. Tautomers A, C and E are 43.1, 43.2 and 33.1 kJmol⁻¹ higher in energy than tautomer B. Tautomer D is the highest energy tautomer and is 121.2 kJ mol⁻¹ higher in energy than tautomer B. These results show that the ligand crystallized in the lowest energy form, tautomer B.

The X-ray structure of the pseudomacrocyle, H₂L9, is more planar than the true macrocycles as it does not have a di(azomethine) linkage unit. The geometry optimized structure of tautomer A of H₂L9 is twisted out of the plane to a greater extent than tautomer A for the true macrocycles as there is no di(azomethine) bridge to limit the degree of twisting and the methyl groups move away from each other. As the pseudomacrocyle is able to twist more than the macrocyclic compounds, it also has a larger RMSD value of 0.984 Å than tautomer A for the macrocycles. Tautomers B and C do not experience the strain relieving twist and are fairly

planar with RMSD values of 0.117 and 0.122 Å, respectively. Similarly, as there is no restricting bridge on the pseudomacrocyclic compounds, the planarity of tautomer D is greatly affected by the strain relieving twist of the pyrrole and imine molecules resulting in a large RMSD value of 1.160 Å.

Tautomer B is the lowest in energy for the pseudomacrocyclic H₂L9. The difference in energy for the other tautomers, however, is not as great as for the true macrocycles with tautomers A, C and D being 21.5, 35.5 and 89.7 kJ mol⁻¹ higher in energy than tautomer B. In the case of the true macrocycles, ring strain will lead to higher relative energies for the tautomers relative to the global minimum. In the case of the non-macrocyclic derivatives, the lack of ring strain and the absence of a conformationally restrictive alkyl bridge lead to lower relative energies.

In general, tautomer B has the most similar structure to the X-ray crystal structure and has the lowest RMSD values of all the tautomers for the ligands. As tautomer B is the lowest energy tautomer, the results also indicate that the ligands all crystallized as the most stable tautomeric form.

In addition to the above molecules, the structures of the ligands that were not studied experimentally by single X-ray crystal diffraction were also calculated. The calculated structures of selected ligands are shown in Figure 6.4. These calculated structures showed very similar results to those already discussed. Tautomers B and C were the most planar structures while tautomers A and D both experience a strain relieving twist. The pseudomacrocyclic structures are able to twist even more out of plane due to the absence of a di(azomethine) linkage. Again, tautomer B for all the calculated ligands is the most stable tautomer.

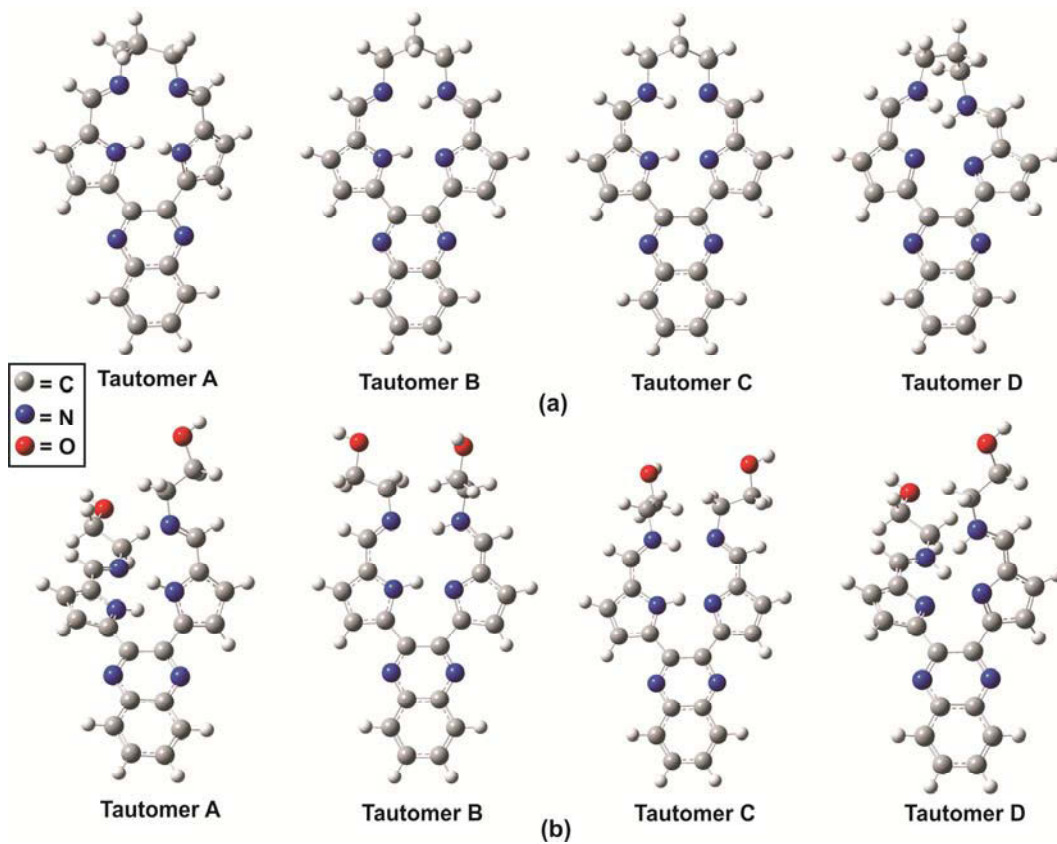


Figure 6.4: DFT-calculated structures of the tautomers of (a) H₂L1 and (b) H₂L11 at the B3LYP/6-311G(d,p) level of theory.

The Mulliken charges for tautomer B of selected ligands were measured to determine the effect of substituents on the quinoxaline moieties and di(azomethine) linkage of the macrocyclic and pseudomacrocyclic ligands. The X-ray crystal structures show that there is intramolecular hydrogen-bonding with the pyrrole N–H atom acting as the hydrogen bond donor and the opposite pyrrole N atom acting as the hydrogen bond acceptor as well as the imine N–H atom acting as the hydrogen bond donor and the opposite imine N atom acting as the hydrogen bond acceptor. This hydrogen bonding seems to further stabilize the compound in this tautomeric form. The Mulliken charges clearly show why this hydrogen bonding pattern is favoured. H₂L1 has a pyrrole proton that has a positive charge of 0.292 e and the opposite pyrrole N atom has a strongly negative charge of -0.528 e. The same is true for the imine moiety where the imine NH hydrogen atom has a positive charge of 0.290 e and the opposite N atom has a charge of -0.413 e. The addition of methyl substituents on the di(azomethine) linkage such as in the case of H₂L2, has little effect on the charges on the core N atoms and their appended hydrogen atoms. The addition of electron withdrawing substituents on the quinoxaline tail (fluorine atom for H₂L7) and alkyl moiety (hydroxyl group for H₂L11) also has little effect on the charge of the core N atoms. This could be due to the large distance between the electron withdrawing groups and the core N atoms. Even when a smaller pyrazine ring replaces the quinoxaline ring, the distance of the electron withdrawing nitrile group (H₂L8a) is too great to affect the charges on the core N atoms. Thus, addition of electron withdrawing or donating substituents to the quinoxaline tail or alkyl moiety, should not affect the hydrogen bonding pattern or the ability of the ligands to coordinate the gold(III) ion.

Table 6.3: Summary of partial Mulliken charges of key atoms for the tautomer B of selected ligands

	N_{pyrrole}	$N_{\text{pyrrole-H}}$	$N_{\text{pyrrole-H}}$	N_{imine}	$N_{\text{imine-H}}$	$N_{\text{imine-H}}$	Electron withdrawing group
H ₂ L1	-0.538	-0.433	0.292	-0.413	-0.351	0.290	
H ₂ L2	-0.539	-0.443	0.293	-0.412	-0.347	0.280	
H ₂ L7	-0.539	-0.433	0.292	-0.411	-0.351	0.289	-0.231 (F)
H ₂ L8a	-0.543	-0.434	0.295	-0.411	-0.347	0.292	-0.191 (C≡N) -0.193 (C≡N)
H ₂ L11	-0.533	-0.440	0.286	-0.396	-0.357	0.276	-0.406 (OH) -0.400 (OH)

6.3.2 Vibrational Frequency Calculation Results for Schiff Base Ligands

The vibrational frequencies of the ligands were calculated for two reasons. Firstly, to verify that there were no negative eigenvalues, which would indicate that the optimized geometry was not a true minimum on the potential energy surface. Secondly, to compare the calculated frequencies with the experimental infrared frequencies to ascertain their accuracy. Figure 6.5 shows an overlay of the experimental and calculated spectra for the tautomeric forms of H₂L1. Table 6.4 summarizes the important stretches in the infrared spectra for the experimental data and calculated tautomeric structures of H₂L1. The absolute difference between the experimental and calculated results was determined using Equation 6.10.

$$\text{diff} = \text{Calc} - \text{Exp}$$

6.10

The calculated IR spectrum of tautomer A of H₂L1 has an N–H stretch at 3624 cm⁻¹ which is at a much higher wavenumber than that of the experimental N–H stretch at 2836 cm⁻¹, corresponding to a 788 cm⁻¹ difference

between the calculated and experimental data. Interestingly, although this tautomer is symmetrical, it also gives two imine C=N stretches at 1700 and 1689 cm^{-1} . The peak at 1689 cm^{-1} is much smaller than the peak at 1700 cm^{-1} and is only visible as a small shoulder on the main peak. Again these imine stretching frequencies are overestimated when compared to the experimental imine stretches. The CH_2 stretch and C-H imine stretch is prominent in the calculated spectra for this tautomer. It is not possible to determine these stretches on the experimental spectrum as all the experimental spectra of the macrocyclic and pseudomacrocyclic ligands have insufficient resolutions spanning 1800- 3000 cm^{-1} . The C-H wagging peaks are also present in both the calculated and experimental spectra. The intensities of the calculated and experimental spectra are relatively similar.

The calculated IR spectrum of tautomer B of $\text{H}_2\text{L1}$ has both a pyrrole N-H and an imine N-H stretch. Both these peaks are intense. The imine N-H stretch is found at 3230 cm^{-1} in the calculated IR spectrum and is an intense band. The stretch may occur in the experimental spectrum but is obscured by the broad band between 1800 and 3000 cm^{-1} . The pyrrole N-H stretch is found at 2960 cm^{-1} in the calculated spectrum which is at a higher wavenumber than the experimental pyrrole N-H stretch, leading to a 124 cm^{-1} difference in the calculated and experimental data. There are also two imine C=N stretches in the calculated spectrum of this tautomer at 1711 and 1656 cm^{-1} . These values have been overestimated in the calculations by 56 and 69 cm^{-1} . The intensity of the stretching mode at 1656 cm^{-1} is much less than the peak at 1711 cm^{-1} . The C-H imine and CH_2 stretch as well as the C-H wagging peaks are much less intense in the calculated spectrum of tautomer B than that of tautomer A.

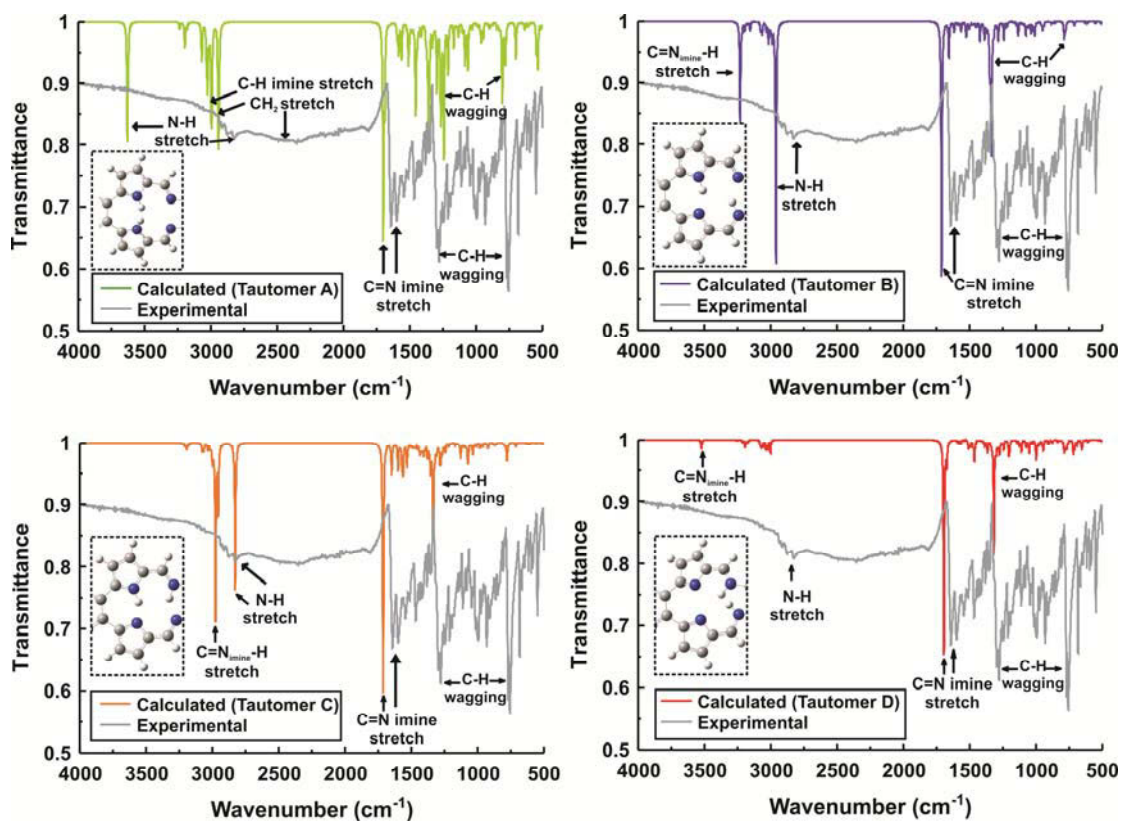


Figure 6.5: Overlay of experimental and calculated Infrared data for all tautomeric forms of $\text{H}_2\text{L1}$.

Tautomer C of H₂L1 has a calculated infrared spectrum that is very similar to tautomer B. This is not unexpected as both tautomers B and C have a pyrrole N and an imine N atom protonated. The spectrum of tautomer C has an intense imine N–H stretch at 2974 cm⁻¹ and an intense pyrrole N–H stretch at 2828 cm⁻¹. The shift of this pyrrole N–H peak is very similar to the experimental value at 2836 cm⁻¹. There are two imine stretching modes present: an intense peak at 1712 cm⁻¹ and a less intense peak at 1648 cm⁻¹. These peaks are at higher wavenumbers than the corresponding peaks in the experimental spectrum. As with tautomer B, the C–H imine and CH₂ stretch as well as the C–H wagging peaks are not intense.

The calculated IR data for tautomer D of H₂L1 shows the absence of a pyrrole N–H stretch and the presence of only a weak peak at 3524 cm⁻¹ corresponding to the imine N–H stretch. There are two imine C=N stretches in the calculated spectrum of tautomer D, an intense stretching mode at 1694 cm⁻¹ and a less intense stretching mode at 1672 cm⁻¹. The C–H imine and CH₂ stretches are weak in the calculated spectrum of this tautomer, but the C–H wagging peak is moderately intense.

Table 6.4: Comparison of selected experimental and calculated vibrational frequencies for all the tautomers of H₂L1.

	Exp. (cm ⁻¹)	Calc. A (cm ⁻¹)	Diff (cm ⁻¹)	Calc. B (cm ⁻¹)	Diff (cm ⁻¹)	Calc. C (cm ⁻¹)	Diff (cm ⁻¹)	Calc. D (cm ⁻¹)	Diff (cm ⁻¹)
C=N	1642	1700	58	1711	69	1712	70	1694	52
	1600	1689	89	1656	56	1648	48	1672	72
N _{pyrrole} –H	2836	3624	788	2960	124	2828	-8		
N _{imine} –H				3230		2976		3524	

The experimental spectrum of H₂L1 is not particularly well described by any one of the spectra of the calculated tautomers with almost all the frequencies for the different stretching modes being overestimated when compared to the experimental data. The calculated IR spectrum of tautomer A has similar relative intensities to that of the experimental spectrum. As the X-ray crystal structure shows the ligands to have the same arrangement of N–H hydrogen atoms as in tautomer B, the calculated spectrum of this tautomer was expected to yield the most accurate results when compared to the experimental data. The spectra of tautomer B for all the ligands are compared in Table 6.5.

The calculations for tautomer B overestimate the frequency of all the vibrational bands when compared to the experimental data. However, the experimental and calculated values only differ by small amounts with H₂L11 having the greatest difference in the experimental and calculated frequency for the imine C=N stretch of 79 cm⁻¹ with H₂L5 having the smallest difference of 23 cm⁻¹ for this stretching mode. The average experimental C=N stretch (for the more intense peak) for all the ligands is 1643(12) cm⁻¹ and the average calculated C=N stretch for tautomer B is 1710(8) cm⁻¹. These values show not only that the experimental and calculated data are in reasonably good agreement, but also that the standard deviation is small indicating that there is little deviation in both the experimental and calculated results.

Table 6.5: Comparison of selected experimental and calculated vibrational frequencies (cm^{-1}) for tautomer B of the Schiff base ligands.

	C=N	Pyrrole N-H		C=N	Pyrrole N-H
	H₂L1			H₂L2	
Experimental	1642, 1600	2836	Experimental	1643, 1601	2819
Calculated	1711, 1656	2960	Calculated	1708, 1654	2953
% Difference	69, 56	124	% Difference	65, 53	134
	H₂L3			H₂L5	
Experimental	1642, 1606	2812	Experimental	1650, 1631	2835
Calculated	1709, 1661	2922	Calculated	1710, 1654	2960
% Difference	67, 55	110	% Difference	60, 23	125
	H₂L6			H₂L7	
Experimental	1647, 1610	2845	Experimental	1640, 1599	2837
Calculated	1709, 1655	2963	Calculated	1710, 1655	2966
% Difference	62, 45	118	% Difference	30, 56	129
	H₂L8a			H₂L8b	
Experimental	1645, 1630	2846	Experimental	1642, 1625	2833
Calculated	1702, 1663	2923	Calculated	1711, 1655	2877
% Difference	57, 33	77	% Difference	69, 30	44
	H₂L9			H₂L10	
Experimental	1650, 1635	2830	Experimental	1643, 1633	2835
Calculated	1718, 1676	2943	Calculated	1707, 1670	2977
% Difference	68, 41	113	% Difference	64, 37	142
	H₂L11			H₂L12	
Experimental	1631	2831	Experimental	1641	2929
Calculated	1710, 1673	2962	Calculated	1699	3644
% Difference	79	131	% Difference	58	715

The difference in calculated and experimental frequencies for the pyrrole NH ranges from 44 cm^{-1} for H₂L8b to 142 cm^{-1} for H₂L10 for the macrocyclic and pseudomacrocyclic ligands. The average experimental pyrrole N-H stretch for all the macrocyclic and pseudomacrocyclic ligands is $2833(21) \text{ cm}^{-1}$ and the average calculated pyrrole N-H stretch for tautomer B of the ligands is $2946(69) \text{ cm}^{-1}$. This again shows that the values are fairly similar; the standard deviations are higher than for the imine bond due to the fact that the NH peak is a much broader peak leading to errors in peak picking.

The acyclic ligand, H₂L12, is in a linear form with both pyrrole N atoms protonated. The calculated IR data for this compound is also overestimated when compared to the experimental data, especially at high frequency vibrational modes. The imine C=N stretch was overestimated by 58 cm^{-1} by the calculations while the higher frequency N-H stretch was overestimated by 715 cm^{-1} .

In an attempt to determine if the errors in the calculations for tautomer B of the macrocyclic and pseudomacrocyclic ligands were systematic or random errors, the frequencies of the experimental bands were plotted against the frequencies of the calculated bands. A straight line would suggest the error is systematic and a correction factor could be applied to the calculated data to improve its accuracy. This technique was applied to the C=N stretching vibration and the pyrrole N-H stretch. No trend was observed for either stretching mode with scattering of the data points suggesting that the errors are random and no

correction factor could be determined. This is not surprising as the fundamental difficulty with interpreting the data in this manner is that the variation between the values is small.

The correlations of the calculated and experimental frequencies for the functional groups are satisfactory. The calculated frequencies of the C≡N stretch for H₂L8a and H₂L8b are 2338 and 2339 cm⁻¹, respectively, while the experimental values are 2227 and 2217 cm⁻¹, respectively. This corresponds to a 111 and 122 cm⁻¹ overestimation of the calculated data for H₂L8a and H₂L8b, respectively. The calculated O–H frequency for H₂L11 is 3843 cm⁻¹ while the experimental frequency is 3300 cm⁻¹ resulting in a 543 cm⁻¹ difference between the calculated and experimental data. This large difference is most likely due to lattice effects in the experimental data as hydrogen bonding present in the solid state is not accounted for in the simulations and have a large impact on the vibrational frequencies.

In summary, the calculated IR data for all the free ligand tautomers overestimates the experimental IR frequencies. The calculated spectra of the tautomers are all different. The spectra of tautomers B and C contain both pyrrole N–H and imine N–H stretching modes while the spectrum of tautomer A has only pyrrole N–H stretches and the IR spectrum of tautomer D has only imine N–H stretches. The calculated IR spectrum of tautomer B and the experimental results compare favourably.

6.3.3 Electronic Transitions for Schiff Base Ligands

The electronic transitions were calculated for all the tautomers of the ligands using the TD-SCF method solving for 30 excited singlet states. The level of theory used was the same as that used for the geometry optimization results: B3LYP/6-311G(d,p). A chloroform solvent model was also used in the calculation to account for any solvent effects in the experimental structures. The calculated results were compared with the experimental UV/visible absorption spectra. These calculations were also done to provide insight into which of the ligand orbitals are involved in the transitions. In general the correlation between the calculated data of the different tautomers and the experimental data was satisfactory. An overlay of the calculated and experimental spectra for the tautomeric structures of H₂L1 is shown in Figure 6.6.

The calculated spectrum of tautomer A of H₂L1 compares favourably with the experimental data. The peak in the calculated spectrum with the greatest oscillator strength is at 333 nm while the peak with the greatest extinction coefficient is at 335 nm in the experimental spectrum. The calculated spectrum has a peak at 447 nm while the corresponding peak in the experimental is at higher energy at 428 nm. In the experimental spectrum there is shoulder to the peak at 335 nm. This shoulder is at 290 nm in the experimental spectrum and in the calculated spectrum it appears as a separate peak at 286 nm.

The overlay of the calculated data for tautomer B of H₂L1 and the experimental data is satisfactory. The peak in the calculated spectrum with the greatest oscillator strength is at 332 nm which is only a 1 nm difference in results between the calculated and experimental data. Although not well defined, there is also a peak at 469 nm in the calculated spectrum which corresponds to the peak at 428 nm in the calculated spectrum. The shoulder that appears in the experimental spectrum at 290 nm is not clear in the calculated spectrum although there is a calculated state at 319 nm which could correspond to this shoulder. The relative intensities of the peaks in the experimental and calculated spectra compare favourably.

The calculated spectrum of tautomer C of H₂L1 does not compare as favourably to the experimental spectrum as that of tautomers A and B. The peak in the calculated spectrum of tautomer C with the greatest oscillator strength is at 347 nm which leads to a 14 nm difference between the calculated and experimental spectra. There is no clear peak in the calculated spectrum that corresponds to the peak at 428 nm in the experimental spectrum; however, there is a calculated state at 441 nm. In the calculated spectrum there is a weak band at 605 nm which does not appear in the experimental spectrum.

The calculated spectrum of tautomer D has a peak at 335 nm which corresponds favourably with the peak which has the greatest extinction coefficient in the experimental spectrum. The calculated spectrum of tautomer D has a shoulder at 383 nm which does not appear in the experimental spectrum of H₂L1. There is a well defined peak at 428 nm in the experimental spectrum which is not present at this wavelength in the calculated spectrum although there are two calculated states at 461 and 454 nm.

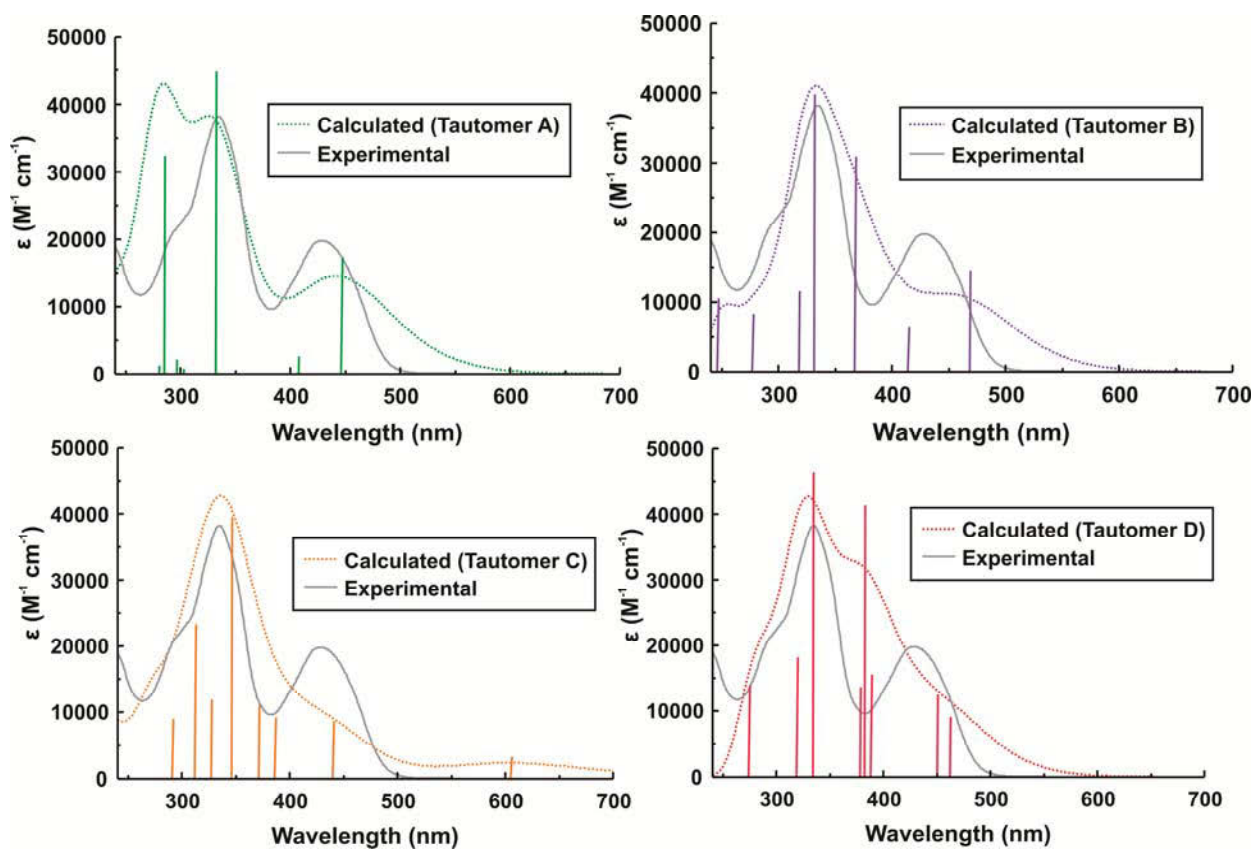


Figure 6.6: Overlays of the calculated electronic spectra (width at half height = 2400 cm^{-1}) of the tautomeric forms of H₂L1 and the experimental data. Calculated states are depicted as vertical lines with intensities given by their oscillator strengths.

The wavelengths and oscillator strengths that are responsible for the calculated spectra of the tautomers of H₂L1 are given in Table 6.6. The corresponding peaks that are present in the experimental spectrum are 335 and 428 nm. The major orbitals that are responsible for these transitions are shown in Figure 6.7. The molecular orbitals of the remaining ligands are very similar to those of H₂L1 and, for brevity, are not shown here. A sample of these orbitals is available in **Appendix F**.

Table 6.6: Summary of the calculated electronic transitions for the tautomeric forms of H₂L1 and the corresponding molecular orbitals

λ /nm ^a	MOs	Coefficient ^b	f^c	Transition Assignment
Tautomer A				
447	93(H)→94(L)	0.690	0.342	$\sigma(\text{brid}), \pi(\text{quin, pyrr, im}) \rightarrow \pi^*(\text{quin, pyrr N, im})$
	92→95	0.129		$\sigma(\text{brid}), \pi(\text{quin, pyrr, im}) \rightarrow \pi^*(\text{quin, pyrr, im, brid})$
408	93→95	0.700	0.0518	$\sigma(\text{brid}), \pi(\text{quin, pyrr, im}) \rightarrow \pi^*(\text{quin, pyrr, im, brid})$
	92→95	0.669		$\sigma(\text{brid}), \pi(\text{quin, pyrr, im}) \rightarrow \pi^*(\text{quin, pyrr, im, brid})$
333	93→96	0.153	0.888	$\sigma(\text{brid}), \pi(\text{quin, pyrr, im}) \rightarrow \pi^*(\text{pyrr, im, brid})$
	91→95	0.406		$\sigma(\text{im, brid}) \rightarrow \pi^*(\text{quin, pyrr, im, brid})$
303	89→94	-0.382	0.0155	$\pi(\text{quin, pyrr, im}) \rightarrow \pi^*(\text{quin, pyrr N, im})$
	89→94	0.449		$\pi(\text{quin, pyrr, im}) \rightarrow \pi^*(\text{quin, pyrr N, im})$
300	91→95	0.399	0.0423	$\sigma(\text{im, brid}) \rightarrow \pi^*(\text{quin, pyrr, im, brid})$
	93→96	0.566		$\sigma(\text{brid}), \pi(\text{quin, pyrr, im}) \rightarrow \pi^*(\text{pyrr, im, brid})$
286	89→94	0.204	0.643	$\pi(\text{quin, pyrr, im}) \rightarrow \pi^*(\text{quin, pyrr N, im})$
	87→94	0.438		$\sigma(\text{brid}), \pi(\text{pyrr}) \rightarrow \pi^*(\text{quin, pyrr N, im})$
282	86→94	0.399	0.0246	$\sigma(\text{brid}), \pi(\text{pyrr}) \rightarrow \pi^*(\text{quin, pyrr N, im})$
Tautomer B				
469	93(H)→94(L)	0.677	0.299	$\sigma(\text{brid}), \pi(\text{quin, pyrr, im}) \rightarrow \pi^*(\text{quin, im})$
	92→95	-0.165		$\pi(\text{quin, pyrr, im}) \rightarrow \pi^*(\text{quin, pyrr, im})$
415	93→95	0.701	0.132	$\sigma(\text{brid}), \pi(\text{quin, pyrr, im}) \rightarrow \pi^*(\text{quin, pyrr, im})$
	92→95	0.600		$\pi(\text{quin, pyrr, im}) \rightarrow \pi^*(\text{quin, pyrr, im})$
368	93→96	0.289	0.637	$\sigma(\text{brid}), \pi(\text{quin, pyrr, im}) \rightarrow \pi^*(\text{quin, pyrr, im})$
	93→96	0.560		$\sigma(\text{brid}), \pi(\text{quin, pyrr, im}) \rightarrow \pi^*(\text{quin, pyrr, im})$
332	92→95	-0.244	0.819	$\pi(\text{quin, pyrr, im}) \rightarrow \pi^*(\text{quin, pyrr, im})$
	89→94	0.400		$\pi(\text{quin, pyrr}) \rightarrow \pi^*(\text{quin, im})$
319	92→96	0.365	0.238	$\pi(\text{quin, pyrr, im}) \rightarrow \pi^*(\text{quin, pyrr, im})$
	91→96	0.624		$\pi(\text{quin, pyrr}) \rightarrow \pi^*(\text{quin, pyrr, im})$
278	92→97	0.206	0.170	$\pi(\text{quin, pyrr, im}) \rightarrow \pi^*(\text{quin, pyrr, im})$
	89→96	0.393		$\pi(\text{quin, pyrr}) \rightarrow \pi^*(\text{quin, pyrr, im})$
247	88→96	0.389	0.216	$\pi(\text{quin, pyrr}) \rightarrow \pi^*(\text{quin, pyrr, im})$
Tautomer C				
605	93(H)→94(L)	0.704	0.0751	$\sigma(\text{brid}), \pi(\text{quin, pyrr N ring, im N}) \rightarrow \pi^*(\text{quin, pyrr NH, im})$
	93→95	0.686		$\sigma(\text{brid}), \pi(\text{quin, pyrr N ring, im N}) \rightarrow \pi^*(\text{quin, pyrr, im})$
441	92→94	-0.155	0.197	$\sigma(\text{brid}), \pi(\text{quin, pyrr, im}) \rightarrow \pi^*(\text{quin, pyrr NH, im})$
	91→94	0.452		$\pi(\text{quin, pyrr, im}) \rightarrow \pi^*(\text{quin, pyrr NH, im})$
387	92→94	0.375	0.209	$\sigma(\text{brid}), \pi(\text{quin, pyrr, im}) \rightarrow \pi^*(\text{quin, pyrr NH, im})$
	93→96	0.552		$\sigma(\text{brid}), \pi(\text{quin, pyrr N, im}) \rightarrow \pi^*(\text{quin, pyrr, im})$
347	92→94	-0.252	0.905	$\sigma(\text{brid}), \pi(\text{quin, pyrr, im}) \rightarrow \pi^*(\text{quin, pyrr NH, im})$
	91→95	0.473		$\pi(\text{quin, pyrr, im}) \rightarrow \pi^*(\text{quin, pyrr, im})$
327	89→94	-0.471	0.273	$\pi(\text{quin, pyrr, im}) \rightarrow \pi^*(\text{quin, pyrr NH, im})$
	89→94	0.462		$\pi(\text{quin, pyrr, im}) \rightarrow \pi^*(\text{quin, pyrr NH, im})$
313	91→95	0.340	0.532	$\pi(\text{quin, pyrr, im}) \rightarrow \pi^*(\text{quin, pyrr, im})$
	87→94	0.595		$\pi(\text{quin, pyrr NH, im}) \rightarrow \pi^*(\text{quin, pyrr NH, im})$
291	86→94	-0.258	0.205	$\sigma(\text{pyrr, im}) \rightarrow \pi^*(\text{quin, pyrr NH ring, im})$
	93→97	0.494		$\pi(\text{quin, pyrr N, im}) \rightarrow \pi(\text{quin, pyrr N, im})$
272	91→96	0.415	0.252	$\pi(\text{quin, pyrr, im}) \rightarrow \pi^*(\text{quin, pyrr, im})$

Table 6.6 continued...

λ / nm^a	MOs	Coefficient ^b	f^c	Transition Assignment
Tautomer D				
464	93(H)→94(L)	0.617	0.109	$\sigma(\text{brid}), \pi(\text{quin,pyrr,im}) \rightarrow \pi^*(\text{quin,right pyrr, im})$
	93→95	-0.297		$\sigma(\text{brid}), \pi(\text{quin,pyrr,im,brid}) \rightarrow \pi^*(\text{quin,pyrr,im})$
451	93→95	0.630	0.150	$\sigma(\text{brid}), \pi(\text{quin,pyrr,im}) \rightarrow \pi^*(\text{quin,pyrr,im})$
	93→94	0.263		$\sigma(\text{brid}), \pi(\text{quin,pyrr,im}) \rightarrow \pi^*(\text{quin,right pyrr,im})$
383	92→95	0.507	0.497	$\sigma(\text{brid}), \pi(\text{quin,pyrr,im,brid}) \rightarrow \pi^*(\text{quin,pyrr,im})$
	93→96	0.255		$\sigma(\text{brid}), \pi(\text{quin,pyrr,im}) \rightarrow \pi^*(\text{quin,pyrr,im,brid})$
379	89→94	0.425	0.164	$\sigma, \pi(\text{quin, pyrr}) \rightarrow \pi^*(\text{quin,right pyrr,im})$
	90→94	-0.283		$\sigma, \pi(\text{quin, pyrr}) \rightarrow \pi^*(\text{quin,right pyrr,im})$
335	93→96	0.521	0.556	$\sigma(\text{brid}), \pi(\text{quin,pyrr,im}) \rightarrow \pi^*(\text{quin,pyrr,im})$
	92→95	-0.207		$\sigma(\text{brid}), \pi(\text{quin,pyrr,im}) \rightarrow \pi^*(\text{quin,pyrr,im,brid})$
320	87→95	0.537	0.218	$\sigma, \pi(\text{quin, pyrr}) \rightarrow \pi^*(\text{quin,pyrr,im,brid})$
	91→96	0.202		$\pi(\text{pyrr}) \rightarrow \pi^*(\text{quin,pyrr,im,brid})$
289	85→94	0.324	0.186	$\sigma(\text{pyrr}) \rightarrow \pi^*(\text{quin,right pyrr, im})$
	86→94	-0.285		$\pi(\text{quin,pyrr,im,brid}) \rightarrow \pi^*(\text{quin,right pyrr, im})$
275	86→95	0.489	0.168	$\pi(\text{quin,pyrr,im,brid}) \rightarrow \pi^*(\text{quin,pyrr,im,brid})$
	89→96	-0.273		$\sigma, \pi(\text{quin, pyrr}) \rightarrow \pi^*(\text{quin,pyrr,im,brid})$

^a6-8 out of the 30 calculated excited states are listed. Abbreviations: quin, quinoxaline ring; pyrr; pyrrole rings, pyrr NH, NH pyrrole ring; pyrr N, N pyrrole ring; brid, di(azomethine) bridge; im, imine bond; H, HOMO; L, LUMO. ^bWhere multiple transitions contribute to an excited state, only the two with the largest transition coefficients have been listed. ^cOscillator strength.

The molecular orbitals for H₂L1, shown in Figure 6.7, are mostly of π -symmetry. The peak at 447 nm in the calculated spectrum of tautomer A of H₂L1 involves a $\sigma, \pi \rightarrow \pi^*$ transition between the HOMO and LUMO orbitals. The σ orbitals of the HOMO are located over the di(azomethine) bridge and the π orbitals are located over the quinoxaline ring, pyrrole ring and imine bonds. The π^* orbitals of the LUMO are mainly located over the quinoxaline ring with some orbitals over the pyrrole rings and imine N atoms. The transition at 333 nm in the calculated spectrum of tautomer A has the largest oscillator strength and involves $\sigma, \pi \rightarrow \pi^*$ transitions between the HOMO-1 and LUMO+1 orbitals as well as the HOMO and LUMO+2 orbitals.

The peak at 469 nm in the calculated spectrum of tautomer B of H₂L1 involves a $\sigma, \pi \rightarrow \pi^*$ transition between the HOMO and LUMO orbitals. The σ orbitals of the HOMO are located over the di(azomethine) bridge and the π orbitals are located over the quinoxaline ring, pyrrole ring and imine bonds. The π^* orbitals of the LUMO are mainly located over the quinoxaline ring and imine N atoms. The transition with the largest oscillator strength in the calculated spectrum is at 347 nm. This calculated state is made up of $\sigma, \pi \rightarrow \pi^*$ transitions between the HOMO and LUMO+2 orbitals as well as $\pi \rightarrow \pi^*$ transitions between the HOMO-1 and LUMO+1 orbitals.

In the calculated spectrum of tautomer C of H₂L1, the peak at 605 nm involves a $\sigma, \pi \rightarrow \pi^*$ transition between the HOMO and LUMO orbitals. The σ orbitals of the HOMO are located over half the di(azomethine) bridge and the π orbitals are over the quinoxaline ring and the pyrrole N ring and imine-N bond. The π^* orbitals of the LUMO are located over the quinoxaline ring and the pyrrole NH ring and imine NH bond. The transition at 313 nm in the calculated spectrum of tautomer C has the largest oscillator strength and involves $\pi \rightarrow \pi^*$ transitions between the HOMO-4 and LUMO orbitals as well as the HOMO-2 and LUMO+1 orbitals.

The peak at 464 nm in the calculated spectrum of tautomer D of H₂L1 involves a $\sigma, \pi \rightarrow \pi^*$ transition between the HOMO and LUMO orbitals. The σ orbitals of the HOMO are located over the di(azomethine) bridge and the π orbitals are located over the quinoxaline ring, pyrrole ring and imine bonds. The π^* orbitals of the LUMO are located over the quinoxaline ring and right hand side pyrrole and imine bonds. The transition at 335 nm in the calculated spectrum of tautomer D has the largest oscillator strength and involves $\sigma, \pi \rightarrow \pi^*$ transitions between the HOMO and LUMO+2 orbitals as well as the HOMO-1 and LUMO orbitals.

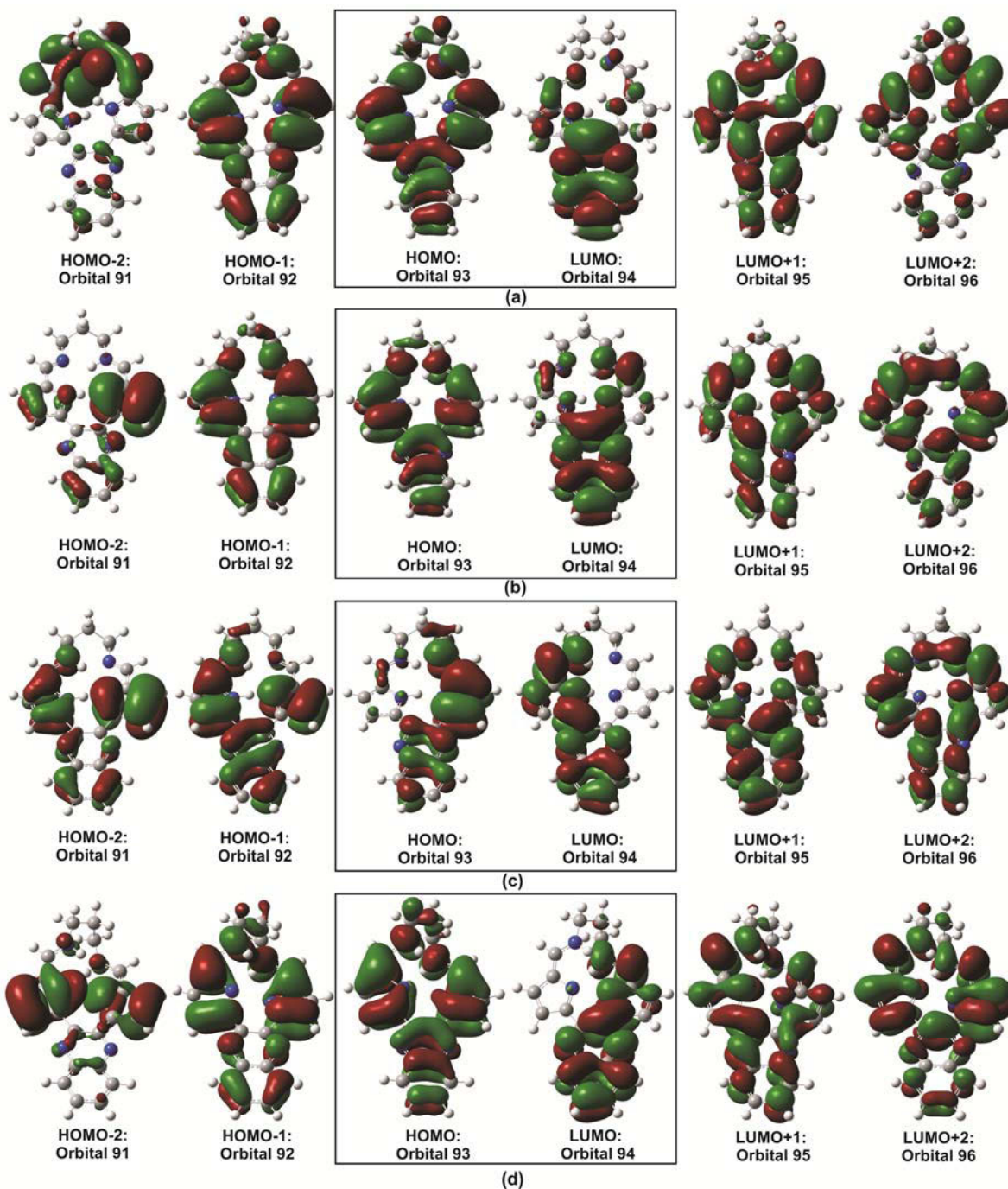


Figure 6.7: The molecular orbitals for the tautomeric forms of H₂L1: (a) tautomer A (b) tautomer B (c) tautomer C and (d) tautomer D, that are responsible for the major electronic transitions.

Table 6.7: Summary of the calculated electronic transitions for tautomer B of the ligands and the corresponding molecular transitions.

Ligand	Exp. λ (nm)	Calc. λ (nm)	MOs	Coef.	f	Transition Assignment
H ₂ L2	427	348	101(H)→102(L)	0.677	0.305	$\pi(\text{quin,pyrr,im}) \rightarrow \pi^*(\text{quin,im})$
			100→103	-0.164		$\sigma(\text{brid}),\pi(\text{quin,pyrr, im}) \rightarrow \pi^*(\text{quin,pyrr,im})$
	334	312	100→103	0.603	0.674	$\sigma(\text{brid}),\pi(\text{quin,pyrr, im}) \rightarrow \pi^*(\text{quin,pyrr,im})$
			101→104	0.286		$\pi(\text{quin,pyrr,im}) \rightarrow \pi^*(\text{quin,pyrr,im})$
	299	312	101→104	0.564	0.836	$\pi(\text{quin,pyrr,im}) \rightarrow \pi^*(\text{quin,pyrr,im})$
			100→103			$\sigma(\text{brid}),\pi(\text{quin,pyrr,im}) \rightarrow \pi^*(\text{quin,pyrr,im})$
		100→104	0.460	0.209	$\sigma(\text{brid}),\pi(\text{quin,pyrr,im}) \rightarrow \pi^*(\text{quin,pyrr,im})$	
		97→102	-0.378		$\sigma(\text{brid}),\pi(\text{pyrr,im}) \rightarrow \pi^*(\text{quin,im})$	
H ₂ L3	421	348	97(H)→98(L)	0.677	0.277	$\pi(\text{quin,pyrr,im}) \rightarrow \pi^*(\text{quin,im})$
			96→99	-0.159		$\sigma(\text{brid}),\pi(\text{quin,pyrr,im}) \rightarrow \pi^*(\text{quin,pyrr,im})$
	346	310	96→99	0.614	0.748	$\sigma(\text{brid}),\pi(\text{quin,pyrr,im}) \rightarrow \pi^*(\text{quin,pyrr,im})$
			97→100	0.262		$\pi(\text{quin,pyrr,im}) \rightarrow \pi^*(\text{quin,pyrr,im})$
	333	310	97→100	0.551	0.670	$\pi(\text{quin,pyrr,im}) \rightarrow \pi^*(\text{quin,pyrr,im})$
			93→98	0.200		$\sigma(\text{brid}),\pi(\text{pyrrN-H ring,quin}) \rightarrow \pi^*(\text{quin,im})$
	299	95→99	0.429	0.326	$\sigma(\text{quin}) \rightarrow \pi^*(\text{quin,pyrr,im})$	
		92→98	-0.322		$\sigma(\text{brid}),\pi(\text{pyrrN-H ring,quin}) \rightarrow \pi^*(\text{quin,im})$	
H ₂ L5	430	349	101(H)→102(L)	0.677	0.335	$\sigma(\text{brid}),\pi(\text{quin,pyrr,im}) \rightarrow \pi^*(\text{quin,im})$
			100→103	-0.166		$\pi(\text{quin,pyrr,im}) \rightarrow \pi^*(\text{quin,pyrr,im})$
	338	315	100→103	0.604	0.747	$\pi(\text{quin,pyrr,im}) \rightarrow \pi^*(\text{quin,pyrr,im})$
			101→104	0.300		$\sigma(\text{brid}),\pi(\text{quin,pyrr,im}) \rightarrow \pi^*(\text{quin,pyrr,im})$
		296	101→104	0.567	0.994	$\sigma(\text{brid}),\pi(\text{quin,pyrr,im}) \rightarrow \pi^*(\text{quin,pyrr,im})$
			100→103	-0.255		$\pi(\text{quin,pyrr,im}) \rightarrow \pi^*(\text{quin,pyrr,im})$
		96→102	0.558	0.247	$\sigma(\text{brid}),\pi(\text{quin,pyrr NH,im}) \rightarrow \pi^*(\text{quin,im})$	
		99→103	-0.354		$\sigma(\text{quin}) \rightarrow \pi^*(\text{quin,pyrr,im})$	
H ₂ L6	430	395	97(H)→98(L)	0.679	0.294	$\sigma(\text{brid}),\pi(\text{quin,pyrr,im}) \rightarrow \pi^*(\text{quin,im})$
			96→99	-0.153		$\pi(\text{quin,pyrr,im}) \rightarrow \pi^*(\text{quin,pyrr,im})$
	336	348	96→98	0.668	0.174	$\pi(\text{quin,pyrr,im}) \rightarrow \pi^*(\text{quin,im})$
			97→99	0.166		$\sigma(\text{brid}),\pi(\text{quin,pyrr,im}) \rightarrow \pi^*(\text{quin,pyrr,im})$
		314	96→99	0.599	0.660	$\pi(\text{quin,pyrr,im}) \rightarrow \pi^*(\text{quin,pyrr,im})$
			97→100	0.303		$\sigma(\text{brid}),\pi(\text{quin,pyrr,im}) \rightarrow \pi^*(\text{quin,pyrr,im})$
		97→100	0.561	0.979	$\sigma(\text{brid}),\pi(\text{quin,pyrr,im}) \rightarrow \pi^*(\text{quin,pyrr,im})$	
		96→99	-0.257		$\pi(\text{quin,pyrr,im}) \rightarrow \pi^*(\text{quin,pyrr,im})$	
H ₂ L7	430	348	97(H)→98(L)	0.682	0.282	$\sigma(\text{brid}),\pi(\text{quin,pyrr,im}) \rightarrow \pi^*(\text{quin,im})$
			96→99	-0.125		$\pi(\text{quin,pyrr,im}) \rightarrow \pi^*(\text{quin,pyrr,im})$
	332	313	96→98	0.584	0.479	$\pi(\text{quin,pyrr,im}) \rightarrow \pi^*(\text{quin,im})$
			97→99	0.299		$\sigma(\text{brid}),\pi(\text{quin,pyrr,im}) \rightarrow \pi^*(\text{quin,pyrr,im})$
		306	97→100	0.518	0.686	$\sigma(\text{brid}),\pi(\text{quin,pyrr,im}) \rightarrow \pi^*(\text{quin,pyrr,im})$
			93→98	-0.297		$\sigma(\text{quin}),\pi(\text{pyrr}) \rightarrow \pi^*(\text{quin,im})$
		93→98	0.553	0.450	$\sigma(\text{quin}),\pi(\text{pyrr}) \rightarrow \pi^*(\text{quin,im})$	
		95→99	0.248		$\pi(\text{pyrr}) \rightarrow \pi^*(\text{quin,pyrr,im})$	

Table 6.7 continued...

Ligand	Exp. λ (nm)	Calc. λ (nm)	MOs	Coef.	f	Transition Assignment
H ₂ L8b		469	94(H)→95(L)	0.696	0.186	$\sigma(\text{brid}), \pi(\text{pyra}, \text{pyr}, \text{im}) \rightarrow \pi^*(\text{pyra}, \text{pyr NH}, \text{im})$
			93→95	0.106		$\sigma(\text{brid}), \pi(\text{pyra}, \text{pyrr}, \text{im}) \rightarrow \pi^*(\text{pyra}, \text{pyrr NH}, \text{im})$
	423	373	93→95	0.546	0.514	$\sigma(\text{brid}), \pi(\text{pyra}, \text{pyrr}, \text{im}) \rightarrow \pi^*(\text{pyra}, \text{pyrrNH}, \text{im})$
			94→96	-0.336		$\sigma(\text{brid}), \pi(\text{pyra}, \text{pyrr}, \text{im}) \rightarrow \pi^*(\text{pyra}, \text{pyrrN}, \text{im}, \text{C-O})$
	364	313	94→97	0.400	0.321	$\sigma(\text{brid}), \pi(\text{pyra}, \text{pyrr}, \text{im},) \rightarrow \pi^*(\text{pyra}, \text{pyrr}, \text{imine})$
	322		88→95	0.346		$\sigma(\text{pyra}, \text{pyrr}, \text{brid}) \rightarrow \pi^*(\text{pyra}, \text{pyrr NH}, \text{im},)$
		298	91→95	0.473	0.523	$\pi(\text{pyrr N-H}) \rightarrow \pi^*(\text{pyra}, \text{pyrr NH}, \text{im})$
			92→96	0.229		$\pi(\text{pyrr N}) \rightarrow \pi^*(\text{pyra}, \text{pyrr NH}, \text{im})$
H ₂ L9		452	90(H)→91(L)	0.681	0.252	$\pi(\text{quin}, \text{pyrr}, \text{im}) \rightarrow \pi^*(\text{quin}, \text{im})$
			89→92	-0.144		$\pi(\text{quin}, \text{pyrr}, \text{im}) \rightarrow \pi^*(\text{quin}, \text{pyrr}, \text{im})$
	420	395	90→92	0.689	0.216	$\pi(\text{quin}, \text{pyrr}, \text{im}) \rightarrow \pi^*(\text{quin}, \text{pyrr}, \text{im})$
			89→92	-0.111		$\pi(\text{quin}, \text{pyrr}, \text{im}) \rightarrow \pi^*(\text{quin}, \text{pyrr}, \text{im})$
	372	345	89→92	0.614	0.721	$\pi(\text{quin}, \text{pyrr}, \text{im}) \rightarrow \pi^*(\text{quin}, \text{pyrr}, \text{im})$
	356		90→93	-0.245		$\pi(\text{quin}, \text{pyrr}, \text{im}) \rightarrow \pi^*(\text{quin}, \text{pyrr}, \text{im})$
	317	307	90→93	0.501	0.409	$\pi(\text{quin}, \text{pyrr}, \text{im}) \rightarrow \pi^*(\text{quin}, \text{pyrr}, \text{im})$
	287		86→91	0.342		$\pi(\text{quin}, \text{pyrr}) \rightarrow \pi^*(\text{quin}, \text{im})$
	269	302	86→91	0.553	0.220	$\pi(\text{quin}, \text{pyrr}) \rightarrow \pi^*(\text{quin}, \text{im})$
			85→91	-0.243		$\pi(\text{quin}, \text{pyrr}, \text{im}) \rightarrow \pi^*(\text{quin}, \text{im})$
		298	88→92	0.454	0.404	$\pi(\text{quin}, \text{pyrr}) \rightarrow \pi^*(\text{quin}, \text{pyrr}, \text{im})$
			85→91	-0.335		$\pi(\text{quin}, \text{pyrr}, \text{im}) \rightarrow \pi^*(\text{quin}, \text{imi})$
H ₂ L10		453	98(H)→99(L)	0.682	0.246	$\sigma(\text{brid}), \pi(\text{quin}, \text{pyrr}, \text{im}) \rightarrow \pi^*(\text{quin}, \text{pyrrNH}, \text{im})$
			97→100	-0.132		$\pi(\text{quin}, \text{pyrr}, \text{im}) \rightarrow \pi^*(\text{quin}, \text{pyrr}, \text{im})$
	420	396	98→100	0.594	0.242	$\sigma(\text{brid}), \pi(\text{quin}, \text{pyrr}, \text{im}) \rightarrow \pi^*(\text{quin}, \text{pyrr}, \text{im})$
			97→99	-0.345		$\pi(\text{quin}, \text{pyrr}, \text{im}) \rightarrow \pi^*(\text{quin}, \text{pyrr N-H}, \text{im})$
	371	345	97→100	0.616	0.742	$\pi(\text{quin}, \text{pyrr}, \text{im}) \rightarrow \pi^*(\text{quin}, \text{pyrr}, \text{im})$
	344		98→101	-0.240		$\sigma(\text{brid}), \pi(\text{quin}, \text{pyrr}, \text{im}) \rightarrow \pi^*(\text{quin}, \text{pyrr}, \text{im})$
	318	308	98→101	0.533	0.545	$\sigma(\text{brid}), \pi(\text{quin}, \text{pyrr}, \text{im}) \rightarrow \pi^*(\text{quin}, \text{pyrr}, \text{im})$
	288		93→99	0.234		$\pi(\text{quin}, \text{pyrr}) \rightarrow \pi^*(\text{quin}, \text{pyrr N-H}, \text{im})$
	270	301	93→99	0.522	0.176	$\pi(\text{quin}, \text{pyrr}) \rightarrow \pi^*(\text{quin}, \text{pyrr N-H}, \text{im})$
			96→100	0.396		$\pi(\text{quin}, \text{pyrr}) \rightarrow \pi^*(\text{quin}, \text{pyrr}, \text{im})$
	299	96→100	0.494	0.271	$\pi(\text{quin}, \text{pyrr}) \rightarrow \pi^*(\text{quin}, \text{pyrr}, \text{im})$	
		93→99	-0.343		$\pi(\text{quin}, \text{pyrr}) \rightarrow \pi^*(\text{quin}, \text{pyrr N-H}, \text{im})$	
H ₂ L11		455	106(H)→107(L)	0.682	0.235	$\pi(\text{quin}, \text{pyrr}, \text{im}) \rightarrow \pi^*(\text{quin}, \text{pyrr N ring}, \text{im})$
			105→108	-0.130		$\pi(\text{quin}, \text{pyrr}, \text{im}) \rightarrow \pi^*(\text{quin}, \text{pyrr}, \text{im})$
	421	395	105→107	0.605	0.177	$\pi(\text{quin}, \text{pyrr}, \text{im}) \rightarrow \pi^*(\text{quin}, \text{pyrr N ring}, \text{im})$
			106→108	-0.298		$\pi(\text{quin}, \text{pyrr}, \text{im}) \rightarrow \pi^*(\text{quin}, \text{pyrr}, \text{im})$
	373	345	105→108	0.615	0.733	$\pi(\text{quin}, \text{pyrr}, \text{im}) \rightarrow \pi^*(\text{quin}, \text{pyrr}, \text{im})$
	358		106→109	-0.239		$\pi(\text{quin}, \text{pyrr}, \text{im}) \rightarrow \pi^*(\text{quin}, \text{pyrr}, \text{im})$
	318	308	106→109	0.516	0.477	$\pi(\text{quin}, \text{pyrr}, \text{im}) \rightarrow \pi^*(\text{quin}, \text{pyrr}, \text{im})$
	288		102→107	0.292		$\pi(\text{quin}, \text{pyrr NH}) \rightarrow \pi^*(\text{quin}, \text{pyrr N}, \text{im})$
	268	303	102→107	0.597	0.220	$\pi(\text{quin}, \text{pyrr NH}) \rightarrow \pi^*(\text{quin}, \text{pyrr N}, \text{im})$
			101→107	-0.211		$\pi(\text{quin}, \text{pyrr}, \text{im}) \rightarrow \pi^*(\text{quin}, \text{pyrr N}, \text{im})$
	299	104→108	0.431	0.357	$\pi(\text{pyrr}) \rightarrow \pi^*(\text{quin}, \text{pyrr}, \text{im})$	
		101→107	-0.415		$\pi(\text{quin}, \text{pyrr}, \text{im}) \rightarrow \pi^*(\text{quin}, \text{pyrr N}, \text{im})$	
H ₂ L12	287	273	65(H)→66(L)	0.701	0.854	$\sigma(\text{brid}), \pi(\text{pyrr}, \text{ime}) \rightarrow \pi^*(\text{pyrr}, \text{im})$
		264	64→67	0.700		0.537

The calculated spectra of tautomers A and B for H₂L1 are most similar to the experimental spectrum. Tautomer B is the dominant tautomeric form in the solid state as seen by the X-ray crystal structures (Chapter Four), but it is unknown whether this is the favoured form in solution, although NMR spectroscopy suggests that it is likely. The calculated spectrum of tautomer B has been used for comparison with the experimental data and Table 6.7 summarizes the calculated electronic transitions for tautomer B of the ligands and gives the corresponding transitions. The calculated spectra of tautomer B for the ligands compares favorably with the experimental spectra. A few calculated states may give rise to a single peak. The peaks at approximately 430 nm and 330 nm in the experimental spectra of the macrocyclic ligands are likely due to a combination of σ , $\pi \rightarrow \pi^*$ and $\pi \rightarrow \pi^*$ transitions according to the calculated spectra. There is little difference in the calculated wavelengths of the different macrocyclic ligands; the substituents have little effect on the calculated absorption spectra. The broad peak at approximately 420 nm and the peaks between 300 nm - 400 nm in the electronic spectrum of the pseudomacrocyclic ligand are due to $\pi \rightarrow \pi^*$ transitions. Again, there is little difference in the calculated wavelengths of the different pseudomacrocyclic ligands. The peak at 287 nm in the experimental spectrum of the acyclic ligand is described by two transitions at 273 nm and 264 nm in the calculated spectrum. These transitions are σ , $\pi \rightarrow \pi^*$ and σ , $\pi \rightarrow \sigma^*$, π^* transitions.

In summary, the calculated spectra of tautomers A and B best describe the experimental electronic spectra of the ligands. The calculated spectrum of tautomer B was used for comparison with the experimental spectra of the ligands. The comparison of experimental and calculated data was favourable. The main transitions for all the ligands are σ , $\pi \rightarrow \pi^*$ and $\pi \rightarrow \pi^*$ transitions.

6.3.4 Calculated NMR Spectral Data of Schiff base ligands

The ¹H and ¹³C NMR spectra of the free ligands were calculated using the GIAO method with the B3LYP hybrid density functional and the 6-311G(d,p) basis set. A DMSO solvent model was also used in the calculation to account for any solvent effects in the experimental structures. The reference used was TMS calculated at the same level of theory in the same solvent continuum. The NMR spectra for all the tautomeric forms of the ligands were calculated and compared to the experimental data. Tables 6.8 and 6.9 give the ¹H and ¹³C NMR shifts for the calculated tautomeric forms of H₂L1 as well as the percentage difference between experimental and calculated values. The numbering scheme for the NMR assignments for the tautomers is shown in Figure 6.8.

Table 6.8: Comparison of experimental and calculated ¹H NMR data (ppm) for the tautomeric forms of H₂L1.

Proton	Tautomer A			Tautomer B		Tautomer C		Tautomer D	
	Exp	Calc	Diff	Calc	Diff	Calc	Diff	Calc	Diff
<i>k</i>	2.06	1.86	-0.20	2.03	-0.03	2.08	0.02	1.49	-0.57
<i>j</i>	4.02	3.80	-0.22	4.02	0.00	4.02	0.00	3.56	-0.46
<i>g</i>	6.98	6.61	-0.37	7.07	0.09	7.17	0.19	7.05	0.07
<i>f</i>	7.43	7.30	-0.13	7.95	0.52	7.90	0.47	7.39	-0.04
<i>a</i>	7.76	7.87	0.11	7.95	0.19	8.18	0.42	7.86	0.10
<i>b</i>	8.00	8.05	0.05	8.21	0.21	7.90	-0.10	8.09	0.09
<i>i</i>	8.25*	8.10	-0.15	8.30	0.05	8.26	0.01	7.06	-1.19
<i>m</i>	12.21	N/A	N/A	11.77	-0.44	14.02	1.81	7.30	-4.91
<i>l</i>	17.71	9.93	-7.78	16.81	-0.90	18.53	0.82	N/A	N/A

*Average of imine chemical shifts

Table 6.9: Comparison of experimental and calculated ¹³C NMR data (ppm) of the tautomeric forms of H₂L1.

C	Tautomer A		Tautomer B		Tautomer C		Tautomer D		
	Exp	Calc	Diff	Calc	Diff	Calc	Diff	Calc	Diff
<i>k</i>	30.80	38.52	7.72	36.24	5.44	35.15	4.35	35.30	4.50
<i>j</i>	54.51	64.55	10.04	58.15	3.64	58.18	3.67	50.69	-3.82
<i>f</i>	116.79	120.74	3.95	121.65	4.86	120.97	4.18	126.18	9.39
<i>g</i>	120.96	118.41	-2.55	126.04	5.08	127.53	6.57	130.64	9.68
<i>b</i>	128.21	133.39	5.18	133.28	5.07	133.67	5.46	133.30	5.09
<i>a</i>	129.62	134.31	4.69	133.71	4.09	133.33	3.71	133.50	3.88
<i>h</i>	131.51	139.46	7.95	136.44	4.93	143.27	11.76	141.29	9.78
<i>c</i>	139.48	144.46	4.98	143.97	4.49	144.29	4.81	144.46	4.98
<i>d</i>	143.63	146.08	2.45	148.07	4.44	147.41	3.78	153.30	9.67
<i>e</i>	143.77	138.55	-5.22	142.65	-1.12	151.97	8.20	164.38	20.61
<i>i</i>	151.67	152.33	0.66	153.09	1.42	154.08	2.41	152.25	0.58

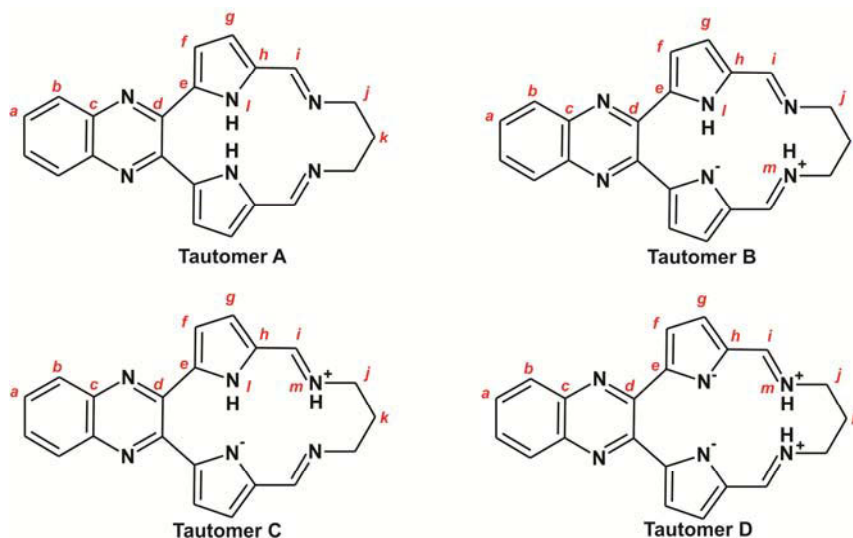


Figure 6.8: Naming scheme used for the ^1H and ^{13}C NMR assignments of $\text{H}_2\text{L1}$.

The calculated shifts of the ^1H NMR spectrum of tautomer A of $\text{H}_2\text{L1}$ are over and underestimated when compared to the experimental spectrum. In general the calculated chemical shifts are in good agreement with the experimental chemical shifts. The main difference between the two spectra is the NH shifts. Tautomer A does not have an imine N atom protonated and therefore the calculated spectrum shows a single peak at 9.93 ppm corresponding to the pyrrole N–H. The experimental spectrum has two NH peaks at 12.21 and 17.71 ppm corresponding to an imine NH and pyrrole NH, respectively. This suggests that tautomer A is not present in solution. The calculated ^{13}C shifts for tautomer A are also over and underestimated. There is a large difference of 7.72 ppm and 10.04 ppm for the calculated and experimental chemical shifts for the central and outer methylene peaks of the bridge, respectively. The rest of the ^{13}C chemical shifts compare favourably (deviations <8 ppm).

The calculated chemical shifts of the ^1H NMR spectrum of tautomer B of $\text{H}_2\text{L1}$ compare favourably with the experimental chemical shifts (differences <1 ppm). The calculated shifts are both over and underestimated when compared to the experimental data. The calculated spectrum of tautomer B has two NH chemical shifts; an imine NH chemical shift at 11.77 ppm and a pyrrole N–H chemical shift at 18.81 ppm. This is consistent with the experimental data leading to only a 0.44 ppm and 0.90 ppm difference between theory

and experiment for the imine NH and the pyrrole NH chemical shifts, respectively. The calculated ^{13}C NMR chemical shifts for tautomer B of $\text{H}_2\text{L1}$ are mostly overestimated. The largest difference in the experimental and calculated ^{13}C NMR shifts is for the methylene protons of the di(azomethine) linkage unit. The rest of the ^{13}C NMR spectrum is well predicted by the calculations with the difference in results below 6 ppm. The calculated and experimental NMR spectra show that it is likely that the ligands adopt tautomeric form B in solution. This is fully consistent with the X-ray structures and the DFT energy order of the tautomers.

The calculated ^1H NMR spectrum of tautomer C of $\text{H}_2\text{L1}$ compares well with the experimental spectrum. The calculated spectrum predicts an imine NH peak and a pyrrole NH peak. Both these values are overestimated in the calculations leading to a 1.81 ppm difference in the calculated and experimental chemical shifts for the imine NH peak and a 0.82 ppm difference in the pyrrole NH peak. Although the rest of the spectrum is well predicted, this large difference in imine N–H shifts suggests that tautomer C is not the favoured tautomeric form in solution. The calculated ^{13}C NMR spectrum for tautomer C overestimates all of the experimental chemical shifts. The largest difference is for the chemical shifts of the methylene carbon atoms; the remainder of the calculated carbon chemical shifts are in good agreement with the experimental chemical shifts.

The calculated ^1H NMR spectrum of tautomer D does not compare well with the experimental spectrum. There is a 0.57 ppm and 0.46 ppm difference between the calculated and experimental data for the central and outer methylene protons of the di(azomethine) bridge, respectively. The imine CH peak is underestimated by the calculations by 1.19 ppm. Tautomer D does not have any pyrrole NH protons and thus the calculations predict only an imine NH stretch at 7.30 ppm, a 4.90 ppm difference in results. The ^{13}C NMR spectra also compare poorly. These large differences in calculated and experimental data suggest that this is not the dominant tautomeric form in solution.

Selected ^1H NMR and ^{13}C NMR shifts for tautomer B of all the ligands are summarized in Table 6.10. The calculated and experimental data compare well for the macrocyclic ligands. In general, the calculated ^1H NMR spectra exhibit a greater error when the chemical shift is further downfield. For example $\text{H}_2\text{L2}$ only has a 0.03 ppm difference in the imine C–H chemical shifts which are situated at 8.20 and 8.23 ppm in the experimental and calculated spectra, respectively. There is a 0.86 ppm difference in the pyrrole NH chemical shift which is situated at 17.85 and 16.89 ppm in the experimental and calculated spectra, respectively. The calculated and experimental data for tautomer B of the pseudomacrocyclic ligands compare less favourably than those of the macrocyclic ligands. In the experimental spectra of these pseudomacrocyclic ligands there is an absence of the peak found at *ca.* 17 ppm in the spectra of the macrocyclic ligands. There is also a large percentage difference in the calculated and experimental values for the NH shift. This suggests that in solution, due to the flexible nature of the imine appendages, the intramolecular hydrogen bonding effects may be overcome and tautomer A may be dominant in solution. The calculated spectra of tautomer A of the pseudomacrocyclic ligands has no imine N–H peak and only pyrrole N–H peaks present at 8.54, 8.60 and 8.58 ppm for $\text{H}_2\text{L9}$, $\text{H}_2\text{L10}$ and $\text{H}_2\text{L11}$, respectively. These values do not, however, compare well with the experimental values for the NH peak which are at *ca.* 11.5 ppm. It may also be that the compounds open up and form new hydrogen bonded structures that could influence the chemical shift of the other N–H peak of tautomer B.

Table 6.10: Comparison of experimental and calculated ^1H and ^{13}C NMR shifts (ppm) for tautomer B of the Schiff base ligands.

	Exp	Calc	Diff	Exp	Calc	Diff	Exp	Calc	Diff
	H₂L2			H₂L3			H₂L5		
Imine CH*: ^1H	8.20	8.23	0.03	8.27	8.39	0.12	8.23	8.28	0.05
^{13}C	152.20	153.89	1.69	153.10	154.50	1.40	151.44	152.78	1.34
Imine NH	12.13	11.80	-0.33	11.24	10.95	-0.29	12.15	11.71	-0.44
Pyrrole NH	17.75	16.89	-0.86	18.38	17.08	-1.30	17.64	16.77	-0.87
	H₂L6			H₂L7			H₂L8a		
Imine CH*: ^1H	8.24	8.28	0.04	8.23	8.22	-0.01	8.40	8.40	0.00
^{13}C	151.57	152.94	1.37	154.79	154.77	-0.02	153.13	154.65	1.52
Imine NH	12.18	11.75	-0.43	12.24	11.83	-0.41	12.51	11.99	-0.52
Pyrrole NH	17.67	16.77	-0.90	17.72	16.76	-0.96	17.56	16.45	-1.11
	H₂L8b			H₂L9			H₂L10		
Imine CH*: ^1H	8.28	8.37	0.09	8.24	8.30	0.06	8.25	8.33	0.08
^{13}C	151.40	154.71	3.31	153.0	156.62	3.62	151.50	156.54	5.04
Imine NH	12.19	11.69	-0.50	11.40	9.75	-1.65	11.41	9.52	-1.89
Pyrrole NH	17.37	16.81	-0.56		17.15			16.91	
	H₂L11			H₂L12					
Imine CH*: ^1H	8.21	7.96	-0.25	8.05	8.24	0.19			
^{13}C	152.80	154.47	1.67	151.47	152.87	1.40			
Imine NH	11.71	9.56	-2.15						
Pyrrole NH		17.06		11.31	8.85	-2.46			

*Average of two imine NH chemical shifts

In order to determine if the errors in the calculations were systematic, the experimental data were plotted against the calculated data. A straight line would indicate that there is a statistical relationship between the calculated and experimental data. There is no such correlation for the ^{13}C NMR shifts suggesting that the errors are random. The only correlation that could be found in the ^1H NMR spectra of the macrocyclic ligands was for the imine NH shifts. The correlation plot is shown in Figure 6.9.

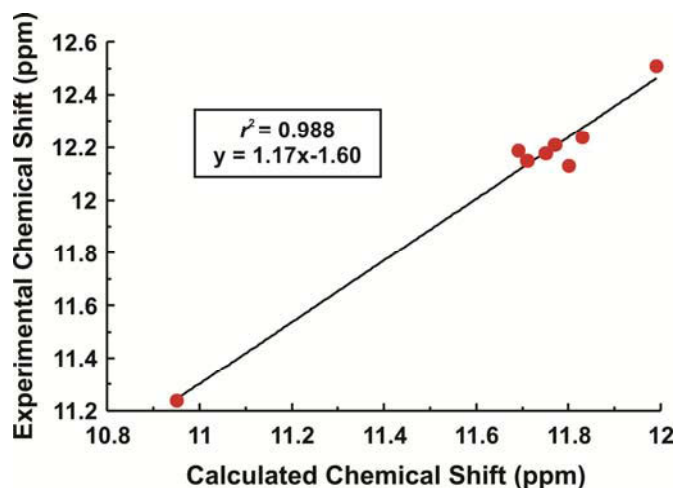


Figure 6.9: Plot of experimental versus calculated ^1H NMR shifts for tautomer B of the imine NH protons of the macrocyclic ligands. The correlation coefficient of the linear fit as well as the equation of the line is shown in the plot.

The plot in Figure 6.9 shows that there is a linear relationship between the experimental and calculated ^1H NMR chemical shifts of the imine N–H atoms of the macrocyclic ligands. This indicates that the errors in the calculations are systematic and can be corrected. Equation 6.11 shows the relationship between the calculated and experimental data.

$$\delta_{\text{imineNH}}^{\text{Exp}} = 1.17 \times \delta_{\text{imineNH}}^{\text{Calc}} - 1.60 \text{ ppm} \quad 6.11$$

In summary, the calculations of tautomer B predict the experimental NMR results of the macrocyclic ligands well. The calculated spectrum has an imine NH peak *ca.* 17 ppm and a pyrrole NH peak at *ca.* 12 ppm, both of which are present in the experimental spectra. The percentage differences between the calculated spectra of tautomer B and the experimental spectra for the macrocyclic ligands are minimal. The calculations of tautomer B of the pseudomacrocyclic ligands do not compare as favourably with the experimental data. There is no peak present in the experimental data at *ca.* 17 ppm of the pseudomacrocyclic ligands indicating the presence of a different tautomer.

6.4 Computational Chemistry of Bis(Pyrrolide-Imine) Gold(III) Chelates

6.4.1 Geometry Optimization Results

The geometries of the bis(pyrrolide-imine) gold(III) chelates were optimized by finding the lowest energy conformation on the potential energy surfaces. The calculations were performed using the PBEPBE hybrid functional in conjunction with the LANL2DZ basis set.

As the calculations are performed in the gas phase, the structures will not be affected by any intermolecular forces. These intermolecular forces have been shown to be present in the X-ray crystal structures. The presence of $\pi \cdots \pi$ and Au– π interactions in the solid state may affect the geometry of the compounds. The calculations show that, in general, the chelates are planar with the gold(III) ion sitting in the plane defined by the four coordinating nitrogen atoms. The bridging unit of the molecule shows some deviation from planarity. This deviation is due to the sp^3 hybridization of the alkyl bis(imine) linkages. The gold(III) cation has a strong preference for a square-planar coordination geometry due to the vacant $d(x^2-y^2)$ orbitals. The extended aromaticity of the ligand also stabilizes a square-planar geometry.

Least squares regression was used to determine the accuracy with which the calculations predicted the geometry of the chelates. The root mean square deviation gives a mathematical means for comparison of the structures. The fits and RMSD values for all the molecules in the asymmetric unit are shown in Figure 6.10. The RMSD values for the ligands and the gold(III) chelates are similar as both the ligands and the chelates are relatively rigid with few torsional degrees of freedom.

The geometry optimized structures of the three-carbon-bridged complexes, $[\text{Au}(\text{L1})]^+$ and $[\text{Au}(\text{L2})]^+$, are completely planar with the exception of a puckering of the central carbon of the three carbon bridge. The X-ray crystal structure of $[\text{Au}(\text{L1})]^+$ shows that the molecule exhibits slight doming of the pyrrole rings, but the rest of the molecule excluding the central methylene bridging carbon is approximately planar. This is reflected in a low RMSD of 0.0771 Å. Both molecules A and B in the asymmetric unit of the X-ray crystal structures of $[\text{Au}(\text{L2})]^+$ show only slight deviations from planarity. Molecule A has a slight domed

configuration while molecule B has the quinoxaline tail slightly rotated out of the plane of the molecule. The calculated and experimental structures are in good agreement with RMSDs of 0.0914 Å and 0.115 Å for molecules A and B, respectively. This shows that the crystal packing effects do not significantly perturb the chelate structure. This illustrates the rigidity of the gold(III) macrocyclic chelates, which evidently resists distortions in geometry.

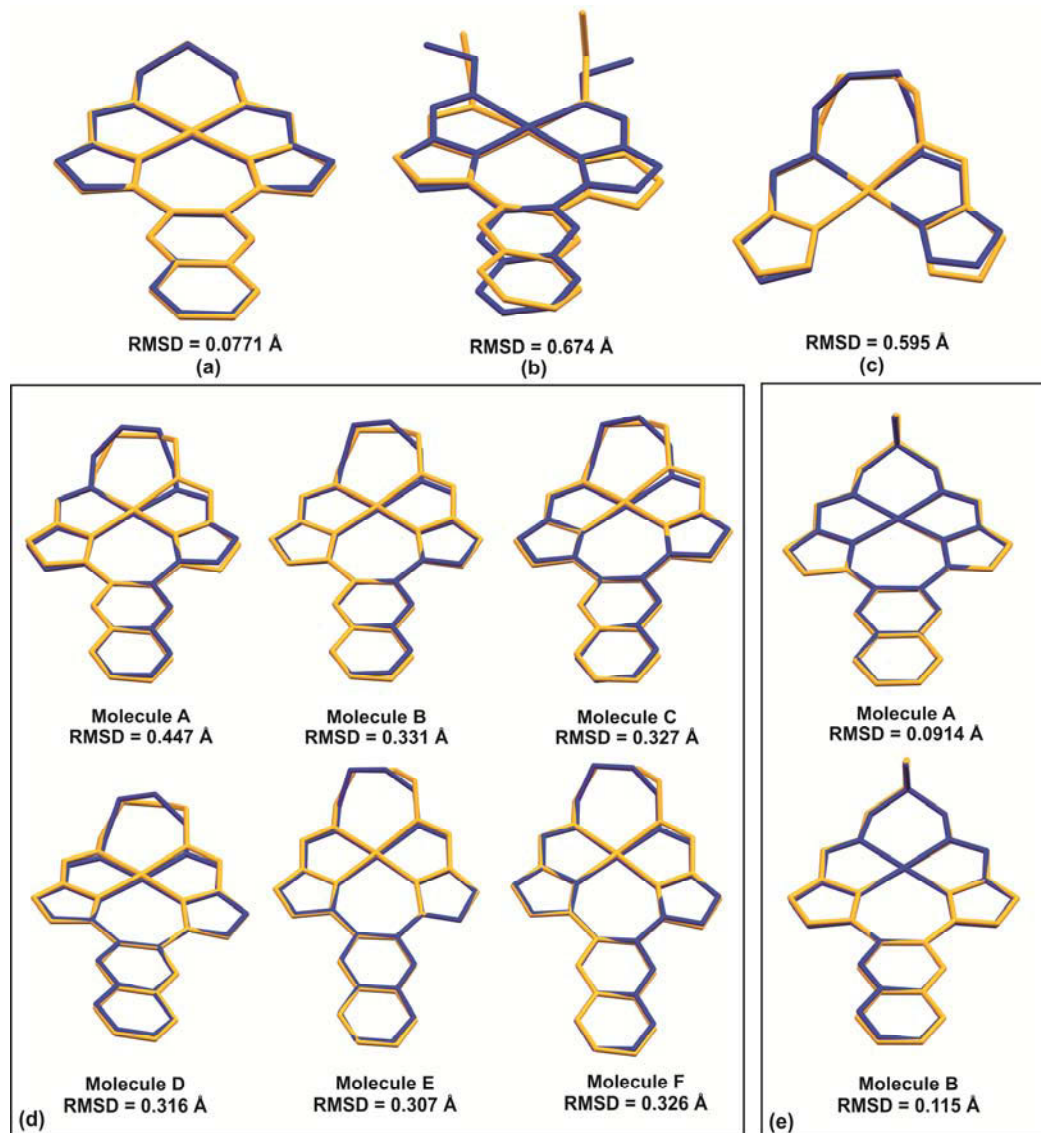


Figure 6.10: Least-squares fits of the non-H atoms of the DFT-calculated structures (yellow) and the molecules in the asymmetric unit of the X-ray crystal structures (blue) for (a) $[\text{Au}(\text{L1})]^+$, (b) $[\text{Au}(\text{L10})]^+$, (c) $[\text{Au}(\text{L12})]^+$, (d) $[\text{Au}(\text{L3})]^+$, and (e) $[\text{Au}(\text{L2})]^+$. The RMSDs are indicated on the diagram.

The calculated structure of the butyl-bridged macrocyclic chelate, $[\text{Au}(\text{L3})]^+$, has a square-planar gold(III) ion with the quinoxaline ring and pyrrole ring tilted out of the plane of the gold(III) ion. This deviation from planarity is due to the buckling of the butyl bridge. In order to accommodate this larger four-carbon bridge, the molecule has to twist out of plane. This same effect is observed in the calculated structure of $[\text{Au}(\text{L12})]^+$. The X-ray crystal structure of $[\text{Au}(\text{L3})](\text{PF}_6)$ has six independent pairs in the asymmetric unit. These molecules

all deviate from planarity to varying degrees typically with one pyrrole ring sitting above the plane and the other below the plane. The quinoxaline ring has also been twisted out-of-plane to varying extents. The least squares fit shows that these deviations of the pyrrole and quinoxaline rings compare favourably to the calculated structure. However, there is a large difference in the geometry of the butyl bridge in the calculated and experimental structures, resulting in higher than expected RMSD values.

The calculated structure of the pseudomacrocyclic, $[\text{Au}(\text{L10})]^+$, also has a square-planar coordination sphere, but the quinoxaline ring and pyrrole rings are tilted out of the plane of the gold(III) ion and the four coordinating nitrogen atoms. As there is no di(azomethine) bridging unit, the molecule is not as rigid and it is therefore possible for the ligand to twist to comfortably accommodate the gold(III) ion. The X-ray structure of $[\text{Au}(\text{L10})]^+$ shows that the molecule is relatively planar with just a slight twist of the quinoxaline tail relative to the pyrrole-imine moiety. The twist results in one pyrrole ring and half the quinoxaline ring sitting below the plane defined by the coordination sphere while the other pyrrole ring and half the quinoxaline ring are sitting above the plane. Although the compounds show similar types of deviation from planarity the RMSD is relatively high, 0.674 Å, due to the flexible nature of the ethyl appendages and the extent of the twisting of the pyrrole and imine rings. The ethyl groups have many torsional degrees of freedom and can be easily distorted from the lowest-energy conformation in the solid state structure.

The calculated and experimental bond lengths and angles of the chelates are summarized in Table 6.11. The calculated and experimental bond distances and angles are in very good agreement. The rigid structure of the gold(III) chelates results in relatively accurate calculations of their structures as indicated by the small difference in bond angles and lengths between the experimental and calculated structures.

Table 6.11: Comparison of the mean bond lengths (Å) and angles (°) of the calculated and experimental structures of the gold(III) chelates: $[\text{Au}(\text{L1})]^+$, $[\text{Au}(\text{L2})]^+$, $[\text{Au}(\text{L3})]^+$, $[\text{Au}(\text{L10})]^+$ and $[\text{Au}(\text{L12})]^+$.

	Au-N _{pyrr}	Au-N _{imine}	N _{pyrr} -Au-N _{pyrr}	Cis- N _{pyrr} -Au-N _{imine}	Trans- N _{pyrr} -Au-N _{imine}	N _{imine} -Au-N _{imine}	C=N _{imine} -C
$[\text{Au}(\text{L1})]^+$							
Exp.	1.99(1)	2.01(1)	99.2(2)	81.8(1)	177.7(1)	97.2(2)	124.1(5)
Calc.	2.001	2.043	99.0	82.1	178.7	96.8	125.0
$[\text{Au}(\text{L2})]^+$							
Exp.	1.98(1)	2.00(1)	100.2(2)	81.7(1)	177.8(7)	96.4(6)	124(2)
Calc.	2.01	2.04	99.1	82.2	178.1	96.3	125.1
$[\text{Au}(\text{L3})]^+$							
Exp.	1.98(1)	2.02(2)	97.1(8)	81.9(8)	177(1)	99.2(4)	121(2)
Calc.	2.01	2.07	97.1	81.8	174	99.8	120
$[\text{Au}(\text{L10})]^+$							
Exp.	1.987(6)	2.059(7)	95.8(3)	81.9(8)	177(1)	99.2(4)	121(2)
Calc.	2.023	2.085	96.5	81.4	174	101.3	119.3
$[\text{Au}(\text{L12})]^+$							
Exp.	1.994(6)	2.043(4)	99.8(2)	80.8(2)	177.1(2)	98.8(2)	120.3(5)
Calc.	2.031	2.085	100.7	80.4	170.4	100.1	120.2

Both the three-carbon and four-carbon bis(imine) bridges exhibit an out-of-plane puckering. This has an effect on the coordination geometry of the gold(III) ion of the macrocyclic ligands. The longer butyl bridge forces the imine N atoms further apart, thus changing the bite angle of the ligand. This effect is also observed in the magnitude of the C=N_{imine}-C angle resulting in a larger N_{imine}-Au-N_{imine} and a smaller N_{pyrrole}-

Au–N_{pyrrole} bond angle for [Au(L3)]⁺ compared to [Au(L1)]⁺ and [Au(L2)]⁺ for both the calculated and experimental structures. Despite the distortion of the coordination geometry of the gold(III) ion, the bond angles about the bis(imine) linkage are approaching ideality. The pseudomacrocyclic complex, [Au(L10)]⁺ has no di(azomethine) bridging unit restricting the N_{imine}–Au–N_{imine} bond angle and thus it has the largest N_{imine}–Au–N_{imine} angle for both the experimental and calculated structures. To accommodate this larger angle, it has a smallest N_{pyrrole}–Au–N_{pyrrole} angle.

The geometry optimized structures of the complexes which could not be crystallized were calculated and are shown in Figure 6.11. The small RMSD values of the structures with three-carbon bridges suggest that the calculated structures of those complexes that were not studied by X-ray diffraction are likely to be a good representation of the actual structures.

The calculated propyl-bridged structures of the compounds depicted in Figure 6.11 are all planar with the exception of the central methylene group. Although the pseudomacrocyclic structure [Au(L9)]⁺ has more degrees of freedom, it still adopts a planar conformation. The geometry optimized structure of the pseudomacrocyclic complex [Au(L11)]⁺ is not completely planar, but has canted quinoxaline and pyrrole rings. This may be due to the added steric bulk of the ethanol appendages which may cause the molecule to deviate from planarity. Interestingly, the geometry optimized structure shows an intramolecular hydrogen bond between the two hydroxyl groups. The bond parameters for this O–H···O interaction are: 1.005, 1.769 and 2.733 Å for the O–H, H···O and O···O distances, respectively. The O–H···O bond angle measures 159.47°. This is a relatively short interaction and is likely to be moderately strong.

The geometry optimized structure of [Au(L4)]⁺ was calculated with the chlorine atom on the di(azomethine) bridge in both the axial and equatorial positions. The geometry optimized structure of the complex with the chlorine atom in the axial position is 7.2 kJmol⁻¹ lower in energy than the structure with the chlorine atom in the equatorial position. This suggests that the axial position of the chlorine atom is favoured.

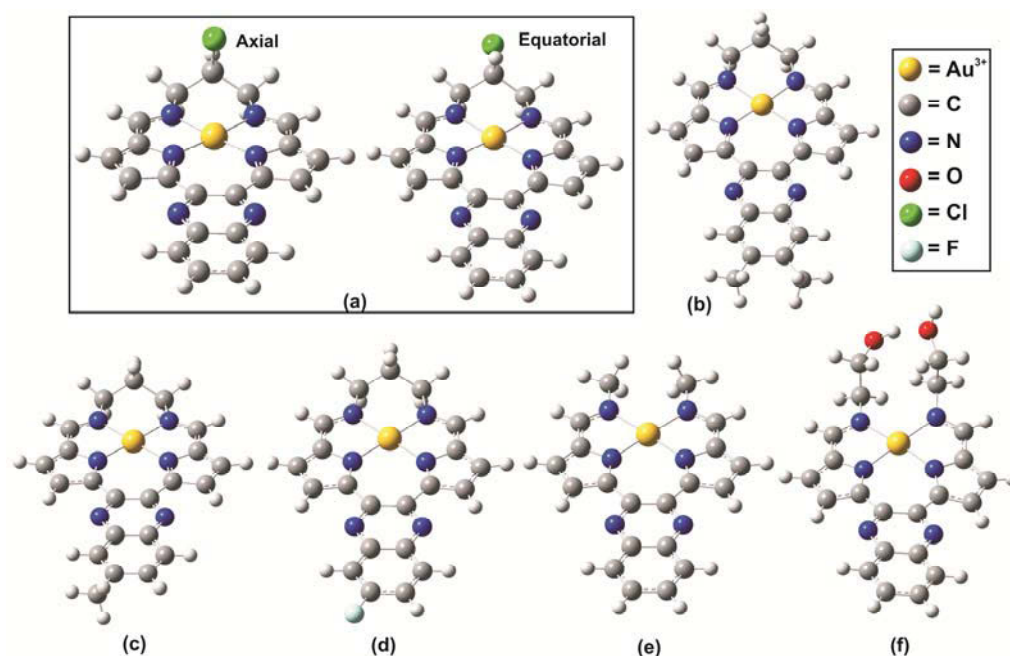


Figure 6.11: Geometry optimized structures of (a) [Au(L4)]⁺, (b) [Au(L5)]⁺, (c) [Au(L6)]⁺, (d) [Au(L7)]⁺, (e) [Au(L9)]⁺, and (f) [Au(L11)]⁺ calculated at the PBEPBE/LANL2DZ level of theory.

6.4.2 Vibrational Frequency Results for the Gold(III) Chelates

The vibrational frequencies of the gold(III) chelates were primarily calculated to ensure that the geometry optimized structures were true minima on the global potential energy surface. Additionally, the calculated frequencies were compared with the experimental IR spectra to determine their accuracy. Figure 6.12 shows an overlay of the calculated and experimental frequencies for the macrocyclic complex $[\text{Au}(\text{L1})]^+$ and the pseudomacrocyclic complex $[\text{Au}(\text{L11})]^+$.

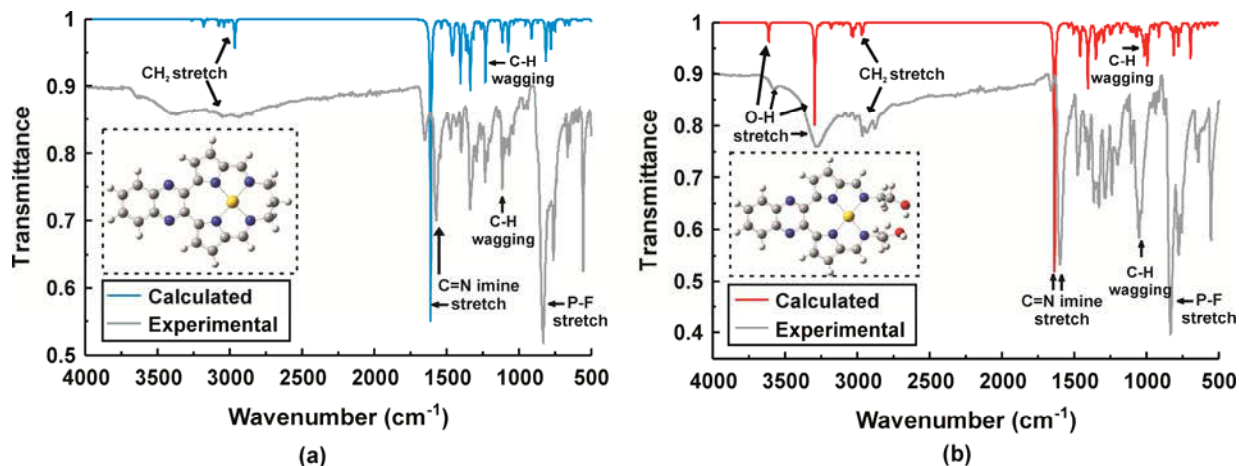


Figure 6.12: Overlay of calculated and experimental frequency data for (a) $[\text{Au}(\text{L1})]^+$ and (b) $[\text{Au}(\text{L11})]^+$.

The relative intensities of the peaks show very good agreement between the calculated and experimental data. The absolute values of the calculated and experimental frequencies are also in good agreement with the calculated frequencies being only slightly overestimated compared with the experimental data. Table 6.12 summarizes the experimental and calculated IR shifts for the C=N stretch and the CH₂ stretch. The errors for the C=N stretch range from 9 cm⁻¹ for $[\text{Au}(\text{L7})]^+$ to 43 cm⁻¹ for $[\text{Au}(\text{L4})]^+$. The errors for the CH₂ stretch range from 27 cm⁻¹ for $[\text{Au}(\text{L9})]^+$ to 82 cm⁻¹ for $[\text{Au}(\text{L4})]^+$. The range of errors in both cases is small, indicating a high degree of accuracy in the calculations. These errors are smaller than those determined for the ligands. As the calculations do not include the anion, the calculated spectra do not contain the strong P-F stretch which dominates the experimental spectrum.

Table 6.12: Comparison of selected experimental and calculated vibrational frequencies (cm^{-1}) for the bis(pyrrrolide-imine) gold(III) chelates presented in this work.

	C=N	CH ₂ stretch		C=N	CH ₂ stretch
	[Au(L1)]⁺			[Au(L2)]⁺	
Experimental	1572	2954	Experimental	1569	2965
Calculated	1610	3008	Calculated	1610	3025
Difference	38	54	Difference	41	60
	[Au(L3)]⁺			[Au(L4)]⁺	
Experimental	1590	2955	Experimental	1569	2963
Calculated	1624	3033	Calculated	1612	3045
Difference	34	78	Difference	43	82
	[Au(L5)]⁺			[Au(L6)]⁺	
Experimental	1573	2955	Experimental	1573	2955
Calculated	1611	3008	Calculated	1610	3008
Difference	38	53	Difference	37	53
	[Au(L7)]⁺			[Au(L9)]⁺	
Experimental	1618	2958	Experimental	1602	2966
Calculated	1609	3009	Calculated	1641	2993
Difference	-9	51	Difference	39	27
	[Au(L10)]⁺			[Au(L11)]⁺	
Experimental	1597	2965	Experimental	1597	2968
Calculated	1631	3002	Calculated	1636	3014
Difference	34	37	Difference	39	46
	[Au(L12)]⁺				
Experimental	1585	2967	Experimental		
Calculated	1625	3034	Calculated		
Difference	40	67	Difference		

The data were analyzed by plotting the experimental frequencies against the calculated frequencies. This gave a straight line plot which suggested that the error in the imine C=N stretching vibration was systematic and a correction could be applied to the calculated data to facilitate more accurate predictions of vibrational mode energies for the assignment of the experimental spectra. This plot is shown in Figure 6.13.

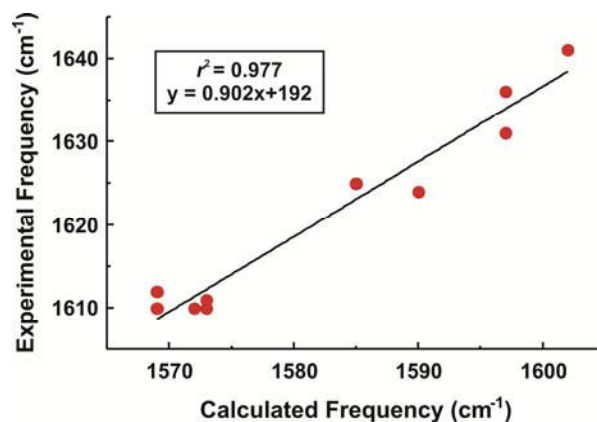


Figure 6.13: Plot of experimental versus calculated imine C=N stretching vibrations of the bis(pyrrrolide-imine) gold(III) chelates. The correlation coefficient and the linear regression are shown on the plot.

Equation 6.12 gives the mathematical relationship between the calculated and experimental vibrational frequencies of the imine C=N stretching vibration. There was no such relationship observed with the other stretching vibrations, indicating that the differences between the experimental and calculated data are due to random errors.

$$\nu_{\text{imine}}^{\text{Exp}} = 0.902 \times \nu_{\text{imine}}^{\text{Calc}} + 192 \text{cm}^{-1} \quad 6.12$$

In general, no negative eigenvalues were noted in the calculated data which suggests the optimized structures were true minimum energy conformations. The calculated and experimental frequencies for the complexes in general compared favourably both in terms of the relative intensities of the spectra and the absolute values of the frequencies.

6.4.3 Electronic Transition for the Gold(III) Chelates

Electronic transitions were calculated for the gold(III) complexes using the TD-SCF method, solving for 30 excited states. An acetonitrile solvent continuum was also used in the calculations to account for any solvent effects in the experimental spectra. The level of theory used was PBEPBE/LANL2DZ. As this basis set makes use of effective core potentials, only the valence electrons are included in the calculations. Core electrons are not involved in electronic transitions, thus it should not affect the accuracy of the simulations. The results were compared with the experimental UV/visible absorption spectra. The purpose of the electronic transition calculations was not only to compare results with experimental data, but also to provide insight into which of the chelate orbitals are involved in the transitions. An overlay of the calculated and experimental results for the macrocyclic complex, $[\text{Au}(\text{L1})]^+$, and the pseudomacrocyclic complex, $[\text{Au}(\text{L10})]^+$, is shown in Figure 6.14 as a representative sample. In this figure the calculated spectrum of $[\text{Au}(\text{L1})]^+$ has been shifted by 30 nm (towards the UV end of the spectrum) in order for the most intense transition peaks in the calculated and experimental spectra to overlap. The calculated spectrum of $[\text{Au}(\text{L10})]^+$ has been shifted by 40 nm (towards the UV region of the spectrum).

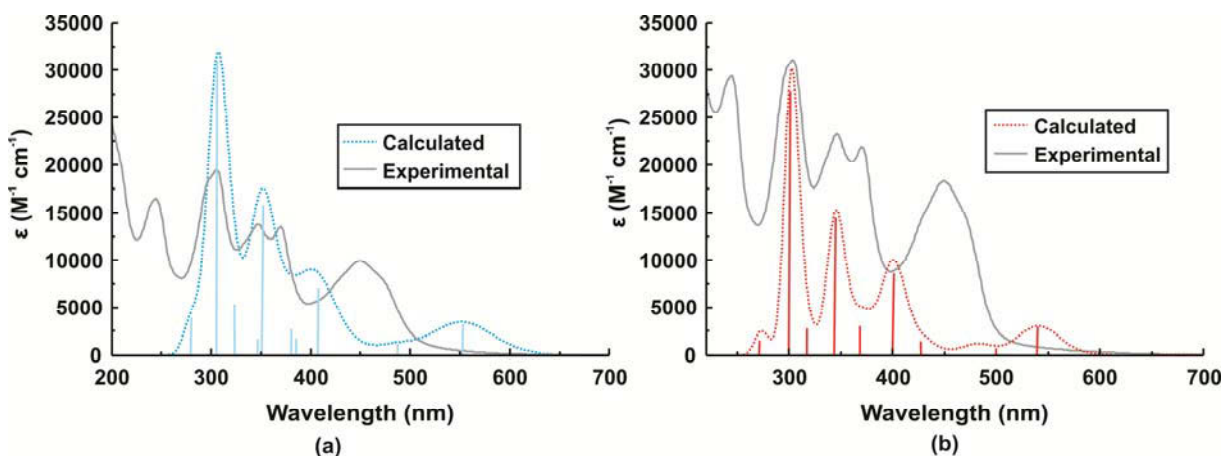


Figure 6.14: Overlay of experimental and calculated UV/visible spectra (width at half height = 1000cm^{-1}) of (a) $[\text{Au}(\text{L1})]^+$ and (b) $[\text{Au}(\text{L10})]^+$ in acetonitrile. Calculated states are depicted as vertical lines with intensities given by their oscillator strengths.

The calculated spectra show multiple transitions and thus multiple absorbance peaks which is consistent with the experimental spectra. The major difference in the calculated and experimental spectra is the shift of the peaks. In the calculated spectrum of $[\text{Au}(\text{L1})]^+$, the peak with the highest oscillator strength is at 339 nm while in the experimental spectrum, the peak with the largest extinction coefficient is at 309 nm. There is also a broad peak in the experimental spectrum at 485 nm, but the corresponding peak in the calculated spectrum is at a lower energy, 586 nm. The experimental spectrum also has a very high energy peak at 246 nm while the calculations do not predict any transitions in this region. Both the experimental and calculated spectra for the macrocyclic complex and the pseudomacrocyclic complex are very similar. This is expected since the alkyl region of the chelates, which determines whether they are macrocycles or pseudomacrocycles, does not have much influence on the electronic properties of the complexes.

The calculated spectrum shown in Figure 6.14 is the result of several electronic transitions between various molecular orbitals. Some of these orbitals are shown in Figure 6.15. Due to the similarity of the orbitals, the remaining molecular orbitals are available in **Appendix F**.

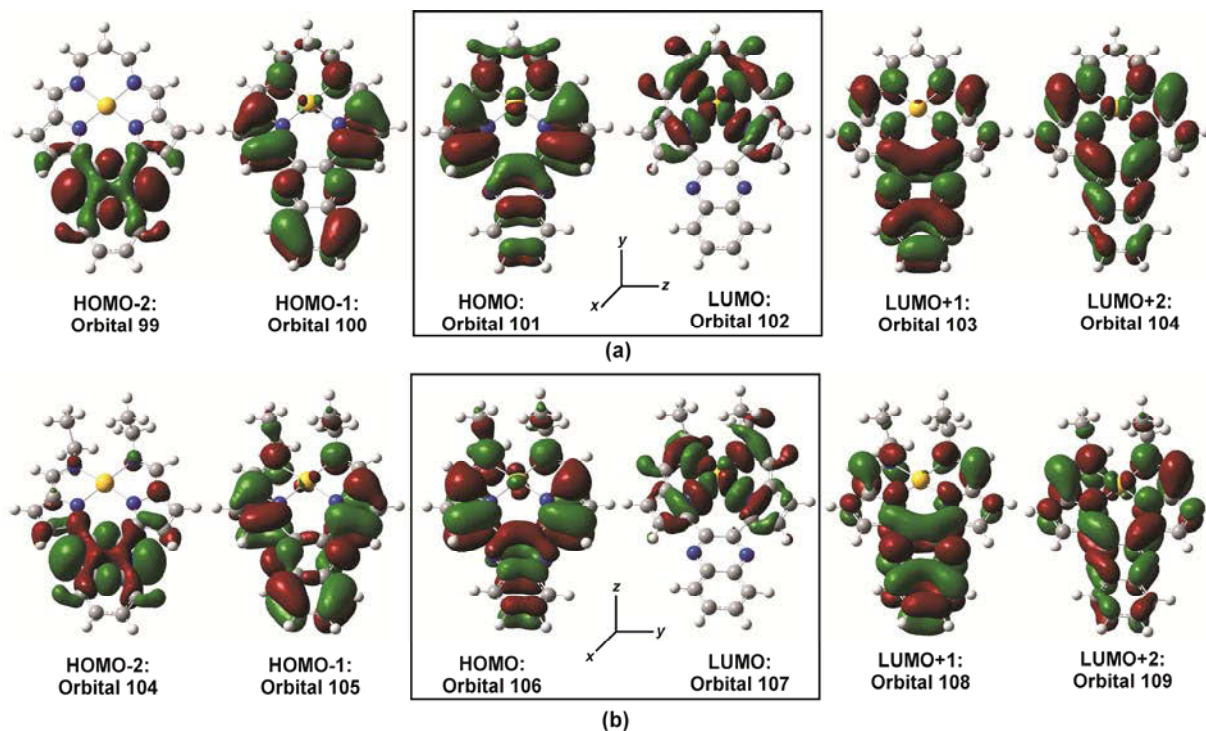


Figure 6.15: Selected electronic orbitals of (a) $[\text{Au}(\text{L1})]^+$ and (b) $[\text{Au}(\text{L10})]^+$.

The orbital plots of the HOMO of $[\text{Au}(\text{L1})]^+$ and $[\text{Au}(\text{L10})]^+$ suggest that the molecular orbital has some π – symmetry with orbitals residing over the quinoxaline ring, pyrrole rings and imine bonds. The HOMO also shows that there are σ orbitals located over the alkyl chains. The HOMO of $[\text{Au}(\text{L1})]^+$ has some metal character with the d_{xy} orbital mixed in with the π orbitals of the ligand. The HOMO of $[\text{Au}(\text{L10})]^+$ has d_{xz} metal orbitals present. The LUMO of $[\text{Au}(\text{L1})]^+$ and $[\text{Au}(\text{L10})]^+$ has σ orbitals located over the pyrrole rings and alkyl groups. The LUMO also has metal character, $[\text{Au}(\text{L1})]^+$ and $[\text{Au}(\text{L10})]^+$ have d_{yz} orbitals mixed with the ligand orbitals. The HOMO-1 for both complexes differs from the HOMO in both cases in that there is less metal character. The LUMO+1 orbital has π –symmetry with orbitals residing over the quinoxaline ring, pyrrole rings and imine bonds.

Table 6.13: Summary of calculated and experimental electronic transitions for the gold(III) complexes.^a

Comp.	Ex. λ	Cal. λ	MOs	Coef. ^b	f ^c	Transition Assignment
[Au(L1)] ⁺		586	101(H)→103(L+1)	0.633	0.0754	$\sigma(\text{brid}), \pi(\text{quin, pyrr, im}), dxz \rightarrow \pi^*(\text{quin, im})$
			100→104	0.256		$\pi(\text{quin, pyrr, imine}) \rightarrow dxz, \pi^*(\text{quin, imine})$
	485	441	101→105	0.470	0.163	$\sigma(\text{bri}), \pi(\text{quin, pyrr, im}), dxz \rightarrow \pi^*(\text{quin, pyrr, im})$
			100→104	-0.450		$\pi(\text{quin, pyrr, im}) \rightarrow dxz, \pi^*(\text{quin, im})$
	455	385	98→104	0.393	0.365	$\pi(\text{pyrr}), dxz \rightarrow dxz, \pi^*(\text{quin, im})$
	373		97→103	0.378		$\pi(\text{quin, pyrr, im}), dxz \rightarrow \pi^*(\text{quin, im})$
	346	357	98→104	0.533	0.123	$\pi(\text{pyrr}), dxz \rightarrow dxz, \pi^*(\text{quin, im})$
	309		97→103	-0.301		$\pi(\text{quin, pyrr, im}), dxz \rightarrow \pi^*(\text{quin, im})$
	246	339	96→104	0.471	0.715	$\pi(\text{quin, pyrr}) \rightarrow dxz, \pi^*(\text{quin, pyrr, im})$
			94→103	0.286		$\sigma(\text{brid}), \pi(\text{quin, pyrr, im}) \rightarrow \pi^*(\text{quin, im})$
	313	97→105	0.559	0.0904	$\pi(\text{quin, pyrr, im}), dxz \rightarrow \pi^*(\text{quin, pyrr, im})$	
		100→106	0.385		$\pi(\text{quin, pyrr, im}) \rightarrow \pi^*(\text{quin, pyrr, im})$	
[Au(L2)] ⁺		719	108(H-1)→110(L)	0.697	0.0207	$\pi(\text{quin, pyrr, im}), dxz \rightarrow dxy, \sigma^*(\text{brid, im}), \pi^*(\text{pyrr})$
		493	106→110	0.663	0.0738	$\pi(\text{pyrr}), d(x^2-y^2) \rightarrow dxy, \sigma^*(\text{brid, im}), \pi^*(\text{pyrr})$
		490	108→111	0.523	0.0678	$\pi(\text{quin, pyrr, im}), dxz \rightarrow dxy, \pi^*(\text{quin, pyrr, im})$
			107→112	0.387		$\sigma(\text{quin}), \pi(\text{pyrr}) \rightarrow dyz, \pi^*(\text{quin, pyrr, im})$
		484	105→110	0.461	0.0145	$\pi(\text{quin, pyrr, im}), dyz \rightarrow dxy, \sigma^*(\text{brid, im}), \pi^*(\text{pyrr})$
			108→112	-0.378		$\pi(\text{quin, pyrr, im}), dxz \rightarrow dyz, \pi^*(\text{quin, pyrr, im})$
		440	104→110	0.494	0.0612	$\sigma(\text{im, brid}), \pi(\text{pyrr}) \rightarrow dxy, \sigma^*(\text{brid, im}), \pi^*(\text{pyr})$
			107→112	-0.416		$\sigma(\text{quin}), \pi(\text{pyrr}) \rightarrow dyz, \pi^*(\text{quin, pyrr, im})$
	481		102→110	0.660	0.0594	$\sigma(\text{quin, pyrr}) \rightarrow dxy, \sigma^*(\text{brid, im}), \pi^*(\text{pyrr})$
	458	419	103→110	-0.122		$\pi(\text{quin, pyrr, im}), dyz \rightarrow dxy, \sigma^*(\text{brid, im}), \pi^*(\text{pyrr})$
	375		108→113	0.434	0.3069	$\pi(\text{quin, pyrr, im}), dxz \rightarrow dxy, \pi^*(\text{quin, pyrr, im})$
	348	414	108→111	0.233		$\pi(\text{quin, pyrr, im}), dxz \rightarrow dxy, \pi^*(\text{quin, pyrr, im})$
	309		106→112	0.452	0.129	$\pi(\text{pyrr}), d(x^2-y^2) \rightarrow dyz, \pi^*(\text{quin, pyrr, im})$
	249	396	104→110	-0.223		$\sigma(\text{im, brid}), \pi(\text{pyrr}) \rightarrow dxy, \sigma^*(\text{brid, im}), \pi^*(\text{pyr})$
	230	368	106→112	0.452	0.110	$\pi(\text{pyrr}), d(x^2-y^2) \rightarrow dyz, \pi^*(\text{quin, pyrr, im})$
			105→112	-0.438		$\pi(\text{quin, pyrr, im}), dyz \rightarrow dyz, \pi^*(\text{quin, pyrr, im})$
		348	104→111	0.529	0.169	$\sigma(\text{im, brid}), \pi(\text{pyrr}) \rightarrow dxy, \pi^*(\text{quin, pyrr, im})$
		105→112	-0.302	$\pi(\text{quin, pyrr, im}), dyz \rightarrow dyz, \pi^*(\text{quin, pyrr, im})$		
	344	104→111	0.383	0.152	$\sigma(\text{im, brid}), \pi(\text{pyrr}) \rightarrow dxy, \pi^*(\text{quin, pyrr, im})$	
		105→112	0.283		$\pi(\text{quin, pyrr, im}), dyz \rightarrow dyz, \pi^*(\text{quin, pyrr, im})$	
	325	101→110	0.440	0.0809	$\sigma(\text{pyrr, brid}) \rightarrow dxy, \sigma^*(\text{brid, im}), \pi^*(\text{pyrr})$	
		102→112	-0.303		$\sigma(\text{quin, pyrr}) \rightarrow dyz, \pi^*(\text{quin, pyrr, im})$	
[Au(L3)] ⁺		580	105(H)→107(L+1)	0.644	0.0734	$\sigma(\text{brid}), \pi(\text{quin, pyrr, im}), dxz \rightarrow \pi^*(\text{quin, im})$
			104→108	-0.267		$\pi(\text{quin, pyrr, imine}) \rightarrow dxy, \pi^*(\text{quin, pyrr, im})$
	485	440	105→109	0.423	0.2087	$\sigma(\text{bri}), \pi(\text{quin, pyrr, im}), dxz \rightarrow \pi^*(\text{quin, pyrr, im})$
	449		104→108	0.394		$\pi(\text{quin, pyrr, im}) \rightarrow dxy, \pi^*(\text{quin, pyrr, im})$
	370	409	105→109	0.458	0.0934	$\sigma(\text{brid}), \pi(\text{quin, pyrr, im}), dxz \rightarrow$
	347		101→107	-0.365		$\pi^*(\text{quin, pyrr, im}) \pi(\text{quin, pyrr, im}), dxz \rightarrow dx^2-y^2,$ $\pi^*(\text{quin, pyrr, im})$
	306		102→108	0.397	0.245	$\pi(\text{pyrr}), dxy \rightarrow dxy, \pi^*(\text{quin, pyrr, im})$
	244	386	101→107	0.365		$\pi(\text{quin, pyrr, im}), dxz \rightarrow dx^2-y^2, \pi^*(\text{quin, pyrr, im})$
		380	98→106	0.642	0.101	$\pi(\text{quin, pyrr, im}) \rightarrow dyz, \sigma^*(\text{pyrr, im, brid})$
		341	100→108	0.460	0.758	$\sigma(\text{brid}), \pi(\text{quin, pyrr, im}) \rightarrow dxy, \pi^*(\text{quin, pyrr, im})$
		98→107	0.244	$\pi(\text{quin, pyrr, im}) \rightarrow dx^2-y^2, \pi^*(\text{quin, pyrr, im})$		

Table 6.13 continued^a...

Comp.	Ex. λ	Cal. λ	MOs	Coef. ^b	f ^c	Transition Assignment	
[Au(L4)] ⁺		579	104(H)→106(L+1)	0.643	0.0716	$\sigma(\text{brid}), \pi(\text{quin,pyrr,im}), dxy \rightarrow \pi^*(\text{quin,im})$	
			103→107	0.286		$\pi(\text{quin,pyrr,im}) \rightarrow dxz, \pi^*(\text{quin,im})$	
		440	103→107	0.473	0.218	$\pi(\text{quin,pyrr,im}) \rightarrow dxz, \pi^*(\text{quin,im})$	
			104→108	-0.409		$\sigma(\text{brid}), \pi(\text{quin,pyr,im}), dxy \rightarrow \pi^*(\text{quin,pyr,im})$	
		481	98→105	0.591	0.0912	$\sigma(\text{quin,pyrr}) \rightarrow dyz, \sigma^*(\text{pyrr, im, brid})$	
		455	100→106	0.237		$\pi(\text{quin,pyrr,im}), dxy \rightarrow \pi^*(\text{quin,im})$	
		376	98→105	0.385	0.260	$\sigma(\text{quin,pyrr}) \rightarrow dyz, \sigma^*(\text{pyrr, im, brid})$	
		348	101→107	-0.359		$\pi(\text{pyrr}), dxz \rightarrow dxz, \pi^*(\text{quin,im})$	
		308	101→107	0.534	0.0975	$\pi(\text{pyrr}), dxz \rightarrow dxz, \pi^*(\text{quin,im})$	
		246	100→106	-0.317		$\pi(\text{quin,pyrr,im}), dxy \rightarrow \pi^*(\text{quin,im})$	
			341	98→107	0.484	0.401	$\sigma(\text{quin,pyrr}) \rightarrow dxz, \pi^*(\text{quin,im})$
				99→107	0.337		$\pi(\text{quin,pyrr,im}) \rightarrow dxz, \pi^*(\text{quin,im})$
			340	98→107	0.509	0.377	$\sigma(\text{quin,pyrr}) \rightarrow dxz, \pi^*(\text{quin,im})$
			99→107	-0.311	$\pi(\text{quin,pyrr,im}) \rightarrow dxz, \pi^*(\text{quin,im})$		
[Au(L5)] ⁺		579	109(H)→111(L+1)	0.634	0.0804	$\sigma(\text{brid}), \pi(\text{quin,pyrr,im}), dxy \rightarrow \pi^*(\text{quin,pyr,im})$	
			108→112	0.298		$\pi(\text{quin,pyrr,im}) \rightarrow dxz, \pi^*(\text{quin,pyrr,im})$	
		484	108→112	0.486	0.2772	$\pi(\text{quin,pyrr,im}) \rightarrow dxz, \pi^*(\text{quin,pyrr,im})$	
			109→113	-0.400		$\sigma(\text{brid}), \pi(\text{quin,pyrr,im}), dxy \rightarrow \pi^*(\text{quin,pyrr,im})$	
		457	109→113	0.525	0.138	$\sigma(\text{brid}), \pi(\text{quin,pyrr,im}), dxy \rightarrow \pi^*(\text{quin,pyrr,im})$	
		378	108→112	0.265		$\pi(\text{quin,pyrr,im}) \rightarrow dxz, \pi^*(\text{quin,pyrr,im})$	
		350	105→111	0.483	0.395	$\pi(\text{quin,pyrr,im}), dxy \rightarrow \pi^*(\text{quin,pyrr,im})$	
		316	106→112	0.306		$\pi(\text{quin,pyrr}), dxz \rightarrow dxz, \pi^*(\text{quin,pyrr,im})$	
		248	102→111	0.524	0.282	$\pi(\text{quin,pyrr,im}) \rightarrow \pi^*(\text{quin,pyrr,im})$	
			104→112	-0.381		$\pi(\text{quin,pyrr,im}), dxz \rightarrow dxz, \pi^*(\text{quin,pyrr,im})$	
		333	104→112	0.383	0.423	$\pi(\text{quin,pyrr,im}), dxz \rightarrow dxz, \pi^*(\text{quin,pyrr,im})$	
			102→111	0.299		$\pi(\text{quin,pyrr,im}) \rightarrow \pi^*(\text{quin,pyrr,im})$	
[Au(L6)] ⁺		581	105(H)→107(L+1)	0.613	0.0756	$\sigma(\text{brid}), \pi(\text{quin,pyr,im}), dxz \rightarrow \pi^*(\text{quin,pyrr,im})$	
			104→108	0.269		$\pi(\text{quin,pyrr,im}) \rightarrow dyz, \pi^*(\text{quin,pyrr,im})$	
		443	104→108	0.463	0.210	$\pi(\text{quin,pyrr,im}) \rightarrow dyz, \pi^*(\text{quin,pyrr,im})$	
			105→109	-0.442		$\sigma(\text{brid}), \pi(\text{quin,pyr,im}), dxz \rightarrow \pi^*(\text{quin,pyrr,im})$	
		484	105→109	0.478	0.118	$\sigma(\text{brid}), \pi(\text{quin,pyr,im}), dxz \rightarrow \pi^*(\text{quin,pyrr,im})$	
		457	104→108	0.270		$\pi(\text{quin,pyrr,im}) \rightarrow dyz, \pi^*(\text{quin,pyrr,im})$	
		375	102→108	0.343	0.334	$\pi(\text{pyrr}), dyz \rightarrow dyz, \pi^*(\text{quin,pyrr,im})$	
		348	100→107	-0.306		$\pi(\text{quin,pyrr,im}), dxz \rightarrow \pi^*(\text{quin,pyrr,im})$	
		310	101→108	0.501	0.143	$\pi(\text{quin,pyrr,im}), dxz \rightarrow dyz, \pi^*(\text{quin,pyrr,im})$	
		247	100→108	0.380		$\pi(\text{quin,pyrr,im}), dxz \rightarrow dyz, \pi^*(\text{quin,pyrr,im})$	
			346	98→107	0.433	0.518	$\pi(\text{quin,pyrr,im}) \rightarrow \pi^*(\text{quin,pyrr,im})$
			100→108	-0.385	$\pi(\text{quin,pyrr,im}), dxz \rightarrow dyz, \pi^*(\text{quin,pyrr,im})$		
		333	98→107	0.355	0.1499	$\pi(\text{quin,pyrr,im}) \rightarrow \pi^*(\text{quin,pyrr,im})$	
			100→108	0.251		$\pi(\text{quin,pyrr,im}), dxz \rightarrow dyz, \pi^*(\text{quin,pyrr,im})$	

Table 6.13 continued^a...

Comp.	Ex. λ	Cal. λ	MOs	Coef. ^b	f ^c	Transition Assignment
[Au(L7)] ⁺		595	105(H)→107(L+1)	0.658	0.0944	$\sigma(\text{brid}), \pi(\text{quin}, \text{pyr}, \text{im}), dxz \rightarrow \pi^*(\text{quin}, \text{pyr}, \text{im})$
			104→108	0.240		$\pi(\text{quin}, \text{pyrr}, \text{im}) \rightarrow dyz, \pi^*(\text{quin}, \text{pyrr}, \text{im})$
	484	443	105→109	0.501	0.106	$\sigma(\text{brid}), \pi(\text{quin}, \text{pyr}, \text{im}), dxz \rightarrow \pi^*(\text{quin}, \text{pyr}, \text{im})$
			104→108	-0.420		$\pi(\text{quin}, \text{pyrr}, \text{im}) \rightarrow dyz, \pi^*(\text{quin}, \text{pyrr}, \text{im})$
	458		102→108	0.421	0.440	$\pi(\text{pyrr}), dyz \rightarrow dyz, \pi^*(\text{quin}, \text{pyrr}, \text{im})$
	371	385	104→108	0.319		$\pi(\text{quin}, \text{pyrr}, \text{im}) \rightarrow dyz, \pi^*(\text{quin}, \text{pyrr}, \text{im})$
	347		102→108	0.514	0.253	$\pi(\text{pyrr}), dyz \rightarrow dyz, \pi^*(\text{quin}, \text{pyrr}, \text{im})$
	309	358	101→107	-0.277		$\pi(\text{quin}, \text{pyrr}, \text{imine}), dxz \rightarrow \pi^*(\text{quin}, \text{pyr}, \text{imine})$
	245		101→108	0.562	0.0699	$\pi(\text{quin}, \text{pyrr}, \text{im}), dxz \rightarrow dyz, \pi^*(\text{quin}, \text{pyrr}, \text{im})$
		350	98→106	0.328		$\sigma(\text{brid}), \pi(\text{quin}, \text{pyr}, \text{imine}) \rightarrow dxy, \sigma^*(\text{brid}, \text{py})$
		100→108	0.470	0.485	$\pi(\text{quin}, \text{pyrr}, \text{im}) \rightarrow dyz, \pi^*(\text{quin}, \text{pyrr}, \text{im})$	
	340	98→107	0.346		$\sigma(\text{brid}), \pi(\text{quin}, \text{pyrr}, \text{im}) \rightarrow \pi^*(\text{quin}, \text{pyrr}, \text{im})$	
[Au(L9)] ⁺		576	98(H)→100(L+1)	0.644	0.0738	$\pi(\text{quin}, \text{pyrr}, \text{im}), dxz \rightarrow \pi^*(\text{quin}, \text{pyrr}, \text{im})$
			97→101	0.284		$\pi(\text{quin}, \text{pyrr}, \text{im}) \rightarrow dxy, \pi^*(\text{quin}, \text{pyrr}, \text{im})$
	448	435	97→101	0.471	0.227	$(\text{quin}, \text{pyrr}, \text{im}) \rightarrow dxy, \pi^*(\text{quin}, \text{pyrr}, \text{im})$
	368		98→102	-0.415		$\pi(\text{quin}, \text{pyrr}, \text{im}), dxz \rightarrow \pi^*(\text{quin}, \text{pyrr}, \text{im})$
	345	406	98→102	0.479	0.0618	$\pi(\text{quin}, \text{pyrr}, \text{im}), dxz \rightarrow \pi^*(\text{quin}, \text{pyrr}, \text{im})$
	302		93→100	-0.381		$\pi(\text{quin}, \text{pyrr}), dxz \rightarrow \pi^*(\text{quin}, \text{pyrr}, \text{im})$
	244	381	93→100	0.408	0.392	$\pi(\text{quin}, \text{pyrr}), dxz \rightarrow \pi^*(\text{quin}, \text{pyrr}, \text{im})$
			95→101	0.385		$\pi(\text{pyrr}), dxy \rightarrow dxy, \pi^*(\text{quin}, \text{pyrr}, \text{im})$
			94→101	0.449	0.739	$\pi(\text{quin}, \text{pyrr}, \text{im}) \rightarrow dxy, \pi^*(\text{quin}, \text{pyrr}, \text{im})$
		338	91→100	0.256		$\pi(\text{quin}, \text{pyrr}, \text{im}) \rightarrow \pi^*(\text{quin}, \text{pyrr}, \text{im})$
[Au(L10)] ⁺		580	105(H-1)→109(L+2)	0.643	0.0739	$\sigma(\text{brid}), \pi(\text{quin}, \text{pyrr}, \text{im}) \rightarrow dyz, \pi^*(\text{quin}, \text{im})$
			106→108	0.277		$\sigma(\text{brid}), \pi(\text{quin}, \text{pyrr}, \text{im}), dxz \rightarrow \pi^*(\text{quin}, \text{im})$
		441	105→109	0.432	0.217	$\sigma(\text{brid}), \pi(\text{quin}, \text{pyrr}, \text{im}) \rightarrow dyz, \pi^*(\text{quin}, \text{im})$
	449		106→110	-0.385		$\sigma(\text{brid}), \pi(\text{quin}, \text{pyr}, \text{im}), dxz \rightarrow \pi^*(\text{quin}, \text{pyr}, \text{im})$
	370	409	106→110	0.484	0.0761	$\sigma(\text{brid}), \pi(\text{quin}, \text{pyr}, \text{im}), dxz \rightarrow \pi^*(\text{quin}, \text{pyr}, \text{im})$
	346		102→108	-0.359		$\pi(\text{quin}, \text{pyrr}, \text{im}), dxz \rightarrow \pi^*(\text{quin}, \text{im})$
	304	385	103→109	0.408	0.3666	$\pi(\text{pyrr}), dyz \rightarrow dyz, \pi^*(\text{quin}, \text{im})$
	245		102→108	-0.400		$\pi(\text{quin}, \text{pyrr}, \text{im}), dxz \rightarrow \pi^*(\text{quin}, \text{im})$
			103→109	0.516	0.0709	$\pi(\text{pyrr}), dyz \rightarrow dyz, \pi^*(\text{quin}, \text{im})$
		358	101→109	-0.315		$\sigma(\text{brid}), \pi(\text{quin}, \text{pyrr}, \text{im}) \rightarrow dyz, \pi^*(\text{quin}, \text{im})$
		101→109	0.444	0.704	$\sigma(\text{brid}), \pi(\text{quin}, \text{pyrr}, \text{im}) \rightarrow dyz, \pi^*(\text{quin}, \text{im})$	
	342	102→108	0.2339		$\pi(\text{quin}, \text{pyrr}, \text{im}), dxz \rightarrow \pi^*(\text{quin}, \text{im})$	
[Au(L12)] ⁺		371	71(H-3)→75(L+2)	0.666	0.0738	$\pi(\text{pyrr}), dxy \rightarrow dyz, \pi^*(\text{pyrr}),$
			70→76	0.219		$\pi(\text{pyrr}, \text{im}), dxz \rightarrow dxy, \pi^*(\text{pyrr}, \text{im})$
	372	344	73→76	0.529	0.0405	$\sigma(\text{brid}), \pi(\text{pyr}, \text{im}), dxz \rightarrow dxy, \pi^*(\text{pyrr}, \text{im})$
	284		72→75	0.365		$\sigma(\text{brid}), \pi(\text{pyr}, \text{im}), dxy \rightarrow dyz, \pi^*(\text{pyrr}),$
			71→76	0.553	0.1104	$\pi(\text{pyrr}), dxy \rightarrow dxy, \pi^*(\text{pyrr}, \text{im})$
		336	72→76	0.320		$\sigma(\text{brid}), \pi(\text{pyr}, \text{im}), dxy \rightarrow dxy, \pi^*(\text{pyrr}, \text{im})$
		69→74	0.522	0.1532	$\sigma(\text{brid}, \text{pyrr}, \text{im}) \rightarrow dyz, \sigma^*(\text{pyrr}, \text{im})$	
	308	70→76	0.424		$\pi(\text{pyrr}, \text{im}), dxz \rightarrow dxy, \pi^*(\text{pyrr}, \text{im})$	

^a6-7 of the strongest transitions of the 30 calculated N states are listed. Abbreviations: quin, quinoxaline ring; pyrr; pyrrole rings; brid, alkyl chain; im, imine bond; H, HOMO; L, LUMO. ^bWhere multiple transitions contribute to an excited state, only the two with the largest transition coefficients have been listed. ^coscillator strength.

There are no visible HOMO to LUMO transitions for any of the complexes. At 647 nm there is a HOMO to LUMO transition, but with an oscillator strength of 0.00. The HOMO \rightarrow LUMO transition would constitute a $\pi \rightarrow \sigma^*$ transition, which is symmetry forbidden and therefore the calculated oscillator strength is 0.00 for this transition. Most of the transitions are from low lying orbitals to the LUMO+1 and LUMO+2 orbitals. Both of these are π symmetry orbitals and therefore transitions to the LUMO+1 and LUMO+2 orbitals are $\pi \rightarrow \pi^*$ which are symmetry allowed transitions. The calculated molecular orbitals show that they are all mixed, with contributions from both the ligand and metal. Therefore, attributing the electronic transitions of the UV/visible spectrum to well defined orbitals on either the ligand or metal is of little value. Instead, each transition in the experimental spectrum needs to be treated as the result of several transitions between several different, mixed orbitals. Most of the transitions are predominantly $\pi \rightarrow \pi^*$ in character which is expected due to the extended aromaticity of the complexes while a limited number of transitions are attributed to LMCT. The electronic transitions and molecular orbitals of the complexes are summarized in Table 6.13. In general, all of the complexes have similar transitions with similar orbitals involved in the transitions.

In conclusion, the calculated results do not compare particularly well with the experimental data. In the future the application of a split basis set could improve the accuracy of the transitions. This split basis set could make use of the LANL2DZ basis set with its effective core potential for the gold(III) ion, but apply the larger 6-311G(dp) basis set to the light atoms of the structure. The calculated molecular orbitals show that they are all mixed, with contributions from both the ligand and metal. Each transition in the experimental spectrum needs to be treated as the result of several transitions between several different, mixed orbitals.

6.4.4 Calculated NMR Spectral Data of Gold(III) Chelates

The ^1H and ^{13}C NMR spectra of the gold(III) complexes were calculated using the same level of theory as that was used for the geometry optimization, frequency and electronic calculations. The LANL2DZ basis set makes use of the D95V basis set for period two elements and ECPs for heavier atoms. A DMSO solvent model was also used in the calculation to account for any solvent effects in the experimental structures. The reference used in both calculations was TMS. The chemical shift of TMS was calculated at the PBEPBE/LANL2DZ level of theory; the calculated chemical shifts are reported relative to this reference. The correlation between the experimental and calculated chemical shifts was relatively good with average differences of 0.3 ppm for the ^1H NMR spectra and 5.6 ppm for the ^{13}C NMR spectra of $[\text{Au}(\text{L1})]^+$. The calculated and experimental ^1H and ^{13}C NMR shifts for $[\text{Au}(\text{L1})]^+$ are listed in Table 6.14. Figure 6.16 shows the labeling scheme for $[\text{Au}(\text{L1})]^+$.

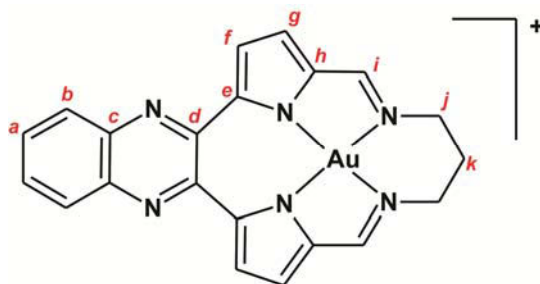


Figure 6.16: Labeling scheme for $[\text{Au}(\text{L1})]^+$.

Table 6.14: Experimental and calculated ^1H and ^{13}C NMR data (ppm) for $[\text{Au}(\text{L1})]^+$.

Proton	Exp	Calc	Diff	Carbon	Exp	Calc	Diff
<i>k</i>	2.42	2.46	0.04	<i>k</i>	33.81	35.18	1.37
<i>j</i>	3.94	3.98	0.04	<i>j</i>	51.27	53.40	2.13
<i>g</i>	7.25	7.23	-0.02	<i>f</i>	118.76	115.27	-3.49
<i>f</i>	7.81	8.57	0.76	<i>g</i>	122.46	114.56	-7.9
<i>a</i>	7.94	8.14	0.20	<i>b</i>	128.48	124.49	-3.99
<i>b</i>	8.06	8.26	0.20	<i>a</i>	131.69	127.34	-4.35
<i>i</i>	8.73	8.09	-0.64	<i>d</i>	135.53	129.57	-5.96
				<i>h</i>	138.99	131.27	-7.72
				<i>c</i>	139.35	133.00	-6.35
				<i>e</i>	147.54	144.50	-3.04
				<i>i</i>	163.05	147.16	-15.89

The calculated chemical shifts were both over and underestimated when compared to the experimental ^1H NMR shifts of $[\text{Au}(\text{L1})]^+$. The calculated ^1H NMR spectrum has the imine CH peak (*i*) much further upfield than in the experimental spectrum with the quinoxaline CH (*a* and *b*) peaks and one of the pyrrole CH (*f*) peaks further downfield. There is a 0.64 ppm difference between the shift of the imine CH peak in the calculated and experimental spectra. There is a 0.76 ppm difference in the shift of the pyrrole peak (*f*). The remaining peaks were calculated more accurately with less than 0.20 ppm difference between the calculated and experimental shifts.

The calculations underestimate the ^{13}C NMR chemical shifts for the alkyl chain of $[\text{Au}(\text{L1})]^+$, but overestimate the bulk of the chemical shifts when compared to the experimental data. The order of the chemical shifts in the calculated ^{13}C NMR spectrum of $[\text{Au}(\text{L1})]^+$ is very similar to that observed experimentally with the only difference being the order of the two pyrrole (*f* and *g*) chemical shifts. The main difference between the calculated and experimental spectra is in the imine C (*i*) chemical shift. The calculations predict this peak at 147.16 ppm, but the experimental spectrum shows this peak to be more downfield at 163.05 ppm, a 15.89 ppm difference between theory and experiment. The remainder of the calculated ^{13}C NMR chemical shifts are within 8 ppm of the experimental frequencies.

Tables 6.15 and 6.16 summarize selected calculated and experimental ^1H and ^{13}C NMR chemical shifts for the bulk of the complexes. These results are very similar to those described for $[\text{Au}(\text{L1})]^+$.

Table 6.15: Comparison of experimental and calculated ^1H NMR data (ppm) for the gold(III) complexes.*

	Exp	Calc	Diff	Exp	Calc	Diff	Exp	Calc	Diff
	[Au(L2)]⁺			[Au(L3)]⁺			[Au(L4)]⁺		
Imine CH (<i>i</i>)	8.83	8.08	-0.75	8.74	7.98	-0.76	8.95	8.15	-0.8
Pyrrole CH (<i>g</i>)	7.44	7.24	-0.2	7.45	7.16	-0.29	7.50	7.27	-0.23
Pyrrole CH (<i>f</i>)	7.99	8.54	0.55	8.06	8.51	0.45	8.02	8.59	0.57
Quinoxaline CH (<i>b</i>)	8.18	8.26	0.08	8.18	8.19	0.01	8.17	8.28	0.11
	[Au(L5)]⁺			[Au(L6)]⁺			[Au(L7)]⁺		
Imine CH (<i>i</i>)	8.83	8.05	-0.78	8.87	8.07	-0.8	8.84	8.09	-0.75
Pyrrole CH (<i>g</i>)	7.40	7.22	-0.18	7.44	7.23	-0.21	7.40	7.33	-0.07
Pyrrole CH (<i>f</i>)	7.93	8.50	0.57	7.99	8.57	0.58	7.90	8.53	0.63
Quinoxaline CH (<i>b</i>)	7.91	8.05	0.14	8.08	8.13	0.05	8.22	8.05	-0.17
	[Au(L9)]⁺			[Au(L10)]⁺			[Au(L11)]⁺		
Imine CH (<i>i</i>)	8.61	7.96	-0.65	8.70	8.10	-0.6	8.62	7.91	-0.71
Pyrrole CH (<i>g</i>)	7.33	7.26	-0.07	7.44	7.21	-0.23	7.49	7.20	-0.29
Pyrrole CH (<i>f</i>)	7.90	8.75	0.85	7.97	8.65	0.68	7.98	8.60	0.62
Quinoxaline CH (<i>b</i>)	8.11	8.25	0.14	8.17	8.21	0.04	8.18	8.22	0.04
	[Au(L12)]⁺								
Imine CH (<i>i</i>)	8.28	7.45	-0.83						

*These protons were selected as they are present in all the macrocyclic and pseudomacrocyclic complexes. The numbering scheme for all the protons are equivalent to those for [Au(L1)]⁺ shown in Figure 6.13.

Table 6.16: Comparison of experimental and calculated ^{13}C NMR data (ppm) for the gold(III) complexes.*

	Exp	Calc	Diff	Exp	Calc	Diff	Exp	Calc	Diff
	[Au(L2)]⁺			[Au(L3)]⁺			[Au(L4)]⁺		
Imine C (<i>i</i>)	164.56	147.61	-16.95	164.83	149.69	-15.14	165.18	148.35	-16.83
Pyrrole C (<i>f</i>)	119.35	115.09	-4.26	118.92	114.73	-4.19	119.78	115.65	-4.13
Pyrrole C (<i>g</i>)	123.39	114.50	-8.89	122.26	114.24	-8.02	124.03	115.25	-8.78
Quinoxaline C (<i>b</i>)	129.08	124.61	-4.47	128.52	124.47	-4.05	129.10	124.64	-4.46
	[Au(L5)]⁺			[Au(L6)]⁺			[Au(L7)]⁺		
Imine C (<i>i</i>)	163.48	146.51	-16.97	163.12	146.95	-16.17	163.40	147.65	-15.75
Pyrrole C (<i>f</i>)	118.48	114.86	-3.62	118.68	114.98	-3.7	118.54	115.41	-3.13
Pyrrole C (<i>g</i>)	122.63	114.37	-8.26	122.65	114.34	-8.31	122.64	114.60	-8.04
Quinoxaline C (<i>b</i>)	127.03	123.15	-3.88	128.08	122.91	-5.17	131.32	127.16	-4.16
	[Au(L9)]⁺			[Au(L10)]⁺			[Au(L11)]⁺		
Imine C (<i>i</i>)	166.35	149.46	-16.9	165.85	150.65	-15.2	167.41	151.29	-16.12
Pyrrole C (<i>f</i>)	118.85	114.52	-4.33	118.95	114.94	-4.01	119.12	114.61	-4.51
Pyrrole C (<i>g</i>)	121.86	114.09	-7.77	122.24	114.16	-8.08	122.59	114.36	-8.23
Quinoxaline C (<i>b</i>)	128.50	124.47	-4.03	128.55	124.46	-4.09	128.58	124.54	-4.04
	[Au(L12)]⁺								
Imine C (<i>i</i>)	164.91	149.46	-15.5						

* The numbering scheme for all the carbons are equivalent to those for [Au(L1)]⁺ shown in Figure 6.13.

The error in the imine chemical shifts in both the ^1H and ^{13}C spectra was seemingly systematic and therefore a correction factor could be determined to enable an empirical correction of the calculated chemical shifts, Figure 6.17. The error associated with the calculation of the remaining protons and carbon atoms was random and so no correction factor could be determined.

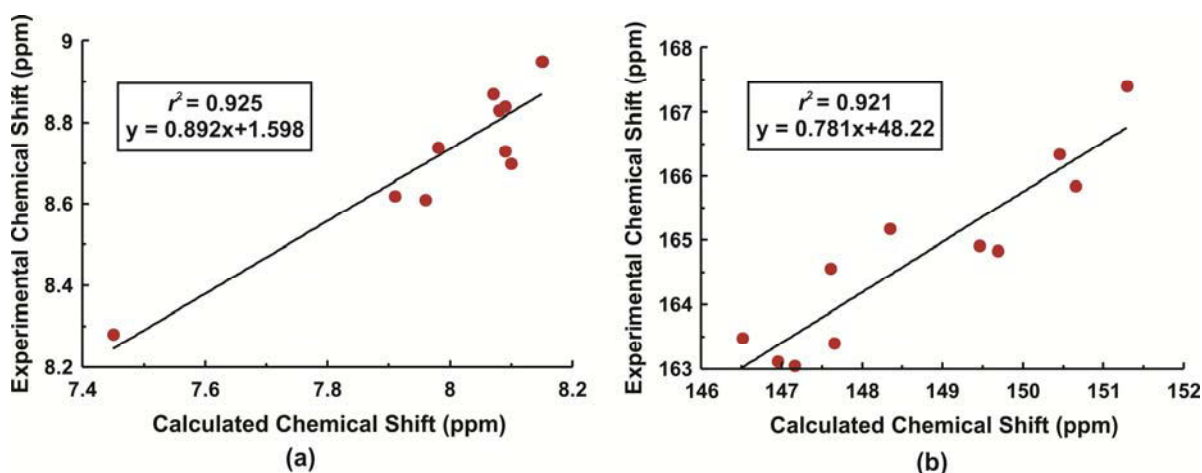


Figure 6.17: Plot of experimental versus calculated (a) ^1H NMR shifts and (b) ^{13}C NMR shifts of the imine protons and carbon atoms of the gold(III) chelates. The correlation coefficients are shown on the plots.

The plots in Figure 6.17 shows that there are linear relationships between the calculated and experimental chemical shifts of the imine group of the gold(III) chelates. The mathematical relationship for the imine proton shift is shown in Equation 6.13 while the relationship for the carbon shift is shown in Equation 6.14.

$$\delta_{\text{imineCH}}^{\text{Exp}} = 0.892 \times \delta_{\text{imineCH}}^{\text{Calc}} + 1.60 \text{ ppm} \quad 6.13$$

$$\delta_{\text{imineC}}^{\text{Exp}} = 0.781 \times \delta_{\text{imineC}}^{\text{Calc}} + 48.22 \text{ ppm} \quad 6.14$$

In summary, the correlation between the experimental and calculated results for the ^1H and ^{13}C NMR data is reasonably good. The data could possibly be improved by using a split basis set, applying a large basis set, 6-311G(d,p) for the carbon, hydrogen and nitrogen atoms while still using the LANL2DZ basis set for the metal ion.

6.5 Summary and Conclusions of DFT Data

Density functional theory (DFT) simulations were used to calculate various electronic properties of the ligands and the gold(III) chelates. The geometry optimized structures as well as the NMR, vibrational and electronic spectra were calculated. These data were compared with experimental data to determine the efficiency of the basis set and hybrid functional used.

The geometry optimization results of the ligands showed that tautomer B was in very good agreement with the experimental X-ray diffraction data, as seen by the lowest RMSD values for the calculated and experimental data. The calculated structure of tautomer D and the experimental structure had the highest RMSD value. Tautomer B was the lowest energy form of all the tautomers. This suggests that tautomer B is the dominant tautomeric form. Geometry optimizations of the gold(III) complexes showed that the propyl-bridged structures have the lowest RMSD values for the calculated and experimental data. The flexible nature of the four-carbon bridge resulted in larger RMSD values for $[\text{Au}(\text{L3})]^+$ and $[\text{Au}(\text{L12})]^+$. The pseudomacrocyclic, $[\text{Au}(\text{L10})]^+$ has many degrees of freedom of movement and therefore has the largest

RMSD value. The gas phase calculations do not take into account $\pi\cdots\pi$ or $\text{Au}\cdots\pi$ interactions which can lead to distortions of the planarity of the complexes.

Comparison of the calculated vibrational frequencies and experimental FTIR spectra for both the ligands and complexes showed that the DFT simulations consistently overestimated the frequencies. Despite the error in estimation of the absolute value of the absorption bands, the relative intensity of the bands was in good agreement with the experimental data, especially for the gold(III) complexes.

The experimental and calculated data for the electronic spectra of the ligands compared reasonably well. The calculated spectra of tautomers A and B matched the experimental data most closely. The main transitions for all the ligands are σ , $\pi \rightarrow \pi^*$ and $\pi \rightarrow \pi^*$ transitions. The calculated electronic spectra of the gold(III) complexes showed larger deviations in the absolute values of the wavelengths compared to the experimental data than was seen for the ligands. The calculated molecular orbitals show that they are all mixed, with contributions from both the ligand and metal.

The ^{13}C and ^1H NMR chemical shifts were calculated for the ligands and gold(III) chelates. The calculations of tautomer B for each compound predicted the experimental NMR spectra of the macrocyclic ligands well, with the percentage differences between the experimental and calculated chemical shifts being minimal. The calculations of tautomer B of the pseudomacrocyclic ligands do not compare favourably with the experimental data suggesting that these ligands may adopt a different tautomeric form in solution. The calculated NMR data for the complexes compared reasonably favourably with the experimental chemical shifts.

The data in general show that the level of theory (B3LYP/6-311G(d,p)) used for the ligands was sufficiently high, yielding results that compared favourably with experimental data. The accuracy of the gold(III) chelate simulations (the PBE/PBE/LANL2DZ level of theory was used in this work) could be improved by using a split basis set. This split basis set could make use of the 6-311G(d,p) basis set for the carbon, hydrogen and nitrogen atoms, while still applying the LANL2DZ basis set with its effective core potentials to the gold(III) ion. The use of the larger basis set for the light atoms should improve the accuracy of the simulations.

6.6 Molecular Mechanics Calculations

Prof. Orde Q. Munro (UKZN) developed new SP4 molecular mechanics (MM) force field parameters to model the structures of the gold(III) complex, $[\text{Au}(\text{L3})]^+$. The force field was used to determine the energetically preferred DNA binding site for $[\text{Au}(\text{L3})]^+$, using a 22-base pair duplex favoured by TOP1. This complex was chosen for these calculations as screening tests showed that $[\text{Au}(\text{L3})]^+$ was the most active of the gold(III) chelates towards several cancer cell lines (Chapter Seven). Prof. Munro ran all the calculations for which the results are summarized below. These results are included in this body of work because they give important insight into the binding mechanisms of the gold(III) complexes.

6.6.1 Introduction

Molecular mechanics is based on a mathematical model of a molecule as a set of balls (atoms) held together by springs (bonds).^{1,2} In this model the energy of the molecules changes with geometry because the springs

resist being stretched or bent from a natural length or angle and the balls resist being pushed too closely together.^{1,2} In other words, MM uses a theoretically mechanical model of a molecule to find its minimum energy geometry. The mathematical expression for the energy and the parameters in it, form a force field.

The potential energy of a molecule can be written as in Equation 6.15.

$$E = \sum_{\text{bonds}} E_{\text{stretch}} + \sum_{\text{angles}} E_{\text{bend}} + \sum_{\text{dihedrals}} E_{\text{torsion}} + \sum_{\text{pairs}} E_{\text{nonbond}} \quad 6.15$$

Where E_{stretch} etc. are energy contributions from bond stretching, angle bending, torsional motion and interactions between atoms or groups which are non-bonded.^{1,2} The mathematical form of these terms and parameters in them form a particular force field. A force field is parameterized by giving numbers to the constants in the force field. A force field can be parameterized using experimental references, such as IR data or X-ray data, or by getting the numbers from *ab initio* or density functional calculations.¹ An accurate practical force field would be parameterized as a best fit to many experimental and calculated results and would have different parameters for different kinds of bonds.¹

MM is a fast technique that is also accurate. It is the most widely-used method for computing the geometries and energies of large biological molecules such as proteins and nucleic acids.¹ This method does, however, have weaknesses. MM makes no reference to electrons and cannot give information on electronic properties. Additionally, a field parameterized for one class of molecules may not perform well for other classes. Also, stationary points calculated from molecular mechanics calculations may not represent global minima.¹ Despite these weaknesses, MM is still the fastest and most accurate technique that could be used to determine the DNA binding site of the gold(III) complex, $[\text{Au}(\text{L}3)]^+$, for this work.

6.6.2 Experimental

A modified SP4 force field was used for the MM calculations. The SP4 forcefield allows for accurate macromolecule simulations. Four distinct nitrogen atom donors were defined for the new force field: npw, npx (the two imine nitrogen atoms); npy, and npz (the two pyrrole nitrogen atoms). Distinct nitrogen donor atom types are mandatory to define the structurally unique *cis* and *trans* N–Au–N angles in the coordination sphere of the square-planar metal ion. Key bond stretching, van der Waals, bond angle, and torsion angle terms were then added to complete the parameter set. The new parameter terms for the force field are listed in **Appendix G** with their standard sp4 definitions.

Gasteiger partial charges and all crystallographic water molecules were used in the calculations. The simulation method involved a genetic optimization algorithm followed by conjugate gradient and truncated Newton optimizations. The lowest energy structures from multiple unique runs were used. The software used was VEGA³⁵ and AMMP (another molecular mechanics program)³⁶.

6.6.3 Results and Discussion of Molecular Mechanics Calculations

The new SP4 molecular mechanics forcefield parameters were developed to model the structures of gold(III) Schiff base complexes. Parameter optimization was used to fit the X-ray structural data. The non-linear least squares fits of the AMMP calculations and X-ray structures of the gold(III) chelates, $[\text{Au}(\text{L}1)]^+$, $[\text{Au}(\text{L}2)]^+$ and

$[\text{Au}(\text{L3})]^+$ was used to validate the forcefield and are shown in Figure 6.18. The RMSD values for these fits are low, indicating that the modified AMMP parameter set affords an acceptably accurate description of the structures as far as their geometric and conformational properties are concerned.

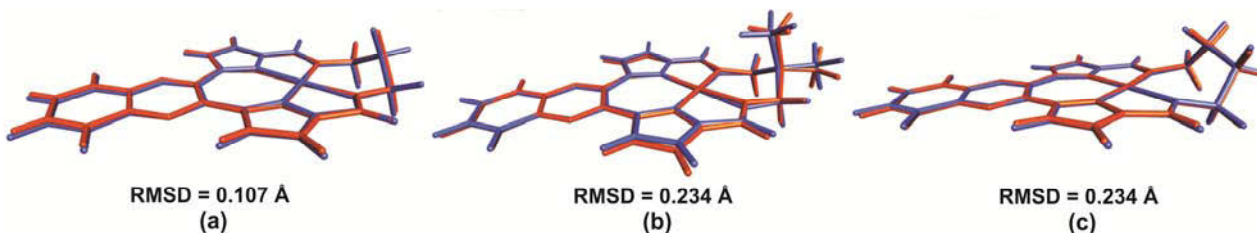


Figure 6.18: Non-linear least squares fits of the AMMP calculated (blue) and X-ray (orange) structures of the compounds (a) $[\text{Au}(\text{L1})]^+$, (b) $[\text{Au}(\text{L2})]^+$ and (c) $[\text{Au}(\text{L3})]^+$. The RMSD errors are shown and were determined from the fit of all atoms in each structure.

In order to further verify the accuracy of the forcefield, AMMP calculations were used to simulate a 22-base pair duplex of DNA (the TOP1 dsDNA Target) and this was compared with the X-ray crystal structure determined by Stewart *et al.*³⁷ The experimental and calculated structures were compared and an overlay of the two structures is shown in Figure 6.19. The similarity index for the two structures is 0.965, indicating that the calculations can accurately simulate the experimental results.

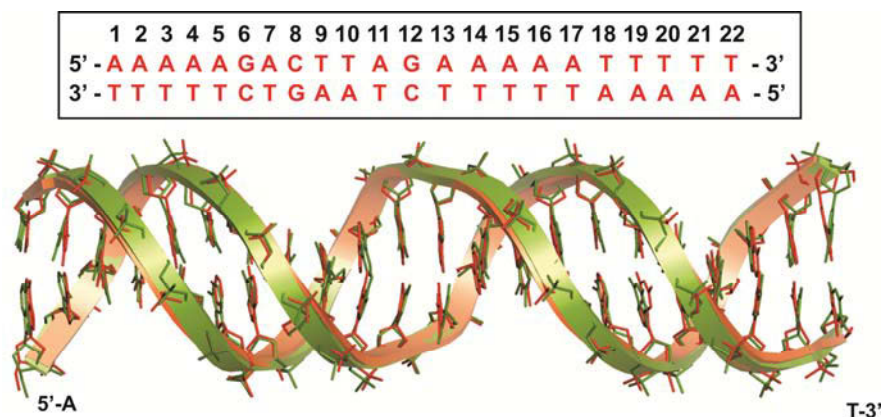


Figure 6.19: Overlay of MM calculated (green) structure and X-ray (orange) structure of a 22 base pair DNA duplex. The H atoms and water molecules have been omitted for clarity but were included in the simulation.

The main purpose of the calculations was to determine the energetically preferred DNA binding site for $[\text{Au}(\text{L3})]^+$. This was done using a conformational search strategy where the energy of the intercalation complex, when $[\text{Au}(\text{L3})]^+$ is intercalated in the major or minor grooves at different binding sites along the 22 base pair DNA duplex, was calculated. The calculations were also carried out with the butyl chain pointing up- or downstream relative to the 5' to 3' reference DNA strand. The search strategy employs the fact that there are four possible ways for $[\text{Au}(\text{L3})]^+$ to intercalate at each dinucleotide pair along the DNA duplex assuming that the quinoxaline ring inserts between π -stacked nucleobase pairs. Each starting conformation was subject to 3–15 independent polytope simplex geometry optimization runs followed by conjugate

gradient and truncated Newton optimizations in a uniform dielectric field ($\epsilon = 80$ D, water). The calculations indicated that the lowest energy intercalation complex is formed when $[\text{Au}(\text{L3})]^+$ it is intercalated in the major groove of the T10–A11 intercalation adduct with the butyl chain facing downstream, Figure 6.20.

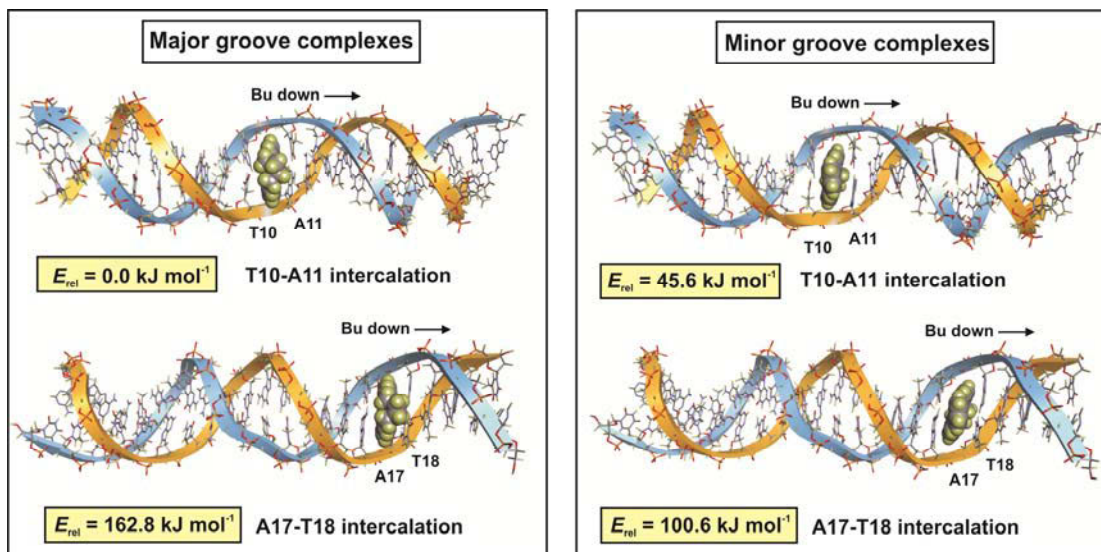


Figure 6.20: DNA base pair specificity for $[\text{Au}(\text{L3})]^+$.

Table 6.17: Intercalation energies of $[\text{Au}(\text{L3})]^+$ in the major and minor grooves of a 22 base pair DNA duplex.

Index	BP	ΔG (kcal/mol)	E_{rel} Major Groove (kcal/mol)	E_{rel} Minor Groove (kcal/mol)
1	AA	0.88		
2	AA	0.88		
3	AA	0.88		
4	AA	0.88		
5	AG	0.67	85.75	94.67
6	GA	1.02	139.65	73.18
7	AC	0.57	78.42	306.15
8	CT	0.67	82.16	125.38
9	TT	0.88	107.26	74.4
10	TA	0.17	0	10.9
11	AG	0.67	85.86	182.15
12	GA	1.02	138.21	96.42
13	AA	0.88	116.4	193.03
14	AA	0.88	111.16	142.56
15	AA	0.88		
16	AA	0.88		
17	AT	0.37	38.91	24.01
18	TT	0.88		
19	TT	0.88		
20	TT	0.88		
21	TT	0.88		

Table 6.17 summarizes the energies of the intercalation complexes at the different DNA intercalation sites along the DNA strand. These conformational energies are relative to the lowest energy conformer (major

groove, T10–A11). Each energy value represents the lowest energy conformation for between 8 to 14 conformations located with butyl chain pointing either up or downstream relative to the 5' to 3' reference DNA strand direction for both the minor and major groove insertion adducts. The ΔG values in Table 6.17 give the stability of the base pairs along the DNA helix. They were determined following the literature method (WEB-THERMODYN).³⁸ The base specificity of $[\text{Au}(\text{L}3)]^+$ in the gas phase is in the order $\text{TA} > \text{AT} > \text{GA} \approx \text{TT} > \text{AC} > \text{CT} \approx \text{AG}$.

The ΔG values from Table 6.17 show that T10–A11 is the lowest stability base pair along the DNA helix with a value of $0.17 \text{ kcal mol}^{-1}$. It is at this lowest-stability T10–A11 site that TOP1 cuts the dsDNA.³⁷ As discussed in Chapter One, TOP I relaxes supercoiled DNA by causing a single-strand nick in the DNA.³⁹⁻⁴¹ It does this by forming a clamp around the duplex DNA. The active-site tyrosine of the enzyme acts as a nucleophile and cleaves a single DNA strand.³⁹⁻⁴¹ Interestingly, $[\text{Au}(\text{L}3)]^+$ forms the lowest-energy intercalation complex at the same T10–A11 site. Hence the drug and enzyme target the same adjacent base pair in a sequence. Figure 6.21(a) shows that there is a good correlation of the relative energy of the $[\text{Au}(\text{L}3)]^+$ intercalation complex with the stability of the base pairs for the major groove intercalation adducts indicating that the more stable the base pair, the higher the energy of the intercalation complex at the same site. Figure 6.21(b) illustrates that the T10–A11 is the lowest stability binding sites.

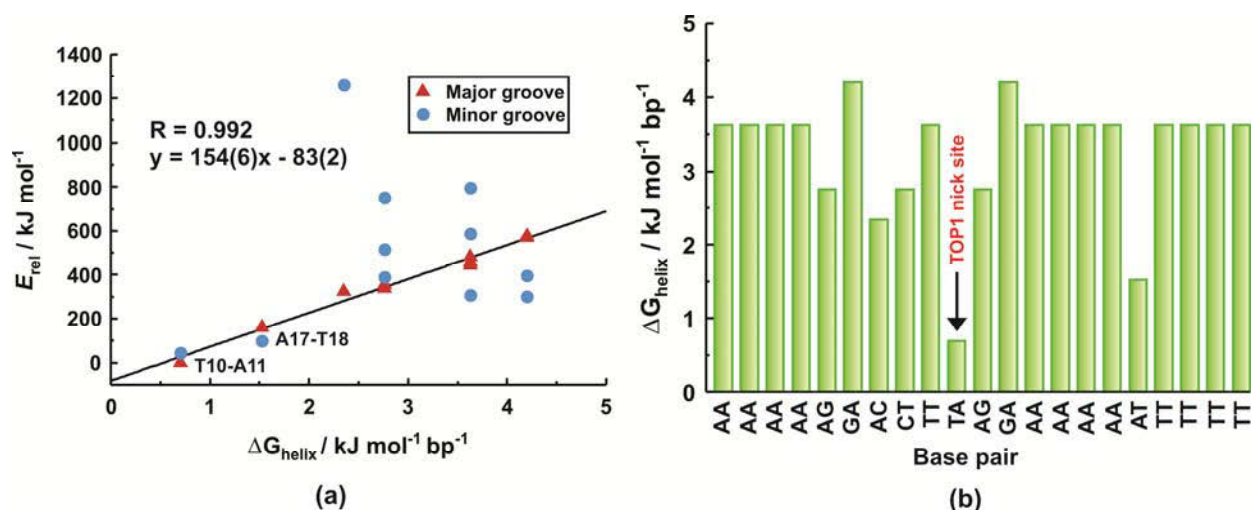


Figure 6.21: (a) Plot of E_{rel} vs ΔG_{helix} for the major and minor groove intercalation adducts. (b) Stabilities of the various base pairs along the DNA helix.

There are many favourable interactions in the T10–A11 lowest energy intercalation complex. Particularly significant is the $\text{Au}(\text{III}) \cdots \text{O}(\text{carbonyl})$ ion-dipole interaction with the π -stacked thymine base (T10). This ion-dipole interaction is shorter than the sum of the van der Waals radii of the interacting atoms at 3.13 \AA . There are also π – π interactions with the pyrrole and quinoxaline rings stacked with the DNA bases. Figure 6.22(a) illustrates these interactions. Other drug binding site interactions include van der Waals attraction and repulsion interactions.

The intercalation complex with $[\text{Au}(\text{L}3)]^+$ bound in the major groove of the T10–A11 site is lower in energy than when the complex is intercalated in the minor groove. The structure of $[\text{Au}(\text{L}3)]^+$ is mostly unchanged upon T10–A11 major groove intercalation relative to the gas phase DFT structure and X-ray structure.

However, when $[\text{Au}(\text{L3})]^+$ intercalates via the minor groove at the T10–A11 site, there is a twisting of the complex's conformation leading to a higher energy structure, Figure 6.22(b).

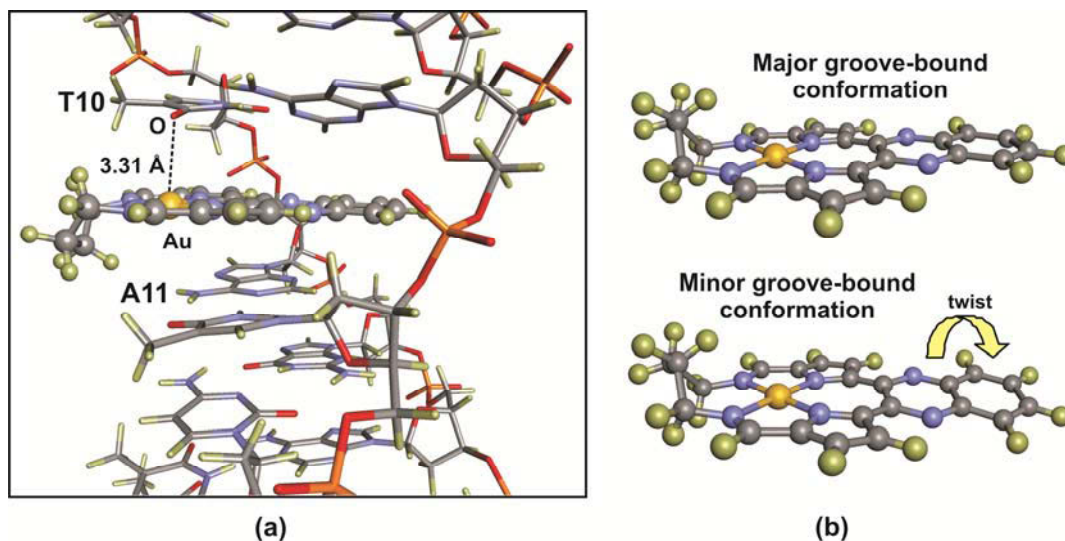


Figure 6.22: (a) Ion-dipole and π - π stacking interactions at the T10–A11 binding site. (b) Major and minor groove-bound conformations of $[\text{Au}(\text{L3})]^+$.

A final enzyme inhibition model was calculated with $[\text{Au}(\text{L3})]^+$ intercalated at the T10–A11 site of the 22-bp DNA duplex in the presence of the TOP1 enzyme, Figure 6.23. Figure 6.24 shows an overlay of this calculated AMMP structure with the complex bound and an X-ray crystal structure of the TOP1–DNA complex without the complex bound. This figure effectively illustrates the effect of the complex intercalation on the DNA strand and the functioning of the TOP1 enzyme.

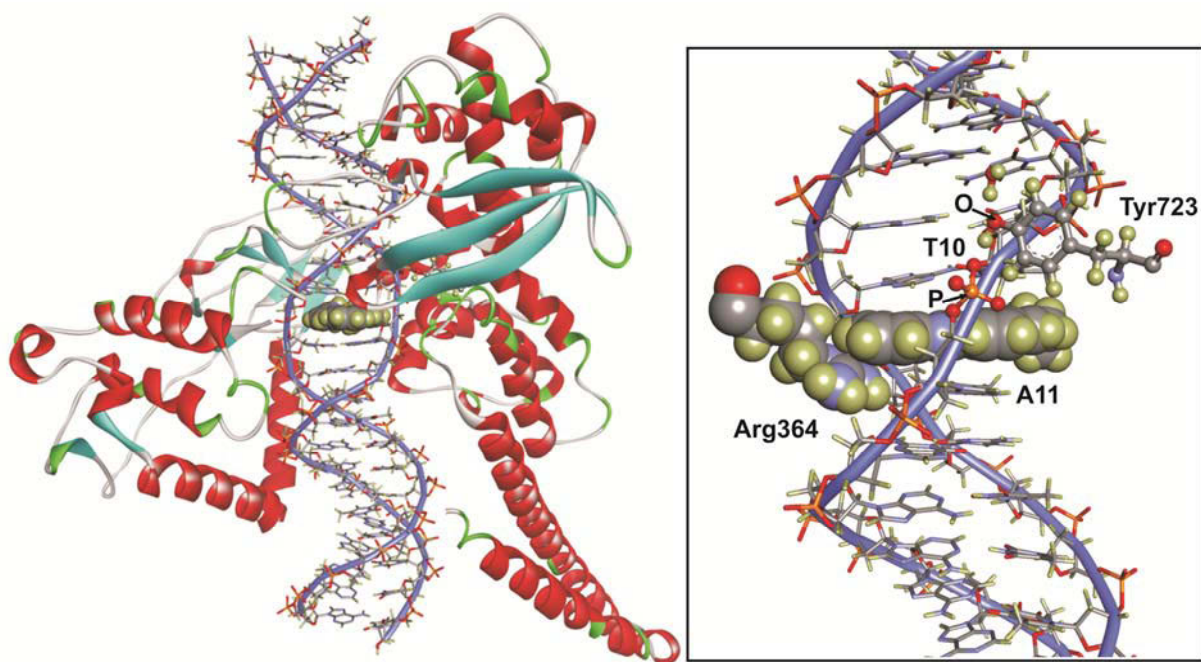


Figure 6.23: Model of the $[\text{Au}(\text{L3})]^+$ DNA intercalation complex in the presence of TOP1.

The key residues for the functioning of TOP1 are Arg 364 and Tyr723. Arg 364 is involved in H-bonding with the A11 base pair of the DNA keeping it in a specific orientation while Tyr723 acts as a nucleophile and cleaves a single DNA strand. It does this by forming a phosphotyrosyl covalent bond with the DNA.³⁹⁻⁴¹ When the complex intercalates between the T10–A11 site these key residues, Arg 364 and Tyr 723, shift. This shift is due to steric repulsion by the quinoxaline ring of the complex causing a downward displacement of Arg 364 in the minor groove. Arg 364 is effectively blocked by $[\text{Au}(\text{L}3)]^+$ from H-bonding to the A11 base. The shift of the residues is also due to the partial unwinding and lengthening of the DNA double helix by the complex intercalation. This moves the scissile strand further downstream and away from Tyr 723. There is a 3.53 Å downstream shift of the scissile strand. The nucleophilic Tyr oxygen atom of the TOP1 enzyme is too far away from the DNA strand to make a cut with an O–P distance of 3.92 Å. The calculated model shows that the DNA substrate sequence recognition by TOP1 is impeded by drug intercalation at the T10–A11 target site of the enzyme. This model suggests that the complex will be a catalytic inhibitor of TOP1.

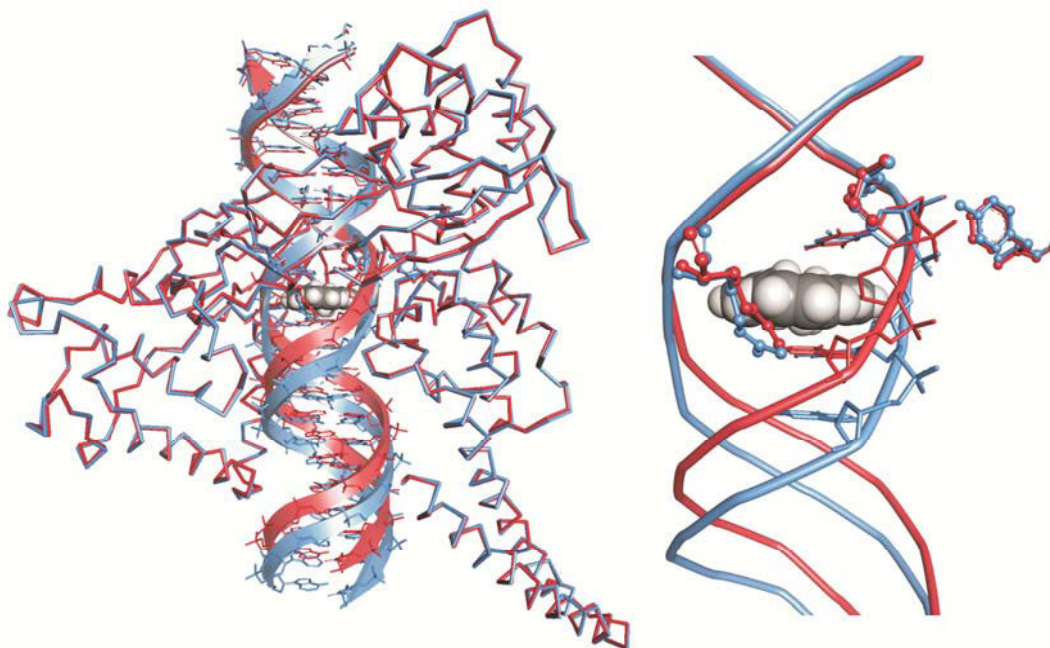


Figure 6.24: Overlay of the pdp1a36 X-ray structure without the complex bound (pink) and the drug-bound MM structure (blue).

In conclusion, new SP4 molecular mechanics (MM) force field parameters were developed to determine the energetically preferred DNA binding site for $[\text{Au}(\text{L}3)]^+$, using a 22-base pair duplex favoured by TOP1. It was determined that $[\text{Au}(\text{L}3)]^+$ binds in the major groove at an adjacent T10–A11 base pair in dsDNA. This is also the cut-site of TOP1. When the complex is bound in this site, it prevents Arg 364 of the TOP1 enzyme from recognizing the adenine base in the TA base pair by steric repulsion from the quinoxaline ring which projects into the minor groove. Binding of the complex also induces elongation at the intercalation site of the DNA. This displaces the scissile strand downstream so that Tyr 723 is too far away to form a covalent P–O–C link to the enzyme. This model suggests that the complex will be a catalytic inhibitor of TOP1.

6.7 References

- (1) Lewars, E. G. *Computational Chemistry, 2nd Edition*; Springer: New York, 2011.
- (2) Jensen, F. *Introduction to Computational Chemistry, 2nd Edition*; John Wiley & Sons Ltd: Great Britain, 2009.
- (3) Grant, G. H., Richards, W. G. *Computational Chemistry*; Oxford University Press: United States, 1996.
- (4) Cramer, C. J. *Essentials of Computational Chemistry Theories and Models*; John Wiley & Sons Ltd: England, 2002.
- (5) Perdew, J. P., Burke, K., Enzerhof, M. *Phys. Rev. Lett.* **1996**, *77*, 3865.
- (6) Perdew, J. P., Burke, K., Enzerhof, M. *Phys. Rev. Lett.* **1997**, *78*, 1396.
- (7) Becke, A. D. *J. Chem. Phys.* **1993**, *98*, 5648.
- (8) Stephens, P. J., Devlin, J. J., Chabalowski, C. F., Frisch, M. J. *J. Phys. Chem.* **1994**, *98*, 11623.
- (9) Hinchliffe, A. *Modelling Molecular Structures, 2nd Edition*; John Wiley and Sons Ltd: Great Britain, 2000.
- (10) Young, D. *Computational Chemistry: A practical guide for applying techniques to real world problems*; Wiley-Interscience: New York, 2001.
- (11) McLean, A. D., Chandler, G. S. *J. Chem. Phys.* **1980**, *72*, 5639.
- (12) Krishnan, R., Binkley, J. S., Seeger, R., Pople, J. A. *J. Chem. Phys.* **1980**, *72*, 650.
- (13) Hay, P. J., Wadt, W. R. *J. Chem. Phys.* **1985**, *82*.
- (14) Wadt, W. R., Hay, P. J. *J. Chem. Phys.* **1985**, *82*.
- (15) Dunning, T. H., Jr., Hay, P. J. *Modern Theoretical Chemistry*; Plenum: New York, 1976.
- (16) Munro, O. Q., Camp, G. L. *Acta Cryst.* **2003**, *C59*, o672.
- (17) Dewar, M. J., Zoebisch, E. G., Healy, E. F., Stewart, J. P. *J. Am. Chem. Soc.* **1985**, *107*, 3902.
- (18) Munro, O. Q., Strydom, S. D., Grimmer, C. D. *Chem. Eur. J.* **2006**, *12*, 7987.
- (19) Toganoh, M., Yamamoto, T., Hihara, T., Akimaru, H., Furuta, H. *Org. Biomol. Chem.* **2012**, *10*, 4367.
- (20) Furuta, H., Ishizuka, T., Osuka, A., Dejima, H., Nakagawa, H., Ishikawa, Y. *J. Am. Chem. Soc.* **2001**, *123*, 6207.
- (21) Senge, M. O., Ema, T., Smith, K. M. *Chem. Commun.* **1995**, 733.
- (22) Barkigia, K. M., Berber, M. D., Fajer, J., Medforth, C. J., Renner, M. W., Smith, K. M. *J. Am. Chem. Soc.* **1990**, *112*, 8851.
- (23) Maity, D. K., Bell, R. L., Truong, T. N. *J. Am. Chem. Soc.* **2000**, *5*, 289.
- (24) Di Bella, S., Fragal, I., Guerri, A., Dapporto, P., Nakatani, K. *Inorg. Chim. Acta* **2004**, *357*, 1161.
- (25) Koleva, B. B., Kolev, T., Spiteller, M. *Inorg. Chim. Acta* **2007**, *360*, 2224.
- (26) Koleva, B. B., Kolev, T., Spiteller, M. *J. Molecul. Struct.* **2007**, *831*, 165.
- (27) Qina, C., Yanga, G., Zhaoa, L., Suna, S., Qiu, Y., Sua, Z., Zhub, Y. *Syn. Metals* **2009**, *159*, 2406.
- (28) Gabbiani, C., Casini, A., Messori, L., Guerri, A., Cinellu, M. A., Minghetti, G., Corsini, M., Rosani, C., Zanello, P., Arca, M. *Inorg. Chem.* **2008**, *47*, 2368.
- (29) Rabuck, A. D., Scuseria, G. E. *Chem. Phys. Lett.* **1999**, *309*, 450.
- (30) Bortoluzzi, M., Paolucci, G., Annibale, G., Pitteri, B. *Polyhedron* **2009**, *28*, 1079.
- (31) Frisch, M. J., Trucks, G. W., Schlegel, H. B., Scuseria, G. E., Robb, M. A., Cheeseman, J. R., Scalmani, G., Barone, V., Mennucci, B., Petersson, G. A., Nakatsuji, H., Caricato, M., Li, X., Hratchian, H. P., Izmaylov, A., F., B., J., Zheng, G., Sonnenberg, J. L., Hada, M., Ehara, M., Toyota, K., Fukuda, R., Hasegawa, J., Ishida, M., Nakajima, T., Honda, Y., Kitao, O., Nakai, H., Vreven, T., Montgomery, J. A. Jr, Peralta, J. E., Ogliaro, F., Bearpark, M., Heyd, J. J., Brothers, E., Kudin, K. N., Staroverov, V. N., Kobayashi, R., Normand, J., Raghavachari, K., Rendell, A., Burant, J. C., Iyengar, S. S., Tomasi, J., Cossi, M., Rega, N., Millam, J. M., Klene, M., Knox, J. E., Cross, J. B., Bakken, V., Adamo, C., Jaramillo, J., Gomperts, R., Stratmann, R. E., Yazyev, O., Austin, A. J., Cammi, R., Pomelli, C., Ochterski, J. W., Martin, R. L., Morokuma, K., Zakrzewski, V. G., V., G. A., Salvador, P., Dannenberg, J. J., Dapprich, S., Daniels, A. D., Farkas, Ö., Foresman, J. B., Ortiz, J. V., Cioslowski, J., Fox, D. J. *Gaussian, Inc.* **2009**, Wallingford CT.

- (32) Dennington, R., Keith, T., Millam, J., Eppinnett, W. L., Semichem, R. *GaussView, Version 5.09* **2009**, Shawnee Mission.
- (33) Mercury Version 2.4 *Cambridge Crystallographic Data Centre: Cambridge, UK* **2010**.
- (34) Allen, F. H., Kennard, O., Watson, D. G. *Perkin Trans. II* **1987**, S1.
- (35) Pedretti, A., Villa., L., Vistoli, G. *J. C. A. M. D.* **2004**, *18*, 167.
- (36) Harrison, R. W. *AMMP - Another Molecular Mechanics Program*, <http://www.cs.gsu.edu/~cscrwh/ammp/ammp.html>.
- (37) Stewart, L., Redinbo, M. R., Qiu, X., Hol, W. G., Champoux, J. J. *Science* **1998**, *279*, 1534.
- (38) <http://www.ncbi.nlm.nih.gov/pmc/articles/PMC16896/>.
- (39) Pommier, Y. *Nature Rev.* **2006**, *6*, 789.
- (40) Koster, D. A., Palle, K., Bot, E. S. M., Bjornsti, M.-A., Dekker, N. H. *Nature Lett.* **2007**, *448*, 214.
- (41) Koster, D. A., Croquette, V., Dekker, C., Shuman, S., Dekker, N. H. *Nature Lett.* **2005**, *434*, 671.

CHAPTER SEVEN:

BIOCHEMICAL STUDIES

7.1 Introduction

7.1.1 Tumour cell line screening

The synthesized gold(III) chelates were designed to act as chemotherapeutic agents, exerting their cytotoxicity through DNA intercalation. This intercalation process is anticipated to induce cell apoptosis by inhibiting the topoisomerase (TOP) enzymes. The cytotoxicity of the gold(III) chelates was determined by *in vitro* testing against the National Cancer Institute's (NCI, USA) sixty human cancer cell lines. These tumour cell lines include melanoma, leukaemia as well as lung, colon, ovary, brain, prostate and kidney cancers. Complexes that were not selected by the NCI, were screened against four human cancer cell lines by the Advanced Materials Division at MINTEK in South Africa.

The cytotoxicity of the gold(III) complexes towards a range of human cancer cell lines was determined by the National Cancer Institute¹ with the Developmental Therapeutics Programme (DTP)². Both are divisions of the American National Institute of Health (NIH). These organizations screen natural products and synthetic compounds against human cancer cell lines to prioritize their further development into commercial anti-cancer agents. The DTP has played an important role in the discovery of more than 40 chemotherapeutic drugs licensed in the United States.² One of these drugs is Paclitaxel which is one of the most widely prescribed anti-cancer drugs on the market. Their recent successes include romidespsin (approved in 2009 for lymphoma), and eribulin (approved in 2010 for breast cancer).²

The *in vitro* screens prioritize compounds primarily by their selectivity towards specific cell lines in the sixty cell line screen. The screening is a two-stage process; the first stage involves the evaluation of all compounds against the 60 cell lines at a single dose of 10 μM .¹ These results determine whether the compound will be tested in the second stage. The second stage is where the compounds are evaluated against the 60 cell lines at five concentrations.¹ Three dose parameters can be calculated from the five-dose screen:

- GI_{50} value: concentration of the compound where there is 50% growth inhibition compared to the control. This is a 50% reduction in the net protein increase in control cells during the drug incubation.
- IC_{50} value: concentration of the compound at which there is total growth inhibition. There is no net increase in the quantity of protein at the end of the experiment.
- LC_{50} value: concentration of the compound resulting in a 50% reduction in the measured protein at the end of drug treatment compared with the beginning. This indicates a net loss of cells following treatment.¹

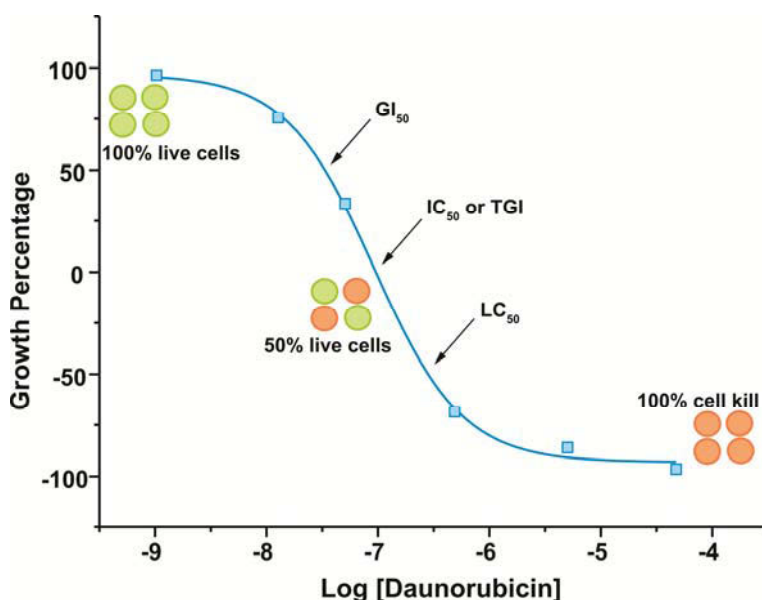


Figure 7.1: Dose-response curve of a central nervous system cancer cell line with the chemotherapeutic agent, daunorubicin.

These values are depicted on the dose response curve of the commercially available anti-cancer agent; daunorubicin, Figure 7.1. Daunorubicin is a DNA intercalator and TOP2 poison.³ The growth percentage is the growth of the inoculated tumour cell line relative to a control batch. It is measured as a net increase or decrease in the mass of protein.

The large amount of data from the *in vitro* screening results allows for the statistical comparison of the activity profile of a compound with the activity profiles of compounds with known modes of action. The statistical comparison can give an indication of the likely mode of action of a potential drug candidate, thus reducing the time taken for mechanism of action determinations. A large data set, such as the one produced by the 60-cell lines, can improve the reliability of these statistical analyses. Screening against 60-cell lines allows for the detection of specificity of a drug candidate towards a particular cell line. This can allow for more effective treatment of specific cancer cell lines.

A drug candidate that shows potential in the *in vitro* screening will then be selected by the DTP *in vivo* with a hollow fibre assay and relevant human tumour xenograft and rodent tumour models. Figure 7.2 shows the hierarchical order of the screening processes done by the DPT and NCI. If a compound does not show further potential at any stage of the screening process, then it will not be selected for subsequent stages.

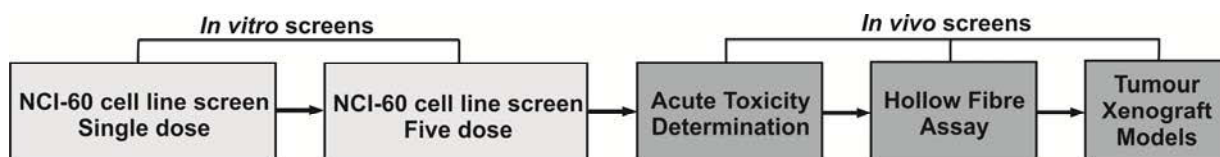


Figure 7.2: Screening processes at the NCI.

Complexes that were not selected by the NCI for *in vitro* screening were sent to the Advanced Materials Division at MINTEK in South Africa. The complexes are screened against four human cell lines: non-small

cancerous, renal, colon and central nervous system (CNS) cancer cell lines. A single dose parameter, the IC₅₀ value, was determined for each cell line. The purpose of these screens was to determine whether the complexes not selected by the NCI were still active against cancer cells and if they showed a preference for a specific cell line.

Further *in vitro* studies were done at the University of Central Florida under the supervision of Prof Mark T. Muller. Three of the gold(III) complexes: [Au(L1)](PF₆), [Au(L2)](PF₆) and [Au(L3)](PF₆), were screened against the HeLa cancer cell line and the IC₅₀ values for the complexes against this cell line was determined. This study was done to compare the cytotoxicity of the complexes to a well-known TOP2 poison and weak inhibitor, etoposide (VP-16).

7.1.2 Elucidation of the Mechanism of Action

Initially when chemotherapy was first developed, it was accepted that malignant tumours could be killed through various inhibitory mechanisms of their cellular division by anti-cancer drugs.^{4,5} With the further development of molecular biology, it has more recently become clear that specific cellular targets can be identified in tumour cells, the function of which are necessary for their replication.^{4,5} Chemotherapeutic agents can, in principle, be specifically designed to target these cellular agents.

As discussed in Chapter One, anti-cancer drugs have a variety of different mechanisms that interfere with tumour cell growth, survival or angiogenesis.^{3,6} Certain drugs interact with the DNA through mechanisms of intrastrand or interstrand crosslinking, intercalation between base pairs or interaction in the minor or major grooves. Drugs such as the antimetabolites affect cell growth by interfering with key biosynthetic pathways while other drugs are classed as hormonal agents and control cell growth by interacting with various hormones.^{3,6} Certain drugs act as vascular targeting agents which prevent angiogenesis by blocking new capillary growth. Table 1.1, Chapter One, gives a brief description of some of the different classes of chemotherapeutic agents and which drugs belong to each class.

Inorganic compounds have seldom been designed for their application in medicine, but are rather fortuitous discoveries.^{4,7} Thus there is often little or no understanding of the molecular basis of their mechanism of action. The success of cisplatin, currently the leading commercially available inorganic anti-cancer drug, has resulted in increased effort to determine the mechanism of action of metal-based compounds.^{4,8,9}

Gold(III) complexes have had success in *in vitro* cytotoxic studies, but their mechanisms of action and biological targets are still debated and likely to be dependent in part on the nature of the ligands bound to the metal ion.¹⁰ The reactivity of some gold(III) complexes with specific biomolecular targets such as DNA and proteins has been studied by various research groups by a number of methods.¹¹ However, the molecular mechanism through which the observed biological effects are produced, remains largely unknown.¹⁰ In some cases, such as with gold(III) porphyrin complexes, there is evidence of direct DNA damage.¹⁰ In other cases, such as with [Au(phen)Cl₂]Cl and [Au(dien)Cl₂]Cl complexes, the effects on DNA and on the cell cycle is minimal so it is unlikely that DNA is the ultimate target.¹⁰ Even in the cases where there is evidence of direct interaction with DNA, the mechanism of DNA damage and cell death is different from those induced by platinum metallodrugs.¹⁰ It has been proposed that gold(III) complexes exert their cytotoxicity by causing mitochondrial damage through modification of specific proteins. Research groups have shown that some gold(III) complexes are inhibitors of the selenoenzyme thioredoxin reductase, a

crucial enzyme for cell protection against oxidative stress. These compounds were found to interfere greatly with the mitochondrial functions.^{12,13} The gold(I) compounds such as auranofin are known thioredoxin reductase inhibitors and antimetabolic agents.^{14,15} Other recent studies also showed the thiol-dependent cathepsin enzymes to be possible targets of gold(III) complexes.^{16,17} These lysosomal enzymes are mainly cysteine proteases responsible for extracellular matrix degradation, bone resorption and joint destruction.¹⁸ It is thus important to determine the mechanism of action of the proposed gold(III) complexes to help shed light on the mechanism of action of other gold(III) complexes.

In order to determine the mechanism of action through which the proposed gold(III) macrocyclic complexes exert their cytotoxicity, gel electrophoresis experiments were used. Gel electrophoresis is widely used as an effective means for the determination of the mechanism of action of new chemotherapeutic agents.^{5,8} The experiments that were performed were determined based on the statistical analysis of the cell screening data. The gel electrophoresis experiments were performed at the University of Central Florida in the United States under the supervision of Prof. Mark Muller. Experiments to determine whether the complexes are TOP1 or TOP2 poisons or inhibitors were also performed in Prof. Muller's laboratory as well as surface Plasmon resonance experiments to determine the binding site of the complexes.

7.2 Experimental

DMSO was used to solubilize the complexes in the aqueous buffer solutions in the following experiments. Prior to any biological work the stability of the complexes in DMSO was determined by recording the absorption spectrum of the complex in DMSO as a function of time. These data showed that the complexes were stable in this solvent system, exhibiting less than 1% change over a 24 hour period. The complexes were stored in frozen DMSO solution prior to all experiments.

The biological experiments reported in this chapter were performed by various third parties. The data processing, interpretation and discussion are, however, the work of the author.

7.2.1 *In Vitro* Cell Screening at the NCI¹

The human tumor cell lines are grown in RPMI 1640 medium containing 5% fetal bovine serum and 2 mM L-glutamine. For a screening experiment, cells are inoculated into 96-well microtiter plates in 100 μ L at plating densities ranging from 5,000 to 40,000 cells per well, depending on the doubling time of individual cell lines. After cell inoculation, the microtiter plates are incubated at 37 °C, 5% CO₂, 95% air and 100% relative humidity for 24 hours prior to addition of experimental drugs.

After 24 hours, two plates of each cell line are fixed *in situ* with tricarboxylic acid (TCA), to represent a measurement of the cell population for each cell line at the time of drug addition (Tz). Experimental drugs are dissolved in DMSO at 400 \times the desired final maximum test concentration and stored frozen prior to use. At the time of drug addition, an aliquot of frozen concentrate is thawed and diluted to twice the desired final maximum test concentration with complete medium containing 50 μ g mL⁻¹ gentamicin (an aminoglycoside antibiotic). Four additional, 10-fold serial dilutions are made to provide a total of five drug concentrations plus control. Aliquots of 100 μ l of these different drug dilutions are added to the appropriate microtiter wells already containing 100 μ l of medium, resulting in the required final drug concentrations.

Following drug addition, the plates are incubated for an additional 48 hours at 37°C, in an atmosphere of: 5% CO₂, 95% air, and 100% relative humidity. For adherent cells, the assay is terminated by the addition of cold TCA. Cells are fixed *in situ* by the gentle addition of 50 µl of cold 50% (w/v) TCA (final concentration, 10% TCA) and incubated for 60 minutes at 4°C. The supernatant is discarded, and the plates are washed five times with tap water and air dried. Sulforhodamine B (SRB) solution (100 µl) at 0.4% (w/v) in 1% acetic acid is added to each well, and plates are incubated for 10 minutes at room temperature. After staining, unbound dye is removed by washing five times with 1% acetic acid and the plates are air dried. Bound stain is subsequently solubilized with 10 mM tris(hydroxymethyl)aminomethane base, and the absorbance is read on an automated plate reader at a wavelength of 515 nm, which corresponds to λ_{max} of the dye. For suspension cells, the methodology is the same except that the assay is terminated by fixing settled cells at the bottom of the wells by gently adding 50 µl of 80% TCA (final concentration, 16% TCA).

Using the seven absorbance measurements: time zero (T_z), control growth (C), and test growth in the presence of the gold(III) complex at the five concentration levels (T_i), the percentage growth is calculated at each of the drug concentration levels. Percentage growth inhibition is calculated using Equations 7.1 and 7.2:

$$\left(\frac{T_i - T_z}{C - T_z} \right) \times 100\% \quad 7.1$$

$$\left(\frac{T_i - T_z}{T_z} \right) \times 100\% \quad 7.2$$

Equation 7.1 is used for concentrations for which T_i ≥ T_z while Equation 7.2 is used for concentrations for which T_i < T_z.

Three dose response parameters are calculated for each compound from the collected data. The GI₅₀ value is calculated using Equation 7.3:

$$\left(\frac{T_i - T_z}{C - T_z} \right) \times 100\% = 50 \quad 7.3$$

The IC₅₀ value can be calculated using Equation 7.4:

$$T_i = T_z \quad 7.4$$

The LC₅₀ value can be determined from Equation 7.5:

$$\left(\frac{T_i - T_z}{T_z} \right) \times 100 = -50 \quad 7.5$$

The values are only calculated for these three parameters if a certain level of activity is reached. If this standard is not reached or is exceeded, the value for that parameter is expressed as greater or less than the maximum or minimum concentration tested.

7.2.2 *In Vitro* Cell Screening at MINTEK

Four cell lines were used for this assay: A549 (non-small lung cancerous cell line), TK-10 (renal cell line), HT-29 (colon cell line) and U251 (CNS cell line). On day one the cells were trypsinised and distributed in a flat bottomed 96-well plate (final concentration of 2×10^5 cells mL⁻¹) and were left to adhere overnight. On day two, the compounds were administered at a final starting concentration of 50 μ M per well with subsequent serial dilutions (eight in total). On day four (72 hours after compound administration), MTS (Celltiter One Solution, Promega, USA) was added and a reading taken after a colour change was observed. Concentrations were triplicated per plate and experiments were repeated at least four times. Sigmoidal curves were fitted to the results using Origin 6.1¹⁹ to calculate the IC₅₀ value.

7.2.3 *In Vitro* cell Screening at the University of Central Florida

The experiment below was performed by Alexander M. Fageson as part of our collaboration with Prof. Muller's group at UCF and is included here for completeness.

HeLa cells were grown in a 96-well plate at 2 500 cells per well for 24 hours. The complex was then added over a 4-log unit concentration scale and the cells were incubated for a further 24 hours. MTS tetrazolium salt was added to the plates and incubated for three hours and the absorbance was measured at 490 nm.

7.2.4 Acute Toxicity Determination at the NCI¹

The determination of the maximum tolerated dose (MTD) is performed in a manner that conserves the compound and minimizes the number of mice used. A single mouse is given a single injection of 400 mg kg⁻¹. A lower concentration is administered if the compound is expected to be extremely potent. A second mouse receives a dose of 200 mg kg⁻¹ and a third mouse receives a dose of 100 mg kg⁻¹. The mice are observed for 17 days and are sacrificed if they lose more than 20% of their body weight or if there are other signs of significant toxicity. If all three mice are sacrificed then the next three dose levels: 50, 35 and 12.5 mg kg⁻¹ are tested in a similar manner. This process is repeated until a tolerated dose is found. This dose is selected as the MTD and used to calculate the amount of material administered during anti-tumour testing. Dose volumes are generally 0.1 ml per 10 g of body weight. The solvent system used for the acute toxicity testing was 100% DMSO.

For the standard hollow fibre assay (HFA), the high and low dose levels are determined, using the MTD using Equations 7.6 and 7.7

$$\text{High dose} = \left(\frac{\text{MTD} \times 1.5}{4} \right) \quad 7.6$$

$$\text{Low dose} = 0.67 \times \text{high dose} \quad 7.7$$

7.2.5 Microtiter well-based assay at the University of Central Florida²⁰

The experiment below was performed by Vidusha Cyril as part of our collaboration with Prof. Muller's group at UCF. The details are reproduced here for completeness.

A fixed number of histidine-tagged TOP1 units (50 μL final volume) were bound to nickel-coated 96-well plates for 2 hours at room temperature. Any unbound enzyme was removed by aspirating off the initial binding solution, followed by three washes (200 μL each) with cold phosphate-buffered saline (PBS) containing 0.05% Tween 20 (PBST). The TOP1 reactions were initiated by the addition of a premix solution of TGS buffer and 100 ng of form I pHOT1 DNA in the presence or absence of test or control drugs. Drugs were dissolved in DMSO, and the final DMSO concentration in the reaction never exceeded 1% (assays tolerate up to 1% DMSO, although matched solvent positive and negative controls must also be included). Reactions were incubated for 1 hour at 37 °C and terminated by the addition of 0.1 vol of 1% (v/v) SDS, followed by 5 minutes incubation at 37 °C. The reaction mixture was next aspirated and washed three times with 200 μL of PBS-T. Pico Green (100 $\mu\text{g mL}^{-1}$) was diluted in TE buffer (1:400) and 200 μL was added to each well, followed by incubation in the dark for 5 min. The relative fluorescence was measured at 485 nm excitation and 525 nm emission wavelength, using a Tecan Ultra plate reader (Tecan, Durham, NC, USA).

7.2.6 Electrophoretic Mobility Shift Assays at the University of Central Florida

The experiment below was performed by Alexander M. Fageson as part of our collaboration with Prof. Muller's group at UCF and is included here for completeness.

For these experiments, 6.3 $\text{ng}\mu\text{L}^{-1}$ of negatively supercoiled pHOT1 plasmid DNA (TopoGEN, Inc.) was used as the dsDNA substrate. Reaction solutions were prepared by mixing 1.0 μL of a 188 $\text{ng}\mu\text{L}^{-1}$ pHOT1 stock solution, 3.0 μL pH 7.9 1X TGS buffer (100 mM Tris-HCl, 10 mM EDTA, 1.5 M NaCl, 1 mM spermidine, 1% BSA, 50% V/V glycerol), and 25.0 μL of deionized water in 1 mL polyethylene microcentrifuge tubes. To these solutions were added 1.0 μL aliquots of standard solutions of ethidium bromide (EB, a cationic DNA intercalator control), $[\text{Au}(\text{L}1)](\text{PF}_6)$, $\text{H}_2\text{L}1$, $[\text{Ni}(\text{L}1)]$ in DMSO (molecular biology-grade, Sigma) to give final control compound concentrations of 500 nM, 5.0 μM , and 50 μM for $\text{H}_2\text{L}1$ and $[\text{Ni}(\text{L}1)]$. In the case of $[\text{Au}(\text{L}1)](\text{PF}_6)$, aliquots of standard solutions of the compound were diluted to give two additional final concentrations such that a more narrowly-stepped range could be investigated (500 nM, 1.0 μM , 5.0 μM , 15 μM , and 50 μM). The solutions were incubated at 37 °C for 15 min before adding 6.0 μL of 6X electrophoresis loading dye (50% aqueous glycerol, 0.025% bromophenol blue) and mixing by vortex centrifugation. Aliquots from each dyed solution (5.0 μL) were loaded on a freshly-cast 1% agarose gel and electrophoresed in 1X TBE buffer (88 mM boric acid, 88 mM TRIS base, 10 mM EDTA, pH 7.8) at 50 V for 60 min. The gel was rinsed in deionized water and stained for 10 min in an aqueous 1X TBE-buffered EB solution (0.5 $\mu\text{g mL}^{-1}$) prior to imaging with UV transillumination (302 nm) on a SyngeneChemGenius system followed by quantification and analysis with ImageJ 1.46r.²¹

7.2.7 Topoisomerase assays at the University of Central Florida

Enzymes, DNA substrates and assay kits were kindly provided by TopoGen Inc. (Port Orange, Florida). By definition, 2 units of TOP I/II enzyme relaxed 100 ng of DNA in 30 minutes at 37 °C. All drugs were dissolved in 100% DMSO and stored at -20°C. Kinetoplast DNA (kNA) was used for the TOP2 experiments. This DNA is mitochondrial DNA and is obtained from trypanosomatid protozoa. For the TOP1 experiments, pHOT1 DNA was used.

The experiments below were performed by Alexander M. Fageson as part of our collaboration with Prof. Muller's group at UCF. The experimental methods are reproduced here for completeness.

a. DNA Unwinding Assay with Human TOP1

Reactions were carried out in TGS buffer (10 mM TrisHCl pH 8.0, 1 mM EDTA, 150 mM NaCl, 5% glycerol, 0.1% bovine serum albumen, BSA, and 0.1 mM spermidine) and 100 U TOP1 and 200 ng supercoiled pHOT1 DNA. Aliquots of the compound were added to the DNA in buffer solution and reactions were incubated at 37 °C for 30 minutes. The reaction was stopped by the addition of SDS (final concentration 4%) and excess protein was degraded by proteinase K (final concentration 1 mg mL⁻¹). Following a phenol:chloroform extraction, DNA dye (bromophenol blue) was added and loaded onto a 1% agarose gel and electrophoresis was carried out for 1 hour 50V. Gel was stained for 5 min in EB (5 ug/ml) and photographed with ChemiGenius Software.

b. kDNA Decatenation Assay by TOP2

Unless otherwise indicated, reactions (30 µl final volume) contained kDNA (100 ng µL⁻¹ final concentration of DNA), TOP2 assay buffer (50 mM Tris-HCl, pH 8, 120 mM KCl, 10 mM MgCl₂, 0.5 mM ATP, 0.5 mM dithiothreitol), 8 units of purified topo II enzyme. Aliquots of compound were added and reactions were incubated at 37 °C for 30 minutes. The reactions were stopped by the addition of SDS (final concentration 4%) and excess protein was degraded by proteinase K (final concentration 1 mg mL⁻¹). Following a phenol:chloroform extraction, DNA dye (bromophenol blue) was added and loaded onto a 1% agarose gel and electrophoresis was carried out for 20 minutes at 100V. EB (final concentration 0.5 ug mL⁻¹) was contained in both the gel and running buffer. Reaction products were then analyzed and quantified through ChemiGenius Software.

7.2.8 Surface Plasmon Resonance at the University of Central Florida

The SPR experiments were performed by Alexander M. Fageson and Dr. Michael Taylor as part of our collaboration with Prof. Muller's group at UCF. They are included here for completeness.

DNA-drug, protein-drug, and ternary DNA-drug-protein interactions were performed using a Reichert SR7000 SPR refractometer (Reichert Inc., Depew, NY, USA). Two sensor chips were utilized in the experiments: a DNA chip and a protein chip.

In the first set of experiments, a biotinylated twenty base-pair duplex DNA segment (synthesized by Dr. Bongyong Lee in the Muller Laboratory) was immobilized to a neutravidin coated sensor slide (Reichert Inc., Depew, NY, USA) at a flow rate of 41 µl /min in a 1X HBS buffer (10 mM HEPES pH 7.4, 150 mM NaCl and 3 mM EDTA, 10% DMSO). A total of 60 ng of DNA flowed over the chip in the HBS buffer to saturate all binding sites on the chip. The gold(III) macrocycles (in a 10% DMSO solution) flowed over the DNA chip at a set concentration of 50 nM to check for binding. The gold(III) macrocycles that bound DNA with a significant SPR response were then titrated over a five-concentration range to establish a K_D (equilibrium dissociation constant). After checking Drug-DNA interactions, TOP1 flowed over the DNA chip as a control to check for binding to the biotinylated DNA. Then, a solution containing drug-TOP1 was flowed over the DNA chip to determine whether the drug blocked the binding of TOP1 to the DNA.

A protein chip was made with the catalytically inactive TOP1 mutant covalently conjugated to the sensor slide (Reichert Inc., Depew, NY, USA) via an anti-TOP1 mouse monoclonal antibody (TopoGEN) cross-link. The sensor slide was activated with N-hydroxysuccinimide (NHS) and 1-(3-(dimethylamino)propyl)-3-ethylcarbodiimide hydrochloride (EDC) in a 1:1 ratio, which serves as a cross-linker for antibody conjugation to sensor slide via amide chemistry. NHS and EDC were prepared as 0.5 M and 0.2 M EDC solutions in deionized H₂O and stored at -80 °C until the time of the experiment. NHS and EDC were mixed in a 1:1 ratio and flowed over the top of the chip. Following activation, an antibody solution containing 950 ng of TOP1 antibody in a sodium-acetate buffered solution (pH 5.4) was applied on top of the sensor chip. Next, 320 ng of TOP1 enzyme was mixed in a solution of 0.05% Tween 20 phosphate-buffered saline (PBS-T) which bound with high specificity to the antibody. First, gold macrocycles were flowed over the chip to establish drug-protein interactions. Second, the same DNA substrate from the DNA chip was flowed over the protein chip to check as a control. Third, a solution containing drug-DNA (equilibrated for 5 min. at 37 °C) was flowed over the chip to see if binding of the DNA to the protein was inhibited in the presence of the drug. Reichert Labview software was used for data collection and Biologic Scrubber 2 software (Campbell, Australia) was used for curve fitting and data analysis. Unless indicated, all experiments were performed at 37 °C with a flow rate of 41 μl min⁻¹.

7.2.8 Data Analysis

All the data was analyzed using KypPlot.²² A statistical multivariate cluster analysis algorithm (group average method, Minkowski distances) was used to formulate the dendrogram in section 7.3.4. For the enzyme inhibition assays (section 7.3.4) standard dose-response functions, Equation 7.8, were fitted to the data:

$$f(x) = 100/(1 + (10^x/A)^B) \quad 7.8$$

where A corresponds to the IC₅₀ value (compound concentration effecting 50% inhibition) and B is the Hill coefficient.

7.3 Results and Discussion

7.3.1 Cytotoxicity Data: NCI-60 Screen

In this work, twelve novel gold(III) Schiff base complexes have been synthesized. Of these twelve complexes, nine have been selected by the NCI for screening against their panel of sixty human cancer cell lines. The complexes that were chosen are: [Au(L1)](PF₆), [Au(L2)](PF₆), [Au(L3)](PF₆), [Au(L4)](PF₆), [Au(L5)](PF₆), [Au(L6)](PF₆), [Au(L7)](PF₆), [Au(L10)](PF₆) and [Au(L11)](PF₆). These nine complexes went through single-dose screening at a concentration of 10 μM and the results from this screening process are promising. The results of the single-dose screen of [Au(L3)](PF₆) are shown in Figure 7.3.

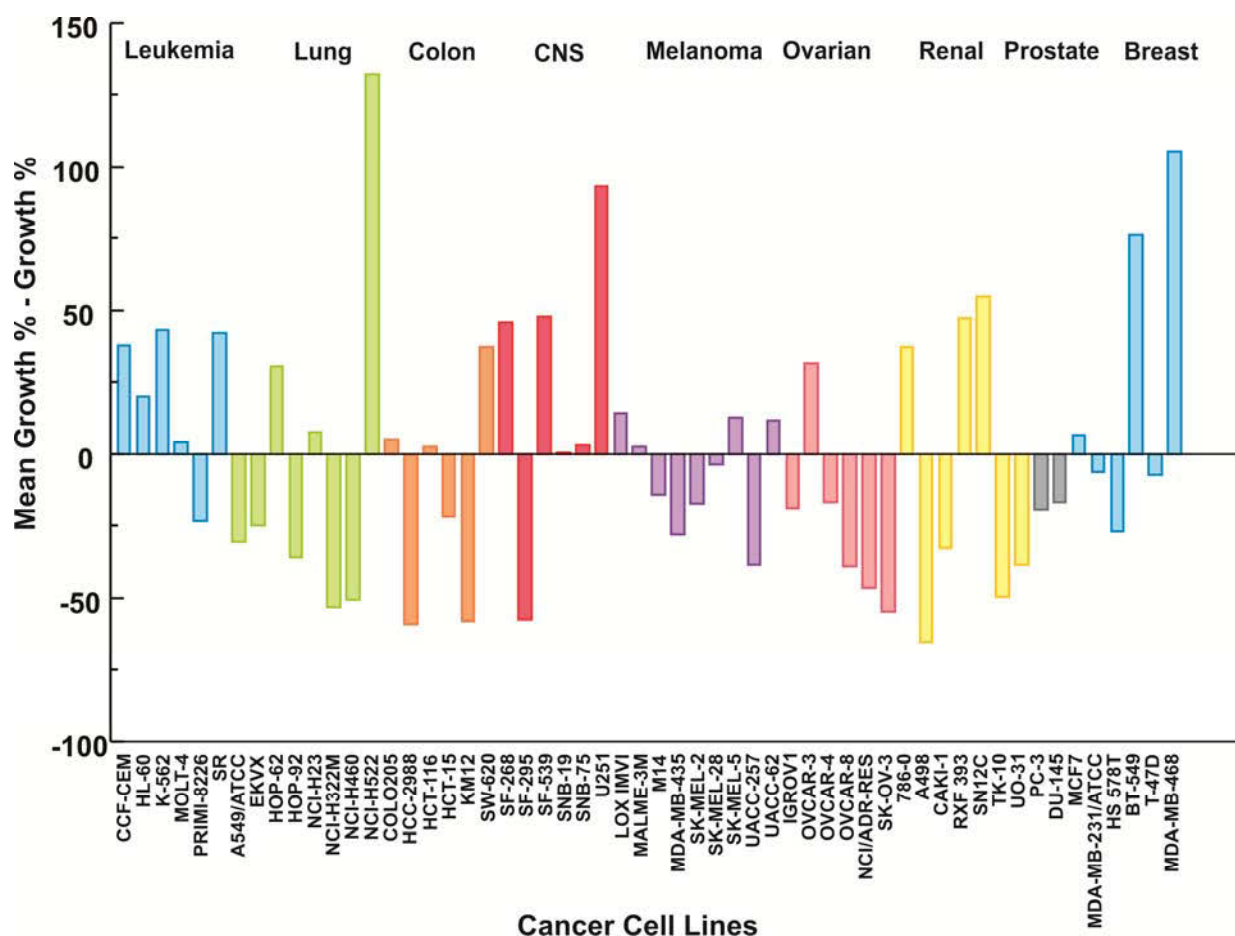


Figure 7.3: Single-dose screening results for $[\text{Au}(\text{L3})](\text{PF}_6)$ over the NCI's panel of sixty human cancer cell lines. The bars are coloured according to the cell line panel, from left to right: leukemia, lung, colon, central nervous system, melanoma, ovarian, renal, prostate and breast cancers.

On the y-axis of Figure 7.3 is the mean growth % - growth %: a high growth percentage of cells relative to the mean growth percentage will lead to small or negative values showing that the drug is ineffective in lowering the growth of that cell line. Large positive values, on the other hand, show that the growth % is low in comparison to the mean growth %, indicating that the drug effectively inhibits growth of that cell line. These results show that $[\text{Au}(\text{L3})](\text{PF}_6)$ is not toxic to all cancer cell lines but seems to selectively target certain cell lines. $[\text{Au}(\text{L3})](\text{PF}_6)$ is mainly effective against leukemia and certain central nervous system and breast cancers while it is largely ineffective against melanomas, ovarian and prostate cancers. This is important as it shows that $[\text{Au}(\text{L3})](\text{PF}_6)$ exhibits inherent specificity towards specific cell lines and it is therefore not a poison, but a potential chemotherapeutic agent with a well defined mode of action. Similar data was obtained for the other gold(III) chelates that were screened; this data is available in **Appendix H**. This data shows that $[\text{Au}(\text{L2})](\text{PF}_6)$, $[\text{Au}(\text{L4})](\text{PF}_6)$, $[\text{Au}(\text{L5})](\text{PF}_6)$, $[\text{Au}(\text{L6})](\text{PF}_6)$ and $[\text{Au}(\text{L7})](\text{PF}_6)$ are all active against central nervous system and leukemia cancer cell lines, but are predominantly inactive against colon and melanoma cell lines. $[\text{Au}(\text{L1})](\text{PF}_6)$ is mainly active against CNS and non-small cell lung cancer lines and inactive against leukemia and colon cancers. The pseudomacrocycles $[\text{Au}(\text{L10})](\text{PF}_6)$ and $[\text{Au}(\text{L11})](\text{PF}_6)$ are active against colon, leukemia and renal cancer cell lines, but inactive against prostate and CNS cell lines. This indicates that small

modifications in the structure of the complex can result in changes to the efficacy of the complex to a specific cell line.

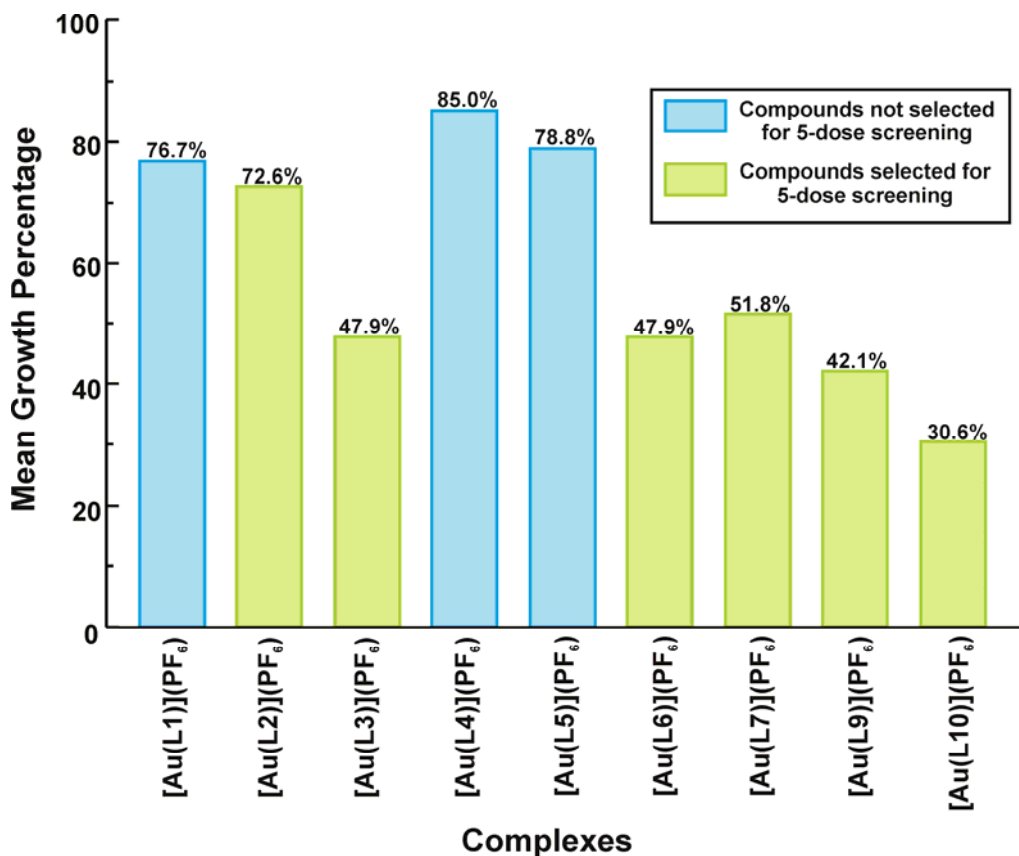


Figure 7.4: Mean growth rate of the NCI's panel of sixty human cancer lines against which the gold(III) complexes were tested in the single-dose screen.

A summary of the single-dose screening data for the complexes is shown in Figure 7.4. This summary gives the mean growth rate of all sixty tumour cell lines for each of the gold(III) complexes. Based on the results from the single-dose screening of the nine complexes, six of the complexes were selected for the next stage of the NCI screening process: five dose screens. The six complexes selected are shown in green in Figure 7.4. These six complexes have the lowest mean growth rate of the nine complexes screened. The most active compound according to the single-dose screening results is the pseudomacrocyclic [Au(L11)](PF₆) with the lowest mean growth rate of 30.6% while [Au(L4)](PF₆) appears to be the most inactive complex with a mean growth rate of 85.0%. There appears to be no correlation between the mean growth rate in the single-dose screens and the electronic or steric nature of the gold(III) complexes. This statement is based upon the fact that the parent compound [Au(L1)](PF₆) with no substituents on the di(azomethine) bridge or the quinoxaline tail was not selected for five-dose screening. The complex [Au(L4)](PF₆) contains an electron-withdrawing chlorine atom on the diazomethane linkage while [Au(L5)](PF₆) contains an electron-donating methyl group on the quinoxaline moiety. Neither of these complexes was selected for five-dose screening. However, other compounds with electron-donating groups: [Au(L2)](PF₆) and [Au(L6)](PF₆), and electron-withdrawing groups: [Au(L7)](PF₆), were selected for further screening.

Six complexes out of the nine selected for single-dose screens, were selected for five-dose screens. These complexes were: [Au(L2)](PF₆), [Au(L3)](PF₆), [Au(L6)](PF₆), [Au(L7)](PF₆), [Au(L10)](PF₆) and [Au(L11)](PF₆). From the five-dose screens, the cell growth parameters for each of the cancer cell lines against each of the metal chelates could be obtained. A summary of the average cell growth response parameters for each of the gold(III) complexes against the NCI₆₀ panel of cell lines is listed in Table 7.1.

Table 7.1: Summary of the average cytotoxicity data over sixty human cancer cell lines for [Au(L2)](PF₆), [Au(L3)](PF₆), [Au(L6)](PF₆), [Au(L7)](PF₆), [Au(L10)](PF₆) and [Au(L11)](PF₆) as well as selected commercial cytotoxic agents.*

Drug	GI ₅₀ (μM)	IC ₅₀ (μM)	LC ₅₀ (μM)
[Au(L2)](PF ₆)	28.7(2)	59.0(3)	96.3(9)
[Au(L3)](PF ₆)	6.4(2)	16.0(2)	>100
[Au(L6)](PF ₆)	3.4(3)	22.0(2)	>100
[Au(L7)](PF ₆)	6.5(2)	31.8(2)	>100
[Au(L10)](PF ₆)	6.7(4)	15.0(3)	>100
[Au(L11)](PF ₆)	2.9(5)	5.6(4)	>100
Cisplatin	2.0(6)	27.0(5)	>100
Carboplatin	99.6(9)	>100	>100
Mitomycin	0.7(3)	6.5(4)	18.2(7)
Camptothecin	0.04(2)	0.9(3)	33(3)
[Au(terpy)Cl]Cl	0.1(2)	10.8(2)	72.7(7)

*Standard deviations are given in parentheses.

The data in Table 7.1 for the commercial chemotherapeutic agents: cisplatin, carboplatin, mitomycin, camptothecin and [Au(terpy)Cl]Cl were obtained from the DTP drug repository database.² The summary of the data shows that the GI₅₀ values for some of the complexes such as [Au(L6)](PF₆) and [Au(L11)](PF₆) compare favourably with some of the commercial anti-cancer agents, in particular cisplatin. The IC₅₀ values of [Au(L3)](PF₆), [Au(L6)](PF₆), [Au(L10)](PF₆), [Au(L11)](PF₆) are lower than those of the platinum(II) drugs, cisplatin and carboplatin. These gold(III) complexes have similar IC₅₀ values to the gold(III) complex [Au(terpy)Cl]Cl, while [Au(L11)](PF₆) is the only complex with a lower IC₅₀ value than the organic drug mitomycin. The LC₅₀ values for the complexes are generally >100 μM. It must be taken into account that these are averages over the sixty cell lines and that the compounds outcompete the commercially available drugs against specific cell lines as will be discussed later.

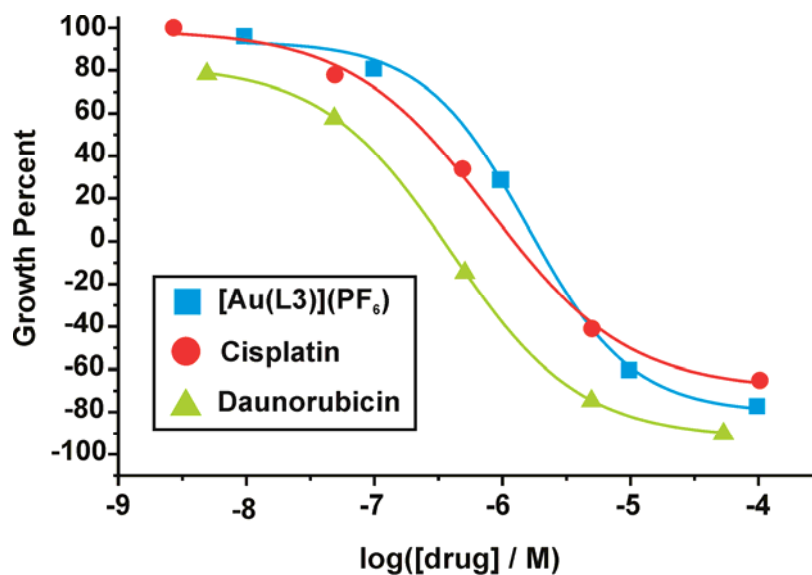


Figure 7.5: Dose-response curves for $[\text{Au}(\text{L3})](\text{PF}_6)$, cisplatin and daunorubicin. The curves measure the response of the breast cancer cell line MDA-MB-468. Data were obtained from the DTP drug repository.²

The compounds synthesized in this work have moderately steeper dose response curves compared to other commercial drugs. Figure 7.5 shows an overlay of the dose response curves for $[\text{Au}(\text{L3})](\text{PF}_6)$, cisplatin and daunorubicin for the breast cancer cell line MDA-MB-468. The steepness of the curve indicates that the initial concentration of $[\text{Au}(\text{L3})](\text{PF}_6)$ required to induce cell death is relatively high. Once this concentration has been reached, small increases lead to high levels of cell mortality. To induce a 50% growth inhibition of the cancer cell line MDA-MB-468, on average a concentration of 0.60 μM of $[\text{Au}(\text{L3})](\text{PF}_6)$ is required. To induce a 75% cell death rate a 11-fold increase of the gold(III) complex is required, giving a concentration of 6.6 μM . For cisplatin to induce the same results, a 36-fold increase in concentration is required i.e. from 0.28 μM to 10.2 μM . These numbers illustrate a moderate difference in the steepness of the dose-response curves with the dose response curve of $[\text{Au}(\text{L3})](\text{PF}_6)$ intersecting the curve for cisplatin, Figure 7.5. Daunorubicin is more effective against this specific cell line than either cisplatin or the gold complex as a much lower concentration of 0.07 μM is required to induce 50% cell growth inhibition while a drug concentration of 1.48 μM is required to induce 75% cell growth inhibition (a 21-fold increase in drug concentration).

The NCI selected the gold(III) complex $[\text{Au}(\text{L3})](\text{PF}_6)$ to go through to the acute toxicity determination and then to the hollow fibre assay. This compound was selected as it had IC_{50} values of $<5 \mu\text{M}$ for 19 out of 57 cell lines. For the acute toxicity determination, three mice were given separate doses of $[\text{Au}(\text{L3})](\text{PF}_6)$ of 100, 200 and 400 mg/kg/dose in 100% DMSO and were monitored for 17 days. If the mice lost more than 20% of their body weight or showed any toxic side effects to the complex, they were to be sacrificed. Seventeen days after being injected with $[\text{Au}(\text{L3})](\text{PF}_6)$ all three mice were alive. Thus the acute toxicity determination showed that the mice could tolerate high doses of $[\text{Au}(\text{L3})](\text{PF}_6)$, even up to 400 mg/kg/dose. This is important as it shows that the complex is not highly toxic to non-cancerous cells. The complex $[\text{Au}(\text{L3})](\text{PF}_6)$ underwent a hollow fibre assay at the NCI and was tested against 12 standard cancer cell lines (results are available in **Appendix H**). The results showed that $[\text{Au}(\text{L3})](\text{PF}_6)$ was insufficiently cytotoxic *in vivo* to justify

xenograft studies. There are several possible causes for this low *in vivo* cytotoxicity, these include: poor physiological and/or cellular transport, off-target binding or possibly excretion from cells by efflux pumps.

Cisplatin is currently the most widely used inorganic anticancer agent worldwide. A comparison of the efficacy of cisplatin with our lead compound $[\text{Au}(\text{L3})](\text{PF}_6)$ against each specific cancer cell line in the sixty cell line screen, shows that each compound has an area of increased activity. These data are depicted as a plot of $-\log\text{GI}_{50}$ of $[\text{Au}(\text{L3})](\text{PF}_6)$ versus the equivalent data for cisplatin, Figure 7.6.

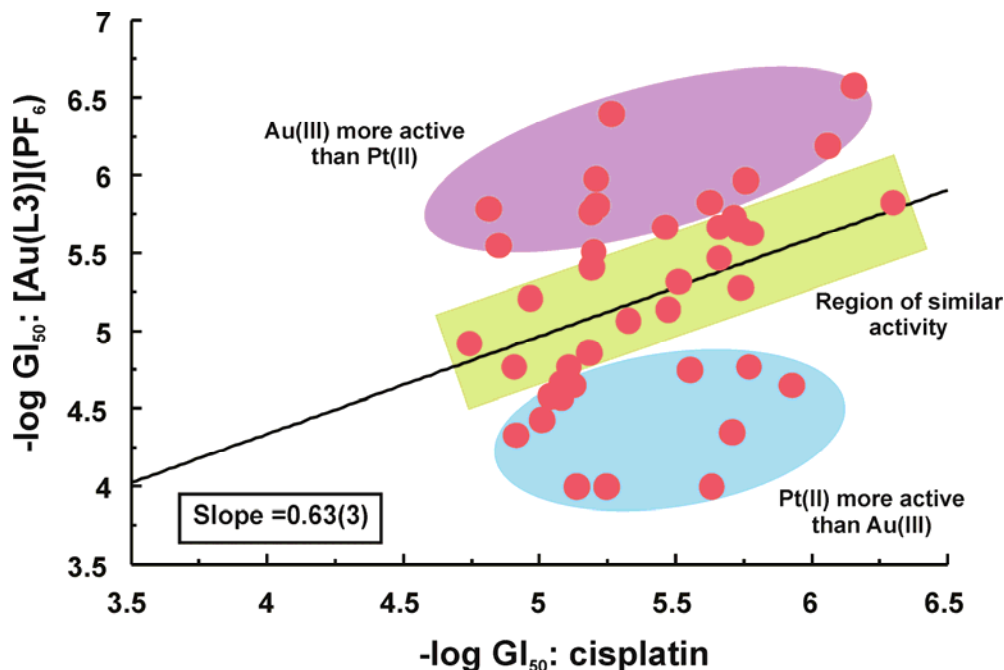


Figure 7.6: Plot of $-\log\text{GI}_{50}$ of $[\text{Au}(\text{L3})](\text{PF}_6)$ versus the equivalent data for cisplatin.

Figure 7.6 shows that $[\text{Au}(\text{L3})](\text{PF}_6)$ shares on average 63% of the growth inhibition activity of cisplatin. The plot also shows that there are three key areas of comparison. There is a zone of increased activity of $[\text{Au}(\text{L3})](\text{PF}_6)$ (purple zone), a zone of increased activity for cisplatin (blue zone) and a zone of equivalent activity (green zone). The purple highlighted area shows that the cytotoxicity of $[\text{Au}(\text{L3})](\text{PF}_6)$ is enhanced for approximately 25% of the cell lines tested. This is a considerable proportion of the cell data.

A comparison of the cytotoxicity of $[\text{Au}(\text{L3})](\text{PF}_6)$ with other commercially available chemotherapeutic agents shows that against specific cell lines $[\text{Au}(\text{L3})](\text{PF}_6)$ is more cytotoxic than those drugs currently in clinical use, Figure 7.7. This is a plot of the $-\log\text{GI}_{50}$ values; a higher $-\log\text{GI}_{50}$ value indicates that the compound is more effective against the cell line. The plot shows that $[\text{Au}(\text{L3})](\text{PF}_6)$ is less cytotoxic than the high activity drug topotecan against these specific cell lines. It is, however, more cytotoxic than cisplatin, ICRF-187 and merbarone against these cell lines. It is also important to acknowledge that, despite the increased cytotoxicity of a drug such as topotecan, it does have side-effects that include diarrhea, anorexia, alopecia and anorexia, which are caused in part by its high cytotoxicity. Topotecan can also only be administered in very small doses and certain cell lines have shown resistance to this drug through mutations. The gold(III) complex $[\text{Au}(\text{L3})](\text{PF}_6)$ exhibits sufficient cytotoxicity to be used as effective chemotherapeutic agents for the treatment of several tumour cell lines, particularly central nervous system cell lines.

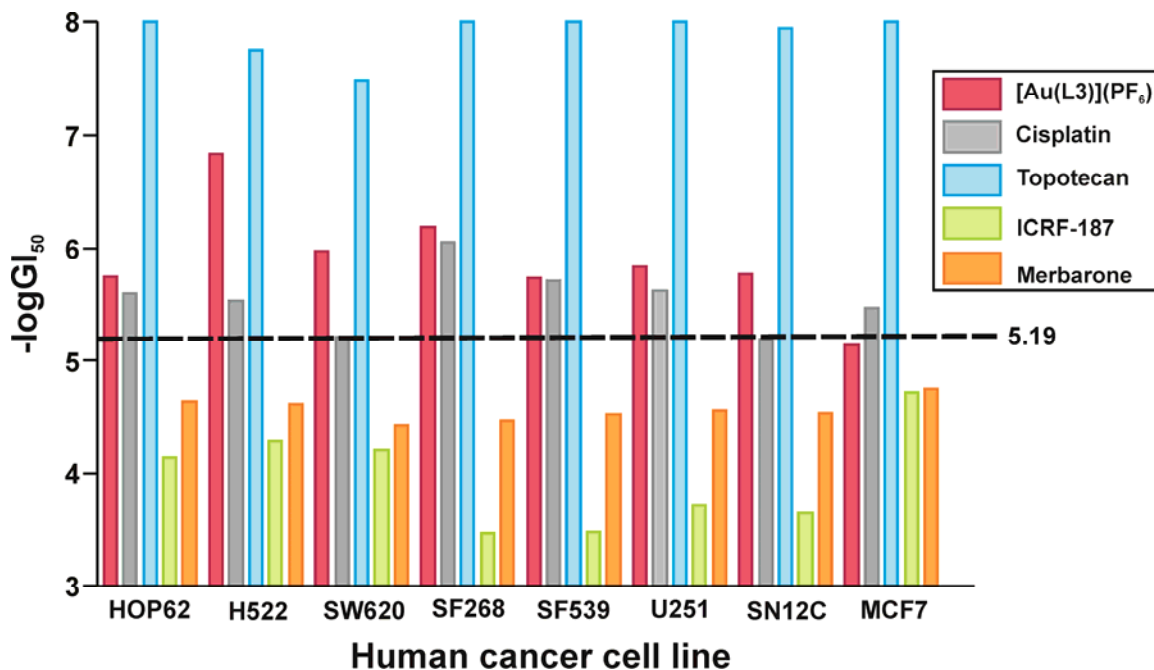


Figure 7.7: Comparison of $-\log GI_{50}$ values of [Au(L3)](PF₆) with commercially available chemotherapeutic agents for specific cancer cell lines. The dashed horizontal line gives the mean GI_{50} value.

As discussed above, six of nine complexes selected for one dose screens by the NCI were further selected for five-dose screening. The data that was obtained from the one-dose screens of the compounds in conjunction with the five-dose data was used to estimate the GI_{50} dose parameter for the remaining compounds that were not selected for the five dose screening. A plot of the mean $-\log(GI_{50}/\mu M)$ versus the mean growth percent of the single-dose screens, Figure 7.8, was used to estimate the $-\log GI_{50}$ values of the compounds for which there was only single-dose data available.

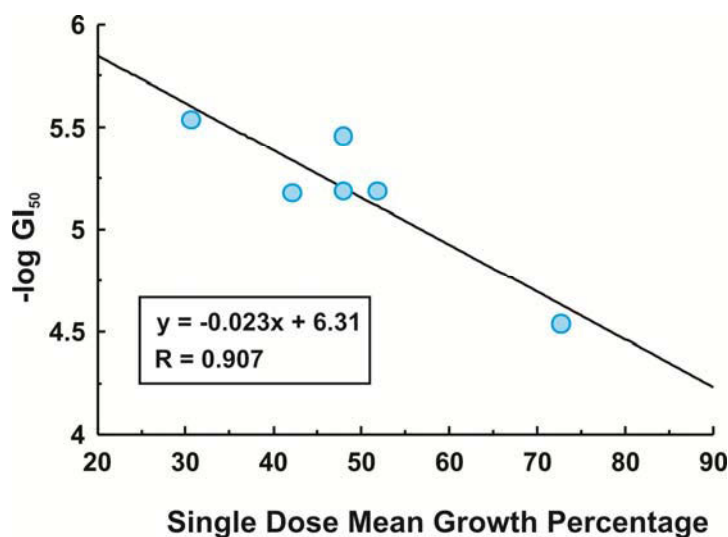


Figure 7.8: Plot of $-\log GI_{50}$ versus single-dose growth percentage.

The GI₅₀ values that were calculated from Figure 7.8 are shown in Table 7.2. As the graph only consists of a few data points, the data given is only a guideline to give a theoretical estimate of the dose response parameter. The estimated GI₅₀ value of [Au(L4)](PF₆) is the highest of all the other gold(III) complexes. This complex has an electron-withdrawing chlorine substituent on the diazomethane linkage. It has been proposed that the electron withdrawing functional groups allow the cancer cells to effectively eliminate the compounds possibly via an efflux pump.²³⁻²⁶ An efflux pump is a known mechanism responsible for the elimination of toxic compounds from cells. It is proposed that electron withdrawing groups allow transport proteins to more effectively bind the metal complexes and thus carry the drugs across the cell membrane and eliminate them from the cell.²³⁻²⁶

Table 7.2: Estimation of the GI₅₀ values of the compounds selected for a single-dose screen only.

Compound	Mean Growth (%)	Estimated GI ₅₀ (μM)
[Au(L1)](PF ₆)	76.7	28.4
[Au(L4)](PF ₆)	85.0	44.1
[Au(L5)](PF ₆)	78.8	31.8

There is no clear correlation between the binding affinity of the gold(III) complexes to DNA and their GI₅₀ values. However, in general, a lower binding constant will result in a higher GI₅₀ value. The complex [Au(L11)](PF₆) has the highest binding constant of $6.61 \times 10^6 \text{ M}^{-1}$ and the lowest GI₅₀ value of 2.86 μM, indicating that potentially DNA intercalation is key to the efficacy of the complexes. This statement is not true for some of the complexes such as [Au(L3)](PF₆) which has the smallest binding constant of $1.20 \times 10^6 \text{ M}^{-1}$, but also a moderate GI₅₀ value of 6.42 μM.

7.3.2 Cytotoxicity Data: University of Central Florida Screen

A cytotoxicity assay for [Au(L1)](PF₆), [Au(L2)](PF₆) and [Au(L3)](PF₆) against HeLa cells was performed in Prof Mark Muller's laboratory (University of Central Florida); the results are shown in Figure 7.9. HeLa cells are a line of cells derived from cervical cancer cells and are often used in scientific research. This experiment involved growing HeLa cells in 96-well plate at 2 500 cells per well for 24 hours. The drug was then added and the cells were incubated for a further 24 hours. MTS tetrazolium salt was added to the plates and incubated for three hours and the absorbance measured at 490 nm. MTS (3-(4,5-dimethylthiazol-2-yl)-5-(3-carboxymethoxyphenyl)-2-(4-sulfophenyl)-2H-tetrazolium is used to assess the viability and proliferation of cells. Enzymes reduce MTS to formazan dyes, giving a purple colour. These reductions only take place when reductase enzymes are active, thus allowing for the measure of viable cells.

Figure 7.9(a) shows that [Au(L3)](PF₆) appears to have the greatest effect on HeLa cell viability when compared to the other complexes and VP-16, a known TOP2 inhibitor and poison. The dose response curves are shown in Figure 7.9(b) and the IC₅₀ values calculated from these graphs are shown in Table 7.3.

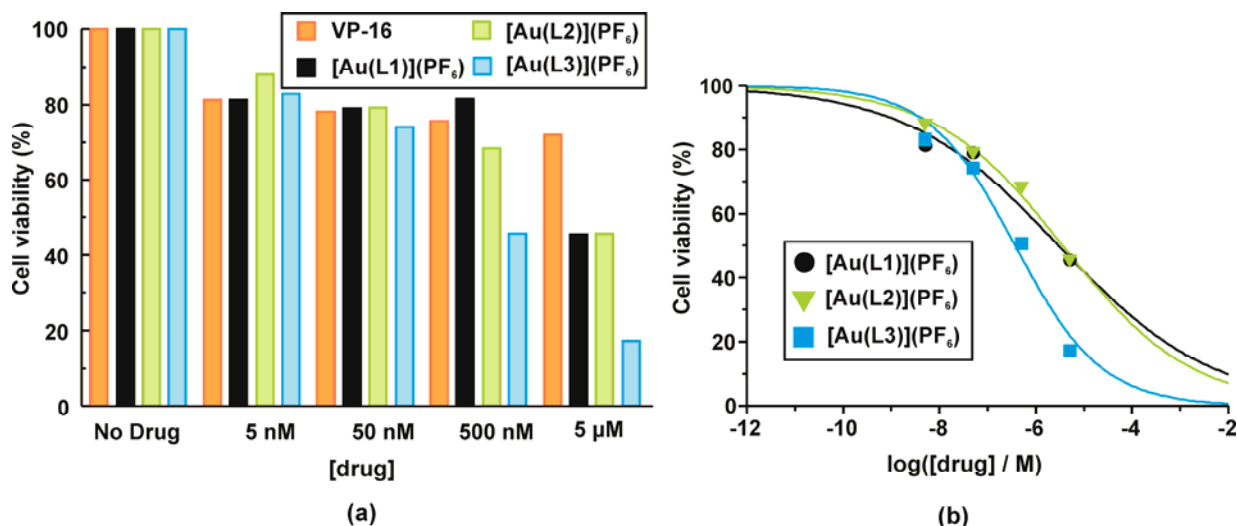


Figure 7.9: (a) Cytotoxicity Assay in HeLa cells for [Au(L1)](PF₆), [Au(L2)](PF₆) and [Au(L3)](PF₆) tested against VP-16. (b) Dose-response function fit for the MTS assay in HeLa cells for [Au(L1)](PF₆), [Au(L2)](PF₆) and [Au(L3)](PF₆).

[Au(L3)](PF₆) has the lowest IC₅₀ value of 0.37 μM against the HeLa cancer cell line. [Au(L3)](PF₆) also has the steepest dose response curve of the three complexes. The steepness of the curve indicates that the initial concentration required to induce cell death is relatively high, but once this concentration has been reached relatively small increases lead to high levels of cell mortality. In order to induce the same or similar cytotoxicity as [Au(L3)](PF₆), higher concentrations of the other two gold(III) complexes are required. At 5 μM, all the complexes are more effective at killing the HeLa cells than VP-16.

Table 7.3: IC₅₀ values for the cytotoxicity assay in HeLa cells for [Au(L1)](PF₆), [Au(L2)](PF₆) and [Au(L3)](PF₆).

Complex	IC ₅₀ (μM)
[Au(L1)](PF ₆)	3.0(2.5)
[Au(L2)](PF ₆)	3.6(1.1)
[Au(L3)](PF ₆)	0.37(27)

7.3.3 Cytotoxicity Data: MINTEK Screen

The complexes [Au(L9)](PF₆) and [Au(L12)](PF₆) were not selected by the NCI for screening. Thus, these complexes were sent to the Advanced Materials Division at MINTEK in South Africa to be screened against four human cancer cell lines. These cell lines are: A549 (non-small lung cancerous cell line), TK-10 (renal cell line), HT-29 (colon cell line) and U251 (CNS cell line). These screens give the IC₅₀ values for these gold(III) complexes against the four cancer cell lines. The results are given in Table 7.4.

Table 7.4: IC₅₀ values for [Au(L9)](PF₆) and [Au(L12)](PF₆) against four human cancer cell lines.

	IC ₅₀ value (μM)			
	A549	TK-10	HT-29	U251
[Au(L9)](PF ₆)	9.2	14.4	14.1	15.5
[Au(L12)](PF ₆)	11.7	11.3	18.5	16.1

The data from Table 7.3 shows that the gold(III) pseudomacrocyclic, $[\text{Au}(\text{L9})](\text{PF}_6)$ is more active against the non-small lung cell line A549 than the CNS cell line U251. The acyclic complex $[\text{Au}(\text{L12})](\text{PF}_6)$ is more active against the non-small cell lung and renal cancer cell lines than the colon and CNS cancer cell lines. On average, across the four cell lines, $[\text{Au}(\text{L9})](\text{PF}_6)$ is more cytotoxic than $[\text{Au}(\text{L12})](\text{PF}_6)$ with a lower mean IC_{50} value.

Figure 7.10 shows a comparison of the two complexes screened by MINTEK and a selection of the complexes screened by the NCI for the four cancer cell lines. This graph is a plot of the $-\log \text{IC}_{50}$ values with the higher values indicating the more active complexes.

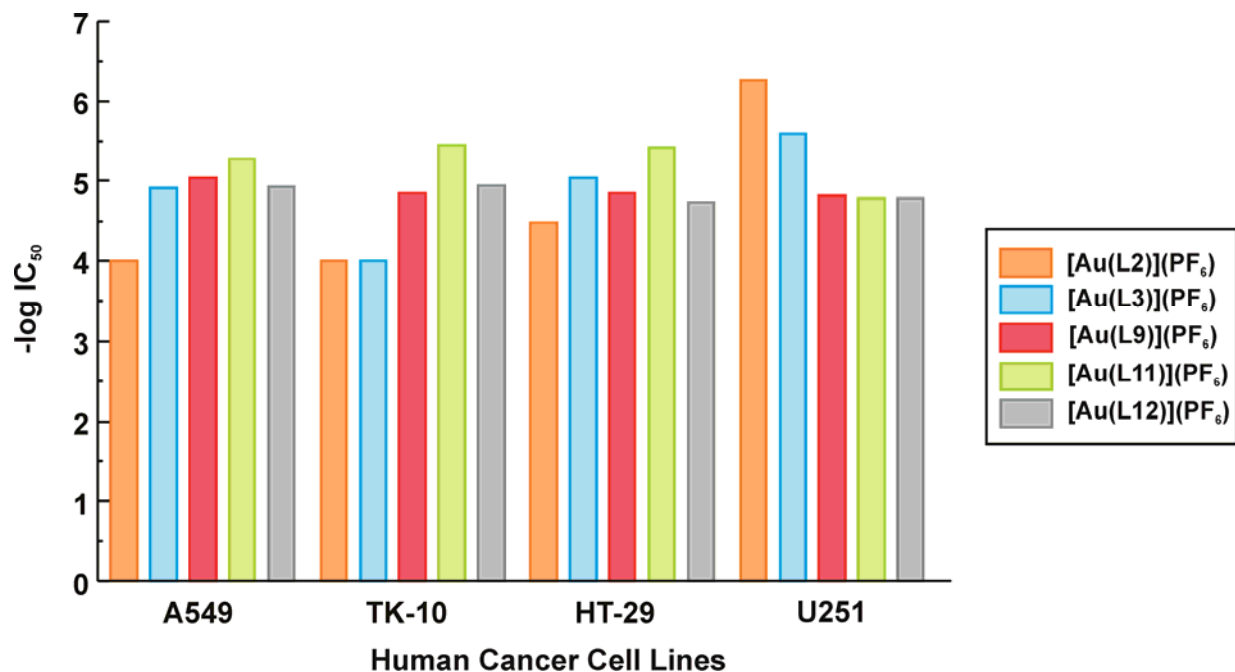


Figure 7.10: Plot of the $-\log \text{IC}_{50}$ values for selected gold(III) complexes for four human cancer cell lines.

The gold(III) complexes screened by MINTEK, $[\text{Au}(\text{L9})](\text{PF}_6)$ and $[\text{Au}(\text{L12})](\text{PF}_6)$, are compared in Figure 7.10 with the complexes $[\text{Au}(\text{L2})](\text{PF}_6)$, $[\text{Au}(\text{L3})](\text{PF}_6)$ and $[\text{Au}(\text{L11})](\text{PF}_6)$ which were screened by the NCI. These compounds were selected for the comparison for specific reasons. $[\text{Au}(\text{L2})](\text{PF}_6)$ was selected as it has the highest mean IC_{50} value for the sixty human cancer cell lines of all the gold(III) complexes tested by the NCI. The gold(III) complex, $[\text{Au}(\text{L3})](\text{PF}_6)$, has the lowest mean sixty cell line IC_{50} value of the gold(III) macrocyclic complexes and was the complex chosen by the NCI for *in vivo* screening. The complex $[\text{Au}(\text{L11})](\text{PF}_6)$ has not only the lowest mean IC_{50} value of the pseudomacrocyclic complexes, but the lowest overall IC_{50} value of all the gold(III) complexes.

Figure 7.10 shows that $[\text{Au}(\text{L9})](\text{PF}_6)$ and $[\text{Au}(\text{L12})](\text{PF}_6)$ compare favourably with $[\text{Au}(\text{L3})](\text{PF}_6)$ and $[\text{Au}(\text{L11})](\text{PF}_6)$ and have greater activity than $[\text{Au}(\text{L2})](\text{PF}_6)$ against the non-small lung cancerous cell line A549 and the colon cell line HT-29. The complexes, $[\text{Au}(\text{L9})](\text{PF}_6)$ and $[\text{Au}(\text{L12})](\text{PF}_6)$, are both more active than $[\text{Au}(\text{L2})](\text{PF}_6)$ and $[\text{Au}(\text{L3})](\text{PF}_6)$ against the renal cancer cell line TK-10. The macrocyclic complexes $[\text{Au}(\text{L2})](\text{PF}_6)$ and $[\text{Au}(\text{L3})](\text{PF}_6)$ are the most active complexes against the CNS cancer cell line U251. In general, the two complexes screened by MINTEK compare favourably to the gold(III) complexes screened by

the NCI. The acyclic complex has similar results to those obtained for the pseudomacrocyclic and macrocyclic complexes and appear to have similar activity. The macrocyclic complexes have a preference for CNS cancer while the pseudomacrocyclic complexes and the acyclic complexes appear to have similar reactivity against the four cell lines.

One of the most important aspects illustrated by the cell screening data is the fact that very small changes in the structure of the gold(III) complexes can lead to a large difference in the cytotoxicity of the complexes. The structures differ in their substituents on both the di(azomethine) linkage and quinoxaline tail for the macrocyclic complexes. The pseudomacrocyclic complexes have varying appendages attached to the imine moiety and the acyclic complex has no quinoxaline tail. Despite the relatively small structural changes, the most active complex, [Au(L11)](PF₆) has a GI₅₀ value of 2.86 μM and the least active complex, [Au(L4)](PF₆) has an estimated GI₅₀ value of 44.1 μM. These structurally different complexes also have different preferences in cancer cell lines.

7.3.4 Determination of the Mechanism of Action

The cell screening data has shown that the proposed gold(III) complexes are effective chemotherapeutic agents, but the determination of their mode of action is a critical aspect of their development as chemotherapeutic agents. There is little known on the mode of action of many chemotherapeutic agents particularly gold(III)-based complexes and the determination of the mode of action of these complexes is therefore important for the further development of metal based therapeutics in general.^{4,8,9}

An advantage of having the gold(III) complexes screened for cytotoxicity by the NCI is that they are tested against a large panel of cancer cell lines and three dose-response parameters are experimentally determined for each cell line. As the compounds are tested against sixty tumour cell lines, there are 180 data points generated for each compound. This large quantity of data makes it possible to accurately compare the cytotoxicity profiles of the gold(III) complexes with compounds that have a known mechanism of action and have gone through the same screening process. The NCI accepts statistical analysis as a valid method for the comparison of new cytotoxic compounds with those of a known mode of action. The DTP have made all the screening data for the compounds they have tested available. This data has made it possible to perform hierarchical cluster analysis. Hierarchical cluster analysis is the only means for achieving a reliable comparison of the cytotoxicity profiles of multiple compounds. This is due to the large amount of data present for each compound. There are several methods available for this type of cluster analysis, but all these methods result in grouping compounds with a similar cytotoxicity profile. The more similar the profile, the tighter the grouping of the compounds. If a compound with an unknown mode of action clusters with several compounds with a known mode of action, which have been determined independently, then it is highly likely that the compound with the unknown mode will have the same mechanism of action as these compounds. A dendrogram, using a group average method and Minkowski distance, was prepared for the lead gold(III) complex [Au(L3)](PF₆) along with 24 compounds of known mode of action, Figure 7.11.

The dendrogram obtained via hierarchical cluster analysis of the GI₅₀ values for a range of commercial chemotherapeutic agents with known mechanism of action indicates a possible mechanism for the novel gold(III) complexes. The cluster analysis shows that [Au(L3)](PF₆) clusters with topotecan and camptothecin. Camptothecin and its synthetic derivative topotecan are well known interfacial poisons of topoisomerase I.^{3,6,27} [Au(L3)](PF₆) also clusters with Zorubicin. Zorubicin is from the anthracycline family which are used to

treat leukemia cancer cell lines.^{3,6,27} These compounds act as TOP2 inhibitors. Thus this cluster suggests that $[\text{Au}(\text{L3})](\text{PF}_6)$ is possibly a TOP1 poison and/or a TOP2 inhibitor. This statistical method does not, however, prove that the complexes are TOP1 poisons and/or TOP2 inhibitors. More unambiguous techniques and experiments were performed at the University of Central Florida to determine the mode of action of the complexes. Experiments were also performed to determine whether the gold(III) ion itself was necessary to induce the cytotoxic effects.

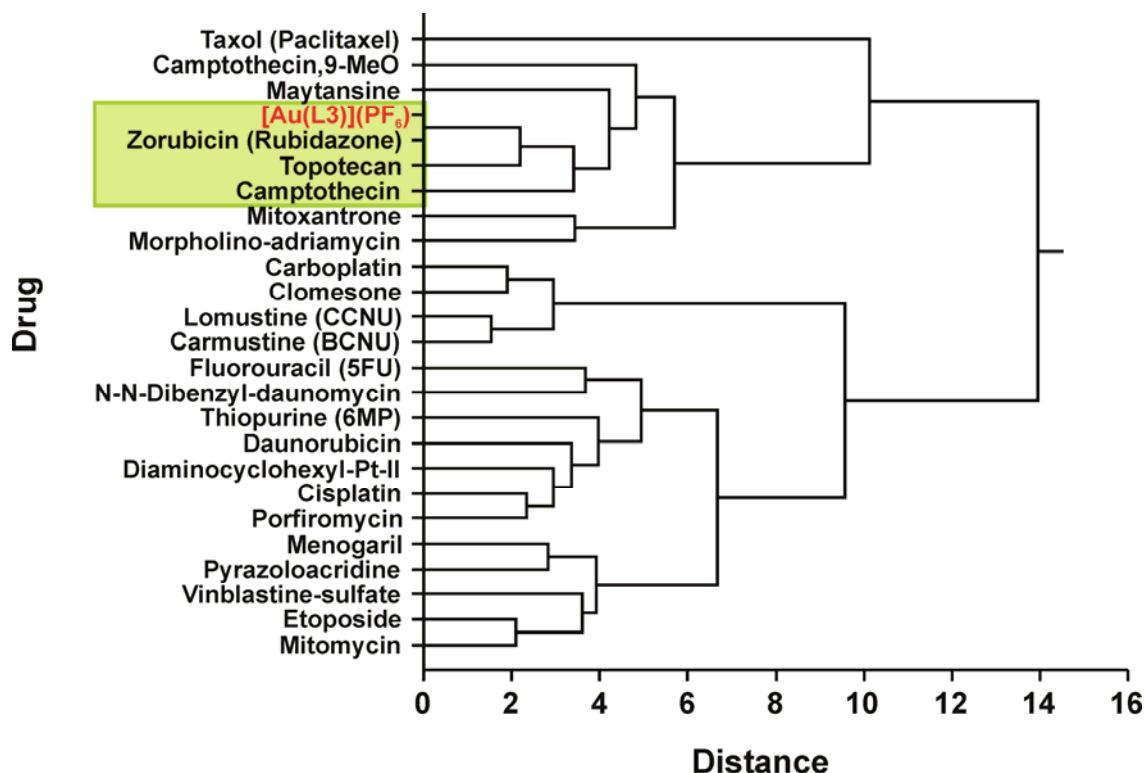


Figure 7.11: Comparison of the activity profile of commercial drugs with a known mode of action and $[\text{Au}(\text{L3})](\text{PF}_6)$.

Prior to discussion of the results of the experiments performed to elucidate the mode of action, a brief explanation on the function of complexes as poisons and inhibitors of the topoisomerase enzymes is given below. As explained previously TOP enzymes relax supercoiled DNA. Figure 7.12 illustrates the cycle in which TOP1 converts supercoiled DNA into relaxed DNA. Step one involves TOP1 binding to the supercoiled DNA with the 5'-TA-3' dinucleotide pair as a target.^{3,28-32} Step two involves the nucleophilic attack on the 3'-phosphate linking the TA pair by the catalytic tyrosine residue (Y723) of the TOP enzyme resulting in a covalent DNA-TOP1 cleavage complex and a nicked strand.^{3,28-32} In step three the intrinsic torque stored in the scDNA drives rotation around the uncut stand until strand relegation occurs with the release of Y723.^{3,28-32} Relaxed DNA is released by the enzyme in Step four.

The TOP enzymes are established anticancer drug targets whose inhibition can initiate cell apoptosis.^{33,34} Drugs that block the TOP1 enzymes can fall into two classes: the well-characterized interfacial poisons (IFPs) and the less common catalytic inhibitor compounds (CIC).³³ Interfacial poisons such as camptothecin intercalate at the 5'-TA-3' nick site.²⁹ This interaction is further stabilized through hydrogen-bonding of the compound to TOP1 to form drug-scDNA-TOP1 adduct, poisoning the enzyme. IFPs prevent stage 3 of the

TOP1 cycle from occurring. Competitive inhibitor compounds function differently. These compounds block either substrate recognition by TOP1, i.e. stage 1 (type 1 competitive inhibitor, CIC1) or they can prevent the formation of the covalent cleavage complex by blocking the nucleophilic attack by Y723, i.e. stage 2 (type 2 competitive inhibitor, CIC2).³³ Compounds inhibiting the first step (CIC1) belong to two groups: conventional competitive inhibitors which bind directly to the enzyme or unconventional competitive inhibitors which bind to the DNA preventing enzyme binding. Unconventional inhibitors exist as DNA intercalators^{35,36} or minor or major groove binders^{37,38} or both.³⁹ Gold(III) porphyrins are TOP1 inhibitors based on scDNA relaxation assays and are possibly unconventional CIC1s.^{40,41}

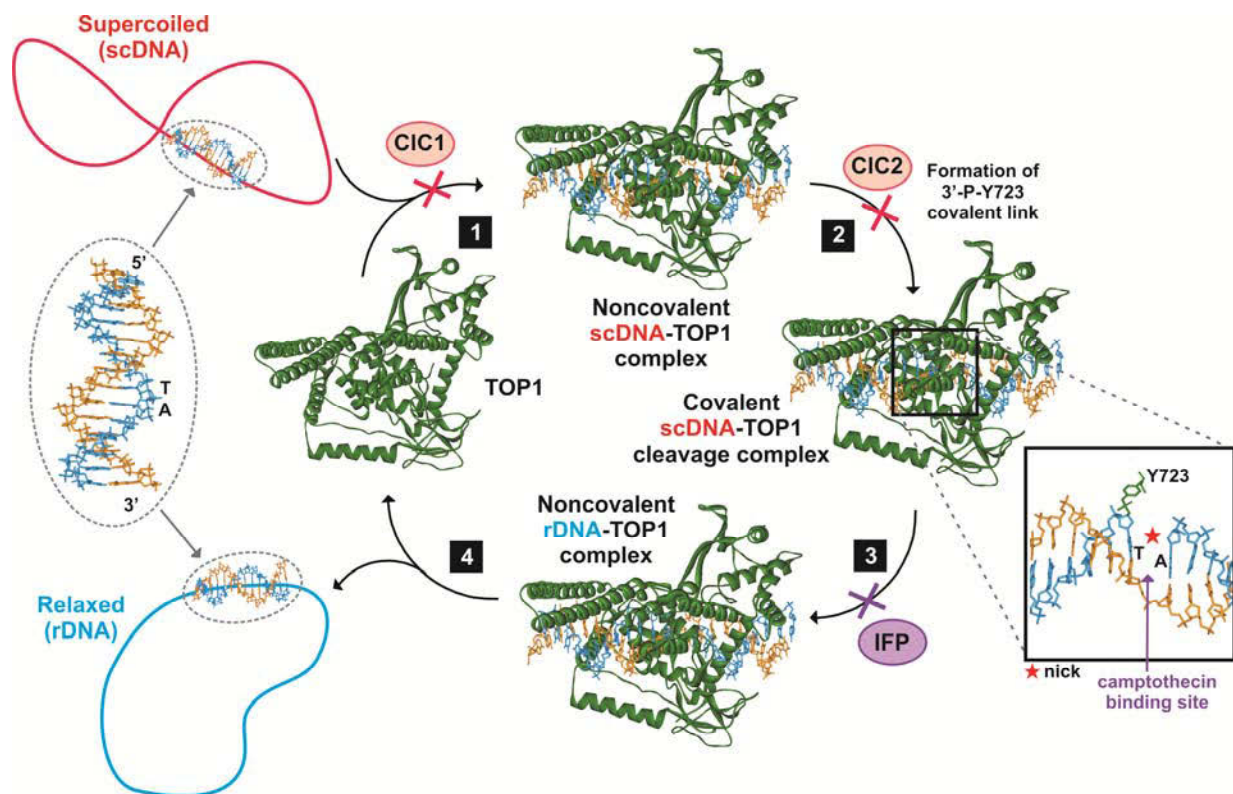


Figure 7.12: Key events in the catalytic cycle of human TOP1.

TOP2 creates a double-stranded break in one DNA molecule, as opposed to TOP1 which causes a single strand break.^{3,6} One DNA molecule is then allowed to pass through the double-strand break of the other DNA molecule thus unwinding the DNA.^{3,6} Similar to TOP1, drugs can act as either TOP2 inhibitors or poisons. TOP2 inhibitors prevent the formation of the DNA-TOP2 complex through competitive inhibition. A TOP2 poison allows the formation of the DNA-TOP2 complex but prevents the religation of the DNA double strand.

In Chapter Five, competitive binding DNA titrations and DNA melting curve experiments were performed to determine the strength of the interaction of the complexes with the DNA but to also determine the binding mode. Both techniques were slightly ambiguous, but suggested that DNA intercalation was a possible mechanism of DNA binding. To further prove that DNA intercalation is the binding technique adopted by the gold(III) complexes, electrophoretic mobility shift assays (EMSAs) with supercoiled and plasmid DNA (pHOT1) substrates were performed, Figure 7.13. Figure 7.13 shows that $[\text{Au}(\text{L1})](\text{PF}_6)$ has a more pronounced mobility shift (lanes 5-9) than the reference compound for DNA intercalation, EB. The effect is great as lane 8

shows a complete loss of mobility and a reversal of the direction of migration of the DNA (lane 9) is observed for $[\text{Au}(\text{L1})](\text{PF}_6)$. The large mobility shifts for the scDNA caused by $[\text{Au}(\text{L1})](\text{PF}_6)$ are due to elongation of the DNA duplex due to intercalation of the gold(III) complex. The binding constant of EB is $5(1) \times 10^6 \text{ M}^{-1} \text{ bp}^{-1}$ and is $2.8(4) \times 10^6 \text{ M}^{-1} \text{ bp}^{-1}$ for $[\text{Au}(\text{L1})](\text{PF}_6)$. Although these binding constants are comparable, $[\text{Au}(\text{L1})](\text{PF}_6)$ induces a greater mobility shift than EB at the same concentration (lanes 3 and 7). This technique shows that the gold(III) complexes act as DNA intercalators.

The macrocyclic ligand, $\text{H}_2\text{L1}$, and the nickel(II) analogue of $[\text{Au}(\text{L1})](\text{PF}_6)$ were also tested using the electrophoretic mobility shift assay. Neither the free ligand (lanes 10-13) nor the nickel(II) complex (lanes 13-15) induced a mobility shift. This is consistent with the results obtained in Chapter Five where neither compound could displace EB from DNA in the competitive binding studies. This assay is important as it shows that the gold(III) ion is essential for DNA intercalation of the compounds. This indicates that the electrostatic attraction of the intercalator to the negatively charged phosphate backbone of the DNA is important as neither $\text{H}_2\text{L1}$ nor $[\text{Ni}(\text{L1})]$ carry a net charge. As shown by the molecular mechanics calculations discussed in Chapter Six, there is also an important ion...dipole interaction between the gold(III) ion and the carbonyl O atom of thymine.

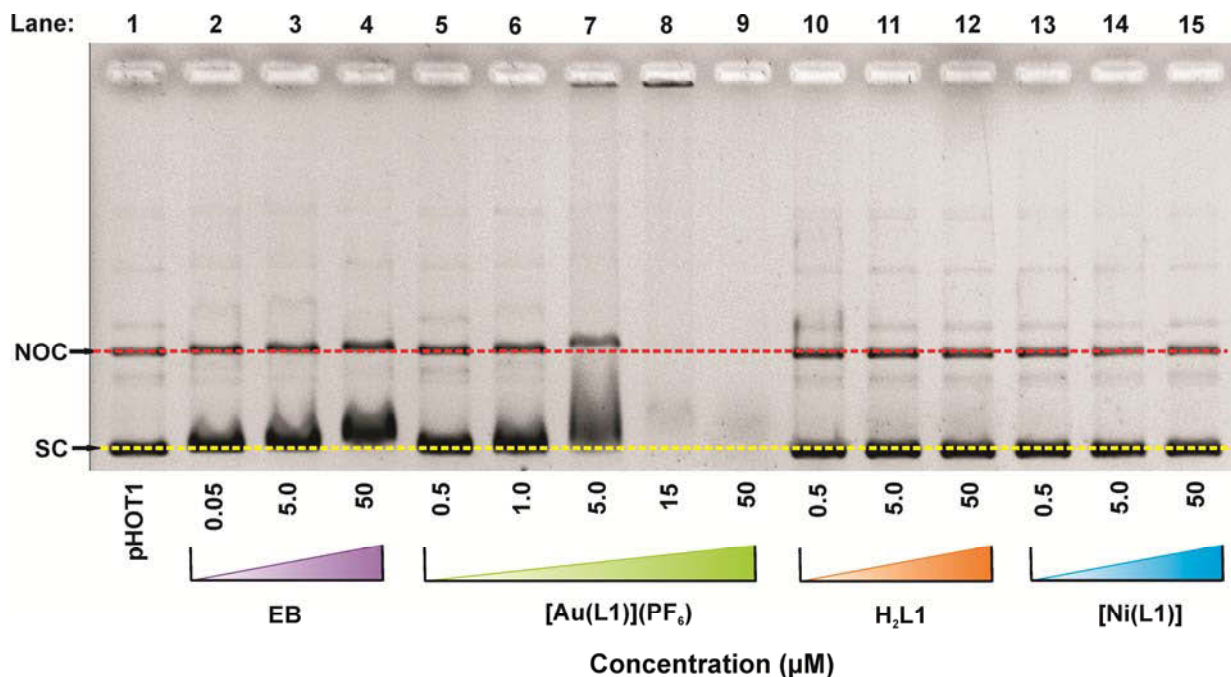


Figure 7.13: Electrophoretic mobility shift assay of selected compounds with supercoiled pHOT1 DNA and Nicked-open circular DNA(NOC).

Prof. Mark Muller has developed a microtiter well-based assay that is capable of distinguishing between TOP1 IFPs and CICs.²⁰ The assay uses genetically-tagged TOP1 to immobilize the enzyme in nickel(II)-coated wells. As discussed above, IFPs trap scDNA-TOP1 cleavage complexes. These cleavage complexes are detected by an enhanced fluorescent signal from picogreen, a DNA sensing dye. TOP1 catalytic inhibitors do not result in covalently trapped DNA and thus lead to diminished emission from the dye with increasing compound concentration. The results of this assay are shown in Figure 7.14.

At concentrations of 100 μM the complexes $[\text{Au}(\text{L1})](\text{PF}_6)$, $[\text{Au}(\text{L2})](\text{PF}_6)$, $[\text{Au}(\text{L3})](\text{PF}_6)$ and $[\text{Au}(\text{L4})](\text{PF}_6)$ give a negative picogreen relative fluorescence. This is similar to the result obtained for the CIC control, mitoxantrone. The other control is the IFP camptothecin which leads to enhanced emission intensity. The assay thus indicates that the complexes: $[\text{Au}(\text{L1})](\text{PF}_6)$, $[\text{Au}(\text{L2})](\text{PF}_6)$ and $[\text{Au}(\text{L3})](\text{PF}_6)$ act as pure catalytic inhibitors of TOP1. $[\text{Au}(\text{L4})](\text{PF}_6)$ has a higher DNA affinity than $[\text{Au}(\text{L2})](\text{PF}_6)$ or $[\text{Au}(\text{L3})](\text{PF}_6)$, but has a weaker response than either of these gold(III) complexes. This could be due to competitive binding of $[\text{Au}(\text{L4})](\text{PF}_6)$ resulting in reduced uptake of the picogreen by the DNA.

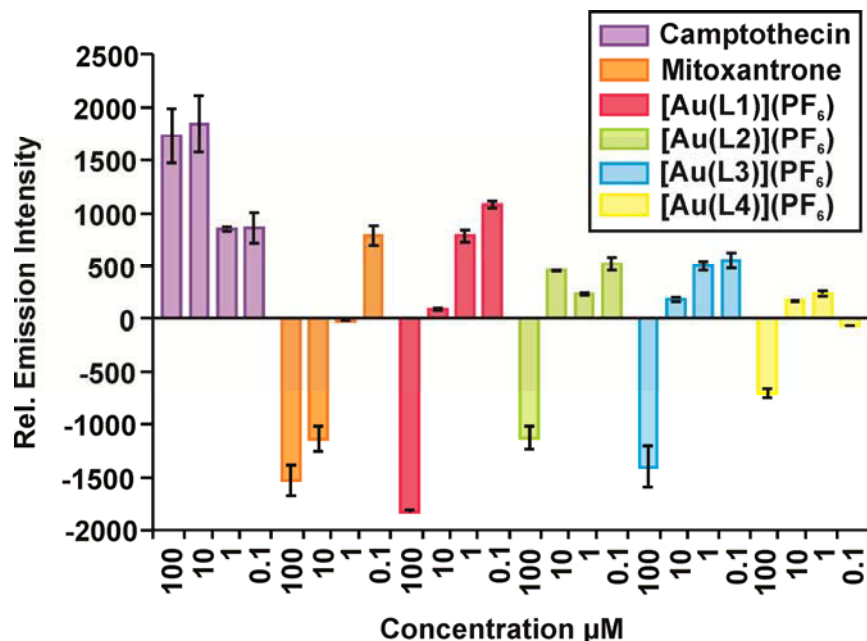


Figure 7.14: Microtiter well-based assay for distinguishing between TOP1 IFPs and CICs.

The preference for the gold(III) complexes to act as catalytic inhibitors of TOP1 rather than poisons was further verified by performing TOP1 DNA relaxation assays, Figure 7.15. In the absence of an IFP or CIC, TOP1 converts scDNA to relaxed DNA as seen by the presence of only nicked-open circular (NOC) DNA. A TOP1 IFP allows the formation of a DNA-TOP1 complex but prevents religation of the double stranded DNA. Thus in the presence of an IFP linear DNA will be detected in the gel assay. A TOP1 CIC prevents the formation of the DNA-TOP1 cleavage complex, thus preventing TOP1 from relaxing the supercoiled DNA. In the presence of a CIC scDNA will be present in the gel assay.

Figure 7.15(a) shows the DNA intercalator control, m-AMSA, in lanes 3-5. At higher concentrations of this compound m-AMSA is shown to inhibit the TOP1 enzyme by the diminishing amount of NOC DNA present and the increasing amount of scDNA present (this is more clearly depicted in Figure 7.13(b), lanes 9-11). Increasing concentrations of the complex $[\text{Au}(\text{L1})](\text{PF}_6)$ have been placed in lanes 6-8 of Figure 7.15(a). It is clear that the complex shows equivalent inhibition of the TOP1 enzyme at one tenth the concentration of the m-AMSA control. At 50 μM of $[\text{Au}(\text{L1})](\text{PF}_6)$ it is clear that the complex inhibits the TOP1 enzyme, indicated by the large amount of scDNA present. Lanes 9-11 and 12-14 of the gel in Figure 7.13(a) show increasing concentrations of $[\text{Ni}(\text{L1})]$ and $\text{H}_2\text{L1}$, respectively. These two compounds induce no change in the DNA shift over the concentration range 0.5 – 50 μM indicating that they do not inhibit the TOP1 enzyme. This again shows the importance of the gold(III) ion to the reactivity of the compounds.

Figure 7.15(b) shows similar results to those described for the $[\text{Au}(\text{L}1)](\text{PF}_6)$ TOP1 DNA relaxation assays in Figure 7.15(a). The TOP1 inhibitor control, m-AMSA (lanes 9-11), shows an increasing amount of scDNA present with increasing concentrations of the compound. In this assay, camptothecin is used as an IFP control (lane 12). This control shows the presence of linear DNA indicating that the DNA has been nicked by TOP1, but not religated. Lanes 3-8 contain increasing concentrations of the gold(III) complex $[\text{Au}(\text{L}3)] \text{PF}_6$. It can be clearly seen that no linear DNA is formed with increasing concentrations of $[\text{Au}(\text{L}3)](\text{PF}_6)$, but there is an increase in the amount of scDNA present. These assays in conjunction with the microtiter assay, show that the gold(III) complexes are catalytic inhibitors of TOP1 rather than poisons.

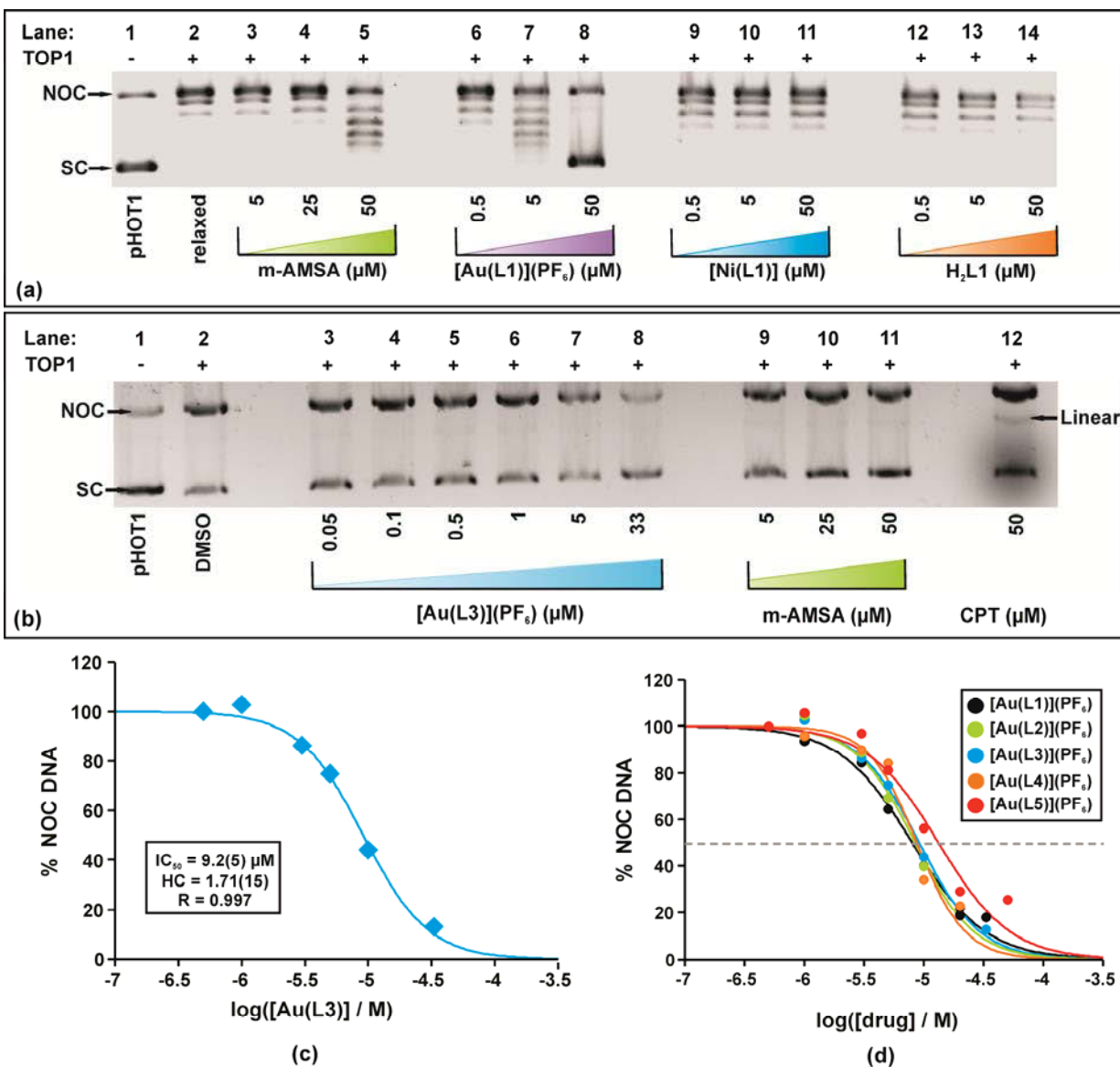


Figure 7.15: TOP1 DNA relaxation assays for (a) $[\text{Au}(\text{L}1)](\text{PF}_6)$, $[\text{Ni}(\text{L}1)]$ and $\text{H}_2\text{L}1$ and (b) $[\text{Au}(\text{L}3)](\text{PF}_6)$. (c) Dose-response function fit for the TOP1 DNA relaxation assay of $[\text{Au}(\text{L}3)](\text{PF}_6)$. (d) Overlapped dose-response function fit for the TOP1 DNA relaxation assay of $[\text{Au}(\text{L}1)](\text{PF}_6)$, $[\text{Au}(\text{L}2)](\text{PF}_6)$, $[\text{Au}(\text{L}3)](\text{PF}_6)$, $[\text{Au}(\text{L}4)](\text{PF}_6)$ and $[\text{Au}(\text{L}5)](\text{PF}_6)$.

Dose response curves were plotted with data from the TOP1 DNA relaxation assays for the five gold(III) complexes: [Au(L1)](PF₆), [Au(L2)](PF₆), [Au(L3)](PF₆), [Au(L4)](PF₆) and [Au(L5)](PF₆), Figure 7.15(c) and (d). These dose response curves are a measure of the percentage of nicked-open circular DNA present with increasing concentrations of the complexes. The curve shows that with subsequent additions of a complex, the percentage of NOC DNA initially remains relatively constant at about 100%, but drops off to 0%. As increasing concentrations of the gold(III) complex are added, it inhibits the functioning of TOP1, as seen from the gels (Figure 7.15 (a) and (b)), this leads to a decrease in the presence of NOC DNA and an increase in the amount of scDNA present.

From the dose response curves, the TOP1 enzyme IC₅₀ values were calculated. These values are recorded in Table 7.5 along with the hill coefficient for each dose response curve. The IC₅₀ value shows the concentration of the complex where there is a 50% reduction in the production of NOC DNA by the TOP1 enzyme. The lower the IC₅₀ value the more effective the complex is as a TOP1 inhibitor, as it indicates that lower concentrations of the drug are required to inhibit the enzyme.

Table 7.5: IC₅₀ values and Hill coefficients determined from dose response curves for TOP1 relaxation assays for [Au(L1)](PF₆), [Au(L2)](PF₆), [Au(L3)](PF₆), [Au(L4)](PF₆) and [Au(L5)](PF₆).*

Complex	IC ₅₀ (μM)	Hill coefficient
[Au(L1)](PF ₆)	8.0(5)	1.43(13)
[Au(L2)](PF ₆)	8.5(6)	1.76(21)
[Au(L3)](PF ₆)	9.2(2)	1.71(15)
[Au(L4)](PF ₆)	8.8(9)	2.15(42)
[Au(L5)](PF ₆)	13(2)	2.45(29)

*Standard deviation for the average is given in parentheses.

In general, the complexes have similar enzyme IC₅₀ values. The complex [Au(L1)](PF₆) has the lowest TOP1 IC₅₀ value of 8.0(5) μM, indicating that this complex is the most effective at inhibiting TOP1. The complex [Au(L5)](PF₆) has the greatest TOP1 IC₅₀ value of 13(2) μM. There appears to be no correlation between DNA binding affinity and the TOP1 IC₅₀ value as [Au(L5)](PF₆) also has the higher apparent DNA binding constant of 2.81 x 10⁶ M⁻¹. A Hill coefficient of less than one indicates negative cooperativity i.e. the binding of one drug molecule by the enzyme substrate reduces its affinity for additional drug molecules. All the Hill coefficients are greater than one which may indicate multiple enzyme binding sites.

DNA decatation assays (kinetoplast DNA) by TOP2 as a function of concentration for [Au(L1)](PF₆), [Au(L2)](PF₆), [Au(L3)](PF₆) were also performed at the University of Central Florida, Figure 7.16. The first four lanes of the gel were set as controls for the experiment. The first lane of the gel contained catenated DNA with no TOP2 present. This is DNA that is interlaced together as links in a chain, it is attached loop to loop (effectively it is supercoiled). As there is no TOP2 present in this lane, the DNA cannot be separated or decatenated and hence there is only one band present. The second lane of the gel contains decatenated DNA and TOP2. This decatanated DNA is in the form of open circular (OC) and closed-covalently circular (CCC) DNA. The third lane contains the solvent control for the decatenated DNA while the fourth lane contains linear DNA. The lane marked VP-16 contains DNA, TOP2 and etoposide (VP-16). The lanes marked 6-14 contain DNA, TOP2 and the gold(III) complex in increasing concentrations.

In the presence of only DNA and the TOP2 enzyme, the TOP2 should form breaks in the double strands of the catenated DNA, thus forming linear DNA. The linear DNA is then religated by TOP2 to form open circular

and closed-covalently circular DNA. Hence in the absence of a TOP2 poison and inhibitor there should be two bands present on the gel; OC and CCC. As a TOP2 inhibitor prevents the formation of the DNA-enzyme complex, no strand-breaks of the catenated DNA should occur in the presence of a TOP2 inhibitor. Thus in the presence of a TOP2 inhibitor, only a band for catenated DNA should be present on the gel. A TOP2 poison on the other hand, allows TOP2 to form a double-strand break leading to the formation of linear DNA but prevents the re-ligation of the DNA. Thus, in the presence of a TOP2 poison, a band for linear DNA should be present on the gel. VP-16 is a commercially available chemotherapeutic agent. The choice of VP-16 as a control is based on the fact that it is a strong TOP2 poison, but is a very weak TOP2 inhibitor. The lane containing VP-16 contains linear DNA and catenated DNA as well as OC and CCC DNA, confirming that it is a TOP2 poison and inhibitor.

At higher concentrations of the complexes (>5 μM), it is clear that only catenated DNA is present and that no NOC or CCC DNA is formed. This indicates that the complexes are all catalytic inhibitors of TOP2. As the TOP2 decatantation assays show an absence of linear DNA in the presence of the gold(III) complexes, this suggests the complexes are not TOP2 poisons.

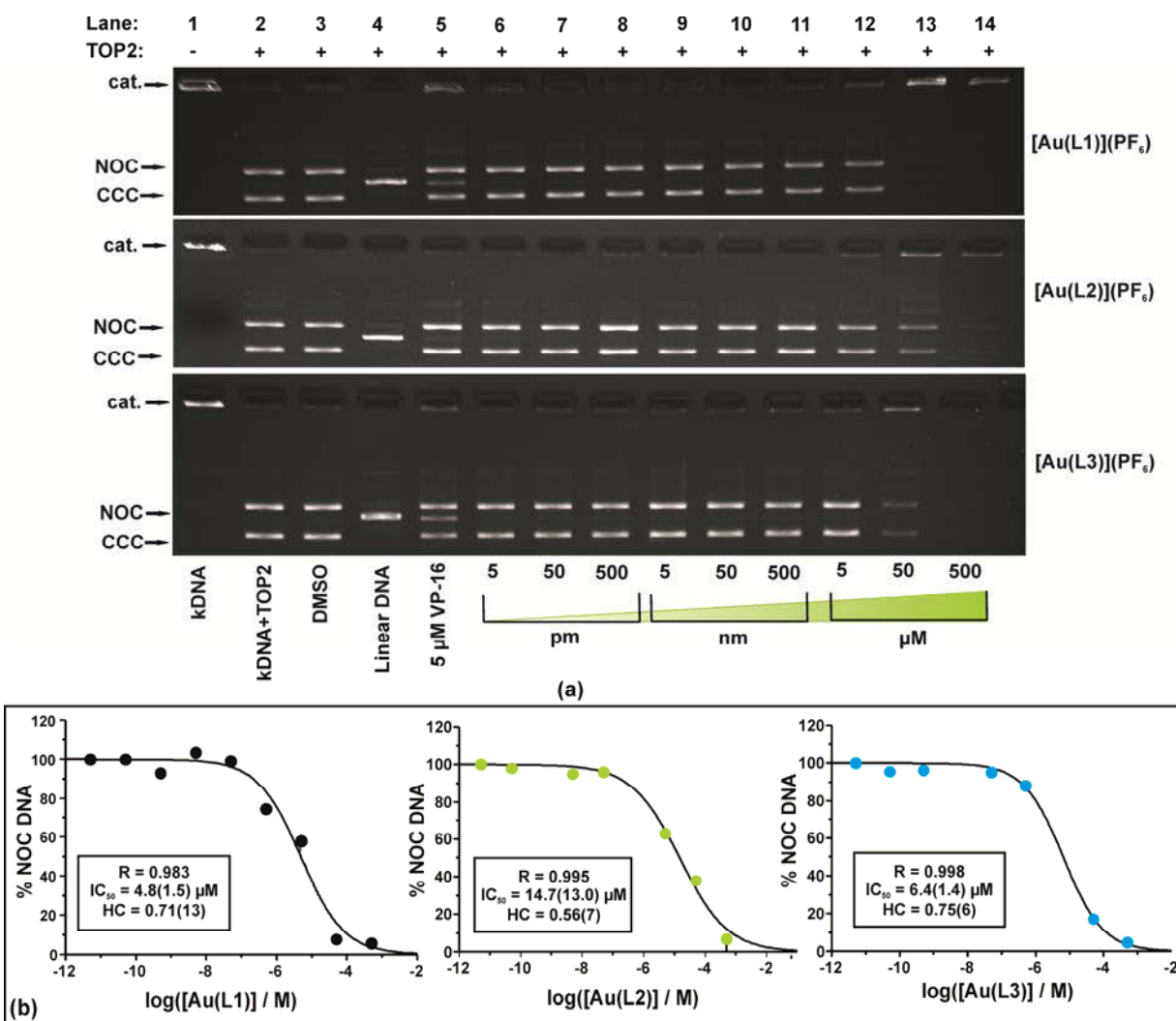


Figure 7.16: (a) TOP2 decatantation assays for [Au(L1)](PF₆), [Au(L2)](PF₆) and [Au(L3)](PF₆). (b) Dose-response curves for the TOP2 decatantation of [Au(L1)](PF₆), [Au(L2)](PF₆) and [Au(L3)](PF₆).

Dose response curves were determined from the TOP2 decatenation DNA relaxation assays for the three gold(III) complexes: [Au(L1)](PF₆), [Au(L2)](PF₆) and [Au(L3)](PF₆), Figure 7.16(b). Similarly to the dose response curves measured for the TOP1 assay, these curves measure the percentage of nicked-open circular DNA present with increasing concentrations of the complexes. The percentage of NOC DNA decreases with increasing concentrations of the gold(III) complexes as they are inhibiting the function of the TOP2 enzyme. From the dose response curves, the IC₅₀ values were calculated. These values are recorded in Table 7.6.

Table 7.6: IC₅₀ values and Hill coefficients determined from dose response curves of TOP2 decatenation assays for [Au(L1)](PF₆), [Au(L2)](PF₆) and [Au(L3)](PF₆).*

Complex	IC ₅₀ (μM)	Hill coefficient
[Au(L1)](PF ₆)	4.8(1.5)	0.71(13)
[Au(L2)](PF ₆)	14.7(3.0)	0.56(7)
[Au(L3)](PF ₆)	6.4(1.4)	0.75(6)

*Standard deviation for the average is given in parentheses.

The compound [Au(L1)](PF₆) has the lowest TOP2 enzyme IC₅₀ value of 4.8 μM. This complex also had the lowest TOP1 enzyme IC₅₀ value. [Au(L2)](PF₆) and [Au(L3)](PF₆) are stronger TOP1 inhibitors than TOP2 inhibitors as they have lower TOP1 enzyme IC₅₀ values. Again there appears to be no direct correlation between DNA binding affinity and the TOP2 IC₅₀ values. All the Hill coefficients are less than one which may indicate a single enzyme binding site.

The AMMP calculations in Chapter Six described the interactions of [Au(L3)](PF₆) with DNA. These calculations showed that [Au(L3)](PF₆) preferentially binds at the TOP1 T10-A11 target and sterically obstructs substrate recognition by displacing R364. Even if TOP1 still managed to bind the DNA with [Au(L3)](PF₆) intercalated at the T10-A11 site, then through the elongation and partial unwinding of the DNA duplex, the covalent cleavage complex could not be formed. These predictions were tested using the technique of surface plasmon resonance (SPR). SPR provides a method for measuring and quantifying equilibrium dissociation constants. This method involved the use of the properties of light reflection (refer to Figure 7.17(a)). A light source is focused at a fixed angle with the incident light ray travelling through a prism until it hits a metal-coated sensor chip.⁴² This will lead to the propagation of an electromagnetic wave in a direction that is parallel to the electromagnetic forces from the chip. The angle of reflection of the light is recorded by a detector after the light travels back through the prism. The angle of reflection is variable and dependent on what is attached to the chip. In a typical SPR experiment, a molecule is covalently conjugated on the topside of the chip and the incident ray is focused on the bottom of the chip.⁴² A buffer containing a second molecule of interest flows over the topside of the chip. Any interaction between the two molecules results in a change of the light reflection angle as the mass on the chip increases.⁴² This change in the light reflection angle is known as a SPR response.

The purpose of the first SPR experiment was to determine whether mTOP1 (a catalytically inactive Y723F TOP1 mutant) is capable of binding to DNA fixed on an SPR chip. The surface of the SPR chip was derivatized with a biotinylated 20-bp DNA duplex and a buffered solution of mTOP1 was allowed to flow over the chip. An SPR response which corresponded to the binding of mTOP1 to the chip (40-100s) followed by saturation (100-160 s) and desorption (>160 s) was obtained. The graph on the right of Figure 7.17(b), shows the SPR response in red when the TOP1 binds the DNA.

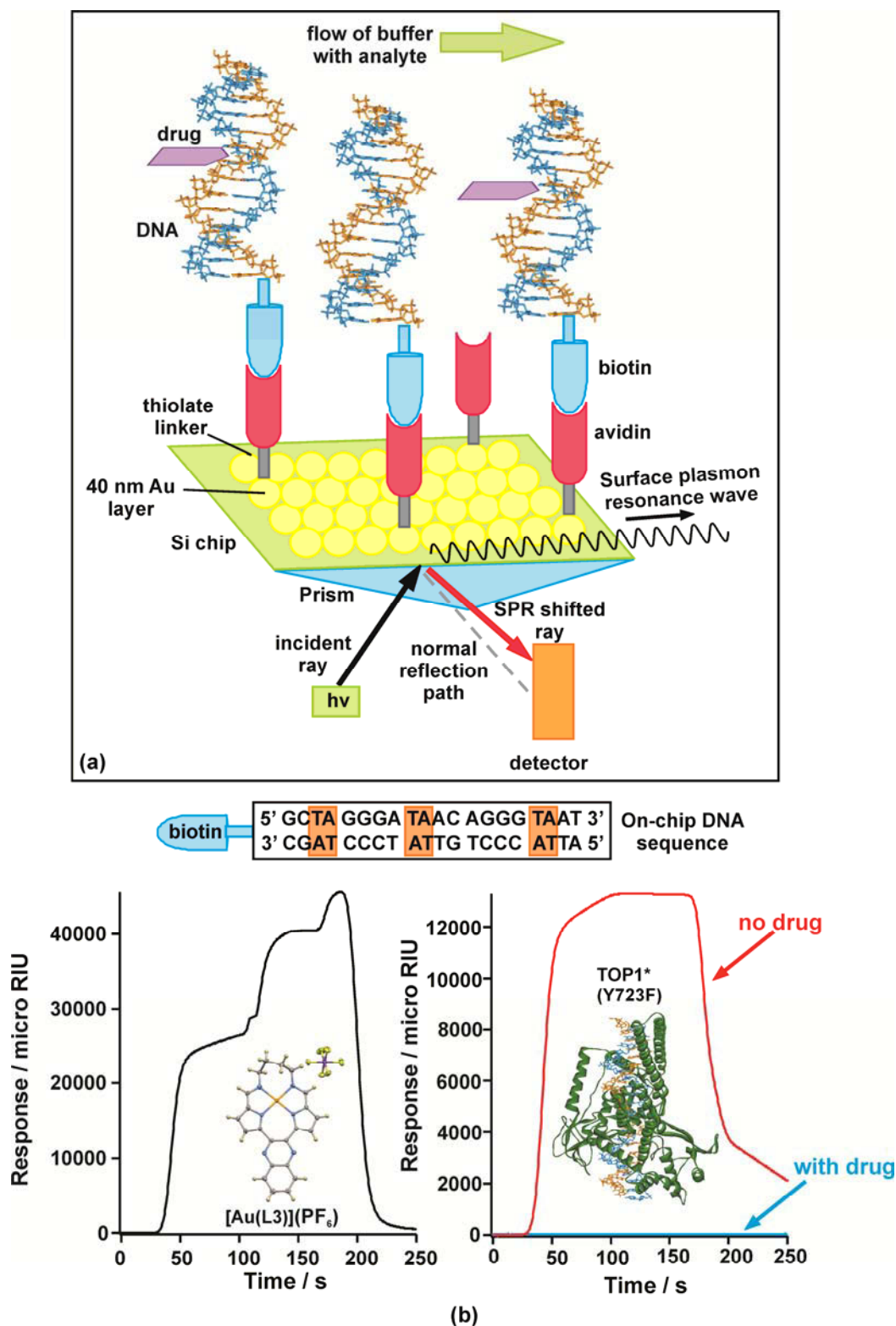


Figure 7.17: (a) Illustration of the key concepts of surface plasmon resonance. (b) On the left, graph showing DNA binding by $[\text{Au}(\text{L}3)](\text{PF}_6)$ and on the right DNA binding by mTOP1 in the presence (blue) and absence (red) of $[\text{Au}(\text{L}3)](\text{PF}_6)$ as determined by SPR. The on-chip duplex DNA sequence is illustrated above the graphs with the enzyme's TA target highlighted.

The second SPR experiment involved flowing a buffered solution of TOP1 and $[\text{Au}(\text{L3})](\text{PF}_6)$ over the chip as before. However, in this case no SPR response was detected (baseline signal). This is consistent with uptake of $[\text{Au}(\text{L3})](\text{PF}_6)$ by the DNA and the inhibition of the enzyme binding to the DNA-complex substrate. The graph on the right of Figure 7.17(b), shows the baseline response in blue when $[\text{Au}(\text{L3})](\text{PF}_6)$ is present with TOP1 and the DNA.

A further experiment was performed whereby a buffered solution containing only the complex $[\text{Au}(\text{L3})](\text{PF}_6)$ was passed over the chip (in the absence of TOP1). Three separate step-wise association response functions were observed. This reflects the presence of the three 5'-TA-3' sites along the 20-bp duplex sequence and that each has a unique microscopic affinity constant. The graph on the left of Figure 7.17(b), shows the stepwise response function of the complex binding to the three 5'-TA-3' sites along the DNA. The same experiments were run for $[\text{Au}(\text{L1})](\text{PF}_6)$. The macroscopic K_D values for $[\text{Au}(\text{L1})](\text{PF}_6)$ and $[\text{Au}(\text{L3})](\text{PF}_6)$ were 2.9 and 15 μM respectively indicating, as confirmed by the apparent DNA binding constants, that $[\text{Au}(\text{L1})](\text{PF}_6)$ binds DNA more strongly than $[\text{Au}(\text{L3})](\text{PF}_6)$.

7.4 Conclusions

Nine of the twelve gold(III) complexes synthesized have been selected by the NCI for single-dose screening against their panel of sixty human cancer cell lines. This data shows that macrocyclic gold(III) complexes are all active against central nervous system cancer cell lines, but are predominantly inactive against colon and melanoma cell lines. The pseudomacrocyclics are active against colon, leukemia and renal cancer cell lines, but inactive against prostate and CNS cell lines. This indicates that small modifications in the structure of the complex can result in significant changes to the cytotoxicity profile of a complex.

Six complexes out of the nine selected for single-dose screens were selected for five-dose screens. The complex $[\text{Au}(\text{L3})](\text{PF}_6)$ had an IC_{50} value of 16.0(2) μM which is the lowest mean IC_{50} value for the gold(III) macrocyclic complexes. The pseudomacrocyclic complex $[\text{Au}(\text{L11})](\text{PF}_6)$ had the lowest mean IC_{50} value, 5.6(4) μM , of all tested complexes. These IC_{50} values are lower than the mean IC_{50} value of cisplatin which is 27.0(5) μM showing that on average the complexes are more effective than cisplatin. The NCI selected the gold(III) complex $[\text{Au}(\text{L3})](\text{PF}_6)$ to go through to the acute toxicity determination and then to the hollow fibre assay. The hollow fibre assay showed that the cytotoxicity of the chelate was greatly reduced in a live animal environment.

The complexes $[\text{Au}(\text{L9})](\text{PF}_6)$ and $[\text{Au}(\text{L12})](\text{PF}_6)$ were not selected by the NCI for screening. These complexes were sent to the Advanced Materials Division at MINTEK in South Africa to be screened against four human cancer cell lines. In general the two complexes screened by MINTEK compare favourably to the gold(III) complexes screened by the NCI. The acyclic complex showed similar activity to the pseudomacrocyclic and macrocyclic complexes.

A hierarchical cluster analysis using the NCI data for a number of complexes with a known mechanism of action showed that $[\text{Au}(\text{L3})](\text{PF}_6)$ clusters with topotecan and camptothecin. Camptothecin and topotecan are well known interfacial poisons of TOP 1.^{3,6,27} $[\text{Au}(\text{L3})](\text{PF}_6)$ also clusters with Zorubicin which acts as a TOP2 inhibitor. This cluster analysis suggests that $[\text{Au}(\text{L3})](\text{PF}_6)$ is possibly a TOP1 poison and/or a TOP2 inhibitor.

At the University of Central Florida, electrophoretic mobility shift assays (EMSAs) were performed to prove that the gold(III) complexes interact with the DNA via intercalation. The assay showed that $[\text{Au}(\text{L1})](\text{PF}_6)$ has a more pronounced mobility shift than EB. The large mobility shifts for the scDNA caused by $[\text{Au}(\text{L1})](\text{PF}_6)$ are due to elongation of the DNA duplex due to intercalation of the gold(III) complex. The macrocyclic ligand, $\text{H}_2\text{L1}$, and the nickel(II) analogue of $[\text{Au}(\text{L1})](\text{PF}_6)$ were also run on the electrophoretic mobility shift assay. Neither the free ligand nor the nickel(II) complex induced a mobility shift. This indicates that the gold(III) ion is essential for DNA intercalation.

A new microtiter well-based assay that is capable of distinguishing between TOP1 poisons and inhibitors was used to test the gold(III) complexes. The gold(III) complexes gave similar results to those obtained for the inhibitor control, mitoxantrone. This experiment showed that the gold(III) complexes are catalytic inhibitors of TOP1. The preference for the gold(III) complexes to act as catalytic inhibitors of TOP1 rather than poisons was further verified by performing TOP1 DNA relaxation assays. In the presence of the complexes TOP1 could not produce linear DNA. DNA decantation assays (kinetoplast DNA) by TOP2 as a function of concentration of the gold(III) complexes were also performed. This assay showed that the complexes were also catalytic inhibitors of TOP2 and not TOP2 poisons. This could be deduced by the presence of catenated DNA and the absence of linear DNA.

Surface Plasmon resonance was used to show that $[\text{Au}(\text{L3})](\text{PF}_6)$ preferentially binds at the TOP1 T10-A11 target and sterically obstructs substrate recognition by the enzyme. In the presence of only the DNA and complex, three clear stepwise responses were observed where the complex binds at the three T-A sites in the DNA. In the presence of the DNA and mTOP1 enzyme, an SPR response was obtained which corresponded to the binding of mTOP1 to the DNA. In the presence of the DNA, mTOP1 enzyme and gold(III) complex, no SPR response was detected. This is consistent with uptake of $[\text{Au}(\text{L3})](\text{PF}_6)$ by the DNA and the inhibition of the enzyme binding to the DNA-complex substrate. Thus the data supports the molecular mechanics calculations discussed in Chapter Six.

7.5 References

- (1) National Cancer Institute; <http://dtp.nci.nih.gov/branches/btb/ivclsp.html> 2012.
- (2) Developmental Therapeutics Programme; <http://dtp.nci.nih.gov> 2012.
- (3) Patrick, G. L. *An Introduction to Medicinal Chemistry, third edition*; Oxford University Press: New York, 2005.
- (4) Kostova, I. *Anticancer Agents Med. Chem.* **2006**, *6*, 19.
- (5) Montaner, B., Castillo-Ávila, W., Martinell, M., Öllinger, R., Aymami, J., Giralt, E., Pérez-Tomás, R. *Tox. Sci.* **2005**, *85*.
- (6) Thurston, D. E. *Chemistry and Pharmacology of Anticancer Drugs*; Taylor & Francis Group: USA, 2007.
- (7) V. Miliacic, D. C., L. Ronconi, K. R. Landis-Piwowar, D. Fregona, Q. P. Dou *Cancer Res.* **2006**, *66*, 10478.
- (8) Danko, P., Kozák, A., Podhradský, D., Viglaský, V. *J. Biochem., Mol. Biol. Biophysics* **2005**, *65*, 89.
- (9) Sun, R. W.-Y., Li, C. K.-L., Ma, D. L., Yan, J. J., Lok, C.-N., Leung, C.-H., Zhu, N., Che, C.-M. *Chem. Eur. J.* **2010**, *16*, 3097.
- (10) Gabbiani, C., Casini, A., Messori, L. *Gol Bull.* **2007**, *40*, 73.
- (11) Messori, L., Marcon, G., Orioli, P., Cinellu, M. A., Minghetti, G. *Eur. J. Biochem.* **2003**, 4655.
- (12) Coronello, M., Mini, E., Caciagli, B., Cinellu, M. A., Bindoli, A., Gabbiani, C., Messori, L. *J. Med. Chem.* **2005**, *48*, 6761.
- (13) Rigobello, M. P., Messori, L., Marcon, G., Bragadin, M., Folda, A., Scutari, G., Bindoli, A. *J. Inorg. Biochem.* **2004**, *98*, 1634.
- (14) Rigobello, M. P., Scutari, G., Folda, A., Bindoli, A. *Biochem. Pharmacol.* **2004**, *67*, 689.
- (15) Omata, Y., Folan, M., Shaw, M., Messer, R. L., Lockwood, P. E., Hobbs, D., Bouillaguet, S., Sano, H., Lewis, J. C., Wataha, J. C. *Toxicol. In Vitro* **2006**, *20*, 882.
- (16) Turk, V., Turk, B., Turk, D. *J. EMBO* **2001**, *20*, 4629.
- (17) Chircorian, A., Barrios, A. M. *Bioorg. Med. Chem. Lett.* **2004**, *14*, 5113.
- (18) Fricker, S. P., Skerjil, R., Cameron, B. R., Mosi, R., Zhu, Y. *Recent Developments in Gold Drugs 2003*; AnorMED Inc: Canada, 2003.
- (19) Origin 6.1 *OriginLab* **2000/9**.
- (20) Cyril, V. M., M. T. *Anal. Biochem.* **2012**, *421*, 607.
- (21) Schneider, C. A., Rasband, W. S., Eliceiri, K. W. *Nat. Methods* **2012**, *9*, 671.
- (22) *KyPlot 5.0.2: Data Analysis and Visualization v. 5.0.2 (KyenceLab Inc., 2011)*.
- (23) Garrett, R. H., Grisham, C. M. *Biochemistry, 2nd edition*; Saunders College Publishing, 1999.
- (24) Prasad, R., Gaur, N. A., Gaur, M., Komath, S. S. *Infectious Disorders - Drug Targets* **2006**, *6*, 69.
- (25) Gupta, A. K., Katoch, V. M., Chauhan, D. S., Sharma, R., Singh, M., Venkatesan, K., Sharma, V. D. *Microbial Drug Resistance* **2010**, *6*, 21.
- (26) Lopez-Ribot, J. L., McAtee, R. K., Lee, L. N., Kirkpatrick, W. R., White, T. C., Sanglary, D., Patterson, T. F. *Anti-microb. Agents Chemother.* **1998**, *42*, 2932.
- (27) Patterson, A. V., Saunders, M. P., Chinje, E. C., Patterson, L. H., Stratford, I. J. *Anti-Cancer Drug Des.* **1998**, *13*, 541.
- (28) Pommier, Y. *Nature Rev.* **2006**, *6*, 789.
- (29) Pommier, Y. *Chem. Rev.* **2009**, *109*, 2894.
- (30) Koster, D. A., Croquette, V., Dekker, C., Shuman, S., Dekker, N. H. *Nature Lett.* **2005**, *434*, 671.
- (31) Koster, D. A., Palle, K., Bot, E. S. M., Bjornsti, M.-A., Dekker, N. H. *Nature Lett.* **2007**, *448*, 214.
- (32) Stewart, L., Redinbo, M. R., Qiu, X., Hol, W. G., Champoux, J. J. *Science* **1998**, *279*, 1534.
- (33) Denny, W. A. *Expert Opin. Investig. Drugs* **1997**, *6*, 1845.
- (34) Solary, E., Dubrez, L., Eymen, B., Bertrand, R., Pommier, Y. *Bull. Cancer* **1996**, *83*, 205.
- (35) Pommier, Y., Covey, J. M., Kerrigan, D., Markovits, J., Pham, R. *Nucleic Acids Res.* **1987**, *15*, 6713.
- (36) Webb, M. R., Ebeler, S. E. *Biochem. J.* **2004**, *384*, 527.
- (37) McKnight, R. E., Onogul, B., Polasani, S. R., Gannon, M. K., 2nd, Detty, M. R. *Bioorg. Med. Chem.* **2008**, *16*, 10221.

- (38) Winkler, D. *Biorg. Med. Chem.* **2011**, *19*, 1450.
(39) Hotzel, C., Marotto, A., Pindur, U. *Eur. J. Med. Chem.* **2003**, *38*, 189.
(40) Che, C.-M., Sun, R. W.-Y., Yu, W.-Y., Ko, C.-B., Zhu, N., Sun, H. *Chem. Commun.* **2003**, *14*, 1718.
(41) Sun, R. W.-Y., Che, C.-M. *Coord. Chem. Rev* **2009**, *253*, 1682.
(42) Tlili, A. *Sensors* **2004**, *4*, 105.

CHAPTER EIGHT:

CONCLUSIONS & FUTURE WORK

8.1 Conclusions

In this work a range of bis(pyrrolide-imine) macrocyclic, pseudomacrocyclic and acyclic ligands have been synthesized. These ligands have been chelated to gold(III) to produce twelve novel complexes. The gold(III) complexes were synthesized with the ultimate aim of producing a new class of potential anti-cancer agents that exert their cytotoxicity through DNA intercalation and the inhibition of DNA-regulating enzymes such as the topoisomerase group of enzymes. Inhibition of these enzymes hampers DNA transcription and replication, which ultimately culminates in apoptosis. The gold(III) chelates were designed to incorporate key design features of commercially available DNA intercalators such as daunorubicin. These features include a large planar aromatic region and an overall positive charge while some of the complexes contain an additional hydrogen bonding region.

The macrocyclic ligands consist of a pair of pyrrole rings joined through a di(azomethine) linkage at the 2-position and a quinoxaline or pyrazine tail in the 5-position; this forms a completely closed structure. The pseudomacrocyclic ligands have a pair of pyrrole rings joined at one end by a quinoxaline tail, but instead of a di(azomethine) linkage completing the macrocycle, they are left open with methyl and ethyl groups joined to the imine moieties. The structure of the ligands was varied through transformations of the di(azomethine) linkage as well as variation of the quinoxaline tail. A Schematic diagram of the gold(III) complexes synthesized is depicted in Figure 8.1.

The macrocyclic and pseudomacrocyclic ligands were synthesized in a four step reaction pathway involving: electrophilic substitution, condensation and Vilsmeier formylation reactions. It was found that these ligands were sufficiently strong π -acceptor and σ -donor ligands to stabilize the gold(III) ion in its high oxidation state. Most of the complexes could be synthesized by metallation of the free ligands with gold(III) directly; however, macrocyclic ligands with substituents on the second carbon of the propyl bridge and those with longer four-carbon bridging groups had to be synthesized by template reactions. Chelation of the metal ion required concomitant deprotonation of the NH groups, resulting in a tetradentate, dianionic ligand. Chelation of the dianionic ligands to gold(III) yielded a monocationic chelate, ideal for interacting with DNA which carries an overall positive charge.

Through the use of single crystal X-ray diffraction, the solid-state structures of nine of the metal free ligands were determined. These ligands include: H₂L2, H₂L5, H₂L6, H₂L7, H₂L8a, H₂L8b, H₂L8c, H₂L9 and H₂L12. The X-ray structures of the macrocyclic compounds are expected to be planar due to the extended aromaticity. This was generally true; however, these compounds all exhibit a slightly domed configuration with the pyrrole rings canted relative to the quinoxaline or pyrazine tail. This doming effect is also observed in other highly conjugated π -systems such as gold(III) porphyrins.^{1,2} The pseudomacrocyclic ligand, H₂L9, is more planar than the true macrocycles. This is attributed to the release of intrinsic structural strain associated with the pseudomacrocycle compared to the genuine macrocycle.

The imine bond distances for all the macrocyclic and pseudomacrocyclic compounds are similar to the standard imine bond length (1.279 \AA)³. Interestingly the $C_{\alpha}-C_{\beta}$ bond lengths ($1.404-1.413 \text{ \AA}$) for the pyrrole rings are longer than the standard value of 1.375 \AA while the $C_{\beta}-C_{\beta}$ bond lengths ($1.375-1.386 \text{ \AA}$) are shorter than the standard value of 1.412 \AA .³ This suggests delocalisation of electron density over the pyrrole ring. The $C=N_{\text{imine}}-C$ bond angle is very similar for all the macrocyclic ligands as they all have a three carbon di(azomethine) linkage. The pseudomacrocyclic ligand, H₂L9, has a smaller $C=N_{\text{imine}}-C$ bond angle, $118.9(1)^{\circ}$, than the macrocyclic compounds. As this bond angle is not determined by the length of the di(azomethine) linkage, it is able to adopt an angle which more closely approaches the ideal angle for an sp^2 hybridized N atom, i.e. 120° .

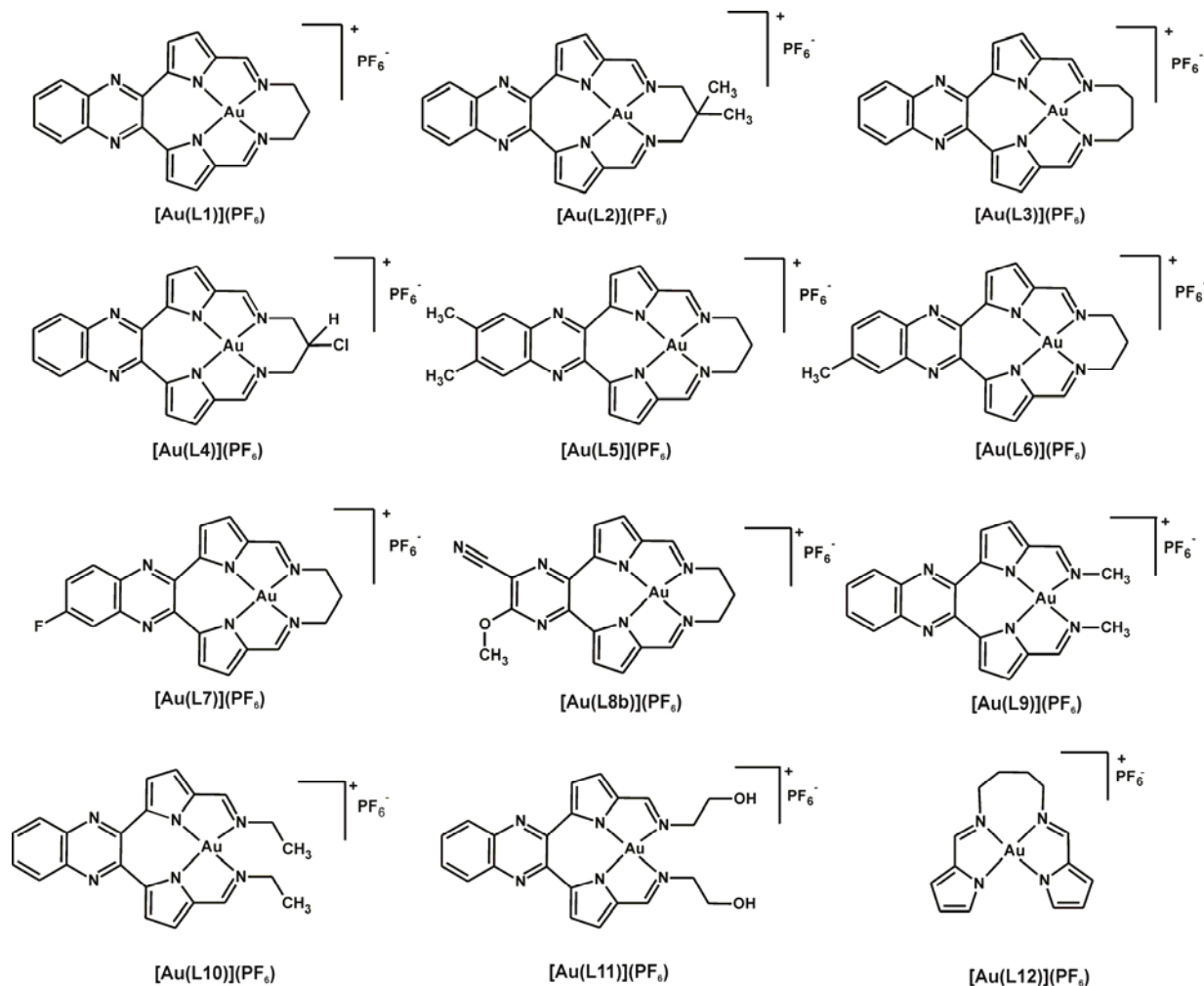


Figure 8.1: Schematic diagram of the gold(III) complexes synthesized in this work.

The X-ray structures highlighted an interesting feature of the macrocyclic and pseudomacrocyclic compounds; the pyrrole N atoms are not both protonated in the solid state. The X-ray data show, in the form of a peak of electron density, that one pyrrole N atom and the diagonally opposite imine N atom are protonated. This is in contrast to the acyclic Schiff base compounds which usually show both hydrogen atoms located on the pyrrole N atoms.⁴⁻⁷ The reported macrocyclic compounds are rigid and cannot adopt a linear configuration and thus protonation of both pyrrolide N atoms would lead to considerable non-bonded

repulsion. Thus, the configuration with the diagonally opposite N atoms protonated is favoured as the steric strain is minimized. H₂L9 does not adopt a linear configuration, but rather a more compact, closed configuration, a true pseudomacrocyclic and thus also has diagonally opposite N atoms protonated. All the macrocyclic and pseudomacrocyclic compounds show two intramolecular hydrogen bonds. The first hydrogen bond has the pyrrole N–H acting as the hydrogen bond donor and the opposite pyrrole N atom acting as the hydrogen bond acceptor. The second hydrogen bond comprises the imine N–H acting as the hydrogen bond donor and the opposite imine N atom acting as the hydrogen bond acceptor.

Five solid-state structures of the gold(III) bis(pyrrolide-imine) Schiff base chelates were also studied by X-ray crystallography. These structures included: [Au(L1)](PF₆), [Au(L2)](CF₃SO₃), [Au(L3)](PF₆), [Au(L10)](AuCl₄) and [Au(L12)](PF₆). The gold(III) ion sits in the plane defined by the four coordinating N atoms, adopting a nominally square-planar coordination geometry. All the gold(III) complexes deviate from planarity to varying extents. The out-of-plane displacements of the rings may be the result of π – π interactions between two neighbouring molecules positioned in close proximity and in a co-planar orientation. In general the complexes are, however, approaching planarity with the exception of the bis(imine) linkage which sits out-of-plane of the complexes. It is important that these complexes are nearly planar as they have been designed as DNA intercalators.

The coordination geometry about the gold(III) ion is approximately square-planar in all cases. This is illustrated by the N–Au–N bond angles for the complexes which are approaching 90° as well as the Au–N distances which are all approximately equal, falling in the range of 1.98–2.06 Å. The average Au–N_{pyrrole} distance for the gold(III) complexes is 1.98(3) Å while the Au–N_{imine} bond distances average 2.03(6) Å. These bond distances are consistent with comparable Au–N bond distances reported in literature, which fall in the range of 1.928–2.216 Å.⁸ Both of the butyl-bridged complexes have larger N_{imine}–Au–N_{imine} bond angles than the propyl bridged complexes. This is because the longer bridge forces the imine N atoms further apart thus changing the bite angle of the ligand. The pseudomacrocyclic complex has no di(azomethine) bridging unit restricting the angle; it therefore exhibits the largest N_{imine}–Au–N_{imine} bond angle of all the complexes.

Very few true intermolecular hydrogen bonds are observed for any of the complexes. This is due to the fact that there are no suitable hydrogen bond donor or acceptor groups positioned on the periphery of the molecules. Although devoid of true hydrogen bonds, the complexes exhibit several weak electrostatic interactions. As the molecules are relatively planar they all exhibit π – π and Au– π interactions which is important for potential DNA intercalation as these interactions will stabilize the DNA-drug conjugate.

The ligands and complexes were fully characterized using Nuclear Magnetic Resonance (NMR), UV/visible and infrared spectroscopy as well as mass spectrometry (MS). These techniques were used to ensure metal chelation had been successful and to investigate interesting structural features of the compounds. Infrared spectroscopy indicated that chelation of the gold(III) ion to the ligand had taken place as the imine (C=N) shift in the range of 1690–1600 cm⁻¹,⁹ underwent a large spectral shift when the ligand was chelated. The pyrrole N–H band also disappeared on chelation.

The ¹H and ¹³C NMR spectra of the gold(III) complexes both showed a downfield shift of their signals in comparison to the free ligand spectra. This result is consistent with the highly polarising and deshielding effect of the gold(III) ion. The same tautomeric form of the ligand present in the solid state with one pyrrole N atom and the diagonally opposite imine N atom protonated, appears to be favoured in solution. The NMR

spectra for the ligands show a peak at *ca.* 11 ppm corresponding to a single imine N–H and another peak at *ca.* 18 ppm corresponding to a pyrrole N–H proton. Neither of these peaks is present in the ^1H NMR spectra of the gold(III) complexes as the protons are lost during metal chelation. Most of the ligands and gold(III) complexes are symmetric with the protons and carbon atoms on each side of the molecule in equivalent chemical environments. This results in a single signal for two equivalent protons in the NMR spectra. The quinoxaline-based macrocycles and complexes $\text{H}_2\text{L6}$, $\text{H}_2\text{L7}$, $[\text{Au}(\text{L4})](\text{PF}_6)$, $[\text{Au}(\text{L6})](\text{PF}_6)$ and $[\text{Au}(\text{L7})](\text{PF}_6)$ are asymmetric. This results in splitting of the ^1H and ^{13}C signals of the atoms on either side of the compound.

The ligands and complexes synthesized have large aromatic chromophores and extended conjugation, resulting in complex absorption spectra. The spectra of the ligands are dominated by $\pi \rightarrow \pi^*$ transitions with all the bands in the UV/vis spectra of the macrocyclic and pseudomacrocyclic ligands being of this type. The quinoxaline-based macrocyclic and pseudomacrocyclic gold(III) complexes have very similar electronic spectra. The electronic spectra of the gold(III) complexes are different to those of the ligands with an increase in the number of bands observed. Substitution on the quinoxaline ring appears to have little impact on the electronic spectra of the complexes, as was the case with the ligands. Based on both DFT calculations and literature information, the bands in the region 450 to 480 nm of the complexes are most likely LMCT bands; the more intense bands below 400 nm are attributed to $\pi \rightarrow \pi^*$ transitions and $\pi \rightarrow \sigma^*$ transitions.

The lipophilicity of the compounds, as measured by $\log P_{o/w}$, range from -0.58(1) to +1.468(3). The order of lipophilicity from most hydrophilic to most hydrophobic compound is as follows: $[\text{Au}(\text{L12})](\text{PF}_6)$, $[\text{Au}(\text{L11})](\text{PF}_6)$, $[\text{Au}(\text{L1})](\text{PF}_6)$, $[\text{Au}(\text{L3})](\text{PF}_6)$, $[\text{Au}(\text{L2})](\text{PF}_6)$, $[\text{Au}(\text{L6})](\text{PF}_6)$, $[\text{Au}(\text{L8b})](\text{PF}_6)$, $[\text{Au}(\text{L4})](\text{PF}_6)$, $[\text{Au}(\text{L9})](\text{PF}_6)$, $[\text{Au}(\text{L7})](\text{PF}_6)$ and $[\text{Au}(\text{L10})](\text{PF}_6)$. All the macrocyclic and pseudomacrocyclic chelates have a high affinity for octanol. This result is expected as the complexes consist of a large organic ligand as well as a bulky hexafluorophosphate(V) counter ion which will lead to increased hydrophobicity. This large positive $\log P_{o/w}$ indicates that the complexes should move readily from the blood serum to the cell membrane. This suggests that the complexes should be able to effectively reach their intended cellular target: DNA. It was also shown that the hydrophobicity of the chelates could be tuned through small changes in the structure of the compounds.

The DNA binding of $\text{H}_2\text{L1}$, $[\text{Au}(\text{L1})](\text{PF}_6)$, $[\text{Au}(\text{L2})](\text{PF}_6)$, $[\text{Au}(\text{L3})](\text{PF}_6)$ was investigated using thermal DNA denaturation studies. The gold(III) complexes all caused an increase in the melting temperature of the DNA at increased concentrations. These results indicate that the complexes are interacting with the DNA and stabilizing it due to increased intermolecular interactions which lead to an increase in the melting point temperature of the DNA. The free ligand, $\text{H}_2\text{L1}$, had little effect on the melting temperature of the DNA which shows that the gold(III) ion is important for interaction with the DNA.

Fluorescence competitive binding DNA titrations were done to determine the affinity of the gold(III) macrocycles for ctDNA. On the addition of increasing concentrations of the complexes to the solution of EB and DNA there was quenching of the initial EB-DNA emission intensity by *ca.* 75 %. This indicates that the complexes bind efficiently and out-compete the EB for binding sites on the DNA. The K_{app} of the complexes range from $4.88 \times 10^5 \text{ M}^{-1}$ to $6.61 \times 10^6 \text{ M}^{-1}$. The gold(III) macrocyclic and pseudomacrocyclic complexes have a relatively high affinity for DNA while the acyclic complex has the lowest DNA affinity. The order of the metal chelates in terms of binding strengths is, from strongest to weakest: $[\text{Au}(\text{L11})](\text{PF}_6) > [\text{Au}(\text{L7})](\text{PF}_6) > [\text{Au}(\text{L9})](\text{PF}_6) > [\text{Au}(\text{L6})](\text{PF}_6) > [\text{Au}(\text{L10})](\text{PF}_6) > [\text{Au}(\text{L8b})](\text{PF}_6) > [\text{Au}(\text{L5})](\text{PF}_6) > [\text{Au}(\text{L1})](\text{PF}_6) > [\text{Au}(\text{L4})](\text{PF}_6) > [\text{Au}(\text{L2})](\text{PF}_6) > [\text{Au}(\text{L3})](\text{PF}_6) > [\text{Au}(\text{L12})](\text{PF}_6)$.

Using the binding constants, $\log P_{o/w}$ values and bridge volumes of $[\text{Au(L1)}](\text{PF}_6)$, $[\text{Au(L2)}](\text{PF}_6)$, $[\text{Au(L3)}](\text{PF}_6)$, $[\text{Au(L4)}](\text{PF}_6)$ and $[\text{Au(L5)}](\text{PF}_6)$, it was determined that the binding constant increases with increasing drug hydrophobicity and decreasing bulk of the bridging unit. This meant that by decreasing the bridge volume of the complex and increasing the hydrophobicity of the complexes, the apparent binding constant could be increased.

The macrocyclic complexes were tested for reduction by glutathione, but as the complexes precipitated out of solution, no rate constant could be measured. However, the complexes appear to be stable to glutathione reduction with the spectra indicating that only precipitation occurs over time rather than precipitation and reduction. The stability of the complexes is due to the macrocyclic ligands that stabilize the gold(III) ion.

Density functional theory (DFT) methods were used to calculate several properties of both the gold(III) chelates and the metal free ligands. The theoretical data were then compared to the experimental data where possible to ascertain the effectiveness of the basis set and hybrid functional used, as well as to better understand the experimental phenomena that were observed. The level of theory used was as follows: for the metal chelates PBE1PBE/LANL2DZ and for the metal-free ligands B3LYP/6-311G(d,p). The geometry optimised structures as well as the NMR, vibrational and electronic spectra were calculated.

The geometry optimization calculations were done for all the possible tautomers of the ligands. The results showed that the tautomer with the pyrrole N atom and the diagonally opposite imine N atom protonated was in very good agreement with the experimental X-ray diffraction data, as seen by the RMSD values of the calculated and experimental data. This was also the lowest energy tautomeric form.

The vibrational frequencies of the gold(III) chelates and metal-free ligands both showed no negative eigenvalues indicating that a true minimum on the global potential energy surface had been reached and the geometry optimised structure was most likely a global energy minimum. Comparison of the calculated vibrational frequencies and experimental FTIR spectra for both the ligands and complexes showed that the DFT simulations consistently overestimated the vibration frequencies. Despite the error in estimation of the absolute value of the absorption bands, the relative intensity of the bands was in good agreement with the experimental data, especially for the gold(III) complexes.

The experimental and calculated electronic spectra of the ligands compared favourably. The main transitions for all the ligands are σ , $\pi \rightarrow \pi^*$ and $\pi \rightarrow \pi^*$ transitions. The calculated electronic spectra of the gold(III) complexes show larger deviations in the absolute values of the wavelengths compared to the experimental data than was noted for the ligands. The calculated molecular orbitals show that they are all mixed, with contributions from both the ligand and metal.

The ^{13}C and ^1H NMR data were calculated for the ligands and gold(III) chelates. The calculations of the macrocyclic ligands predict the experimental NMR results well with the percentage differences between the experimental and calculated results being minimal. The calculations of the pseudomacrocyclic ligands do not compare as favourably with the experimental data suggesting that these ligands may adopt a different tautomeric form in solution. The calculated NMR data for the complexes compared reasonably favourably with the experimental chemical shifts but the results could be improved by using a split basis set.

Prof. O. Q. Munro developed new SP4 molecular mechanics (MM) force field parameters to determine the energetically preferred DNA binding site for $[\text{Au}(\text{L}3)]^+$, using a 22-base pair duplex favoured by TOP1. It was determined that $[\text{Au}(\text{L}3)]^+$ binds in the major groove at an adjacent T10-A11 base pair in dsDNA. This is also the cut-site of TOP1. When the complex is bound in this site, it prevents Arg364 of the TOP1 enzyme from recognizing the adenine base in the TA base pair by steric repulsion from the quinoxaline ring which projects into the minor groove. Binding of the complex also induces elongation at the intercalation site of the DNA. This displaces the scissile strand downstream so that Tyr723 is too far away to form a covalent P-O-C link to the enzyme. This model suggests that the complex will be a catalytic inhibitor of TOP1.

Nine of the twelve gold(III) complexes synthesized were selected by the NCI for single-dose screening against their panel of sixty human cancer cell lines. These complexes are: $[\text{Au}(\text{L}1)](\text{PF}_6)$, $[\text{Au}(\text{L}2)](\text{PF}_6)$, $[\text{Au}(\text{L}3)](\text{PF}_6)$, $[\text{Au}(\text{L}4)](\text{PF}_6)$, $[\text{Au}(\text{L}5)](\text{PF}_6)$, $[\text{Au}(\text{L}6)](\text{PF}_6)$, $[\text{Au}(\text{L}7)](\text{PF}_6)$, $[\text{Au}(\text{L}10)](\text{PF}_6)$ and $[\text{Au}(\text{L}11)](\text{PF}_6)$. The first stage of the screening process is a single-dose screen at a concentration of 10 μM . These tests showed that some of the complexes were indeed highly cytotoxic and were in many cases more cytotoxic than the ubiquitous chemotherapeutic agent, cisplatin. The results of the single-dose screens are as follows from the most cytotoxic to the least cytotoxic compound: $[\text{Au}(\text{L}11)](\text{PF}_6) > [\text{Au}(\text{L}10)](\text{PF}_6) > [\text{Au}(\text{L}3)](\text{PF}_6)$, $[\text{Au}(\text{L}6)](\text{PF}_6) > [\text{Au}(\text{L}7)](\text{PF}_6) > [\text{Au}(\text{L}2)](\text{PF}_6) > [\text{Au}(\text{L}1)](\text{PF}_6) > [\text{Au}(\text{L}5)](\text{PF}_6) > [\text{Au}(\text{L}4)](\text{PF}_6)$. The data showed that the macrocyclic gold(III) complexes are all active against central nervous system cancer cell lines, but are predominantly inactive against colon and melanoma cell lines. The pseudomacrocycles are more active against colon, leukemia and renal cancer cell lines, but inactive against prostate and CNS cell lines.

Based on the data from the single-dose screen, six complexes: $[\text{Au}(\text{L}2)](\text{PF}_6)$, $[\text{Au}(\text{L}3)](\text{PF}_6)$, $[\text{Au}(\text{L}6)](\text{PF}_6)$, $[\text{Au}(\text{L}7)](\text{PF}_6)$, $[\text{Au}(\text{L}10)](\text{PF}_6)$ and $[\text{Au}(\text{L}11)](\text{PF}_6)$ were selected for five-dose screens. From the five-dose screens, the cell growth response parameters GI_{50} , IC_{50} and LC_{50} were calculated. The complex $[\text{Au}(\text{L}3)](\text{PF}_6)$ had an IC_{50} value of 16.0 μM which is the lowest mean IC_{50} value for the gold(III) macrocyclic complexes. The pseudomacrocyclic complex $[\text{Au}(\text{L}11)](\text{PF}_6)$ had the lowest mean IC_{50} value of 5.60 μM . These IC_{50} values are lower than the mean IC_{50} value of cisplatin which is 27 μM . The NCI selected the gold(III) complex $[\text{Au}(\text{L}3)](\text{PF}_6)$ to go through to the acute toxicity determination. The acute toxicity determination showed that the mice could tolerate high doses of $[\text{Au}(\text{L}3)](\text{PF}_6)$, up to 400 mg/kg/dose. This is important as it shows that the complex is not highly toxic to non-cancerous cells. The complex has been submitted for the hollow fibre assay. The hollow fibre assay showed that the cytotoxicity of the chelate was greatly reduced in a live animal environment.

Statistical analysis of the cell screening data, using hierarchical cluster analysis, has shown that the probable mode of action through which $[\text{Au}(\text{L}3)](\text{PF}_6)$ exerts its cytotoxicity is TOP1 and TOP2 inhibition. Based on these results, the mode of action was tested *in vitro* using gel electrophoresis experiments at the University of Central Florida. The TOP1 DNA relaxation assays and the DNA decantation assays (kinetoplast DNA) by TOP2 showed that the complexes were TOP1 and TOP2 inhibitors rather than poisons. This could be deduced by the presence of only supercoiled DNA and the absence of linear DNA. These assays were also run on the free ligand, $\text{H}_2\text{L}1$, and the nickel(II) analogue $[\text{Ni}(\text{L}1)]$. These two compounds showed no change to the DNA shift over the concentration range 0.5 – 50 μM indicating that they do not inhibit the TOP1 enzyme. This again highlights the importance of the gold(III) ion to the activity of the compounds.

In order to further verify the mode of action of the complexes, a new microtiter well-based assay that is capable of distinguishing between TOP1 poisons and inhibitors was used for the gold(III) complexes.¹⁰ The

gold(III) complexes gave similar results to those obtained for the catalytic inhibitor control, mitoxantrone. This experiment showed that the gold(III) complexes are catalytic inhibitors of TOP1.

The theoretical model predicted by the molecular mechanics simulations was verified using Surface Plasmon resonance. This technique was used to show that $[\text{Au}(\text{L3})](\text{PF}_6)$ preferentially binds at the TOP1 T10-A11 target and sterically obstructs substrate recognition by the enzyme, as predicted by the calculations. In the presence of only the DNA and complex, three clear stepwise responses can be seen where the complex binds at the three T-A sites in the DNA. In the presence of the DNA and TOP1 enzyme, an SPR response was obtained which corresponded to the binding of mTOP1 to the DNA. In the presence of the DNA, TOP1 enzyme and gold(III) complex, no SPR response was detected. This is consistent with uptake of $[\text{Au}(\text{L3})](\text{PF}_6)$ by the DNA and the inhibition of the enzyme binding to the DNA-complex substrate.

Thus the aims outlined in Chapter One of this work have been reached:

- A range of macrocyclic, pseudomacrocyclic and open-chain bis(pyrrolide-imine) Schiff base ligands have been synthesized and fully characterized.
- Twelve gold(III) complexes have been synthesized and fully characterized. The complexes were also studied by X-ray crystallography and their exact geometry and solid state interactions were investigated.
- The ligands and complexes were studied by the computational method density functional theory (DFT). The results of the simulations were compared and contrasted with the experimental data.
- The affinity of the complexes for ctDNA was determined using competitive-binding titrations with EB.
- Other characteristics of the complexes such as the octanol/water partition coefficients were determined.
- The gold(III) complexes were screened against sixty different human cancer cell lines by the National Cancer Institute (NCI, USA) to determine their cytotoxicity.
- The mode of action through which the gold(III) complexes exert their cytotoxicity was determined at the University of Central Florida and through molecular mechanics calculations.

This work on the macrocyclic and pseudomacrocyclic gold(III) complexes has been used to secure a patent for the use of this class of gold(III) chelates as chemotherapeutic agents.¹¹

8.2 Future Work

The primary goal of this research was to synthesize and fully characterize a range of gold(III) macrocyclic and pseudomacrocyclic complexes. The potential of these complexes as chemotherapeutic agents and their mechanism of action was also determined. These primary objectives have been achieved; however, during the course of this study several other factors which could improve the cytotoxicity of these complexes have been identified.

Several of the compounds that were synthesized and screened in this work have proven to be effective cytotoxic agents. From the data that has been attained, the complex $[\text{Au}(\text{L11})](\text{PF}_6)$ has the lowest mean IC_{50} value of 5.60 μM and the highest DNA binding affinity of $6.61 \times 10^6 \text{ M}^{-1}$ of all the gold(III) complexes. This is also interestingly the only gold(III) complex synthesized with a region for hydrogen bonding. It is believed

that a new series of macrocyclic complexes with a side chain present that allows for hydrogen bonding with DNA will show enhanced cytotoxicity. Figure 8.2(a) shows an example of the macrocyclic complexes that could be synthesized that would have a hydrogen bonding region as well as extended aromaticity when compared to the current macrocyclic complexes. This structural modification should increase the DNA intercalation ability of the complexes thereby producing more effective TOP1 and TOP2 inhibitors.

The pseudomacrocyclic gold(III) complexes have proven to be strong binders of DNA as well as potent chemotherapeutics, outcompeting most of the macrocyclic gold(III) complexes. As only three of these complexes were synthesized for this work, there is still a large number of complexes that could be synthesized and tested. The three pseudomacrocyclic complexes synthesized in this work contain only alkyl chains. Figure 8.2(b) shows examples of pseudomacrocyclic complexes that could be synthesized with increased aromaticity for enhanced DNA interaction. Hydrogen bonding regions can also be incorporated into these complexes.

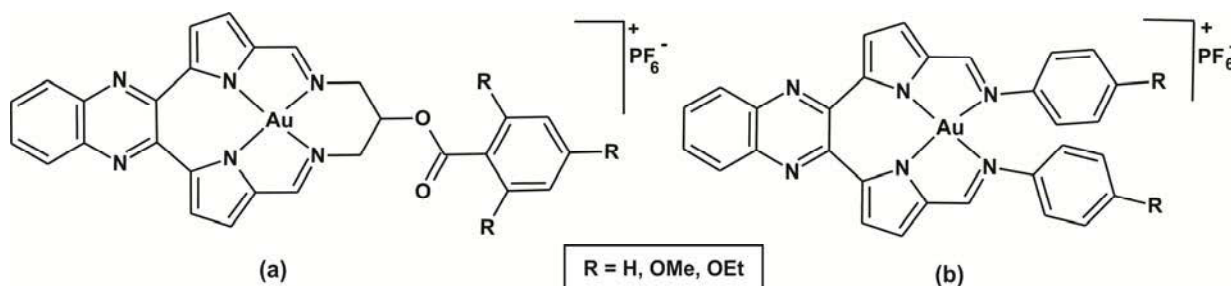


Figure 8.2: (a) Macrocyclic complexes with a region for hydrogen-bonding. (b) Pseudomacrocyclic complexes with increased aromaticity.

A major problem that hindered the spectroscopic studies done in this body of work was the poor solubility of the gold(III) complexes in aqueous buffer solution. A possible strategy for improving the solubility is to exchange the bulky, hydrophobic hexafluorophosphate(V) counter ion for smaller, more hydrophilic anions such as nitrate or chloride. The hexafluorophosphate(V) counter ion was chosen for this work as it is a biologically compatible ion and its large size can aid the crystallization process, but the ion could be exchanged to increase solubility of the chelates for the purposes of spectroscopy. Nitrate and chloride anions would be an ideal choice as they too are biologically compatible. Changing the counter ion would have an effect on some of the properties of the chelates such as the octanol/water partition coefficients.

Another possible strategy to increase solubility is to make use of β - and γ -cyclodextrins which could be used to encapsulate the gold(III) chelates. Cyclodextrins are made up of sugar molecules bound together in a ring. The inner opening consists of primary hydroxyl groups while the outer opening consists of secondary hydroxyl groups,¹² Figure 8.3(a). Due to this arrangement, the interior is less hydrophilic than the aqueous environment and thus able to host hydrophobic molecules in its cavity.¹² The exterior is hydrophilic enough to make the complex water soluble. The cavity diameter of γ -cyclodextrins is 7.5 – 8.3 Å (cavity volume 427 Å³).¹³ The width of the gold(III) complexes is approximately 5 Å across the quinoxaline tail and 7 Å across the di(azomethine) linkage. Therefore although the whole molecule may not fit in the cavity sections of the molecule could be encapsulated, improving solubility. Figure 8.3(b) shows an α -cyclodextrin encapsulating a fairly long molecule.

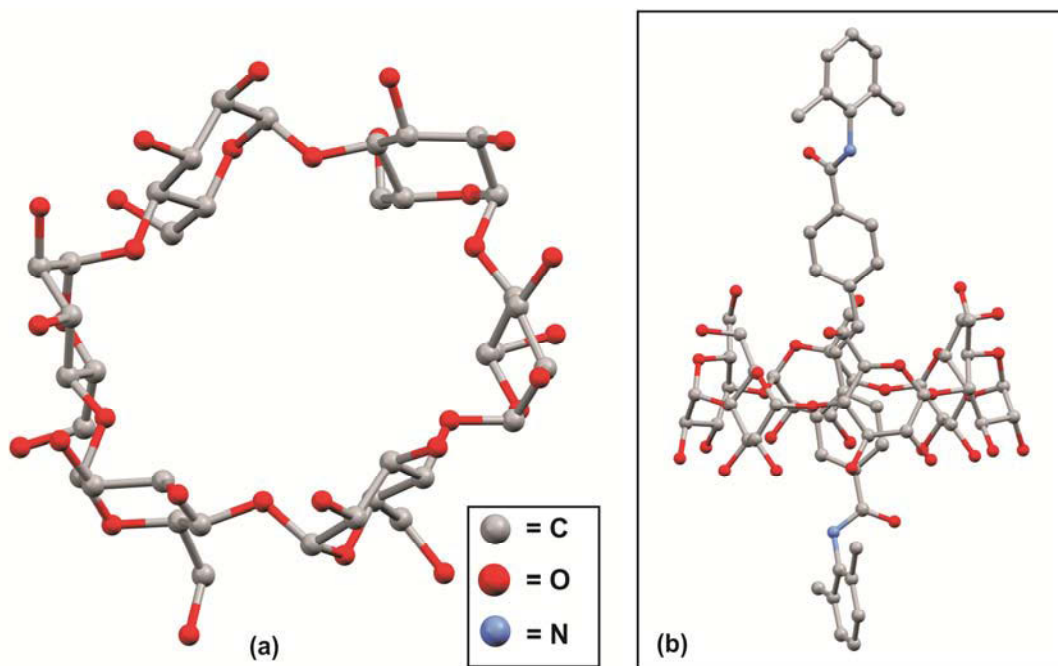


Figure 8.3: X-ray crystal structure of (a) α -cyclodextrin¹⁴ and (b) α -cyclodextrin (*N,N'*-bis(2,6-dimethylphenyl)-4,4'-stilbenedicarboxamide)-rotaxane.¹⁵ The hydrogen atoms and solvent molecules have been omitted for clarity.

Another type of encapsulating agent that could be used is the cucurbiturils which comprise a number of glycouril units and methylene bridges. A study was done to determine if the solubility of the anticancer drug, camptothecin, could be improved through encapsulation by the cucurbiturils.¹⁶ The results showed that with the use of the cucurbiturils, the solubility of camptothecin was increased 70 fold while still maintaining its cytotoxic activity.¹⁶ Although cucurbiturils are another option for encapsulation, the cyclodextrins are the molecules of choice because they are commercially available and inexpensive.

The gold(III) chelates synthesized in this work have been designed with the intention of being DNA intercalator drugs. There is, however, another interesting possibility for drug delivery in the cell: targeted drug delivery. This method exploits receptor sites in cells; an important receptor site that could be targeted is that for the vitamin, biotin. Biotin is an essential nutrient for all living organisms because of its role as cofactor of enzymes involved in carboxylation and decarboxylation reactions.¹⁷ In human cells, there are five biotin dependent carboxylases that catalyze key reactions in gluconeogenesis (glucose generating reactions), amino acid catabolism and fatty acid synthesis.¹⁷ Biotin is also responsible for gene expression as it plays a role in formation of mRNA, which is implicated in DNA transcription.¹⁷ An example of target drug delivery is shown in Figure 8.4 (a) and (b). It is proposed that the alcohol functional groups of the ligand H₂L11 could be used to attach biotin to the molecule through its carboxylic acid functional group, Figure 8.4(c). This could increase uptake of the cytotoxic gold(III) complex by binding to the biotin receptor. As some types of cancers over-express biotin receptors, this could be an effective method of delivering the complex to cancerous cells.

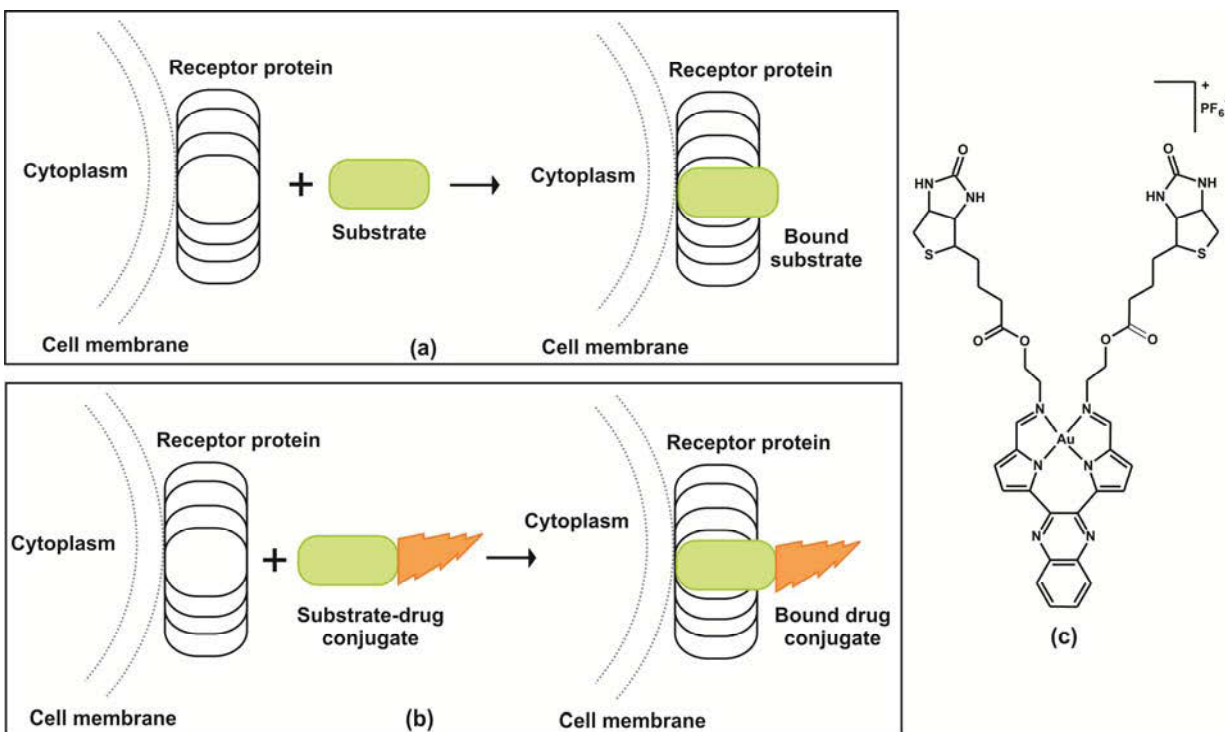


Figure 8.4: An example of targeted drug delivery; (a) normal receptor function and (b) drug bound substrate. The receptor that will be targeted is biotin. (c) $[\text{Au}(\text{L11})]^+$ tagged with biotin.

Another avenue that is currently being explored in our work group is that of radiolabelling the gold(III) complexes and monitoring their biodistribution *in vivo*. This is an exciting new field as the application of ^{198}Au and ^{199}Au in radiopharmaceuticals has remained largely unexplored.¹⁸ This is mostly attributed to the poor stability of gold(III) complexes. The search for agents that can be used for both the diagnosis and therapy of tumours is constantly expanding.¹⁸

^{198}Au with $t_{1/2} = 2.7$ days, $E_{\beta} = 0.97$ MeV and $E_{\gamma} = 411$ keV is the preferred gold isotope for these studies as the high energy γ photons are suitable for external detection by the single-photon imaging instrumentation used in nuclear medicine departments. The diagnostic and therapeutic effects can be achieved using extremely small amounts of the complex, as the effects observed are determined by the radioactivity of the compound and not by the mass of material used.¹⁹

To date in our work group, an acyclic ^{198}Au labelled gold(III) chelate of a bis(pyrrrolide-imine) Schiff base ligand with a three-carbon di(azomethine) linkage has been successfully synthesized with a high isotopic yield of 73% at the South African Nuclear Energy Corporation (NECSA).¹⁹ The biodistribution of the complex in male Sprague Dawley rats was determined by γ -radiation detection in dynamic studies and via counting harvested organs. The γ -ray emission studied showed that the complex was hydrophilic with 21% of the injected dose remaining in the blood pool 4.5 hours after injection with 10.8% still remaining after 24 hours.¹⁹ The organs with a high blood volume, such as the heart and spleen, also contained an elevated amount of the drug. The complex could seemingly be efficiently excreted via the kidneys with over 30% of the compound excreted within 24 hours.¹⁹ The results also showed possible decomposition products or

serum albumin adducts of the complex in the lungs which suggests that the serum stability of the compounds needs improvement.

It is believed that the pseudomacrocyclic complexes synthesized in this work would be ideal candidates for a radiolabelling study. The macrocyclic complexes would not be ideal for this application as it takes 24 hours for chelation to occur and the half life of the ^{198}Au is only 2.7 days. Also the macrocyclic complexes can only be synthesized in small yields. The pseudomacrocyclic complexes, on the other hand, can be synthesized in relatively high yields in a matter of minutes. The complex, $[\text{Au}(\text{L11})](\text{PF}_6)$ is the most suitable complex, because although it is hydrophobic ($\log P_{o/w} = 0.578$), it should still be soluble in a water:DMSO mixture to be injected into the rat. A serum albumin study should be performed before the radiolabelling study is done. It is, however, believed that these complexes will be more stable to decomposition than the open-chained gold(III) complexes previously tested. The macrocyclic ligand serves to stabilize the gold(III) complexes through the macrocyclic effect. This has been illustrated by glutathione reduction studies where the macrocyclic complexes were shown to be stable to reduction which is in contrast to the open-chain gold(III) complex used in the radiolabelling experiment which was completely reduced in 6 hours.

8.3 References

- (1) Che, C.-M., Sun, R. W.-Y., Yu, W.-Y., Ko, C.-B., Zhu, N., Sun, H. *Chem. Commun.* **2003**, 14, 1718.
- (2) Sun, R. W.-Y., Che, C.-M. *Coord. Chem. Rev* **2009**, 253, 1682.
- (3) Allen, F. H. *Acta Cryst.* **2002**, B58, 380.
- (4) Munro, O. Q., Camp, G. L. *Acta Cryst.* **2003**, C59, o672.
- (5) Munro, O. Q., Strydom, S. D., Grimmer, C. D. *Chem. Eur. J.* **2006**, 12, 7987.
- (6) van den Ancker, T. R., Cave, G. W. V., Raston, C. L. *Green Chem.* **2006**, 8, 50.
- (7) Bacchi, A., Carcelli, M., Gabba, L., Ianelli, S., Pelagatti, P., Pelizzi, G., Rogolino, D. *Inorg. Chim. Acta* **2003**, 342, 229.
- (8) Shriver, D. F., Atkins, P. W. *Inorganic Chemistry, 3rd Edition*; Oxford University Press, 2000.
- (9) Pavia, D. L., Lampman, G. M., Kriz, G. S., Vyvyan, J. R. *Introduction to Spectroscopy, 4th edition*; Brooks/Cole: USA, 2009.
- (10) Cyril, V. M., M. T. *Anal. Biochem.* **2012**, 421, 607.
- (11) Munro, O. Q., Akerman, K. J., Akerman, M. P. 2011; Vol. WO2011/158176 A2.
- (12) Lagona, J., Mukhopadhyay, P., Chakrabarti, S., Isaacs, L. *Angew. Chem. Int. Ed.* **2005**, 44, 4844.
- (13) del Valle, E. M. *Process Biochemistry* **2004**, 39, 1033.
- (14) Harata, K. *Bull. Chem. Soc. Jpn.* **1977**, 50, 1416.
- (15) Maniam, S., Cieslinski, M.M., Lincoln, S.F., Onagi, H., Steel, P.J., Willis, A.C., Easton C.J. *Org. Lett.* **2008**, 10, 1885.
- (16) Dong, N., Xue, S.-F., Zhu, Q.-J., Tao, Z., Zhao, Y., Yang, L.-X. *Supramolecular Chem.* **2008**, 20, 659.
- (17) Leon-Del-Rio, A. *J. Nutr. Biochem.* **2005**, 16, 432.
- (18) Berning, D. E., Katti, K. V., Volkert, W. A., Higginbotham, C. J., Ketring, A. R. *Nucl. Med. Biol.* **1998**, 25, 577.
- (19) Akerman, M. P., Munro, O. Q., Mongane, M. van Staden, J. A., Rae, W. I., Bester, C. J., Jansen, D., Zeevaarte, J.-R. *J. labelled compounds and pharmaceuticals* **2013**, submitted.